Fall 1-31-2014

Computational optimization methods for modeling the effect of muscle forces on bone strength adaptation

Catherine Siena Florio
New Jersey Institute of Technology

ABSTRACT

**COMPUTATIONAL OPTIMIZATION METHODS FOR MODELING THE
EFFECT OF MUSCLE FORCES ON BONE STRENGTH ADAPTATION**

by
Catherine Siena Florio

An improved understanding of the mechanical influences that alter the strength of a bone

can aid in the refinement of the wide array of currently available techniques to counteract

the losses of bone strength that occur due to age or disuse both on Earth and in Space. To

address this need, computational modeling methods to quantitatively analyze and

compare the effects of mechanical factors on the strength of a targeted bone within a

multibone, multimuscle system are developed and implemented in this work. Through a

more detailed representation of the system in which the bone acts and the creation of a

model that does not require experimentally based parameters, the developed techniques

eliminate many of the difficulties that have often hindered these musculoskeletal

phenomena from being studied with the tools and methods readily employed in the

investigation of their inert mechanical counterparts.

The computational techniques developed couple the determination of the muscle

forces acting within the system studied, the stresses they induce within the bones of the

system, and the ensuing adaptations of the shape of one of these bones, altering its

strength. This is accomplished through the use of gradient based optimization methods,

finite element methods, and gradientless optimization methods, respectively. The

developed gradientless optimization methods in this work progress the bone shape design

toward one with a more uniform state of stress through the relative effects of measures of

the local stress state, the global stress state, and the variation of the local stress state over

the region being optimized. Quantitative measures of the progression towards a uniformity of the stress state during the optimization process are defined so that relative changes can be directly compared between the various mechanical factors studied. Similarly, methods are developed to independently assess the ability of the conditions studied to induce bone shape alterations that improve the strength of the bone under a standard set of loading conditions.

The implementation of the model in a parametric study of methods to improve the resistance of the tibia bone to stress fractures demonstrates its ability to evaluate the effects of various loading conditions, with forces and stresses studied ranging three orders of magnitude. From this investigation, loading modes are identified that improve the bone's strength in the fracture prone region by up to 20%. The developed computational modeling techniques eliminate the difficulties inherent in the experimental investigation of mechanically based alterations to bone strength and provide a means for the improved understanding and, ultimately, better control of these adaptive phenomena.

COMPUTATIONAL OPTIMIZATION METHODS FOR MODELING THE EFFECT OF MUSCLE FORCES ON BONE STRENGTH ADAPTATION

by
Catherine Siena Florio

A Dissertation
Submitted to the Faculty of
New Jersey Institute of Technology
in Partial Fulfillment of the Requirements for the Degree of
Doctor of Philosophy in Mechanical Engineering

Department of Mechanical and Industrial Engineering

January 2014

.

BIOGRAPHICAL SKETCH

Author: Catherine Siena Florio

Degree: Doctor of Philosophy

Date: January 2014

Undergraduate and Graduate Education:

- Doctor of Philosophy in Mechanical Engineering,
  New Jersey Institute of Technology, Newark College of Engineering,
  Newark, NJ, 2014

- Master of Science in Mechanical Engineering,
  New Jersey Institute of Technology, Newark College of Engineering,
  Newark, NJ, 2001

- Bachelor of Science in Mechanical Engineering,
  Rutgers, The State University of New Jersey, College of Engineering,
  Piscataway, NJ, 1999

Major: Mechanical Engineering

Publications:

Florio, C.S. and K.A. Narh, 2013, "Effect of Modeling Method on Prediction of Cortical Bone Strength Adaptation Under Various Loading Conditions," Meccanica, 48(2), pp. 393-413.

Florio, C.S. and K.A. Narh, 2011, "Development of a Modeling Technique for the Investigation of Muscle Activity and its Effect on Bone Stresses in the Human Leg during an Isometric Exercise," Simulation, 87(4), pp. 313-333.

Acknowledgements in:
Gruen, T.A., Poggie, R.A., Lewallen, A., et al, 2005, "Radiographic Evaluation of a Monoblock Acetabular Component: A Multicenter Study with 2- to 5-Year Results," Journal of Arthroplasty, 20(3), pp. 369-378.

Page, S.J., Levine, P., Sisto, S., et al, 2002, "Stroke Patients' and Therapists' Opinions of Constraint-Induced Movement Therapy," Clinical Rehabilitation, 16, pp. 55-80.

Presentations:

Florio, C.S., 2012, "Use of Optimization to Determine Muscle Activity and Effect on Whole Bone Strength," Eighth Annual NJIT Graduate Student Association Research Day, Newark, NJ.

Florio, C.S., 2011, "Modeling Changes in Whole Bone Strength Due to Muscle-Generated Loads," Seventh Annual NJIT Graduate Student Association Research Day, Newark, NJ.

Florio, C.S., 2010, "Computational Modeling of Bone Strength Adaptation," Zonta District 3 Annual Conference, Atlantic City, NJ.

Florio, C.S., 2010, "Validation of a Model to Predict Load-Induced Geometric Changes in Bone," Sixth Annual NJIT Graduate Student Association Research Day, Newark, NJ.

Florio, C.S., 2009, "Effect of Resultant External Loading Direction on the Stresses in the Leg Bones," Fifth Annual NJIT Graduate Student Association Research Day, Newark, NJ.

Florio, C.S., 2009, "Computational Simulation of the Age-Related Growth of a Femur Bone," Dana Knox Student Research Showcase, Newark, NJ.

Florio, C.S, Poggie, R.A., Sidebotham, C. et al, 2004, "Stability Characteristics of a Cementless Monoblock Porous Tantalum Tibial Implant Without Ancillary Fixation," Fiftieth Annual Meeting of the Orthopedic Research Society, San Francisco, CA.

"Nothing great is ever achieved without much enduring."
- St. Catherine of Siena

ACKNOWLEDGMENT

TABLE OF CONTENTS

TABLE OF CONTENTS
(Continued)

LIST OF TABLES

LIST OF FIGURES

Figure **Page**

Figure | **Page**

Figure **Page**

Figure   **Page**

LIST OF SYMBOLS

English

Scalars

x, y, z	Cartesian coordinates
r ,Θ, z	Cylindrical coordinates
i, j, k, l, m, n, p, q	Indices
A, B, C	Constants (B.4)
A(e)	Area of exposed face of element e (4.19)
Avg	Average (4.22)
c	Subscript representing centroid (4.12)
C	Elastic constant matrix (stiffness matrix) (2.6)
const	A constant (2.18)
D	Characteristic distance (4.11)
d	Moment arm (Figure 3.1)
$d_i(l)$	Distance from node *l* to neighboring node *i* (4.11)
D_{ini}	Initial Diameter of Optimizing Surface (4.36)
ds	Incremental surface area (2.26)
dv	Incremental volume (2.18)
E	Elastic Modulus (Young's Modulus) (2.8)
E	Energy (2.22)
e	index representing element number (4.19)

G	Shear Modulus (Modulus of Rigidity) (2.9) and one of Lamé Constants (2.16)
K	Elastic compliance matrix (2.7)
k	index to indicate optimization iteration count (2.41) and throughout
l	index to indicate node or point on surface being optimized (2.41) or unknown muscle force magnitude (3.1) and throughout
L	Lagrange Equation (3.8)
L, G	Indices representing Local and Global reference systems
m	Mass (2.18)
M	Index representing total number of elements (4.19)
N	index usually representing a total count
PCSA	Physiological cross sectional area of a muscle (3.1)
Q	Energy input to a system (2.22)
Q14Spread	Average(Quartile 4) - Average(Quartile 1) (data sorted ascending in value, divided into four evenly membered groups) (4.38)
R	Characteristic dimension of shape being optimized (4.9)
r	Relaxation factor (4.13)
S	Arbitrary constant (4.9)
S	Shape Function (2.33)
$SED_k(l)$	Strain energy density at point l on optimizing surface at optimization iteration k (4.8)
$SED_k^{EleAWSurfAvg}$	Elemental area weighted surface average of the elemental Strain energy density (4.19)

$SED_k^{EleAWSurfStDev}$	Elemental Area Weighted standard deviation of the elemental strain energy density over optimizing surfaces (4.23)
$SED_k^{SurfAvg}$	Average of nodal strain energy density over optimizing surface at optimization iteration k (4.8)
StDev	Standard deviation (4.22)
t	Time (2.17)
u	Displacement (2.1)
u,v,w	Displacement in Cartesian directions (2.33)
$U_k(l)$	Nodal growth per iteration in direction normal to optimizing surface at point l at optimization iteration k (4.3)
V	Element volume (2.38)
W	Work done by a system (2.22)
W	Work done on a system (2.28)
$w_k(i)$	Weighting factor for ith neighboring node (or element) at optimization iteration k (4.12, 4.13)
x	Location (2.1)
X	Normal distribution of a set of data
$x_k(l)$	coordinate of a node (l) in the growth direction at optimization iteration k (4.3)
Z	Standard distribution (4.22)
$Z(\mathbf{F})$	Optimization Function (goal) in muscle force magnitude model (3.1)
$Z(\mathbf{x}, \mathbf{u}(\mathbf{x}))$	Optimization Function (goal) in shape optimization model (4.1)

Vectors/Matrices

$\mathbf{A^T}$	Coefficients of the unknown muscle force magnitudes in constraint equations of gradientless optimization problem (3.3)
$\mathbf{b}$	Body Force (2.26)
$\mathbf{b}$	Constants in the set of gradient optimization constraint equations (3.3)
$\mathbf{b}$	an unknown vector of length n (A.27)
$\mathbf{B}$	Matrix of derivatives of the Shape Functions of the nodes of an element (2.34)
$\mathbf{B}_k$	Inverse of the Hessian matrix of the optimization objective function $Z(\mathbf{F})$ evaluated at a point k (3.9)
$\mathbf{C}$	Elastic constant matrix (stiffness matrix) (2.6)
$\overline{e}^G$	Unit vector in local coordinate system(4.25)
$\overline{e}^L$	Unit vector in local coordinate system(4.25)
$\vec{\mathbf{F}}$	Driving force for set of nodes in spring smoothing method (4.10)
$\mathbf{F}$	Vector of External Forces applied to an element (2.36)
$\mathbf{F}$	Unknown Muscle Force Magnitudes (3.1)
$\mathbf{G(F)}$	Set of constraint equations in optimization problem (3.3)
$\vec{\mathbf{G}}$	Position vector of a point relative to the global Cartesian coordinate system (B.1)
$\mathbf{I}$	Identity matrix
$\mathbf{K}$	Elastic compliance matrix (2.7)
$\mathbf{K}^{equ}$	Equivalent elemental stiffness (2.39)

$\mathbf{k}_{ij}$	Spring constant in internal node spring smoothing (4.10)
$\mathbf{L}$	Lower triangular matrix
$\vec{\mathbf{L}}$	Position vector of a point relative to the local Cartesian coordinate system (B.1)
$\mathbf{M}$	Moment vector (3.5)
$\mathbf{N}_l$	Unit vector normal to the optimizing surface at node l (4.37)
$\mathbf{N}^{\mathbf{T}}$	Submatrix of $\mathbf{A}^{\mathbf{T}}$ containing constraints of active coefficients (3.12 and A.13)
$\mathbf{P}$	Projection operator (3.11)
$\mathbf{p}$	Nodal coordinates of design variables (4.2)
$\mathbf{P}_o{}^G$	Origin of Global Coordinate system defined in global system (B.8)
$\mathbf{P}_o{}^L$	Origin of Global Coordinate system defined in local system (B.8)
$\mathbf{P}_\chi$	A projection operator to project onto a subspace χ, (A.2)
$\mathbf{P}_\perp$	A projection operator to project onto the orthogonal complement of χ, (A.2)
$\mathbf{Q}$	Square orthonormal unitary matrix
$\mathbf{Q}_\perp$	An orthonormal basis for $\chi_\perp$ (A.9)
$\mathbf{r}$	Moment arm of a force (2.27)
$\mathbf{R}$	Upper triangular matrix
$\mathbf{R}$	Rotational transformation matrix (B.1)
$\mathbf{S}$	Search direction in gradient projection optimization (3.10)

S	Translational transformation matrix (B.2)
t	Surface traction (2.26)
U	Displacement (2.29)
x	Location (2.17)
x	Design variables (nodal positions) in shape optimization problem (4.1)
X	Position of design point (node) on surface being optimized (1.2)
X	an n x p matrix (A.28)
$\mathbf{X_k}^c(i)$	Position of centroid of ith neighboring element to node at point l at optimization iteration k (4.12)
$\tilde{\mathrm{x}}$	Mapping (4.2)
$\Delta\mathbf{x}$	Vector of change in position of nodes in spring smoothing (4.10)
z	A vector (A.1)
$\mathbf{z}_\chi$	projection of **z** onto the subspace χ, (A.1)
$\mathbf{z}_\perp$	projection of **z** onto the orthogonal complement of χ, (A.3)

Greek

Λ	Internal strain energy (2.23)
α	Proportionality constant in growth function (2.41)
α	Step size in gradient projection optimization method (3.10)
β	Scaling factor (4.9)

λ	One of the Lamé constants (2.16)
λ_i	Lagrange multiplier of equality constraint equation in gradient optimization (3.8)
ν	Poisson's ratio (Equation 2.10)
Π	Potential energy (2.28)
ρ	Density (2.17)
$\sigma_k(l)$	Value of measure of actual mechanical state at a node in shape optimization (4.3)
σ_{ref}	Value of measure of desired mechanical state at a node in shape optimization (4.3)
Ω	A region (2.18)
ε_{ij}	Strain tensor component (2.3)
σ_{ij}	Stress tensor component (2.6)
χ	A Subspace of Real Space (A.1)
$\chi_\perp$	The orthogonal complement of χ (A.3)

Vectors/Matrices

$\boldsymbol{\gamma}$	Shear strain (2.2)
$\boldsymbol{\varepsilon}$	Normal strain (2.1)
$\boldsymbol{\lambda}$	set of Lagrange multipliers for the optimization problem using only the active constraints (3.18)
$\boldsymbol{\sigma}$	Normal stress (2.6)
$\boldsymbol{\tau}$	Shear Stress (2.9)

Operators

$\lVert \bullet \rVert_2^2$	Euclidian norm

CHAPTER 1

INTRODUCTION

1.1   Objective

An improved understanding of the mechanical influences that alter the strength of a bone can aid in the refinement of the wide array of currently available techniques to counteract the losses of bone strength that occur due to age or disuse. To address this need, the work presented focuses on the development and implementation of computational modeling methods to investigate the effects of mechanical factors on bone strength.   These modeling methods consist of:

1. The ability to determine the forces acting on a bone, including those produced by individual muscles,

2. The ability to determine the distributions and amounts of local material accretion or resorption that occur due to biological functional adaptation phenomena in the bone structure and that result in changes to the bone's overall shape, and

3. The ability to correlate the shape changes to relative measures of the bone's capacity to resist the loading conditions it typically encounters so that comparisons among various strength changes can be made.

The first part of this work consists of the development of these modeling methods. Their application, through parametric studies of a multimuscle, multibone, single leg system in the second part of this work, demonstrates the capability of these techniques to quantitatively compare the effects of specific mechanical factors on the strength of a fracture prone region of a bone that is part of the musculoskeletal system investigated.

Numerical mathematical optimization methods coupled with finite element structural analysis methods are used in the modeling techniques developed in this work.

Using optimization methods, the forces acting on the bones and the resulting shape changes are determined. Through finite element methods, the stress and strain fields that drive these shape changes are found. The results of the finite element structural analysis are also used to calculate measures of the relative change in the mechanical behavior of the bone due to the alteration of its shape. These measures quantify the ability of each studied set of loading parameters to improve the bone's effectiveness at resisting typically encountered forces and, hence, to improve its strength.

This investigation furthers the understanding of the relationship between mechanical factors and bone strength adaptation and expands and enhances the currently available approaches to its study. By developing these computational modeling methods, means for quantitative, objective comparisons of bone loss mitigation techniques are introduced. Through their use, insight is gained into the effects of the forces produced by the musculoskeletal system on the local changes to the shape and strength of its bones. While applied to one representative system in this investigation, the methods created can be utilized to study any musculoskeletal system desired. The knowledge gained through this work and the subsequent employment of the developed modeling techniques can be useful in the creation of exercise regimens that successfully improve bone strength, particularly in regions that might be especially susceptible to fracture.

1.2   Motivation For Study

The investigation of the strength adaptations of bone and the application of the resulting insight learned about these phenomena to the prevention of the detrimental effects of decreased bone strength has been the focus of much research. A review of the foundation

of this field, with a focus on the areas which currently demonstrate an incomplete understanding and, thus, served as an impetus for the present work, will be discussed.

1.2.1 Strength Adaptation of Bone

"Nature is ever at work building and pulling down, creating and destroying, keeping everything whirling and flowing, allowing no rest but in rhythmical motion, chasing everything in endless song out of one beautiful form into another." - John Muir, Our National Parks, 1901

1.2.1.1 Functional Adaptations of Living Systems. A living organism, like any mechanical system, is comprised of numerous subsystems that each performs a specific, individual, often localized task. Also, as in mechanical systems, these subsystems interact with each other as well to create the overall function of the entire system within the global environment. When the environment of an inert mechanical system changes, either the values of the operating parameters or the design of the system must be altered. In mechanical systems, this must be done either manually by an engineer or operator or automatically through a programmed feedback control system to maintain a relatively constant prescribed level of system performance, which is often related to the system's efficiency. In contrast to the mechanical systems that require external influences to modify system function, biological systems have internal control mechanisms, driven by biological phenomena, to automatically react and adapt to environmental changes. French physiologist Bernard noted in 1857, "All the vital mechanisms, however varied they may be, have only one objective, that of preserving constant the condition of the entire organism." [1]. The resulting changes due to these biological phenomena are called "functional adaptations".

The concept of the "functional adaptation" of individual subsystems to local or global environmental changes is related to Lemarck's early theory of evolution developed in 1809 called "Acquired Inheritance".   This theory stated the widely observed phenomenon of "use and disuse", that "parts of the body used extensively to cope with the environment become bigger and stronger while those that are not used deteriorate" [2], could be inherited and lead to evolution of a species. While this inheritance theory was later disproved and replaced with Darwin's Theory of Natural Selection, the concept inspired further investigation into the processes of "functional adaptation" in individual organisms. In the late 1880's a biologist studying the form and function of bones on the cellular level, Wilhelm Roux, explained that the "functional adaptation" of bones occurs through a "quantitative self-regulating mechanism" controlled by a "functional stimulus" [3].   This inspired more investigation into the processes that drive "functional adaptations".

Use/disuse functional adaptation phenomena have been widely observed in many systems in both animals and plants. One of the most common examples is the increase in muscle size due to weight lifting exercises. For example, the muscles of the arm will grow larger in order to enable the generation of the larger force needed to overcome this increased resistance exerted by their external environment. Similar processes are seen in plants.   Because plants are fixed in place, their responses to environmental changes are often related to the patterns of their growth that create the overall structure of the plant [2] and, therefore, are much more noticeable than many of the adaptations in animals. Thicker regions are observed on the upwind side of tree trunks to resist bending stresses induced by wind [4, 5]. Similar phenomena are observed in the curved nature of tree

branches in response to locally high bending stresses created by the weight of the limb itself [4, 5]. A series of experimental studies based on these observations were performed in the 1970's where weights were hung on growing trees while variations in trunk diameter and material properties at different cross sections along the length of the tree trunks were measured and tracked with time. Correlations made between these measurements and calculated stress field variations showed thicker diameters and denser material ("compression wood") in regions of locally high stress [6, 7].

In addition to changes in the external or global environment, functional adaptations can also occur due to changes within the local environment. Often these happen when some system components are damaged or change their functional efficiency. For example, when one lung is removed, the other lung will often grow to fill the entire chest cavity in order to maintain the total volume of air exchange of the two normal lungs [8, 9]. Other times, changes in one subsystem trigger alterations in a related one. For example, as a muscle grows larger due to increases in external environmental loads, such as during weight lifting, systems that provide nutrients to the muscle must react to this change, just as more coal, air, and water are needed to accommodate the increased power needs when a larger sized turbine is added to a coal power plant. In the biological system, blood vessels provide the nutrients to the muscles. More branches in the vascular system are formed to bring "fuel" to the increased volume of the larger muscle. This increased branching leads to a need for an overall greater supply of blood to the muscle, causing an increased blood flow volume in the vessels leading to the muscle, thereby increasing the pressure in these vessels. To accommodate the increased flow volume, as in the lung example above, the inner diameters of the blood vessels

increase. To counter the increased flow pressure inside the vessels, as in the tree trunk subjected to bending loads, the outer diameters of the blood vessels also increase. In this way, local changes to the circulatory system allow the overall organism to maintain overall efficient functional performance despite changes to its environmental requirements [10-12].

1.2.1.2 Function of Bone and Types of Bone Tissue. Just like the respiratory, circulatory, and muscular systems of animals and the structure of plants, adaptation of the skeletal system occurs based on environmental changes. The changes in bones are related to their two major functions: as a means of structural support and as a reservoir for mineral storage. In order to appreciate the adaptations that occur in bone, an understanding of the basic structure and function of bone is required.

The first role of bone is that of structural support. This function is influenced mainly by the size and the shape of the bone. As in the tree example discussed above, the size and shape of the bone responds to environmental changes by adding volume (material accretion) or removing volume (material resorption) at the bone's surfaces. The hard, dense material that comprises the bone's surface and creates its shape is called cortical bone tissue (Figure 1.1). Cortical bone tissue is a structure of collagen strengthened by calcium phosphate crystals [13]. With its high mineral content, cortical bone has a very low porosity (5-10%) [13-15]. Because of the low porosity, cortical bone acts mechanically like a near-solid material, such as a ceramic [14]. Collagen fiber orientation, degree of mineralization, and porosity variations affect the mechanical properties, and properties can vary with direction, making the material typically transversely isotropic [14]. The rigid, solid behavior of the cortical bone tissue provides

protection to internal systems, for example in bones such as the ribcage and skull, and creates a sort of beam system through which movement is created, for example, in the bones that comprise the extremities like the arms, legs, and fingers. Because a bone made completely of this solid material would be very heavy, and, therefore, require significant energy both to initiate and stop motion, the cortical bone tissue that creates a bone's shape and the majority of its strength is restricted to a relatively thin outer shell [13] (Figure 1.1). The interior of the bone is often hollow or filled with a much less dense, more porous, and, therefore, mechanically different material called cancellous bone tissue (Figure 1.1).
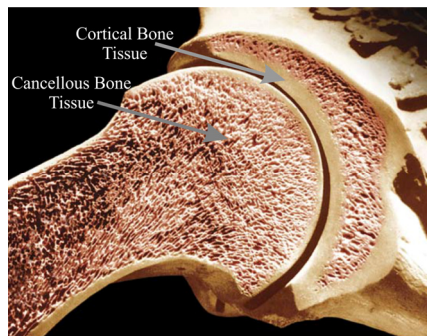
Figure 1.1 Basic structure and location of the two types of bone tissue.

Source: "cancellous bone." [Photograph]. In Encyclopedia Britannica. Retrieved from http://www.britannica.com/EBchecked/media/101316/Longitudinal. Accessed 10/14/13. With permission.

The second role of bone is that of a mineral reserve. This function is mainly the responsibility of this less dense cancellous bone tissue. Cancellous bone tissue is comprised of the same material as cortical bone. However, it is highly porous (50-95%) [15]. In regions that contain both types of bone tissue, the porosity of the bone varies continuously from cortical to cancellous materials (Figure 1.1) so there are no specific geometric, mechanical, and densometric boundary distinctions between two types of bone tissues [14]. Nonetheless, the differences do affect the behavior of the materials.

Mechanically, cancellous bone tissue behaves like an isotropic porous rigid foam-like material [13]. The highly porous structure of cancellous bone tissue is often filled with bone marrow, blood vessels and other structures that allow for direct and easy ion exchange with the mineral crystals that form the cancellous bone tissue structure. Therefore, the mineral content of the cancellous bone tissue is constantly altered, allowing it to rapidly address the calcium, phosphorous, and other mineral needs of the nervous, circulatory, and muscular systems [16]. Alterations in the mineral content affect the structure, mass, density, and, therefore, overall material strength of the cancellous bone tissue.

While the two functions of the bone appear to be separated by the two types of bone material tissues, in fact, both cortical and cancellous bone perform each of these functions, although on different scales. Because of its very high mineral content, cortical bone tissue does provide for mineral needs of the body's systems, especially in response to long term changes. Because of the very large plastic deformation range of cancellous bone tissue and the soft materials that often fill its pores, it has good energy absorbing abilities. Energy from the potentially large forces that can be exerted on bones is attenuated by this porous cancellous material, and its struts act as a truss-like structure to direct stresses away from the more brittle cortical tissue on the bone's surface [13]. Therefore, alterations to both the structure and mineral content of both types of bone tissue have an effect on the overall structural and mineral storage functions of a bone.

1.2.1.3 Functional Adaptation of Bone. The control mechanisms that create the functional adaptations of bone occur through two independent processes to alter the overall strength of the bone, often referred to as "whole bone strength" to differentiate it

from the strength of the bone tissue material itself. In this work, however, the whole bone strength is referred to simply as bone strength. As with all other functional adaptations, a bone's strength modification creates a structure suitable for it to operate appropriately in its immediate environment. As in mechanical design, an object's strength can be adjusted through material choice (thereby adjusting its intrinsic properties) or its shape (hence modifying its extrinsic properties). The example of the functional adaptation of the tree showed that both the density of the trunk and the size of its diameter can be altered to withstand increases in environmental load. The same is true for bone. Changes to bone size or shape can occur by material accretion or resorption on both the endosteal (inner) or periosteal (outer) surface of cortical bone, locally strengthening or weakening the bone structure. Changes to mineral can content occur both in the cortical and the cancellous bone tissue, altering the total mass and, therefore, density, thereby affecting the intrinsic material properties. Modifications to the connections within the network of struts creating the porous structure of the cancellous bone tissue also occur, altering the "stress flow" in the material, thereby affecting its response to applied loading in an additional manner. Thus, both the size/shape of the bone and its material properties can be adjusted to alter the bone's ability to resist applied forces so that a steady level of performance may be maintained while operating efficiently within the whole body system. Figure 1.2 depicts the material regions of a typical long bone and their mechanisms for adaptation.
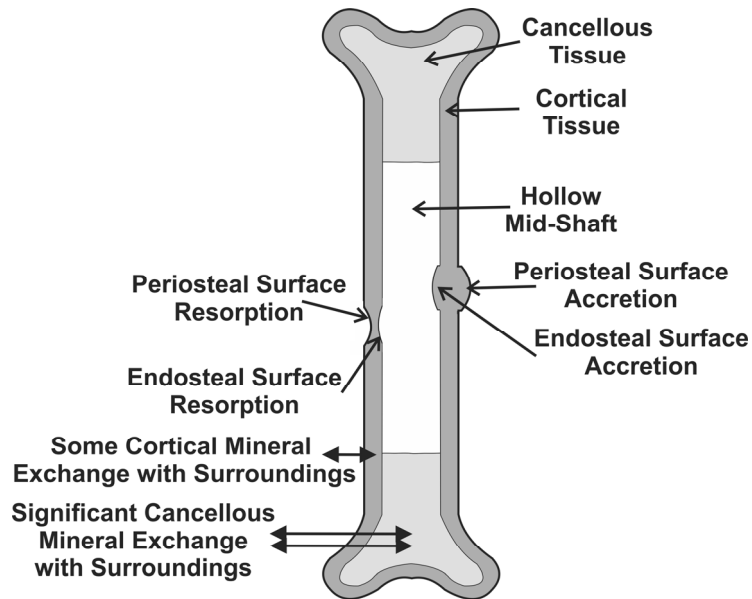
Figure 1.2 Typical long bone structure and strength adaptation mechanisms.

Ties Between Bone Biology and Mechanical Design

Observations of these adaptation phenomena and the relationships between bone's "form and function" have been recorded for centuries. In his seventeenth century studies of human anatomy, Galileo, famous for his interest in mechanical devices, discussed the "mechanical implications of the shapes of bones" [14]. These observations helped give rise to more formal scientific investigations into mechanical design in nature. By the eighteenth century, observations of functional adaptations of individual bones during the lifetime of a living being were documented and concepts about the processes involved in these changes began to be developed. In studying cadavers in 1776, pathologist Alexander Monro described the processes of the adaptive changes of the shape and structure of bone as the "perpetual waste and renewal of the particles which compose the solid fibers of the bone" [17]. Additionally, he noted that there are changes in these processes with time that result in age-related differences in the overall structure of bones. For example, he described the long bones, such as those of the arms and legs, of older

people to be "thinner and firmer in their sides" and to have "larger cavities" than their younger counterparts [17].

In the nineteenth century, as more formal mechanical and material testing methods began to be developed and improved and engineering theory and analysis techniques became more prevalent, more thorough investigations of the causes driving the observed changes to bone's geometric and material properties became possible. A number of human anatomy books, including those by Bougery and by Bell in the 1830's discussed the concept that bone may be optimized for maximum strength with minimum mass [18]. In 1858, a textbook by Humphrey discussed the idea of "absorption and deposition" of bone as part of a process to control the "shape and lightness" of the bone both in its interior volume and exterior surfaces [18]. By 1876, the interdependence of the adaptations to both the bone's material properties and structure and its function was beginning to form as Rauber suggested that a bone's strength depends on "the material, the microscopic structure" as well as "the shape of the whole bone" [18]. While to engineers, this does not seem like a radical concept since it is the basis for the design and analysis of solid objects, the application of mechanical design principles to biological tissues and structures was new to biologists, whose research had traditionally viewed biological materials as unique and who had focused on chemical, cellular, or other innate drivers to their existence and behavior.

Linking engineering theory and analysis to the study of the relationships between form, function and adaptation of bone widened extensively near the end of the nineteenth century. In 1866, a structural engineer regarded for his work on the structural analysis technique of graphical statics, Culmann, noted how the pattern of struts in the cancellous

bone tissue region of a femur, documented in drawings by anatomist von Meyer, was similar to the set of stress trajectories he had recently calculated in a curved bar with a similar loading pattern to that which was said to be imposed on the femur bone [16]. Upon this comparison, von Meyer suggested that cancellous bone "arranged itself along principal stress trajectories" [16, 18]. Though bone biologist contemporaries of Culmann were not well-versed in structural analysis theories themselves, this concept grew amongst their ranks, and, in 1869, a paper summarizing these ideas was published by a surgeon named Wolff. In this publication, Wolff declared that there was a "perfect mathematical correspondence" between the structure of cancellous bone and the bone's stress trajectories and that this mathematical correspondence is "necessary in the structure of bones" [16, 18]. Extending this correspondence to the functional adaptation of bone that he had been studying at the time, biologist Roux defined "pressure or tension" as the stimulus that invokes the observed changes in bone strength [3]. These publications escalated the collective excitement of the researchers studying bone biology about a mathematical "proof" of their centuries worth of observations. The misunderstanding of engineering stress analysis by Wolff and his colleagues relating to differences between the basic material properties of Culmann's beam and cancellous bone tissue and to the nonuniqueness of stress trajectories has since lead engineers to doubt the existence of a "perfect mathematical correspondence" [3, 14, 16]. However, because of its tidiness, this theory sparked an era of study into the relationships between the mechanical properties of bone, its behavior under loading, and the processes behind functional adaptation, with a focus on cancellous bone tissue.

Driven by the quest to find the "mathematical correspondence" described by Wolff and the improved experimental capabilities [18], much of the bone research in the early to mid-twentieth century focused on the material properties of bone. From this research, a better sense of the properties of bone and their variations based on "species, age, sex, diet, state of health...and microscopic structure" [19] lead to theoretical and experimental work in the mid-twentieth century to explain the biological mechanisms behind the functional adaptation of bone. In the late twentieth century and into the twenty-first century, with the increase in computer resource capabilities and numerical analysis methods, work has focused on the mathematical modeling of this phenomenon in an attempt to better understand and predict the mechanical influences on bone strength.

Effects of Bone's Functional Adaptations on its Overall Strength

Influenced by the focus on links between cancellous bone structure and calculated stress trajectories and by the study of the intrinsic material properties of bone tissue, much of the work on the functional adaptations of bone has moved away from the very early observations of size and shape changes and towards the internal alterations in cancellous bone density and composition. Because of the bone's function as a mineral reserve, rapid and significant modifications to mineral composition can occur, allowing for its relatively easy study and experimental alteration. Developments in X-ray and other scanning technologies have readily allowed for the experimental measurement and clinical monitoring of these density changes without the invasive or postmortem methods often necessary to study bone's geometric changes. However, because cortical bone tissue is approximately twenty times stronger and forty times stiffer than cancellous bone tissue [16, 17], these relatively rapid modifications in the cancellous bone tissue can have little

effect on the mechanical performance of the bone [17]. While cortical bone tissue has significantly more calcium content than cancellous bone tissue, its state is less transient, maintaining relatively stable material properties despite fluctuations of the bone's overall mineral content [16, 17]. Consequently, the adaptations of bone's intrinsic properties, while important in its ability to supply minerals for use in the processes of other systems, might have less importance on the bone's ability to sufficiently withstand applied forces.

Studies of the material properties of both cortical and cancellous bone tissue have shown relatively little variation with age, species and even many diseases [13, 20]. Greater strength differences of bone structures have been related to bone shape and size, for instance comparing a rib to a femur to a finger bone. Additionally, strength differences for the same bone of animals, such as the femur bone, have been found to vary almost linearly with size [13]. This follows mechanical stress and design theory that changes in geometry are often more effective at modifying an object's behavior than are changes in the material properties.

While geometric changes in bone typically occur at a slower rate than mineral/density changes, bone growth can occur rapidly to significantly alter bone strength when necessary. For example, temporary structures, called fracture calluses, form in weakened areas of bone, such as surrounding a fracture, to quickly reduce stresses at the fracture site while improving overall bone strength during healing [13, 16, 17, 21]. Figure 1.3 shows an example of a fracture callus that formed near a hip fracture, which has been additionally stabilized by an implanted device. A similar type of structure is a bone spur, which often grows near an arthritic joint to reduce joint stresses by increasing the joint contact area [17]. In addition to these "support patches", slower

changes to overall bone shape can also alter bone strength. Following Monro's eighteenth century observations of the increased inner diameter of older bones, radial expansion of both the inner and outer surfaces of long bones has been observed both with age, disease or paralysis [17, 22]. It is thought that these changes in bone geometry compensate for concurrently observed decreases in the material properties of the bone tissues in these conditions. Additionally, some studies have shown that bone size, not bone density, better predicts an increased risk of stress fractures [23-26]. Based on these observations, a return to the early focus on overall bone geometry in driving and controlling bone strength has been suggested [27, 28].
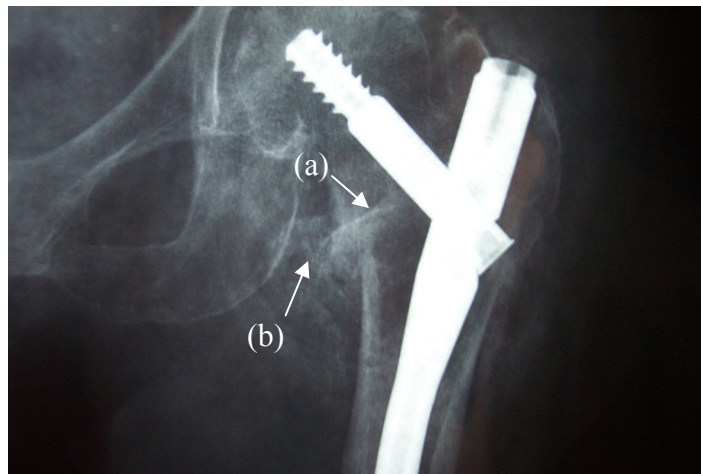
Figure 1.3 Bone callus formed near a fracture of the femoral neck in the hip. (a) fracture (b) callus formation.

Because it is changes in the bone's mechanical environment and bone's role in structural support that often results in adjustments to the way the bone behaves under applied loading, it has been theorized that mechanical factors outweigh any genetic or chemical factors driving modifications to the bone's strength [20, 29]. Accordingly, it is possible for the analysis of the functional adaptations of bone to follow the methods used in the engineering analysis and design of inert mechanical components.

1.2.2 Loss of Bone Strength

The functional adaptations of bone strength create a structure with suitable strength to operate appropriately under the immediate loading conditions that it typically encounters. However, sometimes these adaptations create a bone structure too weak to withstand everyday loads, resulting in an increased risk of fracture. These negative effects of functional adaptation arise for a variety of reasons under various conditions. Because of the potentially detrimental effects, significant research into the causes of this weakening has been carried out.

1.2.2.1 Age and Disease Related Losses. The most common reasons for decreased bone strength are related to age. Age related changes in bone strength have been ascribed to the two main phenomena resulting from changes in bone material quality and the intensity of loading on bone structures. Bone typically has processes to repair damaged areas as a means to prevent the propagation of damage that could eventually lead to fractures and, ultimately, failure of the bone structure. These normal processes remove small sections of bone and replace them with new material over time. On average 5% of cortical bone and 25% of cancellous bone is replaced by these processes per year [14]. During these repair activities, cavities are created where old or damaged bone is removed. The complete replacement of the bone to fill these cavities can take up to six months [17]. With age, the time to complete this repair process increases, leaving more cavities over a longer period of time, and leading to a more porous material at any given time [17]. Additionally, the slower repair rates with age have been found to lead to longer periods of mineralization of the bone structure before removal and replacement. This causes an overall stiffer, though more porous material, increasing the bone material's

brittleness and susceptibility to fracture [30]. Mechanical measurements of bone strength have found a 4-7% decrease in ultimate strain and a 30% reduction in ultimate tensile strength of cortical bone from age 30 to age 80 [17]. Therefore, with age, the bone material becomes, stiffer, more brittle and more likely to fracture under smaller stresses. The increased stiffness with age was what Monro qualitatively noted in his eighteenth century description of the "firmer" quality of older bones. Hence, age can deplete the quality of the bone material itself. Interestingly, similar changes have been observed even in younger people due to diseases that change these bone repair phenomena or the metabolic rates of mineral usage [22]. Figure 1.4 shows the change in bone density near a hip joint with age.

36 Year Old:
Bone Mineral Content
Per Area: 0.8 g/cm^2
(a)

73 Year Old:
Bone Mineral Content
Per Area: 0.4 g/cm^2
(b)
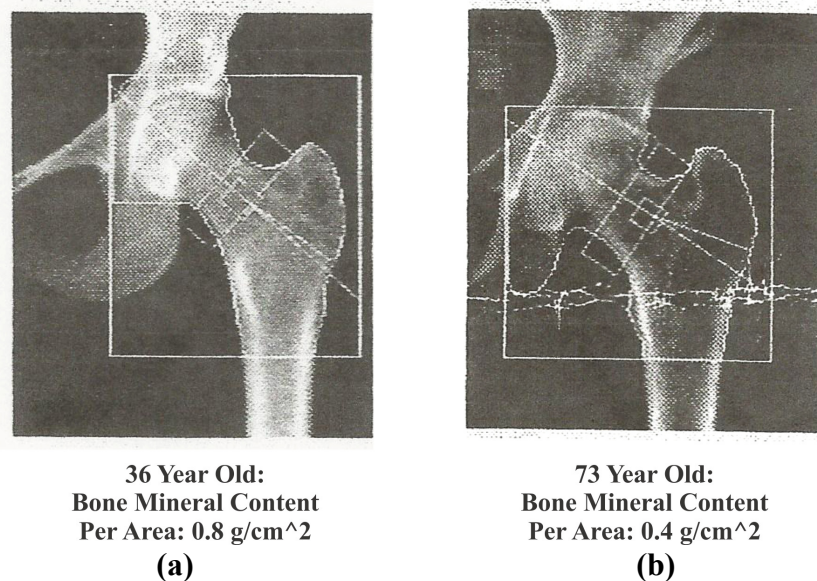
Figure 1.4 Comparison of bone density distribution in the proximal femur (near the hip joint) of a (a) 36-year-old and an (b) 73-year-old bone.

The second phenomenon that can decrease bone strength with age is related to the loads applied to whole bone structure. Muscles have been shown to create larger forces on bones than any associated with gravity, body weight, or impact [13, 14, 20, 31-33]. Muscles are attached to bones near the joints, allowing a large angular rotation to be

generated by small muscle contractions, allowing for efficient motion of the body system. This configuration, however, is opposite to that which would benefit efficient resistance to external forces. It can be thought of in terms of the design of a lever, where the joint is the fulcrum, the weight applied to the end of the bone is the load to be moved, and the muscle applies the necessary force to move this weight. Thus, the closer the force to oppose the weight is to the fulcrum, as is the case with the attachment location of the muscles, the larger its required magnitude to move the weight at the end of the bone. More simply, as noted by seventeenth century mathematician and physiologist Giovanni Borelli, strong muscle forces are required to carry even light weights [14]. These large muscle force magnitudes often create large stresses on the bones to which they are attached and can, therefore, stimulate local functional adaptations in bones. In fact, a strong correlation between muscle strength and bone strength has been observed. As a result, decreases in muscle strength can lead to decreases in bone strength.

A reduction in muscle strength has been noted with age due to a combination of decreased activity and physiological changes. In fact, as much as a 50% reduction in muscle strength can occur by age 75 [32]. This age related decrease in muscle strength alters the mechanical environment of the bones to which the muscles are attached and can directly lead to subsequent age related decreases in bone strength. Similar changes have been observed with other causes of decreased muscle strength such as paralysis, long term immobilization, or significant alterations in exercise activity [34].

1.2.2.2 Losses in Microgravity. In addition to the local changes that result from muscle forces, bone strength can also be altered due to changes in global environmental conditions, for example changes in gravity. Because of the reduced magnitudes of body

forces in microgravity, functional adaptations are initiated upon arrival in the new "weightless" environment to alter the performance of all physiological systems so that the whole body system can operate efficiently within the new global environment. In these cases, the adaptive responses create a weaker bone that may be sufficient for this new environment with typically smaller magnitude loads. However, should larger environmental forces resume, such as return to Earth or arrival on another planet, the potential for fracture of these weaker bones can increase. Therefore, significant research has been performed to understand the effects of microgravity on bone strength.

Measurements of changes in bone density (or mass) have been performed on practically every US and Soviet space mission starting with Gemini and Soyuz [35-39]. Gemini and Apollo missions had X-ray equipment on board to measure hand and foot bone densities. In the Gemini missions, which each lasted no more than two weeks, 3-23% losses in bone density were reported. Apollo missions included calcium balance studies using blood and urine sampling and found significant decreases in calcium balance due to increased calcium excretion over these two-week missions, leading to the conclusion that bone density changes were directly related to systemic calcium losses. The Skylab missions of the early 1970's focused extensively on life science studies. During these one to three month missions, bone resorption markers and calcium excretion were found to increase. However, significant variation in bone density changes were noted between astronauts, ranging from 0-7% decreases from pre-flight measurements [36]. Longer Soviet flights on Soyuz and Mir missions, ranging from two to six months, also showed a wide variety in the amounts of bone loss measured, from no losses at any site to up to a 20% loss in density at the heel [36, 38]. Recent increases in measurement,

medical, and space technologies have lead to more sophisticated studies on the joint Russian, American, and international missions using the Space Shuttle and the International Space Station. Average monthly losses in bone density were determined to correspond to average monthly calcium ion losses [36, 40], and correlations between these losses and muscle atrophy measurements have been made [40, 41].

While significant variations in quantitative measures have been reported, general trends in the musculoskeletal adaptations to microgravity have emerged. Muscle mass, force and power as well as bone mineral density and systemic calcium ion levels all have been found to reduce with time spent in microgravity. Muscle atrophy has been shown to occur much faster than bone strength reductions, with significant muscle loss after only eight weightless days [40] while cancellous bone density changes were not noticeable until almost a month and cortical density decreases after two months [39, 42] in space. Muscle and bone losses were found to be most significant in distal regions, at the ends of the limbs far from the center of the body, [39, 43, 44] with up to a 20% reduction in muscle size in the lower leg muscles that control ankle movement [40] and up to a 20% loss in heel bone density [36, 38]. Corresponding measurements of the strength of muscles that control hip motion diminished less than those of the ankle, ranging only from 10% to 15% of their initial, pre-flight, abilities [40]. The changes in hip muscle strength correlated with the up to 10% decrease in the bone density in the vertebrae of the lower back that has been reported due to weightlessness, near where these muscles act [45]. In addition to the faster rate of losses, the amount of cancellous bone density losses have been measured to be as much as twice those in the cortical bone [39].

Changes in bone and muscle strength have been found to be linear with time in microgravity. Rapid losses in both muscle size and bone density, especially in the cancellous tissue, have been observed upon initial entry into space, followed by slower and more controlled losses that became constant with time [40]. After nine months of one mission, muscle mass approached 70% of the pre-flight value [41].

In addition to a better understanding of the mechanisms of muscle and bone weakening due to microgravity, the recovery due to increased global environmental gravitational conditions has also been monitored. As with measured losses, a significant variation in the amounts and rates of recovery has been reported. However, notable trends have been uncovered. Muscle recovery occurs faster than bone recovery [46], with muscle volume increasing exponentially with time [40]. The rate of bone formation was found to increase upon return from space, while the bone resorption (decay) rates continued to increase, though at slower rates, for some time after return [47]. Additionally, cortical bone mass appears to reach its preflight value faster than the cancellous bone tissue [39]. With time, however, pre-flight strengths returned, indicating the alterations are reversible. It should be noted that while bone density measurements in microgravity changed significantly from pre-flight values during these studies, they were still within clinically normal limits. Therefore, no space-induced osteopenia or osteoporosis has been observed [37] and no osteoporotic fractures have resulted upon reambulation [48].

The potential negative effects of functional adaptations of the musculoskeletal system and the knowledge gained from their study, especially as a result of space travel, has lead researchers to develop ways to artificially invoke or control these phenomena to

modify bone strength even when internal or external environmental conditions would drive changes differently. Such forced, controlled, alterations to the natural bone strength adaptation phenomena target both the intrinsic (material) and extrinsic (shape) bone property changes. Therefore, regardless of the cause, whether it be related to age, disuse, disease or environmental conditions, the levels of bone strength reduction can be lessened and the strength may even be increased by modifying the rates and amounts of bone shape and density changes through the use of various interventions and countermeasures.

1.2.3 Current Countermeasures

Currently, two main methods to artificially alter the functional adaptation of a bone's strength have been developed. Each one targets a different strength modification mechanism to focus on maintaining or improving bone strength through adjustments to both the intrinsic and extrinsic properties of bone's mineral content and shape.

1.2.3.1 Pharmaceutical Based Countermeasures. Pharmaceutical based countermeasures, from nutritional supplements to prescription drugs, target changes to the intrinsic mechanical properties of bone through alterations in the amount or rate of change in bone density by directly controlling its mineral content and porosity. Implementation of this type of countermeasure is often straightforward by administering consistent quantities of certain chemicals that affect the biological bone adaptation processes over time or supplement the minerals that are stored in bones. Because they target the amount and distribution of minerals in the bones, which can be easily measured clinically, their effectiveness can be easily quantified and tracked with time.

Many pharmaceutical based countermeasures specifically target changes in bone density through direct alteration of biochemical processes in the bone tissues and cells.

Specifically, they artificially change the rates of release of minerals, mainly from the cancellous bone tissue, where the quantity of minerals in bone naturally fluctuates significantly. This is accomplished by slowing the repair processes in the bone tissue, thus reducing the release of minerals from the bone tissue and the resulting material porosity that occurs during these repairs [14, 36]. This leaves a denser, and, therefore, stronger material. However, there have been some concerns of potentially unwanted side effects of these pharmaceutical agents, like bisphosphonates, alendronates, and ibandronates, the most significant of which is the potential for increased risk of fracture.

Bone fractures usually begin in the cortical rather than the cancellous region of the bone [28]. The reasons for this are twofold. First, cortical bone tissue is on the outer surface of a bone and is, therefore, subjected to higher stresses simply due to geometry. Second, the dense, nonhomogenous nature of the cortical bone material and the interspersed pores make it more susceptible to the development and propagation of cracks.

In a nonhomogeneous material, cracks form when local variations in a region result in stresses beyond the material's yield strength. They propagate when the strain energy stored in the material due to the deformation caused by the application of an external load is sufficient enough to break the bonds of atoms in the material surrounding the crack [49]. As occurs in inert materials, the relatively large and sparse pores that occur in cortical bone tissue usually dissipate the strain energy, stopping crack propagation. However, if the pores are close enough and numerous enough, and the strain energy stored in the material from the applied load is large enough, cracks can

propagate far enough to span the distance between neighboring pores, resulting in long continuous discontinuities that can potentially result in the structural failure of the object.

In bone, the material in a region with a small localized crack is usually removed and replaced under normal repair processes that occur at a regular rate. However, when the rate of the replacement and repair processes is reduced through the use of pharmaceuticals, a large network of small cracks may result. Under sufficient loading and, therefore, energy input, this network of cracks is prone to combining through the process described above. The resulting larger structural defect can lead to a significant reduction in the bone strength, and with enough crack growth, can result in the structural failure of the bone [14, 20, 28, 50, 51]. By slowing the rate of the natural repair processes, the use of these pharmaceutical agents also results in greater mineralization of the cortical bone tissue. This is believed to create a stiffer, more crystalline, and therefore, more brittle material [30]. Such a brittle material is more susceptible to crack growth and fracture since less internally stored strain energy from the applied forces is dissipated through local plastic deformation and more energy is, therefore, available for crack propagation [49].

Despite the risks, pharmaceutical based methods, which use biochemical means to slow the loss of bone strength, can contribute to a reduced potential for fracture under typically activities for those individuals with significant weakening of their bone structures. However, while these types of countermeasures can successfully limit loss of bone strength, they do not stimulate bone formation [50]. Additionally, because they work systemically, their function cannot be restricted only to specific locations that are weakened and even locations with little or no noted strength reductions are affected [50,

52]. Finally, by targeting the loss of bone minerals, they cause the greatest changes to the cancellous bone tissue rather than the cortical tissue where most fractures initiate [28]. Therefore, alternative or supplemental methods may be necessary to address these limitations. One such method is the mechanical based countermeasures.

1.2.3.2 Mechanical Based Countermeasures. Mechanical based countermeasures, such as exercises, work to improve bone strength by stimulating increased formation of material on the surfaces of the bone [50] despite the reduction in bone material or density that might be naturally occurring in the interior volume in response to internal or external environmental conditions. They target the cortical regions of bone, where fractures most likely occur [28], to change the shape of the whole bone structure as explained in Subsection 1.2.1.3. These shape changes, though usually more subtle than the bone density changes, can often have a greater impact on bone strength [18, 20] and, therefore, might contribute more significantly to the mitigation of losses in bone strength than other countermeasures with the benefit of few potentially adverse side effects.

While external mechanical devices can aid in this means of controlling and altering the bone strength adaptation mechanisms that are related to bone's function as a structural support [10], mechanical countermeasures often act through the dependencies between bone strength and muscle strength that were described in Subsection 1.2.2.2. While nonmechanical factors, like hormones and metabolic and biochemical factors, which are the targets of pharmaceutical countermeasures, do contribute to bone strength, the relationships between changes in muscle strength and changes in bone strength have been shown to be quite pronounced [31]. Additionally, mechanical countermeasures, like exercise, can target specific regions of weakened bone and can have beneficial effects on

other physiological systems that are not possible with biochemical agents that target specific cellular processes consistently throughout the whole skeletal system. A study that directly compared the effects of mechanical and pharmaceutical countermeasures on bone and muscle loss and recovery showed that both intervention methods resulted in a reduction in bone loss over no use of countermeasures. However, those that partook in exercise interventions also showed a reduced amount of muscle loss that was not seen with the pharmaceutical countermeasures, allowing for a quicker recovery to normal function. Therefore, the use of mechanical countermeasures may be beneficial by mitigating the loss of bone strength and concurrently mitigating the negative aspects of the functional adaptations that may also occur in other physiological systems due to the environmental changes.

Despite its potential benefits, quantifying the effectiveness of mechanical based countermeasures is more difficult than it is for pharmaceutical based ones. The reasons for this difficulty are varied and related to the wide variety of available exercise regimens, individual capabilities, the inability to provide specific controlled dosages of exercise as can be done with pharmaceutical methods, and the less direct correlations between clinical measurements of bone geometry and bone strength than have been established for bone density measurements. The effects of mechanical loading and exercise countermeasures on changes in bone strength have, therefore, been the subject of significant research.

1.2.4 Experimental Studies of Mechanical Countermeasures

Although mechanical countermeasures have the potential to maintain and improve bone strength with few adverse effects, the types of mechanical countermeasures are more

diverse than pharmaceutical methods. Additionally, the mechanisms behind their function and the resulting effects are less understood. Therefore, research has been undertaken to examine the relationships between loading magnitude and type of load on changes in bone strength. The study of the functional adaptation of bone can be carried out either by applying or by removing loads that directly interact with the studied bone.

1.2.4.1 Effect of Reduced Load. Studies of decreases in environmental forces can be readily performed and easily controlled. Through investigations of immobilized subjects, trends in the functional adaptations of bone that lead to a loss of bone strength can be examined. The effects of immobilization on bone strength can be observed in the paralyzed, those subjected to long hospital stays, or even in those who have to wear a cast due to a fracture. Therefore, experimental methods for studying the ways bone adapts to immobilization typically mimic these three conditions. Animals have been subjected to severed nerves, tendons, spinal cords. They have had their limbs plastered in casts, wrapped in bandages and even suspended. Humans have also been subjected to casting and periods of time of restricted activity while confined to a bed. In fact, human bed rest studies began as early as the 1940's [53] where plaster casts immobilized subjects from waist down while they lay in hospital beds.

From these studies [16, 54, 55], a number of trends in bone density and mineral content have emerged. The initial response to immobilization has been found to occur in the highly changeable cancellous bone tissue region through increased resorption of bone material and increased levels of minerals, especially calcium, in blood and urine. The net amount of loss becomes constant with time of immobilization, when losses temporarily stop. A brief increase in strength is usually then noted, sometimes returning to pre-

immobilization levels. Then, the decrease in strength occurs again, at a slower rate than initially upon immobilization, until a new steady state strength level is achieved, which is lower than that prior to immobilization. Cortical bone tissue has been observed to follow the same trends although the response is slower and less dramatic. The change in bone density has been shown to be fully reversible upon remobilization. These trends in bone density due to immobilization follow those observed due to microgravity described above. In addition, comparison of the results of bed rest studies with observations of the losses incurred by astronauts and cosmonauts in space show analogous amounts of mineral changes [56].

While fewer investigations have examined the geometric changes of cortical bone due to reduced environmental forces, a series of canine studies in the late 1970's examining the changes in the geometry of the cortical regions of long bones over time due to cast immobilization [54, 55] provided insight into significant trends. These studies found that the decreases in bone size were greater the more distal the location on the immobilized limb so that the bones in the toes had a greater response than those near the shoulder. Changes were found in both in the porosity of the cortical bone tissue and its overall shape. While the changes in the porosity were initially rapid and transient, even returning to pre-immobilization levels despite being immobilized, changes to geometry were slower in response and longer in duration. Losses of bone material were noted on both the inner and outer surfaces of the cortical bone. These trends in cortical bone geometry changes with location and time were consistent with those observed in other studies for bone density due to immobilization and spaceflight.

1.2.4.2 Effect of Increased Load. While immobilization has proven to be a good model for loss of bone strength, the experimental study of the response of bone to increased loading has been more challenging. Experiments have been performed on many different animals, often involving the surgical implantation of load application fixtures and strain measurement devices. Through X-rays, changes in bone density and shape with time are typically tracked as a result of specified loading protocols. Additionally, at the completion of the study, animals are often sacrificed to obtain histological data such as bone mineral content and types and distributions of bone cells present.

Similar to the studies of the effects of loading on trees where specified weights were hung and changes in trunk geometry were noted [7], these animal studies often involve the external application of specified loads to individual bones so that changes in bone structure can be observed with time. One of the first of these studies was a series of experiments using rabbits [57, 58]. Ferrous wires were surgically inserted through the tibia bone of rabbits and bending loads were repeatedly induced by alternating the direction of a magnetic field surrounding the ends of these wires induced by an electromagnet. After a number of weeks of repeated load application, measurements taken from X-rays of the loaded bones were compared to those from initial X-rays. New growth was found to occur at both the inner and outer cortical surfaces in the regions perpendicular to the bending axis where large bending stresses are expected. A similar study was later performed on turkeys [59]. While the loading mechanism was different (bending loads were induced through mechanically loading a pin inserted through a turkey's leg), the resulting growth in the turkey's bone subjected to the bending load corresponded well to the observations seen in the rabbit experiment. Differences in the

amounts of growth observed due to the variations of the magnitudes and durations of the applied forces in these studies indicated to these researchers that there is a strong relationship between the load magnitude and the amount of bone strength adaptation.

Instead of inducing a specified external load on an animal's bone, artificial manipulation of the internal environment of a sheep's leg has also provided insight into relationships between applied forces and functional adaptation of bone [60]. The front leg of a sheep is comparable to the arm of a human, where the lower part contains two parallel bones: a radius and an ulna. In this study, one bone, the ulna, was removed. Changes in the density and measured surface strains of the remaining bone, the radius, were examined. Similar to the study of adaptation in the lungs explained in Subsection 1.2.1.1, over time, new bone volume was added to the side of the radius where the ulna was such that it eventually replaced almost the entire volume that was removed. Under normal walking loads, the measured strains on the outer surface of the radius initially increased significantly upon removal of the ulna. With the added bone volume, however, these strains returned to values similar to those before the ulna was removed.

These early experimental studies provided measurable evidence of the existence of a direct relationship between applied forces and alterations in bone shape. Based on these results, researchers began to investigate how to actively control the strength adaptations of bone through prescribed loading modes and activities.

1.2.4.3 Effect of Exercise Mode. The first step in the study of controlled bone strength adaptation was the understanding of the effects of currently performed exercises. Because increases in applied loads have been shown to increase bone size and density and because the changes in bone mass have been shown to lag behind, but parallel, the

changes in muscle mass, the effects of different exercises on bone strength have been extensively studied both in animals and in humans in order to identify loading patterns that trigger the greatest increases in bone strength. Both prospective clinical investigations, comparing prescribed exercise regimens to carefully controlled groups whose exercise activities were limited, and retrospective studies, examining the bone geometry and density of bones from athletes of various sports, have been performed. Additionally, significant work has been conducted to develop exercise routines for astronauts that help maintain bone and muscle strength while accommodating both the time and space limitations typical to a space station environment.

Animal studies of the effects of exercise on geometric changes, and, therefore, likely strength changes, of bones have been numerous. The exercise studies eliminate the need for the complex fixtures, invasive surgeries to attach load applying mechanisms to the bones, and the artificial loading patterns of the earlier experiments reviewed above. Additionally, because actual motions and activities are used, their results have more direct clinical implications. These animal studies usually compare the effects of activities on measures of bone strength such as geometric dimensions or density. Non-exercising groups that just went about normal activities are often used as a reference. An early study of this type done in the 1970's [61] examined the timing as well as the amounts of change in cortical bone geometry of adult hamsters that were allowed access to an exercise wheel. Both initiation and termination of increased rates of bone growth were found to lag behind initiation and termination of exercise. This showed that the benefits of exercise exceed the time spent performing the activity.

Treadmills have often been used as a means of controlling increases in environmental loading for these animal studies. Such studies have successfully verified trends in loading intensity on bone mass increases by comparing conditions in animals that are immobilized, normally ambulating, and subjected to increased activity through controlled "exercise" speeds using these treadmills [62]. Under such activities, the beneficial increases in extrinsic (geometric) properties were found to be greater than those for intrinsic (material) properties of cortical bone tissue [63]. Additionally, these controlled speed treadmill investigations have been able to show the importance of atypical loading modes of the same intensity as typical modes on the changes in bone strength, such as swimming versus walking at the same rate for a land mammal [64].

Based on the results of these animal studies, human clinical investigations into the effects of various exercise types on bone strength adaptation have been undertaken. Because of the difficulties in controlling the behavior of humans as exactly as can be done with animal experiments, more varied conclusions have resulted. Some studies have shown that exercise in adults produces only a slight impact on skeletal geometry and a moderate impact on bone density [65]. Others have concluded that exercise does not add new bone material, but only acts to prevent bone loss [27, 65, 66]. Still others have shown significant impact of exercise on both bone size and density [67].

The variation in the conclusions drawn by these studies is related to the difficulties in quantifying changes in both environmental loading and bone strength. Many studies have only measured reaction forces between the whole body and the ground [26] or whole body accelerations [68] to estimate the magnitude of bone loading. In these investigations, measures of bone strength changes were often limited to bone

mass [65, 66]. While both of these types of measurements are easy to obtain, they do not accurately depict the complete mechanical conditions or adaptive responses.

Additional complications to these studies of the effects of exercise regimens in humans are related to the study protocols themselves as well as to the subject's compliance to these protocols. Mixed loading modes are often used, with combinations of high and low intensity activities, such as running, jumping, and isometric exercise, allowing no means to isolate effects of the type of activity on observed strength changes. Compounding all of these issues are significant difficulties in accounting for activities outside the study time and the small amount people who actually complete the full study from start to finish [66, 68].

Retrospective studies comparing the properties of bones of different athletes have provided means for more control in the identification of loading parameters, since the athletes studied often partake in the specialized activities over longer periods of time in more repeatable patterns than the non-athlete subjects enrolled in short-term exercise programs. Such studies have resulted in similar conclusions as those drawn from the animal experiments. For example, activities, like squash or soccer, that provided "novel strains" most different from those of typical activities, have been found to induce the greatest changes in bone strength regardless of the intensity of the activity [69]. Unlike the animal studies where the local mechanical environment was usually measured through the use of strain gages, in these human investigations typical or atypical loads were classified based on measurements of whole body reaction forces. In this manner, the variations in the local mechanical environment that may have induced the changes was not identified in these studies.

Effect of Exercise Mode in Microgravity

Like the studies in space that have helped to better understand bone loss mechanisms, studies of the effects of exercise on bone strength gains are more controlled in microgravity with better compliance than Earth-bound investigations. Such studies are valuable in applying the knowledge gained from animal and clinical experiments of adaptation mechanisms to the implementation of practical and efficient exercise regimens. While early space missions by the US and Soviets used mainly treadmill and stationary bikes [44, 52], these activities have since proven to be better suited for reducing the cardiovascular deconditioning "functional adaptations" that also occur in microgravity rather than attenuating the musculoskeletal losses [33, 70]. Bungee cord harnesses in combination with a treadmill were found to be better at reducing losses in bone density in space through simulating an increased gravitational force, but they did not fully eliminate the losses caused by living in microgravity [71]. These results led to a focus on methods to increase the whole body loads. Weight systems, flywheels and friction ramps have all been studied with limited success [33, 36, 38, 52, 71]. Because increased bone formation in addition to reduced bone resorption has been observed in bed rest studies where resistance exercises were incorporated [71], such exercises became the prominent loading mode in many studies. Of the different types of resistance exercises, isometric loading methods have shown a great benefit in reducing losses to muscle strength during global reductions in environmental mechanical forces [70] and in improving bone strength during recovery upon return to "normal" conditions [46]. Isometric exercises are those where a constant force is supported in a constant position, such as when holding up a weight or attempting to move a fixed object. Based on this

information, resistance exercises have dominated bone and muscle loss mitigation exercise protocols for space flight programs.

Resistance bands have been on every US space flight since Skylab, even the early Soviet missions, and are still currently available on the International Space Station [44]. However, the bands have had persistent problems including the inability to generate sufficient force intensities to induce bone formation and the breakage of the bands due to overuse [72, 73]. In 2009, a more complex resistance force exercise mechanism was installed on the International Space Station. Through the use of vacuum cylinders, a flywheel mechanism to simulate movement of free-weights, and a cable pulley mechanism to control the stroke of each exercise, this machine could provide twice the resistance of the bands. The software interface of the system could provided feedback on the magnitude and direction of the resulting force generated so that user-customized goals could be created and performance could be analyzed. The astronauts currently using this equipment are required to perform heel raises, squats and deadlifts to target the muscles controlling ankle, knee, and hip [72, 74-76] for thirty to sixty minutes a day, three to six days a week [77, 78]. Early results have shown that, although some post-flight losses were still noted, the use of this equipment improved the attenuation of bone loss, during a six to eight month timeframe, over previously used exercise devices [78, 79]. Through the more controlled studies performed in the development of efficient exercise regimes for those spending long times in space, resistance exercises have emerged as the prominent means of maintaining musculoskeletal fitness in microgravity. However, as evidenced by the lengthy bone loss mitigation exercise regimens currently required on the

International Space Station, the most economical and efficient routines that also minimize both exercise time and complexity of exercise equipment have yet to be developed.

Experiments on animals and humans both on Earth and in Space have provided significant insight into the effects of various types of loading modes on bone strength adaptation responses and have directed researchers towards the basic types of exercise countermeasures to losses of bone strength with the most potential for benefit. However, a wide range of approaches to mechanical means of maintaining bone strength is still being used which has lead to an equally wide range of reported effectiveness. Therefore, before mechanical based countermeasures can be efficiently and effectively implemented both on Earth and in Space, further investigation is necessary. Strength loss mitigation methods that target regions of bone with the most the significant consequences of or susceptibility to weakening must be identified. Additionally, methods to quantify the changes in bone strength for a more scientific comparison must be developed. Computational analysis methods and simulations often have been used to help understand physical systems that are difficult to study experimentally. Therefore, they may be beneficial in the investigation of exercise countermeasures to losses of bone strength.

1.3   Computational Modeling of Bone Strength

Studies of living subjects have been able to show basic correlations between the applied forces and bone strength adaptation, demonstrating the relative effects of loading modes and intensities. In animal experiments, due to variations in animal ages, species, sizes, and types of bone studied as well as duration of study and methods used to quantify strength changes, absolute correlations and trends have been difficult to identify [55, 57, 63]. In addition to the inter-subject variations, significant problems in study design,

patient compliance and uncontrolled external influences have limited the successful isolation of loading parameters on bone strength adaptation in human exercise studies [80]. The quantification of strength changes in these experimental and clinical studies has often focused on the easily measured bone mineral density, considering only the intrinsic material property changes and ignoring the extrinsic geometric changes that may better correlate with bone strength [27]. Because computational models are often used in mechanical analyses to gain insight into phenomena that are difficult to measure, isolate, or see through experimental means, they are well suited to examine the relative effects of specific parameters that have the potential to induce the greatest bone strength adaptations without the variability in study subject and restrictions in measurements that have limited experimental and clinical investigations. A review of this use of computation modeling methods follows.

1.3.1 Application of Computational Modeling to Study Bone Strength Adaptation

Computational modeling methods have been used to complement physical experiments. For example, to quantify the effects of bone loss countermeasures that were studied experimentally, finite element analyses have been employed [78, 81]. In such work, imaging scans of actual bones are made before treatment and at regular intervals. The scanned images are analyzed, the material properties and geometric boundaries are deduced, and finite element models are generated. The response of the whole bone structure to various sets of boundary conditions can then be predicted to determine the effects of the combined changes in density or geometry that resulted from the experimental alterations in the bone's mechanical environment. Such studies can reveal the interactions or the effects of treatments on material property and geometric variations

within a bone as well as the relative effects of these changes on bone strength in ways that cannot be achieved through standard experimental measurements alone.

Modeling methods can also be used independently of physical studies to simulate the bone strength adaptation phenomena. Because changes to both intrinsic and extrinsic properties occur under mechanical loading simultaneously, experimental and clinical researchers are unable to separate the two types of adaptive responses of bone strength. Computational modeling and simulation techniques, however, can be developed to isolate each adaptive response and systematically alter input loading parameters so that specific trends and relationships can be revealed and quantified.

Following the physical experiments, previous computational studies have often focused on material property changes. The predictions of these models are often based on images of density distributions of strut configurations in cancellous bone tissue regions from experimental or clinical studies. However, because geometric changes are not as easily examined experimentally, even though they are thought to significantly affect bone strength, the computational study of shape changes of bone may be quite beneficial in understanding and controlling bone strength adaptation phenomena.

1.3.2 Bone Shape Adaptation Modeling Methods and Current Limitations

Despite the many different computational models that have been developed to simulate bone shape adaptation, all follow the same basic iterative optimization procedure. They start with the numerical solution of the structural analysis of the bone being optimized under the given loading conditions. The response of the bone to this loading that drives the shape adaptations can be represented through various measures of the mechanical state, such as deformation, strain, stress, strain energy density, or even components or

gradients of these measures, that are calculated at discrete points along the bone's surfaces from the numerical structural analysis. Based on the distribution of the local mechanical state of the bone, local material accretion or resorption is determined using numerical models that represent the effects of the bone's strength adaptation phenomena, moving the local mechanical response measures toward a specified optimization goal. The shape changes of the bone are simulated by moving the locations of the discrete points on the boundary surfaces, typically either nodes or shape control points, where the local mechanical state was calculated.

Using such methods, the governing conservation equations are usually solved quasi-statically, and the shape optimization progresses iteratively, so that the total mass of the system remains constant for each structural analysis. The same boundary conditions are typically applied to the new shape at each iteration, though variations in loading regimes can be incorporated as well. The simulations are run until a specific goal or a physical size limit is reached. Alternatively, iterations may represent physical quantities of time, such as days, and simulations may be run over a specified time period. While finite element methods are most common, because only the surface profiles are changed in these models, boundary element methods have also been employed [82-84].

While this basic modeling method has been followed since the computational modeling of bone strength adaptation began in the 1970's, significant research has focused on three major areas to improve the model predictions. The first area relates to the specific mathematical model simulating the effects of the bone's strength adaptation phenomena. The second area relates to the selection of mathematical optimization

method and convergence criteria. The final area relates to the representation of the physical system and boundary conditions. Each area will be discussed in detail.

1.3.2.1 Model Drivers and Parameters. Many different types of measures have been proposed as the "functional stimulus" (measure of the local mechanical state and threshold values to trigger bone loss or growth) cited by early researchers as the driver and controller of bone's functional strength adaptations. The review of models presented here is representative of the majority of previously proposed models. Early studies focused on strain tensor components as the "functional stimulus" driving the geometric changes in bone, indicating that there may be a different response for each tensor component [85-89]. Later studies used more averaged effects like strain energy density [90-93] or von Mises stress [94, 95]. Other studies have driven the strength changes by principal stresses and strains [96-98], strain rates [99-101], and spatial gradients of strain or strain energy density [100, 102-105]. Some studies have compared experimental results of bone shape adaptation to computational models, either simulating the adaptation process itself or just representing the mechanical response to the applied load, to compare trends in bone growth or decay with trends in various mechanical measures to determine which measure may be the most appropriate growth driver [96, 99, 100, 103, 104]. Despite these numerous and diverse studies, no mechanical measure has been conclusively found to be directly proportional to observed changes in bone shape. In fact, some studies have even indicated that different measures may control accretion and resorption [85, 102].

Because the modeling methods of bone strength adaptation follow a basic feedback control system, threshold values of the mechanical measure are required to

trigger the cellular activities causing strength adaptation and to define the amounts of change at each surface location. Similar to the determination of the mechanical measure that acts as this functional stimulus, many researchers have attempted to determine these threshold values. The growth and decay thresholds have been the same value [87, 91] or different values [85, 93, 106] and even varied by location [107]. The use of different threshold values for accretion or resorption results in a range of mechanical responses to external loading that trigger no strength adaptations to the bone often, called the "lazy zone" [29, 59, 106]. Researchers using the lazy zone believe that there is a range of typically encountered mechanical states over which nonmechanical factors control the slight amount of adaptation that occurs [103]. Despite the many studies, ranging from the application of strain gages on actual bones in living subjects to finite element modeling, like the functional stimulus, no definitive conclusions have been made about the number of thresholds, their values or even the actual existence of any such parameter [108].

In addition to the mechanical measure driving the model and the threshold values triggering adaptation phenomena, the rates of material accretion or resorption are often specified within the developed computational model. Like the threshold values, these rates can be constant or based on location, such as the outer (periosteal) or inner (endosteal) surfaces, and may even vary based on whether accretion and removal occurs [91, 92]. It has even been proposed that the rate is different for different model measures, such as each strain tensor component in a strain tensor driven model [89].

The parameters discussed in this section, especially the rates and threshold values, are often specified for the particular conditions studies. Most parameters are typically selected that correlate experimental observations with the model prediction [89, 92, 109-

112]. Yet, the selection of model parameters in this manner may limit the application of the model to systems and conditions similar to the experiments on which the parameter selections were based. Therefore, alternative means of determining the parameters or formulating the numerical model are necessary.

1.3.2.2 Optimization Methods and Stopping Criteria. The second area of significant research in the development of bone strength adaptation models is the selection of the mathematical optimization method and convergence or stopping criteria. Because the shape strength changes of the bone are thought to be a response to an external trigger or "functional stimulus", the adaptations are believed to be moving the bone's strength towards a particular goal. The use of computational modeling methods to simulate the strength adaptation phenomena in bone and to predict the resulting changes to the bone's shape requires the understanding and specification of this optimization goal.

Conceptually, the goal of the functional strength adaptation of bone is to create a structure suitable to withstand the forces likely to be imposed on it. Similar to the design of mechanical components, this implies that certain strength requirements are necessary. For example, the failure stress of the bone structure must be greater than stresses caused by applied loads. Observations of bone strength adaptations have noted that growth occurs in regions of high stress/strain and decay occurs in regions of low stress/strain. The growth and decay threshold values used in many of these computational models actually function as optimization goals, causing greater amounts of growth or decay in regions with greater variances from the threshold values. By driving the local surface stresses or strains towards the threshold values, the variation over the surface is reduced. The threshold values (or optimization goals) can easily be arbitrarily selected in

computational models. For example, they can be a specific design criterion, such as a maximum or minimum stress during the function of an inert mechanical part. However, the global designation of a singular absolute stress or strain value that bone cells use to drive adaptation in all circumstances seems unlikely. Rather, a relative measure of variation is more probable. Nonetheless, the simplicity of this type of model has lead to its widespread selection of threshold values often only to match an experimental result.

Models that are driven by selected "threshold values" that trigger growth or decay usually follow the form:

$$\text{Local Growth} = \text{Rate} * (\text{Local Value} - \text{Threshold Value}) \tag{1.1}$$

$$\mathbf{X}_{new} = \mathbf{X}_{old} + \text{Local Growth} \tag{1.2}$$

where $\mathbf{X}$ is the location of a point on the surface and the optimization goal is minimization of (Local Value - Threshold Value). The calculation of the growth at each discrete point on the surface is repeated iteratively as the measure of the local mechanical state changes with each iterative change to the boundary surfaces. Such a routine is often called a gradientless or zeroth-order optimization scheme because the gradient of the optimization function is not used in the search for the optimal solution [113]. Because only the optimization function itself is used, as in Equation 1.1, gradientless optimization methods are less mathematically rigorous than traditional gradient based methods. These gradientless optimization methods do not achieve a unique solution and do not find global optima. Instead, the identification of specific, somewhat arbitrarily selected, convergence criteria to define when the model has reached its "optimal state" is required. Nonetheless, when systems start close to their optimal state, as in bone shape

optimization where the amount of shape changes are limited, or when a precise optimum is not necessary, such methods can be efficiently employed [113, 114].

Some models have been developed that take advantage of the mathematical simplicity of the gradientless optimization methods without the burden of selecting model convergence criteria by attempting to choose a rate (Equation 1.1) that represents actual progress with time [93]. Models are then run until a specific length of time is reached rather than until a specific convergence criterion is met. These rates are often arbitrarily selected to create shapes that correspond to a validation case of a specific experimental set of conditions and, therefore, may not be applicable to other situations. While these might allow simulations to more closely replicate experimental results, difficulties can arise when trying to compare effects of different loading or boundary conditions using these same model parameters.

The need for the selection of specific threshold values, growth rates, and convergence criteria can be eliminated through the use of gradient-based methods. In such cases, an optimization goal, such as minimizing the variation of stress or strain over the surface, is written in the form of a function, the gradient of which leads the search for unique local, and sometimes global, optimization solutions. Because these methods require the determination of the gradient of the optimization function with respect to each design parameter (here discrete points on the boundary surfaces of the bone), the number of gradient calculations required and their subsequent application can be computationally prohibitive, especially for complex, three dimensional shapes [115]. Thus, while they are more mathematically rigorous and more apt to result in unique optima, gradient-based mathematical optimization techniques are more difficult to execute and require more

computational resources than gradientless method, limiting their applicability to the simulation of bone strength adaptation.

Despite the significant number of computational models of bone strength adaptation that simulate the shape changes of bone, there has been no consensus on the most appropriate optimization methods, growth driver measures and modeling parameters (thresholds, rates, etc.). Many models are based on correlations to specific experimental studies and few use specific convergence or stopping criteria. Therefore, the ability to use such computational models to quantitatively compare the effects of a wide range of loading and geometric conditions is currently limited.

1.3.2.3 Representation of Physical System. Many of the current computational models that predict adaptive shape changes of bone simplify the bone geometry, the boundary conditions, or both. As in any numerical model of a physical system, such simplifications are used to reduce the computational resources and the total study time required. Research has been undertaken to understand the effects of the simplifications on the ability of the models to appropriately simulate the strength adaptations.

The first area of simplification studied is the geometry. In general, the more complete the representation of the shape of an object, the more accurate its resulting structural analysis. However, because modeling of bone shape changes in response to external loading conditions is computationally intensive, geometric simplifications are often employed. The most basic of these is the study of a two-dimensional cross-section of the midshaft of a long bone, simplified as a thick circular or oval annulus [85, 86, 92, 93]. While the relative trends in load-based strength adaptations are properly reflected in these models, the simplifications ignore the effects of axial variations and may, therefore,

limit the accuracy of the actual shape predictions. Three dimensional geometries [116], and models that account for regions of both cortical and cancellous bone tissues have been shown to give a better representation of the mechanical state of the bone [112]. The use of multibone, multisegment systems [117, 118] and the inclusion of supplemental structures such as cartilage, tendons, and ligaments [119] can provide even more accurate predictions.

Like geometry, the effect of the representation of the boundary conditions has been extensively studied. Because muscles often produce the major forces on bones, the way these forces are included in the computational model can significantly affect the structural analysis. Studies have shown that simplifications of the distribution of the forces on the bone's surface [120, 121] can cause significant variations in predicted mechanical behavior. The appropriate distribution of the muscle loads considers both the inclusion of individual muscles, as compared to grouping the effects of muscles with similar functions [122], and the accurate representation of the connection of the muscle to the bone, both in size of contact area and amount of contact rigidity [119-121, 123].

An investigation of the extent of model complexity necessary to appropriately simulate the behavior of a femur bone under loading at the hip has been performed [123]. In this study comparisons were made between the deflection predicted by a model with varying levels of geometric and boundary condition accuracy and those measured experimentally. While the most complete model produced results most similar to the experimental measures, the study found that the simplifications made to the boundary conditions had a much greater impact on the model results than did the geometric simplifications.

1.3.2.4 Current Bone Shape Adaptation Models. Despite the realized need, most current bone shape adaptation models are still limited in their incorporation of more realistic geometries or boundary conditions. This is, in part, due to the computational intensity required to alter the bone shape while maintaining the integrity of the discretization, which increases with increased model complexity. The lack of significant advancement of bone shape adaptation modeling methods is also related to the historic and ongoing experimental focus on material property adaptations to alter bone strength. While many of the numerical bone strength adaptation models have focused on changes in bone density, insight into the effects of various modeling features can also be applied to bone shape adaptation simulations.

Computational models of the adaptation of material properties of bone have shown the effects of the model complexity on the predicted adaptive changes. Models with more complete representations of the muscle activity have resulted in more conservative changes in bone density because the grouping of muscles imparts larger localized forces, resulting in regions of high stresses that drive greater adaptive responses [122]. Studies have shown that even small changes in the load distributions on the bone can result in significant differences in the resulting changes in density distributions [120, 121]. Some models have included both shape and material property adaptations, showing a better prediction of the mechanical state of the bone and resulting density distributions with the more accurate depictions of the cortical and cancellous tissue [124].

Despite these recommendations, many of strength adaptation models still have significant simplifications. Because many studies have focused on the adaptations of the upper (proximal) part of the femur bone, the geometry modeled is often limited only to

this region [122, 124]. The artificial, fixed boundary constraints placed on the cut surface in such truncated models can significantly affect the stress distributions and, therefore, adaptation predictions [123]. Other models have used more complete geometries but have reduced the boundary conditions either by applying only resultant forces instead of individual muscle forces [44] or by reducing the attachment of a muscle to the bone to a single node [112]. Each of these simplifications results in higher stress values near the regions of force applications than if more realistic boundary conditions were applied.

As shown, the ability of current bone strength adaptation models to accurately represent the system studied is currently limited, restricting the reliability of the predictions made. While more complex to develop and more computationally intensive to execute, numerical models including more complete physical systems, such as multiple bones and individual muscles, can reduce the need for artificially imposed boundary conditions, improving the predicted stress state and the ability to accurately simulate bone strength adaptations. Additionally, computational models that are not dependent upon the arbitrary selection of parameters that control the initiation, execution, and termination of the model can lead to more equitable quantitative comparisons between varied bone loss mitigation methods. Models that include both of these aspects may significantly improve the current capabilities in the development of effective countermeasures to reductions in bone strength.

1.4   Scope

This work addresses the limitations of current bone shape adaptation models, particularly the difficulties in their widespread use for comparative studies of the effects of loading conditions on local changes in bone strength. The developed modeling method directly couples the determination of the activity of individual muscles in a multisegment leg system with the structural analysis of the bones to which they attached and the prediction of the resulting changes in bone strength, allowing for a more complete representation of the physical system. Numerical optimization and finite element methods are employed in the first part of this work (Chapter 2 through Chapter 4) to create a shape adaptation model that is independent of experimentally matched or arbitrarily selected parameters, allowing for the ability to directly compare widely varied conditions. The capabilities of the validated model are revealed in the second part of this work (Chapter 5) when the developed model is used to identify combinations of hip, knee and ankle joint angles and net forces generated by the leg acting on a fixed surface that achieve the greatest improvements in the strength at a specified location within the bone system. Through this work, the developed modeling method is shown to enhance the current capabilities to predict bone shape adaptation, allowing for more exacting analyses of these phenomena. More importantly, the development and application of the method presented here demonstrates its potential for improving the effectiveness of mechanical countermeasures to losses of bone strength, specifically those that can target regions which may be especially prone to fracture.

CHAPTER 2

PROBLEM FORMULATION

To achieve the research goals of this work, the development and application of a modeling method that can be used to compare the bone shape adaptations in a musculoskeletal system under various conditions, the problem investigated must be well defined. It was desired that the model could accurately predict both the individual muscle activities and the resulting bone shape strength adaptations under various conditions in a detailed representation of a musculoskeletal system independently of experimentally or arbitrarily selected parameters. The motivation behind this work was to develop means to assess the effectiveness of mechanical countermeasures to bone loss and to determine combinations of bone joint configurations and loading conditions that may be most beneficial to improving bone strength in critical locations in a musculoskeletal system. This chapter discusses the details of the development of the modeling technique, the system modeled, including modeling assumptions, and the process for the application of the developed method.

2.1   System Modeled

The leg was selected as the focus of studies performed to illustrate the effectiveness of the modeling method developed in this work, although the modeling methods can be applied to any musculoskeletal system. The leg muscles, which are typically the largest and strongest of the whole body, can generate forces spanning a number of orders of magnitude, resulting in significant variations in the stress and strain distributions in the bones to which they are attached. Because bone strength adaptations, which are driven

by these distributions, are thought to be closely associated with changes in muscle forces, applying the developed bone shape adaptation model to such a system verifies its function under a broad domain of loading conditions.

The weakening of the bones in the leg may result in a reduced functional mobility, potentially leading to a loss of independence or even serious injury. Consequently, a focus on methods to counteract these losses may be of importance for conditions both on Earth and in long term space travel. As reviewed in Chapter 1, experimental and clinical studies have shown that the majority of disuse related bone loss occurs in the lower extremity, with increasing amounts of loss the more distal the location (further towards the foot) [36, 54, 125]. Therefore, this distal leg region (Figure 2.1b) may most benefit from bone strengthening methods.

The function of the entire leg musculoskeletal system, from pelvis to foot, was modeled in this study, and strength adaptations were simulated for the tibia bone. A local region of this bone was targeted for strengthening because of its susceptibility to fractures that may result in impaired mobility. Figure 2.1 illustrates the system investigated.

(a)

(b)

(c)
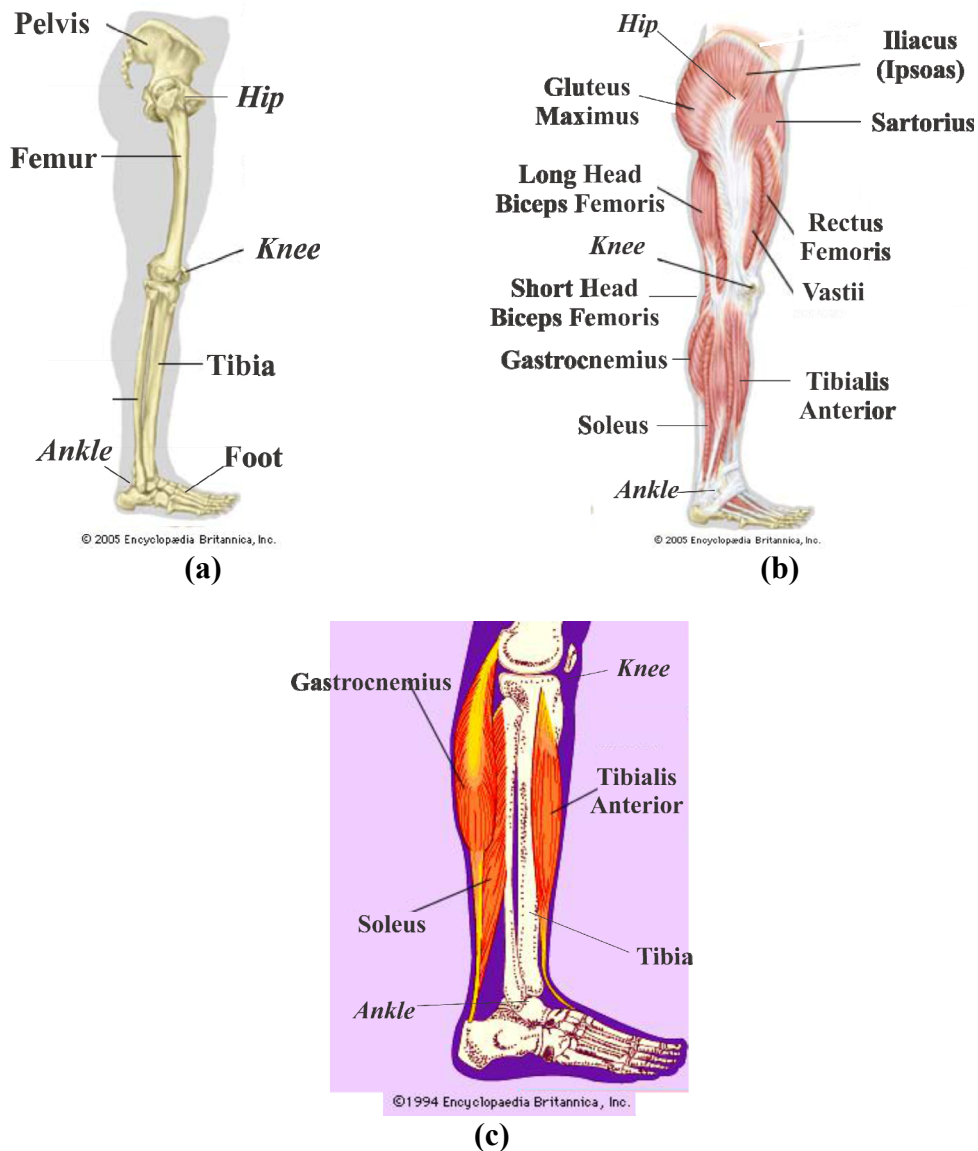
Figure 2.1 Full leg musculoskeletal system studied. (a) Included bone segments from pelvis to foot (b) Included muscles and joints (c) Distal portion of the leg from knee to foot: location of potential significant bone loss selected for strength adaptation investigation.

Figure 2.1a and 2.1b Source: "patella."[Art]. In Encyclopedia Britannica. Retrieved from http://www.britannica.com/EBchecked/media/47969/Skeletal-and-. Accessed on 10/14/13. Copyright 2005 by Encyclopedia Britannica, Inc. With permission.

Figure 2.1c Source: "clam: muscles." [Art]. In Encyclopedia Britannica. Retrieved from http://www.britannica.com/EBchecked/media/2567/Rigid-skeletons-. Accessed 10/14/13 Copyright 1994 by Encyclopedia Britannica, Inc. With permission.

2.1.1 Anatomical Model of the Leg

The function of the modeled leg was limited to that which occurs in the two-dimensional plane depicted in Figure 2.1a, a sagittal plane in which forces are directed either anteriorly (towards the front), posteriorly (towards the back), superiorly (up towards the head) or inferiorly (down towards the foot). Any forces out of this plane were assumed to be negligible and, therefore, were not included. As a result, some modifications to actual anatomical geometry of the leg system components were made are noted as necessary.

The model included four bony segments and ten muscles. The muscles selected were those that cause flexion and extension of the hip, knee, and ankle joints. The selection of the included muscles was verified through comparison to muscle sets used in experimental investigations of muscle activity for similar leg functions [126, 127]. The bony segments included were selected based on the attachment locations of the included muscles. In this way, the complete function of each muscle was internal to the system studied, limiting the artificial boundary conditions applied to the system modeled.

The ten major leg muscles included in this model are listed in Table 2.1. The bones to which they are attached, whether they are located on the front (anterior) or back (posterior) of the leg, and their main functions are also listed in this table. Because only two-dimensional forces in the sagittal plane were simulated in this study, the locations of muscle attachment on all bony segments were projected onto a sagittal plane through the midline of the long bones (femur and tibia).

Based on the locations of attachment of the included muscles, four bony segments, the pelvis, femur, tibia and foot, were chosen for inclusion in the system

modeled. The geometry of the pelvis was projected onto the same sagittal plane through the midline of the long bones as the muscle force vectors. Because of the two-dimensional simplification of the muscle forces in this model, the offset geometry of the femoral neck was not included. Because the fibula neither carries weight bearing loads nor shows significant changes with age or exercise [128-130] it was excluded from this model and the lower leg segment consisted only of the tibia. The foot segment was represented as a solid structure, without the representation of individual bones.

Table 2.1 Muscles Included in the System Studied

Muscle	Location	From	To	Function
Sartorius	Anterior	Pelvis	Tibia	Hip Flexion/ Knee Extension
Rectus Femoris	Anterior	Pelvis	Tibia	Hip Flexion/ Knee Extension
Iliacus (Ipsoas)	Anterior	Pelvis	Femur	Hip Flexion
Gluteus Maximus	Posterior	Pelvis	Femur	Hip Extension
Long Head Biceps Femoris	Posterior	Pelvis	Tibia	Hip Extension/ Knee Flexion
Tibialis Anterior	Anterior	Tibia	Foot	Ankle Flexion
Soleus	Posterior	Tibia	Heel	Ankle Extension
Gastrocnemius	Posterior	Femur	Heel	Ankle Extension/ Knee Flexion
Vastii (Vastus Lateralis)	Anterior	Femur	Tibia	Knee Extension
Short Head Biceps Femoris	Posterior	Femur	Tibia	Knee Flexion

The basic representation of the musculoskeletal system of the leg is described above. As with any mechanical model, assumptions were made in order to create a well defined system to investigate. These assumptions allowed the model to be analyzed using mathematical approximations of system behavior with acceptable efficiency and accuracy and will be described in the next section.

2.1.2 Model Definitions and Assumptions

A number of assumptions were employed in the definition of this model to clarify the system components included, simplify the system representation, and specify the range of conditions over which the model is valid. Specifically, assumptions were made regarding the representation of the geometry and function of the bone and muscle components, and the types of activities that could be simulated using the developed model.

2.1.2.1 Representation of the Bone Segments and Interfaces. As described in Subsection 2.1.1, the model contained four bone segments: the pelvis, the femur, the tibia, and the foot. Because the muscle forces were limited to two-dimensions, as described above, the bone geometry, while three-dimensional, was simplified. The femur and the tibia were approximated as circular cylinders along their entire lengths, except at the joint ends. The pelvis and the foot were approximated as linear extrusions of appropriate cross-sections, each with a unique, uniform thickness.

The overall geometry of the bones in the model was based on one published source and represented an average healthy adult male, based on a height of 1.77m and mass of 66.5kg [131]. In the reference study used, major bony landmarks were measured for a number of cadaveric and skeletal specimens and then scaled to the average size. These locations were reported based on four local coordinate systems, one on each bone segment: the right anterior superior iliac spine (ASIS) for the pelvis, the greater trochanter for the femur, the tibial tuberosity for the tibia, and the calcaneus, or heel, for the foot, with the pelvis coordinate system also used as the global coordinate system. The locations of the bony landmarks, relative to each segment's local coordinate system found in the literature [131, 132], were used to guide the development of their

representative geometries. Figure 2.2 depicts the bone segments and coordinate systems used for this model.
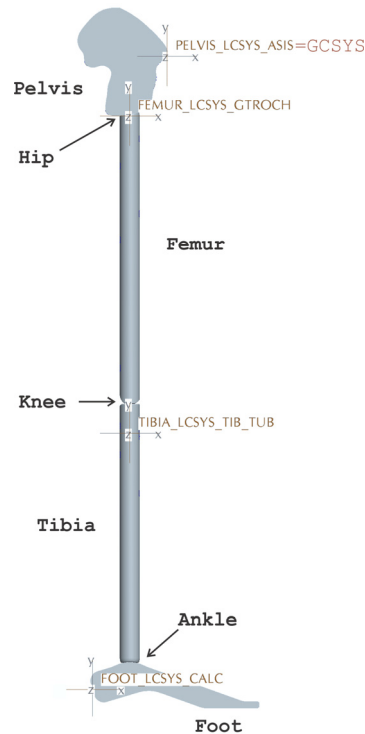
Figure 2.2 Bone segments and reference coordinate systems used.

Femur and Tibia

The overall shapes of the femur and tibia bones were created as initially circular cylinders with concave/convex joint ends (see Figure 2.3). The length of the femur, 0.435m, was taken as the distance from the center of the hip joint to the bottom of the femoral condyles [131]. The length of the tibia, 0.386m, was determined to be the distance between the knee and ankle joint centers [131]. The greater trochanter was used to approximate the location of the hip joint center [133]. Figure 2.3a shows an anterior view of the bones near the hip joint and the approximation used in this model and Figure 2.3b, the sagittal view. The locations of the knee and ankle joint centers within the defined local coordinate systems were taken directly from the published reference [131].

(a)   **(b)**
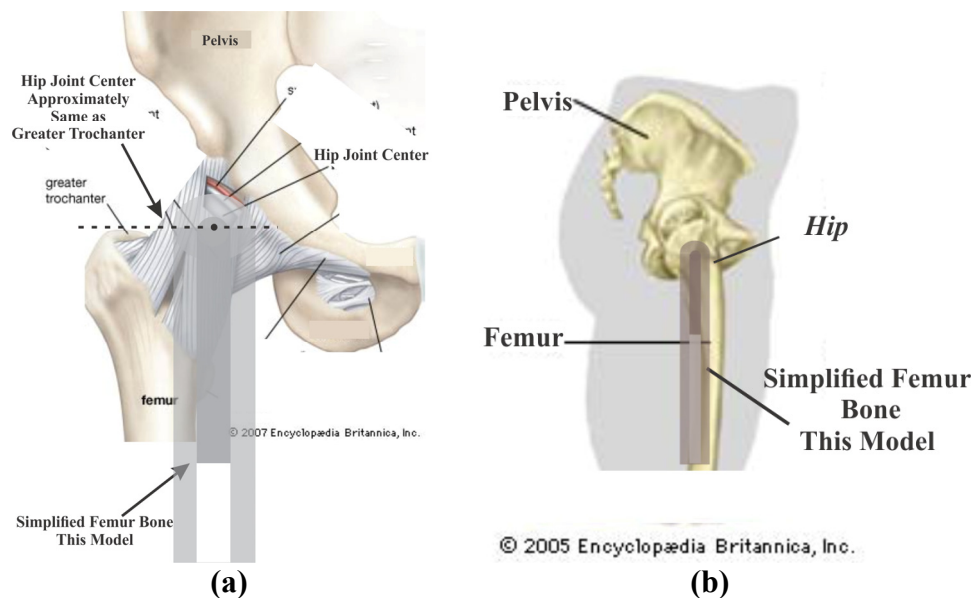
Figure 2.3 Skeletal system near hip joint and simplified model used in this study (a) anterior view (b) sagittal view.

Figure 2.3a: Source: "pelvic girdle". [Art]. In Encyclopedia Britannica. Retrieved from http://www.britannica.com/EBchecked/media/47813/Anterior. Accessed on 10/14/13. Copyright 2007 by Encyclopedia Britannica, Inc. With permission.

Figure 2.3b: Source: "patella."[Art]. In Encyclopedia Britannica. Retrieved from http://www.britannica.com/EBchecked/media/47969/Skeletal-and-. Accessed 10/14/13. Copyright 2005 by Encyclopedia Britannica, Inc. With permission.

The dimensions of the widths, or outer diameters, of the femur and tibia used in this model were selected based on a survey of measurements of cadaveric bones from the literature. Because the human femur and tibia do not have uniform or circular cross-sections, like in the simplified geometry used in this study, much variety in reported measurements of the dimensions of these bones was found depending on the location along the shaft and the orientation of the measuring device with respect to the bone's planes (eg. frontal, or z-y in Figure 2.2, and sagittal, or x-y in Figure 2.2). While the dimensions vary significantly at the end regions of the bones near the joints, the midshaft, or diaphyseal region, has been reported as fairly uniform and nearly even in the frontal and sagittal planes. For the average human adult male the femoral shaft diameter has

been reported as 29mm with less than 10% difference between frontal and sagittal dimensions [134, 135], and the tibial width has been reported as 28mm [136]. Because the width of the tibia has been reported to be similar to that of the femur, and for simplicity in the model approximation, the outer diameters of both the tibia and the femur were 30mm in this study. This value has been used previously in published computational models of the long bones of the leg [93, 95].

Because the midshaft of the diaphyseal region of the long bones, such as the femur and the tibia, is hollow, the thickness of this cortical shell must be properly represented. The cortical wall thickness in the shafts of long bones is often assumed to be uniform [86, 87]. An outer radius twice that of the cortical shell thickness in the long bone shafts has been consistently measured for humans as well as many other land mammals [13, 14, 134, 137-140]. If both the tibia and femur bones are represented as simple hollow circular cylinders with a 30mm outer diameter, then this ratio gives a cortical wall thickness of 7.5mm and an inner diameter of 15mm. These dimensions fall within the range of published measurements of actual human adult bones [135].

At the ends of the femur and tibia bones, near the hip, knee, and ankle joints, the hollow cortical shell is filled with cancellous bone. The necessity of simulating this tissue configuration was the subject of a preliminary study. Models were created depicting the femur and tibia as either solid structure made of cortical bone tissue, a hollow structure made of cortical bone tissue, or a composite structure with a hollow cortical shell and cancellous bone tissue-filled end regions each comprising 12% of the total length of the bone [140]. For simplicity, the material composition of the pelvis and foot followed the same options: either completely made of cortical bone tissue,

completely hollow, or completely filled with cancellous bone tissue. A single static load was applied to the foot, and the bottom surface of the pelvis was constrained in all degrees of freedom. These preliminary studies were carried out using ANSYS v.12.1 [141], the commercial finite element code that was used throughout the work presented.
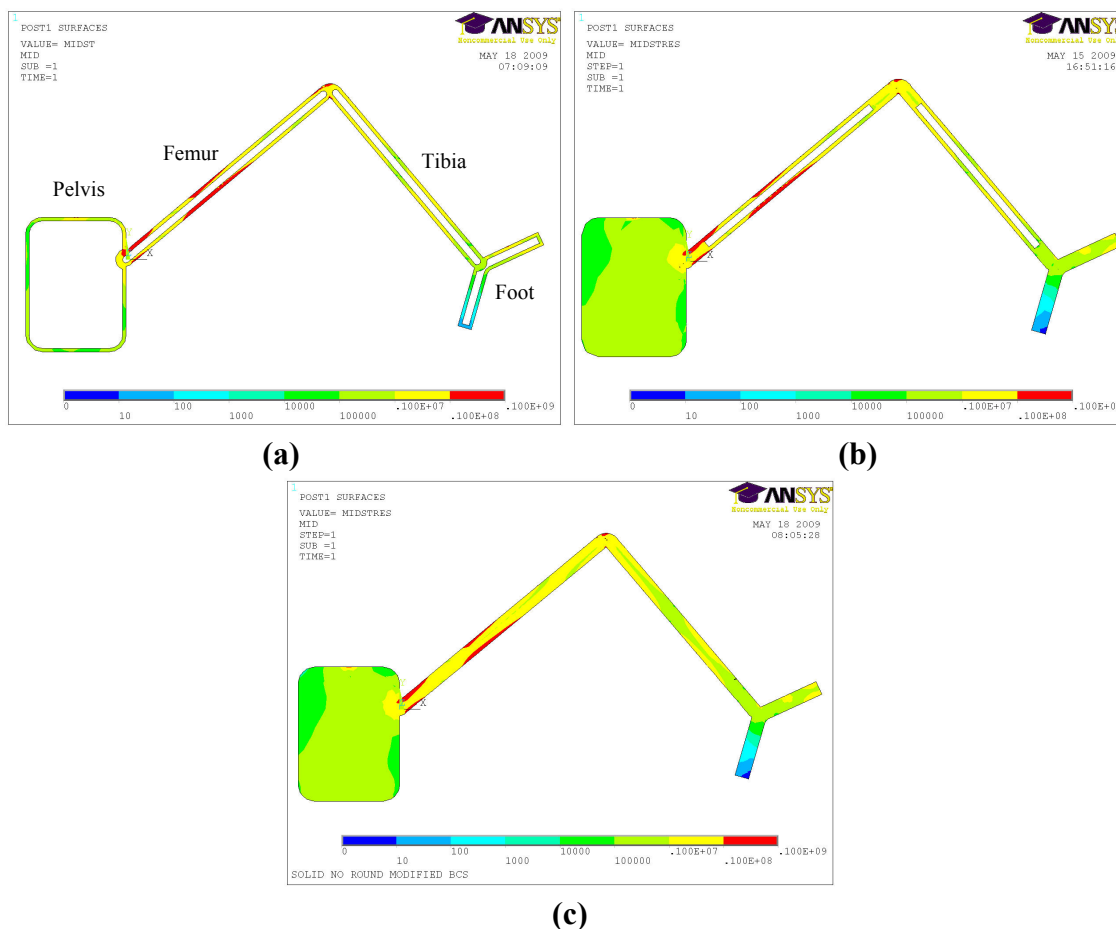
Figure 2.4 Comparison of von Mises stress distributions for same loading and boundary conditions and geometry for (a) hollow cortical shell (b) cortical shell with cancellous where appropriate (c) solid cortical geometries.

The comparison of the stress and displacement distributions in models representing the femur and tibia as solid cortical components, hollow cortical shells, or hollow cortical shells with cancellous bone tissue at the ends showed that, while the solid cortical model was the most rigid and the hollow the most flexible, nearly identical stress

distributions resulted for all cases except at the locations of highest displacement and at the locations of the joint interfaces (Figure 2.4). On average, the inclusion of the cancellous bone tissue showed a 13% reduction in the deflection over the completely hollow case but a 20% increase in deflection over a completely solid case. Similarly, the stresses in the model with cancellous bone tissue at the ends of the long bones showed approximately a 5% decrease in maximum stress values over the completely hollow case and about a 5% increase in the maximum stress values of the completely solid case. The inclusion of the cancellous bone reduced the stress concentrations at the joint interfaces compared to the completely solid geometry while also decreasing the maximum stresses due to the large deflections of the completely hollow geometry. Therefore, the inclusion of the cancellous bone tissue at the ends of the femur and tibia and in the interior regions of the foot and pelvis was justified. In all the bony volumes, the two regions of different bone tissue material were modeled as independent volumes in perfect contact with each other through the use of shared nodes at the interfaces [16, 17, 119]. Figure 2.5 depicts the simplified geometry and the actual bone geometry for the femur (Figure 2.5a) and the tibia (Figure 2.5b).
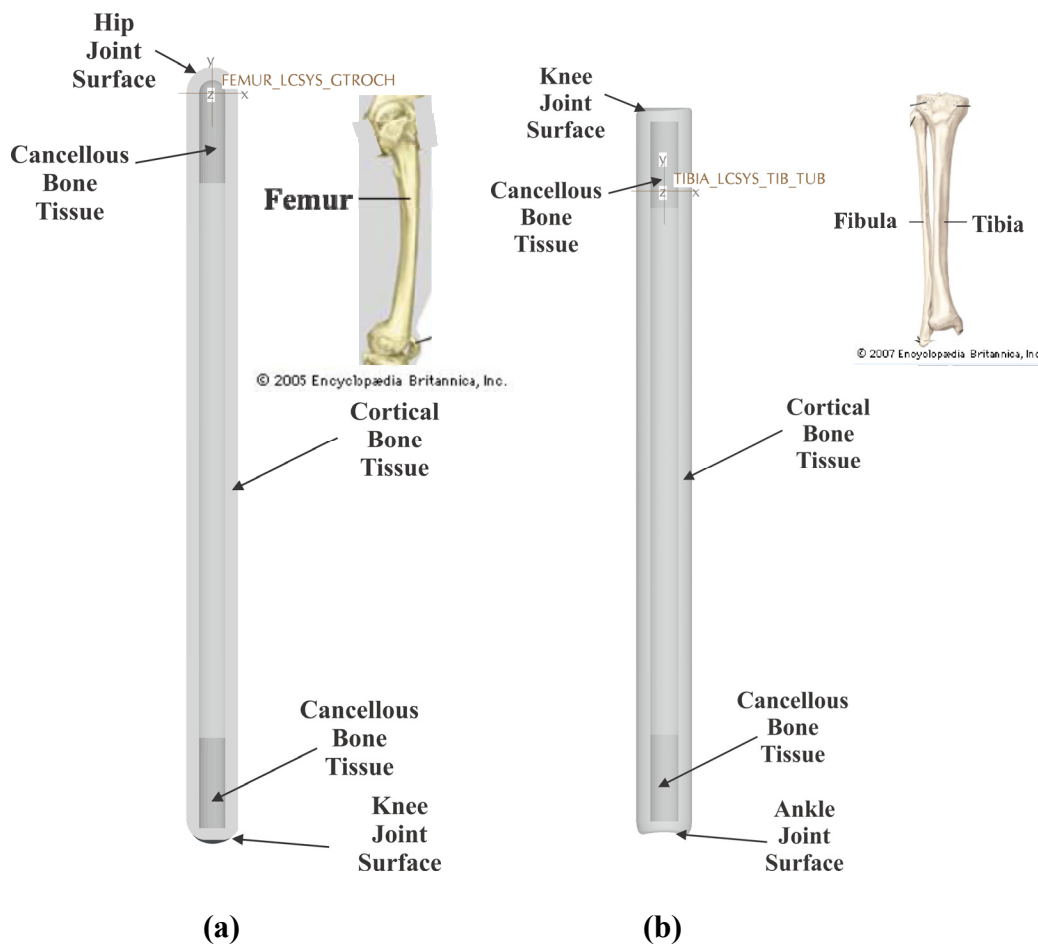
Figure 2.5 Model representations of the (a) femur (sagittal view) (b) tibia (anterior view) used in this investigation. Insets show image of actual bone.

Figure 2.5a inset: Source: "patella." [Art]. In Encyclopedia Britannica. Retrieved from http://www.britannica.com/EBchecked/media/47969/Skeletal-and-muscular. Accessed 10/14/13. Copyright 2005 by Encyclopedia Britannica, Inc. With permission.

Figure 2.5b inset: Source: Adapted from "radius: radius, ulna, fibula, and tibia." [Art]. In Encyclopedia Britannica. Retrieved from http://www.britannica.com/EBchecked/media/47235/The-radius.   Accessed 10/14/13. Copyright 2007 by Encyclopedia Britannica, Inc. With permission.

Pelvis

The pelvis geometry was modeled as a two-dimensional, sagittal view of the adult human

pelvis, extruded by a uniform thickness. The profile geometry was created from a series

of thirty-five points taken from a three-dimensional mapping of the human pelvis of a

medium sized male (1.74m tall, 76kg mass) [132]. This published study mapped 123

bony landmarks from a number of skeletal pelvises and then averaged these mappings for

six size groups for both male and female human adults. The thirty-five points selected for the creation of the pelvis profile used in this work were those that created a cross section slice of the pelvis at a location that aligns with the midplane of the femur bone. Care was taken to ensure that all points of attachment of the muscles used in this study to the model of the pelvis developed for this work were accommodated for in the creation of this cross-sectional profile either directly or as a projection onto this plane. Verification of this placement of the muscle attachment points was made through comparisons to published drawings of the sagittal view of the entire human leg [142]. Similarly, the profile of the pelvis developed here was verified through visual comparison to publications of the human skeleton [143, 144].

As described above, the developed two-dimensional profile became a three-dimensional bone segment through a linear extrusion of uniform depth, which was twice the diameter of the femoral bone, or 60mm. This value was selected to reduce artificial numerical effects that might result at the hip joint interface between the simplified pelvis and femur bone geometries.

The pelvis was modeled as a cortical shell with the entire inner volume filled with cancellous bone tissue [17]. (See Figure 2.6.) For simplicity, the cortical wall thickness of the pelvic bone segment in this model was approximately the same as that used for the femur and tibia bones. However, to accommodate the profile shape, a 7.2mm shell thickness was used.
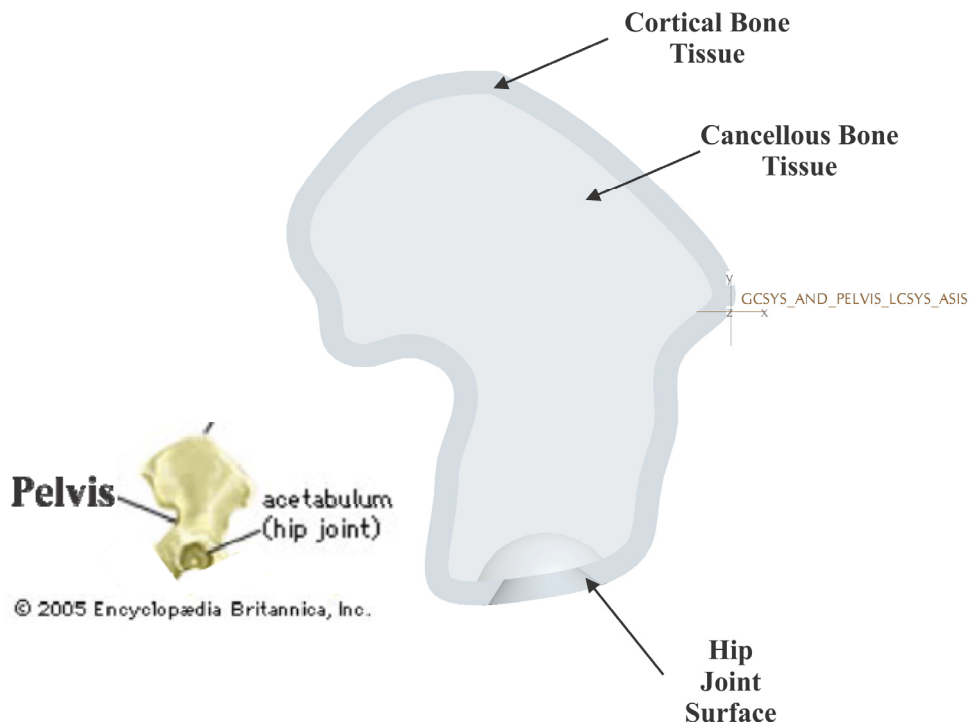
Figure 2.6 Model representation of the pelvis used in this investigation. Inset shows actual bone.

Inset Source: "chimpanzee: pelvis." [Art]. In Encyclopedia Britannica. Retrieved from http://www.britannica.com/EBchecked/media/45433/Comparison-of-the-pelvis. Accessed 10/14/13. Copyright 2005 by Encyclopedia Britannica, Inc. With permission.

Foot

As with other bone segments, the foot geometry was modeled based on published measurements of the locations of boundary-defining bony landmarks for an averaged sized adult male [131, 145]. Similar to the pelvis, the foot boundary was based on a slice through the midplane of the adjoining long bone, here, the tibia. The locations of the ends of the heel and the long toe (or second toe) were used to define the overall length of the foot, 252mm. The length of the calcaneous, or heel bone, measured 57mm from the end of the heel to the approximate center of ankle joint. The profile was verified through comparisons to published anatomical drawings of the foot [146]. The simplified foot generated for this model had a uniform depth defined as the distance from the first to the

fifth metatarsal (toe bones) and measuring 60mm [131]. Because the forefoot is comprised of many small bones, it was assumed to be a solid volume of cortical bone tissue. Cancellous bone tissue was included only in the hind foot region, from the heel to the navicular tubercle [131, 146]. In this region, a uniform cortical shell 7.5mm in thickness was assumed, following the cortical thickness used for the femur, tibia, and pelvis bone segments. (See Figure 2.7.)
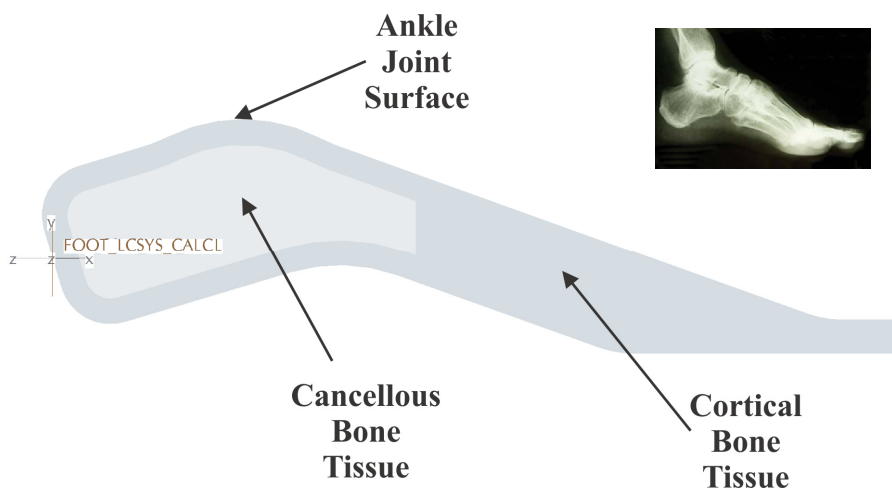
Figure 2.7 Model representation of foot used in this investigation. Inset: X-ray of actual human foot for comparison.

Inset Source: "X-ray: X-ray of a human foot." [Photograph]. In Encyclopedia Britannica. Retrieved from http://www.britannica.com/EBchecked/media/136119/X-ray-of-a-human-foot. Accessed 10/14/13. With permission.

Joints

Based on the studies reviewed in Subsection 1.2.4.3, static, isometric loading may lead to the best improvement in bone strength. The joint interfaces in the models developed in this work were created to simulate the function of the hip, knee, and ankle joints under this kind of activity, which maintains constant joint angles. Under these kinds of static loading conditions, the proper transfer of forces from one bone segment to the next is of importance. Therefore, ensuring the appropriate simulation of the joint function over a

large range of motion was not necessary. As such, the mating geometries at the joints were simplified considerably.

Contacting geometries at the hip joint were modeled as a concave hemisphere in the inferior (bottom) region of the pelvis and a convex hemisphere at the superior (top) end of the femur bone (Figure 2.8a). For the ankle joint, matching concave and convex linearly extruded curves were used (Figure 2.8c). The knee joint geometry was the most complex of the three joints included in this model (Figure 2.8b). The basic shape was approximated using published anatomical drawings of the mating ends of the femur and the tibia [143, 144, 146]. The femoral condyles on the distal end of the femur bone were included, but only roughly approximated. The geometry was further modified to prevent interference between the femur and the tibia as the knee joint was rotated through 90° of flexion. The joint geometry was verified through a comparison of the distance between the tibial tuberosity, which is the location of the origin of the tibia's local coordinate system, and the knee joint surface on the superior (top) end of the tibia in this model to the approximately 32mm reported in published literature [147].
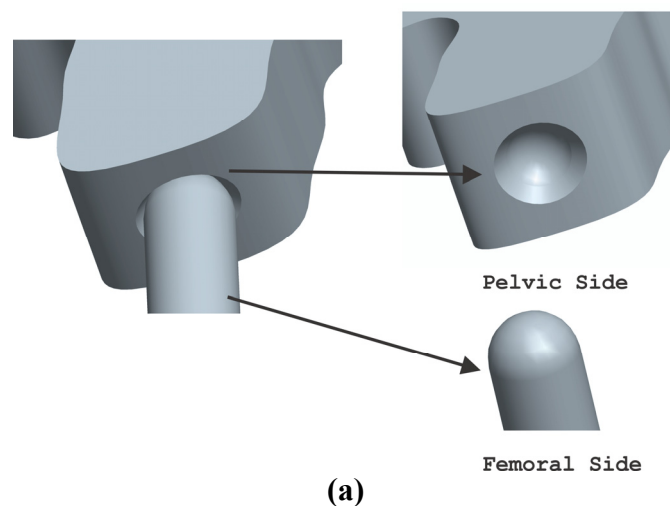
Pelvic Side

Femoral Side

(a)

Figure 2.8 Joint interfaces used in this model for (a) hip (b) knee (c) ankle.

Femoral Side

Tibial Side

(b)

Tibial Side

Foot Side

(c)
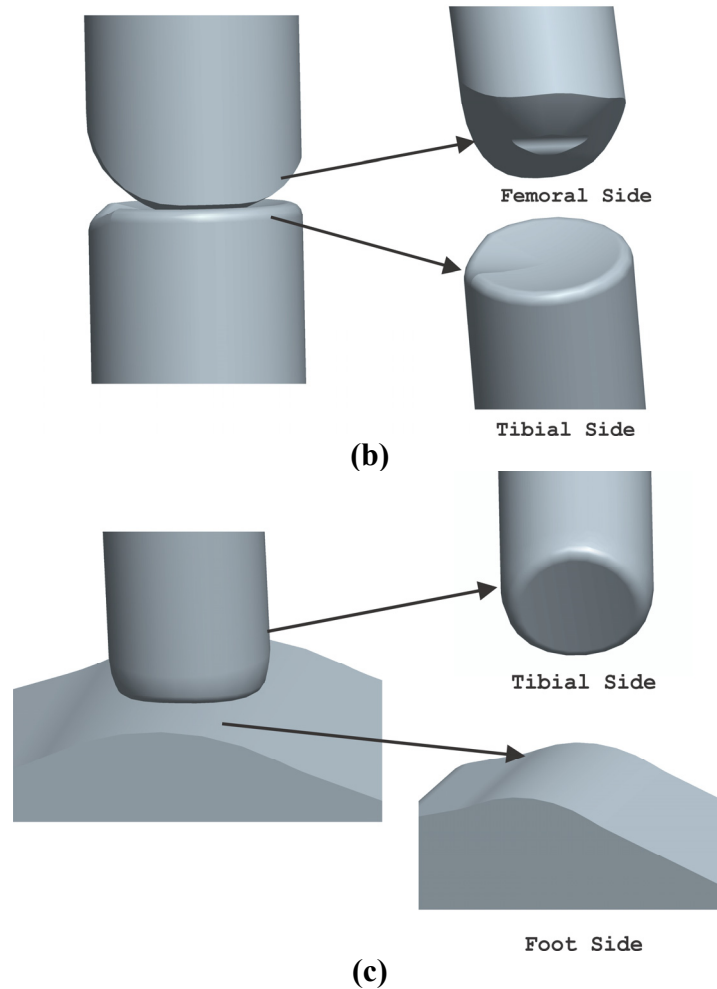
Figure 2.8 Joint interfaces used in this model for (a) hip (b) knee (c) ankle. (Continued)

The mating joint surfaces of the four bone segments in this model were in direct contact and remained so during loading and unloading of the bones. The soft tissues at the joints, cartilage and ligaments, were not modeled directly. Instead a joint contact model that simulated compliance between mating surfaces was employed to simulate the function of these soft tissues under the fixed limb conditions investigated. The joint contact model allowed mating nodes, elements and surfaces to remain independent for each bone volume but simulated the interactions of these components during load application. A series of preliminary studies was performed to determine the appropriate joint contact modeling parameters.

In simulating the cartilage-on-cartilage mating surfaces, frictionless joint contact was assumed and an augmented Lagrange multiplier contact algorithm with flexible-flexible contact pairs was used [148, 149]. ANSYS's built in contact module, which uses this method, was employed. ANSYS provides five standard contact models to simulate such an interaction. Each has a series of accompanying parameters that allow the contact algorithm to be adjusted for the particular conditions simulated. During these preliminary joint surface interaction studies, each of these contact models and their associated parameter settings were compared to a reference case in which the joints of the leg were modeled as rigidly united mating volumes with shared nodes and, therefore, included no joint compliance.

The contact models and parameters investigated varied in the type and the amount of relative motion allowed between mating surfaces and how the pairs of mating nodes were identified. The three main joint interaction (contact) models available in the software used were evaluated. These models selected mating (contacting) nodes by directly comparing the nodal coordinates from the contacting pair of surfaces. The first model ties the contacting nodes to prevent motion both tangential to (sliding) and motion normal to (separation) the contacting surfaces. The second model allows for tangential but not normal motion (sliding but not separation). The third model allows for both normal and tangential motion (sliding and separation) of contacting nodes. Two additional models were studied that were slight modifications of the first two described. These used tolerance bands, rather than exact positions, to determine nodal contact status for the tied node and no separation, sliding only, surface interactions, respectively. The

range of the tolerance band used in these contact models was a percentage of the thickness of the element directly adjacent to the contacting surface.

Modeling parameters related to how much motion between mating nodes (or compliance) is allowed for each of the five motion model types considered were studied. Compliance at the joint interface was simulated in the contact models through the use of a contact spring stiffness. The contact stiffness value was a percentage of the elastic modulus of the contacting materials. Comparisons were made for contact stiffness values equaling 1%, 10% and 100% of the cortical bone elastic modulus. Because the contact model is solved iteratively, the contact stiffness value can either be adjusted by the contact algorithm based on the values calculated at each iteration or held constant for the entire solution. Both methods were compared in this preliminary study. The five contact models and their additional parameters were evaluated for solution stability and run time. The maximum von Mises stress and maximum deflection within the entire model and locally at each joint were compared. Based on the results of the preliminary investigation, the joint contact model parameters used for the remainder of the study were chosen.

The five main types of contact models were first examined. When compared to the model that allows for no separation or sliding through tied contacting nodes, it was found that models that allowed for sliding or both sliding and separation resulted in a two and four fold increase in runtimes, respectively, and the same order of magnitude decrease in measures of solution stability. The sliding or sliding and separating models also resulted in 80% and 60% higher contact stresses, respectively, compared to the tied node models. The models that allowed for separation and sliding had slightly lower contact stresses than the model that allowed only for sliding due to the ability for gaps or

openings to form between the contacting surfaces, thus releasing the contacting node couples from the calculations. These separation and sliding models also allowed for nearly twice the overall model maximum deflection than the tied node models because more motion at the joint was allowed. This increased motion lead to decreased stresses at locations far from the joints and significantly increased stresses locations near the joints, for example, at locations where impingement between mating volumes occurred due to the reduced restriction on the motion at the joints. Such models that allow for freer motion may be most appropriate when large alterations in joint angles due to the applied loads are expected, which was not the case for the desired modeling conditions.

When compared to the rigidly fixed model, the tied node model had the most similar overall von Mises stress distributions, with a slight (5-10%) increase in overall deflection and significantly decreased stresses near the joints due to the greater joint compliance. Hence, even though relative motion (sliding and separation) between contacting surfaces was restricted by the tied node model, the compliance added by the contact model improved the representation of the loading response at the joints without affecting the overall prediction of the bone stresses due to applied loads. Therefore, this type of restriction might be most appropriate for modeling a static loading condition for a fixed limb configuration where no changes in joint angles are expected.

The inclusion of a tolerance band to determine the contact status of node pairs improved the solution stability by as much as 80%. The tolerance band used in this study was 5% of the thickness of the model element underlying the contact element. Therefore, the element size in the joint region can affect the amount of stability improvement. To investigate this effect, the mesh near the joint contact surfaces was varied up to 50%.

While no changes in overall stress magnitudes or distributions were found far from the joints, significant differences were noted in the contact stresses and in the von Mises stresses in regions surrounding the contacting surfaces.   Thus, the mesh size near the joints in models that include a tolerance band based selection of contacting pairs should be selected to ensure stability of the contact model solution while limiting the stress concentration effects of boundary condition discontinuities at the contacting surfaces.

As the value of the contact stiffness parameter increased, the overall maximum model deflection and the maximum von Mises stress near the joints decreased. However, the relationships between the stiffness parameter and these results were not linear. The greatest differences with variation in the contact stiffness, 40% in deflection and 60% in stress, occurred between joint contact stiffness values of 1% and 10% of the elastic modulus of cortical bone, while only a 10% decrease in deflection and a 1% decrease in stress occurred between joint contact stiffness values of 10% and 100% of the elastic modulus of cortical bone.   The run times varied only slightly due to these differences in joint compliance. A 15% overall decrease in run time with similar nonlinear trends was found over the range of contact stiffness values studied. In contrast to using a constant value of contact stiffness, when this parameter is allowed to vary during the solution of the contact model, the run time increased eightfold and the maximum stress varied as much as 150%. Based on this study, a contact stiffness of 10% of the elastic modulus of the underlying cortical bone showed the most significant beneficial effect on local and contact stresses without adverse effects on the solution stability or the overall stress distributions. This value correlates, in order of magnitude comparison when considering

the element size of the mesh used in this study [150], to the modulus of the actual cartilage that comprises the actual joint interfaces [151].

Based on this study of the available joint contact models and related parameters, the model selected for use in this work included tied nodes to prevent relative motion of contacting surfaces, but allowed for a 90% reduction in material compliance at the joints (10% contact stiffness). It was desired that the stiffness value remained constant during the solution of the contact model and that a tolerance band of 5% of the underlying element thickness was used to determine the contact status of selected tied nodes. With the representation of the bones and their interfaces established, the representation of the muscles within the model was next determined.

2.1.2.2 Representation of Included Muscles. Of the almost fifty muscles/muscle segments in the human leg [152], ten muscles which are known to contribute most to the production of sagittal plane forces were selected for inclusion in this model (See Table 2.1). While other muscles may contribute to the activities studied, their major function is out of the plane considered here, and, so, their effect is assumed to be negligible [153-156].

As described in Subsection 1.3.2.3, an accurate representation of the boundary conditions, especially the muscle forces, is important in predicting realistic responses of musculoskeletal systems to applied loads. As such, care was taken when selecting modeling parameters related to the muscle forces, particularly the bone attachment areas over which the muscle forces were applied, the lines of action of the muscle forces within the system studied, and the cross sectional areas of the muscles, which were used in the determination of the muscle force magnitudes.

The first consideration in the representation of the muscles in the model developed for this work was related to the way in which the forces functioned in the model. Physically, muscles attach to bones via connective tissue called tendons, which have much smaller cross-sectional areas than do the muscles. As described in Subsection 1.2.3.1, previously published studies have shown that stress concentrations can develop if a muscle force is represented through only a single node. Therefore, in this model, the muscle forces acted on bones over areas representing the average cross sectional diameter of human tendons, regions 9mm in size [13, 157-159].

The next modeling area to be defined is the representation of forces generated by the muscles. Muscles were not modeled physically. Instead, the geometric model developed contained only the bones of the musculoskeletal system analyzed, and the muscles were represented as forces acting upon these bones. Accordingly, the locations and areas of the force application and the directions of the muscle force vectors had to be defined. Because a multi-bone system was considered in this work, muscles acted completely within the system analyzed so equal muscle force magnitudes were applied at both locations of attachment. (See Figure 2.12 for a definition of these points.) These locations were determined from the literature [131]. The muscles were assumed to act as straight lines between these origin and insertion points [160]. When necessary, such as when this straight line passed through the bone geometry, intermediate points were used to better define the muscle force path [156]. (See Figure 2.9.) Additional forces were not applied at these intermediate points. They were only used to change the direction of the force vector around a joint, such as around the knee. These lines of action of each muscle force were dependent on the relative orientation of the bony segments.
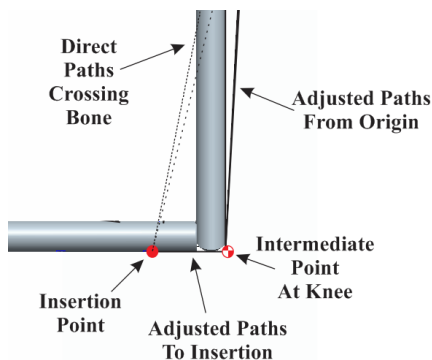
Figure 2.9 Example of use of intermediate point in muscle force line of action about the knee joint.

By defining the joints crossed by each muscle and where they act on each bone in the system, the effects of each muscle on the motion or stability of each joint can be better understood. Table 2.2 defines the joints crossed by each muscle included in the model used in this work. It also lists whether the muscle acts on the front (anterior) or the back (posterior) of the leg system modeled, giving an indication of whether it increases the angle of the joint it crosses (called extension) or decreases it (called flexion). Figure 2.10 shows the overall physical model of the musculoskeletal system of the leg used in this work. The included bony segments, joints, and the lines of action of the muscles for a straight leg configuration are shown. In this figure, an illustration of an average sized adult male is placed alongside the developed model for reference.

Table 2.2 Joints Crossed By Each Muscle

MUSCLE	Location	HIP	KNEE	ANKLE
Sartorius (SART)	Anterior	✓	✓	
Rectus Femoris (RF)	Anterior	✓	✓	
Iliacus (Ipsoas) (IL)	Anterior	✓		
Gleuteus Maximus (GM)	Posterior	✓		
Long Head Biceps Femoris (LHBF)	Posterior	✓	✓	
Tibialis Anterior (TA)	Anterior			✓
Soleus (SOL)	Posterior			✓
Gastrocnemius (GAST)	Posterior		✓	✓
Vastii (VAST)	Anterior		✓	
Short Head Biceps Femoris (SHBF)	Posterior		✓	
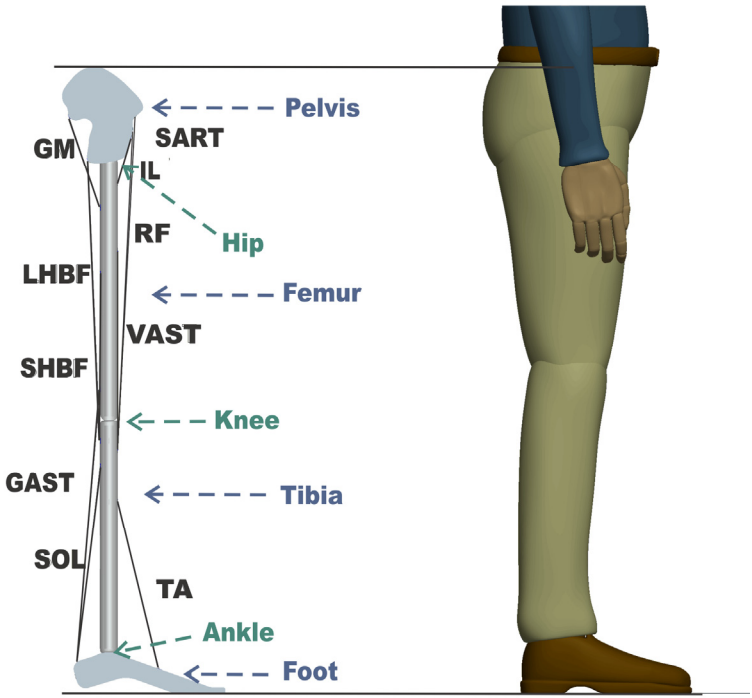
Figure 2.10 Full musculoskeletal model of the leg system used in this study with same-scaled image of average adult male, indicating appropriate assembly height of model.

A geometric parameter not included in the physical model, but important in the determination of individual magnitudes of muscle forces as described in Chapter 3 is the physiological cross sectional area of the muscle (PCSA). The PCSA is widely used as a measure of the overall size of the muscle and is an indicator of the relative muscle strength [161]. The PCSA is calculated as the ratio of the volume of the muscle to its length. Both of these physical parameters are usually measured from cadaveric or MRI studies. While their values can vary significantly between individuals for a given muscle or even between different states of muscle activation for the same activity performed, the relative sizes of the muscles within a system and, therefore, their relative force producing capabilities and strengths are similar between different individuals.

Because the PCSA is often used to determine the individual muscles forces, the effect of the variability of the values of the PCSA used in these models has been the subject of much study. While the values of the muscle PCSA used to predict muscle forces have been shown to significantly affect the muscle force magnitudes, the trends in the relative muscle forces in a given musculoskeletal system are repeatedly predicted, regardless of the PCSA values used [162, 163]. This is important because these trends can be directly compared to trends in experimental measurements of the electrical activity produced by active muscles. Interestingly, resultant forces made from the sum of individual muscle forces, have been shown to be less sensitive to the values of PCSA used, as the sum acts to "balance out" the differences [163].

The physiological cross sectional areas of the ten muscles used in this study were defined as the average of the measurements reported in eight published studies [163-171]. Because of the wide range of values reported for many of the muscles, the average was

taken excluding the extreme reported values. Table 2.3 shows the average and extreme

PCSA measurements from the literature surveyed for the muscles included in this model.

In order to understand the effects of these exclusions, the differences between the average

including and excluding the extremes are reported. Refer to Table 2.2 for key to muscle

name abbreviations.

Table 2.3 Average Physiological Cross Sectional Areas (PCSA) Reported in the
Literature for the Muscles Used in this Study (cm^2)

Muscle	Average	Max	Min	Average Excluding Extremes	Difference of Average Excluding to Average Including Extremes
SART	3.9	5.9	2.7	3.6	-8%
RF	33.9	54.1	9.2	36.5	8%
IL	21.7	31.0	8.8	23.0	6%
GM	49.4	60.8	32.3	51.0	3%
LHBF	30.2	48.0	9.1	31.6	5%
TA	18.0	39.5	8.5	18.1	1%
SOL	118.0	230.0	38.0	97.8	-17%
GAST	44.6	68.0	17.0	40.9	-8%
VAST	79.1	147.8	16.5	90.0	14%
SHBF	9.3	19.4	4.7	9.9	6%

Note: Data averaged from values reported in [163-171].

The musculoskeletal model described above, while developed to sufficiently

represent all of the basic functional components of the musculoskeletal system studied,

does contain significant simplifying assumptions. Therefore, the use of this model, as is

the case for any model, whether numerically or experimentally based, is valid only under

the circumstances specified. The valid system conditions selected in this work were

based on those that have experimentally produced the most significant effects on overall

bone shape, and, therefore, bone strength adaptations, as reported in Chapter 1. The specific system conditions studied will be explained next.

2.1.3 System Configurations Studied

The assumptions used in the generation of the models of the bone geometry and muscle placement and in the models of the interfaces of the bony segments at the joints described in Subsection 2.1.2 limited the types of activities that could be simulated using the developed system representation. The limitations restricted the types of forces generated by the system investigated. The model of leg musculoskeletal system studied used in this work, from pelvis to foot, while three-dimensional in geometry, was symmetric at the midplane and considered only forces in the sagittal plane. Therefore, the actions studied using this model were limited to this plane and included flexion or extension of the hip, knee or ankle joints. Torsion about the long axis of the leg and out-of-plane forces or motions, such as abduction or adduction, were considered negligible. As follows, muscles whose main actions were these kinds of out-of-plane forces were excluded from the model. Such an assumption simplified the process for the determination of the individual muscle forces by limiting the size of the set of unknowns, and this approach has been widely used [153-156].

The joint contact model chosen for this work, described in Subsection 2.1.2.1, restricted the relative motion at the hip, knee, and ankle joints. Therefore, the model was limited to the study of static activities or dynamic activities simulated through iterative, quasi-static approximations. The current study did not consider any dynamic loads and focused only on static, isometric exercises. Isometric exercises are those where the joint angles do not change due to muscle activity, such as when applying a resultant force

against an immovable object or when holding a weight at a particular location for a given period of time.

2.1.3.1 Specific Limb Configurations Studied and System Parameters Used. The study of isometric loading of the leg using the developed model was applied to three different limb configurations. While all other aspects of the musculoskeletal model and finite element mesh were identical for each configuration studied, by varying the hip, knee, and ankle joint angles, the joint interfaces and muscle force vectors varied. Therefore, the effects of a range of loading conditions could be compared as is discussed in Chapter 5. Figure 2.11 shows the three configurations studied, including the lines of action for each included muscle. The global coordinate systems and the local coordinate systems for each bony segment are shown as are the boundary constraints. The top of the pelvis was fixed in all degrees of freedom, representing the mass of the upper body. The toe, through which the resultant load was applied to a fixed surface in the parametric loading studies conducted in the second phase of this research, was also constrained in all degrees of freedom. The three limb configurations are named for the angle created between the longitudinal axis of the tibia bone and the global y-axis so that the 0° configuration is that shown in Figure 2.11a, the 45° configuration is that shown in Figure 2.11b, and the 90° configuration is that shown in Figure 2.11c.
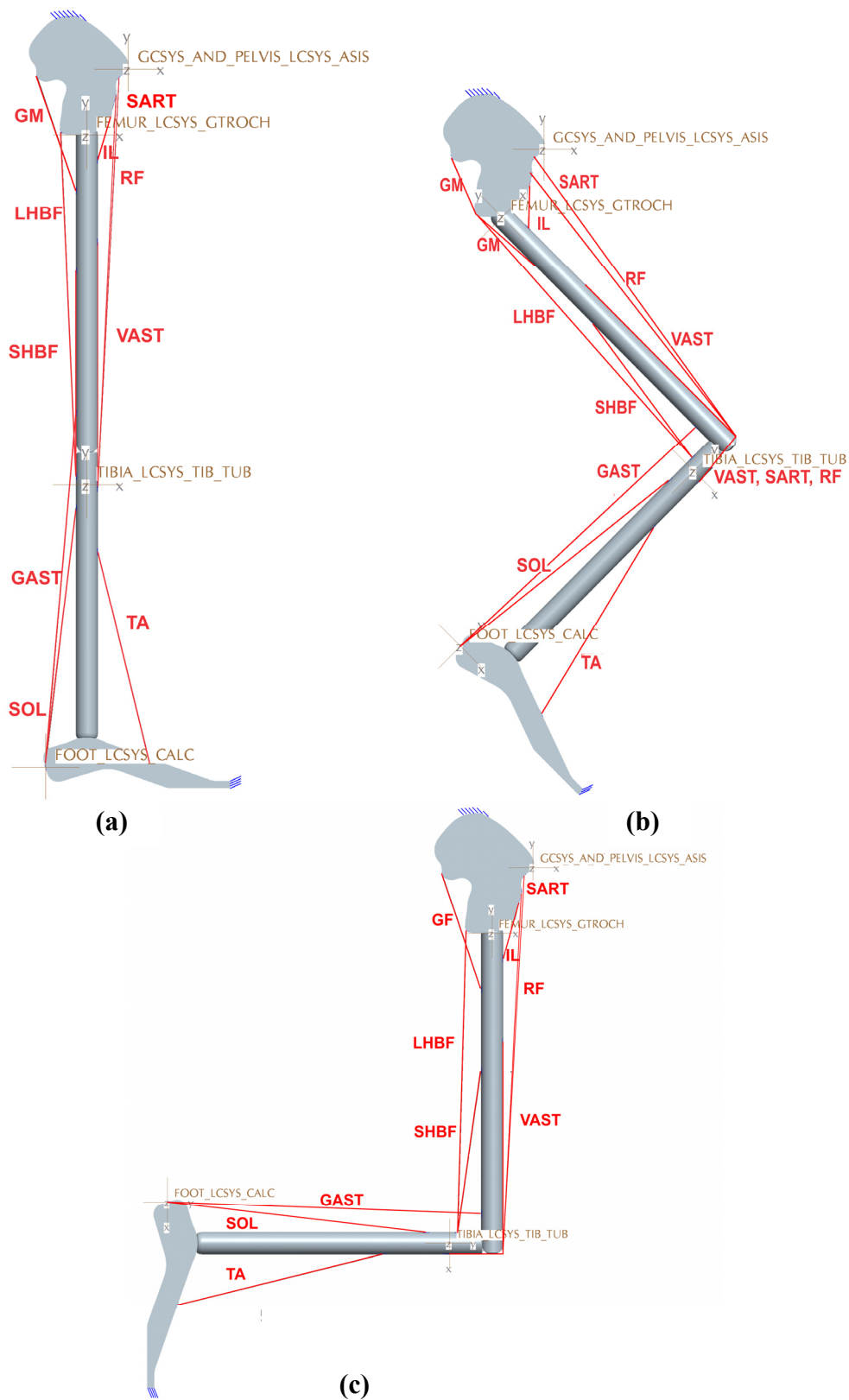
Figure 2.11 Bone segments, lines of action of muscle forces, local and global coordinate systems, and boundary constraints for (a) 0° (b) 45° (c) 90° limb configurations studied.

The geometry was created using three-dimensional solid CAD modeling techniques and then discretized. This process is now explained in detail. Because a joint contact model was used in analyzing this leg system, each bony segment, the pelvis, the femur, the tibia, and the foot, remained an independent volume. The geometries for each volume were created separately using the three-dimensional CAD modeling software Pro/Engineer Wildfire 4.0 [172]. The local coordinate systems for each bone volume defined in Subsection 2.1.2.1 were created. From these local coordinate systems, each set of muscle origin and insertion points defined in [131] were marked. The bone volumes were then assembled using this same CAD software to create the configurations shown in Figure 2.11. The assembly global coordinate system coincided with the local coordinate system of the pelvis. Lines, which denoted the muscle force vectors, were drawn connecting the origin and insertion points for each muscle in each assembly.

A number of geometric measurements were taken from this model, using the CAD software's built-in tools for use in determining the individual muscle forces, bone stresses and relative orientation of the bone segments in each configuration studied. Translation and rotation measurements were taken between the global assembly system and the local coordinate system for each segment in each limb configuration assembly for the cases shown in Figure 2.11. These measurements were used in the finite element and the bone shape adaptation models to transform the nodal positions from the global to the local coordinate systems or to move bone segments to the desired study configurations. Table 2.4 lists the coordinate system transformation parameters.

Table 2.4 Coordinate Transformations from Global to Local for Each Bony Segment

Configuration	Coordinate Name	Pelvis LCSYS (Anterior Superior Iliac Spine)	Femur LCSYS (Greater Trochanter)	Tibia LCSYS (Tibial Tuberosity)	Foot LCSYS (Calcaneous)
0°	X (m)	0.0000	-0.0560	-0.0560	-0.1120
	Y (m)	0.0000	-0.0894	-0.5393	-0.9521
	Theta Z (deg)	0.0	0.0	0.0	0.0
45°	X (m)	0.0000	-0.0560	0.2000	-0.1116
	Y (m)	0.0000	-0.0894	-0.4274	-0.6598
	Theta Z (deg)	0.0	45.0	-45.0	-45.0
90°	X (m)	0.0000	-0.0560	-0.1139	-0.4987
	Y (m)	0.0000	-0.0894	-0.5094	-0.4534
	Theta Z (deg)	0.0	0.0	-90.0	-90.0

Additionally, the directions of each of the muscle vectors were defined for the three limb configuration cases in Figure 2.11 as the angle between the "muscle lines of action" and the global y-coordinate (see Figure 2.12). The directions of each muscle force (Figure 2.11) acting on each bone segment as defined in Figure 2.12 are provided in Tables 2.5 through 2.7. Note that the "origin bone" is the bone connected to the muscle that is located most proximal (closest to whole body center), while the "insertion bone" is the bone connected to the muscle that is located most distal (furthest away from whole body center).
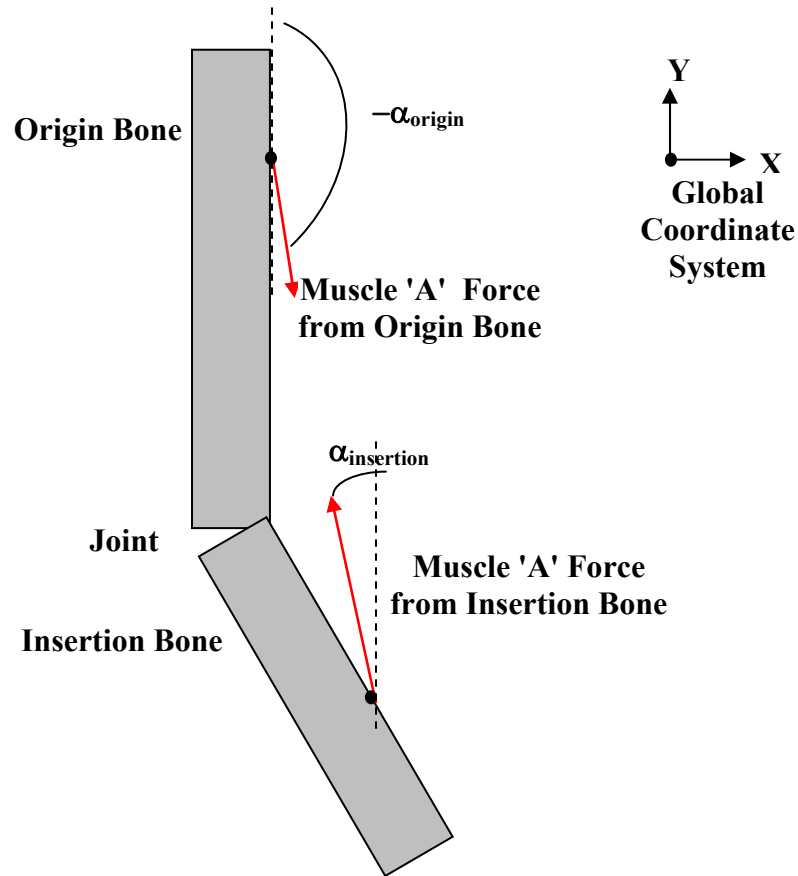
Figure 2.12 Definition of angle, α, used to define the direction of the muscle force on each bone segment. All angles are defined with respect to the global Y-coordinate, with counterclockwise as positive.

Table 2.5 Angular Direction, α, of Muscle Force Application on each Bone Segment for the 0° Configuration (degrees)

Muscle	Origin Bone	Origin α	Insertion Bone	Insertion α
SART	Pelvis	177.044	Tibia	-2.956
RF	Pelvis	177.321	Tibia	-2.679
IL	Pelvis	164.173	Femur	-15.827
GM	Pelvis	-161.278	Femur	18.722
LHBF	Pelvis	-177.568	Tibia	2.432
TA	Tibia	-166.182	Foot	13.818
SOL	Tibia	173.370	Foot	-6.629
GAST	Femur	175.145	Foot	-4.855
VAST	Femur	180.000	Tibia	0.000
SHBF	Femur	180.000	Tibia	0.000

Table 2.6 Angular Direction, α, of Muscle Force Application on each Bone Segment for the 45° Configuration (degrees)

Muscle	Origin Bone	Origin α	Insertion Bone	Insertion α
SART	Pelvis	-144.008	Tibia	-45.000
RF	Pelvis	-141.915	Tibia	-45.000
IL	Pelvis	177.440	Femur	-2.560
GM	Pelvis	-156.614	Femur	48.676
LHBF	Pelvis	-138.266	Tibia	41.723
TA	Tibia	148.818	Foot	-31.182
SOL	Tibia	128.371	Foot	-51.629
GAST	Femur	132.857	Foot	-47.143
VAST	Femur	-135.000	Tibia	-45.000
SHBF	Femur	-143.1585	Tibia	-31.183

Table 2.7 Angular Direction, α, of Muscle Force Application on each Bone Segment for the 90° Configuration (degrees)

Muscle	Origin Bone	Origin α	Insertion Bone	Insertion α
SART	Pelvis	176.720	Tibia	-90.000
RF	Pelvis	177.039	Tibia	-90.000
IL	Pelvis	164.173	Femur	-15.827
GM	Pelvis	161.278	Femur	18.722
LHBF	Pelvis	178.405	Tibia	-1.594
TA	Tibia	103.818	Foot	-76.182
SOL	Tibia	83.370	Foot	-96.629
GAST	Femur	87.857	Foot	-92.143
VAST	Femur	-180.000	Tibia	-90.000
SHBF	Femur	171.841	Tibia	-8.159

With the locations of the muscle force application and force directions defined, the moments arms that each muscle created about each joint it spanned were determined from the CAD model assemblies for each of the 0°, 45° and 90° configurations defined in Figure 2.11. (Refer to Table 2.2 for identification of the joints crossed by each muscle in this model.) The muscle force moment arms were also measured from the assembled geometric models using the software's built-in tools. To calculate the moment arms, an imaginary cut was made in the leg system studied just above (proximal to) each joint working from the foot towards the pelvis. The muscles force lines that were severed with

this cut were identified. Lines perpendicular to the severed muscle force lines (or projections of these lines) were drawn and extended to the joint centers. The lengths of these lengths were the measured joint moment arms. Figure 2.13 shows an example of how the joint moment arms were calculated for the 45° configuration.
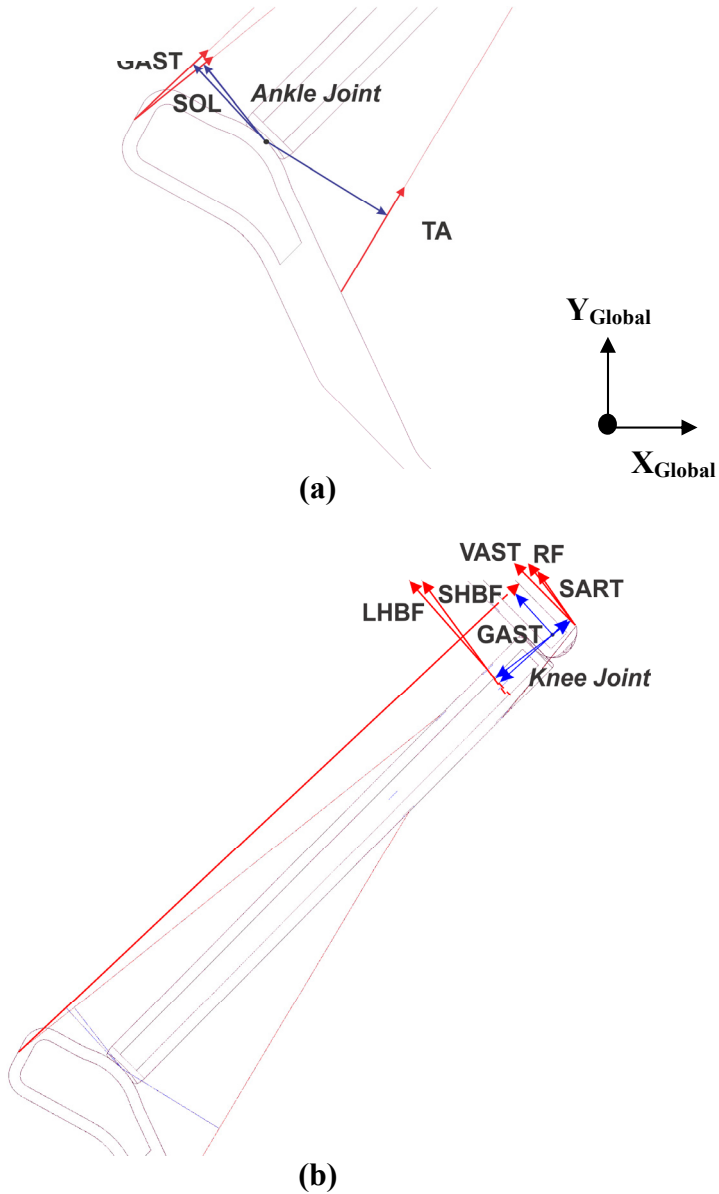
(a)

(b)

Figure 2.13 Determination of muscle force moment arms about each joint in the system studied. Representative case: 45° configuration for (a) ankle (b) knee and (c) hip joints.

(c)
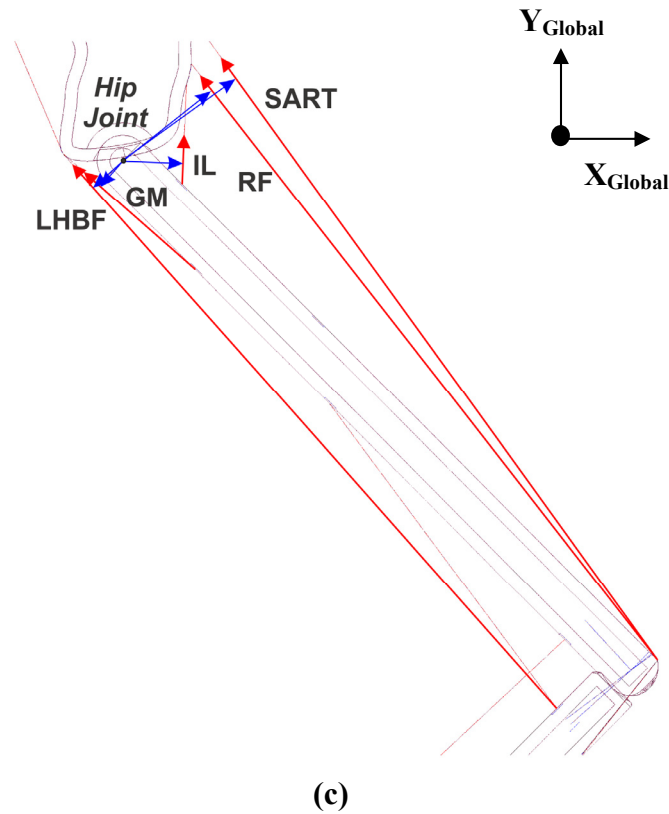
Figure 2.13 Determination of muscle force moment arms about each joint in the system studied. Representative case: 45° configuration for (a) ankle (b) knee and (c) hip joints. (Continued)

The muscle moment arm values used in this model for each configuration studied are listed in Table 2.8. The sign of the muscle force moment arm in the "direction" of the moment arm length was determined based on the direction of the moment created by the severed muscle force. For example, if the muscle created a counterclockwise (positive) moment about the joint, the moment arm of the muscle about this joint was positive. If the muscle created a clockwise (negative) moment about the joint, the moment arm of the muscle about the joint was negative. (Refer to Figure 2.13.)

Table 2.8 Moment arms of Muscles Forces about Joints (m)

Hip Muscles			
Muscle	**0° Configuration**	**45° Configuration**	**90° Configuration**
SART	0.039857	0.081664	0.039402
RF	0.037319	0.066296	0.037032
IL	0.023704	0.035214	0.023704
GM	-0.038279	-0.019778	-0.038279
LHBF	-0.034780	-0.023170	-0.035110
Knee Muscles			
Muscle	**0° Configuration**	**45° Configuration**	**90° Configuration**
SHBF	-0.015000	-0.480569	-0.048057
LHBF	-0.016955	-0.047179	-0.046797
GAST	-0.018331	-0.039411	-0.039411
VAST	0.015000	0.015000	0.015000
RF	0.017690	0.015728	0.015339
SART	0.018198	0.015903	0.015393
Ankle Muscles			
Muscle	**0° Configuration**	**45° Configuration**	**90° Configuration**
TA	0.074938	0.074938	0.074938
GAST	-0.052330	-0.054429	-0.054429
SOL	-0.050894	-0.050874	-0.050894

Note: Direction indicates the creation of a CCW (+) or CW (-) moment.

The identification of the locations of the joint centers was necessary in order to measure these moment arms. (Refer to Figure 2.13 for illustration of each joint center). Some deviations from the locations listed in the reference used [131] were made to accommodate the bone volume geometries created for this model. Because the muscle forces were assumed to act only in a two dimensional plane, and because the end geometries of the long bones in this model ignored the widening as the joints were approached, the location of the greater trochanter listed in [131], which is also the location of the femur's local coordinate system, was used as the center of rotation of the hip [133].   The center of the arc on the distal geometry of the femur was used at the

center of rotation of the knee. The center point of contact between the tibia and foot geometries was taken as the center of rotation of the ankle joint. Despite the deviations from the locations of the joint centers reported in [131], the position of these landmarks in this model with respect to each local coordinate systems correlate well with those reported in the literature.

It should be noted that many different methods have been developed in the published literature to determine muscle moment arms [163, 170, 173-175]. These methods often rely on complex curve fits to experimental measurements of muscle lengths and joint centers over a range of joint angles in a functioning system. The methods described here were based on straight line connections between measurements of bony location markers which were averaged over a wide range of subjects and, hence, are approximations of the actual distances which may be measured in a singular functioning musculoskeletal system. However, the current method is repeatable, not reliant upon curve fit approximations, and, therefore, suitable for the purposes of the comparative studies in this work.

Because static isometric conditions were studied in this work, the net force by the leg system was constant, acting at a fixed region between the toe and an immovable surface (Figure 2.11). Therefore, to solve the conservation of angular momentum equations for each static set of loading conditions in this, the moment that was generated by the reaction force from the fixed surface about each joint was required. The distances between the joint centers and toe region over which the force acts, with respect to the global coordinate system, were measured in CAD model assemblies for each

configuration (set of joint angles) studied using the same built in software tools used to measure the muscle force moment arms and are listed in Table 2.9.

Table 2.9 Resultant/Reaction Force Moment Arms About Joints (m)

Moment Arm Component (Global CSYS)	0° Configuration	45° Configuration	90° Configuration
HIP			
X	0.195000	0.105597	-0.465663
Y	-0.0639824	-0.764144	-0.615000
Z	0.0	0.0	0.0
KNEE			
X	0.195000	-0.191388	-0.195000
Y	-0.465663	-0.467159	-0.465663
Z	0.0	0.0	0.0
ANKLE			
X	0.195000	0.0926434	-0.195000
Y	-0.0639824	-0.183128	-0.639824
Z	0.0	0.0	0.0

With the geometry and the boundary conditions defined, the model was next prepared for the structural analyses under the varied loading conditions studied. This analysis was performed through the use of finite element modeling methods. Therefore, the CAD model bone volumes were discretized into a finite element mesh. Each bony segment volume was only meshed once. The parameters in Table 2.4 were used to transform the meshed volumes into each of the three configurations in Figure 2.11.

2.1.4 Discretization of the Geometry

The preprocessing for the finite element analysis of the bone volume geometries created to represent the pelvis, femur, tibia, and foot was performed using the commercial finite element software package ANSYS/Mechanical APDL [141]. The geometry developed in the CAD software (Pro/Engineer Wildfire 4.0 [172]) was imported into the finite element

software through the use of neutral IGES files. Each bone volume was imported separately and assembled within the finite element software using the global coordinate system defined in Subsection 2.1.3. The interior volumes for the cancellous regions were created in the ANSYS pre-processor as well. Following the preliminary contact material model studies in Subsection 2.1.2.1, common surfaces between the cancellous and cortical bone regions were shared so that no relative motion at the material interfaces occurred. Additionally, regions where loads were applied or constraints were induced were separated from the rest of the bone surfaces. However, common lines were shared at the interfaces. These load/constraint regions were appropriately labeled for ease of subsequent selection. Finally, the local coordinate systems of each bone segment used in the development of the geometry and its transformations were added to the finite element model for each of the three configurations shown in Figure 2.11. The bone volumes were next discretized to create the finite element mesh used in the analysis (Figure 2.14).

A combination of 20-node tetrahedral elements and 8-node hexahedral elements were used. In general, hexahedral elements were used for regular geometry, such as the cylindrical regions of the femur and tibia, allowing element sizes to be directly controlled. As described in Chapter 4, hexahedral elements with no mid-side nodes were used so that the shape adaptations could be simulated through customized subroutines in ANSYS. The tetrahedral elements were used for interior volumes or exterior volumes with irregular geometry, such as the pelvis, foot, and the regions of the femur and tibia near the hip, knee and ankle joints as well as the central core in each cylindrical region. Figure 2.14 shows the designations of element types for each region of the model. A transition layer of pyramidally shaped elements was used at interfaces between the

hexahedral and tetrahedral element types. At the contacting surfaces of the joints, special surface elements necessary for the execution of the joint contact analysis were placed on top of the tetrahedral elements at the mesh at the end regions of each bone segment volume. Figure 2.15 shows the meshed contacting surfaces used.
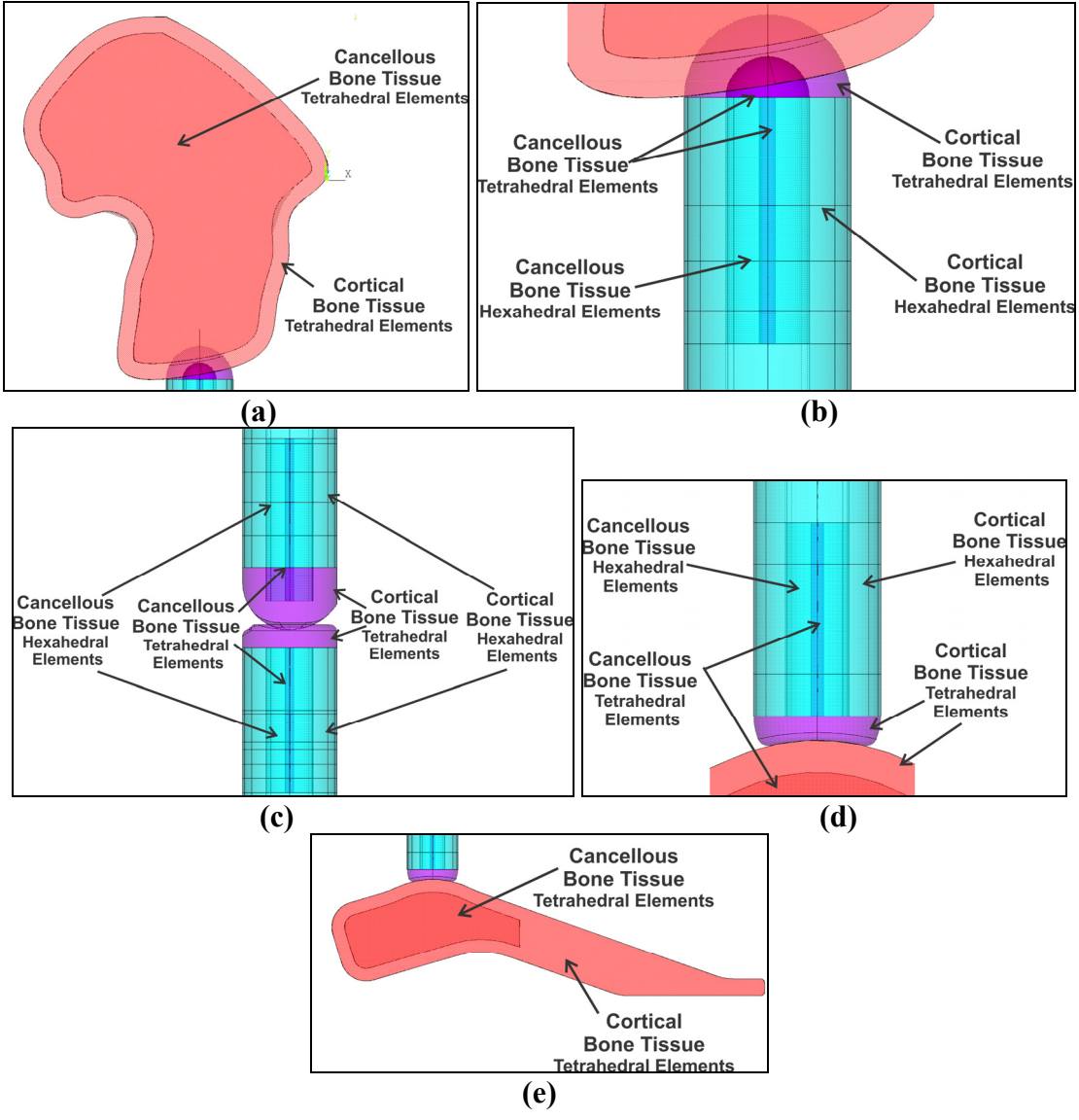
Figure 2.14 Locations of types of elements used (a) pelvis (b) near hip joint (c) near knee joint (d) near ankle joint (e) foot.

Hip Joint

Knee Joint

Ankle Joint

Pelvis Side

Femur Side

Femur Side

Tibia Side

Tibia Side

Tibia Side

Foot Side

(a)

(b)

(c)
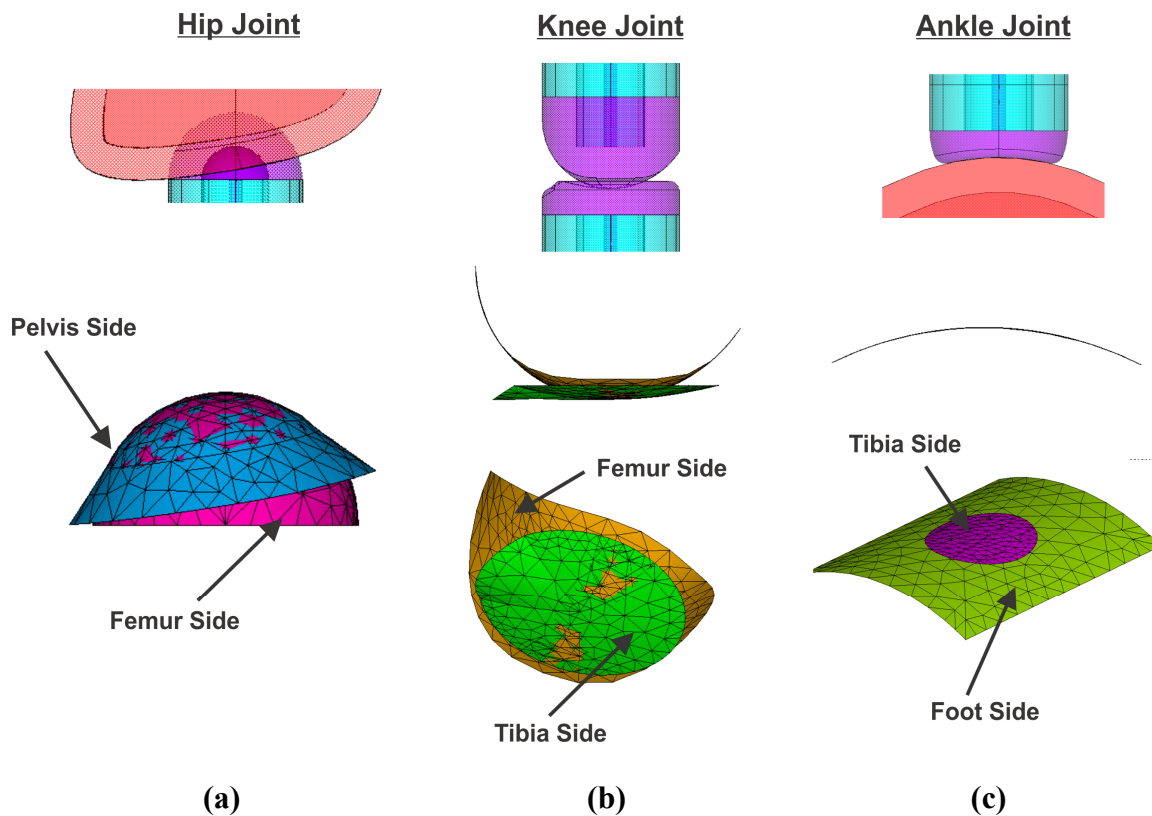
Figure 2.15 Meshed contacting surfaces for (a) hip (b) knee (c) ankle joints.

The development of the mesh for the leg bone system studied was constrained by two factors. The first factor is related to the approximation of the porous bone material as a continuum. Both cortical and cancellous bone are porous materials made of structural units called osteons. Therefore, they are not uniform homogeneous continua as assumed in the finite element analysis methods used in this work. In order for the continuum assumption to be valid, the element size of the model's finite element mesh must be at least an order of magnitude greater than the characteristic size of the material modeled [176]. Because the focus of this study was on cortical bone strength, the element size for the entire model was limited by the characteristic size of the cortical bone tissue material. Since the cortical bone tissue is much less porous than cancellous

bone tissue, [13, 15, 17], its characteristic size was assumed to be that of an osteon, which ranges in size from 100-300μm [16]. As a result, the minimum element size for the mesh created in this model was one millimeter. The second factor that limited the mesh developed in this work is related to the maximum model node limit of 256,000 nodes imposed by the available software license.

The cylindrical regions of the femur and the tibia meshed with hexahedral elements were divided into a number of volumes in order to control the element size and to create a mapped mesh. (Refer to Figure 2.16 during this discussion of the mapped mesh). The mesh in the cortical region in these bone volumes had a radial spacing of 1.875mm. The mesh in the corresponding cancellous region had a radial spacing of 2mm, graded by a ratio of 0.5 so that the element size started out the same as the adjoining cortical elements, and got smaller as the radial coordinate decreased. In the theta direction, around the circumference of the cylindrical regions, element sizes were also graded to be smaller in the anterior and posterior regions, where the muscle forces were applied, and larger 90° from these regions. Because the sagittal (symmetry) plane was closest to the region of applied muscle forces, the smallest elements were placed in this region. The angular size of the elements was 4.3° for the first ±17.2°. It increased to 6.4° until ±36.4° when the element size increased again to 10.72° until the ±90° location. In the axial direction, the mesh was varied so that the smallest element sizes were in locations of muscle force or constraint application. The mesh gradually transitioned to larger elements away from these regions. The cancellous regions, with hexahedral elements, had identical mapping to the corresponding cortical regions in the angular and axial directions in regions where both types of tissue were present.

In regions with tetrahedral elements, meshes were automatically created using ANSYS's built in meshing algorithms. Various levels of refinement, using the built in refinement tools, were applied so that the tetrahedral elements were visually similar in size to the mapped, hexahedral element region. Further refinement was applied to the regions of muscle force application. The mesh at the contacting surfaces was based on preliminary study of the effect of element size on contact model results discussed above.

Each muscle force was applied over a region the size of an average tendon, as explained in Subsection 2.1.2.2. If the muscle force occurred in where tetrahedral elements were used, this region was circular. If it occurred where a hexahedral mesh was used, the region was square. The force application area was divided into two zones to allow for a stepped transition from a central core of highest magnitude forces to a region with a moderately lower magnitude located next to the surrounding nonloaded elements. The nodes in the central one-third of the total muscle force application area incur twice the load applied to nodes in the surrounding 2/3 of the total application area. Because of the mapped hexahedral mesh in the femur and tibia regions, the muscle force attachment areas were assigned a constant element size in both these inner and outer zones for all muscle force areas. In the pelvis and foot regions with the tetrahedral mesh, however, the number of nodes in each region and at each muscle force area varied because the mesh could not be directly controlled. This variation in the node count in the muscle force application area was accounted for in the assignment of the nodal muscle force values.

Preliminary mesh sensitivity studies were performed for the effect of mesh on both the von Mises stress distributions and on the resulting shape changes to the bone's surface geometry. Refinement of the mesh was limited, however, due to the limits on the

maximum allowable number of nodes within an analyzed model. The selected mesh created the least alterations in results with node distribution variation while meeting the node limit criteria. The final finite element model contained a total 184,067 elements and 242,066 nodes. Figure 2.16 shows the final mesh used arranged in the 0° configuration. With use of the coordinate system transformations described in Subsection 2.1.3.1, this mesh was the same for each limb configuration studied.
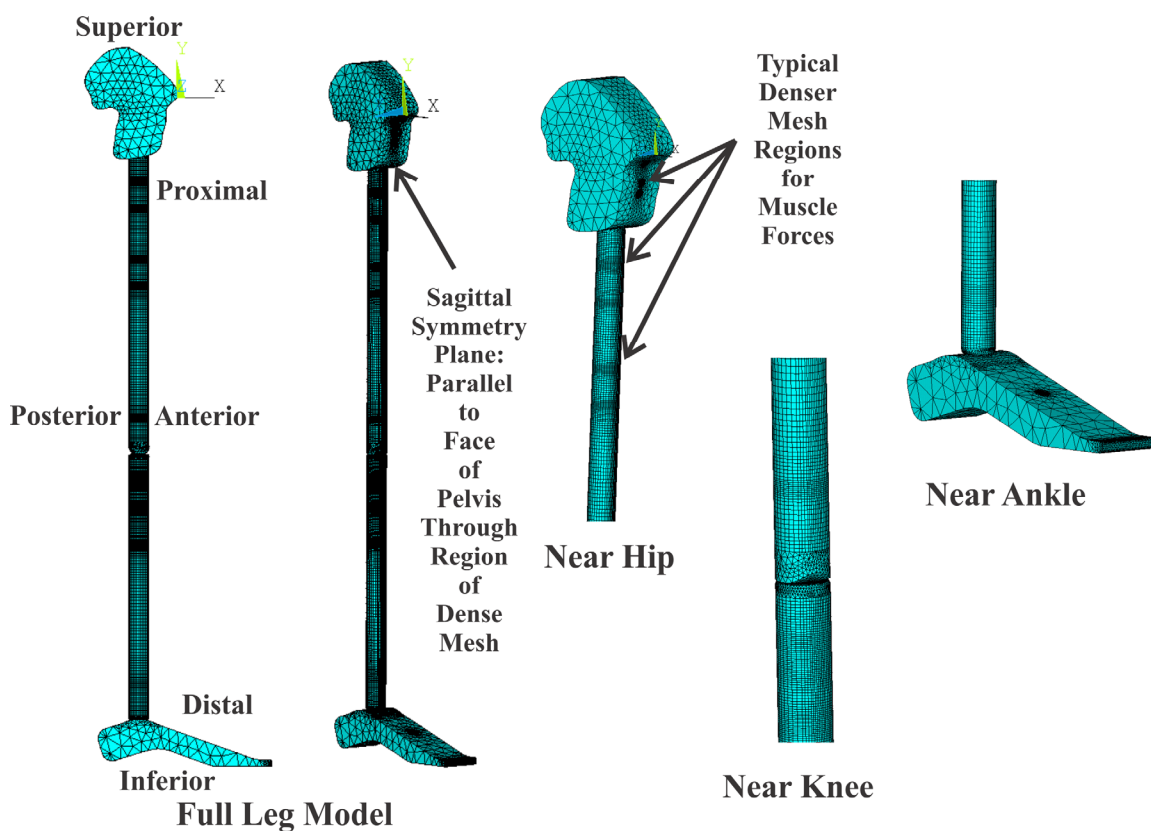
Figure 2.16 Final mesh used for all studies in this work.

2.2 Material Models

The appropriate modeling of the behavior of a material is crucial to its analysis. Therefore, a significant amount of research has been published on the material properties of cortical and cancellous bone tissue. As a living structure, these material properties can

vary. This is due to a wide number of factors including density, which is related to porosity and amount of mineralization, age, species, previous load history, location within the body or position within an individual bone, loading orientation, type of load, and even genetic factors. Hence, unlike many manmade materials, the material properties of bone tissue, even of "healthy" individuals, can have a wide range of reported values [13, 177-180].

Because of this variation, significant research has been undertaken to develop empirical models, through both experimental and computational means, relating the factors listed above and the material properties so these models can be used to predict bone behavior [13, 31, 178, 179, 181, 182]. Most models contain correction factors and other constants that fit the mathematical model to a particular set of experimental data. Therefore, such models may be limited in their universal application. Nonetheless, some generalized descriptions of bone material behavior can be made.

Bone tissue, both cortical and cancellous, behaves elastically, and sometimes viscoelastically. It is generally agreed that bone tissue is an anisotropic, composite material that can behave nonlinearly at increased strain rates. However, depending on the model's application, the specific system conditions, the scale of the system considered (cellular vs. tissue level vs. whole bone level), and even the type of bone studied, simplifications can be made that significantly reduce the computational complexity. Such simplifications include assumptions of linear elasticity and transverse or full isotropy [14]. Of the physical parameters that affect the mechanical properties of cortical and cancellous bone tissue, density and orientation are most influential [14].

Because the intent of this work is a comparative study of the relative effects of various loading regimens on the cortical bone strength adaptation, a detailed, highly accurate model of the material behavior of cortical and cancellous bone is not necessary. The selection of the material properties used in this model is explained below.

2.2.1 Properties of Cortical Bone Tissue

Many of the material properties of cortical bone tissue are affected by load magnitudes and rates of loading [14, 90, 178, 182]. Therefore, simplifications to the material models can be achieved by limiting the range of applied loads. The loads considered in this study were selected so that developed stresses remained in the elastic range, justifying the use of elastic material models in this work.

The yield strength of cortical bone material has been reported to range from 80-150 MPa under tensile loads, 100-160 MPa under compressive loads, and 160-180 MPa under bending loads [178]. While cortical bone tissue is viscoelastic with the stiffness, strength, and brittleness all increasing with increased strain rate [14], the viscous effects have a negligible effect on the bone's response under a wide range of loading frequencies [178]. Because only static loading is considered in this work, viscoelastic effects were assumed to have a negligible effect.

The strength of cortical bone varies linearly with porosity and with mineralization, and, hence, linearly with density. However, because only shape changes are considered in the strength adaptations simulated in this investigation, the density of cortical bone is assumed to be uniform throughout the bone volumes and constant with time. Therefore, the strength of the cortical bone was considered a constant in this work.

For reference purposes in this study, an average value of those listed above, 150 MPa, was considered to be the yield strength of cortical bone tissue.

The elastic modulus of cortical bone is reported to vary exponentially with porosity and also exponentially with mineralization. However, because the density of the bone is assumed to be constant with location and time in this study, a constant modulus was used in this work. Cortical bone tissue, especially in the long bones like the femur and tibia, is typically considered to be transversely isotropic, with the properties in the transverse plane about half those in the longitudinal plane, or along the longitudinal axis [16]. Nonetheless, cortical bone tissue has often been modeled as an isotropic material [183, 184]. Because of the complex loading in the bone system studied in this work, the transversely isotropic material model for the cortical regions of the long bones (femur and tibia) was warranted. Because there is no dominant loading direction in these foot and pelvis regions, fully isotropy was assumed in these regions. Table 2.10 summarizes the material properties used in this model. Note that the directions x and z describe the local transverse plane while direction y describes the local axial direction of the long bone as in Figure 2.11. Because the Poisson's ratio of cortical bone ranges from 0.28 to 0.48, a mid-range value was used in this work.

Table 2.10 Cortical Bone Tissue Material Properties (GPa except ν)

For Femur and Tibia from [185]		For Pelvis and Foot	
Material Property	**Value**	**Material Property**	**Value**
Ex	9.55	E from [183]	16.35
Ey	9.55		
Ez	16.61		
Gxy	3.28		
Gyz	4.74		
Gxz	4.74		
ν	0.37	ν from [184]	0.34

2.2.2 Properties of Cancellous Bone Tissue

Cancellous bone tissue is significantly more porous than cortical bone tissue (Figure 1.1), with its porosity ranging from 50-95%. This porosity varies significantly with location and time, causing the measurement of cancellous bone properties to be appreciably more difficult than that of cortical bone tissue. Because of its considerable porosity, empirical and analytical relations developed for engineering foams are often used to determine the mechanical properties of cancellous bone tissue [13]. In addition, because of its very porous nature, the material properties of cancellous bone tissue are affected not only by the density, but also by the orientation of the struts that create the porous structure of the material [14].

While the yield strain of the cancellous bone tissue is a constant that is equal to the slope of the yield stress versus stiffness curve, this material does not reach an ultimate stress and fail after yielding [14]. Instead, the stress remains fairly constant or increases slightly with strain as the pores collapse upon each other as a result of buckling, not a bending failure of their struts [14]. As a result, the cancellous bone tissue has significant plastic deformation after yielding and, therefore, energy absorption ability [13].

Because of the wide range of reported values of the material properties of cancellous bone tissue and the transient nature of the strut orientation and material density, it is often modeled as an isotropic material [16]. This simplification is acceptable in the current work because of the focus on the cortical bone tissue and strength of the whole bone structure. Because the Poisson's ratio of cancellous bone tissue is difficult to measure due to its porosity, a value of 0.3 is often used in the published literature [16] and was used in this study.

The modulus of elastic of cancellous bone tissue is, on average, 70-80% of that of cortical bone tissue and is widely reported to range from 8-14 GPa [16]. However, to determine the most appropriate value of the elastic modulus of the cancellous bone tissue for use in this work, a preliminary study was performed to compare the effects of three different values of an isotropic elastic modulus of cancellous bone tissue: 8 GPa, 11 GPa, and 14 GPa. In these studies, the cortical bone tissue of all bone components was modeled as an isotropic material (modulus of 16.35 GPa, Poisson's ratio of 0.34). A number of loading conditions with these different cancellous bone material properties were compared in order to ensure the effect was due to choice of the material property and not that of the boundary conditions. The geometry of the model was as described in the preliminary study of the effect of the inclusion of cancellous bone tissue in Subsection 2.1.2.1 and Figure 2.4. Over the three modulus values considered, the variation in the maximum model deflection was slight (<5%) and decreased linearly with increasing stiffness. There was little difference (<0.5%) in the maximum model von Mises stress. Because of the small effect of the cancellous bone elastic modulus on the overall behavior of the system modeled, a mean value of the reported range of the cancellous bone elastic modulus, 11 GPa, was chosen for use in this work.

With the geometric and material models of the system studied fully established and the boundary conditions and loading parameters identified, the system is fully described and can be analyzed. The analysis is achieved through mathematical modeling methods which use equations that govern the behavior of the system in terms of the response due to the material properties and the response due to the system configuration. The governing equations and the solution methods used in this work are now described.

2.3   Governing Equations and General Modeling Techniques

Just as with any mechanical system, the musculoskeletal system studied in this work must satisfy basic governing and constitutive equations. The behavior of the materials within the system can be described by material model constitutive equations. The operation of the defined musculoskeletal system itself is described by the basic laws of conservation of momentum, mass, and energy. The additional observed behavior of biological systems, like the bone strength adaptation studied in this work, that occur due to physiological processes can also be described mathematically with the development of relations that express the results of these processes in terms of the parameters that control the processes. The explanation of the mathematical modeling of the behavior of the bone tissue and the governing equations related to the conservation of system mass, momentum and energy that are implemented in this work are discussed in detail as are methods for their solution. Basic methods used in this work to predict the individual muscle activity and bone strength adaptation, the focus of Chapters 3 and 4, respectively, are introduced.

2.3.1 Constitutive Equations of the Cortical and Cancellous Bone Material

The bulk (also called tissue level or apparent level) properties of bone tissue under the loads imparted by everyday activities are usually represented using continuous, homogeneous, linear, elastic, isotropic or transversely isotropic models [16]. Therefore, the bone is considered to be a Hookean material, and there is a linear relationship between stress and strain in the bone materials studied in this work. The constitutive equations for a Hookean, isotropic and transversely isotropic material are presented in the

Lagrangian coordinate system using tensor notation unless otherwise noted. The descriptions, relations, equations and derivations written here are based on [16, 186].

The relationships between strain and displacement are called the kinematic relations and are written in Voigt (engineering) form as (from [186]):

$$\varepsilon_i = \frac{\partial u_i}{\partial x_i}$$

where i= 1, 2, 3 or x, y, z

(2.1)

for normal strains depicting the change in length and as

$$\gamma_{ij} = \frac{\partial u_i}{\partial x_j} + \frac{\partial u_j}{\partial x_i}, \quad i \neq j$$

where i, j = 1, 2, 3 or x, y, z

(2.2)

for shear strains depicting the change in angle.

The expressions for strain can be written in tensor form as (from [186]):

$$\varepsilon_{ij} = \frac{1}{2}\left(\frac{\partial u_i}{\partial x_j} + \frac{\partial u_j}{\partial x_i} \right)$$

where i, j = 1, 2, 3 or x, y, z

(2.3)

Normal strains are indicated by i=j and shear strains are indicated by i≠j. The strain tensor is symmetric. It should be noted that shear strains written in engineering or Voigt form (γ_{ij}, i≠j) are twice those written in the strain tensor form (ε_{ij}, i≠j) [186] so that the values of the engineering shear strain components (γ_{ij}, i≠j) are twice the tensor shear strain component values:

$$\varepsilon_{ij} = \tfrac{1}{2}\gamma_{ij}, \; i \neq j$$

(2.4)

For a given body (in this work, the bone) to remain homogeneous and continuous during the deformation due to an applied load, thus ensuring that no voids open within the material, a piecewise continuous strain and displacement field must be maintained [186]. This means that the strain tensor at a point (ε_{ij}, i,j=1, 2, 3 or x, y, z) must be a continuous function of displacement (u_i, i=1, 2, 3, or x, y, z). In other words, the strain tensor in Equation 2.3 must be twice differentiable in x_i. This requirement leads to six compatibility (or continuity equations) [186, 187].

$$\frac{\partial^2 \varepsilon_{11}}{\partial x_2^{\ 2}} + \frac{\partial^2 \varepsilon_{22}}{\partial x_1^{\ 2}} = 2\frac{\partial^2 \varepsilon_{12}}{\partial x_1 \partial x_2} \tag{2.5a}$$

$$\frac{\partial^2 \varepsilon_{22}}{\partial x_3^{\ 2}} + \frac{\partial^2 \varepsilon_{33}}{\partial x_2^{\ 2}} = 2\frac{\partial^2 \varepsilon_{23}}{\partial x_2 \partial x_3} \tag{2.5b}$$

$$\frac{\partial^2 \varepsilon_{11}}{\partial x_3^{\ 2}} + \frac{\partial^2 \varepsilon_{33}}{\partial x_1^{\ 2}} = 2\frac{\partial^2 \varepsilon_{13}}{\partial x_1 \partial x_3} \tag{2.5c}$$

$$\frac{\partial^2 \varepsilon_{11}}{\partial x_2 \partial x_3} = \frac{\partial}{\partial x_1}\left(-\frac{\partial \varepsilon_{23}}{\partial x_1} + \frac{\partial \varepsilon_{13}}{\partial x_2} + \frac{\partial \varepsilon_{12}}{\partial x_3}\right) \tag{2.5d}$$

$$\frac{\partial^2 \varepsilon_{22}}{\partial x_3 \partial x_1} = \frac{\partial}{\partial x_2}\left(-\frac{\partial \varepsilon_{31}}{\partial x_2} + \frac{\partial \varepsilon_{12}}{\partial x_3} + \frac{\partial \varepsilon_{23}}{\partial x_1}\right) \tag{2.5e}$$

$$\frac{\partial^2 \varepsilon_{33}}{\partial x_1 \partial x_2} = \frac{\partial}{\partial x_3}\left(-\frac{\partial \varepsilon_{12}}{\partial x_3} + \frac{\partial \varepsilon_{23}}{\partial x_1} + \frac{\partial \varepsilon_{31}}{\partial x_2}\right) \tag{2.5f}$$

Directions 1, 2, and 3 are any orthogonal set of directions, typically Cartesian x, y, and z.

Because cortical bone is modeled as a linearly elastic material for the small strains considered in this work, the constitutive equation describing this Hookean material is simply (from [16]):

$$\sigma_{ij} = C_{ijkl}\varepsilon_{kl}$$
$$\text{where i,j,k,l} = 1, 2, 3 \text{ or x, y, z}$$

(2.6)

C_{ijkl} results in a 6x6 matrix of the elastic constants called the elastic constant matrix (or stiffness matrix).

Taking the inverse of Equation 2.6 leads to [16]:

$$\varepsilon_{kl} = K_{klij}\sigma_{ij}$$
$$\text{where i,j,k,l} = 1, 2, 3 \text{ or x, y, z}$$

(2.7)

K_{klij} is the inverse of C_{ijkl}, is also a 6x6 matrix, and is referred to as the elastic compliance matrix.

The thirty-six unique components of the elastic constant matrix, C_{ijkl}, describe the elastic behavior of the material. With thirty-six unique components, there are no relationships between the material orientation and behavior, and the material is anisotropic. The number of unique components in the elastic constant matrix (and, therefore, its inverse, the elastic compliance matrix) can be reduced if the material displays some degree of symmetry with respect to the three orthogonal directions (1, 2, 3 or x, y, z). Such orthotropic materials have planes of symmetry where material properties are independent of direction within the plane.

Orthotropic materials exhibit orthotropic symmetry, meaning they have three mutually perpendicular planes of mirror symmetry [16]. In such materials, there are three

main planes in which the material properties do not depend on direction. These planes are mutually orthogonal and their normals define three orthogonal directions. This reduces the number of unique constants in the elastic matrix in Equation 2.6 to nine [186]. Specifically, the elastic constant matrix of an orthotropic material is composed of relationships between three Young's moduli (E_i) that are used to describe the dependency of normal stress on normal strain,

$$\sigma_{ii} = E_i \varepsilon_{ii}$$
$$\text{where } i = 1,2,3 \tag{2.8}$$

three shear moduli (or moduli of rigidity) (G_{ij}) that describe the dependency of shear stress and shear strain,

$$\tau_{ij} = G_{ij}\gamma_{ij} \quad \text{or} \quad \sigma_{ij} = 2G_{ij}\varepsilon_{ij} \quad i \neq j$$
$$\text{where } i,j = 1,2,3 \tag{2.9}$$

and three unique Poisson's ratios (v_{ij}) that describe the lateral contractions of the volume that result from axial strains.

$$v_{ij} = -\frac{\varepsilon_{ii}}{\varepsilon_{jj}}, \quad i \neq j$$
$$\text{where } i,j = 1,2,3 \tag{2.10}$$

For orthotropic elastic materials, the elastic compliance matrix is symmetric, shown in engineering form as:

$$\begin{bmatrix} \varepsilon_{11} \\ \varepsilon_{22} \\ \varepsilon_{33} \\ 2\varepsilon_{23} \\ 2\varepsilon_{13} \\ 2\varepsilon_{12} \end{bmatrix} = \begin{bmatrix} \dfrac{1}{E_1} & \dfrac{-v_{21}}{E_2} & \dfrac{-v_{31}}{E_3} & 0 & 0 & 0 \\[2mm] \dfrac{-v_{12}}{E_1} & \dfrac{1}{E_2} & \dfrac{-v_{31}}{E_3} & 0 & 0 & 0 \\[2mm] \dfrac{-v_{13}}{E_1} & \dfrac{-v_{23}}{E_2} & \dfrac{1}{E_3} & 0 & 0 & 0 \\[2mm] 0 & 0 & 0 & \dfrac{1}{G_{23}} & 0 & 0 \\[2mm] 0 & 0 & 0 & 0 & \dfrac{1}{G_{13}} & 0 \\[2mm] 0 & 0 & 0 & 0 & 0 & \dfrac{1}{G_{12}} \end{bmatrix} \begin{bmatrix} \sigma_{11} \\ \sigma_{22} \\ \sigma_{33} \\ \sigma_{23} \\ \sigma_{13} \\ \sigma_{12} \end{bmatrix} \qquad (2.11)$$

where

$$\frac{v_{12}}{E_1} = \frac{v_{21}}{E_2}, \quad \frac{v_{13}}{E_1} = \frac{v_{31}}{E_3}, \quad \text{and} \quad \frac{v_{23}}{E_2} = \frac{v_{32}}{E_3} \qquad (2.12)$$

The relationships listed in Equation 2.12 ensure that work cannot be extracted from the closed system process of elastically deforming the material so that the changes to the material system satisfy the Second Law of Thermodynamics [186].

Transversely isotropic materials, where two of the three orthogonal planes exhibit the same uniform properties, further reduce the number of unique elastic constants to five. In addition to the three orthogonal planes of symmetry, there is a plane of isotropy (constant properties). The five unique elastic constants are created by imposing these additional restrictions on the orthotropic material model:

$$E_1 = E_2, \qquad v_{12} = v_{21}, \qquad v_{31} = v_{32}, \qquad G_{23} = G_{13}, \qquad G_{12} = \frac{E_1}{2(1+v_{12})} \qquad (2.13)$$

Finally, an isotropic material displays full isotropic symmetry where all planes are planes of mirror symmetry and planes of isotropy and where material properties are the same in all directions. This reduces the elastic compliance matrix to depend on only two unique elastic constants, representing a common Young's modulus (E) and a common Poisson's Ratio (v), with the restrictions that:

$$E_1=E_2=E_3=E, \qquad v_{12}=v_{21}=v_{31}=v_{32}=v_{13}=v_{23}=v,$$

$$G_{23}=G_{13}=G_{12}=G=\frac{E}{2(1+v)} \tag{2.14}$$

The elastic constant matrix (stiffness matrix) is found by taking the inverse of the elastic compliance matrix, so that the constitutive equation of an orthotropic material, in engineering form, becomes (from [16]) :

$$
\begin{bmatrix} \sigma_{11} \\ \sigma_{22} \\ \sigma_{33} \\ \sigma_{23} \\ \sigma_{13} \\ \sigma_{12} \end{bmatrix}
=
\begin{bmatrix}
\dfrac{1-v_{23}v_{32}}{\Delta E_2 E_3} & \dfrac{v_{12}+v_{31}v_{23}}{\Delta E_1 E_3} & \dfrac{v_{13}+v_{12}v_{23}}{\Delta E_1 E_2} & 0 & 0 & 0 \\
\dfrac{v_{12}+v_{31}v_{23}}{\Delta E_1 E_3} & \dfrac{1-v_{13}v_{31}}{\Delta E_1 E_3} & \dfrac{v_{23}+v_{21}v_{13}}{\Delta E_1 E_2} & 0 & 0 & 0 \\
\dfrac{v_{13}+v_{12}v_{23}}{\Delta E_1 E_2} & \dfrac{v_{23}+v_{21}v_{13}}{\Delta E_1 E_2} & \dfrac{1-v_{12}v_{21}}{\Delta E_2 E_1} & 0 & 0 & 0 \\
0 & 0 & 0 & G_{23} & 0 & 0 \\
0 & 0 & 0 & 0 & G_{13} & 0 \\
0 & 0 & 0 & 0 & 0 & G_{12}
\end{bmatrix}
\begin{bmatrix} \varepsilon_{11} \\ \varepsilon_{22} \\ \varepsilon_{33} \\ 2\varepsilon_{23} \\ 2\varepsilon_{13} \\ 2\varepsilon_{12} \end{bmatrix}
\tag{2.15}
$$

where

$$\Delta = \frac{1-v_{12}v_{21}-v_{23}v_{32}-v_{31}v_{13}-2v_{21}v_{32}v_{13}}{E_1 E_2 E_3}$$

For transversely isotropic and isotropic materials, the simplifying restrictions in Equations 2.13 and 2.14 can be substituted into the Equation 2.15, respectively. For fully

isotropic materials, the two unique constants have special names, the Lamé constants, λ and G, and the constitutive equation in engineering (Voigt) form in Equation 2.15 can be written in terms of the Lamé constants as (from [186]):

$$
\begin{bmatrix} \sigma_{11} \\ \sigma_{22} \\ \sigma_{33} \\ \sigma_{23} \\ \sigma_{13} \\ \sigma_{12} \end{bmatrix} =
\begin{bmatrix}
\lambda+2G & \lambda & \lambda & 0 & 0 & 0 \\
\lambda & \lambda+2G & \lambda & 0 & 0 & 0 \\
\lambda & \lambda & \lambda+2G & 0 & 0 & 0 \\
0 & 0 & 0 & G & 0 & 0 \\
0 & 0 & 0 & 0 & G & 0 \\
0 & 0 & 0 & 0 & 0 & G
\end{bmatrix}
\begin{bmatrix} \varepsilon_{11} \\ \varepsilon_{22} \\ \varepsilon_{33} \\ 2\varepsilon_{23} \\ 2\varepsilon_{13} \\ 2\varepsilon_{12} \end{bmatrix}
\tag{2.16}
$$

where the constants are defined as $\lambda = \dfrac{E\nu}{(1+\nu)(1-2\nu)}$ and $G = \dfrac{E}{2(1+\nu)}$.

Cortical bone tissue is typically modeled as a transversely isotropic material in the long bones, with the radial and circumferential directions having the same properties and the longitudinal (or axial in the long bone) having different properties [13, 17, 178]. It has also commonly been represented as a fully isotropic material [184]. In this work, the transversely isotropic material models were applied to the cortical bone in the femur and tibia while fully isotropic cortical bone models were applied to the pelvis and the foot as explained in the previous section.

Cancellous bone tissue is typically described as anisotropic due to its extreme porosity and its very labile (or constantly changing) nature [16]. However, unless the behavior of cancellous bone is the focus of the study, its material properties are most frequently approximated using isotropic material in models [16] and will be done so in this study as explained previously.

2.3.2 Governing Equations

With the material properties of the bone defined, the governing equations were applied to ensure that mass, energy and momentum are conserved within the musculoskeletal system studied. This section reviews the mathematical descriptions of these "balance principles" used in this work. The equations presented here are general for any continua [188]. In this section, the system will be explained and its governing equations, especially as applied to the developed models, will be discussed.

2.3.2.1 Conservation of Mass. In the model used in this research, both the cortical and the cancellous bone tissue materials were assumed to be a uniform continuum and their properties constant with time. All intrinsic material properties in this model were, therefore, homogenous. Hence,

$$Grad(\rho(\mathbf{x},t)) = \mathbf{0} \tag{2.17}$$

for all times t during the analysis and all locations $\mathbf{x}$ in the model. In Equation 2.17 ρ is the density.

While the material properties remain constant with time in the bone strength shape adaptation model in this work, the overall volume changed as the bone's shape iteratively adapted to the applied loads. Because the density is assumed to be constant, this volume change results from an addition or removal of bone material, or mass, over time. However, because the developed model simulates the effects of the shape strength adaptation and not the actual biological processes, the analysis is performed in such a way that the incremental mass changes are not considered. Specifically, the

shape/strength adaptation phenomena investigated in this work are separated into two distinct phases, the load application phase and the shape adaptation phase.

In the first phase, the bone volume, in its current state, is loaded by a set of external forces. Under the load application, the shape changes have yet to occur, and so the total system mass remains constant. This phase determines the measures of the system's response to the load that are used to drive the adaptation of the bone's shape towards a more uniform stress/strain distribution. In this way, this stress analysis is performed for a closed mass system each time the load was applied. This can be represented mathematically by:

$$m = \int_{\Omega} \rho(\mathbf{x}, t) dv = const > 0 \tag{2.18}$$

for all times t during the load application phase of the iterative analysis and for each bone segment volume v defined by the region, Ω, of the bone system geometry with a mass of m.

In the second phase of the modeled phenomena, the results of the first phase are used to simulate the strength adaptation of the cortical bone region. While the model did not directly simulate the biological adaptation processes themselves, it predicted the resulting effects on the bone's shape. Because the shape is changed in this second phase of the analysis, the mass of the entire system does change with iteration (representing time). Therefore, in the second phase of the analysis, the adaptation model indirectly accounted for the changes to the system mass through the prediction of the shape changes to the whole bone surface, or boundary, profile. The shape change is assumed to occur instantaneously directly after the load was applied.

By separating the model in two distinct phases, the analysis of the response to the applied mechanical load in the first phase occurs for a closed mass system. Because the analysis is repeated iteratively with "time", the boundary of the closed mass system changes between analysis iterations. The total mass of the closed system at each iterative cycle of the load application and adaptive response to the load (m_i) is equal to sum of the mass at the end of the previous iteration and the instantaneous, incremental change in mass that resulted from the alterations of the profiles of the bone's boundary surfaces in response to the applied loading at the completion of the adaptation prediction phase of the current iteration. Therefore, while the total mass of the bone may vary from one iteration to the next, during the performance of the mechanical (finite element stress) analysis, the system mass remains constant. This conservation of mass during subsequent mechanical analyses after shape adaption is summarized in Equations 2.19 through 2.21.

$$m_1 = \rho \int_{\Omega_{iteration=1}} dv = const_1 > 0 \;\; \text{during iteration 1} \tag{2.19}$$

$$m_2 = \rho \int_{\Omega_{iteration=2}} dv = const_2 > 0 \quad \text{during iteration 2} \tag{2.20}$$

$$\vdots$$

$$m_n = \rho \int_{\Omega_{iteration=n}} dv = const_n > 0 \;\; \text{during iteration n} \tag{2.21}$$

$$m_1 \neq m_2 \neq \ldots \neq m_n$$

2.3.2.2 Conservation of Energy. In addition to the changes in the physical system controlled by the conservation of mass, the energy within the system studied must be preserved. The application of this balance principal to the models developed in this work is discussed.

First Law of Thermodynamics

The First Law of Thermodynamics, or the conservation of energy in a closed system, can be represented over a particular time interval as (from [189]):

$$\Delta E_{system} = Q_{net} - W_{net} \qquad (2.22)$$

where E is the total energy, Q is the amount of energy input to the closed system and W is the work done by the closed system. Like the conservation of mass, the First Law (conservation of energy) was not considered directly in this model. Instead, an explanation of the energy transfer of the studied system is presented here. The system boundaries are the bone surfaces, and only the set of bones, not the muscles, are included. Therefore, a closed system was considered. The muscles are considered force generators to supply energy to the bone system examined. This energy is assumed to trigger the bone's adaptive response. The energy applied to the bone system from the muscles is used to deform the bone material. Because the bone is assumed to be perfectly elastic, when the load was released, the energy is fully released from the system. However, the deformation of the bone structure during the load application is assumed to trigger cellular processes that result in the removal or addition of material to the bone's surface through energy sources in addition to the strain energy created by the mechanical deformation of the bone under the external load. This cellular energy is not directly

considered in this work, but its effects are modeled as the changes to the bone's surface geometry.

Second Law of Thermodynamics

The Second Law of Thermodynamics states that entropy production must be nonnegative for any material system. The Second Law of Thermodynamics is satisfied in the modeling techniques employed in the current research through the use of a compliant set of constitutive equations describing the material behavior. These constitutive equations established the relationships between the material property parameters: the Young's moduli (E), the shear moduli (G) and the Poisson's ratios (ν). Based on the material symmetry, these properties may vary with direction as discussed in the previous section.

To comply with the Second Law of Thermodynamics, the work done on a perfectly elastic material, such as the one in this model, to deform it must be nonnegative. Strain energy per unit volume is a measure commonly used to quantify this energy transferred to a material during deformation. Therefore, by the First Law of Thermodynamics, this strain energy is equal to the work done on a perfectly elastic material to deform the material, since there are no losses due to heat and no other means of energy dissipation are considered [16, 186, 188]. Thus, the strain energy per unit volume (or strain energy density) of the deformed perfectly elastic material can be expressed as:

$$\Lambda / volume = \frac{1}{2} tr(\boldsymbol{\sigma\varepsilon}) = \frac{1}{2}\left(\sigma_{11}\varepsilon_{11} + \sigma_{22}\varepsilon_{22} + \sigma_{33}\varepsilon_{33}\right) + \sigma_{23}\varepsilon_{23} + \sigma_{13}\varepsilon_{13} + \sigma_{12}\varepsilon_{12} \qquad (2.23)$$

where Λ is the strain energy and σ_{ij} and ε_{ij} are the stress and strain tensors components in Voigt notation.

This Law imposes additional restrictions on the elastic constants for orthotropic materials, where properties varied only along three orthogonal planes. For such a material, compliance to the Second Law of Thermodynamics requires the following:

$$E_1>0, \quad E_2>0, \quad E_3>0, \quad G_{23}>0, \quad G_{13}>0, \quad G_{12}>0,$$

$$1-v_{23}v_{32}>0, \qquad 1-v_{13}v_{31}>0, \qquad 1-v_{12}v_{21}>0,$$

$$1-v_{12}v_{21}-v_{23}v_{32}-v_{31}v_{13}-2v_{21}v_{32}v_{13}>0, \qquad (2.24)$$

$$v_{12}/E_1 = v_{21}/E_2 , \qquad v_{13}/E_1 = v_{31}/E_3 , \qquad v_{23}/E_2 = v_{32}/E_3$$

The relations in Equation 2.24 can be reduced for transversely isotropic and isotropic materials using the simplifications in Equations 2.13 and 2.14. The isotropic material, the simplest form of these material property restrictions is:

$$E>0, \qquad\qquad G>0,$$

$$1-v^2>0, \qquad\qquad 1-3v^2-2v^3>0 \qquad (2.25)$$

2.3.2.3 Conservation of Momentum. The final balance principle that must be satisfied in the system's governing equations is the conservation of momentum. The model studied in the proposed work was statically or quasi-statically loaded. Thus, there is no net linear or angular momentum changes in the system at each analysis iteration. As such, the sum of the forces acting on the system and the sum of the moments acting on the system were both zero. [188]

Because the system studied is the set of bones only, surface forces, or tractions, are applied to the surfaces of the bone to account for externally applied forces including the muscles forces, the weight of the soft tissues surrounding the bones of the body

segment (for example the upper leg on the femur), and other externally imposed forces. The body forces acting on the bones are related to the gravitational forces, or the weight of the bones. For the conservation of momentum analysis of these multibone systems, contact forces are assumed to be internal to the system. Under these static conditions, the conservation of linear momentum (balance of forces) can be expressed as:

$$0 = \int_{\partial\Omega} \mathbf{t} ds + \int_{\Omega} \mathbf{b} dv \qquad (2.26)$$

where $\mathbf{t}$ is the surface traction, ds is the incremental surface area, $\mathbf{b}$ is the body force per unit volume, dv is the incremental volume, $\partial\Omega$ is the surface boundary and Ω volume studied. Because isometric loading conditions where joint angles remained constant, the conservation of angular momentum with $\mathbf{r}$ as the force moment arms is expressed as:

$$0 = \int_{\partial\Omega} \mathbf{r} \times \mathbf{t} ds + \int_{\Omega} \mathbf{r} \times \mathbf{b} dv \qquad (2.27)$$

In this study, the momentum due to the weight of the bones and soft tissues is assumed to be small compared to that due to the muscle forces and externally applied forces. Therefore, no body forces are included in these models, and the surface tractions do not include the weight of the tissues surrounding the bones. Conservation of linear momentum is achieved through balancing these surface tractions. Conservation of angular momentum is achieved by balancing the moments created by these surface traction forces about the system joints (hip, knee, ankle, etc.). The methods used to solve these balance equations are reviewed in Subsection 2.3.4 and discussed in detail in Chapter 3.

2.3.3 Finite Element Approximations

The constitutive and governing equations described in Section 2.3.1 were used to find the stresses and strains within the bone that drive its strength adaptations modeled in this work. Because of the complex geometry, loading conditions, and material models used in the multi-bone system studied in this work, finite element methods were employed to determine the local variations of the "shape adaptation drivers" so that they may be used in subsequent shape adaption prediction models. The specific finite element methods used in this work and applied to the bone system modeled are described following [190].

The basic steps of any finite element analysis can be described as applied to the bone system in this work. The geometry of the bone is discretized into distinct elements. The elements are defined by a set of distinct points, or nodes. The external forces applied to the bones are distributed over each element through the application of the forces onto these discrete nodes. The constitutive and governing equations are applied to each element. Continuity between elements is ensured at each node. Finally, based on the governing equations, displacements, stresses, and strains are calculated at each node to describe the bone system's response to the applied surface loads and boundary constraints.

The loads applied to the surfaces of the system studied (surface tractions) are found using the momentum balances Equations 2.26 and 2.27. The specific solution methods used for the musculoskeletal system studied in this work will be discussed further in the next section. Through the application of the constitutive equations, the principles of minimum total potential energy and virtual work are utilized at each element

to create the expressions required to find the nodal displacements that resulted from these external loads.

The cancellous and cortical bone materials that comprised the system modeled are assumed to be perfectly elastic so that the potential energy of each element, Π, as described by the application of the First Law of Thermodynamics (Equation 2.22) to this system, is simply defined as the difference between the internal strain energy, Λ, stored in the element and the work, W, done by the external forces, $\mathbf{F}$, acting on the element [186] (remembering that the body forces were considered negligible in this model):

$$\Pi = \Lambda - W \tag{2.28}$$

The work done on the element is simply the product of the forces, $\mathbf{F}$, and the nodal displacements that they cause, $\mathbf{U}$.

$$W = \mathbf{F}\mathbf{U} \tag{2.29}$$

The internal strain energy stored in each element Λ is written as the integral of the strain energy density (strain energy per unit volume of the element) defined in Equation 2.23 over the elemental volume v so that:

$$\Lambda = \frac{1}{2} \int_{\Omega} \boldsymbol{\sigma}^T \boldsymbol{\varepsilon} \, dv \tag{2.30}$$

where Ω is the elemental volume and $\boldsymbol{\sigma}$ and $\boldsymbol{\varepsilon}$ are the stress and strain tensors.

The strain energy of the perfectly elastic material element is written in terms of strain only using the constitutive equation for a linearly elastic material (Equation. 2.11). In matrix form, this is expressed as:

$$\boldsymbol{\sigma} = \mathbf{C}\boldsymbol{\varepsilon}$$
(2.31)

where $\mathbf{C}$ is the symmetric elastic constant matrix described in Equation 2.15. Substituting Equation 2.31 into Equation 2.30 resulted in an expression for the strain energy in terms of strain only:

$$\Lambda = \frac{1}{2}\int_{\Omega}\boldsymbol{\varepsilon}^T\mathbf{C}\boldsymbol{\varepsilon}\,dv$$
(2.32)

In finite element analysis modeling, the calculations above are performed at each of the elements and the solutions are stored only at the nodes. The spatial variation of any calculated parameter (such as the displacement) throughout an element is, therefore, determined by the use of a type of interpolation within the element using a shape function. The shape function, S, defines the variation of the displacement within the entire element in terms of the displacement at each of the nodes associated with the element. The number of shape functions used to describe this spatial variation over an element is equal to the number of nodes in the element. The form and complexity of these shape functions are based on the number of nodes in the element and the node positioning within the element and are unique for each element type. The displacement at any point can then be found through the sum of the products of the shape functions S and displacements U at each node. For example, for the 8-node hexahedral elements

used in this model, the displacements u, v, and w in the local x, y, and z directions are described as the sums below where i represents the nodes of the element:

$$u = \sum_{i=1}^{8} S_i U_{xi}$$

$$v = \sum_{i=1}^{8} S_i U_{yi} \qquad (2.33)$$

$$w = \sum_{i=1}^{8} S_i U_{zi}$$

With the displacements defined, the strain-displacement relations in Equation 2.3 can be used to describe the strain as the derivative of the displacements in Equation 2.33. Because the nodal displacements are constant values at a given solution iteration, the nodal strain and displacement are related through the derivatives of the shape functions and can be written in the matrix form presented in Equation 2.34, where $\mathbf{B}$ is a matrix of the derivatives of each of the shape functions with respect to the coordinate directions (for example x, y and z).

$$\varepsilon = \mathbf{BU} \qquad (2.34)$$

Substituting Equation 2.34 into the expression for the strain energy, Equation 2.32, yields:

$$\Lambda = \frac{1}{2} \int_{\Omega} \mathbf{U}^T \mathbf{B}^T \mathbf{CBU} dv \qquad (2.35)$$

Substituting Equations 2.35 and 2.29 into the expression for the potential energy of each element in Equation 2.28 results in:

$$\Pi = \frac{1}{2}\int_{\Omega} \mathbf{U}^T\mathbf{B}^T\mathbf{C}\mathbf{B}\mathbf{U}dv - \mathbf{F}\mathbf{U}$$

(2.36)

To find the minimum potential energy, which is required for the stability of the perfectly elastic element, the derivative of Equation 2.36 with respect to displacement U must be equal to zero. So that:

$$\frac{\partial}{\partial \mathbf{U}}\left(\frac{1}{2}V(\mathbf{U}^T\mathbf{B}^T\mathbf{C}\mathbf{B}\mathbf{U})\right) - \frac{\partial}{\partial \mathbf{U}}(\mathbf{F}\mathbf{U}) = \mathbf{0}$$

(2.37)

$$\text{or } V\mathbf{B}^T\mathbf{C}\mathbf{B}\mathbf{U} - \mathbf{F} = \mathbf{0}$$

(2.38)

where V is the element volume, a scalar.

In this finite element formulation, each element can be seen as a spring so that the nodal displacements of an element **U** are linear functions of the forces applied to the nodes of a particular element, **F**, and the proportionality constant is called the equivalent element stiffness or $\mathbf{K}^{equ}$. Thus, the spring-like behavior of the element can be described through the relation:

$$\mathbf{F} = \mathbf{K}^{equ}\mathbf{U}$$

(2.39)

Therefore, substituting Equation 2.39 in Equation 2.38, the equivalent elemental stiffness $\mathbf{K}^{equ}$ can be expressed in terms of the element shape functions and the material constitutive properties as:

$$\mathbf{K}^{equ} = V\mathbf{B}^{\mathrm{T}}\mathbf{C}\mathbf{B} \qquad (2.40)$$

In summary, at each element, the external forces applied to the nodes, the volume of the element, the initial locations of the nodes, the constitutive and strain-displacement relations, and the shape functions are used in the relations in Equations 2.39 to find the nodal displacements of the element as a result of the applied nodal forces. In turn, the nodal displacements are used with the strain displacement relations Equation 2.34 to find the nodal strains. Finally, the constitutive equations of the material being modeled, as in Equation 2.31, can be used to find the nodal stresses. Force balances are applied from one element to the next to ensure continuity of the solution and to determine the nodal displacement, strain and stress throughout the body studied. The distribution of these nodal values describes the overall response of the solid body to the applied loads and can then be used in further studies such as failure analyses or bone strength adaptations.

The constitutive and governing equations and the finite element methods presented here were the basis for the means to analyze the response of the system described in Sections 2.1 and 2.2 under various loading conditions. Two additional model components were required in order to complete the development of the methods used to simulate bone shape adaptation in the work. The first component is the determination of the magnitudes of the muscle forces imposed on the bones which is necessary to specify the bone's mechanical environment. The second component is the determination of the bone shape adaption which is necessary to convert the response of the bone to the loading, as determined by the finite element methods described in this section, to the changes to the surface profile that ultimately alter the bone's strength. A

brief description of the methods used to develop these modeling components is now explained. More details on the muscle force model and the shape adaptation model are provided in Chapters 3 and 4, respectively.

2.3.4 Muscle Force Model

Because the number of muscles in a musculoskeletal system typically far exceeds the number required satisfy the momentum balance equations (Equations 2.26 and 2.27), the system is indeterminate. As a result, it cannot be solved using standard systems of equations means, and a number of methods have been suggested to find the magnitudes of the muscle forces. Both methods developed in the field of engineering mechanics as well as applications assumptions about the system based on its anatomy or physiology have been employed. Early solution methods developed by researchers applied simplifying assumptions so muscle with common functions were grouped and others were eliminated to make the system determinate [191]. More recently, mathematical optimization methods have been employed [192]. A detailed review of the methods that have been applied to a muscle system is given in Chapter 3. However, a general overview of optimization based solution methods, criteria used to design the specific methods applied to the current work, and the associated modeling assumptions relevant to the system studied, is now presented.

Mathematical optimization methods find the optimal (minimum or maximum) solution to a problem given a specified goal. Usually, a series of constraints over which the solution must be valid are also imposed. The goal and constraints are often a function of the design variables, which are the set of unknowns for which the solution is required. Mathematical optimization methods can be as simple as taking the derivative of a

function and finding the values of the independent variables that make the derivative equal to zero. These methods can also be quite complex, iteratively finding a set of values that satisfy the given criteria through a series of numerical calculations that attempt to progress towards a stated goal and adjusting the direction of this progression whenever it moves away from this goal. Mathematical optimization methods are often used in many different engineering design problems including the modification of physical features, such as the values of an object's critical dimensions to meet weight or strength criteria, the modification of system functional parameters, such as flow rates, to meet thermal criteria, and the adjustment of system inputs values, such as temperature and chemical quantities, to meet power efficiency criteria.

In applying the same kinds of optimization methods to determine the muscle force magnitudes in a musculoskeletal system, it is assumed that, while many different combinations of muscles can produce the same results, a given group of muscles functions in a repeatable manner. Furthermore, there is a particular combination of muscle forces that make the set of muscles operate most efficiently to perform a given function. The optimization goal, therefore, is a mathematical definition of the efficient operation of a muscle set.

The selected goal of the optimization of the muscle force activity has varied significantly among the models developed in the published literature, ranging from minimizing the sum of individual muscle forces [127], to minimizing muscle stresses [193], to minimizing muscle fatigue [192]. The muscle forces used in these optimization goals are usually weighted to reflect the relative force-generating ability in each muscle [127, 194]. The weighting factor can be a reference force [192] or a physical measure of

the muscle such as size [193] or the anatomical makeup of the muscles themselves [195]. The mathematical terms in the optimization goals comprised of the unknown muscle forces can be linear [191] or nonlinear [127]. Despite the wide variety of optimization goals that have been used in previous investigations, published comparative studies showed no significant differences in the resulting muscle forces [194, 196-199] given an adequate level of complexity of the physical representation of the system.

As with the optimization goal, the particular mathematical optimization method used has also been the subject of much study. Both linear and nonlinear optimization goals using both analytical and numerical solution methods producing both global and local solutions have been suggested [127, 163, 193, 196, 198]. A number of methods were compared in this work and will be discussed in Chapter 3. Based on this comparison, one method was selected for its suitability to both the specific system and boundary conditions studied as well as its ability to be incorporated into the methods for the prediction of the adaptations of bone strength developed in this work. Because the developed model was intended to be used to compare the effects of various activities on bone strength adaptations, the ability of the model to be applied to many different loading cases with no changes to the programming code was important.

As with any mathematical model of a physical system, the validity of the muscle force optimization technique is contingent upon a series of limiting assumptions. In the development of a model to determine the individual muscle forces in this work, the following assumptions were used. Muscle forces can only produce tensile forces [127]. This assumption was represented by the set of constraints in the mathematical optimization model. The musculoskeletal system studied was assumed to undergo

isometric loading only such that joint angles remained constant, and there was no net angular momentum about each joint in the system. This assumption became the second set of constraints in the mathematical optimization model, which ensured the balance of moments created by the fixed-joint angle musculoskeletal leg system.

Other assumptions limiting the operation of the muscle force magnitude model were related to the physiological function of the muscles themselves. Typically, the magnitude of the force generated by a muscle is influenced by changes in the muscle length and the rate of these changes. However, because joint angles were assumed to remain constant in the activities studied in this work, the effects of these force-velocity relationships were assumed to be negligible [155] and, so, not included in the developed model. The magnitude of the force generated by a muscle is also affected by the instantaneous length of a muscle during the activity studied in relation to a reference length in the "resting" position of the particular limb containing the muscle. Because the joint angles were not at the extremes of their ranges of motion for the activities studied in this work, the instantaneous and resting lengths were not significantly different. Therefore, the effect of the force-length relationships was assumed to be negligible [156] and was not included in the developed methods.

The developed optimization method used in this work was based on previously developed methods from the literature. Modifications were made to improve its function and stability for the particular application examined in this study. The function of the specific muscle force magnitude optimization model created for this work was validated through quantitative comparisons to published numerical and experimental studies of the

individual muscle force activity for a given isometric exercise. The development and validation of this model is presented in Chapter 3.

As with the determination of individual muscle force magnitudes that create a particular function of a musculoskeletal system, predicting the changes in strength of a bone due to variations in these muscle forces can also be thought of as an optimization problem. The goal of the resulting modifications to the bone's shape is defined in relation to the desired behavior of the bone with respect to these forces. Therefore, mathematical optimization methods were also applied to the simulation of bone shape strength adaptations in the developed computational model. A brief description is next presented. Details are provided in Chapter 4.

2.3.5 Bone Shape Adaptation Model

While experimental and clinical studies of shape adaptations to bone strength have been performed for centuries, the numerical simulation of these phenomena has only been investigated for about fifty years. It was during this time that computational capabilities and resources became sufficient to simulate and analyze the complex geometry and behavior of systems such as bones. Early theoretical and analytical mathematical models [87, 106] were soon followed by numerical simulations of these theoretical models [88, 91]. As the field of computational engineering modeling and analysis grew, methods to address the numerical difficulties specifically related to simulating bone shape alterations were found and more extensive numerical studies were possible. A brief summary of the basic concepts of these types of modeling methods and their application to the current work is now presented. A more detailed review of the published work that lead to the

development of the final model in this work is found in Chapter 4 as is a thorough description of the currently developed model.

Most of the computational models simulating the shape alterations that result in the strength adaptation of cortical bone follow some basic modeling assumptions. As noted previously, the computational model of bone strength/shape adaptation developed in this work did not directly simulate the actual biological processes that contribute to the initiation, propagation, and termination of the shape strength adaptations. The simulation simply linked the changes in the loading environment with the changes in bone surface profile in a way that was representative of known biological phenomena. Therefore, the energy input required to grow new bone material and the energy release when bone material is removed was not directly modeled (see Subsection 2.3.2.2) [87, 200]. In many of these kinds of studies, the nodes of the finite element generated during the discretization of the geometry for the finite element analyses represent the bone cells that collect and relay the signals of changes in mechanical conditions as well as produce the resulting structural changes to the bone surface [201, 202]. Applying this assumption to the developed model, the locations of the surface nodes are moved as a result of measures of the local (nodal) stress state. In this work, only the shape adaptations in skeletally mature adults were considered. Therefore, material accretion or resoption did not occur in the longitudinal, or axial, direction, and the bone shape was only modified normal to the "cylindrical" surfaces as represented in Figure 1.2 [16, 17]. Finally, the current model assumed that the direction of the loading (tensile vs. compressive or clockwise or counterclockwise torsion and moments) had no effect on the predicted adaptations [57].

As described in Chapter 1, the alterations in the shape and, therefore, strength of the cortical bone tissue region of long bones function to reduce the locally high stresses or to increase the locally low stresses, resulting in a more uniform distribution of surface stresses. As a result, the prediction of the surface profile changes due to variations in its mechanical stress state can be thought of as a type of optimization problem with the goal of creating uniformity in the surface stresses, or more generally, in the state of stress of the bone's surface. Like the optimization methods used to determine the muscle force magnitudes discussed in the previous section, many different numerical models have been developed to predict the shape and strength changes of cortical bone. The methods vary both in the particular measure used to describe the stress state at the bone's surface, often referred to as the "mechanical stimulus", and in the mathematical method used to solve the optimization problem.

A large amount of both numerical and experimental research has been devoted to determining the local mechanical measure that drives the shape changes. Average, equivalent, and principal stresses and strains, individual components of the stress and strain tensors, energy measures such as strain energy density have all been suggested as the mechanical stimulus behind bone strength adaptations, as have gradients of these values with time and space [87, 96, 100, 106]. Preliminary studies in this work examined the effects of using different measures of the mechanical state of the bone as the part of the optimization goal and are more thoroughly discussed in Chapter 4.

An equally large number of studies in the literature have examined the specific mathematical optimization methods used to predict these shape changes. Gradient-based methods, such as the ones used in the model to determine the muscle force magnitudes,

and less mathematically rigorous ones, such as gradientless optimization methods, that find both local and global optima have been employed [203-208].

The techniques that have been developed to simulate bone's shape and strength adaptations are similar to the shape optimization methods created to design inert mechanical components based on size and strength criteria. In these shape optimization methods, the set of unknown "design variables" is typically the locations of the points defining the surface profile. In this work surface node positions are used, but shape control points that describe geometries, like those used in the b-splines and Bezier curves to approximate surfaces can also be used as the design variables [209]. However, because of the geometric complexity of the typical bone surface, even with significant simplifications, the number of unknown design variables in these shape optimization problems is often very large, even when using line or surface control points rather than finite element nodes. The optimization methods selected for this work were required to function relatively efficiently to calculate the changes to the locations of surface nodes on a three-dimensional mesh.

The optimization usually proceeds iteratively. The local mechanical stress state of the bone is typically determined through finite or boundary element methods based on a prescribed set of boundary conditions (loads or constraints). To obtain loading conditions on bone due to the muscles, the magnitudes of the independent muscle forces must be found. The local growth or decay of the bone at discrete points along the surface is simulated through a mathematical relation that converts the value of the measure of local mechanical stress state of the bone to the amount of change of the local positions of points (nodes) describing of the bone's surface. The boundary conditions are applied

again, the distribution of the local mechanical state determined, and the new surface profile formed. The process is repeated until a prescribed stopping criterion is achieved.

The mathematical equation used in many of these models is:

$$Growth_k(l) = \alpha \left(Measure_k(l) - Measure_{threshold} \right) \tag{2.41a}$$

$$\mathbf{X}_{k+1}(l) = \mathbf{X}_k(l) + Growth_k(l) \tag{2.41b}$$

where l is the lth node or control point, α is a constant (but can also be a function of system variables), "Measure" is the selected measure of the local mechanical state of the bone, such as von Mises stress, strain, or strain energy density and "threshold" is a reference value of this measure against which each local measure is compared. The nodal position $\mathbf{X}_k(l)$ is changed at each optimization iteration to $\mathbf{X}_{k+1}(l)$ by the amount calculated by the "Growth" relation. This process is applied to each surface node or control point after the solution of structural analysis, which is usually performed using finite element or boundary element methods, to determine the new position of each surface point. Values of local measures below the threshold value trigger resorption, and values above the threshold trigger material accretion. This threshold value may be a constant value determined by experimental measures [210] or a failure limit of the material, such a maximum allowable stress [211, 212]. It can vary with location [89], magnitude of applied load [91] or even iteration, such as an average measure calculated from the current mechanical state of the bone [213]. The threshold may also include a range of values over which no material shape changes occur [214]. The α value scales the amount of growth or decay and is sometimes taken as the rate of adaptation or step size of the optimization process.

Because the value/values of the mechanical state measure's threshold, the rate of shape change, α, and the growth relation itself (i.e. changing from linear to nonlinear) can all alter the local nodal positions and the overall predicted bone shape, much research has been undertaken to determine the values of these parameters that can properly predict experimental observations. However, because, in many of these models, the parameters are chosen to match experimental measurements of accretion or decay of the cortical bone surface at a particular time or a particular load, this often results in models that are applicable only to the conditions of the experimental study used to determine the model parameters. Therefore, despite the significant amount of different bone strength and shape adaptation models in the published literature, their universal application is often limited. Because the intent of the current work was to develop modeling techniques to compare the effectiveness of various loading conditions on improving local bone strength, a model with results independent from the arbitrary selection and adjustment of parameters driving the predictions was required. Extensive effort to develop a computational bone shape adaptation model that meets these more universal application criteria was put forth in this work and is described in detail in Chapter 4.

In addition to adaptation modeling methods, stopping or convergence criteria must also be defined. Many bone shape adaptation models simply choose α to be a rate and run the simulation over a specific period of time [88, 90, 93, 112]. By stopping the model this way, no indication of the level of approach to the optimization goal of lowering peak stress and improving uniformity of the stress distribution in the bone is calculated. While, as with the selection of modeling parameters, this may be suitable when comparing the numerical predictions to experimental observations, difficulties arise

when trying to compare the effects of different loading modes or conditions different than in the particular experiment from which the model was generated. Therefore, significant work was performed as part of this study to develop such model convergence criteria, and this work is discussed in Chapter 4.

A model that is universally applicable to many different loading conditions must be able to appropriately predict the mechanical response and the resulting shape adaption over the entire bone surface and then compare the resulting change in the behavior of the bone that has developed for the different loading conditions. Progress towards methods for such a comparison is subject of the final phase of the model development.

2.4   Method for Comparison of Effectiveness of Strength Adaptation Techniques

The modeling methods developed in this work not only must accommodate the numerical determination of the alterations to the surface profile of the bone resulting from changes to the boundary conditions and loading environment of the bone, but also must permit the tracking of the resulting variations in stress and strain distributions at discrete locations within the bones studied. By complying with these conditions, the methods of this work are capable of quantitatively comparing measures of the effectiveness in improving bone strength of the shape change that result from each set of loading conditions studied. The development of such a comparative measure is described.

2.4.1 Typical Geometric Measures of Bone Strength

Since the early clinical observations and experimental models, a direct correlation between bone size and strength has been noted. Many experimental models simply tracked the amount of bone growth either by changes in a particular linear dimension,

such as a radius or bone thickness measured at a discrete point, or changes in more regionalized dimensions, such as the area of a cross-section, as the quantitative measure of the improvement in bone strength under a particular load [57, 59, 60, 63, 69]. If these dimensional measurements increased, the bone was said to be strengthened and the loading conditions mitigated bone losses. If the values of these measurements decreased, the bone was said to be weakened and the loading conditions were not conducive to bone strengthening. These dimensional measurements are simple to repeatedly track with time using a series of X-rays.

As medical imaging technology became more sophisticated, more complex measures of bone geometry could be compared between living subjects. Area moments of inertia about particular axes and polar moments of inertia could be automatically calculated using the software supplied in CT or similar imaging devices. The ability of the bone to resist bending or torsional loads could be directly compared [100, 130, 215].

With the increased use of computational models to analyze medical imaging scans or even to simulate bone shape changes as a result of loading conditions, more specific and numerous quantitative measures of the changes to a bone's geometry became available. Geometric measures such as the perimeter [25, 130] of the endosteal (inner) and periosteal (outer) surfaces, measures of circularity [130], section modulus, [130], radius of gyration, center of gravity, and principal axes of the principal moments of inertia [216] have all been reported in addition to the radii [93], area (both of the entire cross-section and just the cortical region) [95, 112, 130], moments of inertia [112, 130, 217], and cortical thicknesses [64, 218-221] previously used.

All of these measures can be correlated to an object's strength. However, the universality of the conclusions drawn based on each of these measures is often limited to changes in the ability of the bone to resist a particular mode of loading. For example, cross-sectional areas are related to compressive loads; area moments of inertia are related to bending loads about particular axes; polar moments of inertia are related to torsional loads; section moduli combine bending and torsional loading as do measures of eccentricity like centers of gravity and circularity. However, bones are subjected to combinations of numerous modes of loading. It has been shown that measures of combined loading strength, such as section moduli, correlate better with measures of bone density [130], which are often used as an indicator of whole bone strength.

There are limitations to the use of such geometric measures to indicate strength changes. First, these measures are often taken at one particular location and, therefore, indicate a local strength, not the overall strength of the whole bone studied. Some attempt at addressing this concern has been made by performing these calculations at multiple cross-sections over the length of the bone and considering the changes in the extreme values of these measurements [217]. In doing so, however, the understanding of relative changes at particular locations is lost. Second, because these measures are often indicators of one particular mode of loading, changes that increase the resistance to one particular loading mode may make the bone weaker in another. Finally, attempts to create quantitative values that are combinations of these geometric measurements that address strength resistance to a number of loading modes, such as through the use of dimensionless parameters, are often not possible. This is because dimensional analysis methods assume that the relative shapes remain the same and only size changes. Bone

shape adaptation, like shape optimization in mechanical design, is not a simple scaling of the geometry, but a complete alteration of the surface profile.

While geometric measures can give a rough idea of strength changes, if a more precise quantitative comparison of strength resistance is desired, alternative methods are needed. Because bone strength adaptation through alterations in shape is similar to structural shape optimization in the design of inert mechanical components, research in that field was examined to determine an effective means of comparison in this work.

2.4.2 Measures of Strength Changes in Shape Optimization

The general mechanisms for the strength adaptations of bone and the shape optimization in mechanical component design are similar. Both involve the accretion or removal of material on the surfaces of the object. Likewise, their goals are related to the reduction in the overall variation of the stress distribution on the object's surface or a reduction of the overall maximum stress within the object [203]. Often the goal of structural shape optimization is a reduction in the maximum stress in the component due to a particular load set to a value below the yield strength. This load set is usually the most extreme load typically encountered by the device studied. Thus, the inert mechanical component is designed such that its weakest location will not fail under this specific condition. Similarly, the adaptive changes to bone alter its strength to reduce extreme stress at locally weaker locations in response to the typical mechanical environment.

Such a concept is applicable to the determination of comparison criteria for various bone strengthening loading schemes. While the different exercises or loading sets usually produce improvements in bone strength under the particular applied load or the exercise, the strength improvements may not result in the ability of the newly shaped

bone to resist a different set of loads than those applied to create this new geometry. Therefore, a beneficial means of comparison would be to subject the newly shaped bones that are created by the different loading conditions studied to a common set of loads and calculate the strength measures under this one loading condition using the newly adapted (optimized) bone shapes. As the design of mechanical components employs shape optimization to improve strength for an extreme loading condition, the choice of the comparison load set for bone strengthening analysis should represent an extreme typically encountered load. Improvements in the ability of the newly shaped bone to resist this common comparison load would represent a measure of effectiveness of the exercise on improving the bone's strength.

2.4.3 Selection of the Comparison Load Set

As discussed in Chapter 1, disuse models, from bed rest an immobilization studies on earth to measurements of those spending time in near weightlessness, have shown that loss of bone and muscle strength (often measured by bone density and muscle volume) increases at locations that are more distal along the leg. Thus, a bone strengthening routine that can target the losses in the distal portion of the leg may be beneficial. The strengthening of a targeted location was the objective of the studies in the second part of this work (Chapter 5) where the developed modeling methods were applied.

2.4.3.1 Observed Bone Fractures in the Distal Portion of the Leg. There have been many reports of stress fractures in the tibia upon relatively significant and sudden changes in muscle forces. For example, stress fractures occur after resuming weight bearing following immobilization due to a previous bone fracture [222]. Stress fractures of bone have also been reported after surgeries that alter the muscle force balance in

otherwise normal bones, such as after joint replacement surgery [222]. Finally, these fractures have been reported after increasing physical activity due to job demands [223], sporting activities [25, 26, 224], or military activities [24, 225]. Most of these stress fractures do not occur upon the first episode of increased load, but after a few weeks of the new loading pattern [224, 226, 227]. These observations indicate the potential hazards of suddenly subjecting a bone to significantly increased loading. This intensified loading condition can occur not only in those conditions described above but also upon changes in gravitational forces, such as a return to Earth or arrival to another planet after spending long times in a near-weightlessness environment. Therefore, the methods to prevent such fractures can be beneficial.

2.4.3.2 Specific Location of Fracture. Most of these kinds of fractures, especially due to increased activity, occur in the distal portion of the tibia. Stress fractures due to running have been observed at a location one-third of the length of the tibia measured from the ankle joint [228]. Fractures typically are located in the cortical tissue only, usually on the posterior (back) side of the bone, and rarely go through the entire diameter of the bone [224]. Fractures frequently occur eight to twelve weeks after increased activity [223, 224, 227, 229]. This might be enough time for muscles to increase their strength but before the bone strength is fully increased. Interestingly, a thickening of the cortical bone has been observed in the region of the stress fracture immediately after the fracture but before a callus has the chance to form [224]. This could be related to the initiation of strength adaptation of the bone shape due to increased stress/strain in the region even before the fracture caused noticeable failure of the bone structure. The common observations in the locations of stress fractures due to increased weight bearing

activities, particularly walking, running, or marching seem to indicate a common cause.

2.4.3.3 Loading Modes related to Stress Fractures of the Tibia. Much research has been undertaken to determine why stress fractures often occur in the distal tibia. Through the use of gait analysis and subsequent kinematic calculations, greater impact forces, hip and ankle angles, muscle forces and loading rates have all been associated with stress fractures in the tibia [230]. More detailed studies have attempted to separate the effects of each of these possibilities to determine the activities or conditions that may induce such failures to the otherwise healthy bone structure. A study of drop jumps, simulating the impact forces upon landing during running or marching, measured the strains on the bone directly through surgically attached strain gages [231]. While high impact forces between the body and the ground were found during drop impact, the values of the recorded maximum bone strains were no higher for running, implying that the positioning of the upper body and joint angles throughout the leg improved the ability of the musculoskeletal system to "absorb this impact" and prevent its transmission to the bones. Similarly, calculations of the stress in the bone of an averaged size person under loading conditions that represented increased "training exercises" were found to be well below the fracture strength of bone tissue material [232].   From these observations, it has been suggested that stress fractures might occur in regions where large amounts of remodeling, which temporarily weakens the bone, coincide with regions of high stress.

More specific studies correlating the phases of gate to ground reactions and muscle forces have provided additional insight into the mechanisms of stress fractures. Significant bending moments in the sagittal plane have been found to increase distally from the knee to the ankle during the stance phase of gait, with the maximum moment

occurring at mid-stance [26, 233]. This bending stress, thought to be related to the large muscle forces required to oppose the reaction forces generated at the knee and to keep the knee joint stable, has been shown to cause large tensile loads on the posterior side of the bone, the location most noted for distal tibia stress fractures. Measurements of the ground reaction forces during running have shown that the most variability between individuals in the magnitude and direction of the ground reaction force also occurred during mid-stance, presenting the possibility of large, odd-directed loading in the tibia [234]. These studies demonstrate the likelihood of a relationship between high muscle forces and stress fracture. They also implicate the forces generated during mid-stance, rather than the impact forces imposed during landing, as a probable cause of these fractures. This explanation correlates well with the previously noted observations that the stress fractures often occur after a few weeks of altered activity as muscles strengthen.

Although the reviewed studies seem to explain the conditions conducive to stress fracture in the tibia, the development of stress fractures in the presence of these factors is not universal. When comparing the ground reaction forces generated by people who have developed stress fractures to those who have not, no significant differences in the magnitude or direction of these loads were found [26]. Likewise, stress fractures of the distal tibia do not occur in every individual who experiences a sudden increase in weight-bearing loads. In mathematical terms, the loading conditions may be "sufficient" for the stress fracture to occur, but other factors are required to provide the "necessary conditions" for the fracture to actually form. Therefore, much research has been performed to identify the unique factors that are specific only to the group of individuals

that have incurred stress fractures. The identification of such factors would allow for the prediction of increased susceptibility to this type of bone damage.

2.4.3.4 Correlations of Bone Strength Measures to Stress Fractures in the Tibia. Various measures of the intrinsic and extrinsic properties of bone have been compared between people who have sustained stress fractures to those who have not but have undergone identical military or athletic training. The occurrence of stress fractures has not been found to correspond to specific trends in the intrinsic material properties of the bone such as bone mineral density, mineral content, or cortical porosity [24-26, 226]. However, correlations between stress fractures and the extrinsic geometric properties have been uncovered. Smaller absolute geometric measures, such as total cross-sectional area, cortical area, diaphyseal width, and moments of inertia related to bending in the sagittal plane have all been associated with increased incidence of stress fractures [24-26, 225, 226]. Even when these measures were weighted by body size for a more direct comparison between subjects with and without stress fractures, those who sustained fractures were found to have smaller sized tibial shafts, especially at the "fracture prone" distal third of the tibia, than those who had no fractures [24, 26]. Therefore, it has been suggested that measures of the size of the distal tibia could be used to identify an increased risk for stress fracture. Such an identification could permit these individuals to undergo additional exercises to increase the bone's size prior to the standard military or athletic training [24] or even prior to increased activity after prolonged disuse from injury, disease or time spent in microgravity.

2.4.3.5 Comparison Case Definition. The review above indicates that the likelihood of the development stress fractures in the distal tibia during increased activity is directly

related to the tibia bone's geometry and that the cause of the stress fracture is directly related to muscle forces induced on the tibia bone itself. Therefore, the prevention of stress fractures may be achieved through the development of exercises (or sets of muscle loads) that improve the strength of the tibia bone in the commonly damaged region located one-third of the length of the tibia from the ankle joint.

These clinical observations can be translated to mechanical design criteria for application in the computational modeling and analysis methods developed in this work. The loading conditions that cause stress fractures of the distal tibia in those individuals that are at risk for such failure of the cortical bone structure were selected as the critical design load. As such, the ability of the distal tibia to resist loads that may cause stress fractures was selected as the comparison criteria for the analysis of the effectiveness of the various exercises examined in this study. Specifically, the maximum stress developed at the location of most of these fractures, the cross-section at one-third of the length of the tibia from the ankle joint, under stress-fracture inducing loads, was chosen as the quantitative measure of comparison of the effectiveness of the individual exercise loading and bone configuration cases studied in this work. The lower this maximum stress value when the shape adapted bone system is placed in the comparison case configuration and subject to the comparison case "design" load, the further away the bone material is from the yield or fracture strength of the cortical bone tissue and the less likely the stress fracture is to occur.

In order to more clearly define the stress fracture inducing, critical design load, the conditions at mid-stance during running were further analyzed. Based on the review in Subsection 2.4.3.3, it is this loading environment where large bending moments are

induced in the distal tibia, increasing the potential for stress fractures.   To incorporate

this loading environment into the developed model, the limb configuration (joint angles),

joint moments, and lines of action of the muscle forces must be explicitly defined. From

this information, the magnitudes of individual muscle forces and the resulting stress

distributions on the bones of the leg system can be determined.

The mid-stance phase of running, jogging, or walking corresponds to the time

when the foot is in most contact with the ground. At this time, maximum support

moments develop at the joints, minimum horizontal forces, and maximum vertical thrust

ground reaction forces, up to three times the body weight, occur as the foot prepares to

lift the leg or, depending on the speed of gait, the entire body off the ground in a phase of

gait called "push off" [235-241]. At this stage of gait, the ankle acts to generate the

impending liftoff power, the knee acts to absorb energy from the recent landing and the

hip acts to stabilize the upper body [241]. Many experimental measurements have been

performed on human subjects walking, running or jogging in order to determine joint

angles and joint moments through the complete gait cycle, including the mid-stance

point.   Therefore, the joint moments and angles necessary to defined the system

configuration for the comparison analysis in this work were obtained from the published

literature. The particular values of the joint moments and angles used, which are listed in

Table 2.11 were taken from a study of a healthy adult male of weight 79kg (170lb)

jogging at 2.72m/s (6mi/hr) [241]. These values were consistent with those derived from

a number of other similar studies [236-238, 240]. Because stress fractures are prevalent

both in runners and in the military where significant marching occurs, jogging was

deemed a suitable comparison activity that averaged the speeds of these two common

activities. The descriptions of the local bone segment coordinate systems with respect to the global coordinate system as described in Subsection 2.1.3 are presented in Table 2.12. The angles defining the lines of actions of the muscle forces as in Subsection 2.1.3 and Figure 2.12 are presented in Table 2.13. The muscle moment arms, determined using the same methods as Subsection 2.1.3 and Figure 2.13 are listed in Table 2.14.   In this preliminary study, the resultant force created by the system for this comparison case was identified through prescribed moments about the hip, knee and ankle joints.

Table 2.11 System Parameters for Comparison Case - Midstance Jogging

Joint	Joint Moment (N-m) CCW+	Joint Angle (deg)
Hip	-30	20
Knee	180	45
Ankle	160	20

Table 2.12 Coordinate Transformations from Global to Local for Each Bony Segment

Transformation	Pelvis LCSYS (Anterior Superior Iliac Spine)	Femur LCSYS (Greater Trochanter)	Tibia LCSYS (Tibial Tuberosity)	Foot LCSYS (Calcaneous)
X (m)	0	-0.0560	0.0632	-0.1568
Y (m)	0	-0.0894	-0.5366	-0.8749
Theta Z (deg)	0	0	0	0

Table 2.13 Angular Direction, α, of Muscle Force Application on Bone Segment (Refer to Figure 2.12) (degrees)

Muscle	Origin Bone	Origin α	Insertion Bone	Insertion α
SART	Pelvis	-166.244	Tibia	-25.000
RF	Pelvis	-165.113	Tibia	-25.000
IL	Pelvis	169.688	Femur	-10.312
GM	Pelvis	-156.615	Femur	30.183
LHBF	Pelvis	-161.505	Tibia	18.495
TA	Tibia	168.096	Foot	-11.904
SOL	Tibia	148.570	Foot	-31.430
GAST	Femur	152.886	Foot	-27.114
VAST	Femur	-160.000	Tibia	-25.000
SHBF	Femur	-166.329	Tibia	13.671

Table 2.14 Perpendicular Distance Between Muscles and Joints (m)

Muscle	Hip
SART	0.06135
RF	0.53141
IL	0.02967
GM	-0.028
LHBF	-0.0318

Muscle	Knee
SHBF	-0.0407
LHBF	-0.0428
GAST	-0.0395
VAST	0.015
RF	0.01556
SART	0.01567

Muscle	Ankle
TA	0.07189
GAST	-0.0543
SOL	-0.0498

Unlike the static isometric loading conditions compared in this work, where the joint angles remain constant during loading, jogging is a dynamic activity. Therefore, the angular acceleration of the joints and linear acceleration of the bone segments must be considered in the conservation of momentum equations used to calculate the individual muscle forces (Equations 2.26 and 2.27). However, only one particular instance of the jogging cycle, midstance, was considered as the condition with the greatest potential for stress fracture in this comparison case. At midstance, the leg is fixed to the ground and the linear acceleration of each body segment and the angular accelerations of each segment about the ankle, knee and hip joints are typically small [242, 243]. Therefore,

acceleration can be neglected, and the system can be considered static at the moment in the jogging cycle used as the "critical load" condition in this study. In verification of this assumption, the published literature has shown that comparisons of calculations made using balances of linear and angular momentum that include or neglect the body segment linear and joint angular accelerations result in small overall differences, even at the hip, which is the location of the largest accelerations at the midstance point of gait [243].

To compute the effects of the studied loading conditions on the improvement of the bone's strength, the optimized geometry was subjected to the "critical design conditions" of mid-stance jogging. The same geometry, mesh, material properties, joint contact model, and methods of applied loads as in the predictions of the shape changes of the tibia bone resulting from these exercises as described earlier in Chapter 2 were employed. Additionally, the same set muscles were assumed to be involved in this activity and to act at the same locations on the bones of the system. Therefore, only the locations of the boundary constraints had to be determined for this comparison condition.

At midstance of the gait cycle during jogging, the center of pressure of the foot in contact with the ground is at a location approximately 70% of the foot length from the heel [244]. Based on this, in the model used in this work, a square region centered at a location 70% of the model's foot length from the foot reference coordinate system at the calcaneous, or the heel, was fully constrained against translation in all directions. This region was the full width of the foot bone volume and had a length of one half of this dimension. The top of the pelvis was similarly constrained to indicate connection with the upper half of the body. The final limb configuration for this comparison case is

shown in Figure 2.15. The lines of action of muscle forces are represented in red, and the applied boundary constraints are shown in blue.
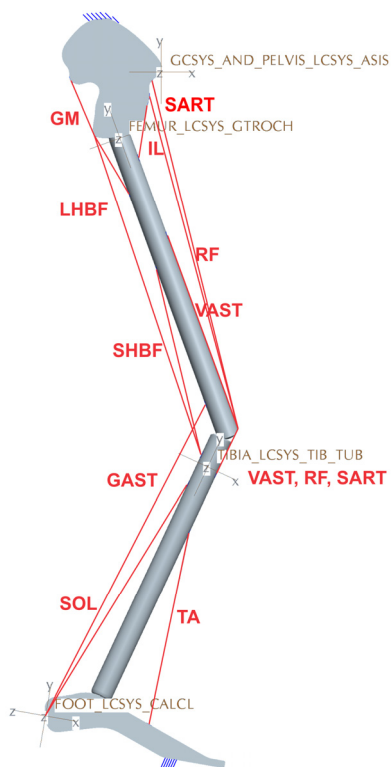
Figure 2.17 Limb configuration and boundary conditions for comparison case.

2.5   Summary

This chapter has provided the full definition of the problem investigated in this work and the basic methods used for its analysis. The system studied was the bones of the leg from pelvis to foot. Contact between the bones at the hip, knee and ankle joints was simulated. Cancellous bone tissue and cortical bone tissue were included at the appropriate locations. Cortical bone tissue was modeled as a transversely isotropic material, while cancellous bone tissue was given fully isotropic material properties. The forces acting on the leg were restricted to a two-dimensional sagittal plane. The bone geometry, however,

was three-dimensional in shape, though simplified to accommodate the two dimensional forces. Ten major muscles imparted the loads on the bone system.

The strength shape optimization of the tibia was predicted under a number of different isometric loading conditions. Under all conditions, the resultant force between the toe and a fixed surface was prescribed as were the hip, knee and ankle joint angles. Varying the resultant force direction, the effect of the set of muscle force magnitudes was studied, while varying the joint angles allowed for the investigation of the effect of muscle force direction. The effectiveness of the new bone geometries that resulted from the adaptation processes due to these various conditions in improving the bone strength was compared by subjecting each to a common loading case. Because stress fractures in the distal portion of the tibia have been identified as a potential hazard to ambulation in many situations, the newly shaped tibia bone was studied, as part of the whole leg system, under conditions of mid-stance during jogging, a condition where stress fractures are likely to occur. The reduction in the maximum von Mises stress at the location likely to fracture from that induced on the pre-adapted shape was then compared for the shape adapted geometry produced by each loading condition/set of joint angles studied. The case that demonstrated the greatest decrease in this measure was deemed most effective at improving the tibia bone strength.

In order to complete these comparative studies, significant work was done to develop the necessary computational modeling methods. These techniques coupled optimization methods with structural analysis methods to determine the magnitudes of the individual muscle forces, the response of the bone system to these forces and the ensuing shape changes to the tibia bone. The modeling methods were developed in this

work so that they could be used to study the diverse system configurations and boundary conditions desired for the comparative studies explained with no changes to the computational code and with no dependency upon experimentally or arbitrarily selected parameters. The developed methods had a basic iterative algorithm. From the given joint angles and net resultant isometric force, the individual muscle forces were fully determined through a mathematical optimization method and applied to the multi-bone system. A structural analysis was performed using finite element methods to determine the local mechanical state along the bone's surfaces. Based on a measure of this state, the changes in the positions of local discrete points on the surface, representing local material accretion or resorption, were calculated using another optimization method. These surface points were then moved accordingly. Criteria to indicate the completion of the simulation were checked and the process was either repeated or was terminated. The goal of the muscle force magnitude optimization is related to the efficient operation of the set of muscles studied. The goal of the bone shape adaptation optimization is related to improved uniformity of the bone's structural response to these muscle forces.

The remaining chapters discuss the development and application of modeling methods to analyze these problems. Much work was done in the development of the modeling methods in order to meet the goals of independence from experimentally based or arbitrarily selected parameters, of universal application with no alterations to the programmed code, and of the direct quantitative comparisons of the effectiveness of each set of loading conditions/configurations on improving the strength of the bone. The components of the full modeling method, the muscle force magnitude model, the finite element model, and the bone shape strength adaptation model were developed and

validated independently. They were then coupled for use in the comparative study described above.

The work described in Chapter 3 constitutes the first component of the methods developed in this work to predict and compare bone strength adaptations due to variations in muscle activity. Specifically, the chapter focuses on the development and validation of the modeling methods to determine the individual muscle force magnitudes that are applied to the multi-bone system.

CHAPTER 3

MUSCLE FORCE MODEL

3.1   Introduction

The mechanical environment of any bone is directly related to the muscles that act on and around it. As discussed in Chapter 1, because the musculoskeletal system has evolved with a focus on movement rather than force resistance, muscles act on the bones near the joints. This allows for more efficient motion control as small linear displacements of the muscle (small contraction) can result in large angular displacements of the limb. However, the close location between the muscle force attachment point and the joint center results in the necessity for relatively large muscle forces to resist the moments generated when a weight or other force acts at the end of the limb (Figure 3.1). As a result, muscle forces are often some of the largest forces acting on a bone or system of bones, and the proper simulation of the mechanical environment of a bone relies on the proper estimation of the muscle forces acting on it.

$$\Sigma Moments_E = 0$$
$$Fm_y d1 - Fw_y d2 = 0$$
$$Fm_y = Fw_y (d2/d1)$$
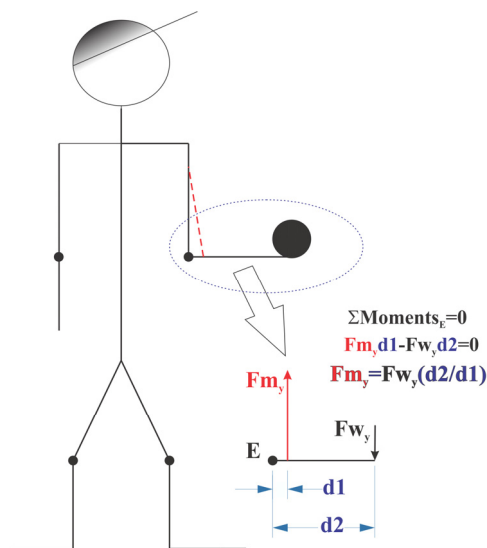
Figure 3.1   "Mechanical disadvantage" of muscle forces in external load resistance.

The studies reviewed in Subsection 1.3.2.3 emphasized the importance of the accuracy in the representation of the boundary conditions over the accuracy in the representation of the physical geometry in predicting the response of a bone to encountered loading. Therefore, the development of the appropriate methods to determine the magnitudes and distributions of the muscle forces acting on the surfaces of a system of bones was necessary in this study of the adaptations of bone strength to changes in its mechanical environment. This chapter discusses the development and validation of a modeling method to determine the individual muscle forces acting on a bone, specifically within a multi-segment, multi-bone system.

3.2   Background

As discussed in Chapter 2, the resolution of the magnitude of the force generated by each individual muscle in a system is a redundant, indeterminate problem. Because the accurate representation of the activity of individual muscle forces is important in the analysis of the behavior of bone systems, many different methods that have been developed in the field of solid mechanics have been applied to these musculoskeletal systems to resolve the indeterminacy. The suitability of these methods has often been determined though comparisons of the trends in muscle force magnitudes predicted by models to trends in the electrical currents generated by active muscles as measured through electromyography or EMG. A review of some of the methods that have been used is given here.

3.2.1 Numerical Models to Determine Muscle Force Magnitudes

Early methods of determining muscle force magnitudes involved reducing the number of unknown values in the momentum conservation equations to the same number of these balance equations, thereby converting the indeterminate system of equations to a determinate one. This was achieved through simplifying the defined system model [191]. Muscles that were known to work together or act over the same regions and result in the same function were grouped together to form a single unknown force. Additionally, the inactivity of other muscles was assumed to eliminate them from the system of unknowns. As computational resources began to increase in the 1960's, many numerical methods to solve more complete mathematical models of physical systems began to be developed. One of these emerging fields was that of numerical optimization, where indeterminate problems could be solved through iterative "searches" towards mathematically stated "goals" or "objectives". Such methods were initially applied to musculoskeletal systems by researchers studying the muscle activity during walking or "gait" in the early 1970's, when linear optimization goals, such as finding the minimum sum of muscle force magnitudes, were used to find the "optimal configurations" of muscle forces in the walking leg [191]. These optimization problems were usually constrained by compliance to the momentum balances in the system and by ensuring that only tensile muscle forces resulted, since muscles cannot produce compressive forces [127]. While the constraints applied to these models have not varied significantly between these early models and present times, many different objective functions, depicting the optimization goal, have been used.

To explore which goal may be the most appropriate in predicting muscle activity, more complex goals were developed in response to advances in more evolved computational methods and resources, and relative comparisons were made among the resulting muscle force predictions for different goals and to EMG measurements. These later developed optimization goals were often nonlinear and involved weighting factors to account for variations in load carrying capacity of different muscles in the systems analyzed. An early study of these more complex goals compared the predictions of the minimization of linear and nonlinear, weighted and nonweighted sums of muscle forces [127]. The muscle forces were weighted through the normalization of each muscle force by the maximum possible static, or isometric, force the muscle could exert. While the different numerical models resulted in similar force magnitudes for many of the muscles studied in the walking leg system modeled, the nonlinear, weighted optimization goals were found to best match EMG data in terms of predicted muscle activity and intensity. In order to prevent overprediction of muscle force magnitudes, additional constraints of the maximum allowable muscle forces were incorporated into these methods. As a result of this early investigation by Pedotti and Krishnan [2], muscle force prediction models began to focus on the application of various nonlinear optimization methods and the inclusion of various weighting factors.

In the early 1980's, an optimization criterion [193] was developed by Crowninshield and Brand based on previous studies of the relationships between muscle force magnitude, geometry, and ability of muscles to hold a constant force over time. Because it had previously been shown that the maximum time a muscle could hold a force of a particular magnitude (intensity) was inversely related to the magnitude of the

force raised to a power, *p*, and that the maximum force a muscle can produce is linearly proportional to the size of the muscle, this optimization criterion used a nonlinear sum of muscle forces weighted by the muscle size to represent a maximum of muscle endurance. This endurance optimization was thought to be important in repetitive activities such as walking.   By weighting the muscle force magnitude by the size of the muscle generating the force, a measure of muscle "stress" was created. The muscle size was represented by a standard anthropometric measure of the average muscle cross sectional area, called the physiological cross sectional area or PCSA, which is calculated as the muscle volume divided by its length [245].   The basic optimization criterion developed is shown in Equation 3.1, where *n* is the number of muscles in the system studied and F_l, is the lth muscle's force magnitude, and *PCSA* and *p* are as defined above.

$$Z(\mathbf{F}) = \sum_{l=1}^{n} \left(F_l \Big/ PCSA_l \right)^p \tag{3.1}$$

In studies of the application of this criterion, the methods' developers used a Euclidean norm of this optimization goal, the pth root of the sum, to ensure the optimization function has equivalent units to the optimized variable, the muscle stress, and to reduce the overall magnitude of the objective function as they investigated the effect of the value of *p*.   However, they noted that this normalization is not required. Parametric studies involving this power, *p*, showed that the predicted muscle force magnitudes were relatively insensitive to powers (*p*) of greater than two.

Later models expanded on these two main forms of the optimization criteria, the muscle force normalized by maximum muscle force magnitude or the muscle force normalized by the muscle size. Additional linear and nonlinear weighting factors were incorporated to better represent muscle structure and physiology. For example, the inclusion of measures of the relative amounts of muscle fiber types were thought to better predict fatigue resistance, and, therefore, endurance [246]. As the understanding of the function of muscle fibers grew, additional terms were added to the optimization goals to include the specific aspects of their anatomy and behavior. These types of goals focused on the activation of the muscle rather than the amount of muscle force generated [195]. Rather than absolute muscle forces [127] or stresses [193], optimization goals that considered these values in other models were normalized by the maximum generated forces or the maximum allowable stresses [247] under the assumption that the musculoskeletal system "recruits" additional muscles to generate the necessary forces only as single muscles approach their individual maximum strengths.

As the number of muscle force prediction models and the methods for solving numerical optimization problems grew, the research began to shift focus towards studies comparing these numerical models and developing tools to determine which might be most applicable to the study of musculoskeletal systems. Despite the large number of these kinds of studies, researchers have failed to show one model to be superior to the others in predicting the muscle force activity and intensity. Yet, the results of these comparative studies provided important insight into both the function of the models and the function of muscle force activation and activity in actual systems.

3.2.2 Comparison Studies of Muscle Force Prediction Models

Studies have been undertaken to compare optimization goals, constraints, and solution methods for determining the individual muscle force magnitudes in these indeterminate musculoskeletal system models. Comparisons have been made both between different models and between models and experimental results. Because there is no proven method to convert quantitative measures of electrical activity in muscles to resulting magnitudes of generated forces, comparisons to EMG activity are usually qualitative, comparing relative intensities of muscle forces within the system studied to those of the electrical currents in the muscles measured by EMG [127, 245]. Some general conclusions from these works will be reviewed.

It is widely agreed that nonlinear optimization criteria result in muscle force activities and intensities that correlate more closely with experimental measurements than do linear criteria and nonlinear optimization criteria are, therefore, preferable [127, 192-194, 196, 197, 248]. Linear optimization methods have been found to "unnaturally" require the orderly addition of muscle forces where one muscle force is maximized before another is activated, necessitating not only the appropriate designation of the maximum muscle forces in the constraint equations, but also accurate enforcement of inter-muscle relationships, both of which are difficult to define [192, 248]. Nonlinear schemes have been found to predict more muscle activity for force sharing in synergistic muscles (with similar functions) and opposition forces for stability in antagonistic muscles (with opposing functions), higher joint contact forces, and "improved continuity of predicted muscle activity" during a gait, or walking, cycle than linear schemes [196, 248]. It has also been suggested that while both the sum of the squares or cubes of the

muscles stresses are able to achieve muscle force predictions that are very similar to each other and to trends in EMG activity, the cubed criteria may be less dependent upon constrained values of minimum or maximum force [197]. The minimization of the sum of the cubes of the muscle stresses, thus, may predict extensive load sharing to keep the individual muscle forces as low as possible [248] while the minimization of the sum of the square methods may be implemented more efficiently [197] and may provide more realistic load sharing than the minimization of the sum of linear or cubic terms [248]. Other studies have concluded that these nonlinear schemes eliminate the need for maximum or minimum force criteria altogether [193].

Methods that weighted the muscle forces with physiological parameters such as PCSA, moment arms, and relations between muscle forces and activity properties like amounts and rates of muscle length changes, fiber content, or activation, improved correlation with experimental EMG data trends over methods that use linear or nonlinear sums of muscle force magnitudes alone [192, 194, 195, 197, 246]. For example, it was found that minimizing the sum of muscle forces alone gives greater preference and, therefore, greater predicted muscle force magnitude to muscles with the largest moment arms. This may result in unrealistically large forces for very small muscles [192] and, depending on the muscle location/moment arm, result in an equal force for all muscles regardless of their state [194]. The minimization of muscle stresses (forces weighted by areas) accounts for the relationships between the force generation capability and the muscle size by giving preference to muscles with the largest product of the muscle moment arm and the cross-sectional area [192]. However, use of the minimization of muscles stresses may overestimate the forces in larger muscles [194].

These weighted optimization models are quite sensitive to variations in the values of the physiological parameters used [163, 194, 197, 198].   Therefore, highly reliable, well established or subject-specific data are required as values for these weighting parameters.   Alternatively, when these values are not verifiable or available, the optimization method should depend on as few physiological parameters as possible. For example, while PCSA, joint center locations, and muscle attachment points have been long studied and are widely available for various populations, relative amounts of different types of muscle fibers or relationships between amounts and rates of change of muscle length and resulting forces for specific muscles and across different populations are much less established and, therefore, less reliable for use in generic or general models [195, 197, 198, 245]. In addition to being used as "weighting values", the parameters involved in the physical model of the system studied, including the dimensions of the system components, muscle attachment points, and joint centers, as well as the number of degrees of freedom allowed, can also significantly affect the predicted muscle force magnitudes [198, 199].

The results of most studies have demonstrated that the minimization of the sum of nonlinear powers of muscle stresses sufficiently predicts observed trends in muscle activity and intensity for both force sharing over muscles of similar function and joint stability in muscles of opposing functions without significant dependence on artificial force limitation constraints and choice of physiological parameters [153, 192, 193, 197, 247-249]. Additionally, such a model is thought to be most appropriate when studying static or quasi-static activities within a normal range of motion such as isometric exercises, where a force is generated but the joint angles do not change, and walking,

where the joint angles vary over a relatively small range and the forces are not generated too rapidly [248, 250].

Based on this review, the minimization of a sum of nonlinear powers of muscle stresses was selected as the optimization criterion for the models developed in the current study. Because of the relative indifference to powers greater than two in early studies [193] and the concern of over-dispersing the resultant load to individual muscles when minimizing the sum of cubic terms in more recent studies [248], the minimization of the sum of the squares of the muscle stresses was selected. Further, the model was constrained to satisfy the momentum balances and to prevent the development of compressive muscle forces. However, even with the optimization criteria and constraints established, the published literature has presented significantly varied numerical optimization solution routines. Therefore, initial investigations were undertaken to select an appropriate solution method that could be incorporated into the overall bone strength adaptation model developed in this work.

3.3 Muscle Force Model Development

The overall goal of this research was to create a computational model to predict the effects of various loading conditions on changes in bone strength. The model was to appropriately simulate both the local mechanical environment acting on the bone and its response to changes in this environment. The model was then to be used in a variety of conditions to compare the resulting strength adaptations. Therefore, the model must be capable of handling many different loading conditions and must be able to automatically and iteratively determine and apply individual muscle forces to a discretized bone

geometry so that local changes in bone shape can be determined. Using these criteria, preliminary studies were first performed to determine an appropriate numerical optimization routine to use in the overall modeling routine component responsible for generating the required muscle forces. The selected optimization method was then incorporated into a subroutine that could automatically be called from within a finite element code to calculate and apply the muscle force loads. The developed model was validated through comparisons to published studies.

3.3.1 Preliminary Studies

A number of numerical optimization methods have been used in published literature to determine the individual muscle forces given a nonlinear optimization goal with linear constraints as chosen for the conditions studied in the current work (Chapter 2). In general, optimization schemes work by searching for a point within a feasible solution space that minimizes (or maximizes) an objective function (goal) [251]. In unconstrained numerical optimization methods, the search direction moves through all space in a way that iteratively reduces (or increases) the objective function until a minimum (or maximum) is found. In constrained optimizations, the solution space can be reduced as the search is limited to only the subset of space that satisfies the equality and inequality constraint equations. The various optimization methods differ by how the feasible space is searched for this optimal solution set [252].

As described in Section 3.2.2, the selected optimization problem for the determination of the muscle force magnitudes is in the general form shown in Equations 3.2 and 3.3 for muscle forces acting in a two-dimensional plane.

$$\text{Minimize } Z(\mathbf{F}) = \sum_{l=1}^{n} \left(\frac{F_l}{PCSA_l} \right)^2 \qquad (3.2)$$

$$\text{Constrained by } \mathbf{g}(\mathbf{F}) \leq \mathbf{0}$$

$$(3.3)$$

$$\text{Where } \mathbf{g}(\mathbf{F}) \text{ is in the form } \mathbf{g}(\mathbf{F}) = \mathbf{A}^{\mathbf{T}}\mathbf{F} - \mathbf{b}$$

$Z(\mathbf{F})$ is the optimization goal (objective function). $\mathbf{F}$ is an array of the force magnitudes for the l muscles studied (the design variables or "unknowns"). F_l is the magnitude of the lth muscle force in a direction along the length of the muscle. $PCSA_l$ is the physiological cross-sectional area of the lth muscle, n is the total number of muscles in the system. $\mathbf{g}(\mathbf{F})$ is an array of length $n+m$ containing the system constraints. m is the number of momentum balance equations to be satisfied (depends on degrees of freedom of the defined system). $\mathbf{A}^{\mathbf{T}}$ is a matrix of coefficients of the muscle force magnitudes in the constraint equations. $\mathbf{b}$ is an array of the constants in the constraint equations.

In the specific problem investigated in this study, there are n inequality constraints and m equality constraints. The first n constraints (inequality) ensure that no compressive forces are generated and are of the form:

$$\mathbf{g}_q(\mathbf{F}) \leq 0, \, q = 1 \ldots n, \, \mathbf{g}_q(\mathbf{F}) = -\mathbf{F}_l \qquad (3.4)$$

where $\mathbf{F}_l$ is the force vector generated by the lth muscle.

The last m constraints (equality) ensure the momentum balance equations are satisfied and are of the form:

$$\mathbf{g}_q(\mathbf{F}) = 0, \; q = n+1 \ldots n+m,$$

$$\mathbf{g}_q(\mathbf{F}) = \mathbf{M}_m = \sum_{l=1}^{n} \mathbf{r}_{lm} \times \mathbf{F}_l$$

(3.5)

where $\mathbf{M}_m$ is the moment vector due to the net reaction force acting between the system studied and the external environment about the mth joint, and $\mathbf{r}_{lm}$ is the vector defining the lth muscle's moment arm about the mth joint.

Because the function defining the optimization goal is continuous and differentiable with respect to the design variables, and functions defining the constraints are linear with respect to the design variables, a number of standard numerical or analytical methods could be employed. In the literature, three main methods have been used to solve similar problems: a Lagrange multiplier method [127, 163, 192, 194, 249], sequential quadratic programming [163, 198], and gradient projection optimization [193]. Each of these was explored for its effectiveness of implementation based on the requirements discussed above. For each method, a code was specifically written or a commercial code was implemented to solve a representative optimization problem obtained from the literature. Results were compared to each other and to those published in the literature for the cases considered. Because of their more widespread use, the Lagrange multiplier and the sequential quadratic programming methods were considered first.

The Lagrange multiplier method is an analytically based type of optimization procedure [252]. In this method only equality constraints are considered. Therefore, in the current problem, only the constraints in Equation 3.5 were used where m, the number of rotational degrees of freedom in the system (joints in the system). The constraint

equations $\mathbf{g}_q(\mathbf{F})$ in Equation 3.5 are rearrange so each is in the form $\mathbf{g}_q(\mathbf{F}) = 0$ in Equation 3.6, and the objective equation, or optimization goal $Z(\mathbf{F})$ is restated as shown in Equation 3.7. $\mathbf{F}$ is a vector consisting of the set of all the design variables for the optimization problem, the muscle force magnitudes.

$$\mathbf{g}_q(\mathbf{F}) = \sum_{l=1}^{n} \mathbf{r}_{lm} \times \mathbf{F}_l - \mathbf{M}_m = \mathbf{0}, \text{ where } q = 1\ldots m \tag{3.6}$$

$$Z(\mathbf{F}) = \sum_{l=1}^{n} \left(\frac{F_l}{PCSA_l} \right)^2 \tag{3.7}$$

The optimization goal $\mathbf{Z}(\mathbf{F})$ in Equation 3.7 is then combined with the equality constraint equations $\mathbf{g}_q(\mathbf{F})$ in Equation 3.6 to form a Lagrange Equation in Equation 3.8 where λ_q are the Lagrange multipliers.

$$L = Z(\mathbf{F}) + \sum_{q=1}^{m} \lambda_q \mathbf{g}_q(\mathbf{F}), \text{ where } q = 1\ldots m \tag{3.8}$$

The partial derivative of the Lagrange Equation (Equation 3.8) is found for each unknown muscle force (design variable) in $\mathbf{F}$ and each Lagrange multiplier in λ. Each partial derivative is set to zero and the system of equations is solved for the unknown muscle forces and Lagrange multipliers. Because the inequality constraints (Equations 3.4) cannot be directly incorporated into the Lagrange equation, their compliance has to be ensured after the basic Lagrange Multiplier optimization scheme is completed. Any member of $\mathbf{F}$ (design variables) that is found to be negative is set to zero and eliminated from the system of equations. The remaining members of $\mathbf{F}$ are "reset" to unknown, and the optimization routine is repeated until all remaining muscle force magnitudes are

positive. This solution set is the set of "active" muscles and the magnitudes of these muscles are the optimum solution.

The sequential quadratic programming method requires a quadratic optimization goal (optimization function) and linear equality or inequality constraint equations. If either the optimization function or the constraint equations are of higher order, they are reduced into a series of equations of the appropriate order, hence the name "sequential quadratic programming", or SQP [253]. In general, this method uses a function of the gradient of the objective function as the search direction along which the optimal solution is thought to be located. Specifically, the potential optimal solution set, **F**, is updated at each iteration through the use of the following equation:

$$\mathbf{F}_{k+1} = \mathbf{F}_k - \mathbf{B}_k \nabla Z(\mathbf{F}_k) \tag{3.9}$$

where $\mathbf{B}_k$ is an approximation of the inverse of the Hessian matrix of the objective function $Z(\mathbf{F})$ evaluated at a specific point in the design space, k. The search direction is then iteratively updated until a local optimum is found [254]. The specific SQP method used in these preliminary studies was applied directly from a commercial mathematical programming and analysis package. This package uses a second order Quasi-Newton general-use formulation of the SQP method called the Broyden-Fletcher-Goldfarb-Shanno method (BFGS) to update the search direction, This method approximates the gradient of the nonlinear objective function through a Taylor series expansion, thus approximating the Hessian matrix of the objective function (optimization goal) [255]. The BFGS formulation, used in this method, for updating the approximation of $\mathbf{B}_k$ is thought to be "superior to all such known...algorithms" [203]. However, the SQP

method finds only local optima. Therefore, multiple repetitions of the solution must be performed with different starting values to determine global optima.

Because the Lagrange multiplier and the SQP methods have been the optimization methods most extensively used to resolve individual muscle force magnitudes in the reviewed literature, their application to the model developed in this work was investigated thoroughly. The SQP method was applied through the use of the commercial mathematical programming and analysis software MATLAB [256]. For simplicity of comparison the code for the Lagrange multiplier method was also written using the MATLAB software, which has a C-based programming language and an extensive library of predefined mathematical functions.

These two optimization methods were applied to a musculoskeletal system previously analyzed using these same two methods as reported in the literature [163]. This system was also previously studied experimentally [126]. In the conditions studied, the nine-muscle leg system generated a specified resultant force between the foot and a fixed plate through isometric muscle contraction so that the joint angles remain constant. Twelve loading conditions were studied. The resultant force was generated in twelve directions, one every 30° with the same magnitude for each. All twelve loading directions were studied to give an indication of the effectiveness of each method for application to a variety of loading conditions. The model predicted muscle activity for each configuration using each optimization model was compared. Figure 3.2 shows the basic system investigated. The nine muscles included in this simplified system (Figure 3.3) were two ankle extensors (Gastrocnemius and Soleus), two knee extensors (Rectus Femoris and Vastii), two hip extensors (Gluteus Maximus and Long Head Biceps

Femoris), two hip flexors (Rectus Femoris and Iliacus), and three knee flexors (Gastrocnemius, and Short and Long Heads of the Biceps Femoris). The moment arms and muscle PCSAs for these muscles included in this muscle force model are listed in Table 3.1.
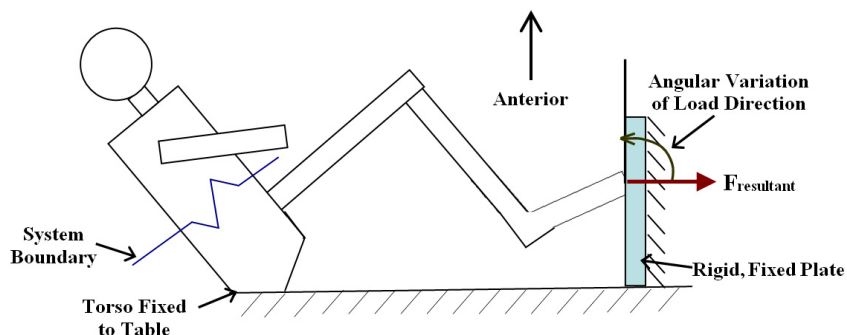
Figure 3.2 General depiction of system configuration and activity investigated in the preliminary muscle force validation model, including boundary conditions and resultant force generated by the leg.
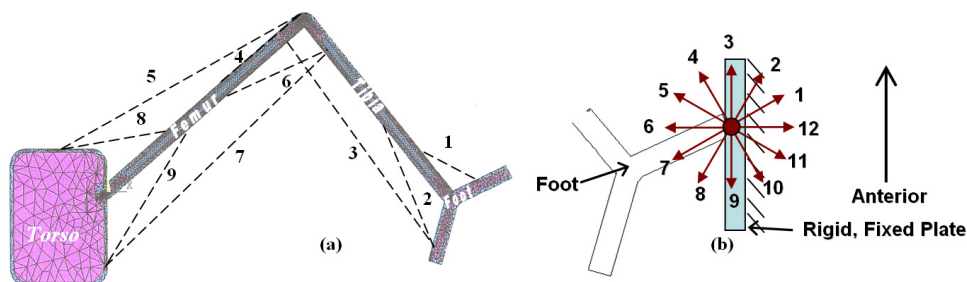
Figure 3.3 (a) Musculoskeletal model used in the preliminary muscle force validation model, depicting the included muscles and approximate functional locations. (b) Specific directions studied of resultant force depicted in Figure 3.2. See Table 3.1 for muscle names corresponding to numbers.

Table 3.1 Geometric Data for Muscles Used in Preliminary Muscle Force Model

ID	Muscle	Function	PCSA (cm²)	Moment Arm about Ankle (m)	Moment Arm about Knee (m)	Moment Arm about Hip (m)
1	Tibialis Anterior	Ankle Flexor	11.5	0.0298	---	---
2	Soleus	Ankle Extensor	92.5	0.044	---	---
3	Gastrocnemius	Ankle Extensor, Knee Flexor	44.3	0.044	0.0138	---
4	Vastii	Knee Extensor	98.1	---	0.0329	---
5	Rectus Femoris	Knee Extensor, Hip Flexor	20.1	---	0.0329	0.0279
6	Short Head of Biceps Femoris	Knee Flexor	6.1	---	0.025	---
7	Long Head of Biceps Femoris	Knee Flexor, Hip Extensor	45.5	---	0.025	0.0619
8	Iliacus	Hip Flexor	31.0	---	---	0.0317
9	Gluteus Maximus	Hip Extensor	44.3	---	---	0.0368

In the previously published work [163] used as a basis for this comparison to the methods developed here, extensive algebraic manipulations were employed to apply the Lagrange multiplier method, and the commercial software, MATLAB, was selected to apply the SQP method. To reduce the required algebraic manipulations in the implementation of the Lagrange Multiplier method in the current work, the full sum of the squares of the individual muscle stresses was used to define the objective function in this current work, not the normalized sum as described in [193]. Because the SQP method results in only local optima, four different initial guesses were used in this study: All muscles were initially either 0N, 100N, 500N, or 1000N.

In undertaking the current study, conditions were found where both the Lagrange multiplier and SQP method may predict the same optimal solution for each loading case. However, extensive manual manipulations of each of these optimization models were required in the current work to properly implement each method. For the SQP method,

the initial guess had to be repeatedly modified until a global solution was found. For the Lagrange multiplier method used in this work, iterative 'zeroing' of negative resulting muscle forces and repeated solving of the optimization problem was required. The published literature used as a comparison in this study [163] reached the global optimal solution through extensive algebraic manipulations of the Lagrange multiplier equation and by subjecting the muscle force magnitudes to additional constraints, such as maximum values. When applying the same "manual modeling adjustments" to different resultant loading directions (but same loading magnitudes) for the system studied, different solutions resulted for each modeling method compared (Lagrange multiplier and SQP). Therefore, different initial guesses or algebraic manipulations were required for each loading condition and studied and each solution method. Additionally, in some directions, the "zeroing" procedure in the Lagrange multiplier optimization method implemented in this work resulted in only two remaining unknowns that were required to satisfy three unique constraint equations. Because this created an undetermined optimization problem, additional constraints on muscle force magnitudes, such as maximum values, were imposed, as in the comparable published work using this method.

Figures 3.4 and 3.5 show representative results for an individual muscle's predicted magnitude for the Lagrange multiplier method and the SQP method developed in this work. The local optima found with the SQP method for each of the initial guesses are also presented. For some muscles, such as the Tibialis Anterior shown in Figure 3.4, all methods predicted nearly the same muscle activity (zero or nonzero magnitude) and intensity (magnitude value), and the results of the SQP method were insensitive to the initial guess under all loading conditions. For other muscles, such as the Gastrocnemius

(Figure 3.5), there was significant variation in both the predicted muscle activity and intensity with the optimization method used for some loading directions while other loading directions showed relative independence from the optimization method.
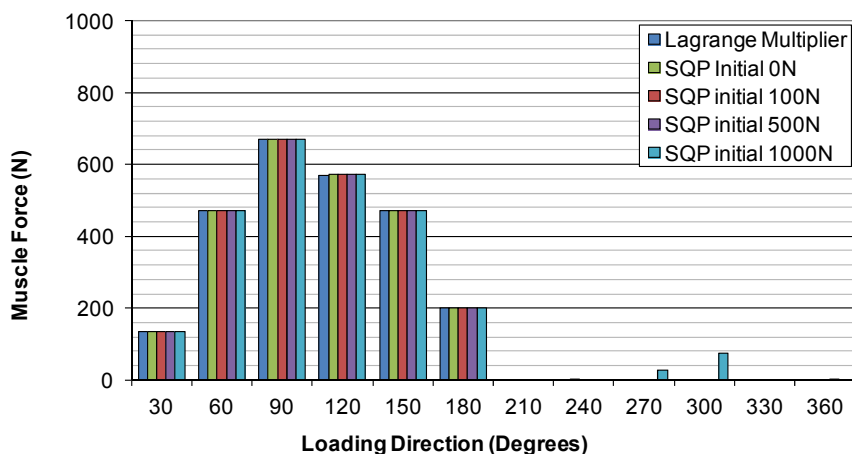
Figure 3.4 Predicted force magnitudes for tibialis anterior muscle for various net loading conditions using different optimization methods during the muscle force model validation studies.
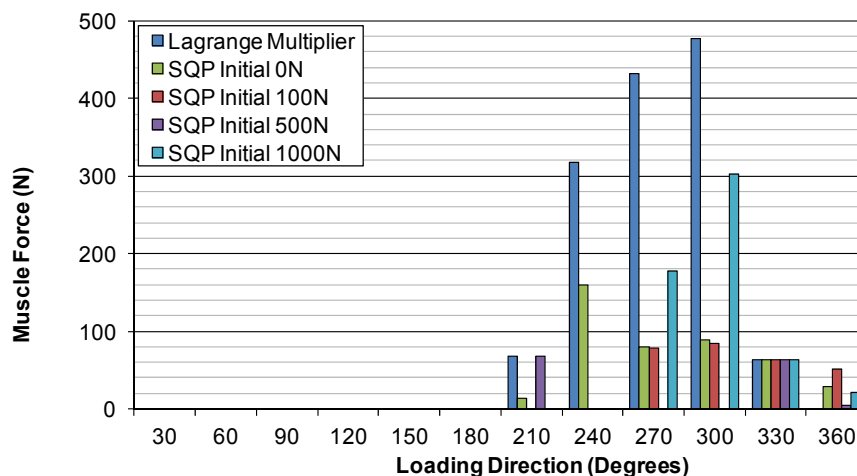
Figure 3.5 Predicted force magnitudes for gastrocnemius muscle for various net loading conditions using different optimization methods during the muscle force validation studies.

Figure 3.6 shows the values of the optimization goal for the runs conducted for the SQP method starting with different initial values. For example, for the 60° loading direction, different initial guesses for the SQP method resulted in different goal values,

requiring multiple runs to find the lowest optimization goal value. Yet, for the 120° direction, all initial guesses resulted in the same optimization goal, indicating the global optima was reached regardless of the initial guess. Still for others, such as the 30° direction, multiple, but not all, initial guesses resulted in the same optimization goal value. This may indicate that for some loading directions there may be multiple local optima over the range of force magnitudes studied and the initial guess selected, while for others there may be only one local optima over the range investigated.
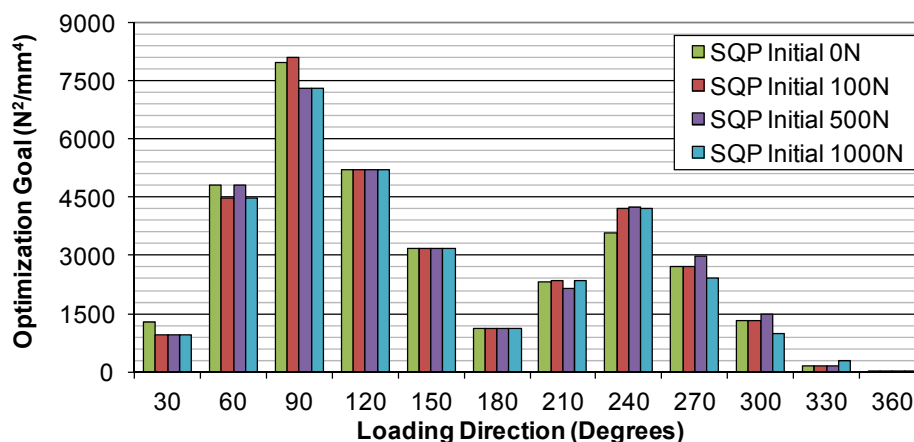
Figure 3.6 Resulting optimization goal (minimum sum of the muscle stresses) for various net loading conditions using different optimization methods during the muscle force validation studies.

In Tables 3.2 though 3.6 the model predicted relative muscle force intensities for groups of muscles with the same function are compared. Regardless of absolute magnitude of the forces, if a true "optimal" solution was found, the distribution of the muscle forces to achieve a net action (such as moment about a particular joint in a particular location) should be the same regardless of the model used. The variations in the predicted muscle forces shown in the tables for the different optimization methods and initial guesses are an indication of the inconsistency in the solutions using these Lagrange multiplier and SQP methods for a range of loading conditions of interest.

While the optimization methods compared in this preliminary study may be sufficient for investigating a single loading condition, their automated application to a variety of loading conditions, as required in the model developed in this work, is cumbersome due to the manipulations required and the need for multiple initial guesses. Additionally, the resulting solutions are often inconsistent. Therefore, an alternative optimization method was used that resulted in the determination of a global optimum with the application of only one initial feasible solution and no modifications to the programming code for different conditions or systems studied.

Table 3.2 Muscle Force Model Validation: Comparison of Ankle Extensors Prediction: Gastrocnemius Force as a Percentage of Soleus Force

	30°	60°	90°	120°	150°	180°	210°	240°	270°	300°	330°	360°
Lagrange	None	None	None	None	None	None	G only	G only	G only	G only	22.69%	S only
SQP 0N	None	None	None	None	None	None	23.55%	99.75%	22.95%	22.76%	28.56%	33.33%
SQP 100N	None	None	None	None	None	None	S only	S only	22.25%	21.42%	22.94%	80.90%
SQP 500N	None	None	None	None	None	None	G only	S only	S only	S only	22.94%	3.56%
SQP 1000N	None	None	None	None	None	None	S only	S only	65.32%	135.06%	22.94%	22.94%

Table 3.3 Muscle Force Model Validation: Comparison of Knee Extensors Prediction: Rectus Femoris Force as a Percentage of Vastii Force

	30°	60°	90°	120°	150°	180°	210°	240°	270°	300°	330°	360°
Lagrange	41.74%	64.16%	84.50%	114.00%	213.42%	None	None	None	None	None	V only	2.26%
SQP 0N	160.32%	161.98%	341.77%	114.00%	213.40%	None	None	None	None	None	V only	21.87%
SQP 100N	41.74%	64.17%	410.44%	114.00%	213.40%	None	None	None	None	V only	V only	17.28%
SQP 500N	41.74%	163.19%	84.49%	114.00%	213.40%	None	None	None	None	None	V only	7.71%
SQP 1000N	41.74%	64.17%	84.49%	114.00%	213.40%	None	None	None	None	None	V only	2.28%

Table 3.4 Muscle Force Model Validation: Comparison of Hip Extensors Prediction: Gluteus Maximus Force as a Percentage of Long Head Biceps Femoris Force

	30°	60°	90°	120°	150°	180°	210°	240°	270°	300°	330°	360°
Lagrange	None	None	None	None	None	None	L only	L only	L only	L only	56.51%	219.08%
SQP 0N	None	None	None	None	None	None	L only	L only	L only	L only	56.53%	167.39%
SQP 100N	None	None	None	None	None	L only	L only	L only	L only	L only	56.51%	318.65%
SQP 500N	None	None	None	None	None	L only	L only	L only	L only	L only	56.51%	107.34%
SQP 1000N	None	None	None	None	None	L only	L only	L only	1.06%	L only	L only	224.40%

Table 3.5 Muscle Force Model Validation: Comparison of Hip Flexors Prediction: Rectus Femoris Force as a Percentage of Iliacus Force

	30°	60°	90°	120°	150°	180°	210°	240°	270°	300°	330°	360°
Lagrange	41.14%	39.59%	38.94%	38.42%	37.74%	I only	None	None	None	None	None	R only
SQP 0N	142.26%	78.57%	86.11%	38.41%	37.75%	I only	I only	I only	I only	I only	None	R only
SQP 100N	41.14%	39.60%	92.25%	38.41%	37.75%	I only	I only	I only	I only	I only	None	R only
SQP 500N	41.14%	78.91%	38.93%	38.41%	37.75%	I only	I only	I only	I only	I only	None	R only
SQP 1000N	41.14%	39.60%	38.93%	38.41%	37.75%	I only	I only	I only	I only	I only	None	R only

Table 3.6 Muscle Force Model Validation: Comparison of Knee Flexors Prediction: Short Head Biceps Femoris Force as a Percentage of Long Head Biceps Femoris Force

	30°	60°	90°	120°	150°	180°	210°	240°	270°	300°	330°	360°
Lagrange	None	None	None	None	None	L only	179.16%	88.60%	38.09%	8.03%	L only	L only
SQP 0N	None	None	None	None	None	22.23%	10.86%	9.88%	6.45%	4.37%	L only	L only
SQP 100N	None	None	None	None	None	22.23%	10.86%	8.59%	6.40%	4.39%	L only	L only
SQP 500N	None	None	None	None	None	22.23%	9.21%	10.48%	6.69%	4.37%	L only	L only
SQP 1000N	None	None	None	None	None	22.23%	10.86%	8.86%	6.58%	2.92%	L only	L only

3.3.2 Optimization Method Used in Developed Model

While the Lagrange multiplier and sequential quadratic programming methods (SQP) may be more widely used in the published literature for the determination of individual muscle force magnitudes, the gradient projection method has also been used, specifically in the work that initially established the sum of the squares of the muscle forces as a potential optimization goal [193]. Like the SQP method, the gradient projection method finds only local optima. However, if the objective function (optimization goal) is convex, then the optima found by this solution method are also global [114]. A convex function has a positive semidefinite Hessian. In the particular problem used in this study, the objective function is the sum of the squares of the muscle stresses, where the muscle stresses are defined as the ratio of the muscle force magnitude to the muscle PCSA (Equation 3.2). Therefore, the set of unknowns are the muscle force magnitudes and the Hessian of the objective function is a diagonal matrix of all positive numbers whose (l,l)

terms are all constant and equal to $\dfrac{2}{(PCSA_l)^2}$. The determinant of this Hessian matrix is

constant and always positive, making the Hessian of the objective function positive definite and satisfying the criteria of a convex function. All constraints in this model are linear and their second derivatives are zero. Therefore, the Hessian of the constraint matrix was positive semidefinite. Both the objective function and the constraints were positive semidefinite, making the complete optimization problem analyzed in this work a

convex problem. Thus, the gradient projection method will find its global optima. The use of the gradient projection method for determining the muscle force in the current work, may, therefore, resolve some of the issues with universal applicability of the solution method found with the use of the Lagrange multiplier and SQP methods as reported in the preliminary studies discussed in Subsection 3.3.1.

The gradient projection optimization method, a form of the method of steepest descent, uses the gradient of the objective function as the search direction [257]. This search direction, normal to the objective function, produces the most rapid reduction in the objective function value towards a local minimum. The gradient projection method restricts the search for optima to the subspace of the feasible solution space that is tangent to the set of constraints that are exactly satisfied (equal to zero) at the current solution point. These constraints include all equality constraints and those inequality constraints that are equal to zero. The subset of constraints that are exactly satisfied is called a "working set" of active constraints. They indicate the extreme locations, the boundary, of the feasible space thereby reducing the search region from a volume to a surface and reducing an inequality problem to one comprised solely of equality constraints. Restricting the search to only this subset is done by projecting the gradient of the objective function onto this surface defined by the active constraints. This provides the sufficient conditions for any point found along any search direction using this method to be a potential local optimum.

The method proceeds iteratively by finding a working set of active constraints, a search direction, and a step size along the search direction to move from one set of values of the unknown variables to another until an optimum value of the objective function is

reached. Each working set is a "guess" of the actual set of active constraints that produces the optimal solution. Therefore, this working set is modified at each iteration. Because the search direction is projected onto this active working set, the search can also change direction at each iteration. The step size along this search direction towards the optimization goal can affect both the efficiency and accuracy of the solution. As a result, many different methods have been developed to determine this step size. The one followed in this study was developed specifically for problems with linear constraints, and it is often referred to as Rosen's Gradient Projection Method [253, 257]. For any version of the gradient projection method, if the initial guess of the optimal point is within the feasible region and the initial search direction is feasible (tangent to the working set of active constraints), then all subsequent iterations will also produce feasible solutions for the unknown set of design variables, working set and search direction. [254]. A basic description of the method and the procedure for its implementation [114] will be explained followed by specific modifications employed for the current work.

3.3.2.1 Gradient Projection Optimization Method. The problem to be optimized is as in Equation 3.2 and Equation 3.3, where a set of design variables, $\mathbf{F}$, will produce the smallest value of the defined objective function, $Z(\mathbf{F})$, within a set of n inequality and m equality constraints, $\mathbf{g}(\mathbf{F})$. By rearranging the linear constraints so they are all in a form of $\mathbf{g}(\mathbf{F}) \leq \mathbf{0}$, the coefficients of the unknown variable $\mathbf{F}$ in this set of equations can be placed into matrix, $\mathbf{A}^T$, and a vector of the constant terms in these constraint equations, $\mathbf{b}$, can be created. At each iteration the "working set" of active constraints consists of all equality constraints and any inequality constraints with a value when evaluated at the particular set of values of the design variables $\mathbf{F}$ equal to zero. The coefficient matrix of

active constraints $\mathbf{N}^T$ is a submatrix of $\mathbf{A}^T$. Because the constraints are linear, these coefficient matrices $\mathbf{A}^T$ and $\mathbf{N}^T$ also define the gradient $\nabla \mathbf{g}(\mathbf{F})$ of all or just the active constraint functions, respectively. At each iteration, the active constraint matrix $\mathbf{N}^T$ is modified so that gradients of inequality constraints are added or removed. The gradients of equality constraints are always part of the active constraint matrix $\mathbf{N}^T$ and are never removed.

The feasible solution is updated at each iteration through the relation:

$$\mathbf{F}_{k+1} = \mathbf{F}_k + \alpha \mathbf{S} \tag{3.10}$$

$\mathbf{S}$ is a vector defining the search direction and α is the step length along the search direction. The procedure requires the calculation of $\mathbf{S}$ and α along with $\mathbf{F}$ at each iteration.

The first step in the gradient projection optimization method is the determination of the search direction, defined as:

$$\mathbf{S} = -\mathbf{P}\nabla Z(\mathbf{F}) \tag{3.11}$$

$\mathbf{P}$ is the projection operator on the gradient of the objective function $Z(\mathbf{F})$. The negative ensures the reduction of the value in a progression towards the solution minima. In problems with linear constraints, such as the one in this work, $\mathbf{P}$ is a square matrix with dimensions equal to the length of the vector of design variables $\mathbf{F}$. Specifically, $\mathbf{P}$ creates an orthogonal projection (See Appendix A) of the gradient of the objective function onto the set of gradients of active constraints ($\mathbf{N}^T$) and is defined as:

$$\mathbf{P} = \mathbf{I} - \mathbf{N}(\mathbf{N}^T\mathbf{N})^{-1}\mathbf{N}^T \qquad (3.12)$$

The calculated search direction $\mathbf{S}$ is tangent to the set of active constraints, and, thus, is feasible [203] if:

$$\mathbf{N}^T\mathbf{S} = \mathbf{0} \qquad (3.13)$$

Because $\mathbf{N}^T$ and $\mathbf{S}$ change with each iteration, the validity of this equation must be checked at each iteration.

With the search direction found, the step length along the search direction is next calculated. The gradient projection method works by modifying the "working set" of active constraints until one is found that minimizes the objective function (optimization goal). If Equation 3.10 is substituted into Equation 3.2, then the constraints, $\mathbf{g}(\mathbf{F})$, are shown to be linear functions of the step length, α. Additionally, because the working set of active constraints is updated at each iteration, inactive constraints can become active constraints at points (sets of design variables $\mathbf{F}$) when the constraint, evaluated at the particular point in the design space, $\mathbf{F}$, is equal to zero. As a result, the step length, α, can be calculated along the search direction as the distance between the current point, $\mathbf{F}_k$, and the updated solution point, $\mathbf{F}_{k+1}$, where an inactive constraint becomes active and thus added to the "working set" of constraints. This step length can be derived through the substitution described above and subsequent algebraic manipulation noting that active constraints $g_j\left(\mathbf{F}_{k+1}\right) = 0$:

$$\alpha_j = -\frac{g_j\left(\mathbf{F}_k\right)}{\mathbf{A}_j^T\mathbf{S}} \text{ , j are inactive constraints only} \tag{3.14}$$

$$\text{where } g_j\left(\mathbf{F}_k\right) = \mathbf{A}_j^T\mathbf{F}_k - \mathbf{b}_j$$

Because $\mathbf{F}_k$ is always a feasible solution and only the inactive constraints are considered, $g_j(\mathbf{F}_k)$ are always less than zero and so negative. Therefore, because the constraints, $\mathbf{g}(\mathbf{F})$, are a function of the step length, α, the sign of the derivative of each inactive constraint, $g_j(\mathbf{F}_k)$, with respect to α, $\partial g_j\left(\mathbf{F}_k\right)/\partial\alpha$, gives an indication of whether there is movement to or from the inactive constraint along the positive search direction. Because the goal is to add a new constraint to the "working set", the step should be towards the constraint or in the positive α direction. This is achieved through the consideration of only the sets that achieve positive derivatives or:

$$\frac{dg_j}{d\alpha_j} = \mathbf{A}_j^T\mathbf{S}\Big|_{\mathbf{F}_k} > 0 \text{ , j are inactive constraints only} \tag{3.15}$$

In determining this step size, it is desired to move to the next nearest inactive constraint along the search direction. Therefore, the set of step lengths to reach all inactive constraints is first restricted only to those with positive steps (so that they may be encountered while traveling along the search direction). Of these, the closest inactive constraint, the one with shortest step length, is selected as a candidate for possible inclusion into the working set. This shortest step length required to get to this constraint from $\mathbf{F}_k$ is selected as the α in Equation 3.10. The added constraint expands the feasible solution surface in the search for the local optima.

If a local optimum is encountered along the current search direction between the current position and the next closest inactive constraint, then there is no need to add or remove constraints. In this case, the location of the local optimum (minimum) is considered to be the next solution set, $\mathbf{F}_{k+1}$. The step along the search direction that moves from the current position to the local minimum, $\mathbf{F}_{k+1}$, is defined such that, by using Equation 3.10 in the objective function $Z(\mathbf{F}_{k+1})$ in Equation 3.2, Z is minimized.

As currently inactive inequality constraints can be added to the "working set", currently active inequality constraints can be removed from the "working set", constricting the feasible solution space to a smaller range. The Kuhn-Tucker conditions provide a means for this removal and set the necessary conditions for a feasible point to be a local optimum. These Kuhn-Tucker conditions are now defined and their use in the gradient projection optimization method is explained.

The projection of the gradient of the objective function over the set of active constraints can be expressed as the gradient of the Lagrangian of the optimization problem itself evaluated at the new feasible solution set $\mathbf{F}_{k+1}$ such that:

$$L = Z(\mathbf{F}_{k+1}) + \lambda_i g_i(\mathbf{F}_{k+1}) \text{ , } i \text{ are active constraints only} \tag{3.16}$$

$$\nabla L = \nabla Z(\mathbf{F}_{k+1}) + \lambda_i \nabla g_i(\mathbf{F}_{k+1}) \text{ , } i \text{ are active constraints only} \tag{3.17}$$

with k as the optimization iteration counter. Solving for the Lagrange multipliers λ_i using only the active constraint matrix $\mathbf{N}^T$ gives:

$$\lambda = -\left(\mathbf{N}^T\mathbf{N}\right)^{-1}\mathbf{N}^T\nabla Z\left(\mathbf{F}_{k+1}\right) \tag{3.18}$$

The Kuhn-Tucker conditions state that if $\mathbf{S} = -\mathbf{P}\nabla Z(\mathbf{F})$, the projection of the negative gradient of the objective function onto the set of active constraints, is zero and the Lagrange multipliers of the active inequality constraints are nonnegative, then the point may be a local optimum. Therefore, in order for the working set of active constraints to form a solution set that contains a local optimum, the inequality constraints that produce negative Lagrange multipliers must be removed from the "working set". This removal is done one at a time, with the most negative Lagrange multiplier removed first. The new set of active constraints is used to create a new $\mathbf{N}^T$ matrix and the resulting new search direction is found based on this updated, smaller "working set". The Lagrange multipliers of this new "working set" are found and the process is continued until all Lagrange multipliers of the active inequality constraints are nonnegative.

If the updated search direction, based on the removal of all active constraints with corresponding negative Lagrange multipliers, evaluated at the current feasible solution point $\mathbf{F}$ is equal to zero, then $\mathbf{F}$ is a local optimum. If this updated search direction is not zero, then the new active constraint found during the determination of the step length may be added to the "working set" of active constraints only if the derivative of that new active constraint with respect to the step size, as in Equation 3.15, evaluated for the updated search direction, is positive. This positive derivative means that the constraint that is to be added is in the direction of minimizing the objective function and so will help to further reduce the objective function's value. Once the constraint is added, the Lagrange multipliers of the new "working set" are found, and the "working set" of active constraints is again adjusted until all of their Lagrange multipliers are nonnegative. If constraints are again removed, the search direction, $\mathbf{S}$, in Equation 3.4 is again updated.

If the search direction is still not zero, a new step length α and an updated feasible solution $\mathbf{F}_{k+1}$ are found in the execution of the next solution iteration. The iterative process stops when the search direction, $\mathbf{S}$ in Equation 3.4, which is the projection of the gradient of the objective function onto the feasible solution surface, is equal to zero, indicating that a local optimum (minimum) of the objective function is found.

3.3.2.2 Application of Gradient Projection Optimization to Current Model. A code was written, based on published descriptions of the basic gradient projection optimization method [114] and its numerical implementation [203, 253, 254], as explained in Subsection 3.3.1 and Subsection 3.3.2.1, specifically to solve the problem analyzed in this work: the determination of the magnitudes of the muscle forces in a musculoskeletal system by minimizing the sum of the muscle stresses. For more effective and efficient code development, MATLAB [256] software was used to generate the gradient projection method code, to take advantage of its extensive built in mathematical functions, especially in linear algebraic operation. However, the developed though the method could be written in any general programming code. The major code components are described below.

A main program was written to define the physical constants of the model, listed in Table 3.1 as well as the moments about each joint resulting from the reaction between the fixed plate and the net force generated by the leg system in Figures 3.2 and 3.3. The initial feasible guesses for the set of muscle force magnitudes $\mathbf{F}_l$ for each of the twelve resultant load direction cases studied were also included in this main program. The main program calls a function (subroutine) to execute the gradient projection optimization method. The subroutine evaluates the solution at each iteration of the optimization

method to check if the solution conforms to the stopping criteria (either optimal solution found or maximum number of iterations achieved) and either executes the next optimization iteration or stops the program.

The objective function, its gradient, and all of the constraint equations, which would need to be updated depending on the system analyzed, are contained in the subroutine that implements each gradient projection iteration. Prior to the execution of the initial optimization iteration, the convexity of the defined problem and the feasibility of the initial guess are verified and the initial search direction is calculated. The subroutine performs the gradient projection optimization routine to find the updated feasible solution $\mathbf{F}_{k+1}$, the updated search direction $\mathbf{S}$ and the updated value of the objective function $Z(\mathbf{F}_{k+1})$ for each iteration and passes this information back to the main program to determine whether or not an optimal solution has been found. In addition to executing the gradient projection algorithm, this subroutine creates and maintains an accounting of the current "working set" of active constraints. A separate subroutine was written to handle the addition and removal of constraints from the "working set". This subroutine is called by the gradient projection optimization subroutine as necessary.

Some modifications to the optimization method described in Subsection 3.3.2.1 were made in the code written for this work to aid in the numerical stability of the routine. A widely noted concern with the computational implementation of the gradient projection method of optimization is a tendency to "zigzag" around the optimal solution but never reach it [114, 203, 253, 254]. This usually occurs as active constraints are repeatedly added and removed because of their small, nonzero values. Therefore, the first change was the use of a ±0.01 tolerance band to select active inequality constraints.

Similarly, the second modification involved the use of a small tolerance band, on the order of 10^{-5}, to address issues resulting from roundoff error when other comparisons to zero were required, such as may occur in determining compliance to the Kuhn-Tucker conditions. Finally, **QR** factorization was employed to simplify many calculations and to ease concerns of illconditioning in calculating the projection, determining compliance to the Kuhn-Tucker conditions and when adding and removing active constraints to the system [203, 254] (See Appendix A). **QR** factorization decomposes any matrix into the product of a square orthonormal (unitary) matrix **Q** and an upper triangular matrix **R**. **LQ** factorization is similar, but uses a lower triangular matrix **L**. The inverse of the orthornormal **Q** matrix is not only easier to calculate but also better conditioned than terms such as those involving the constraint coefficient (gradient) matrix such as $\mathbf{N}^T\mathbf{N}$. Additionally, the triangular matrix is particularly useful when solving for the Lagrange multipliers required in both the Kuhn-Tucker evaluations and in the adjustments of the active set. While both **QR** and **LQ** factorization were tested in the program written for this work, no differences in the resulting optimal solution sets were found. Because of **QR** factorization's more widespread use and its reduced susceptibility to roundoff errors when solving the least squares problem to find the Lagrange multipliers in the optimization routine [258], the **QR** factorization method was incorporated into this code.

The code written to perform the muscle force optimization was validated before being implemented in the full multisegment bone strength adaptation model. This validation is next discussed.

3.3.2.3 Validation of Muscle Force Optimization Model. To verify the code developed to find individual muscle force magnitudes using the gradient projection optimization

method described in Subsection 3.3.2.2, predictions of muscle force activity using this code were compared to those of two alternative optimization methods: Sequential Quadratic Programming optimization using a commercial software package [256] and the results of published computational studies using a Lagrange Multiplier method [163, 259] for the system described in Subsection 3.3.1 under each of the twelve loading directions described in Figure 3.3. Additionally, these predicted values were judged against trends in published experimental EMG measurements [126] of the same segment of the musculoskeletal system and under the same loading conditions.

Comparisons between the individual muscle activities for each loading condition studied predicted by the model and recorded from the EMG data are shown in Figure 3.7, where the intensity of each muscle's generated force is normalized by the maximum force value (or EMG signal strength) generated by that muscle over the twelve loading directions examined. This normalization was necessary because EMG, which measures the intensity of the electrical signals generated by the muscles from locations on the surface of the skin, cannot be directly correlated to muscle force magnitudes but can indicate only relative trends in muscle activity [193]. Very good agreement between all of the numerical models compared was shown. Additionally, the numerical models showed similar trends in the relative muscle intensity with each resultant loading direction as the experimental EMG measurements. Differences between the numerical and experimental models were more significant and caused by a number of reasons. First, the numerical models predicted the muscle forces that were necessary to only create the given resultant force, while the experimental measurements recorded additional muscle activity such as the muscle force required to hold the leg at the studied, static

configuration [126]. This is well displayed for the muscles that act on the ankle and hip joints, such as the soleus and the gluteus maximus which function near the constrained model locations. Second, the numerical models assumed that the muscles acted within one plane. Actual musculoskeletal geometry and attachment is three-dimensional, producing out of plane forces and moments that were assumed negligible in the model but whose effects on the included models were recorded in the reference experimental studies. Finally, because the muscle force magnitudes were predicted using an optimization routine with a mathematically based optimization goal, the relative amounts of activity in muscles that have the same function may be different from EMG measurements since the actual recruiting of muscle activity may not exactly follow the mathematical rules numerically applied.
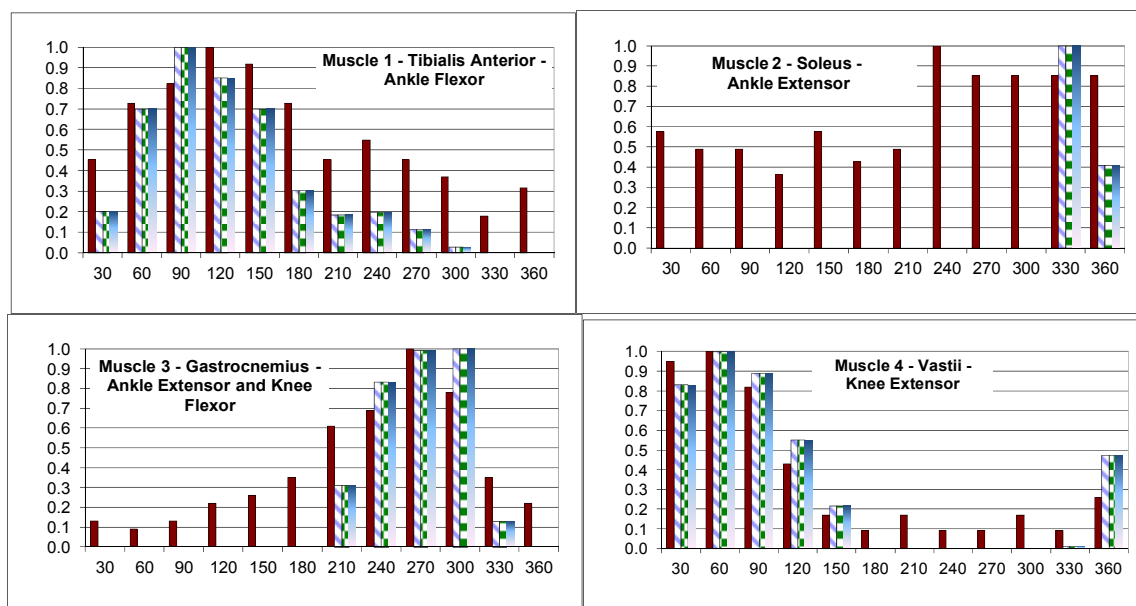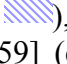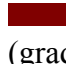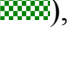
Figure 3.7 Comparisons of the normalized muscle forces magnitudes predicted by the various optimization models for the twelve loading directions considered.

Gradient projection model (hashed ▨), EMG Measurements [126] (solid ▬), Lagrange Multiplier method [163, 259] (checkered ▦), SQP method [256] (graded ▬)
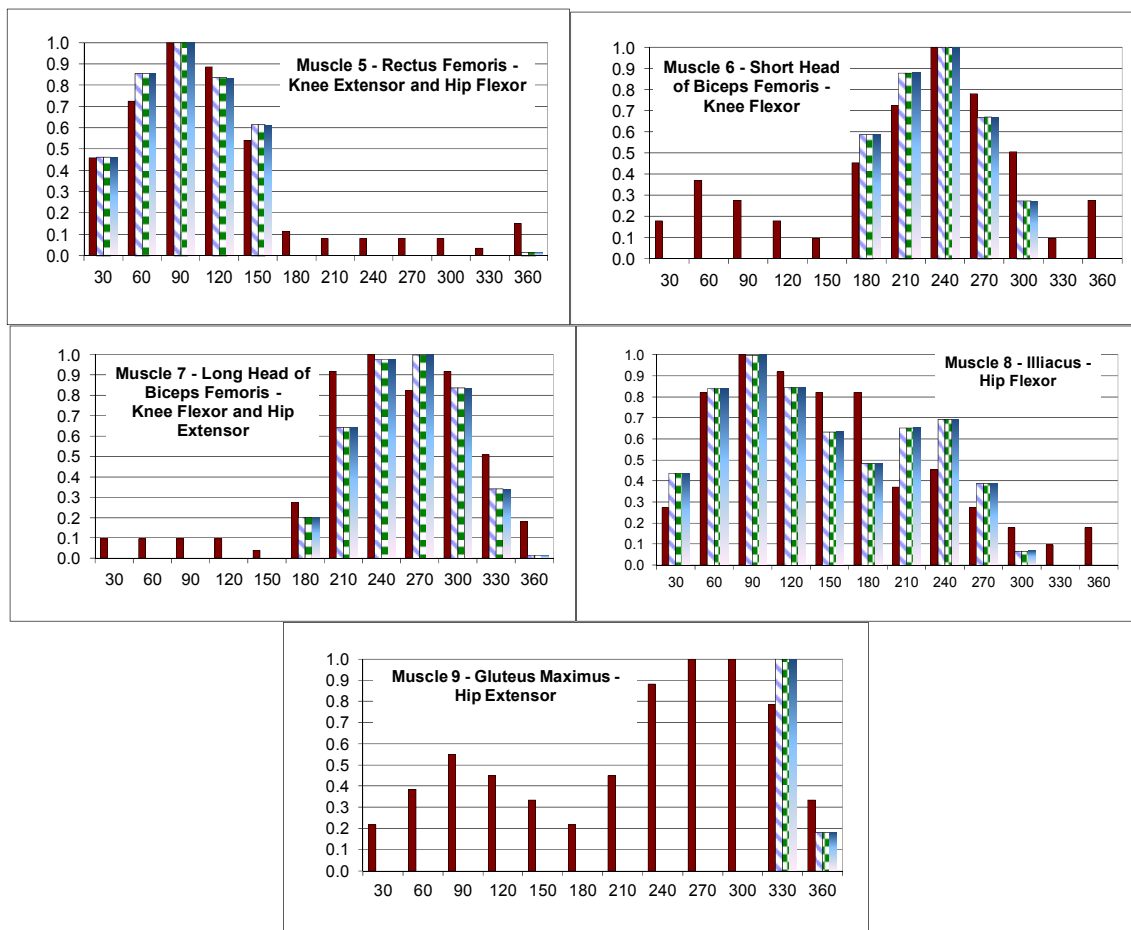
Figure 3.7 Comparisons of the normalized muscle forces magnitudes predicted by the various optimization models for the twelve loading directions considered. (continued.)

Gradient projection model (hashed ▧), EMG Measurements [126] (solid ▬), Lagrange Multiplier method [163, 259] (checkered ▨), SQP method [256] (graded ▨)

Comparisons of the muscle force magnitudes predicted by the three numerical models show little differences. For most muscles and loading directions, any difference was under 0.001%. The largest differences, though still less than 0.1%, were seen in predictions of the 180°, or posteriorly directed, force. Using a maximum stress of the muscle tissue of 1MPa (100 N/cm^2) [193], no muscle was found to have a safety factor less than two, indicating that failure of the muscle tissue under the forces predicted by the model was unlikely and implying that the predictions were physiologically reasonable.

The analysis of the muscle stresses also showed that the muscle force optimization model used in this work did not predict that any one muscle loading was at the maximum allowable load as has been seen with other models [192]. This indicates that the developed model distributed the required loads over a number of muscles with common function and did not maximize the force in one muscle before recruiting another. The combined comparison and analysis of numerical solution to commercial optimization software and published methods and of the predicted trends to experimental measurements validates the proper function of the developed code for the gradient projection optimization of muscle force magnitudes for isometric actions of the leg.

To examine the efficiency of the author developed gradient projection optimization method program when compared to other numerical optimization methods studied, including the sequential quadratic programming from the commercial software, the number of iterations required by each method to solve each loading case studied is presented in Figure 3.8. In general, trends in the number of iterations with loading direction were similar for each optimization method, with more iterations required for the posteriorly directed resultant (180° through 360°) forces than for the anteriorly directed ones (30° through 150°). However, the sequential quadratic programming method required two to four times more iterations to find the optimal set of muscle force magnitudes than did the gradient projection method. The number of iterations presented for the SQP method did not include the multiple restarts for necessary multiple initial guesses.
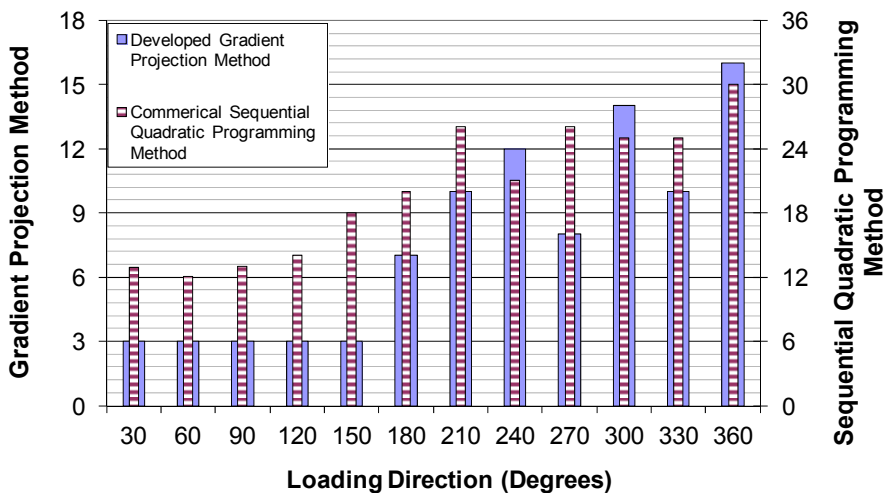
Figure 3.8 Comparisons of number of iterations to solution for the numerical optimization methods studied.

Computational studies of muscle activity and intensity that predict actual force magnitudes can reveal relationships between the forces generated by muscles within a studied system not seen from trends in the electrical activity recorded by EMG. For example, each muscle's relative contribution to the net moments about each joint (ankle, knee and hip) can be quantified. Additionally, each muscle's contribution to the defined function of the muscle in the musculoskeletal system operation as described in Table 3.1 can be determined. In this way, dominant synergistic (same function) and antagonistic (opposing function) muscles can be identified. The number of synergistic or antagonistic muscles may also indicate the level of difficulty of the optimization process.

To understand the predicted relative influence each muscle had on the total muscle-generated joint moment, the ratio between the signed moment produced by each individual muscle and the total signed joint moment due to the reaction forces generated in the system from the net resultant load could be calculated. Positive values would indicate that the muscle force produced a moment in the same direction as the reaction

force, while negative values would indicate that the muscle produced a moment in the opposite direction. By using the signs of these moments, synergistic (same functioned) and antagonistic (opposing functioned) muscle activities could be identified. The relative magnitudes of these ratios provide an idea of which muscles dominate which actions. Ratios with a magnitude of one would indicate the moment produced by the muscle was equal to that produced by the reaction force. A magnitude greater than one would indicate that the muscle produced a moment larger than that produced by the reaction force. For a static system such as the one considered in this investigation where there is no net angular momentum and no net moment, these muscle-generated moments that are larger than those produced by the reaction force should always be balanced by a moment generated in the opposite direction by an antagonistic muscle to produce a net muscle moment equal to that caused by the reaction force. This method also provides an additional method to verify the model's function. This model appropriately predicted both synergistic and antagonistic muscle activity.

Likewise, the relative contribution of the predicted forces between muscles that perform the same function about a joint (synergistic muscles) could be analyzed and compared to the relative values of their physiological parameters (such as moment arms and cross-sectional areas). Flexor and extensor muscles for the ankle, knee and hip were each compared separately (Table 3.7). In this validation study, the relative contributions of such synergistic muscles to the total force varied with the resultant loading direction studied and were not directly proportional to the relative size of the muscles or location of action of the muscles relative to the joints. Thus, while the physiological parameters

did affect the resulting values of the individual muscle forces, they did not have sole influence over the results predicted by this model.

Table 3.7 Muscle Force Model Validation: Predicted Relative Influence of Geometric Parameters on Synergistic Activity

		30°	60°	90°	120°	150°	180°	210°	240°	270°	300°	330°	360°
Ankle Extensors: Gastrocnemius as % of Soleus	Force	neither	neither	neither	neither	neither	neither	Gast Only	Gast Only	Gast Only	Gast Only	23%	Sol Only
	Moment Arm	100%											
	Area	48%											
Ankle Flexor: ONLY Tibialis Anterior	Force												
	Moment Arm												
	Area												
Knee Extensors: Rectus Femoris as % of Vastii	Force	42%	64%	84%	114%	213%	neither	neither	neither	neither	neither	Vastii only	2%
	Moment Arm	100%											
	Area	20%											
Knee Flexor: Gastrocnemius as % of Long Head Biceps Femoris	Force	neither	neither	neither	neither	neither	LHBF only	16%	29%	33%	40%	13%	LHBF Only
	Moment Arm	55%											
	Area	97%											
Knee Flexor: Short Head Biceps Femoris as % of Long Head Biceps	Force	neither	neither	neither	neither	neither	22%	10%	8%	5%	2%	LHBF only	LHBF Only
	Moment Arm	100%											
	Area	13%											
Hip Extensors: Gluteus Maximus as % of Long Head Biceps Femoris	Force	neither	neither	neither	neither	neither	LHBF only	LHBF only	LHBF only	LHBF only	LHBF only	57%	219%
	Moment Arm	59%											
	Area	97%											
Hip Flexor: Rectus Femoris as % of Iliacus	Force	41%	40%	39%	38%	38%	IL Only	IL Only	IL Only	IL Only	IL Only	neither	RF only
	Moment Arm	88%											
	Area	65%											

These studies have validated the use of the developed program to predict the individual muscle forces in a musculoskeletal system using a gradient projection optimization method and an optimization goal to minimize the sum of the squares of the muscle stresses. The developed model does not require the artificial constraints of arbitrary maximum muscle force values and can be used for a variety of loading and sets of joint angles (geometric configurations) with only minor manual interaction to input the specific momentum balance equations for the system investigated. Additionally, these studies have shown how having quantitative values of individual muscle force magnitudes can provide significant insight into the locally generated muscle forces,

which are often difficult to measure experimentally, to determine how they contribute to the net resultant force, which is more readily measured through experimental means. Finally, the ability to determine muscle force magnitudes allows for the study of the response of the bone to the muscle loads, the intent of the next phase of the model development which is discussed in Chapter 4.

3.3.3 Application of the Muscle Force Model

Next, a method was developed to integrate the validated muscle force optimization model with the structural analysis used to predict the effect of these individual muscle forces on the stress state of the bones to which they are attached. The goal of the method is to take a given physical activity or resultant force generated by the whole musculoskeletal system, determine the individual muscle forces that create this net force, and apply these loads a model of the bone system to the local stress distributions in these components. The modeling method developed here can then be used to drive the bone strength adaptation models as discussed in Chapter 4. In this section, the method to couple the muscle force optimization and the structural analysis will first be explained. Then representative applications will be presented in order to demonstrate its function and usefulness towards the understanding the behavior of skeletal system under muscle loads.

3.3.3.1 Model Linking Muscle Force Optimization to Bone Stress Analysis. The analysis of the response of the bone system to applied muscle loads and appropriate boundary constraints was performed through the use of commercial finite element software ANSYS [141]. The finite element code was customized through the development of a user-defined Fortran subroutine (called a User Programmable Feature

or UPF) to execute the muscle force magnitude optimization code that was described in Subsection 3.3.2. The muscle force optimization program is an independently operating executable program that outputs the muscle force magnitudes to ANSYS through the use of a C-shell around the developed MATLAB code described in Section 3.3.2. This executable program was called from a Fortran subroutine in ANSYS, the structural analysis solver. As stated in Subsection 3.3.2.2, the use of MATLAB is not required for the operation of this modeling method. The same procedure could have been carried out completely within a user defined Fortran subroutine if additional code was written to replicate the built-in MATLAB linear algebra functions used for modeling efficiency in the developed code. To automate the execution of the model for any system studied, a script written in the ANSYS programming language (ANSYS Parametric Design Language or APDL) was used to assign the modeling parameters for both the muscle force model and the finite element model, run the muscle force optimization, apply the appropriate muscle forces returned from the user subroutine, apply other boundary conditions, run the structural analysis and examine the results. In this way, the individual muscle force magnitudes found from the optimization program were directly applied to the finite element model of the system of bones studied.

3.3.3.2 Effect of Muscle Force Activity on Stress Distribution in Bones. The procedure described in Section 3.3.2.2 was used to analyze the effects of the muscle forces on the bones in the system described in Subsection 3.3.1 under a number of loading conditions. Specifically, the effect of variation of the direction of the resultant force generated between the foot and the fixed plate was studied. Four of the twelve resultant force directions in Figure 3.3, representing the 90°, 180°, 270° and 360°

directions, all with the same magnitude, were examined. The resulting von Mises stress distributions and displacement distributions were compared to examine the trends in the response of the bones in the system to variations in the muscle force activity and intensity.

A similar physical model to the one described in Chapter 2 was used for this investigation as shown in Figure 3.9. However, the shapes of many of the bone components were simplified. The geometry of the pelvis was represented as a rectangle with rounded corners. The foot geometry was reduced to a symmetric inverted V-shape with the heel at one end and the toe at the other. All hip, knee and ankle joints were represented by concave and convex hemispheres. Cancellous bone tissue was included as described in Chapter 2. In the configuration investigated in this study, the joint angle at the hip was 45° while that at the knee and ankle was 90°. The bottom surface of the pelvis (torso) section was fixed in all degrees of freedom as was the flat surface representing the toe region of the foot. Because this was a comparative study to examine the function of the model, the simplification of the geometry was justified. All material properties and joint interaction models described in Chapter 2 were used in this study. Figure 3.9 shows the model used.
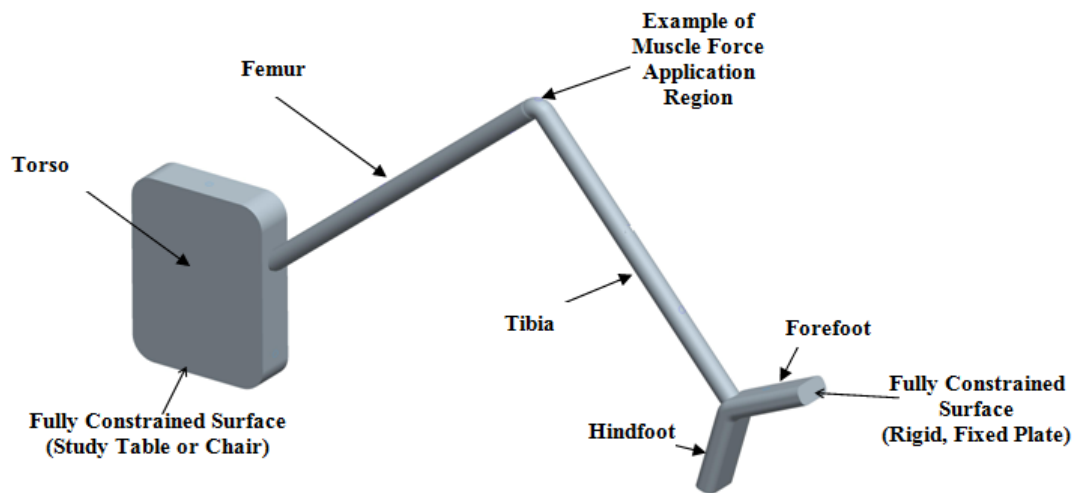
Figure 3.9 Simplified skeletal model used in study of lower extremity isometric loading.

The distributions and extreme values of the von Mises stress and displacement within the complete model as well as each individual bone volume were compared. Additionally, stresses at the contacting interfaces, such as contact pressures and frictional stress, contact convergence measures, like chatter, were all examined to understand the model function and the effects of the muscle force. Significant results for the von Mises and displacement distributions as well as the joint contact pressures are discussed here.

The muscle activity for each resultant loading direction studied is presented in Table 3.8, depicting both the predicted magnitude and the relative intensities of the muscle forces based on the ratio of the individual muscle's magnitude to the maximum magnitude of any active muscle force that contributes to the resultant force. The table also identifies the muscle both by relative position (front of leg (anterior) or back of leg (posterior)) and resulting muscle action (flexion or extension). In general, the muscle force magnitudes that act to create an anteriorly or posteriorly (front or back) directed resultant force were the greatest, with the anteriorly directed resultant force requiring the greatest muscle magnitudes. A superiorly (towards the torso) directed resultant force

required muscle force magnitudes about half of the anteriorly directed resultant. An inferiorly (away from the torso) directed resultant force required muscle forces an order of magnitude smaller than all of the other loading directions studied.

Table 3.8 Muscle Activity and Intensity for Loading Cases Studied

Muscle	Location	Action	90° (Anterior)	180° (Superior)	270° (Posterior)	360° (Inferior)
1 - TA	Anterior	Ankle Flexor	671 (41%)	201 (25%)	77 (5%)	0
2 - SOL	Posterior	Ankle Extensor	0	0	0	114 (28%)
3 - GAST	Posterior	Ankle Extensor, Knee Flexor	0	0	484 (33%)	0
4 - VAST	Anterior	Knee Extensor	758 (46%)	0	0	403 (100%)
5 - RF	Anterior	Knee Extensor, Hip Flexor	640 (39%)	0	0	9 (2%)
6 - SHBF	Posterior	Knee Flexor	0	65 (8%)	75 (5%)	0
7 - LHBF	Posterior	Knee Flexor, Hip Extensor	0	294 (37%)	1460 (100%)	23 (6%)
8 - IL	Anterior	Hip Flexor	1640 (100%)	796 (100%)	639 (44%)	0
9 - GM	Posterior	Hip Extensor	0	0	0	50 (12%)

Joint moments from the net resultant force can also help to explain muscle activity. The joint moments caused by the reaction force on the foot due to the leg acting on the fixed plate are listed in Table 3.9. Positive joint moments from the reaction force at the plate required ankle extensors, knee flexors and hip extensors to counterbalance them. Negative joint moments required ankle flexors, knee extensors and hip flexors for counterbalance. Additional antagonistic muscle activities were necessary to fully balance the total moments about each joint. As expected, the joint moments created by opposing net resultant forces (anterior/posterior and superior/inferior) had nearly equivalent magnitude.

Table 3.9 Input Joint Moments due to Reaction Force (N-m) (CCW+)

	Ankle	Knee	Hip
90° (Anterior)	-20	-46	-70
180°(Superior)	-6	9	-7
270°(Posterior)	19	45	70
360°(Inferior)	5	-13	3

By considering these net joint moments, as in Table 3.9, in the analysis of the muscle activity, an understanding of the relative intensities of the muscle forces between resultant force cases emerges. This is a useful tool when comparing system behavior under varied loading conditions. For example, in this study, to create an interiorly directed resultant force, ankle and hip flexors and knee extensors were required. To create a superiorly directed force, ankle, knee, and hip flexors were needed. One of the active knee flexors also acts as a hip extensor, causing the hip flexor muscle force magnitude to be greater than if the hip flexor was acting alone to achieve the desired net hip joint moment. To create the posteriorly directed force, knee flexor and hip and ankle extensors dominated, but they were modulated by their respective antagonistic muscles. Of these active muscles, those that spanned both the knee and hip joints were most influential. Finally, to generate the inferiorly directed resultant force (360°), the knee extensors created the majority of the force. Ankle extensor activity was also significant, while hip muscle activity was slight, mostly due to the activity of the knee extensor muscles that spanned both ankle and knee joints. The activity of the knee extensor was modulated by antagonistic muscle activity that created an opposing moment about the ankle to adjust the net moment to meet the equilibrium conditions.

These descriptions of active muscle forces and their relative magnitudes for each net resultant force can in understanding the responses of the bones to different loading

conditions in the system studied. The stress and displacement distributions in the bones due to the muscle activity are described next and compared for the four net resultant loading directions studied. This analysis provides an example of how a model such as the one developed here could be used to improve the understanding of the behavior of a musculoskeletal system beyond the standard experimental measurements of EMG activity, net resultant forces, and joint angles.

Von Mises Stress and Displacement Distributions and Joint Contact Pressures

As the direction of the resultant load at the toe changed direction from forward towards the front of the body (anterior 90°) to inwards towards the torso (superior 180°) to back away from the body (posterior 270°) to outwards towards the foot (inferior 360°), the locations of maximum deflection and stress resulting in the musculoskeletal system shifted from the hip towards the foot (Figures 3.10 and 3.11). The largest deflections and stresses occurred for anteriorly and posteriorly directed forces. The smallest stresses and displacements (by an order of magnitude) occurred for the inferiorly directed forces. Stress concentrations were observed at all edges of the joint contact regions, at the locations where boundary condition discontinuities occur, and at areas of muscle force application. High contact pressures were found at the knee and ankle especially for the posteriorly (270°) directed load (Figure 3.12). Less extreme but relatively high contact pressures were found at the hip for the anteriorly directed load. The smallest contact pressures were found at the joints for the superiorly and inferiorly directed loads. Basic trends with loading direction in each bony segment and joint are briefly discussed to provide a better understanding of regional variations due to the change in direction of the resultant force. For comparisons of active muscles and resulting displacement

distributions refer to Figure 3.10. In all descriptions of von Mises stress distributions, refer to Figure 3.11. For changes in joint contact pressure refer to Figure 3.12.
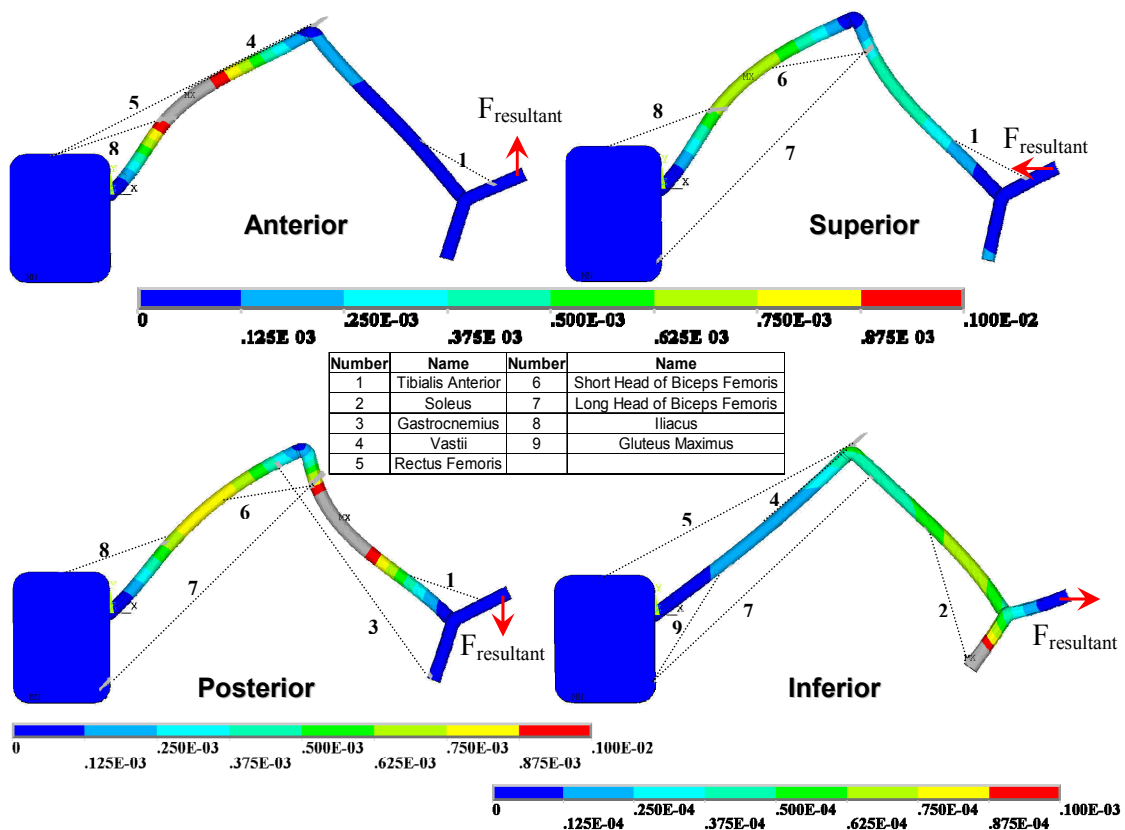
Figure 3.10 Active muscles and displacement distributions for muscle force model verification study.

Torso (Pelvis)

For the anterior and superior resultant loads, the location of highest stress was at the upper, or anterior side edge of the hip joint (Location A in Figure 3.11) while for the posterior and inferior loading cases, two high stress regions occurred. One was at the bottom, or posterior side, edge of the hip joint (Location A1 in Figure 3.11). The second was at the common attachment point of the hip extensor muscles (the gluteus maximus and the long head of the biceps femoris) on the posterior side of the pelvis bone on the

same side as A1, but further down the vertical face of the pelvis. This area corresponds

to the zone where large hip flexor muscle force magnitudes in the anterior and superior

loads and the large hip extensor forces in the inferior load were applied.
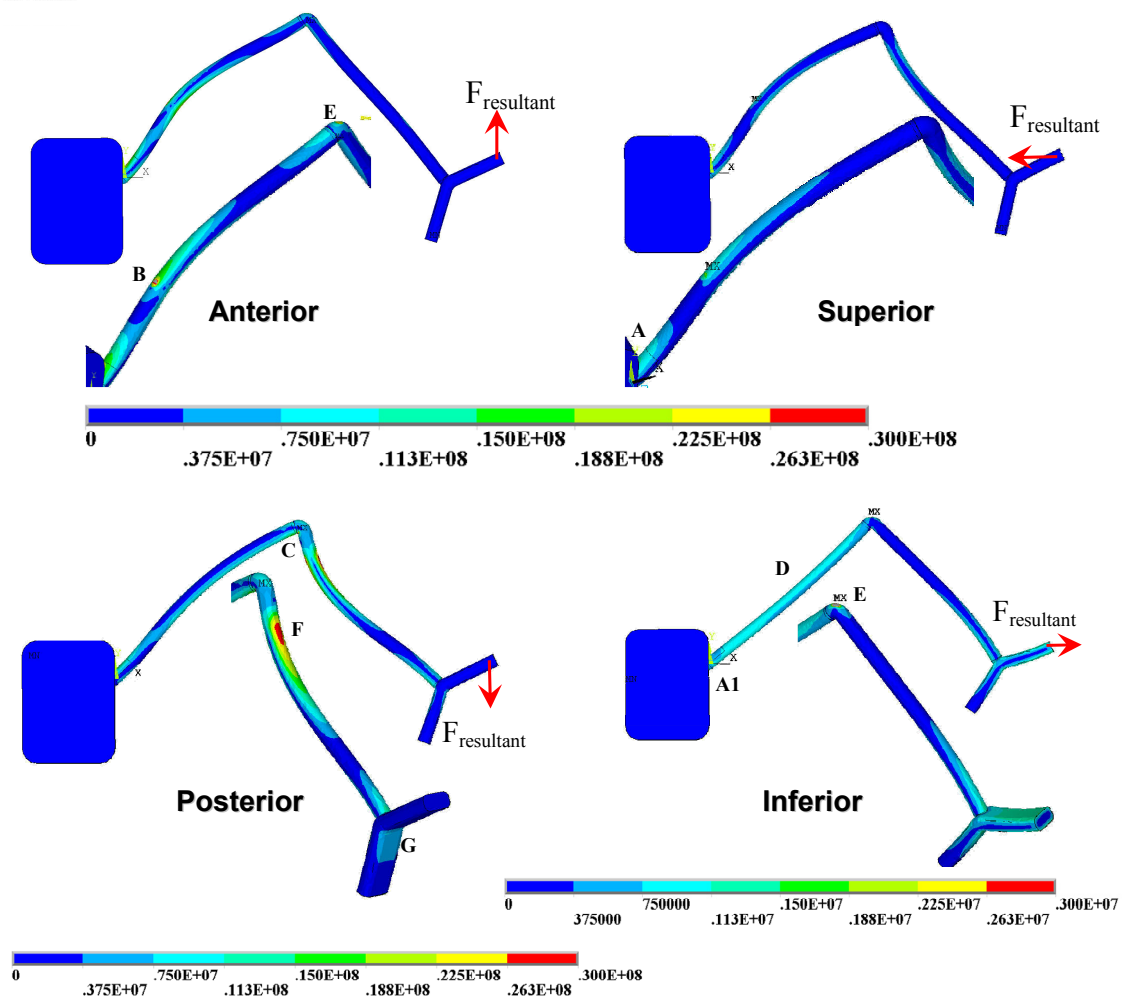
Figure 3.11 von Mises stress distributions for muscle force model verification study.

Hip

The contact pressures at the hip joint followed the trends in the maximum stresses at the

torso with high stresses on the anterior side near point A in Figure 3.12 on the anteriorly

directed load to the posterior side near point B on the inferiorly directed load case (at the

edges of the contact region). The superior and posterior loading cases showed a transition in the location of maximum contact pressure within the contact area from a more anterior to a more posterior location, between the edges of the contact region. The posterior shift in the location of maximum contact pressure was related to the shift from active hip flexor muscles in the anteriorly directed and superiorly directed resultant load cases to active hip extensors in the inferiorly directed resultant load as well as the slight joint compliance allowed by the joint contact model. For the posteriorly directed load, hip flexors were joined by knee flexors working both to pull the femur in the posterior direction. This shifted the location of the contact pressure posteriorly, resulting in a more intermediate location of high contact force.

Femur

The largest stresses in the femur under the anteriorly and superiorly directed resultant forces occurred at the location of attachment of the hip flexor muscle as it had the largest force magnitude (location B in Figure 3.11). While this very large force acted over a small area, its effect on the bone stress was modulated by the deflection of the largely hollow bone (Figure 3.10). Depending on the resultant load and the direction of the net joint moments, contact occurred at the hip and knee joints resulting in a region of relatively high stresses, for example as near location A in Figure 3.11. For the inferiorly directed case, the effects of the maximum muscle force in the femur were modulated by the bending caused by other muscle activity for a more evenly distributed stress over the femur surface (Location D in Figure 3.11).
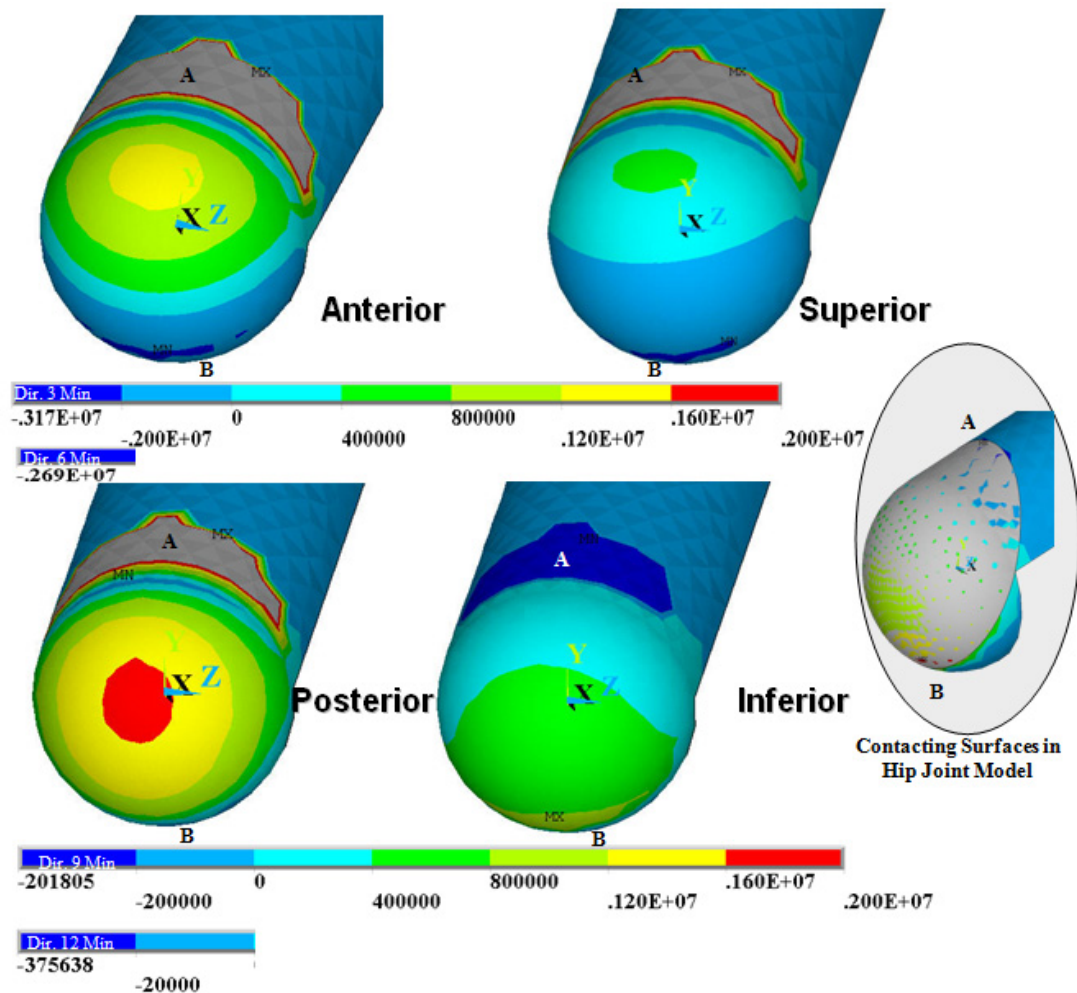
Figure 3.12 Contact pressures in hip joint for muscle force model verification study.

Knee

The analysis of the contact pressures at the knee joint follows the same characteristics as those of the hip. In the anteriorly directed resultant load, knee extensors were active, trying to pull the tibia anteriorly to increase the angle between the femur and the tibia. This loading increased the contact pressure on the anterior side of the knee joint. In the superior and posterior directions, knee flexors dominated, working to reduce the knee joint angle. This lower angle brought the contacting surfaces closer together due to the compliance imposed by the joint contact model. To create the inferiorly directed

resultant force, both knee flexors and extensors were active. Since one muscle force no longer dominated, the contact pressures at the edges of the mating joint surface regions on each bone volume were reduced.

Tibia

The regions of high stress in the tibia were mainly the areas near the muscle force application (Figure 3.11) and near the joints. For the anteriorly and the posteriorly directed loads, a localized region of high stress occurred near the knee joint, on the posterior side where the femur and tibia contact at point C in the Figure 3.11. For the anteriorly and inferiorly directed load, knee extensors contributed to the majority of the load on the tibia, causing a region of very high stress at muscle attachment (point E in Figure 3.11). The region of attachment of the knee extensors on the posterior side of the tibia was the zone of highest stress in the superior and posterior loading directions. Under these conditions, the pull of these muscle forces on the tibia caused large deflection (Figure 3.10) and a resulting region of high bending stress on the anterior side (point F in Figure 3.10).

Ankle

The trends in the contact pressure described the hip and knee were consistent with those at the ankle joint. The anteriorly directed resultant load caused a high positive contact pressure on the anterior side of the joint. This opposite trend was observed for the superior, posterior and inferior loading directions, where a high contact pressure was found on the posterior edge of the joint. This shift corresponded to the decreased magnitude of the ankle flexor muscle force moving from the anteriorly directed resultant force to the superiorly directed and posteriorly directed forces, for which the ankle

extensor forces were also required. For the inferiorly directed force, no ankle flexor activity occurred and only the ankle extensor soleus was active, increasing the pressure at the posterior side of the joint as the muscle attempted to increase the angle between the foot and tibia.

<u>Foot</u>

The changing muscle activity in the region surrounding the ankle joint for each resultant load direction impacted the stresses and displacements in the foot. The region of high stress and displacement in the foot shifted from the toe and ankle flexor muscle attachment point in the anteriorly directed load, to the heel and attachment of the ankle extensor muscles in the inferiorly directed load (Figures 3.10 and 3.11). Localized regions of high stress are also found under the arch of the foot for the posteriorly and inferiorly directed resultant loads (point G in Figure 3.11), likely due to the combination of the ankle flexor muscle loads on the heel and the displacement constraint at the toe (Figure 3.9).

3.3.3.3 Conclusions. The modeling techniques to determine the individual muscle forces that generate a known resultant force and directly couple these calculated muscle force magnitudes to the analyses of the resulting response of the skeletal system to which the muscles are attached have been proven to be useful in examining the relationships between resultant loads generated by the bone/muscle system, the muscle activity and intensity of the forces generated by each of the muscles considered in the leg system studied, and the resulting state of stress of the bones and the joints within the system. For example, the use of the modeling methods in a verification study revealed how the stress state of the bones in a musculoskeletal system can be significantly altered simply

by changing the direction of a constant magnitude net resultant force generated by the system of muscle forces studied. This verification study demonstrated the ability of such a model to determine the individual muscle forces generated within a given system that together to produce a desired activity and the resulting changes to the local mechanical environment of the bones within this system that they induce. The use of these techniques can not only provide insight into the system behavior, but can also provide the input necessary to study subsequent system responses, such as bone shape adaption. In Chapter 4, the tools to predict the alterations in bone strength due to the variations in the local mechanical environment of the bone are discussed.

CHAPTER 4

BONE STRENGTH ADAPTATION MODEL

4.1 Background

As discussed in Chapter 1, because both the intrinsic properties of bone, such as material density, and the extrinsic properties, such as the overall shape, change in response to variations in the bone's mechanical environment, it is not possible to separate these two effects using physical experiments or clinical studies. However, through the use of numerical simulations, the effects of each mode of adaptation can be isolated and the intersubject variation introduced by studying living systems can be eliminated to reveal insight into the adaptive behavior of a musculoskeletal system in a more controlled fashion.

The computational modeling of the phenomena of bone strength adaptation emerged in the 1960's to 1970's after the rise of computational resources and the related development of numerical tools to solve more complex mechanical problems. At the same time, significant research focused on using these new computational tools, like finite element analysis and numerical optimization, to efficiently automate mechanical design processes. Because both bone strength adaptation processes and mechanical design processes have a similar goal, to prevent failure of a system component, the modeling and analysis methods developed for one area of study can often be applied to the other.

Bone strength adaptation occurs both by changing the internal structure of the bone, thereby modifying its porosity and density (intrinsic properties), and by modifying its external surface, thereby altering the overall shape (extrinsic properties). Similarly,

the automated design of inert mechanical components, structural optimization, is divided into two main areas [260]. In topology optimization, the internal structure is altered, such as the arrangement of struts in a truss or the local mechanical properties. In shape optimization, the boundary surfaces of the object are altered, changing the external structure that interfaces with the environment. A subset of shape optimization is size optimization, where the overall profile remains the same, but the dimensions change, such as modifying the diameter of a cylinder or the length of a beam. Because the fields of modeling bone shape strength adaptation and structural optimization parallel one another both in their theories and in the processes involved, the application of numerical solution methods to these two fields is similar. The development of new methods and techniques for improved solution efficiency and stability in one of these fields can be applied to benefit studies in the complementary field.

The general numerical methods for modeling both the intrinsic and extrinsic property adaptations in both fields of study follow the same procedures [88, 91, 98, 207, 261-263]. A structural analysis is performed, usually through finite element or boundary element methods. A mathematical model that relates the local mechanical state of the object under loading to the adaptive changes in the local structure of the component (i.e. the incremental changes to the bone or component size/shape) is applied. The discretized geometric model is modified at control points (such as nodes) based on the adaptation model. The control point positions may then be additionally adjusted to ensure that the discretized geometric model retains its integrity after the design modifications. The process is repeated iteratively until the optimization goal, such as a sufficient decrease in the maximum stress in the model, is reached.

Following the experimental investigations of bone strength adaptation, most of the attention of the complementary numerical studies has been on the intrinsic design properties, or the modification of the bone density and cancellous bone structure. The reasons for this are mainly twofold. First, because the modification of the bone density and cancellous structure has been more extensively studied experimentally and because methods to measure and visualize these changes with time are readily available, experimental validation to the developed modeling methods is more feasible [110, 264]. Second, the modeling methods used to simulate the changes to the internal structure are simpler to execute than those related to shape optimization. The modeling of internal adaptation of bone strength (or topology optimization in inert objects) consists of modifying the material properties of each element in the discretized geometry based on its local mechanical state [90, 265]. While methods are needed to prevent extreme discontinuities between the properties of neighboring elements or nodes [109, 202, 266-268], the mesh structure remains constant and so there is no need to modify the geometric discretization during the analysis.

In contrast, during the shape optimization process and simulations of bone strength shape adaptation, the entire mesh structure is modified based on local variations of the bone's (or mechanical component's) response to the applied loads as calculated through the stress analysis. Although the necessity of altering the mesh as the simulation progresses is noted in reported computational models of bone shape adaptation [93, 95], much of the work in developing methods to maintain the integrity of the model during the optimization process has been accomplished by those in the field of structural optimization. Even in some of the first numerical shape optimization methods developed

in the 1970's [269, 270], it has been noted that the movement of the surface boundary may result in extreme mesh distortions causing inaccurate and, therefore, unreliable, results from the structural analysis. For this reason, automatic node smoothing or remeshing on both the external surfaces and in the interior volume has been suggested to ensure an appropriate mesh is consistently maintained throughout the analysis [204, 209, 212, 271-278].

The validation of bone shape adaptation models is more difficult than that of bone density adaptation models because accurate cross sectional slices of the bone often give the best views of the changing profiles. However, measurements of these sections cannot be easily obtained on living subjects. Traditionally, comparisons of model results were made to actual bone systems by examining the bones of animals sacrificed at the end of the experimental period. As such, only one snapshot in time was used to show the effect of the loading on the bone adaptation which provided no indication of the state of "convergence" of the growth. While newer imaging methods can obtain geometric data without the need to sacrifice the subject, the issue of the "stopping point" remains. As a result, numerical models of bone shape adaptation are often developed to create the same growth patterns as observed in experimental studies [82, 89, 112], and their function is limited to studying the same systems that were investigated experimentally. Similarly, many of these shape optimization modeling methods have been developed to study a singular problem, such as determining the radius of a fillet in a mechanical component that sufficiently reduces a stress concentration [209, 261, 272, 279-281], limiting the region of optimization to a small portion of the overall component investigated. In contrast to these previously defined methods, the objective of the current research was to

compare diverse system conditions using only one model. The modification of the currently available techniques to meet this modeling design goal was the focus of this segment of the current study.

4.2   Model Development

The model developed in this work followed the same basic procedure described in Section 4.1. However, to achieve the research goal of universal applicability of the developed model, the definition of the main model features, the shape adaptation model driver, the optimization solution methods, the mesh refinement methods, and all the solution parameters, including stopping criteria, had to allow for more general use. Each of these modeling components will be reviewed in terms of previously developed models as reported in the literature and how these components were modified towards meeting the model design goals of this work.

4.2.1 Optimization Method

The methods used to determine the set of unknown design variables that define the optimal surface shape in the simulation of bone adaptation or in the design of mechanical components fall into two main categories: gradientless and gradient-based optimization. Gradient-based optimization methods were described in Chapter 3 and used for finding the muscle force magnitudes. Gradientless optimization methods are less mathematically rigorous. They merely iteratively step a calculated value towards a target value along a linear path. Descriptions of these methods and their use in shape optimization/bone shape adaptation will be reviewed, and conclusions will be drawn about their potential benefit to the current research objectives.

4.2.1.1 Gradient-based Optimization Methods. Gradient-based optimization routines are mathematically rigorous methods that result in a unique local optimum. They are often described in the function form by:

$$\begin{aligned} &\text{minimize } Z(\mathbf{x}, \mathbf{u}(\mathbf{x})) \\ &\text{with the constraints } \mathbf{g}(\mathbf{x}, \mathbf{u}(\mathbf{x})) \le 0 \end{aligned} \tag{4.1}$$

where $\mathbf{x}$ is the set of design variables and $\mathbf{u}$ is any function of these design variables. In structural shape optimization, the optimization goal Z can be a function of any calculated parameter derived from the structural analysis. In the finite element formulations for shape optimization [213], the design variables $\mathbf{x}$ are often simply the nodal coordinates. However, they can also be parameters or values derived from the nodal coordinates or can be some intermediate "control" points that influence the locations of the nodes. These control points are often used to reduce the number of design variables for which to solve [269]. In these situations, a mapping is employed such as:

$$\mathbf{p} = \tilde{\mathbf{x}}(\mathbf{x}) \tag{4.2}$$

where $\mathbf{p}$ are the nodal coordinates, $\mathbf{x}$ are the design variables, and $\tilde{\mathbf{x}}$ maps from the design variables to the nodal coordinates.

The gradient-based methods that have been used in the past in structural optimization problems are diverse and include the Method of Steepest Descent, Gradient Projection (used in the developed muscle force magnitude optimization model of Chapter 3), Conjugate Gradient (Fletcher-Reeves), Davidson-Fletcher-Power, Broyden-Fletcher-Goldfarb-Shanno, the Penalty Methods, Lagrange Multiplier Methods, and Newton and

Quasi-Newton Methods [203, 252]. Each requires the calculation of the gradient of the objective function $Z(\mathbf{x})$ and the constraints $\mathbf{g}(\mathbf{x})$ with respect to the design variables $\mathbf{x}$ [269]. Because the objective and constraint equations are typically a function of the results of the structural analysis, they depend on the shape of the object described by the design variables $\mathbf{x}$. These methods require sensitivity analyses, which are the individual perturbations of each design variable to examine its effect on the optimization goal [269]. Specifically in shape optimization, sensitivity analyses evaluate the gradient of the response measure (Z) with respect to the shape parameters (design variables ($\mathbf{x}$)) that describe the geometry of the domain being optimized [282].

Difficulties arise in calculating these gradients and performing these sensitivity analyses in two major ways. First, the number of gradient calculations depends on the number of design variables. While the finite element nodes are the best choice for design variables because, due to their close proximity, they allow for the most variation of the surface geometry. However, their use comes at high computational expense. Methods to reduce the number of design variables to alleviate the computational burden focus on averaging or regionalizing surface nodes through the use of superelements [204] and B-splines, Bezier curves, and the like [207, 261]. However, even with these smaller sets of design variables, the number of required gradient calculations can be quite significant, especially when examining three-dimensional surfaces [207, 269]. Second, because they are based on structural analyses, the optimization goals and gradients are often nonlinearly dependent upon the design variables [269]. While differentiation by finite differences as well as analytical and semi-analytical approaches have been developed to estimate these gradients, the approximations can be a large source of error and often

require extensive code development and access to the finite element structural source code itself [207, 283]. Because of these difficulties, less computationally intensive and mathematically rigorous methods were sought in the practical execution of structural shape optimization, especially when studying three-dimensional, complex shapes as in the current work.

4.2.1.2 Gradientless Optimization Methods. While gradient-based methods result in a unique optimal solution, their implementation in shape optimization is often difficult. Zero-order, or gradientless, methods eliminate the computational difficulties of the gradient-based methods and can be implemented completely external to the numerical structural analysis solvers, which is especially useful when utilizing commercial software with little direct access to the source code [284]. These mathematical methods were originally developed in the 1950's, not specifically for mechanical design applications, but they were dismissed by mathematicians in the 1970's because of their slow rate of convergence and lack of absolute proof of convergence. Interest in gradientless optimization methods was revived in the 1990's with the increased use of high performance computing and "simulation-based optimization" [113].

There are two main types of gradientless optimization methods. Direct search methods step along a varying direction with a varying step size while looking for smaller and smaller (or larger and larger) numbers in a "sequential examination of trial solutions" [113]. Examples of these kinds of methods are the Simplex, Compass, Pattern Search, Coordinate Search, Line Search, and Powell methods, which differ based on how to find the step size [113]. The second type is often referred to as "biologically based" methods due to their widespread use in simulating natural phenomena. These methods are even

simpler to implement than direct search methods as they just move a design variable to a new guess based on the difference between the value of a measure related to the design variable and that of a selected "goal" [94].

While gradientless methods are much easier to implement and less computationally intensive to execute than gradient based ones, there are some limitations. Many of the direct search methods are often restricted in the relationships between the optimization goal and the design variables. For example, Simplex methods require linear relationships [113]. Other methods may be able to handle highly nonlinear optimization functions but do not converge for a large number of design variables [203]. Still other methods may be simple to execute but are very inefficient. Examples of these include many of the univariate methods that essentially just "change one design variable at a time" [114]. In all of these direct search methods, termination criteria is important, as improperly selected criteria can miss the optimum and either never converge or converge to the wrong solution [113].

The so-called "biologically-based" optimization methods do not have a prescribed mathematical algorithm. Instead, they systematically step towards a particular goal using the form:

$$
\begin{aligned}
& x_{k+1}(l) = x_k(l) + U_k(l) \\
& where\ U_k(l) = \alpha\left(\sigma_k(l) - \sigma_{ref}\right)
\end{aligned}
\tag{4.3}
$$

where $x(l)$ is the design variable at a particular location (point) l, $\sigma(l)$ is a measure of the local stress state at a point, σ_{ref} is a desired stress state, α is a coefficient, usually controlling the rate of change, and k is the optimization iteration counter. In structural

shape optimization of a mechanical component, the reference value is usually a specified stress value such as a yield strength, which is often scaled by a safety factor. For bone shape adaptation simulations, it is typically the threshold value that is thought to trigger bone growth or decay. The idea behind the use of this type of model in studying the functional adaptations of living components is based on the observation that "biological" systems progress towards a state with few variations [7, 94, 285, 286]. Critics believe these kinds of methods cannot guarantee a mathematical optimum and may even fail to reduce the maximum stresses in mechanical component design [213]. Nonetheless, because of their ease of use and similarity to feedback control system models, this type of gradientless optimization method has been widely implemented to predict shapes of both biological and inert objects [4, 11, 87, 90, 112, 209, 281, 287-294] and has even been used to simulate the internal adaptation of bone density and in structural topology optimization [265, 267, 295].

While not as commonly applied to solve shape optimization and bone adaptation problems, global optimization methods such as evolutionary, simulated annealing, and particle swarm have been implemented [206, 252]. These are gradientless methods that have the potential to reach a global optimum. In these methods, local optima are first found near different initial conditions. Then, the optimum of these local optima is found. Global optimization methods follow stochastic processes which have no iterative improvements, requiring many cycles of trial and error with a number of starting values or initial conditions. The chances of finding an optimum value with these methods often decrease with an increasing number of design variables, and it has been suggested that for three-dimensional shapes, a small number of design variables should be used and the

design domain should be limited to a small local range surrounding these points [208]. For these reasons, their practical application to structural optimization is limited.

Based on this review of the types of shape optimization and bone adaptation simulation methods that have been developed, the gradientless, biologically-based method was chosen for application to this work. A gradient-based method, such as the one developed for the muscle force magnitude model would ensure a unique, optimal solution and such gradient-based methods were investigated for their potential application to the shape adaptation models in this work. However, the large number of design variables involved in the three dimensional models of interest and the use of commercial finite element software for the structural analyses, which limits access to the data necessary to compute the required gradients, prohibited the feasible application of the gradient based methods in this work.

In choosing to use the least mathematically rigorous of the available gradientless optimization methods to compare the effects of various loading conditions on the ensuing bone shape changes, the appropriateness and repeatability of the resulting optimal solution must be assured. Work was undertaken in a number of areas to ensure the ability of the developed model to produce a unique and repeatable solution. Significant work was done in selecting the model parameters: the factor, α, in Equation 4.3 and the reference value stress, $\sigma_{ref,}$ in the same equation. Additionally, the development of a uniform stopping or convergence criteria was required so that direct comparisons could be made between the conditions developing in the various systems studied which may have different configurations, geometry, and loading. Finally, a mechanical measure of

the local mechanical state had to be selected to drive the shape adaptation model. The development of each of these modeling components is discussed in detail.

4.2.2 Model Driver: Measure of Local Stress State

There are many different measures of the state of stress of a local region in an object. Some common measures include the stress and strain tensors, principal stresses and strains, von Mises stress, and strain energy density. Each one provides unique insight into the behavior of the object under the applied load as the measure explains the response of the object to the applied load in a different way. For example, some are directional measures, while others depict the overall state in all directions. Still other measures describe the intensity of the particular type of behavior induced in the object as a response to the applied load. A wide variety of measures have been used by others to drive the bone shape adaptation simulations in previously developed models. Accordingly, a number of measures were considered for the model developed in this work. Because many different models have been published with many different conclusions as to which measure best correlates with changes in bone strength, a review of the application of these model drivers to the gradientless optimization methods in previously published works and their potential for inclusion in the model developed in this work will be discussed.

4.2.2.1 Strain or Stress Tensors. Many models of bone strength adaptation have been driven by stress or strain values [17]. Early quantitative models of bone adaptation related peak strain values to changes in the curvature of long bones and suggested that stresses above a "minimum effective stress" activated adaptive responses in bone tissue.

Because strain gages are often used in animal studies to determine the mechanical state of the bone [296-298], the value of this "minimum effective stress" was often represented by experimentally measured strain taken in regions of bone with observed load-induced growth or decay [299]. Based on these early conceptual models, more rigorous mathematical adaptation models were developed, correlating the contribution of each strain tensor component to the local changes in bone shape in a direction normal to the bone's surface through a relation similar to that used in Equation 4.3: [87]

$$U_k(l) = \alpha_{ij}(l) \left[\varepsilon_{ij}(l) - \varepsilon_{ij}^{ref}(l) \right] \tag{4.4}$$

where $U_k(l)$ is the change in the position of the point l on the surface of the bone in the direction normal to the surface for the optimization iteration k. In this model, each strain tensor component may have a different growth rate coefficient (step size), α_{ij}, and reference value, ε_{ij}^{ref}, each of which can vary from point to point on the surface. It was expected that these model parameter values would be determined experimentally, and, while they were permitted to vary from point to point, it was implied that they were likely the same for all points on the surface considered. This model allowed for each component of the strain tensor to affect the local bone adaptation in a different manner and with a different weight. For example, normal strains could be made to cause greater changes than shear strains with the proper selection of the α_{ij} and ε_{ij}^{ref} parameters. As a result many subsequent studies looked for evidence of these direction dependent and localized effects to quantify these relationships.

While some techniques found the values of these model parameters through trial and error until the model predicted shapes or amounts of growth matched those found experimentally [89], others tried a more rigorous approach. Finite element analyses of the experimental loading conditions were performed on geometries representing the bones studied experimentally. Magnitudes of strain tensor components were compared to determine their correlation with regions where large amounts of growth or decay were observed experimentally. However, the conclusions drawn by comparing finite element results to experimental observations were often conflicting. For example, various models have correlated growth with either high circumferential strains [181], longitudinal strains [59] or shear strains [300]. While this tensor based model in Equation 4.4 allows the adaptation to be dependent on loading mode, not just magnitude, difficulties arise when the effect of the sign of the strain tensor components is considered. Again, conflicting conclusions have been drawn about this effect as well, with various studies either including or neglecting the sign of the component in the model [85, 301, 302]. Strain and stress tensor based methods may be very generalized and may be able to account for the effects of each type of directional load. However, in addition to the complexity of having to vary the effects of all the individual tensor components, the experimental based nature of obtaining the modeling parameters and the conflicting results amongst varying applications limits the global applicability of such tensor based models.

4.2.2.2 Scalar Stress/Strain Measures. The use of an averaged, scalar measure of the local stress state eliminates the need to determine the relative importance or effect of each strain mode (tensor component) on local bone shape adaptation, which was a major drawback of the tensor based model. One of the first mathematical models of bone

adaptation used differences between the values of a scalar measure of the actual stress on the bone's surface and an optimal stress value, which was a measure of the failure stress of the bone weighted by a factor of safety [303]. The use of such a failure-based measure is similar to many of the structural shape optimization models that were being developed contemporaneously. Because many of these shape optimization models were developed by those in engineering structural analysis fields, the influence of failure analysis methods led to the use of scalar measures of the local state of stress as model drivers. For example, many of the structural shape optimization models for predicting "optimal" designs of inert mechanical components being developed at the same time as bone adaptation models used stress values such as von Mises stress [94] or maximum principal stress [211] that were typically compared to maximum limits in failure theories. Other models chose a single tensor component deemed most influential for the loading conditions studied, such as maximum tangential stress when optimizing the curvature of a stress concentration [212]. These scalar-based models reduced the complexity of the growth equations tremendously to:

$$U_k(l) = \alpha(l)\left[\sigma_k(l) - \sigma_{ref}\right] \tag{4.5}$$

where $\sigma_k(l)$ can be any measure of the state of stress at a point l for the current iteration k. Although they follow the same form as the tensor based model, only a single set of parameters is needed, not one for each strain tensor component. The reference value, σ_{ref}, in these models, is usually considered to be the same for all locations in the system.

Likewise, while the scaling factor coefficient could vary by location, it typically is a constant $\alpha(l) = \alpha$ with both location on the surface $x(l)$ and optimization iteration k.

As in the selection of an appropriate failure theory to analyze the potential of an object to break under a particular loading condition, the selection of this scalar stress measure in these shape optimization methods is usually based on the particular loading conditions studied. This is often suitable for structural shape optimization where the component is designed to resist a particular extreme loading condition based on its function. However, this method of selecting the model driver measure might present difficulty in bone adaptation models because bones are subjected to a wide variety of loading conditions daily.

4.2.2.3 Strain Energy. A scalar measure of the mechanical state of a system that incorporates all the stress and strain tensor components is the strain energy. This is a measure of the energy that is stored within a body due to the work on the system from the applied force and the ensuing deformation. Originally, strain energy was used as a measure of the state of local stress (or model driver) in bone adaptation simulations modeling the change of the density of cancellous bone with loading [304]. Based on its successful use in that application, strain energy based adaptation drivers were later applied to bone shape change adaptation models [90]. The idea of energy transfer to the bone from the external loads as the driver for bone strength adaptation is based on the "hysteresis energy theories" of material fatigue and thermodynamic considerations of biological processes, where the mechanical energy applied to the bone can be used to induce the chemical reactions that result in the addition or removal of bone material.

The relevance of energy as an adaptation driver becomes more apparent when considering the function of "mechanoreceptor" cells, which are located in many biological tissues, including bones, and are affected by mechanical deformation. Cell membranes, the outer boundaries of individual cells, contain channels through which ions can pass [2]. The ions are used in local chemical processes to alter biological functions, from regulating fluid flow to activating a muscle fiber. Their release can be triggered by any number of stimuli. In mechanoreceptor cells, the ions are released or absorbed as a result of a mechanical stimulus. In these cells, deformation of the cell membrane causes the ion channels to open or close. It had been proposed that this deformation implies that the mechanoreceptor cell actually "measures" the amount of deformation (strain) as a stimulus for subsequent biological phenomena [84]. However, more recent theories suggest that the process is based on an energy transformation.

In these energy based theories, the work done to achieve the elastic deformation of the cell membrane results in a change in the free energy of the open or closed state of the ion channel [305]. There are fibers in the interior of the cell, which are connected to the ion channels, that rearrange upon the mechanical stimulus. This occurs in part for structural support and in part for storage of the strain energy from the applied mechanical load. It is the rearrangement of these fibers that causes the channels to open or close [306], altering the chemical state and physical configuration of the cell, and driving physiological processes.

The use of strain energy as a driver in computational bone shape adaptation models has two benefits. First, it is a scalar measure that incorporates all stress and strain tensor components. This allows all modes of the mechanical behavior to be taken into

account without concern about the orientation of the coordinate systems or the direction of the load. Second, while the complete system energy balance has not been fully considered in the discussion above, the information regarding the relationships between the cellular response to a mechanical stimulus and the transfer of mechanical energy to the chemical energy for biological processes provides a sound physical basis for the use of strain energy density as a driver for bone strength adaptation models. This is an improvement over a model based on arbitrary correlations to experimental observations. Many bone shape adaptation and structural shape optimization methods have used strain energy density as the driving measure [90, 93, 307-309]. Additionally, an object with a uniform strain energy density is often regarded as the most strong and stiff design possible [310].

4.2.2.4 Gradients. In addition to the measures of the state of stress, some studies have suggested that it is not the local values of these measures but their spatial gradients in various directions that drive the adaptive response in bones. Most of these studies have been based on comparing experimental observations to the results of numerical stress analyses of the initial and final geometries. Some investigators have found high circumferential strain gradients correlate best with regions of bone formation [100, 311, 312]. Others have proposed that strain gradients drive bone growth, while strain magnitudes drive decay [313]. Still others have stated that adaptation is controlled by strain energy density magnitudes but the results of the adaptation produce a more uniform strain energy density distribution, reducing the high strain energy density gradients [103]. Based on many of the shape optimization models, all with optimization goals of uniformity of stress or reductions in peak stress/strain concentrations, this explanation of

the strain energy density driving the adaptation towards more uniform strain energy distribution seems most feasible and consistent with experimental observations.

4.2.2.5 Comparisons of Adaptation Model Drivers.   Because of the wide range of measures of the mechanical state of an object and the equally wide range of proposed drivers of bone strength adaptation models (or functional stimuli for the strength adaptations of bone), numerous studies have been performed to determine which measures correlate most closely with experimental observations of bone growth or decay. In some of these studies, stress analyses were performed on models created from images bone shapes made at different times in experimental studies and trends in the distribution of the mechanical measures of the local stress state over the system predicted by the model were compared with trends in the experimentally observed alterations in bone geometry [96, 100, 311, 313, 314]. In other studies, experimental measurements from strain gages directly applied to bones were compared to macroscopic and microscopic changes in bone structure and shape [181, 300, 301]. In still other studies, models with different drivers were developed, and the resulting geometries were compared to experimentally observed changes in the bone structure [103, 104]. Strain and stress tensor components, von Mises stress and strains, principal stresses and strains, strain energy density, gradients of all of these quantities in Cartesian and cylindrical coordinates, and even rates of changes of these measures with time have been examined. Not surprisingly, the conclusions of these studies varied greatly. In general, however, they all indicated that models in which multiple components of stress, strain or both were incorporated in some form produced better correlation with observed trends in changes in bone shape with load.

In order to understand the effects of different model drivers on the predicted bone shape adaptations, a preliminary study was undertaken [315] to examine the abilities of these various adaptation models over a wide range of loading conditions. The results of models driven by strain tensor components (developed and coded in this preliminary study of the current work), and models driven by Mises stress [95] and strain energy density [93] reported in the literature were compared for a simple initially circular cylinder under basic and combined loading modes. Specifically, axial, torsional, and bending loads as well as combinations of axial and bending, of axial, bending, and torsion, and of bending, torsion, and surface forces, which roughly approximate the loading modes induced by the muscle forces, were examined. Because the strain tensor component driven model was developed and run in this work, a better understanding of its function was also achieved from this study.

Each model followed the same "biological-based" gradientless optimization model (Equation 4.3). The strain tensor model followed Equation 4.4 (written here in summation form, rather than tensor notation, for simplicity) :

$$x_{k+1}(l) = x_k(l) + \sum_{i=1}^{6} \alpha(i)\left(\varepsilon_k(l,i) - \varepsilon_{ref}(i)\right) \tag{4.6}$$

The reference strain $\varepsilon_{ref}(i)$ and coefficient $\alpha(i)$ for each of the $i=6$ strain tensor components (three Cartesian normal and three Cartesian shear strains in Voigt notation) could be different, but in the model used in this preliminary study these parameters were held constant over the optimizing surface and with iteration for each set of conditions studied. This is similar to the von Mises stress driven and strain energy density driven

models used for comparison that had a constant growth rate and reference value, which varied only for each loading case studied.

The initial geometry of each model compared in this preliminary study was a circular hollow cylinder. However, the published strain energy density driven model was two-dimensional, varying only the radial and angular dimensions, while the von Mises based and tensor component based models were three dimensional, allowing for variation in the axial direction. Each used linear elastic material models. The strain energy density driven model considered the cortical bone to be transversely isotropic, while the other models used fully isotropic material properties. Each model incorporated some form of nodal smoothing or mesh adaptation to prevent largely skewed elements as the element shapes were altered. All models also allowed for the independent change of both the inner (endosteal) and outer (periosteal) surfaces of the cylinder (bone), applying the same growth model to each surface. No specific convergence criteria were used; instead the models were stopped either arbitrarily or as the amount of growth per iteration decreased.

While the basic features of the resulting shapes of the bones were similar for the different models, the characteristics of the execution of these models differed significantly. Each model, the two from the literature [93, 95] and the one developed in this work, used arbitrarily selected loading and reference values, with no common correlation between these values, especially in the mixed mode loading case. Additionally, in each model examined, the reference value was different for each loading case studied. For the strain tensor based model, each tensor component had a different reference value, even for the same loading case. Because of these differences in the particular values of the applied loads and model parameters used, only qualitative

comparisons of resulting shapes were performed. Figure 4.1 shows the shape changes for each of the six loading modes considered as predicted by the strain tensor based model developed in this work.
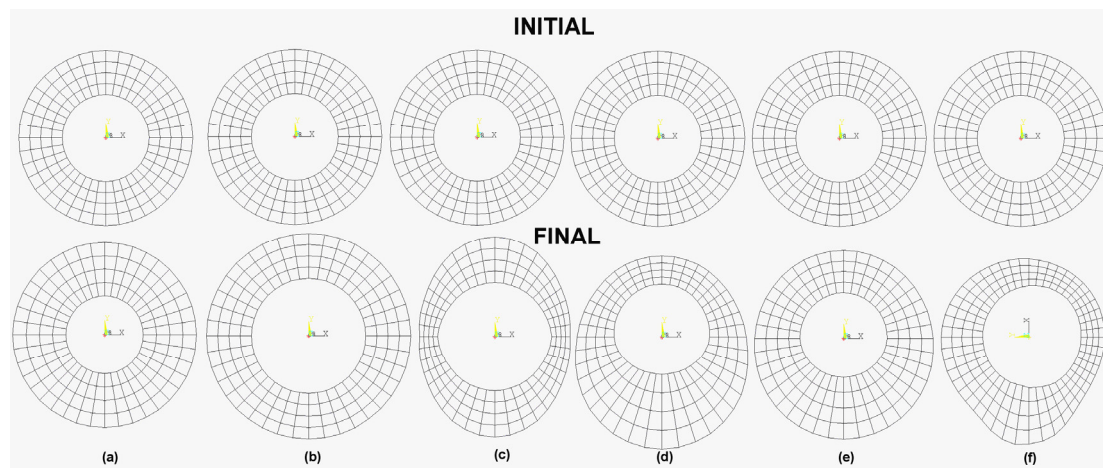
Figure 4.1 Changes in shape predicted by developed strain tensor based model for the basic and mixed load modes considered. (a) Axial compression (b) Torsion (c) Bending (d) Bending + axial compression (e) Bending + axial compression + torsion (f) Bending + torsion + surface force.

The descriptions of the behavior of the bone shapes under the various loading modes were very similar amongst the three model drivers compared. Because of the differences in the nodal measures and the threshold or reference stress values, the relative magnitude of the nodal measure with respect to that of the threshold determined whether growth or decay (apposition or resorption) would occur. However, the relative trends in shape change with the surface locations were consistent between the three models, regardless of the reference values and values of applied load chosen. Axial loading (Figure 4.1a) resulted in uniform and equal growth (or decay) on both inner and outer surfaces. Torsional loads (Figure 4.1b) caused uniform surface changes in the opposite direction on the inner and outer surfaces, with greater amounts of change on the outer

than on the inner surface. Bending (Figure 4.1c) brought growth to the inner and outer surfaces near the region of maximum stress and decay to both surfaces along the neutral bending axis. Combination loads produced asymmetric shapes. Adding a bending load to the uniform axial compression (Figure 4.1d) resulted in an egg-shaped geometry where the inner and outer surfaces were no longer concentric. This is similar to many of the images of the resulting shape changes to actual bones undergoing this type of mixed mode loading in experimental studies [58, 59]. Adding torsion to this combination (Figure 4.1e) rounded out the shape, producing less variation in wall thickness around the bone's circumference. Finally, the combination loading with surface forces (Figure 4.1f) produced an asymmetric geometry at a cross section through one of the force application areas similar to the shape of a femur bone cross-section [316, 317].

While the three distinct model drivers, strain tensor components, von Mises stress, and strain energy density produced very similar trends, the direction and amount of movement of the surfaces were directly dependent upon the relative differences in the magnitudes of the reference value and the value of the measure of the nodal stress state. Therefore, model predictions were directly controlled by the choice of reference value in relation to the magnitude of the applied load. In the author developed strain tensor model, the "sign" of these measures was also a factor. The effect of direction was removed with the use of two reference values of the same magnitude but of opposite signs for each strain tensor component, the proper reference value was used based upon corresponding nodal value.

The use of six strain tensor components allowed for the effect of each tensor component on growth to be revealed. However, because the model in Equation 4.6

summed the difference between nodal tensor component values and their respective reference values, one mode of loading could dominate over another simply by the choice of the reference value used. For example, if a reference value for a shear strain tensor component is chosen to be a non-zero number, but the particular loading mode on the bone being studied results in no shear strain at the node in question, then the difference between nodal and reference values might be relatively large, resulting in a significant amount "growth" predicted by the model due to this shear strain component even though no shear strain existed. This would seem to violate energy balance laws (First Law of Thermodynamics) as the model would predict growth without any mechanical energy input. The model could be altered to eliminate the terms that reference nonexistent tensor components loads. However, the implementation would be difficult as the model would have to be varied for each individual node. To avoid this, in applications of the strain tensor-based model, even by its original developers, only the dominate tensor component(s) have been used in Equation 4.6 [84].

In most bone adaptation models, the gradientless optimization parameters, the reference value, ε_{ref}, the scaling coefficient, α, and even the stopping criteria, are arbitrarily selected or based on experimental measurements. This might be sufficient for qualitative comparisons, for the identification of basic trends in strength changes for a given load, or to simulate an experimental study to gain further insight [84]. However, in order to be able to use computational techniques to compare various conditions that are not studied experimentally, as is desired in this work, a less empirically based model with no case-dependent alterations is required. These preliminary computational studies have demonstrated the interdependency of the parameters involved in biologically based

gradientless optimization methods, complicating their independent selection. Such an independent selection of parameters is necessary for a general application model, as is the objective of this work. Therefore, the more consistent definition of these modeling components was a significant focus of the current research. The determination of the modeling methods and parameters that allow for general non system-specific bone adaptation modeling is the subject of the following sections.

For the remainder of this work, the strain energy density was used as the model driver measure. This selection was made, in part, because of the appeal of using a single scalar, nonnegative value that accounts for the complete stress state rather than a series of values, each with their own sets of parameters and signs, as in the strain tensor based models. Additionally, because the strain energy density measure is based on the fundamental transfer of energy within the musculoskeletal system, from the mechanical energy imparted on bones from their environment, to the energy that is used in the biological processes that produce bone strength adaptations, the use of such a driver allows the function of the complete system to be considered. Similar conclusions about the benefits of the use of this strain energy density measure have been drawn in the literature [90].

4.2.3 Reference (Threshold) Value

While the goal of many optimization problems is the minimization or maximization of the value of some measure or function of a measure, the goal of gradientless "biological-based" or "feedback control-based" optimization methods is to minimize the difference between the value of a measure of the system performance and a particular reference value. Therefore, unlike more structured optimization methods, an additional

requirement for biologically based gradientless optimization methods is the selection of this particular reference value. In models of bone strength adaptation, like in feedback control systems, this reference value is often referred to as a "threshold". When the system measure is above threshold, the bone is strengthened through the addition of bone material. When the measure is below the threshold, the bone is weakened through the removal of the material. In theory, the process continues until the system measure becomes equal to the threshold value throughout the "design set".

The threshold values in many previously developed bone shape adaptation models have been based on experimental measurements, often using strain gages attached to the surfaces of animal bones. In these experimental observations, it was noted that the magnitude of the strain required to initiate the apposition (growth) of bone material on the cortical surface was not the same as the value at which the resorption (decay) of bone material from the surface started [59, 60, 298]. These kinds of observations have led researchers to believe that there was a range of strains (or, more generally, mechanical stimuli), corresponding to typical daily activities, under which no adaptation occurs [29, 299]. Developers of numerical models to simulate the bone strength adaptation then began to use two threshold values, one to trigger "decay" and one to trigger "growth" (Figure 4.2).
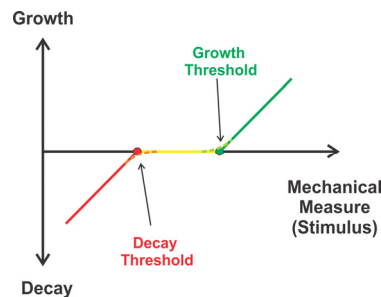
Figure 4.2 Typical shape adaptation model. Note: The curves for growth and decay need not be linear nor their slopes equal.

The range of values between these two thresholds has been referred to as the "lazy zone" or "equilibrium zone" [106] (yellow line in Figure 4.2). Some models have used continuous transitions to the lazy zone (orange and light-green dashed curved corners in Figure 4.2) to improve numerical stability [82, 309] or to improve the representation of the observed phenomena [51, 106, 299]. Without these threshold transition regions, the solution near the threshold may oscillate between growth and decay or growth and no growth, resulting in a zigzagged surface pattern as the nodes oscillate individually such as in Figure 4.3a. Figure 4.3b depicts the oscillation of the mechanical stimulus, here the strain, about the unitary threshold value, alternatively moving the node from a state of decay to a state of no change.
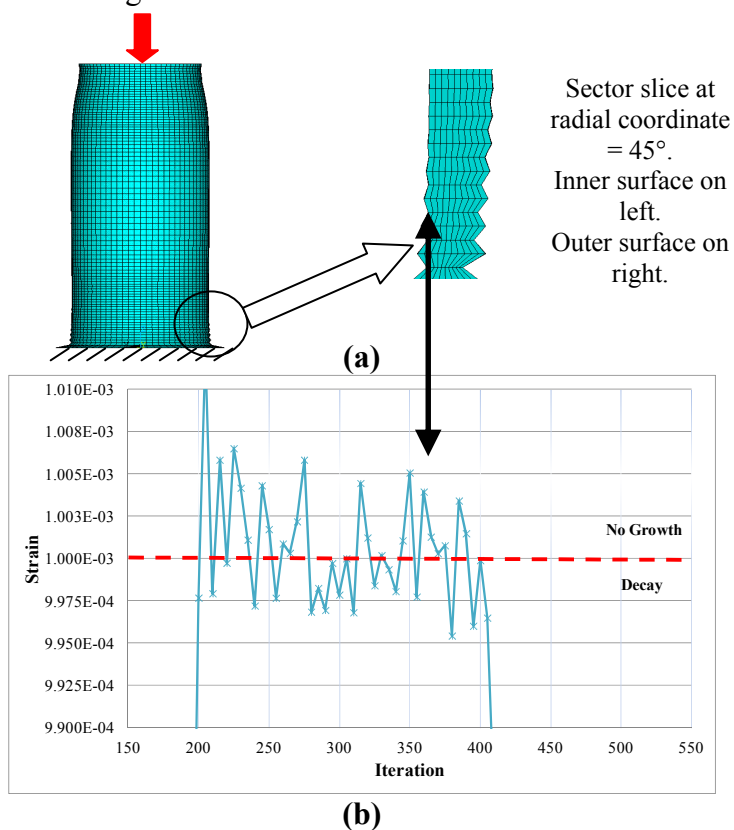
Figure 4.3 Effect of stimulus-growth curve. Preliminary model using a lazy zone and no transition region near thresholds. (a) Oscillations of nodal growth on both inner and outer surfaces of a hollow cylinder. (b) Oscillations of strain value at a node about the threshold value (red dashed line).

The particular values of the thresholds used in many numerical models are often obtained from experiments and, consequently, are in terms of strain, denoted by ε. The value of the "growth threshold" typically used in the literature is $3000\mu\varepsilon$, and that of the "decay threshold" is $1000\mu\varepsilon$ [17, 29, 59, 299]. This "growth threshold" value corresponds with peak strain under everyday activities measured in many different animal studies [17]. Because the experimental methods used to obtain these "threshold values" often involved strain rosettes, the reported magnitudes most closely correspond to maximum principal strains rather than specific strain tensor components [60, 318]. This makes the use of these multiple threshold values somewhat difficult in models that do not use the maximum principal strain as a driver measure. Though it is possible to calculate the strain energy density from strain rosette measurements, values for all principal stresses are required, not just the maximums that are often reported in the literature [307]. The use of experimentally based strain measurements for threshold values makes the model highly dependent upon experiments and on the particular loading modes for which test data exists. Many models have avoided this complication by setting the width of the "equilibrium" or "lazy" zone to a percentage of the threshold [82, 90, 93, 309, 319]. Under such assumptions, the reference value is usually either arbitrarily selected or based on the specific loading condition studied. In a sort of "compromise", it is also possible to set a trigger for growth or decay based on the principal strain values obtained experimentally but with an adaptation model driven by the nodal value of a more complete measure of the local state of stress, such as strain energy density.

Many studies have been undertaken to understand the effect of threshold value on model predictions [85, 86, 95, 104, 112, 319, 320]. Each study has emphasized the

significant effect of the value of the threshold relative to the value of the local mechanical measure at the location along the bone surface that is being altered, regardless of whether the same threshold value is used to trigger growth or decay or whether two separate threshold values are used. The relationship between the threshold value and that of the local stress state defines not only the amount of shape change, but also its direction (adding or removing material).

For example, Figure 4.4 shows data from two preliminary versions of the model using the strain tensor reference measure and either a point threshold value or a range of reference values (lazy zone) [315]. By tracing how the values of the strain tensor components at a particular node compare to the reference values selected by each threshold type model, the effect on the growth (decay is negative growth) per iteration of the use of either a point threshold or a lazy zone can be clearly understood. In this figure, the nodal strain tensor component values are identical for each type of reference model used (point (a) or range (b)). However, their relationships to the reference values (identified by the regions noted as "Grow" "Decay" or "No Change") are not. The different threshold types employed lead to differences in the amount of growth, as seen in the outer surface growth curves (solid lines) in Figure 4.4 for the two threshold models examined. As the mechanical conditions change, the value of one strain tensor component at the node may meet its threshold and move into the "lazy zone" of no growth, eliminating its further contribution to the overall nodal growth. With this component no longer affecting the nodal growth, another tensor component may begin to dominate the growth behavior, generating an abrupt change in the amount of nodal growth per iteration as seen in the inner growth curve (dashed line) between 60 and 80

iterations for the threshold range, lazy zone model in Figure 4.4. The large discontinuity in the growth trends at the inner surface for the range threshold model results from the shift from radial strain dominated growth and axial strain dominated growth.

Because of the high dependency of the predicted shape changes on the threshold value in all of these models, it has been suggested that altering the specific threshold value of the actual physiological bone system through pharmaceutical methods could beneficially alter the bone structure with no mechanical intervention [51]. However, this interdependency between threshold value and bone shape change has limited the practical application of these models for use in quantitative comparisons of relative amounts of shape strength change. Further, the employment of a "lazy zone" has been said to "thwart a unique solution" since its results in many "equilibrium" states [321]. A recent experimental study has even questioned the existence of the lazy zone completely. The study reports a linear relationship, with no discontinuities ("lazy zone"), in both cortical and cancellous bone adaptations in response to both small applied strain values usually associated with disuse weakening and to large applied strains associated with overuse strengthening (300$\mu\epsilon$ to 5000$\mu\epsilon$) [322]. This suggests that there may not be a standard or even any threshold value at all.
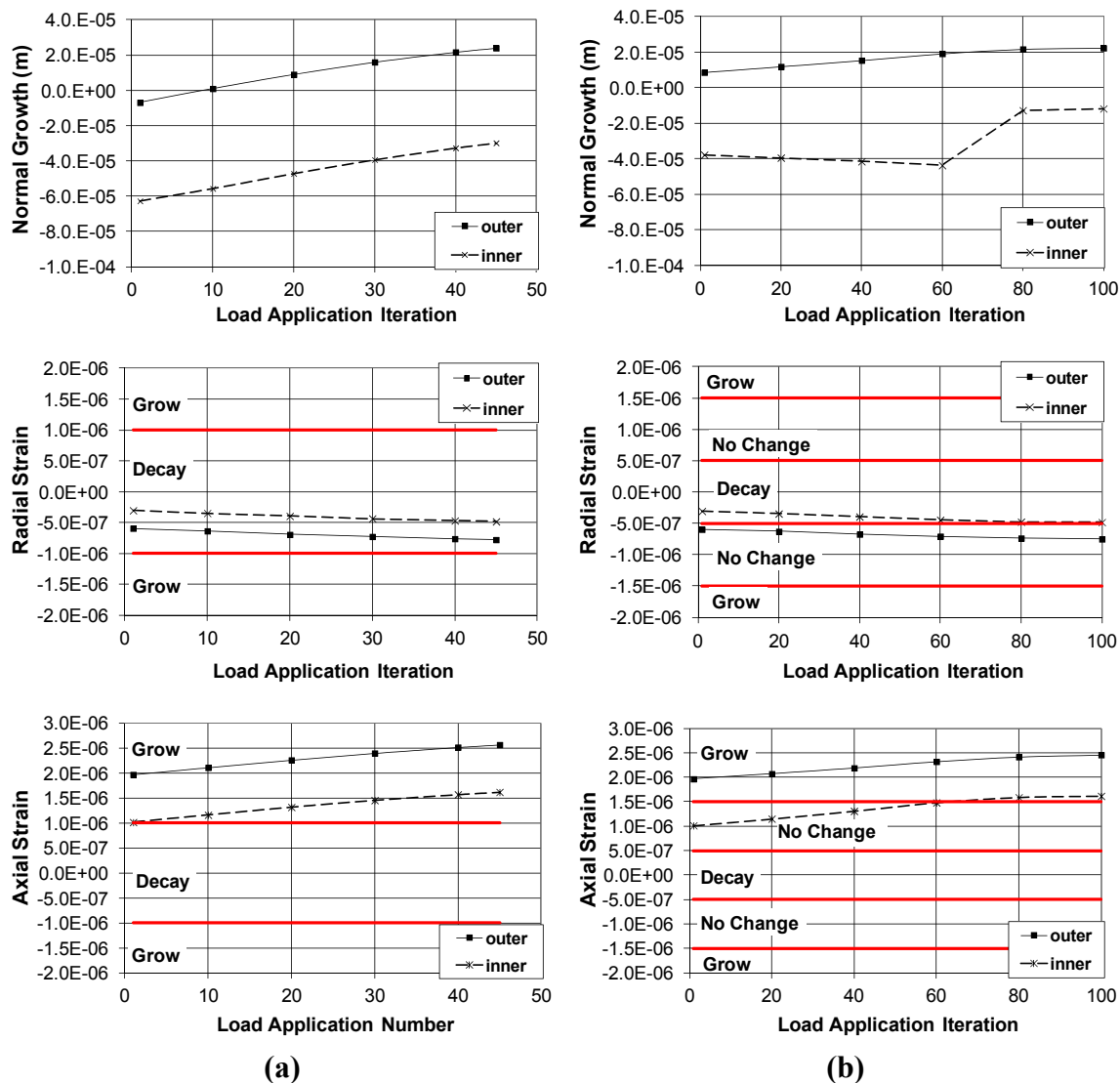
Figure 4.4 Effect of reference value: preliminary model using strain tensor based reference measure and either (a) a point reference value or (b) a range reference value. Note: To eliminate the effect of strain direction, growth behavior (and threshold values) were equal in magnitude for either positive or negative strains.

In line with this recent observation the changes in bone shape with amount of local strain induced in the bone, mechanical structural shape optimization models are not normally based on "universal" threshold values. Instead, the optimization "goal" (reference/threshold) is often specific to the loading conditions studied, such as a maximum allowable stress. The goal of these shape optimization studies is to drive the

design towards a stress measure level in the high stress region that is lower than the level under which failure is likely. In many of these structural shape optimization models, the growth driver portion of the optimization goal expression is normalized by the threshold value to reduce amount of growth predicted due to the amount of variation within the optimization design set [211, 212, 281] as in:

$$U_k(l) = \alpha \frac{\left[\sigma_k(l) - \sigma_{ref}\right]}{\sigma_{ref}} \tag{4.7a}$$

A few bone shape adaptation models have applied a condition-specific goal, rather than the more common physiologically based, threshold trigger value. For example, the effect of a disturbance to a bone system was investigated using the pre-disturbed conditions as the optimization goal so that each design variable had its own individual optimization goal, its pre-disturbance stress, and the shape of the bone was modified to attempt to eliminate the effect of the disturbance on the system's behavior [90], leading to the growth equation:

$$U_k(l) = \alpha \frac{\left[\sigma_k(l) - \sigma_{ref}(l)\right]}{\sigma_{ref}(l)} \tag{4.7b}$$

where $\sigma_{ref}(l)$ is the "undisturbed" reference value for node l.

Some structural shape optimization models also have not used a constant reference value. Instead, the reference value has changed with each optimization iteration based on the current mechanical state of the object studied. Alternatively, some models have used the stress at a point far from the region of high stress [323] or the

maximum or minimum stress on the surface to be optimized as the reference value [324]. Others have used more global measures of stress, such as averaged values over the boundary of the surface being optimized [213, 281, 325]. By using global reference values that are calculated based on the current stress state of the object rather than a predetermined value, a reduction in local stress variations is achieved that inherently considers the applied boundary conditions. This eliminates the potential to artificially push the system behavior toward an arbitrarily selected, irrelevant state. It also removes the need to modify the model based on the particular conditions studied.

While the reference value or threshold discussed in this section are generally tied to a physical quantity or measure in these gradientless optimization models, the scaling factor (coefficient), α, is more abstract. Although the parameter could be correlated with time, the scaling factor has often been used to control the stability of the "search" for the optimal state. The selection of this factor in both bone adaptation and shape optimization models is reviewed next, with a focus on the relevance to the needs of the comparative type model to be developed in this work.

4.2.4 Growth Rate (Step Size)

In creating a computational model that represents the effects of bone strength shape adaptation processes, challenges arise in balancing model behavior with computational stability. Because the "gradientless" optimization methods neither directly depict specific physiological phenomena nor result in mathematically rigorous solutions, much care must be taken to ensure the parameters used result in physically realistic predictions as well as unique and repeatable solutions. Upon initial examination of Equation 4.3, the scaling factor coefficient (growth rate or step size) α seems of little consequence.

However, the factor has a strong association with model features such as convergence, numerical stability, and mesh distortion, and plays a significant role in the overall model function and predicted shape. The methods for selecting the value for the scaling factor and the effects of these selections are now discussed.

Like the threshold measure, the "growth rate," α, in bone shape and strength adaptation models has traditionally been based on physical observations of changes in size and shape of a bone with time for a particular load. While a single value for the growth rate is normally used for all points on the adapting surface in many of these models, the constant can theoretically vary with location and even direction of growth [86, 87, 89]. For example, experimental observations have noted that the apposition (growth) of bone material is more prevalent on the periosteal (outer) surface of long bones while resorption (decay) is more often noted on the endosteal (inner) surface [17, 29]. In terms of a numerical model, this implies that the growth rate is not only different on the inner and the outer surfaces but also, on each surface, the rate of decay is different from the rate of growth. This can be visualized as different slopes for the red (decay) and green (growth) curves in Figure 4.2 and different shape adaption models plots entirely to describe the behavior of the inner and outer surfaces.

The rate of change of inner and outer diameters of hollow, long bones has been the subject of both controlled prospective studies, where current bone changes based on given loads were investigated, and retrospective studies, where dimensions of bones of different ages were measured and trends determined. Reported values from controlled experiments have ranged from a decay rate of 5.4 μm/day on the inner surface of the bones of immobilized dogs to a growth rate of 260 μm/day in forced distraction of

fractured bones in rats [216]. Measured diameters of human bone specimens from various aged subjects have been used to calculate growth rates that have ranged from 1 µm/year to 50 µm/year [317, 326-328]. Figures 4.5 and 4.6 summarize the data reported from two sources for the changes in a leg bone and finger bone respectively. These experimental measurements, however, cannot be used as the growth rate constant α in the models because these values represent the entire "growth" $x_{k+1} - x_k$ in Equation 4.3. Nonetheless, they provide an order of magnitude basis for this parameter.
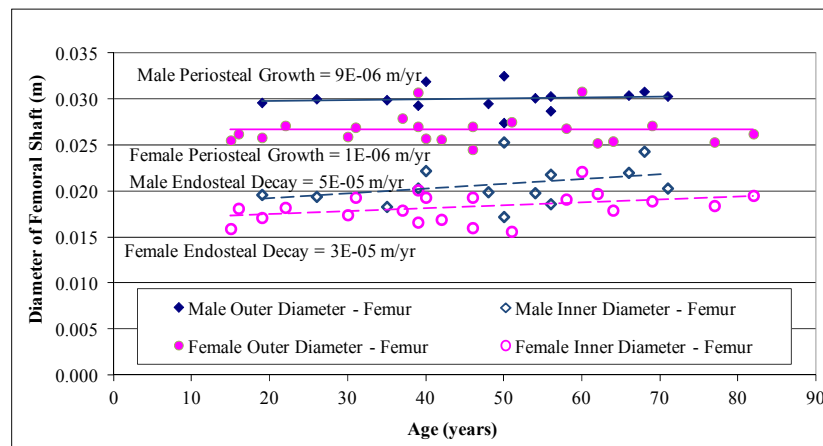
Figure 4.5 Changes in femoral shaft diameter with age. Data plotted based on values reported in [317].
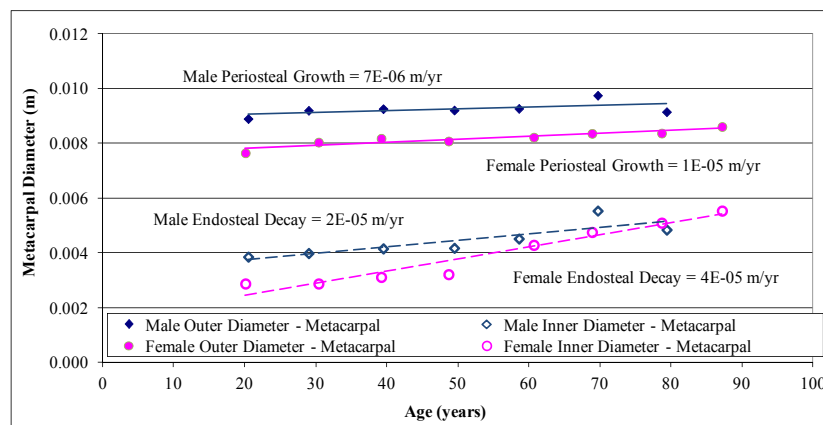
Figure 4.6 Changes in metacarpal diameter with age. Similar trends are seen as in the much larger femur bone where increases in inner diameter (decay) occurred at a greater rate than increases in outer diameter (growth). Note: Data plotted based on values reported in [22].

While it is clear that the coefficient, α, of Equation 4.3 is not truly an independent value, a parametric study was performed using one of the loading conditions discussed in Subsection 4.2.2.5 to understand the effects of changes in the "growth rate" coefficient (step size) and to potentially select values for the currently developed model. To ensure that the results were not dependent upon the loading mode chose, the mixed torsion, bending, muscle force load was applied to an initially circular cylinder (image (f) in Figure 4.1). Because the data in Figures 4.5 and 4.6 suggest there may be different rates for growth and decay on the inner and outer surfaces, ten combinations of periosteal (outer) growth rate (OGRTE) and decay rate (ODRTE) and endosteal (inner) growth (IGRTE) and decay rate (IDRTE) listed in Table 4.1 were investigated. A strain energy density driven model was used, with the reference value taken as the current surface average strain energy density. A normalized difference from nodal to reference value was incorporated as in Equation 4.8 so that the nodal growth model was written as:

$$U_k(l) = \alpha^* \frac{\left[SED_k(l) - SED_k^{SurfAvg} \right]}{SED_k^{SurfAvg}}$$

(4.8)

where α^* is either OGRTE, ODRTE, IGRTE or IDRTE depending on the surface on which the node is located and the sign of $\left[SED_k(l) - SED_k^{SurfAvg} \right]$.

Table 4.1 Parameters Used for Study of Effect of Growth Rate

	OGRTE	ODRTE	IGRTE	IDRTE
Rate Set 1	1.00E-04	1.00E-07	1.00E-07	1.00E-05
Rate Set 2	1.00E-04	1.00E-05	1.00E-06	1.00E-04
Rate Set 3	1.00E-05	1.00E-05	1.00E-05	1.00E-05
Rate Set 4	1.00E-05	1.00E-07	1.00E-07	1.00E-04
Rate Set 5	1.00E-05	1.00E-07	1.00E-07	1.00E-05
Rate Set 6	1.00E-05	1.00E-07	1.00E-07	5.00E-05
Rate Set 7	1.00E-05	1.00E-07	1.00E-07	2.50E-05
Rate Set 8	1.00E-05	1.00E-06	1.00E-06	2.50E-05
Rate set 9	1.00E-05	1.00E-07	1.00E-07	1.50E-05
Rate set 10	1.00E-05	1.00E-07	1.00E-07	2.00E-05

The final geometry for each of these ten sets of growth rates (scaling factors or step sizes) is shown in Figure 4.7. While each showed the same basic trends that resulted from the use of the strain tensor based model and arbitrary growth rate and threshold value as presented in Figure 4.1, significant differences were noted in the local amounts of growth. The variations in the shapes shown in Figure 4.7 indicate that the "growth rate factor" coefficient does not simply scale the shape changes because each node moves independently based on its local state of stress. Hence, the selection of this value will likely affect any quantitative comparisons between different loading conditions.
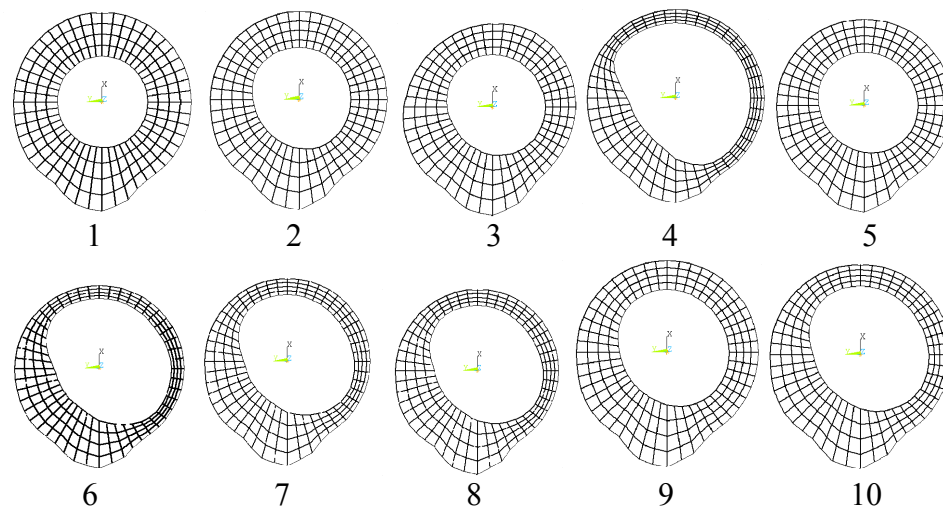
Figure 4.7 Variations in shape changes resulting from the use of different growth rate factors.

Because the experimental data of bone dimensions did not offer a repeatable and consistent rate of growth with time or for different load application, and because preliminary studies using the growth rate factor showed that its selection can alter the shape predictions, computational mechanical shape optimization methods were consulted to investigate their non-biological use of the "scaling factor" coefficient α in an attempt to find methods to be used for quantitative comparisons of the strengthening ability of

various loading modes. In the study of optimizing inert mechanical component design, the coefficient α from Equation 4.3 does not have a physical meaning. It is simply an arbitrarily selected "scaling factor" used to control model stability and convergence. Because the "gradientless" biologically based optimization methods are not mathematically rigorous and, therefore, do not result in a unique solution, the effect of this scaling factor, or step size, is important and has been the subject of much study.

The scaling factor, α, in shape optimization models, as in Equation 4.3, is a parameter that is used to improve convergence, reduce instability, decrease the amount of mesh distortion, and control the progression of the solution [212, 289, 323, 324, 329]. If this value is too large, the solution may diverge [289] or cause extreme mesh distortion [212]. In some models this factor has been selected through a series of iterative preliminary studies [324, 329]. In others, it was a function of the mesh [209, 212, 330]. In determining this mesh-dependent factor, α, has been required to limit the step size (change in node/point position) for each node, or design point, to a specified fraction of the current element size, such as 5% or 10% [212, 330]. Some models have decreased this scaling factor with each iteration to force "convergence" [212]. Other models have suggested that choosing α to maintain a constant step size throughout the optimization [289]. Still others have proposed decreasing this scaling factor (step size) if the difference between the nodal and reference values increases (diverges) and increasing the scaling factor if the difference decreases (converges) [323]. The inclusion of limits for minimum or maximum changes in element size per iteration have also been recommended [331].

Based on these previous model designs, a preliminary study was undertaken to modify the currently developed model in Equation 4.8 to incorporate a variable growth rate scaling factor (step size) and add growth per iteration limits in an attempt to reduce the model dependency on the arbitrary selection of this parameter. One structural shape optimization technique included a method to alter this scaling coefficient/step size to control the progression of the optimization using a three term factor where R is a characteristic dimension of the shape being optimized and S and β are defined as shown in Eq. 4.9 [323]:

$$
\begin{aligned}
\alpha &= RS\beta \\
&0 < S < 1 \text{ is an arbitrary constant} \\
\beta &= 0.5 \text{ if diverging } (SED_k(l) - SED_{SurfAvg}) > (SED_{k-1}(l) - SED_{SurfAvg}) \\
\beta &= 1.1 \text{ if converging } (SED_k(l) - SED_{SurfAvg}) \leq (SED_{k-1}(l) - SED_{SurfAvg})
\end{aligned}
\tag{4.9}
$$

l is the location (node) being optimized.

The initial radius of the surface being optimized, either the inner radius or outer radius of the initially circular cylinder, was selected as the characteristic dimension R used in this preliminary model that automatically alters this growth rate (step size), α, based on model conditions. Following the suggestions from the literature, the value of S used in this model was 0.2 [323]. Using the recommendations from the structural shape optimization models reviewed, the growth at each node per iteration was limited by a maximum change of 5% of the element's characteristic size in the direction of growth.

Despite the automated selection of this model parameter, the use of this modified model resulted in similar issues as were faced when using any arbitrarily chosen constant α (Figure 4.7). By plotting the change in the variable α, which is calculated

automatically by this new model, with iteration (Figure 4.8a) and comparing it to the average growth with iteration over the surfaces being optimized (Figure 4.8b), it is clear that the growth is directly affected by the value of this scaling factor (step size) α. Additionally, it was discovered that the criteria used to alter the scaling factor with iteration caused the factor to follow the local oscillations in the nodal strain energy density with iteration (Figure 4.9).

(a)   (b)
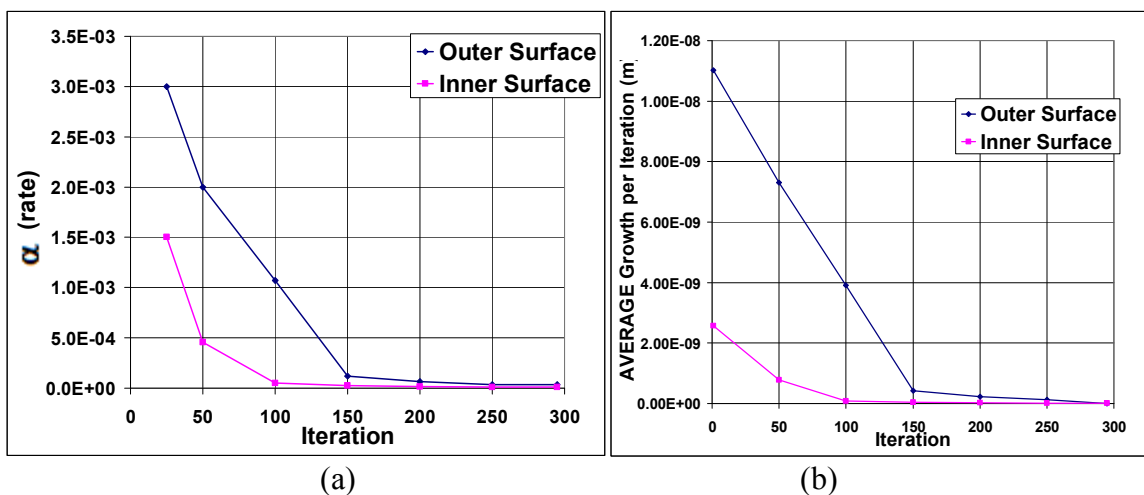
Figure 4.8 Trends in growth per iteration follow those of scaling factor (growth rate) that change with iteration (a) growth rate factor (b) nodal growth averaged over the optimized surface.
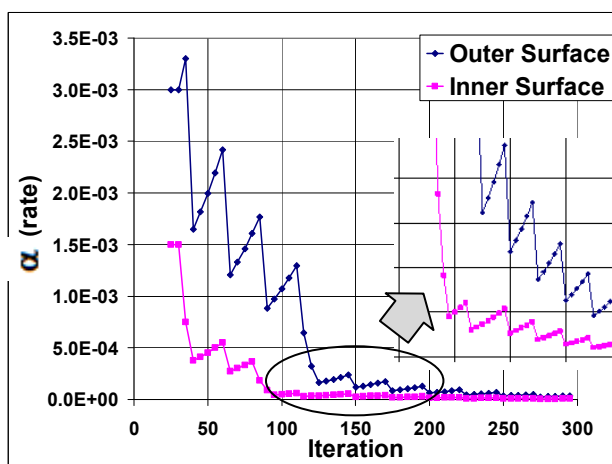
Figure 4.9 Oscillations in a formulation of the scaling factor that changes with iteration.

These preliminary studies showed that the currently available means for determining the growth rate coefficient (step size), α, in the shape optimization and bone adaptation models reviewed are inappropriate for use in a more general purpose model, such as the one developed, in this research because they do not allow the model to function independent of α and do not provide a consistent means for defining its value. This dependency is one of the main reasons the gradientless optimization method used does not ensure a unique optimum. As stated previously, this gradientless optimization method does not result in the "strongest" design. Instead, it simply "enhances the strength" of the design [324]. Therefore, the determination of the amount of strength enhancement that is sufficient to reduce concern of failure of the object under anticipated loading conditions is another modeling component required in a universally applicable modeling tool that uses biologically-based gradientless optimization methods. The "sufficient" modifier on the reduction in the likelihood of failure is quantified through the selection of convergence criteria and is the subject of the next section of this chapter.

4.2.5 Convergence Criteria and Convergence Measure

As with the other components of the gradientless optimization method used in this work, the criteria selected to indicate that the strength of the component has been "sufficiently enhanced" due to the alterations in shape have varied greatly amongst bone strength adaptation and mechanical shape optimization models. Many of the bone shape adaptation models have described the growth rate factor as an actual measure of change with time, thereby using time as a measure of model progress. However, as was demonstrated thus far, the optimized shape is directly influenced by the value of the

growth rate coefficient (step size) α in the majority of these models. In addition, the effect of this parameter is interrelated with the effect of the reference threshold value σ_{ref}. Therefore, to use the developed modeling methods to directly compare the effects of varied boundary conditions and configurations, a strong and repeatable convergence (stopping) criterion that is not influenced by the other modeling components is required.

In structural shape optimization methods, where the goal is to reduce the maximum stress over a design field (surface or curve) to a level such that the structure is less likely to fail, the strength depends mainly on one specific geometric feature, such as the curvature of a fillet or the shape of a hole. In such conditions, there are a small number of design variables, usually at node where boundary conditions are not applied, and one mode of loading. Many of these models define convergence simply based on a measure of the approach to the threshold value at each design variable (node). Usually, the minimum and maximum values of the mechanical measure for the set of design variables are identified. Convergence is, therefore, declared in these methods when these values become acceptably close to the reference threshold value [209, 211]. Alternatively, convergence can be declared when the difference between the minimum and the maximum values of the measure of the state of stress at each of the design variables is less than a prescribed value, indicating a decrease in overall variation [323].

In problems with a large number of design variables, such as those nodes that define an entire surface rather than a small design region or curve, applied boundary conditions at the design variables may prevent the singular absolute maximum or minimum nodal value from successfully approaching the threshold value. In such cases more global measures of the reduction in the variation of the mechanical measures of the

local stress state at the design variables are implemented. For example, the standard deviation of the differences between the local mechanical measures over the design field and the reference value has been used as a measure of convergence [281]. Other models have used a ratio between the local stress value and a stress value far from the design field as a normalized measure of the stress at the surface that is undergoing the optimization process [289]. Each of these techniques is a method to quantify the variation of the mechanical state of stress within the set of design variables (nodes).

Alternatively, some structural shape optimization methods have not used solely a measure of the variation of the stresses in the design field at the current state (or shape) as a measure of convergence. Instead, the methods have compared values of the variation in the stress field over an optimizing surface from one iteration to the next [289] or from the initial to the current configuration [209]. This eliminates the need to set a particular value of acceptable variance, which may depend on the conditions in the system studied, and, instead, considers only the relative changes as a result of the alterations to the shape of the body being optimized.

Because the objects that are being optimized are often only one component of a larger system, the range of possible locations of the design variables that comprise the optimizing region is not infinite. Instead, the potential changes to the object's shape are limited by physical constraints. These size limits are imposed as additional criteria by which to stop the optimization solution. Therefore, the final shape may not achieve the necessary reduction in the failure potential of the object but would, instead, reach a dimensional limit of its functional range.

The three-dimensional bone geometries being optimized in this work, while relatively simple in initial shape, have a large number of design variables, on the order of thousands of nodes. Boundary conditions are directly applied on some of these nodes. The large number of design variables prohibits the use of many of the convergence methods discussed above. The direct application of loads and constraints to nodes that are included in the design space presents a difficulty when determining measures of the design goal, a reduction in the variation of the local mechanical state over the surface being optimized. Where boundary conditions are applied, any measure of the mechanical state of the design variables (nodes) at that location may never be significantly altered. Because of the large number of design variables and the application of loading/boundary conditions on the optimizing surface inherent to a three-dimensional bone shape adaptation model, the reviewed methods for determining convergence criteria cannot be used. Because clearly defined and consistently applied stopping criteria are important in comparative use of a shape adaptation model, a number of preliminary studies were developed and carried out to examine means of defining convergence criteria that are independent of the applied boundary conditions or system studied.

With this goal of facilitating independent modeling methods in mind, a number of convergence criteria were investigated. In these preliminary studies, the growth driver in Equation 4.8 was used, repeated here for convenience.

$$U_k(l) = \alpha \frac{\left[SED_k(l) - SED_k^{SurfAvg} \right]}{SED_k^{SurfAvg}}$$

$$(4.8)$$
redisplayed

Based on this growth equation, three main convergence measures were investigated: the local measure of the mechanical state, $SED_k(l)$, the local mechanical measure normalized by the reference value $\dfrac{SED_k(l)}{SED_k^{SurfAvg}}$, and the growth driver term (excluding the direction of growth), $\left| \dfrac{\left[SED_k(l) - SED_k^{SurfAvg} \right]}{SED_k^{SurfAvg}} \right|$, which is a measure of how different the local measure at a particular node is from the average at all locations. Trends in minimum, maximum, average, median, and standard deviation of each of these measures were examined as were the changes in these measures with iteration. A direct difference between the measure quantities at given iterations, $Measure_k(l) - Measure_{k-5}(l)$, and a relative difference in the measure quantities between iterations, $\dfrac{Measure_k(l) - Measure_{k-5}(l)}{Measure_{k-5}(l)}$, were both investigated. In addition, averages and standard deviations of these differences over a number of iterations were also computed and compared. Despite the many measures considered in these preliminary studies, all failed to produce a strong, repeatable correlation with observed reductions in the variation of the stress state over the surface being optimized. Additionally, trends with the measures considered were found to be dependent upon other model components, especially the growth rate factor (step size) α. However, these preliminary studies provided insight into the behavior of the distribution of the local mechanical stress state of an object during the alterations in its shape with the intention to reduce the variation in this distribution. These results of these studies will be briefly summarized.

In these preliminary studies, to investigate the influence of the convergence criteria, a three-dimensional initially circular hollow cylinder was examined. Both the inner and outer surface profiles were automatically altered based on local values of the strain energy density as in Equation 4.9. The bottom surface was fixed in all degrees of freedom, and a uniform compressive force was applied normal to the top surface. In this loading configuration, the strain energy density on the cylindrical side surfaces that were being optimized was fairly uniform except near the regions of applied load and constraint. As the shape changed with the optimization, the values of both the minimum and maximum nodal strain energy density decreased, but the average nodal value of the strain energy density over the optimizing surface actually increased. Figure 4.10 shows the distribution of the nodal strain energy density values. While the spread in the strain energy density values at the nodes decreased with iteration, the number of nodes at the extremes of the range of energy density values remained fairly constant. Therefore, a simple measure of the nodal stress state may not provide sufficient information about the uniformity of the set of design variables necessary to determine model convergence.
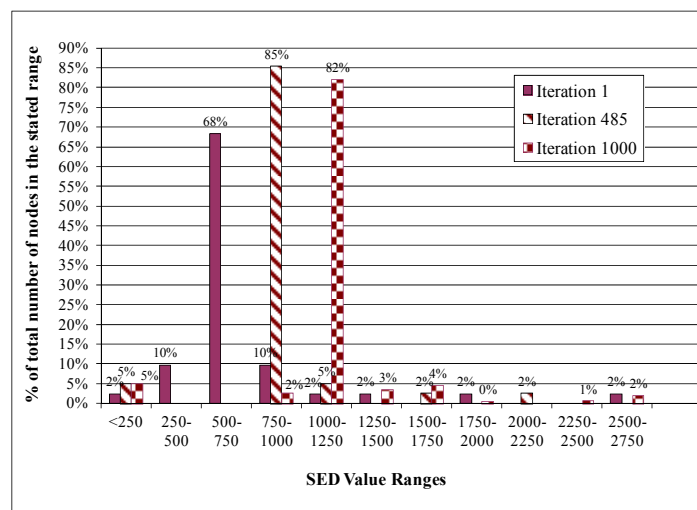
Figure 4.10 Distribution of nodal SED values for representative case with shape adaptation iteration.

The use of a convergence measure that includes a more global representation of the mechanical state of the shape being optimized, such as the local strain energy density normalized by the surface averaged value of this measure, provided a better indication of the increased uniformity in the strain energy density with optimization iteration in the case studied. However, the effects of locally extreme values still played a significant role in the trend and value of the convergence measure with iteration. For example, the maximum difference, $\max\left(\dfrac{SED_k(l)}{SED_k^{SurfAvg}} - \dfrac{SED_{k-1}(l)}{SED_{k-1}^{SurfAvg}}\right)$, showed discontinuities with iteration. These discontinuities corresponded to the shifts in the location of the node at which the convergence measure was at its maximum value each iteration (Figure 4.11).
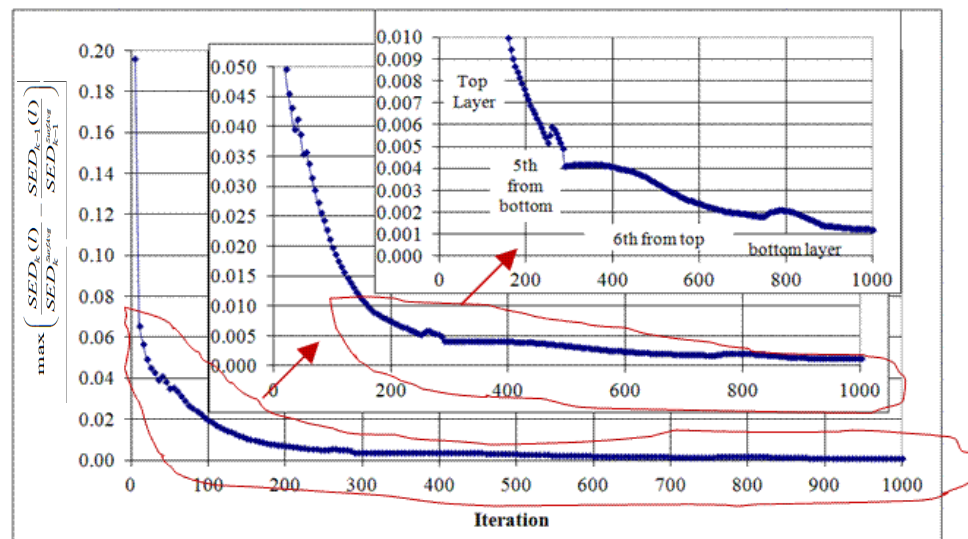
Figure 4.11 Potential convergence measure of maximum change in ratio of nodal to surface average strain energy density between iterations. Discontinuities resulting from changes in location of maximum value of convergence measure make it unacceptable.

When using the absolute value of the full ratio used in the growth driver equation

(Equation 4.9), $\left| \left[\dfrac{SED_k(l) - SED_k^{SurfAvg}}{SED_k^{SurfAvg}} \right] \right|$, a better behaved trend in the decrease of the

convergence measure with iteration was found. Additionally, when the surface averaged value of this measure was used, rather than the absolute extrema of the nodal values for the basis, a smoother curve resulted (Figure 4.12a). With a constant growth rate factor, this curve shows that, on average, the amount of growth per iteration was getting smaller because the nodal values were approaching the surface average value.

To find when the change in the convergence measure from one iteration to the next was sufficiently small to stop the optimization computation, differences in this surfaced average measure between iterations were plotted (Figure 4.12b). As noted in the figure, false convergence may be triggered depending on the convergence threshold selected. A smoother (more averaged) variation with iteration was obtained using standard deviation over a number of iterations instead of just the difference between sequential iterations (Figure 4.12c). The use of the standard deviation was suggested in the literature for optimization with a large number of design variables [281]. While the results showed a convergence measure that did generally decrease with increased number of iterations, the measure did not have a single minimum, making it unclear as to where the proper stopping point should be defined. Additionally, depending on the relative values of the nodal mechanical measure and the reference threshold in the optimization function (Equation 4.8), an absolute convergence threshold value selected for one system/parameter set may not achieve the same convergence for another.
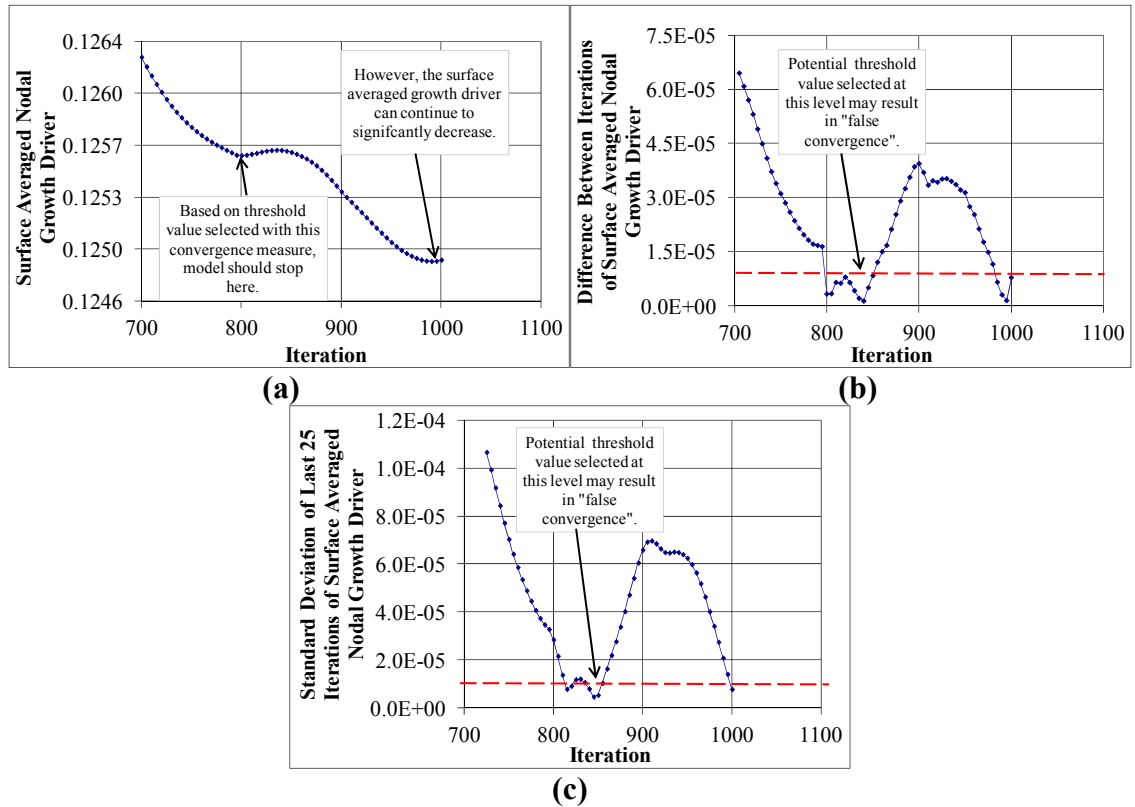
Figure 4.12 Issues developed with the use of the change in the average of the nodal growth drivers over the optimizing surface. (a) Average of nodal growth drivers over the surface being optimized (b) Difference between iterations of the average of nodal growth drivers over the surface being optimized (c) Standard deviation over twenty-five iterations of average of nodal growth drivers over the surface being optimized.

When applying the convergence measure shown in Figure 4.12 to the model where the growth rate factor changed based on the value of the convergence measure, as in Equation 4.9, the interdependency of the two modeling components was exposed (Figure 4.13). What initially seemed to be model convergence may simply be an effect of the change in the growth rate coefficient (step size), α, since based on the model used, as the convergence measure decreases the α value is lowered, reducing the growth per iteration.
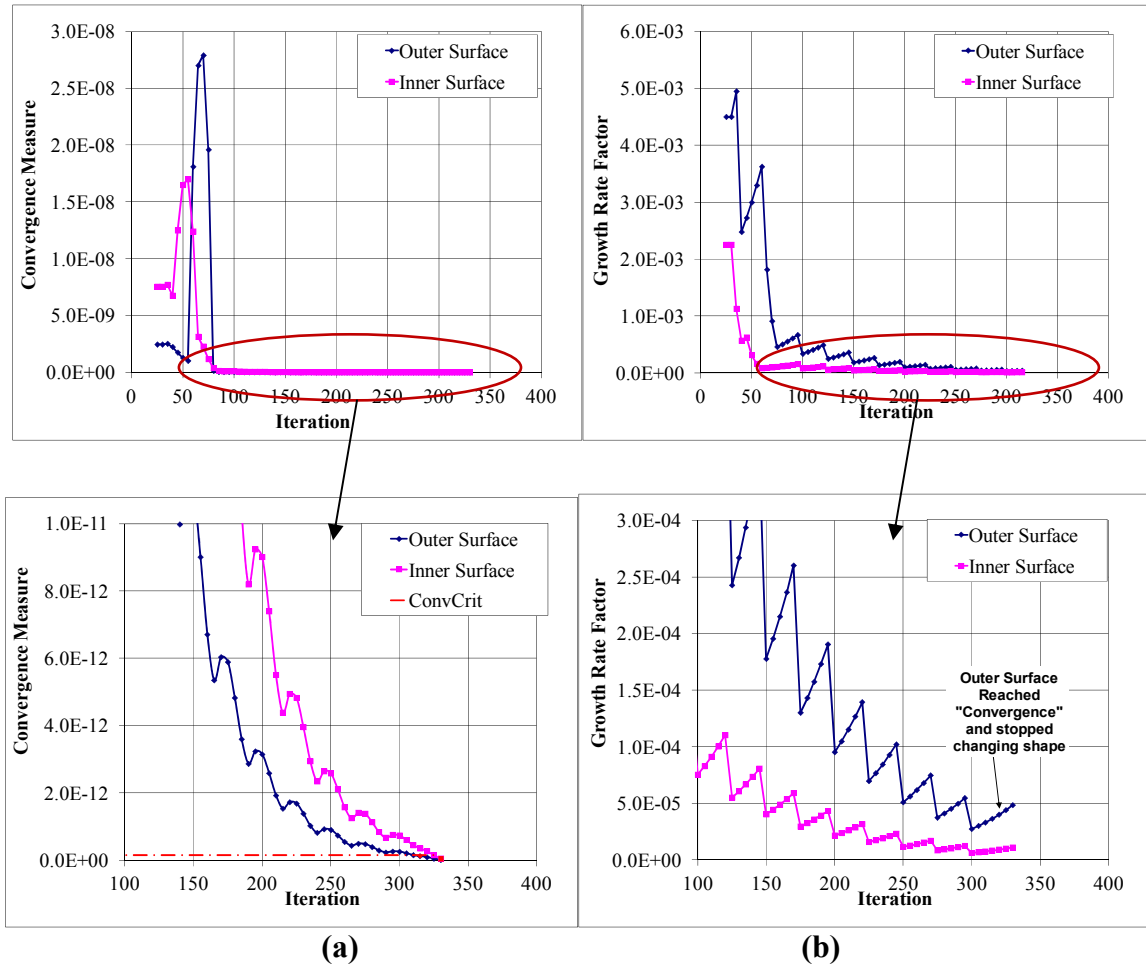
Figure 4.13 The trend in convergence measure as ratio of difference in nodal and surface average strain energy density to surface average strain energy density (a) in a model where the growth rate coefficient α changes with iteration (b). Varying the way the growth rate changed based on the convergence measure did not significantly alter these trends.

These preliminary studies using convergence measures common to shape optimization models demonstrate the need for the development of a new convergence measure for use in the universally applied model developed in this work. Such a convergence measure must not only be independent of the influence of other model parameters, such as the growth rate, but also must consider the possible effects of the extreme nodal values. Finally, the convergence measure must focus on quantifying changes in the level of uniformity of the mechanical state on the optimized surface rather

than a reduction of either extreme or average values. The development of the convergence measure ultimately used in this work as further discussed in Section 4.3.

The ability of the convergence measure to appropriately capture the conditions at which the uniformity produced by the object's response to the applied boundary conditions has sufficiently improved to increase the object's strength is dependent upon the accuracy of the calculated nodal values of the mechanical measure of the local stress state. The accuracy of the solution of the structural analysis when using finite element methods is directly dependent upon the quality of the discretization, or the mesh. Therefore, the maintenance of the quality and integrity of the mesh during the shape optimization process is necessary. Methods to achieve this are discussed as the final required modeling component in the development of computational methods to predict the adaptations of the shape and strength of bone.

4.2.6 Mesh Adjustment Methods

Because shape optimization methods alter the overall geometry of an object, the discretization of this geometry, required for the numerical structural analysis, is affected by the iterative changes to the boundary surfaces as the mesh is stretched, compressed, and distorted. The need to adjust the mesh during the iterative geometric has been a noted requirement for bone shape adaptation and mechanical shape optimization routines regardless of the optimization solution method chosen or system parameters defined [93, 94, 204, 205, 207, 212, 213, 261, 271, 272, 276, 281, 330, 332-334]. As with all the other model components reviewed thus far, a wide range of methods have been suggested to adjust the mesh during the shape optimization process in order to maintain its integrity

despite the geometric changes. These methods are first reviewed before their application to the model developed in this work is discussed.

Two main types of mesh adjustment methods are used in shape optimization routines: nodal smoothing and relocation, known as mesh adaptation, and mesh refinement and coarsening, known as remeshing. In mesh adaptation the same number of elements and nodes are kept, but the locations of the nodes that define the size and shape of the elements are adjusted to eliminate large distortions. In mesh refinement new elements are formed and old elements are removed either by combining or dividing current elements or by completely removing all nodes and elements and creating a new mesh without the limitations imposed by the current mesh structure. As described in Section 4.4, the shape adaptation modeling methods developed in this work require the continuous identification of a constant number of surface nodes. Therefore, in incorporating mesh adjustment methods to the current model, only the mesh adaptation, node smoothing methods were considered. In the current model, these methods were used to adjust the nodes on the optimized surfaces as well as the nodes in the internal volume of the modeled bone geometry.

Two methods of mesh adaptation, where nodes are relocated but not eliminated or added, were used in this work. In the first method, often referred to as Laplacian smoothing, the coordinates of all nodes are changed based on some weighted local measurement, for example, a weighted average of a characteristic of all the elements attached to a given node [335]. This weighting factor can be related to the shape of the elements, such as skewness, or the nodal solution such as stress, strain, displacement, strain energy or gradients of these measures [336]. In the second method, referred to as

spring smoothing, the edges of the elements that connect nodes are idealized as a network of springs. As the element boundaries are "displaced" due to the shape changes, the "springs" are stretched or compressed, imparting "forces" within the spring system proportional to the amount of "displacement" (change) of the boundary surface. The nodes are moved to restore an equilibrium of the "spring forces" connecting them [337].

4.2.6.1 Interior Node Smoothing. Although the outer surface nodes are the focus of the shape optimization processes, the importance of modifying the locations of the interior nodes is directly related to the consistent accuracy of the finite element analysis required for the proper prediction of the shape alterations [204, 209, 273]. Without moving these interior nodes, the elements near the optimizing surface become extremely distorted, as the nodes on the surface move, but the interior nodes of those surface elements remain fixed as in Figure 4.14. Interior node smoothing methods typically move the internal nodes in proportion to the changes in the locations of the external nodes. The simplest requirement is to maintain the original even spacing between the interior nodes as the boundary surfaces are altered. Such a requirement was used in this work. Spring smoothing mesh adaptation methods were followed to fulfill this requirement [337].
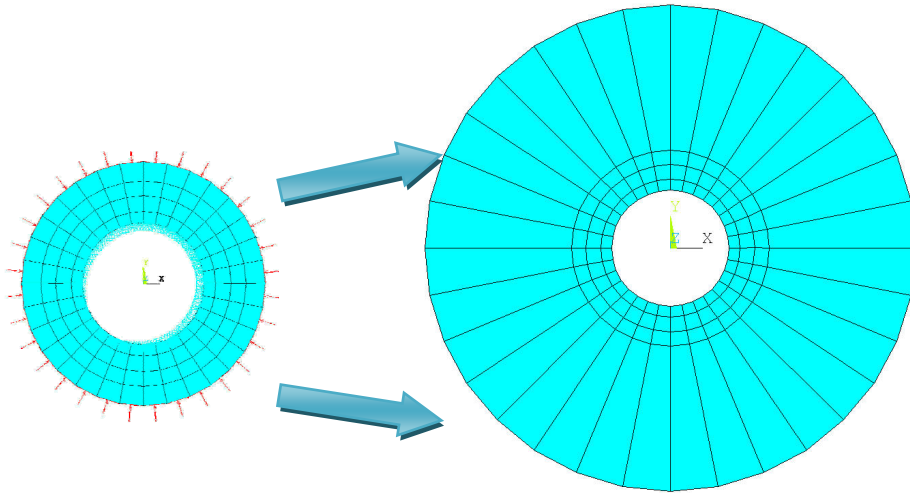
Figure 4.14 Extreme element distortion without interior node smoothing.

In the spring smoothing method, the system of connected nodes in the meshed geometry is represented as a system of connected linear springs. At the initial nodal positions, before any surface shape adaptation occurs, the spring system is in equilibrium. As the adaptation simulation moves the surface nodes, dimensionless "spring forces", proportional to the displacement along the imaginary springs connected to each of the surface nodes, are generated following a dimensionless form of Hooke's law. The forces are propagated through the connected nodes as:

$$\mathbf{F}_i = \sum_j^{n_i} k_{ij} \left(\Delta \mathbf{x}_j - \Delta \mathbf{x}_i \right) \tag{4.10a}$$

where j represents the index of the neighboring node, i is the node with the force $\mathbf{F}_i$ and n_i is the number of neighboring nodes connected to node i. The effective spring constant k_{ij} of the spring connecting node i to node j is defined as:

$$k_{ij} = \frac{1}{\sqrt{\left(\mathbf{x}_i - \mathbf{x}_j\right) \bullet \left(\mathbf{x}_i - \mathbf{x}_j\right)}} \tag{4.10b}$$

Thus, the movement of the internal nodes as a result of the smoothing is inversely proportional to the pre-smoothed distance between neighboring nodes i and j before the surface nodes are moved by the shape adaptation model in the given solution iteration.

With the amount of displacement of the outer nodes known from the shape adaptation model, the displacements of the interior nodes required to create uniform element sizes in the system are calculated through a system of equations patterned after force equilibrium equations for a system of connected linear springs. For a geometry such as the hollow cylinder used in this work, the interior nodes are moved in proportion to the shape adaptation model predicted changes in the positions of the inner and outer surface nodes of the hollow cylinder representing the bone volume, denoted as $\Delta\mathbf{x}_1$ and $\Delta\mathbf{x}_N$, respectively. The amount of change to the locations of the interior node, therefore, propagates from these known displacements on the boundaries to maintain the uniform mesh.

In the model used in this work, the use of hexahedral elements in the adapting bone region and the limitation no axial growth, the direction of shape adaptation is limited only to changes normal to the adapting surface. Thus, only interior nodes were only required to be adjusted along radial lines. The application of the spring smoothing method to the model in this work, therefore, reduces the general model to a one-dimensional set of springs where each interior node is only connected to two "springs", and each surface node is connected only to one "spring". This reduces the coefficient matrix in the system of force equilibrium equations in Equation 4.10a to a simple band

matrix. Preliminary studies using a customized code to perform this smoothing demonstrated that a uniformly spaced radial mesh can be achieved maintained regardless of whether the surface is decaying (Figure 4.15a) or growing (Figure 4.15c).

(a)   (b)   (c)
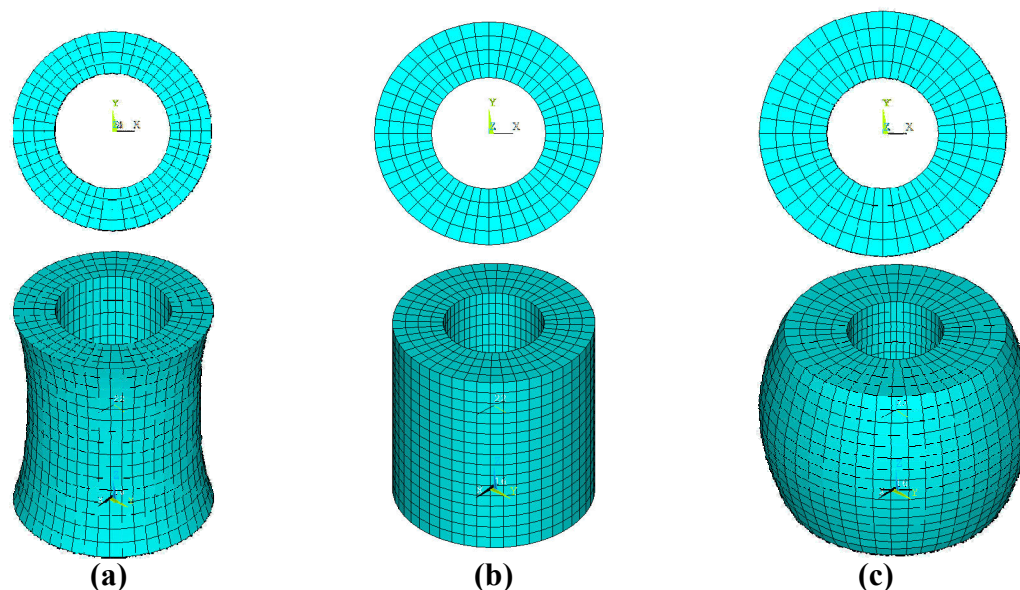
Figure 4.15   Effect of interior node smoothing routine to maintain equally spaced radial nodes. (a) initial mesh (b) decaying outer surface (c) growing outer surface.

4.2.6.2 Surface Node Smoothing. Because the discrete points on the boundary surface move independently from one another in the gradientless shape optimization routines, locally high values of the measure of the local mechanical state (stress, strain, strain energy density, etc) could result in significant mesh distortions even though the interior nodes are uniformly distributed from the implementation of the spring smoothing routine. For example, in Figure 4.16a one location may grow much more than the others if a stress concentration occurs. Alternatively, there can be an abrupt transition in growth; for example when going from a loaded to an unloaded region (Figure 4.16b). In order to allow for a more gradual transition between the abrupt changes in amounts of predicted growth, smoothing methods are generally applied to these surface nodes.
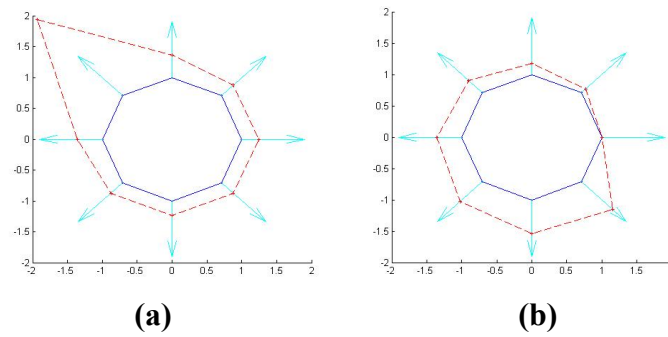
Figure 4.16 Examples of extreme local variations in nodal growth during shape optimization. (a) Effect of a local stress concentration. (b) Effect of a change in loading state.

As with the other components of bone strength adaptation models, methods devised to handle model-developed discontinuities are based in physiological phenomena. In the development of numerical models of the changes in the distribution of bone density (modifications of intrinsic material properties) due to loading, researchers have found that discontinuities in the material properties resulting from model predicted strength often caused numerical instabilities. To address these instabilities, it was hypothesized that the model should incorporate "communications" between cells that may alter their individual response to mechanical stimuli [202, 338]. Mullender et. al. developed a "spatial influence function" to simulate this phenomena [202]. In such a model, the response at a location Q to a mechanical stimulus is the sum of the response of all surrounding locations, each weighted by a function related to the distance between the locations of the growing node and that of its neighbors. The further the neighbor is from the node, the less influence it has on the node's growth. Specifically, the response at a location Q is modified from Equation 4.6 to:

$$U_k(l) = \alpha \sum_{i=1}^{N} e^{-\left[\frac{d_i(l)}{D}\right]} \left(\sigma_k(i) - \sigma_{ref} \right) \tag{4.11}$$

where $d_i(l)$ is the distance from location l to a neighboring location i, D is a reference dimension (an arbitrarily selected characteristic distance) and $\sigma_k(i)$ is the measure of the mechanical state at the neighboring node i at the current iteration k. While originally developed for models of changes to bone density distribution, in this work, the method was applied in preliminary studies as a means to adjust the surface nodes near the large growth discontinuities such as those in Figure 4.16.

Upon application of this modified shape adaptation model with integral nodal smoothing, some issues emerged. At a particular cross section, the smoothing effect was increasingly noticeable as the value characteristic distance, D, in Equation 4.11, was found to increase. This characteristic distance controls the reach at which the mechanical state of one location is allowed to influence the state at another. Therefore, with the selection of a large value for the characteristic distance compared to the typical element size in the mesh used, the state of neighboring nodes has a larger effect on the response at a particular location. As seen in Figure 4.17, when this distance value becomes sufficient enough, the local variations are lost, and the predicted shape may no longer be representative of the variations in the local mechanical state.

The limited practical application of the spatial influence smoothing method of Equation 4.11 to three-dimensional shapes is largely due to two main features: the required summing of all the effects of nodes and the selection of the arbitrarily parameter D. First, the "spatial influence" smoothing method sums the effects that the mechanical states of all nodes have on the change in the location of the given node, weighted by their distance from the changing node. This essentially gives nodes in the middle of the volume twice as many influential neighboring nodes as those nodes located at the ends of

the volume, causing disproportionate changes. To adjust for this skewed influence of neighbors, it is possible to modify the characteristic distance of influence, D, based on the location of the particular node. However, this introduces additional arbitrarily selected modeling parameters, including the distances at which adjustment need to be made and the level of adjustment, further complicating the model and making its universal application unlikely. Additionally, because the method sums the effects of all nodes, the growth at each node is greater than the growth that would be caused by its own mechanical state, potentially inflating the predicted shape changes.

| (a) | (b) | (c) | (d) |
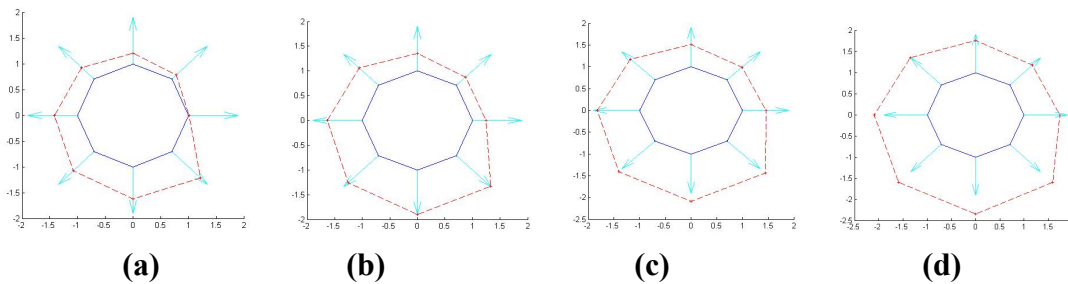
Figure 4.17 Effect of characteristic distance in spatial influence function. (a) 25% (b) 65% (c) 90% and (d) 130% of initial distance between neighboring nodes.

Second, in the simple two dimensional model presented in Figure 4.17 the characteristic distance, D, can be manually adjusted based on visual inspection of the resulting geometry or can be set to a value based on the discretization of the geometry, such as the average element size (similar to Figure 4.17c). In a more complex three-dimensional mesh or with more involved boundary conditions, however, the element size is not likely to be uniform. Applying the spatial influence method of Equation 4.11 to a non-uniform mesh results in an inconsistent distribution of the effect of the neighboring nodes simply due to the manner in which the geometry studied was discretized. Additionally, because the method depends on the arbitrary selection of the characteristic

distance, and because it does not directly consider the local variations in mechanical state of neighboring nodes, extreme and discontinuous amounts of growth can still result, especially in regions surrounding the boundary conditions.

Because of these limitations, as with the other modeling components reviewed thus far, studies of structural shape optimization methods, rather than bone strength adaptation models, were consulted to find more consistently surface node smoothing methods that could be universally applied to a wide range of geometries and boundary conditions. In these shape optimization methods, the "smoothing" is not integrated directly into the optimization function itself. Instead, changes to the nodal positions predicted by the shape optimization models are first calculated and then adjusted based on specified smoothing routines.

In many structural shape optimization routines, nodal smoothing methods that are typically employed use some form of an averaged value of the predicted local change in the nodal position to modulate the amount of nodal growth and smooth the new profile that results. In the simplest of these methods, the nodal growth is modified so that the final changes to the position of a node become the arithmetic average of the shape optimization predicted changes in the position of that node and those of its nearest neighbors [281]. Other methods further scale this value by a constant fraction [213], making a weighted average. Such weighted averages can be used on their own or can evolve into more complex smoothing methods.

One of the most popular grid smoothing methods was developed in the late 1960's based on an approximation of the discrete Laplacian, since it was observed that numerical approximation to the solution of the Laplace equation has an averaging effect [336]. This

method uses the locations of the centroids of the elements that share a common node to relocate that common node in the following way:

$$\mathbf{X}_k^{Smooth}(l) = \frac{\sum_{i=1}^{N}\mathbf{X}_k^c(i)w_k(i)}{\sum_{i=1}^{N}w_k(i)} \tag{4.12}$$

where $\mathbf{X}_k^{Smooth}(l)$ is the smoothed location of the node at the current optimization iteration. This node is shared by N elements. $\mathbf{X}_k^c(i)$ is the location of the centroid of the ith neighboring element at the current iteration and $w_k(i)$ is a weighting factor associated with that element. The weighting factor can be any nodal parameter that varies smoothly, such as nodal positions, displacements, strains, or stresses, or it can be an arbitrarily selected value $0 < w_k(i) \le 1$.

A variation of this method adds a relaxation factor to the nodal position expression. This is referred to as "relaxed weighted barycentrage" technique [335]:

$$\mathbf{X}_k^{Smooth}(l) = (1-r)\mathbf{X}_k^{Orig}(l) + \frac{r}{N}\sum_{i=1}^{N}w_k(i)\mathbf{X}_k^{Orig}(i)$$
$$\sum_{i=1}^{N}w_k(i) = 1 \tag{4.13}$$

where N is the number of directly neighboring nodes (attached by element edges) or centroids of elements that share the common node. In this method, the weighting factors must sum to unity, with a relaxation factor $0 \le r \le 1$ used to further smooth the nodal positions. Variations of this method have been applied to "regularize" meshes during shape optimization processes and even in some bone adaptation simulations [112].

These smoothing methods are intended to be used iteratively until a sufficient amount of smoothing is reached (multipass filtering) [335, 336]; however, a single iteration can be applied when only a small amount of smoothing is desired [112, 213, 281]. Many methods have applied mesh adaptation only in regions of the mesh that have triggered a flag indicating high mesh distortion. Alternatively, it has been used over the entire mesh as a means for promoting progress towards mesh regularization. For additional control of the mesh alterations during the shape optimization processes, limits to the amount of node motion that can occur during each optimization iteration, referred to as move limits, have been imposed as a method to maintain mesh integrity [330]. It has been suggested that these limits be used in conjunction with the Laplacian smoothing methods, especially those with relaxation [335], to prevent large changes in nodal positions due to the smoothing process. The move limits function similar to the constraints limiting the maximum allowed muscle forces values used in some gradient-based muscle force magnitude optimization routines.

Based on this review, a preliminary model using iterative Laplacian smoothing with relaxation and move limits was developed for the three-dimensional bone shape adaptation model in this work. The iterative smoothing in this preliminary model was stopped when the maximum change in the nodal position over the surface being smoothed was less than 10% of the average nodal move limit on the adapting surface per shape adaptation iteration. The move limit per shape adaptation iteration was defined based on preliminary studies which showed that when an element shrank by more than approximately 20%, the element Jacobian became inverted, indicating significant mesh

distortion. The move limit imposed in this model was related to the prevention of this element inversion before the internal spring smoothing method could be employed.

Because of the computational intensity of the internal node smoothing method described in Subsection 4.2.6.1, it was implemented only once every five shape optimization iterations in the developed model. The move limit was such that the total change of the element size over these five iterations could not exceed 20% before the internal smoothing was invoked. Consequently, the move limit per iteration of each surface node was defined as 4% of the distance between the current positions of surface node and the first closest interior node along the radial line (direction of growth) at each optimization iteration. This is consistent with models in the published literature that prevent more than a 5% change in nodal position per shape optimization iteration [330].

In this preliminary model, the following smoothing equation was used based relaxed weighted barycentrage model in Equation 4.13 as:

$$U_k^{Smooth}(l) = (1-r)U_k^{Orig}(l) + \frac{r}{N}\sum_{i=1}^{N} w_k(i)U_k^{Orig}(i)$$
$$w_k(i) = \frac{\nabla SED_k(i)}{\sum_{j=1}^{N} \nabla SED_k(j)} \tag{4.14}$$

where $U_k(l)$ is the change in nodal position at node l calculated from current optimization iteration, N is number of surrounding nodes and the gradient of the nodal strain energy density is used as the weighting function. The calculation of this nodal SED gradient is explained in Appendix B. The use of strain energy density is often employed as a measure of deformation as well as material behavior. The gradient

provides information about the direction of this deformation. Therefore, the strain energy density gradient is a good measure of the element distortion with which to weight the repositioning of the surface nodes [334]. This smoothing was applied to all surface nodes, regardless of the level of difference in growth between their neighbors. Despite its ability to successfully smooth regions of large discontinuities and growth levels overall convergence could not be achieved using this relaxed form of the Laplacian smoothing method.

The reason for this is related to the relaxation component of the smoothing routine. In regions of nearly uniform nodal growth and SED values, Equation 4.14 reduces to:

$$U_k^{Smooth}(l) = \left(1 - \frac{r}{N}(1-N)\right)U_k^{Orig}(l) \qquad (4.15)$$

and convergence is never achieved, regardless of the choice of the relaxation factor r, since the term $\left(1 - \frac{r}{N}(1-N)\right)$ will always be greater than 1. Additionally, confounding effects described by Equation 4.15 is still the issue of selecting the relaxation factor, r. In the implementation of this method, the selection of an appropriate relaxation factor for the particular model studied typically requires a series of preliminary trials. This precludes its implementation in a more universally applied model. Therefore, alternative methods to the relaxed Laplacian smoothing of the surface nodes were investigated.

One such method was previously developed [334] to eliminate the arbitrary selection of the weighting or relaxation factors by prescribing an expression for their determination. This is a weighted Laplacian smoothing method without the additional

relaxation, following the basic form in Equation 4.12. The conditions at the node being smoothed and those of the neighboring nodes, rather than at the centroids of attached elements as in Equation 4.12, are included in the calculations. The movements of the node along the individual coordinate direction (for example Cartesian X, Y, and Z) are computed separately in this method. The smoothing equations follow accordingly:

$$x_k^{Smooth}(l) = \frac{\sum_{i=1}^{N+1} w_k^x(i)x_k^{orig}(i)}{\sum_{i=1}^{N+1} w_k^x(i)}, \quad y_k^{Smooth}(l) = \frac{\sum_{i=1}^{N+1} w_k^y(i)y_k^{orig}(i)}{\sum_{i=1}^{N+1} w_k^y(i)}, \quad z_Q^{Smooth} = \frac{\sum_{i=1}^{N+1} w_k^z(i)z_k^{orig}(i)}{\sum_{i=1}^{N+1} w_k^z(i)} \quad (4.16)$$

The weighting factors $w_k^x(i)$, $w_k^y(i)$, and $w_k^z(i)$ are based on the gradients of the nodal strain energy density in each of these coordinate directions and are dependent upon the magnitude of the directional strain energy density gradients. Specifically,

$$w_k^c(i) = \begin{cases} 1 & \text{if } \max_i \left|\left(\nabla_c SED_k(i)\right)\right| = 0 \\ \dfrac{\left|\left(\nabla_c SED_k(i)\right)\right|}{\sum_{i=1}^{N+1} \left|\left(\nabla_c SED_k(i)\right)^i\right|} & \text{if } \max_i \left|\left(\nabla_c SED_k(i)\right)\right| > 0 \quad c = x, y, z \end{cases} \quad (4.17)$$

While the surface nodes only change position in the radial direction in the current work, to capture the complete variation of the SED gradient that could lead to the growth discontinuities, the entire gradient of the SED was used instead of the gradient only in the direction of node movement. Therefore, the smoothing model in this work is:

$$U_k^{Smooth}(l) = \frac{\sum\limits_{i=1}^{N+1} w_k(i) U_k^{orig}(i)}{\sum\limits_{i=1}^{N+1} w_k(i)},$$

$$\text{where } w_k(i) = \begin{cases} 1 & \text{if } \max\limits_i \left|(\nabla SED_k(i))\right| = 0 \\ \dfrac{\left|(\nabla SED_k(i))\right|}{\sum\limits_{i=1}^{N+1} \left|(\nabla SED_k(i))\right|} & \text{if } \max\limits_i \left|(\nabla SED_k(i))\right| > 0 \end{cases} \qquad (4.18)$$

The ability of this SED gradient based method to smooth the changes in positions of the surface predicted by the shape adaptation model developed in this work, in conjunction with the spring based interior node smoothing method described in the previous subsection, was investigated in another preliminary study in this work. An initially circular hollow cylinder with a series of regional forces applied to its outer surface was subjected to the shape optimization model with the iterative surface node smoothing method invoked every iteration and the single-pass interior node smoothing method invoked every five iterations. The surface node smoothing iterations stopped when the maximum change in the nodal growth due to the smoothing was 10% of the nodal move limit (described above). The effect of the inclusion of the surface node smoothing is shown in Figure 4.18. The dramatic difference between these two meshes demonstrates the import of the inclusion of node smoothing methods on the accuracy of the bone shape adaptation and mechanical shape optimization predictions.
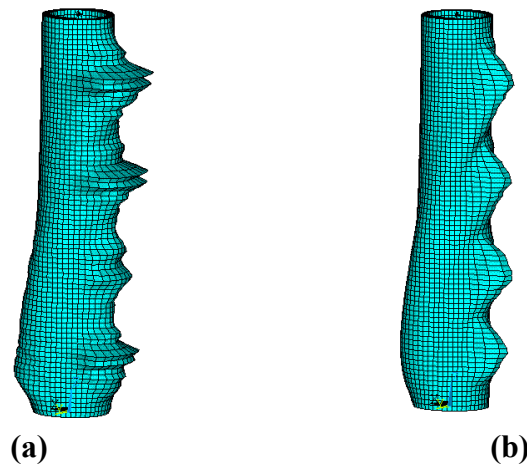
Figure 4.18 Shape optimization routine run using (a) no nodal smoothing methods and (b) with nodal smoothing methods.

4.2.7 Summary

When first conceived, the numerical prediction of the alterations in a bone's shape that occur as a result of its strength adaptation phenomena paralleled the methods being developed to optimize the mechanical design of structural components. As computational capabilities improved and the interest in the prediction of bone strength adaptation grew, more researchers entered the field, and the study of the optimization of the strength of living material diverged from that of the inert. The focus of the bone strength adaptation model development became the development of means to represent the actual biological phenomena rather than the prediction of their effects. Empirical models, developed to correspond to experimental measurements of bone surface strains or high-tech images of bone shapes, have driven the recent literature in this field. Though much progress has been made since start of the field of study, when it was said, "The whole subject of adaptive ontogenic changes in bone is of great interest and has attracted a thick fluffy coating of wooly thinking," [339] the lack of a sound

mathematical and theoretical basis still limits the usefulness of these computational model of bone strength adaptations.

Because of the wide variety of experimental observations and measurements, many empirical based models currently used in numerical bone adaptation studies are valid only for the singular situation used to develop them. Because they must be reformulated for each condition studied, they cannot, and often are not, used to compare the effects of various mechanical loading conditions or configurations. As shown in this chapter, the goals of structural shape optimization are the same as those of bone strength adaptation, a reduction in the local variation of the bone's response to the mechanical environment. Therefore, the methods used in their study are often similar. As demonstrated in this section, the progress made in the computational techniques for mechanical shape optimization, which often have a more rigorous mathematical, scientific, or engineering basis, can be applied to the study of the bone strength adaptation. Such modeling methods are less dependent upon experimentally determined or arbitrarily selected parameters. The set of modeling techniques developed and described in this chapter can be used to study a variety of conditions so that direct comparisons can be made between different systems. Therefore, these model components help reach the goal of this study, the independent and universal modeling analysis of mechanical bone adaptation.

Based on the requirements of the current structural bone adaptation modeling method developed in this work, the reviews of previous work and the results of the preliminary studies presented here, a structural shape optimization based numerical bone adaptation model has been devised that has made significant progress towards an

universally applied bone adaptation modeling technique that need not dependent upon experimental parameters and need not be adjusted based on the conditions or system examined. The specific modeling components developed and included will now be discussed.

4.3   Final Developed Bone Shape Adaptation Model

The model to predict the alterations to the shape of a bone under the influence of its mechanical environment developed as part of this research was intended to simulate the relationship between the local mechanical state and the local amounts of accretion or resorption of cortical bone tissue material on the endosteal (outer) and periosteal (inner) surfaces of a bone that was part of a three-dimensional representation of a multi-segment musculoskeletal system. While many models have been previously developed with a similar purpose, the goal of this work was to improve the universal applicability of such a model. Specifically, the design of techniques developed in this work focused on a decreased dependence on experimentally based or arbitrarily selected parameters and providing a more consistent definition of the main features of the model so that it could be used to quantitatively compare the effectiveness of various loading conditions in improving the strength of targeted regions of the bone. Using the insight gained from the review of previously developed bone strength adaptation and structural shape optimization models discussed in Section 4.2 combined with the results of the preliminary studies presented, a modeling method was established that met these design objectives. In this section, the creation of the final form of the developed bone shape adaptation model and the procedure for its implementation are presented.

4.3.1 Interrelationships Between Reference Value, Growth Rate, and Convergence

The alterations in the bone's shape were determined using the gradientless biologically based shape optimization method of the general form in Equation 4.3, repeated here for convenience:

$$x_{k+1}(l) = x_k(l) + U_k(l)$$
$$U_k(l) = \alpha(\sigma_k(l) - \sigma_{ref})$$

(4.3)

where $x_k(l)$ is the current position of node l, $\sigma_k(l)$ is the value of the local measure of the current state of stress, σ_{ref} is the threshold value of this measure, α is the growth rate constant (step size), $x_{k+1}(l)$ is the new position of node l, and $U_k(l)$ is the amount of change in the location of node l. The strain energy density was selected as the measure of the local state of stress used as the "functional stimulus", or mechanical driver, for the bone strength adaptation processes simulated in this work (See Section 4.2). Based on the assumption of no axial growth, the shape modifications occurred only in the local radial direction so that $x_k(l)$ represented the radial coordinate of the location of the surface node l with reference to a local cylindrical coordinate system over the optimization process.

Despite the extensive study of the effects of the reference (threshold) value, σ_{ref}, growth rate (step size), α, and convergence criteria, the definition of these main model features were not selected in Section 4.2. Instead, their interrelationships were examined. Individually and in combination, they directly control the amount of change in the position of each node at each shape optimization iteration as well as the total amount of growth that forms the final optimized shape. The preliminary studies also demonstrated

the current difficulties in determining methods for the consistent definition of these parameters independent of the conditions or the system studied. However, insight into their necessary features was also gained. For example, the use of a model derived reference value that is calculated based on the current state of stress in the body being optimized was found to induce alterations to the objects shape that were more relative to the conditions being studied than driving the object to an arbitrarily selected stress state. Additionally, the interactions of the bone segments in this model with each other as well as with the muscles that exert forces on them and the conditions external to system examined that restrict their motion, the three-dimensional models for which the simulation techniques are developed contain regions of locally high or low stress that will always remain high (or low) regardless of the geometric alterations that occur around them. Finally, because the growth rate (step size) directly controls the amount of change with iteration, convergence measures that simply compare one iteration to the next may not give a true representation of the progression of the geometry to an optimized state but may really only indicate the effects of this growth rate. These issues must be resolved in order for the developed model to achieve the desired modeling design objectives.

In the preliminary studies reviewed in Subsection 4.2.3, a number of model derived reference values based on the current state of the optimized body were suggested. A stress at a region far from the stress concentration area, a maximum or minimum value and an average value of stress over the optimized surface were all considered for use in this model. However, because the geometry being optimized in this study is three dimensional with a large number of nodes (design variables) and directly applied boundary conditions, the use of an absolute maximum or minimum nodal value does not

give a good representation of the state of the entire body since regions of high stress will remain near the loaded or constrained areas. Additionally, the selection of a region far from the stress concentration would be dependent upon the loading condition and, thus, vary between cases studied, limiting the universal applicability of the developed modeling techniques. An average value over the set of design variables studied could give a more global measure of the overall stress state over the surface being optimized, it can represent a goal in the progress towards its uniformity of the local stress state in the design region. Therefore, the surface averaged strain energy density (SED) was pursued as a potential reference value in the developed model.

In the discretization of a three-dimensional body, some variation in element size and node location is necessary to appropriately capture the mechanical state of the object. For example, more nodes are often required near the boundary conditions where the state of stress may vary significantly with location, and fewer nodes may be needed far from these locations where more constant distributions of stress are expected, as shown in Figure 4.19. If an arithmetic average of nodal strain energy densities is used, weight is given to locations with a large number of nodes, even if these regions account for a relatively small portion of the overall surface area. To eliminate this artificial mesh-dependent weighting, which would tend to skew the average value towards the stress concentration values, an elemental area weighted average was employed. Instead of being weighted by node density, the average strain energy density used in this model was weighted by surface area of the exposed face of each element belonging to the optimizing surface. In this way, elements with small areas (where there is a high node density)

would carry less weight than elements with large areas, and a more sparse node density, reducing the heavy contribution of the denser spaced nodes near areas of high stress.
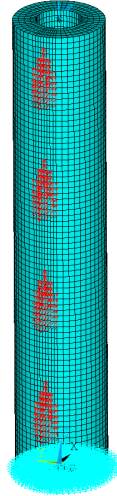
Figure 4.19 Variation of nodal distribution in locations of applied boundary conditions.

Specifically, the elemental area weighted average strain energy density was calculated using nodal values of the strain energy density and coordinates of these surface nodes. First, an elemental strain energy density was found by taking the arithmetic mean of the strain energy density of the nodes that create the exposed face of the element on the optimizing surface. Using the coordinates of these nodes, the area of this face was also calculated. The surface area weighted average elemental strain energy density was then defined as follows:

$$
SED_k^{EleAWSurfAvg} = \frac{\displaystyle\sum_{e=1}^{M} SED_k(e) A_k(e)}{\displaystyle\sum_{e=1}^{M} A_k(e)}
$$

$$
SED_k(e) = \frac{\displaystyle\sum_{n=1}^{N} SED_k(n)}{N}
$$

(4.19)

where $SED_k(n)$ is the strain energy density at each of the nodes at the N corners of exposed face of the element e on the optimizing surface, and $SED_k(e)$ is called the elemental strain energy density for that element e. Accordingly, $A_k(e)$ is the area of this exposed face of element e. M is the total number of elements with exposed faces on the optimizing surface. N is the number of nodes that define the element face, for example $N=4$, for an eight-node hexahedral element. Using this element area weighted surface averaged strain energy density as the reference (threshold) value, in growth (shape optimization) equation becomes:

$$U_k(l) = \alpha \left(SED_k(l) - SED_k^{EleAWSurfAvg} \right) \tag{4.20}$$

This formulation eliminates the arbitrary or experimentally based selection of the reference (threshold) value and allows the optimization to be driven towards uniformity based on a global measure of the current stress state of the body being optimized.

In the growth driver equation (Equation 4.20), the wide range of nodal strain energy density values (Figure 4.20a) among the nodes in one system with one load as well as between nodal results for various systems under a range of loading cases hinders the widespread application of this driver. The value of the step size (growth rate) α must continually be adjusted for each node, often by orders of magnitude, to prevent extreme element distortion and to ensure maintain consistency with the move limit defined in Section 4.2. Preliminary studies showed that the currently available methods to alleviate the dependence on and automate the selection of the growth rate (scaling) factor α artificially alter the shape optimization process and interfere with the accurate prediction of effects of the local mechanical or stress state on the bone shape and strength.

Different methods to reduce the range of variation in an attempt to make this parameter, α, independent of the loading conditions have been previously suggested. Many shape optimization methods have used a normalized growth driver [211, 212, 281] resulting in a growth (shape optimization) equation as in Equation 4.21:

$$U_k(l) = \alpha \frac{\left(SED_k(l) - SED_k^{EleAWSurfAvg} \right)}{SED_k^{EleAWSurfAvg}}$$

(4.21)

When implemented in the optimization of a three-dimensional surface with thousands of design variables (nodes) and directly applied boundary conditions, the normalization does sufficiently reduce the variation of the growth driver value so as to avoid the prohibitive extreme mesh distortion that results without adjustment of α (Figure 4.20b).

In statistical analyses, many predictions of the behavior of a population are based on calculations over a standard distribution. In such a group of normally distributed data, their average is equal to zero and their standard deviation is equal to one. An arbitrary normally distributed set of data can be converted into a standard by normalizing the difference between the individual value and the group's average by the standard deviation of the group, allowing for easier calculation of subsequent measures. This transformation method from an arbitrary normal distribution *X* of a set of data to a standard distribution, *Z*, called standardization, can be written as [340]:

$$Z = \frac{\left(X - Avg \right)}{StDev}$$

(4.22)

Similar to normalization, standardization imposes the added advantage of controlling the mean and the spread of the transformed population in a predefined and repeatable manner.

The standardization transformation is of a similar form to the growth driver expression in the current model, and its application to the shape adaptation model would reduce the dependency on the growth driver (step size), α, because the large spread of values would be reduced to a manageable and predictable range. In the application of this "standardized growth driver" to the shape optimization function (Equation 4.20), the elemental area weighted standard deviation was used for a more equitable measure of the conditions across the optimized surface and was calculated following a similar process to that described for the elemental area weighted surface average:

$$U_k(l) = \alpha \frac{\left(SED_k(l) - SED_k^{EleAWSurfAvg}\right)}{SED_k^{EleAWStDev}} \tag{4.23}$$

$$SED_k^{EleAWStDev} = \sqrt{\frac{\sum_{e=1}^{M} A_k(e)\left(SED_k(e) - SED_k^{EleAWSurfAvg}\right)^2}{\frac{(M-1)\sum_{i=1}^{M} A_k(e)}{M}}} \tag{4.24}$$

where $A_k(e)$, $SED_k(e)$ and M are as described in Equation 4.19.

As shown in Figure 4.20c, when implemented, the standardized growth driver appropriately reduces the variation in the nodal growth that resulted from the non-normalized difference between the local and global measures of the stress state was used to drive the adaptive behavior (Figure 4.20a). While the distribution of the nodal strain

energy density over a typical bone surface is not a true normal distribution, it is a sufficient approximation for the purposes of this application. The few nodes that still produce growth values outside of this standard deviation of one are likely nodes that involve the direct application of boundary loading or constraints and can be handled through the implementation of the move limits without a detrimental effect on the resulting shape predictions. Consequently, the standardization of the growth driver was used in this work.
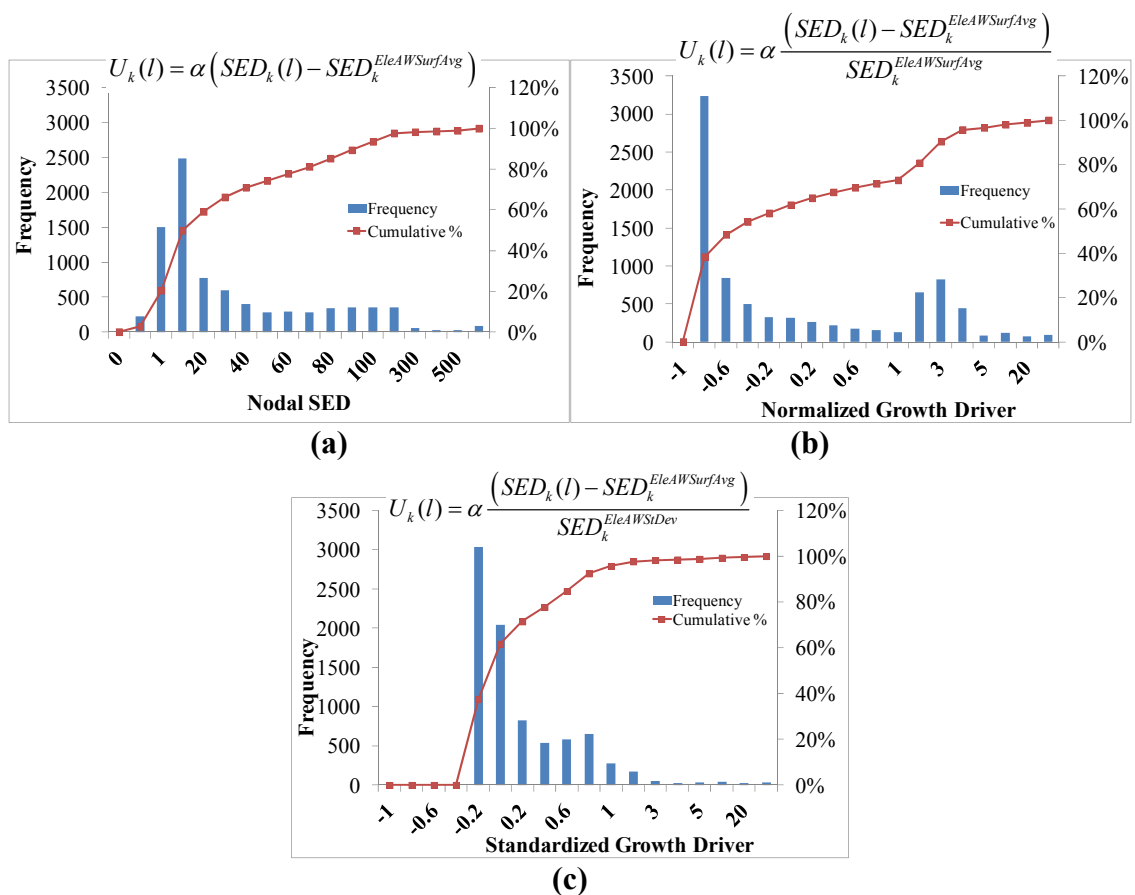
Figure 4.20 Histogram of growth driver measures for nodes on the optimizing surface of a 3-D cylinder (a) basic (b) normalized (c) standardized.

In order to ensure that this new growth driver in the shape optimization function really does eliminate the model's dependency upon the growth rate scaling factor (step

size), α, a preliminary study was performed using this new model. Mixed bending and compressive loads were applied to an initially circular hollow cylinder with a fixed bottom surface. The applied force levels were varied by orders of magnitudes with a constant growth rate (step size), α, to test the model dependence on this parameter. Although the nodal strain energy density values differed by two orders of magnitude over the cases studied, the distribution of the strain energy density with location was the same for the different loads (Figure 4.21a). More importantly, after hundreds of shape adaptation iterations, the resulting shape predictions were identical in both magnitude and distribution independent of the load magnitude (Figure 4.21b). By using the standardized growth driver, the model's dependency upon the growth rate (step size) factor was eliminated, furthering the models progress towards the stated research goal of universal applicability.
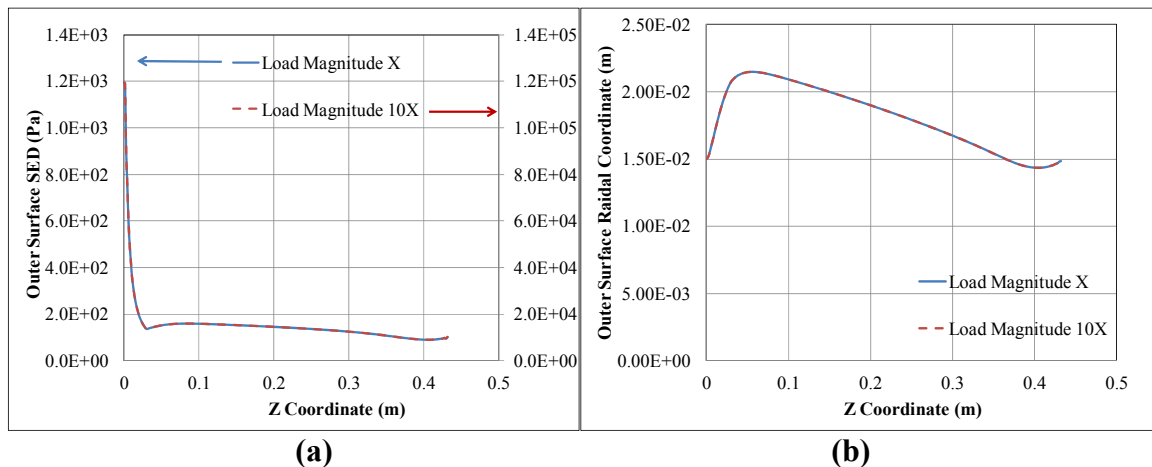
Figure 4.21 Representative results of shape optimization using standardized growth driver. Final (a) strain energy density (b) radial coordinate of surface nodes along the length of the cylinder (Z coordinate) at angular coordinate, Θ = 0°.

The last modeling component needed to resolve the development of the bone shape adaptation modeling technique in this research was the conditions required to stop

the optimization process. As discussed in Subsection 4.2.5, because of its mathematical laxity and inability to determine a unique optimum, there is no consistent, definitive way to note the completion of a biologically based gradientless optimization process. Techniques similar to those for defining convergence of other iterative numerical methods are often employed, where either the change in a measure is tracked from one iteration to the next or the process continues until a measure reaches a threshold value. The use of such criteria implies that the measure used to track convergence will stop changing when the goal is achieved. The implied goal of the shape optimization models developed in this work is the uniformity of the strain energy density over the surface being optimized. As previously mentioned, the persistent outliers in the strain energy density levels that result from the imposed boundary conditions prevent a fully uniform state of stress over the optimized surface. Therefore, criteria to define "nearly uniform" were required.

Convergence measures for shape optimization models have handled outliers in different ways. In some models, these outliers denote targeted regions for the design optimization, and, therefore, convergence is measured by the reduction in the magnitudes of the maximum values, minimum values, or the variance between them. Such criteria is most beneficial when the number of design variables is small, such as the optimization of a fillet curve in a two dimensional representation [209, 323]. In other models, these outliers are extraneous and so are eliminated from the convergence calculations. Because of the large number of design variables in the shape optimization methods developed in this work, the nodes that are outliers and the nodes that are targeted for mediation depend upon both the geometry and the loading conditions. Because statistical analysis methods

are useful in determining outliers of large populations through prescribed quantitative means, the use of statistical analysis methods was explored in the development of convergence criteria for this work.

The most commonly used statistical methods for extracting outlier members of a dataset rely on standard deviations. Outliers are typically defined as any points greater than three standard deviations away from the average of a set. A potential convergence criterion using this concept was investigated. In this preliminarily developed convergence model, the number of design variables (nodes) with strain energy density values more than three standard deviations away from the surface averaged value was tracked. Convergence was said to be achieved when the number of these outliers was reduced by a particular amount. When this modeling concept was implemented, however, the number of these defined outliers did not significantly change because these outlier values were related to the nodes closest to the boundary loads and constraints. Various multiples of standard deviations were also considered; however, none resulted in a reliable method for identifying improved uniformity.

In statistical analysis, the most typical members of a dataset are often defined by creating a subset called the "interquartile range". Here, the set members are sorted numerically. The data is then divided into four groups with an equal numbers of members in each group. The most typical data is said to lie in the middle two groups, the "interquartile range". In an attempt to exclude outliers in the measure of convergence in the bone shape optimization model developed in this work, only data in the interquartile range was considered. The convergence measure was the average strain energy density value of this range, and convergence was said to be achieved when this measure was

reduced a specified amount or stopped changing. Upon use of this attempted convergence criteria, however, it was found that the strain energy density average sometimes increased and the amounts of change varied based on the conditions modeled, limiting the potential use of the method as a universal convergence criteria.

The concept of the quartiles inspired another potential method for determining the achievement of the optimization goal. Instead of examining the most common values, the first and last quartiles, the extreme values, were considered. These subsets consisted of the top and bottom 25% of the data values. Therefore, they represented the "extreme" nodal strain energy densities. By representing the first quartile as the arithmetic mean of the members of this subset, extremely low nodal values (absolute minimums) are tempered. Similarly, the use of the average of the members of the fourth quartile moderates the extremely high values and eliminates the reliance on the absolute maximums. This method ensured a consistent number of data points to be analyzed and a well-defined convergence value.

The averages of the first and fourth quartiles, can be considered equivalent "maximum" and "minimum" model values, and so can be used in the same manner that the absolute nodal maximum and minimum of the model strain energy density have been previously employed to signal convergence in shape optimization models. Specifically, the change from the initial difference between the equivalent model minimum and maximum (called the "Q14Spread" in this work) at each optimization iteration can be used as a convergence measure. Convergence can be said to be achieved at the iteration when the Q14Spread is reduced from its initial value by a specified amount.

The effectiveness of such a convergence method at quantifying the change in the variation of the mechanical state of the surface nodes (design variables) was demonstrated through the use of histograms of nodal strain energy density with iteration of the shape optimization process as in Figure 4.22. Between the initial (Figure 4.22a) and final (Figure 4.22b) shape optimization iteration of a representative shape optimization problem, the variation of the nodal strain energy densities was clearly reduced even though the number of extreme values (in the bins labeled "more" in Figure 4.22) increased slightly and the mode and median of the dataset increased. The change in the Q14Spread from that of the initial (pre-optimized) shape presents a quantitative measure of the reduction in variation of the state of stress over the optimizing surface. In this example, the Q14Spread is reduced by about 50%. A 50% reduction in the Q14Spread was selected as the convergence criterion in this work.
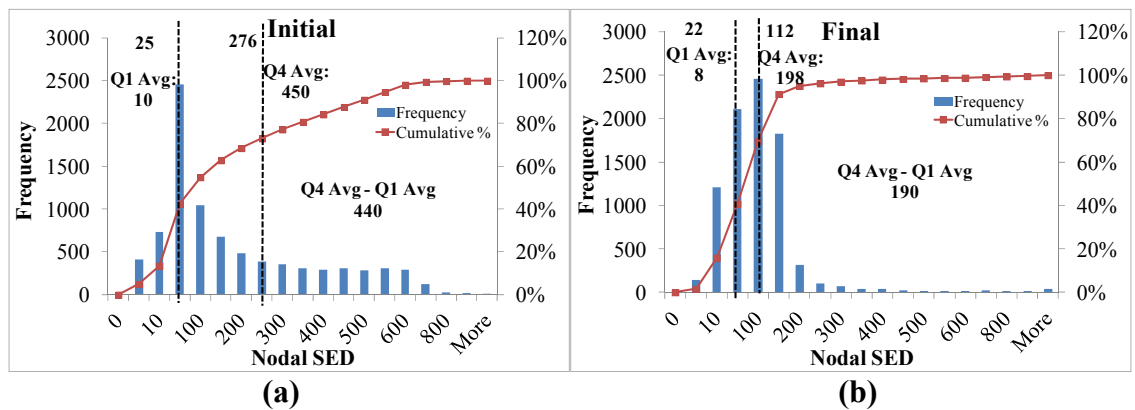
Figure 4.22 Histogram of nodal SED values depicting quartile average method for convergence (a) initial (b) final nodal variation over the optimized surface.

4.3.2 Summary

This bone shape strength adaptation model, which is independent of any experimentally derived or arbitrarily selected parameters, does not require any modifications or additions to its modeling parameters, components, or techniques based on the system or conditions

studied. Moreover, it uses predefined, quantitative criteria to determine when sufficient improvement of the uniformity of the stress state over the optimized surface is achieved, and contains means to maintain the integrity of the mesh, ensuring accuracy of the structural analysis on which the shape optimization is based.

The basic function of the modeling method developed is as follows. Changes to the profile of the bone's outer (periosteal) and inner (endosteal) cortical surfaces are simulated through the movement of surface nodes in the local radial direction (normal to the surface) by an amount that is directly proportional to the statistically standardized value of the nodal strain energy density on the optimizing surface. Spring based smoothing of the interior volume nodes and strain energy density gradient based Laplacian smoothing of the external surface nodes as well as a maximum "move limit" and a constant growth rate (step size) that does not depend on the modeled conditions are used to prevent extreme mesh distortion during the optimization process. The changes to the shape of the bone studied are stopped when the change in the difference between the average of the upper and lower quartiles of the nodal strain energy density over the optimizing surface is reduced from its initial value by 50%.

The components of developed model allow for the consistent prediction of the alterations to the shape of the bone in response to the local variations in the state of stress. Because all system conditions studied with this model are subjected to the same features, parameters and stopping criteria, the response of the adapted bone to different environmental conditions could be directly quantitatively compared. Hence, the developed model has realized the desired design objective of universal applicability to aid in the evaluation of the strengthening ability of a wide range of conditions. The

conversion of the theoretical description of the bone shape adaptation model to practical implementation using numerical computational methods is next presented.

4.4   Implementation of the Developed Bone Shape Adaptation Model

The developed computational bone shape adaptation model described in this chapter is based on the accurate calculation of local measures of the mechanical state in order to modify the shape at discrete, but close, points over the optimizing surface. Because finite element methods divide a volume into many smaller volumes joined together by discrete points, or nodes, numerical shape optimization and finite element analysis have been a natural pairing since their early development [204, 269, 280]. Following this coupling, the developed bone shape adaptation model was incorporated into a commercial finite element code through the use of customized subroutines, just as was the muscle force magnitude optimization model (Chapter 3). The implementation of the customized code incorporates all of the modeling components described in this section. To provide a complete presentation of the modeling technique created in this work, the programming methods for linking of the numerical muscle force magnitude optimization model presented in Chapter 3 with the computational shape optimization model presented in this chapter is also described. While the method will be explained in detail, the general process is depicted in a flow chart in Figure 4.24, which can be referred to as needed. The shape optimization function will first be discussed, followed by its function within the whole muscle developed model.

4.4.1 Shape Adaptation Model Function

For the shape optimization model to function within a commercial finite element code, tools to access and modify the finite element model and its solutions were used. The commercial code used in this work, ANSYS Version 12.1, has two types of programming features to access the model database and control its function: a Fortran-based scripting language (ANSYS Parametric Design Language (APDL)) that contains many built in functions to execute ANSYS commands and extract model data, and user-defined subroutines (called User Programmable Features (UPF)) that work directly within the ANSYS solver allowing the user to alter the solver function or model data directly. As with the muscle force magnitude optimization, both features were used for the bone shape strength optimization simulations.

The shape optimization process used in this work is an iterative procedure where the bone's surface boundary is progressively adjusted based on the current conditions until sufficient uniformity of its stress state is achieved. These iterations involve both the determination of the state of stress on the optimizing surfaces and the resulting shape changes. In the computational implementation of the model developed in this research, an APDL script was created to input the model parameters, control the iterations, track convergence, and execute both the structural analysis and the shape changing procedures. The movement of the surface and the calculation of the measures to drive this movement were commanded through a UPF Fortran subroutine functioning within a customized version of ANSYS. The simulation of the shape adaptation was achieved through the movement of each node on the optimizing surface by an amount dependent upon the state of stress (mechanical state) at that node. The developed subroutine used data directly

from the ANSYS finite element model database, such as the nodal coordinates and solution of the structural analysis, along with geometric model and shape optimization model parameters input using the APDL script. These parameters, such as basic geometric dimensions, growth rate (step size), move limits, and size limits, were entered into the APDL script so that they could easily be changed, as required, based on the loading and model conditions studied, without having to recompile the customized ANSYS executable.

The developed node moving (shape optimization) subroutine (UPF) has five main functions. First, it calculates the unit normals (moving directions) and converts nodal coordinates from the ANSYS database from global to required local Cartesian and cylindrical coordinates. Second, it calculates the strain energy density and its gradient. Third, it calculates the amount of growth per node. Fourth, it smoothes these nodes and imposes move limits. Finally, it checks if the new surface boundaries reach any growth limits, requiring the model to stop before convergence is reached, and it checks for convergence. Each one of these functions is discussed.

In order to perform these functions, various data are passed to the growth predicting subroutine from the APDL script from which the subroutine is called. Flags are passed identifying the iteration, load case, and surface being optimized (endosteal or periosteal). Information about the "design variables", or set of nodes defining the optimizing surface, including identification numbers, global coordinates, and strain tensor components, is sent from the ANSYS database as is information about the orientation of the bone cylinder being optimized via the identification of its local coordinate system. Geometric parameters like the initial element spacing of the initially mapped mesh,

which are used to calculate the move limits are also passed. In addition, data regarding the grouping of the nodes by location are necessary as are data regarding the constraint status of the nodes, which are used to identify the nodes on the optimizing surface that are restricted from moving. The locations of the transition from hollow to cancellous filled the interior bone volume are also passed from the script, as the identities of the nodes on the internal surface in the cancellous region does not change shape. Predefined geometric boundary limits, like values of the maximum and minimum cortical thickness and radius allowed are passed from the APDL script to the UPF subroutine, as they are necessary when checking for the need to stop the optimization process before convergence is reached. Finally, the material properties are passed to the growth model subroutine so that the nodal strain energy densities can be calculated.

4.4.1.1 Growth Direction and Coordinate Transformations. The first function of the shape optimization subroutine is to determine the direction along which each surface node moves. Based on the assumptions listed in Chapter 2, adult bone only changes shape in the transverse planes (no longitudinal (axial) growth). Therefore, this model allows growth of each node only in the local radial direction. A unit vector along the central axis of the initially circular cylinder, with the origin at the distal end near the ankle, is defined as the local z-axis in the growth region of the bone being optimized. A unit vector is drawn from the origin of this local coordinate system to each surface node and then projected onto a plane perpendicular to the local z-axis through the given surface node. This projected vector, defined in the global coordinate system, identifies the growth direction, $\mathbf{N}_k(l)$, at any optimization iteration k, for each node l.

In addition to the determination of the growth direction, many aspects of the node moving shape optimization model require transformations of the nodal coordinates from the global coordinate system in which nodal coordinates are stored in the ANSYS model database to coordinate systems local to the orientation of the bone whose shape is being optimized within the musculoskeletal system configuration studied. This Cartesian transformation is performed knowing the local z-coordinate direction and the local coordinate system origin as defined above. To ensure that the orientation remains consistent between cases studied, the transformation is made without introducing any extraneous spin about the global z-axis. The orientation of the local coordinate system is defined by assuming that the local y-axis is aligned with a vector normal to the plane framed by the local z-axis and the global x-axis [341]. Specifically, with the local z-axis $\overline{e}_z^L$ defined as above, the coordinate transformations are as follows:

$$\overline{e}_y^L = \frac{\overline{e}_z^L \times \overline{e}_x^G}{\left|\overline{e}_z^L \times \overline{e}_x^G\right|} \tag{4.25a}$$

$$\overline{e}_x^L = \overline{e}_y^L \times \overline{e}_z^L \tag{4.25b}$$

where L represents the local bone coordinate system and G represents the global model coordinate system. Details on the numerical implementation of this procedure are provided in Appendix B. Because of the cylindrical geometry of the bone volume studied, the cylindrical representation of the local coordinate system is also calculated. This cylindrical representation of the local coordinate system and the subsequent nodal positions are useful in identifying, grouping, and sorting nodes throughout the shape optimization process.

4.4.1.2 Calculation of the Strain Energy Density and its Gradient. The second function of this shape optimization user defined subroutine was to calculate the mechanical measure driving the gradientless optimization procedure. As discussed in Subsection 4.2.2, the strain energy density was selected as the measure of the nodal state of stress from which the amount of nodal growth was calculated. This measure is calculated using the nodal strain tensor values and the material properties. The strain tensor data is obtained directly from the model database. The material properties are input to the ANSYS structural analysis model through the APDL script and passed to the user defined Fortran subroutine from this script. For simplicity, the strain energy density, *SED*, was calculated solely as a function of strain through the equation [85]:

$$SED = \frac{1}{2} tr\left(\boldsymbol{\sigma}\boldsymbol{\varepsilon}\right)$$

and substituting in $\boldsymbol{\sigma} = \mathbf{C}\boldsymbol{\varepsilon}$

$$(4.26)$$

where $\boldsymbol{\varepsilon}$ and $\boldsymbol{\sigma}$ are the engineering strain components and stress components (using strain components in Voigt (vector) form so that $\varepsilon_{k\ (k=4,5,6)}$ are $\gamma_{ij} = 2\varepsilon_{ij}$ for $i{\neq}j$ in the strain tensor matrix) and $\mathbf{C}$ is the elastic constant matrix. As described in Chapter 2, the cortical bone material was assumed to be transversely isotropic with the following material property relations (Equation 2.13 repeated here for convenience).

$$E_1{=}E_2, \quad v_{12}{=}v_{21}, \quad v_{31}{=}v_{32}, \quad G_{23}{=}G_{13}, \quad G_{12} = \frac{E_1}{2(1+v_{12})} \qquad (4.27)$$

Therefore, the elastic coefficient matrix is (modified from Equation 2.15 which presented this matrix for an orthotropic material):

$$\mathbf{C} = \begin{bmatrix} \dfrac{(1-\nu_{32}\nu_{23})E_1}{\Delta_N} & \dfrac{(\nu_{21}+\nu_{31}\nu_{23})E_1}{\Delta_N} & \dfrac{\nu_{32}(1+\nu_{21})E_1}{\Delta_N} & 0 & 0 & 0 \\[2ex] \dfrac{(\nu_{21}+\nu_{31}\nu_{23})E_1}{\Delta_N} & \dfrac{(1-\nu_{32}\nu_{23})E_1}{\Delta_N} & \dfrac{\nu_{32}(1+\nu_{21})E_1}{\Delta_N} & 0 & 0 & 0 \\[2ex] \dfrac{\nu_{32}(1+\nu_{21})E_1}{\Delta_N} & \dfrac{\nu_{32}(1+\nu_{21})E_1}{\Delta_N} & \dfrac{(1-\nu_{12}^2)E_3}{\Delta_N} & 0 & 0 & 0 \\[2ex] 0 & 0 & 0 & G_{23} & 0 & 0 \\[1ex] 0 & 0 & 0 & 0 & G_{23} & 0 \\[1ex] 0 & 0 & 0 & 0 & 0 & G_{12} \end{bmatrix} \qquad (4.28)$$

Where $\Delta_N = 1 - \nu_{21}^2 - 2\nu_{23}\nu_{32} - 2\nu_{21}\nu_{32}\nu_{13}$

The strain energy density is then calculated as follows [21, 186]:

$$\begin{aligned} SED = {} & \frac{1}{2}C_{11}\left[\varepsilon_{11}^2 + \varepsilon_{22}^2\right] + \frac{1}{2}C_{33}\varepsilon_{33}^2 + \frac{1}{2}C_{12}\varepsilon_{11}\varepsilon_{22} \\ & + C_{13}\varepsilon_{33}\left[\varepsilon_{11} + \varepsilon_{22}\right] + 2C_{44}\left[\varepsilon_{23}^2 + \varepsilon_{13}^2\right] + 2C_{66}\varepsilon_{12}^2 \end{aligned} \qquad (4.29)$$

where C_{ij} are the components of the elastic coefficient matrix in Equation 4.28 and ε_{ij} are the strain tensor components.

Finite difference methods were used to find the discrete approximations of the gradient of the strain energy density [342]. These gradients were necessary for the node smoothing routine and are calculated in each cylindrical direction separately(r, θ, z). From these components, the magnitude of the total gradient is found for all nodes i:

$$\nabla \boldsymbol{SED}(i) = \frac{\partial SED(i)}{\partial \theta}\boldsymbol{\theta} + \frac{\partial SED(i)}{\partial z}\mathbf{z} + \frac{\partial SED(i)}{\partial r}\mathbf{r} \qquad (4.30a)$$

$$\left|\nabla \boldsymbol{SED}(i)\right| = \sqrt{\left(\frac{\partial SED(i)}{\partial \theta}\right)^2 + \left(\frac{\partial SED(i)}{\partial z}\right)^2 + \left(\frac{\partial SED(i)}{\partial r}\right)^2} \qquad (4.30b)$$

At most locations, the fourth order accurate finite difference approximation was used. However, in some locations, such as for the gradient in the radial direction or near the ends of the optimizing surface in the z direction, second order accurate or central difference approximations were necessary. The ends of the optimizing surface were considered to be the top and bottom of the cylindrical growth region at the outer surface and the start of the cancellous filled regions at the inner surface. Appendix B has more details on the calculations of the nodal strain energy density gradients.

In order to identify the neighboring nodes in the gradient calculations, the surface node identifier numbers are sorted first by their local theta coordinate and then by their local z-coordinate and assembled into a matrix. Because of the large number of nodes to be sorted, the heap sort procedure was employed as it is an efficient $N\log_2 N$ process that sorts the data directly in place with no need for extra memory to use as temporary auxiliary storage [258]. Heap sorting is also used for other sorting processes in this developed model as required. Details on this sorting routine are found in Appendix B.

4.4.1.3 Calculation of Amount of Nodal Growth. The third function of the shape optimization/node moving subroutine was to calculate growth. In Subsection 4.3.1, the growth equation chosen for this work was stated as:

$$U_k(l) = \alpha \frac{\left(SED_k(l) - SED_k^{EleAWSurfAvg}\right)}{SED_k^{EleAWStDev}}$$

(4.23)
restated

This equation allows for the arbitrary selection of the growth rate (step size), α, without affecting the resulting shape change predictions because the standardized nodal strain energy density used to drive the growth typically results in a value on the order of -1 to 1.

Because its value did not affect the predicted shape, the growth rate (step size) was selected to ensure a small change in element size per shape optimization iteration for most nodal strain energy densities. Because growth only occurred in the radial direction in this model, the initial radial step size of the mapped hexahedral mesh in the adapting volume, a value of 1e-5 was used as the growth rate (step size), α.

The calculation of the element area weighted average and standard deviation of the elemental strain energy density is described in Subsection 4.3.1. The sorted node matrix, with the theta-coordinate increasing in each row and z-coordinate increasing in each column, is employed to identify the nodes that define each element face so that their coordinates and strain energy densities can be properly used. The element exposed surface area is approximated as:

$$A(e) = r_{avg} \Delta \theta \Delta z \tag{4.31}$$

$$r_{avg} = \frac{1}{4} \sum_{i=1}^{4} r_i \tag{4.32}$$

$$\Delta \theta = \left(\theta_j - \theta_{j+1} \right) \tag{4.33}$$

$$\Delta z = \left(\theta_k - \theta_{k+1} \right) \tag{4.34}$$

i are the nodes on the four corners of 8-node hexahedral element on the optimized bounding surface, j and $j+1$ are neighboring nodes along the theta direction, and k and $k+1$ are neighboring nodes along the z direction. Because the mapped mesh was regular in theta and z coordinates, the element surface areas remained rectangular and the method of area calculation remained valid throughout the analysis. Using these elemental areas,

the weighted average and standard deviation of the local strain energy over the optimizing surface are calculated from Equations 4.19 and 4.24 and the nodal growth is subsequently determined through Equation 4.23 and stored.

4.4.1.4 Mesh Adjustment. Before the nodes are moved, adjustments to the calculated magnitudes of growth are imposed through the surface nodal smoothing routines. This is the fourth function of this user defined subroutine. First adjusted are the nodes which should not move based on their imposed constraints or their locations within the model. Information about the constraint status of each node from the model database is used in the customized subroutine to prevent any constrained nodes from moving. Those nodes are marked as constrained and have their growth magnitudes set to zero, regardless of the calculated value from shape adaptation model. Additionally, nodes at the very ends of the optimizing surfaces that connect to nonadapting elements in other regions of bone are prevented from moving by also forcing zero-magnitude growth. Specifically, on the outer surface, there was a zero growth row of nodes at each end of the cylindrical region before the knee and ankle joint geometries. On the inner surface, the row of nodes that first share cortical and cancellous elements was also restricted from growing.

Because one layer of nodes at the transition elements is prevented from moving, significant distortion may arise as the free nodes of these elements begin to change position. Such distortion can cause stress concentrations that propagate into the surrounding elements. Additionally, these transition regions already have high stress concentrations as they are typically either near areas of large force application at the joints and muscle attachments on the outer surface or near material or geometric transitions like from the hollow to cancellous filled inner bone volume. Because of the

large strain energy density values that develop in these transition regions and the resulting large amount of growth that would occur based on the nodal adaptation model (Equation 4.23), mesh distortion is likely to occur in these regions. This situation is not addressed with the smoothing methods developed in this model thus far. Instead, special rules were established for the movement of the nodes in this transition region that were not based on the nodal strain energy densities or their gradients.

On the outer surface, where boundary conditions may be directly applied to the nodes, the stress concentrations are potentially very large. A transition region with a length equal to the diameter of the initial cylindrical outer surface was defined, following Saint-Venant's principle [186]. A quadratic adjustment is imposed in this region of the outer surface as follows:

$$U_k^{Smooth}(l) = \left(\frac{(Z(l) - Z_{zero})}{D_{ini}} \right)^2 U_k^{Orig}(l) \tag{4.35}$$

where l is the nodal point, $Z(l)$ is the local axial coordinate of node l, Z_{zero} is the local axial location at the border with the boundary condition, $U_k^{Orig}(l)$ is the pre-smoothed nodal growth, D_{ini} is the initial diameter of the optimizing surface, and $U_k^{Smooth}(l)$ is the post-smoothed growth. The effect of creating this transitional growth region on the outer surface is shown in Figure 4.23a.

On the inner surface, the strain energy density variations are less extreme and are mainly a result of the discontinuities between the material properties, geometry and element type from the hollow region to the cancellous filled region. Because the magnitude of the strain energy density variation is likely less extreme on this inner

surface than on the outer surface, the model assigns a linear transition in nodal position over the first three node layers from the start of the inner surface. Figure 4.23b shows representative adjusted regions on the inner surface.

(a)

(b)
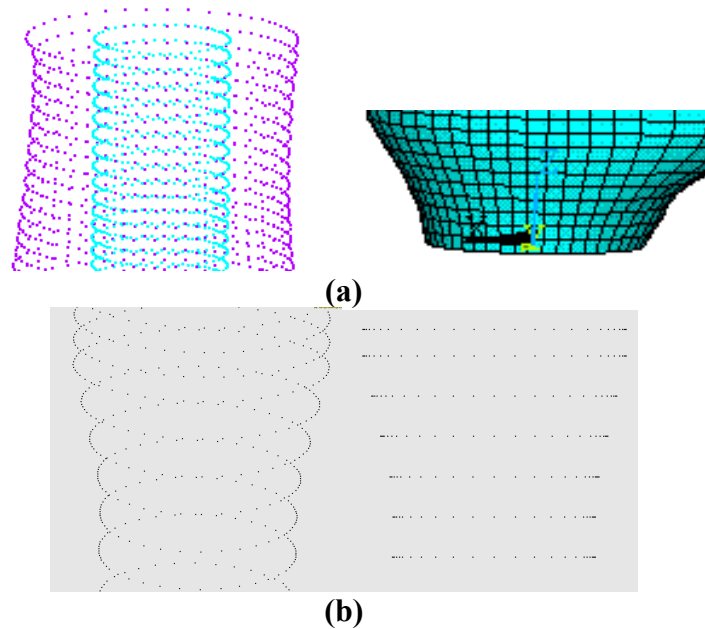
Figure 4.23 Node adjustment on external (periosteal) surface near nongrowing regions. (a) quadratic on outer (periosteal) (b) linear on inner (endosteal) surface.

One final set of nodal adjustments was performed based on a check of violations of prescribed move limit. As described in Subsection 4.3.1, the maximum allowable amount of change in the position of each surface node per iteration was 4% of the element size. Limits are imposed on both the amounts of increase and decrease in element size in the developed model. If the change in a node's position is found to exceed its move limit in the direction of its predicted growth, the growth is adjusted to be the value of the corresponding move limit. Because too high a value of decay can cause element inversion and the inability to solve the structural analysis, every surface node has its own decay limit to prevent element inversion. This decay limit is calculated from the

distance between the node and the first interior node with the same theta and z coordinates. These limits are imposed on the growth control the distortion of the elements, especially between the interior node smoothing iterations (Subsection 4.2.6.1). Because the consequences of high elemental growth are not as dire as that of high elemental decay, the move limit in the growth direction is based on the original element size and, hence, remains the same for every node throughout the optimization.

In the execution of the mesh adjustment procedure, the special transition conditions described above are implemented first. The gradient based smoothing methods described in Subsection 4.2.6.2 (Equation 4.18) are then implemented only on the nodes that were not already adjusted as a result of these special conditions. The smoothing based adjustments to the nodal growth are made sequentially based on the location of the nodes on the optimizing surface, starting from the node with theta, θ, and z values of zero. Because more variation typically occurs in the z rather than the theta direction, smoothing proceeds first in the direction of increasing z before theta is updated. Once one full sweep of node smoothing over the optimized surface is completed, the process is repeated iteratively until the maximum change in any one node position due to the smoothing is less than 10% of the average nodal decay growth limit over the surface being optimized.

Because these smoothing operations are all adjustments to the magnitudes of the growth, the change in nodal position is found only after nodal smoothing through:

$$\mathbf{X}_{k+1}(l) = \mathbf{X}_k(l) + U_k(l)\mathbf{N}_k(l) \tag{4.36}$$

where $\mathbf{X}_k(l)$ defines the current location of the node l in the global Cartesian coordinate system, $U_k(l)$ is the amount of growth (positive is grow, negative is decay), and $\mathbf{N}_k(l)$ is a vector defining the growth direction in the global Cartesian system described above. The global coordinates of each of the nodes in the design set are updated in the ANSYS model database to these newly calculated values and the shape of the meshed representation of the bone is altered.

4.4.1.5 Calculation of Convergence Measures. The fifth and final function of the shape optimization subroutine is the calculation of the convergence measures. As described in Subsection 4.3.1, the model may be stopped when either convergence is achieved or a size limit is reached.

As described in Section 4.3, the developed convergence measure is based on the equivalent extreme values of the range of the nodal strain energy density over optimizing surface. These equivalent extreme values and their difference (Q14Spread) are calculated in the developed Fortran subroutine with the help of the heap sort method to identify the upper and lower quartile sets. The value of the convergence measure is found for each surface at each shape optimization iteration and passed to the APDL script to check for sufficient reduction from the initial value of this measure to stop the process.

There were four size limits used to stop the model independent of the convergence measure: maximum outer diameter, minimum inner diameter, and maximum and minimum cortical (wall) thickness. All size limits are parameters identified through the APDL script and passed to the Fortran subroutine for comparison to the calculated values of these measures based on the nodal growth at each iteration.

Flags are triggered when these size limits are reached, sent back to the APDL script, and used to stop the analysis.

The limits for the maximum outer diameter and minimum inner diameter were based on the distances between the surface nodes and the central cylindrical axis (local z-axis). For the minimum inner diameter limit to be reached, the minimum distance must be less than the initial element size in the radial direction of the mapped mesh. For the maximum outer diameter limit to be reached, the maximum of this distance must be greater than half of the maximum outer diameter of the human tibia bone. While the average maximum measured mid-shaft diameters for bones of various ages and races has been reported as 38.5mm [343], this value was increased 50% to 58mm for the stopping criteria in this work because the developed shape optimization program was expected to predict large growth at areas of direct load application.

The maximum and minimum thicknesses were calculated by finding the maximum distance between pairs of nodes on the inner and outer surface with same theta and z coordinates. The threshold for the minimum cortical thickness of 2mm was derived from measurements of the bones of the paralyzed [344]. As with the maximum outer diameter, the maximum cortical thickness of the normal human bone, 12.5mm [345, 346], was increased 50% to 19mm for the maximum thickness threshold value.

The calculations of the convergence and stopping measures complete the operation of the shape adaptation subroutine. This routine to move the nodal positions based on their stress state is one part of the overall developed model to predict the strength adaptations of a bone. The basic function of the complete numerical process from the establishment of the geometric model to the optimal design is next discussed.

4.4.2 Complete Shape Optimization Routine

Because the model was designed to function completely within a commercial finite element program, the numerical shape optimization routine in this work is directed through a script written specifically to command the commercial finite element code as well as to perform necessary programming functions using data from the finite element program's model database. The overall numerical procedure is presented in the flow chart in Figure 4.24. The APDL script directs the ANSYS processes by defining the system modeled and the system and other model parameters and controlling the simulation and its subsequent analyses. It has four main functions: to set and apply model parameters for both the built-in numerical structural analysis and the customized shape optimization, to establish the means for efficient simulation and subsequent analysis based on this strength adaptation modeling, to execute all user programmable subroutines (that calculate growth, assign node motion, carry out node smoothing, implement growth constraints, and calculate convergence measures), and to control the flow of the simulation including its initiation and termination. Each one of these functions is discussed in detail within the context of the overall function of the developed bone shape strength adaptation modeling methods.
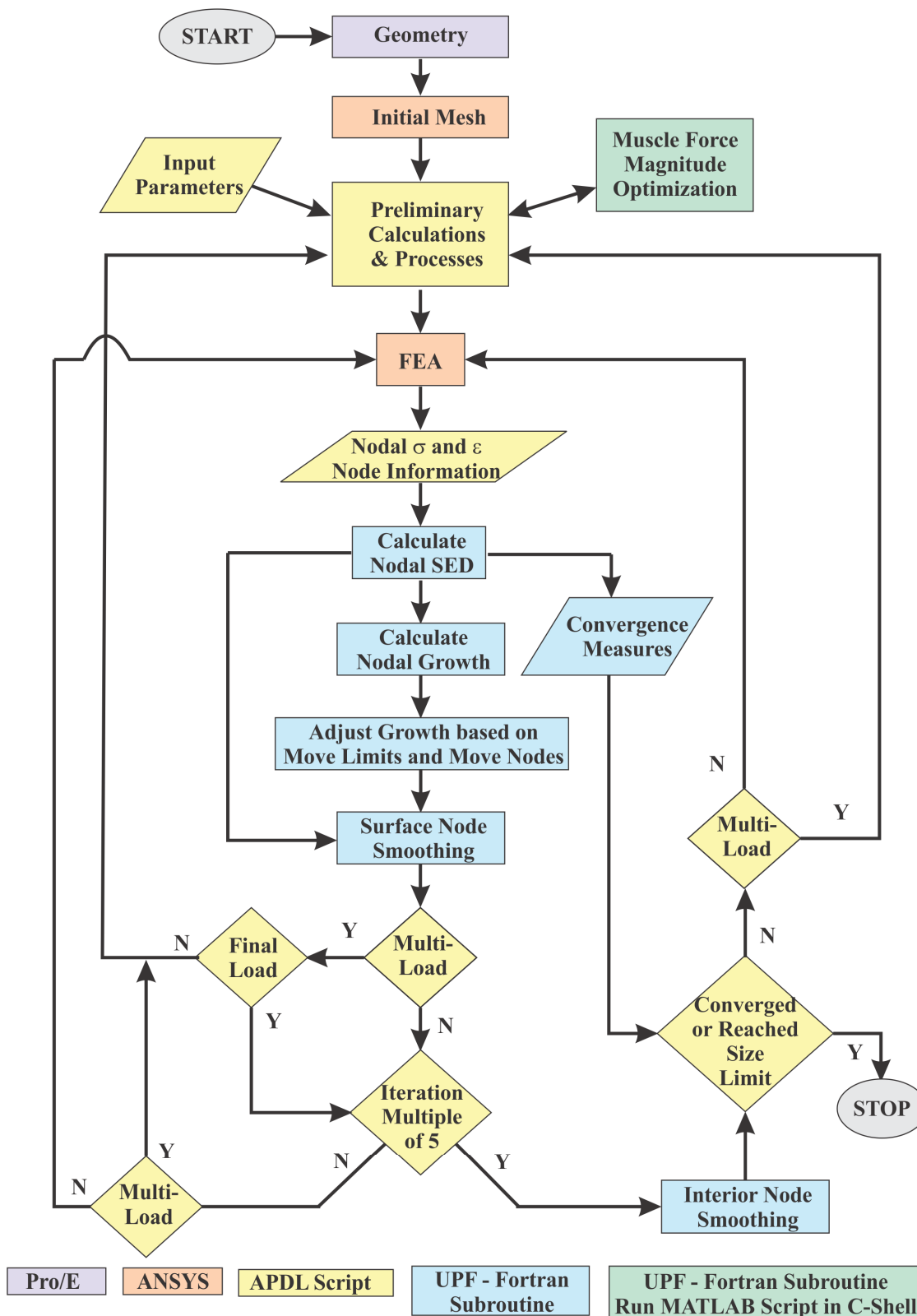
Figure 4.24 Basic operation of computational bone shape adaptation model.

4.4.2.1 Preliminary Tasks. Before the iterative shape adaptation optimization procedure was carried out, a number of preliminary processes were performed to establish the geometry, the discretization, and the parameters used during the analysis.   These preliminary tasks are first described. While the development of the geometry and mesh were done manually, the majority of this preliminary work was accomplished through automating the tasks using the APDL scripting. In this way, the developed program could be applied to any geometric model with few modifications.

The bone volume geometries and their assembly into the limb configurations studied (Figure 2.8 or Figure 5.1) were first created using a three-dimensional CAD software (Pro/Engineer Wildfire 4.0 [172]). Using the CAD software and the definition of the muscle attachment points from the literature [131], the muscle force angular directions (Tables 2.5 through 2.7) were found, as were the moment arms of the defined reaction force at the toe about each joint in the system (Table 2.8).   While each configuration was made using the CAD software to determine these physical parameters, only the assembled bone geometry of the 0° configuration (Figure 2.8a) was imported into the finite element software, through a neutral format file, and meshed as described in Chapter 2. Contacting regions were identified and appropriate properties were assigned based on the preliminary studies discussed in Chapter 2.

Groups of nodes and elements were created and named to aid in the execution of the structural analysis and the shape adaptations. The cortical and cancellous bone regions of each bone segment were defined as were the areas where the muscle forces and displacement constraints were applied. Groups of nodes to define the growth region on the endosteal (inner) and periosteal (outer) surfaces were established.   Using the

mapped mesh of the growth region of the bone, lists of unique theta and z coordinate values were established to ease the selection of desired nodes during the adaptation and surface smoothing processes. Additionally, groups of radial nodes with common z and theta coordinates, sorted from inner to outer surface, were established for use in the internal spring smoothing routine.

The geometric modeling components were defined and established. The local coordinate systems described in Table 2.4 were defined. These local coordinate systems were used to transform the discretized straight leg bone system model to the proper system configurations studied including the 0°, 45°, and 90° configuration models (Figures 2.8b and 2.8c), directly within the finite element model. In each of these discretized multibone leg models, the mesh was disassociated from the bone volumes and the volumes were removed so that the nodes of the mesh were free to move as directed by the bone shape adaptation simulations.

Next, the information used by the muscle force magnitude optimization program was established. The data in Tables 2.3, 2.8 and 2.9 defining the physiological cross sectional area, and the moment arms between the locations of the applied muscle forces and the joint centers were entered through the APDL script and stored in the model database for each of the three limb configurations studied (0°, 45°, and 90°). A flag system was established to signal the appropriate set of data to be used by the Fortran subroutine that performs the muscle force optimization procedure for the conditions studied in each investigation. Parameters to store the resulting individual muscle force magnitudes were created in the APDL script so the values could be used in subsequent procedures.

Then, the parameters directly related to the bone strength adaptation studied were identified in the APDL script. By defining the parameters this way, they became part of the model database, but they could still be easily altered so that the developed numerical model could be used for different systems or configurations without significant changes to the user defined subroutine and customized version of ANSYS. The initial cylindrical dimensions (inner and outer diameters and length) and relative locations of the transition between cancellous filled and hollow regions of the bone undergoing the shape optimization were then identified and assigned. The points used to define the central axis of the growing bone cylinder were created. The constant growth rate factor (step size) used in the shape optimization procedure was defined. Finally, all the parameters used to stop the progress of this optimization process were set. These include the convergence threshold, the maximum size limits, and the maximum number of iterations allowed.

Finally, the material properties selected in Chapter 2 for the particular cortical and cancellous bone regions identified in Figures 2.5 through 2.7 were defined in the APDL script and applied to the appropriate groups of elements during the execution of the structural analysis. Through this automated manner of assigning the material properties, the values used could be easily modified, if necessary.

4.4.2.2 Execution and Control of the Bone Strength Adaptation Simulation. As mentioned previously, the optimization routine is run through the execution of a developed APDL script. This iterative process applies the boundary conditions, performs the finite element structural analysis, calculates the change in nodal position and alters the surface profiles accordingly, smoothes the mesh as required, checks the model results for compliance with stopping criteria and ends the simulation as appropriate. Because the

developed adaptation model allows for the study of the effects of multiple load sets, the script tracks not only the optimization iteration, but also stores the specific load set being applied, so that these multi-load simulations can be undertaken. Data necessary to understand the model function and analyze changes in the bone strength are collected, stored, and output for use in subsequent calculations

Each iteration starts with the application of the boundary conditions. Constraints are applied as defined in the problem statement in Chapter 2. The muscle forces are calculated directly through the user programmable feature subroutine described in Chapter 3 using the appropriate data for the system configuration studied, which was passed directly from the APDL script. From the magnitudes of the muscle forces returned from the muscle optimization program and the muscle force angles and the node groups established in the preliminary processes, individual forces are applied to each node in the predefined muscle force groups as explained in Chapter 2. If a node is subjected to more than one muscle load, the force components are simply added. Because the model is capable of applying a repeated series of load sets, the muscle force magnitudes are cleared at the end of each adaptation iteration and reapplied in the next.

With these boundary conditions applied, the finite element structural analysis is performed. The components of the strains at each of the nodes on the outer and inner surfaces determined from the structural analysis are extracted from the model database and stored in previously defined vector parameters in the defined surface groups. This data is used to calculate the nodal growths in the shape adaptation subroutine. Additionally, the strain component values at the first two radial levels of interior nodes from each surface were also extracted from the model database and stored into a series of

matrix parameters. These strain values are necessary in determining the strain energy density gradients used in the surface node smoothing routine. These strain tensor data as well as information identifying corresponding nodes are passed to the shape optimization routine, which is executed twice for each load set at each iteration, once for the set of nodes on the outer surface and then again for those on the inner surface. A series of flags is used to control the information passed to the optimization subroutine. The flags indicate the surface currently being optimized, ensuring proper data is sent to the subroutine and the appropriate data is returned and stored.

While the calculations of the changes in the positions of the surface nodes are carried within the UPF subroutine, the amount of change for each node is passed back from the growth subroutine to the ANSYS database through the ADPL and stored for use in the interior node smoothing routine. Because the interior node smoothing is performed only every fifth iteration, the total change of the surface node positions over five iterations is retained from the growth routine and is summed for input into the interior smoothing routine. If the iteration is a multiple of five, the interior node smoothing procedure is executed in another Fortran subroutine to calculate the amount of change in the interior node positions based on the changes to the boundary surfaces as per Subsection 4.2.6.1. The values of the global coordinates of these interior nodes are updated in the ANSYS model database, resulting in the regular maintenance of evenly spaced radial nodes over the course of the optimization process.

While the shape optimization subroutine checks on the size limits and sets flags if conditions are met for the termination of the optimization simulation at each iteration, if the size limits are not reached, achievement of convergence is tested only every five

iterations within the APDL script. At this time the Q14Spread from the current iteration is compared to Q14Spread at the start of the optimization simulation through the relation previously defined in Subsection 4.3.1:

$$if\left(\frac{Q14Spread_k - Q14Spread_1}{Q14Spread_1} \geq 0.5\right), \text{ then}$$

Stop Growth: Convergence is Achieved

(4.38)

where k is the iteration count. Because the inner and outer surfaces could converge independently, one surface may continue growing while the other may have stopped. While the continued growth of one surface may influence the strain energy distribution on the other surface, growth was not restarted if the Q14Spread on the converged (stopped) surface fell below this 50% threshold. If a multiload case is studied, the changes to the surface profile continue until the convergence criteria is met for all of the load sets. After both inner and outer surfaces achieve convergence or a size limit is reached, a final stress analysis is performed using the final bone shape, and the process ends.

Data necessary for the subsequent analyses are output from the shape adaptation subroutine and APDL script at each iteration for later use. Such data include the individual growth and final nodal coordinates, strain component values, and strain energy density values and their gradients for each optimization iteration. Convergence data and surface averaged measures at each iteration are also retained. Additionally, images of von Mises stress or displacement distributions or the mesh itself are automatically obtained and stored through the APDL script.

If convergence thresholds are not achieved and no size limits are reached, the optimization process continues. If a single load case is being studied, the muscle force magnitudes calculated in the first iteration can be reapplied in subsequent iterations. In this situation, the iteration count is updated, and the shape optimization is repeated without the re-execution of the muscle force magnitude optimization program. If a multiload case is being studied, additional checks are required to determine if the load just applied is the final case in the set. If it is not, the iteration count is not updated. However, the load set count is updated. The new muscle force magnitudes are calculated through the execution of the muscle optimization subroutine. The new forces are applied to the model for structural analysis and the next shape optimization iteration is performed. If the final resultant force of the multiload case has been applied, then the iteration count is updated, the load set count is reset. Because one optimization iteration may contain a number of subsets for the multiload cases, the growth rate scaling factor α defined in Subsection 4.3.1, which is set based on internal node smoothing occurring every five iterations, is scaled by the number of load cases in the multiload set so that the extreme mesh distortion can be better controlled.

After repeated iterations of this process, either convergence, a size limit, or a maximum number of iterations criterion is met and the process is terminated. The resulting shape is then used in the comparison case study described in Chapter 2. The newly optimized system geometry is placed in the comparison configuration through the coordinate transformations in Table 2.11. Using the comparison case resultant joint moments in Table 2.10 and the physical system parameters in Tables 2.12 and 2.13, the individual muscle force magnitudes are calculated and applied to the system containing

the optimized tibial shape. A single structural analysis in this comparison configuration with the system containing the new tibia shape is performed, and data are collected to quantify the effectiveness of each "optimized" shape at improving the bone's ability to resist this comparison (critical design load) condition at a fracture prone region. This completes the bone shape strength adaptation optimization process.

While the function of each modeling component was validated during its development, a preliminary study was performed to verify the function of the complete numerical model, without the final comparison. The straight leg configuration (0°) was examined under the four loading directions used in the model defined in Figure 4.1. Visual comparisons were made of the change in geometry and the von Mises stress distribution in a cross section at one third of the tibia length from the ankle for each individual case (Figure 4.25). The applied boundary conditions are also shown, with the net generated resultant force at the toe shown for reference along with the resulting displacement distributions.

The comparison, while only visual, clearly shows the different shapes and effects on the von Mises stress distribution that can result by altering the mechanical environment of the tibia bone. Depending on the resultant force direction, for a constant magnitude load, either increases or decreases in the uniformity of the state of stress in a local region can result. The final cross sectional shapes in this figure are similar to the results in Figure 4.1, the preliminary study of the adaptations under the basic combinations of loading modes. For example, the anteriorly directed loading case (Figure 4.25a) in this straight leg configuration showed bending dominate loading at the comparison location (Similar to Figure 4.1c), while the inferiorly directed loading case

(Figure 4.25d) more closely reflected the effects of the combination of compression and bending (similar to Figure 4.1d). The similarities in the local shape changes under similar loading modes predicted using the currently developed methods with model based parameter values and those of the preliminary studies using arbitrarily selected parameters adds to the validation of the function of the current bone shape strength adaptation model. The comparisons of the initial to final local von Mises distributions for each optimizing loading case over the course of the optimization show that the model can demonstrate an improvement of the uniformity state of stress induced by a repeated load under a particular loading condition. The variation of the resulting changes between these cases confirms the need to use a singular, independent load set under which to compare the relative changes in bone strength due to the varied loading conditions.

Load Sets and Displacement

Note:
Displacement contour scale is the same for all cases.

Note:
von Mises stress contour scales are different for each case but are the same for initial and final within a case.

Shape and von Mises Stress Distribution

Initial

Final

(a)   (b)   (c)   (d)
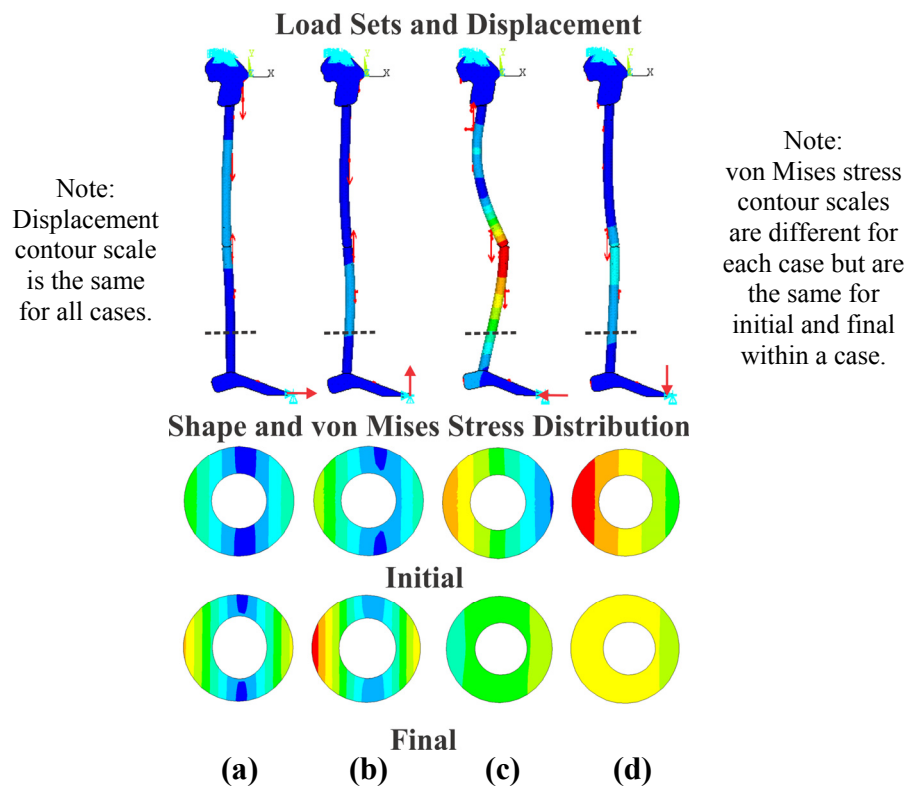
Figure 4.25 Preliminary study to verify function of complete bone shape adaptation model. (a) anteriorly (b) superiorly (c) posteriorly and (d) inferiorly directed resultant.

The modeling method described in this section has met the design goals established for the first part of this research. It functions repeatably without the dependency on arbitrarily selected parameters and without any modifications based on the conditions studied. It has a clearly defined convergence measure which is directly related to the optimization goal of improved uniformity and is not artificially altered by isolated extreme values. Additionally, the direct coupling of the muscle force optimization model provides a more complete representation of the mechanical environment under which the bone strength adaptations occur. Finally, the multisegment skeletal model, with joint contact and appropriate depiction of the cortical and cancellous bone tissue, improves the accuracy in the structural analysis used to drive the shape adaptations. These modeling improvements allow for the direct quantitative comparison of vastly different conditions on shape-based strength changes in bone, a task which has been difficult using previously developed models. The application of the developed model is the subject of the second part of this research and the topic of Chapter 5.

CHAPTER 5

COMPARATIVE STUDIES

5.1 Description

The objective of the first phase of this work was to create a means to quantitatively compare the effects of various loading conditions on the predicted shape strength adaptations of a bone through the development of a computational modeling method. This was successfully completed as described in Chapters 3 and 4. The objective of the second phase of this work was to use the developed model to compare the effects of different loading conditions on the changes in strength of a fracture prone region of bone. In addition to identifying loading modes that may reduce the risk of fracture in a particular region of bone, the "design goal" of the shape optimization studies in this second phase of work, these comparative studies were intended to demonstrate the ability of the developed modeling method to quantitatively evaluate the effects of specific mechanical factors on the strength of a fracture prone region within a system of bones. The leg system chosen for this investigation, and the targeted strengthening region, susceptible to stress fractures, was located a distance one-third of the length of the tibia from the ankle.

The use of the developed model to determine targeted and efficient strengthening methods is especially useful in environments where mechanical countermeasures to bone weakening may be limited by physical space, gravitational forces, and time available to devote to exercise. It was with this focus that the comparative studies presented here were performed using the modeling method developed in the first phase of this work.

5.1.1 Cases Studied

In these comparative studies, the strength adaptations of the tibia bone were investigated under the isometric generation by a leg system of a force at the toe against a fixed surface. Under the static conditions studied, the direction of this net resultant force of the ten muscles and four bony components included in the model of the system studied (Figure 5.1) was varied, but the magnitude of this force remained the same for all cases considered. The resultant forces directions studied were defined to coincide with each of the four global coordinate directions, as shown in Figure 5.1. Note that in Figure 5.1 these selected loading directions are referenced in three ways: by global direction vectors, angular coordinate, and anatomical direction. In this chapter all three descriptors are used interchangeably. In addition to the repeated generation of a force between the toe and the fixed surface in each of the four loading directions depicted, the sequential generation of pairs of these single resultant forces was also studied, for example, the repeated generation of an anteriorly directed load, followed a posteriorly directed load, rather than another anteriorly directed load. Lastly, the sequential generation of all four loading directions in a clockwise rotation, anteriorly, then inferiorly, then posteriorly, then superiorly, as in pedaling a bicycle, was studied. The examination of the shape optimization (strength adaptations) of the tibia bone as a result of these eleven loading conditions was repeated for the leg system arranged into each of the three configurations depicted in Figure 5.1. These configurations, 0°, 45°, and 90° were named based on the orientation of the axis of the tibia bone with respect to the global y-axis. The leg system with the optimal tibial bone geometry created under each of the thirty-three conditions studied was then arranged into a configuration representing the mid-stance phase of

jogging, a condition thought to induce stress fractures of the distal tibia. The muscle forces generated during this jogging condition were applied to the leg bone system modeled and a static structural analysis was performed. Stresses generated in the tibia bone, particularly at the targeted region susceptible to stress fractures, were then compared for each "optimal" bone geometry under this common loading condition, as outlined in Section 2.4. The specific single and multiload cases examined in these comparative studies for each limb configuration studied are listed in Table 5.1. The load cases in this table were used in each of the three limb configurations in Figure 5.1 for a total of thirty-three optimization studies.

Table 5.1 Loading Cases Studied for Each Limb Configuration

	Direction (As in Figure 5.1) and Name
One Load Case	[1,0,0] (Anterior or A) 0°
	[0,1,0] (Superior or S) 90°
	[-1,0,0] (Posterior or P) 180°
	[0,-1,0] (Inferior or I) 270°
Sequence of Two Load Cases	[0,1,0] and [0,-1,0] (S-I) 90°-270°
	[1,0,0] and [-1,0,0] (A-P) 0°-180°
	[0,1,0] and [1,0,0] (S-A) 90°-0°
	[-1,0,0] and [0,-1,0] (P-I) 180°-270°
	[1,0,0] [0,-1,0] (A-I) 0°-270°
	[-1,0,0] [0,1,0] (P-S) 180°-90°
Sequence of Four Load Cases	[1,0,0] [0,-1,0] [-1,0,0] [0,1,0] all around (A-I-P-S) 0°-270°-180°-90°
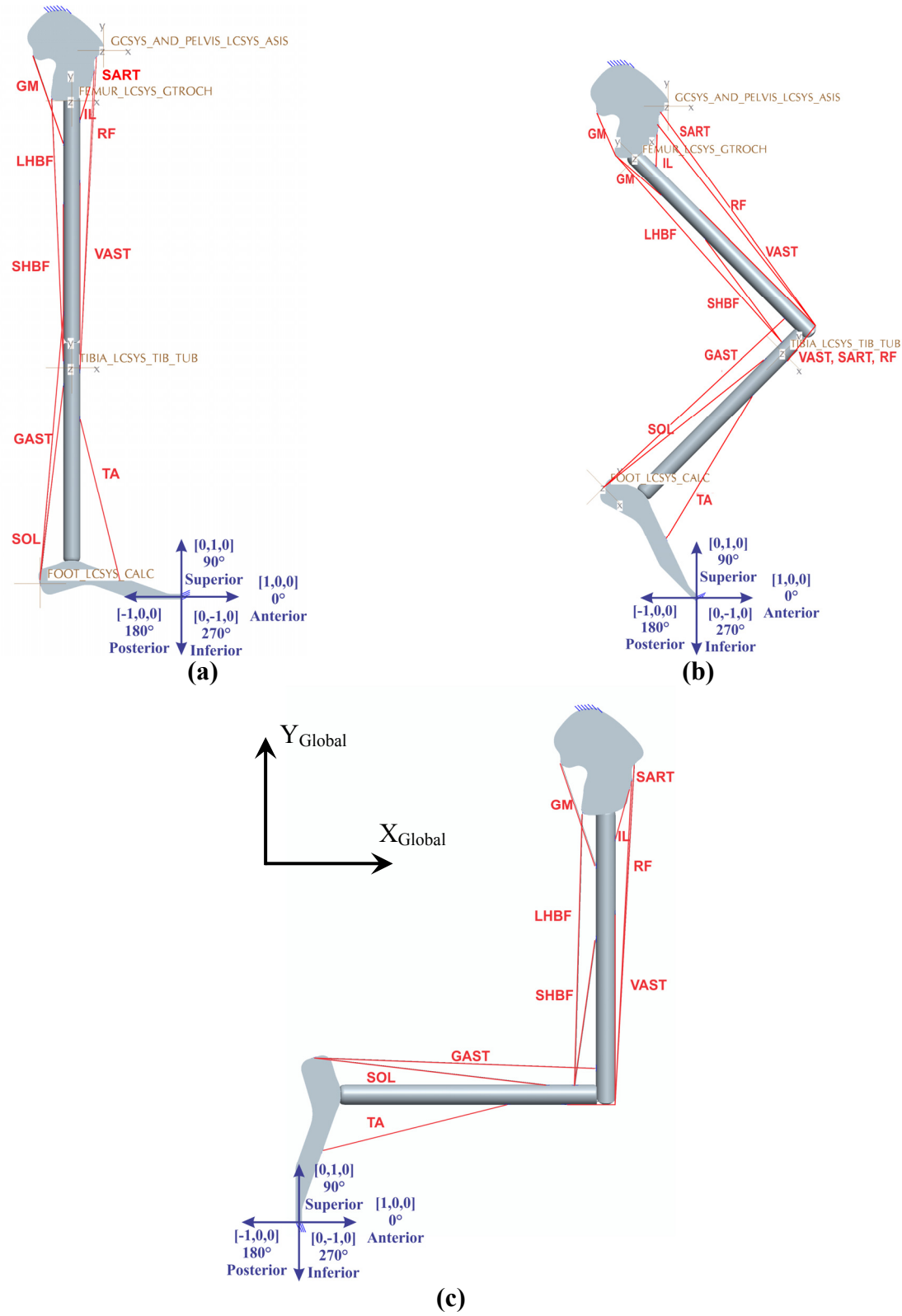
Figure 5.1 Loading conditions and system configurations used for comparative studies, indicating the definition of the net resultant force directions. (a) 0° (b) 45° and (c) 90° configurations.

To compare the effects of each loading case and leg configuration on the resulting shape changes and strength adaptations of the tibia bone, certain data were tracked with iteration and at convergence, so that they could be used in subsequent analyses for each optimization case studied. Global changes to the tibia bone were understood through the tracking of four parameters that were defined in Chapter 4, namely the Q14Spread, the convergence measure, the element area weighted surface average and standard deviation of the elemental strain energy density. To reveal local trends, nodal strain energy density, amount of change in nodal position, and the local radial coordinate of each surface node (based on the local tibial Cartesian coordinate system in Figure 5.1) were tracked over the optimization process at representative locations over each surface studied. In particular, trends at local angular coordinates of 0°, 90°, 180° and 270° around the circumference of the bone and at local axial coordinates of one-sixth, one-third, one-half, two-thirds, and five-sixths of the total length of the optimizing region on both the inner (endosteal) and outer (periosteal) surfaces gave a representation of the behavior over the entire surface. Additionally, for each cross-section created normal to the axial direction at these five axial locations, the minimum and maximum von Mises stress and strain energy density of nodes on the outer circumference were recorded for each iteration. Because geometric measurements have been suggested as indicators of strength, the area, moment of inertia, and the polar moment of inertia at each of these cross-sections defined in the local tibial coordinate system (Figure 5.1) were also tracked with iteration. As an indication of the asymmetry and overall size of the optimized shape, the center of gravity as well as the maximum radial coordinate of the outer surface were measured for these cross-sections at each optimization iteration. Once the optimal

tibial geometry for given set of conditions was determined, measures of the state of stress in the bone under the common ("critical design load") mid-stance jogging conditions, such as the nodal von Mises stress and displacement, were determined and compared amongst all the optimized geometries resulting from the thirty-three cases studied based on combinations of loading conditions studied in Table 5.1 and limb configurations in Figure 5.1. Through the analysis and comparison of the values and trends in these measures, insight can be gained into not only the most and least effective loading conditions to strengthen the distal tibia, but also into the causes of the shape alterations that occur for each loading case studied. These analyses work towards achieving the goals of this phase of the study to better understand the function of the developed shape optimization (strength adaptation) model and to use the model to determine the effects of specific mechanical factors on the strength of a fracture prone region of a bone.

All cases were run on one of two workstations: A 64-bit LINUX Redhat v5.3 machine with dual quad core 2.40 GHz processors and 12 GB RAM and a 64-bit Windows7 machine with dual quad core 2.70 GHz processors and 16 GB RAM. ANSYS v12.1 was used for each analysis. The customization with user defined subroutines was compiled using the Intel Fortran Compilers v10.1 for LINUX and for Windows respectively. MATLAB v2010b (for LINUX or Windows 7) was used to run the muscle force magnitude optimization program and either GCC 4.1 (for LINUX machine) or Visual Studio 2008 (for Windows machine) was used to create the independent executable of this muscle force magnitude code. Run times ranged from two to twelve days, depending on the particular conditions studied.

Because the study was one of comparisons, it was important to ensure that the use of the different software and hardware did not affect the results. To allay this concern, one identical case was run on both machines. The Q14Spread was used as a comparison measure because it is a function of the finite element analysis, the muscle force magnitude optimization, and the calculations within the user defined Fortran subroutine. Throughout the shape optimization studies, the difference in the Q14Spread calculated by each machine was 0% (to seven decimal places). It was, therefore, concluded that the use of two different machines did not adversely affect the results of the comparative studies and helped to expedite its execution.

Before the initiation of this thirty-three case parametric study, two issues had to be resolved. The first was related to the order of the load application in the sequential multiload cases. The second was related to the choice of the constant magnitude of the resultant force whose direction changes with each case studied. These issues were the subject of two final preliminary studies.

5.1.1.1 Effect of Load Order. The effect of the order of the sequence of load application for multiload cases on the resulting system performance and shape predictions was investigated. For this study, the superiorly and inferiorly directed loads were sequentially generated in the straight leg 0° configuration (Figure 5.1) either with the superiorly directed load generated before or after the inferiorly directed resultant load. The cases were run to convergence or maximum size limit, whichever was first achieved. The data described above resulting from the superiorly directed resultant force portion of the sequential multiloadset was then compared. Specifically, convergence measures and element area weighted surface averaged strain energy density were tracked with iteration

for both the inner and outer surfaces under each load order studied. Additionally, plots of the variation of the nodal strain energy density, growth per iteration and local radial coordinate for the last iteration for both inner and outer surfaces were created for each load order case studied. Finally, the geometric measures of the optimal tibial bone shapes generated from each case were calculated at the one-third length cross section. Based on the comparisons of these measures, conclusions could be drawn about the order of load application to be used in the comparative studies.
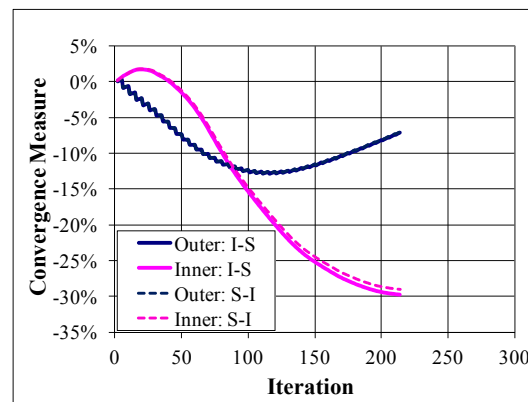
Figure 5.2 Comparison of convergence measure with iteration for the superiorly directed load as the first or the second load in the multiple load sequence.

The average difference in the convergence value over the course of the study was 1% on the outer surface and 8% on the inner surface. Because the inner surface (pink lines in Figure 5.2) proceeded in the converging direction at the start of the optimization before diverging, the larger difference on the inner surface was due to the difference in the iteration where the change from converging to diverging occurred. The difference is noticed because comparisons were made in the convergence measure of only one of the two loadsets in the multiload case examined. That is, when this superiorly directed resultant load was the second in the series, it underwent one additional shape optimization step (that under the inferiorly directed loadset) than the case where it was

applied first (before the inferiorly directed loadset). While small, the presence of this additional shape change iteration was noted when the sign of the convergence measure changed. Of the measures studied, the series order had the greatest effect on the Q14Spread because it considered the extreme values over the surface and, therefore, represented the largest possible differences in nodal values over the optimization domain. Both the average and maximum difference of the element area weighed surface averaged strain energy density resulting from the superiorly directed loadset applied either first or second in the multiple load case studied differed by less than 0.5%.

Visually, the trends in nodal strain energy density, growth per iteration, and radial dimension for both the inner and outer surfaces showed little difference as a result of the applied load order. As a representation of these observed trends, the nodal strain energy density with axial position along the $\Theta=0°$ location of the outer surface is presented in Figure 5.3a. Similarly, the nodal growth per iteration of the inner surface along the same location is shown in Figure 5.3b. Finally, the geometric measures listed above of each of the cross-sections studied differed by less than 1%, most by less than 0.1%.
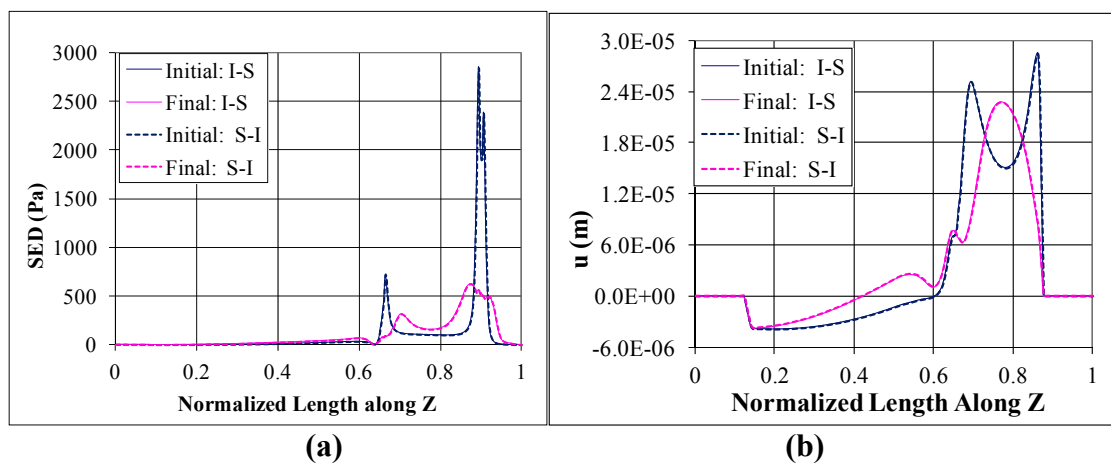
Figure 5.3 Comparison of (a) nodal strain energy density and (b) growth at $\Theta = 0°$ on outer surface for initial and final iterations for the superiorly directed load as the first or the second load in the multiple load sequence.

This study demonstrated that the order of the sequential load application in multiload set cases does not significantly affect the resulting distributions of strain energy density or shape changes. Therefore, the order of application of loads of a multiload case was not critical in these parametric studies.

5.1.1.2 Effect of Load Magnitude. In the comparative studies in this work, the direction, not the magnitude of the resultant force generated by the leg against a fixed plate, is varied. In order to select this magnitude, a series of preliminary studies were performed for the same single, anteriorly directed resultant force case using a number of values spanning an order of magnitude: 50N, 75N, 100N, 125N, 150N, 200N, 500N. To ensure that the trends found were not simply an effect of the particular direction selected, the anteriorly directed force, this analysis was also performed for an inferiorly directed resultant force.

For both directions of the resultant force studied, the change in its magnitude did not change the distribution of the individual muscle force magnitudes (muscle activity) calculated using the muscle force optimization model, as the optimization resulted in muscle force magnitudes that were scaled by the same amount as the input resultant force direction. In general, the von Mises stress distributions, nodal strain energy densities, and final optimized tibial bone geometry varied little with each magnitude of the generated muscle force direction studied. This can be seen from a comparison of the von Mises stress distribution for the 50N, 100N and 500N cases shown in Figures 5.4a through 5.4c with the stress contour scales as appropriate multiples of that used for the 50N case (2x for the 100N and 10x for the 500N). These figures depicts the optimal shape predicted by the model and the resulting stress distributions in the tibia bone on the

outer surface and at a cross section one third of the bone's length from the ankle joint, the targeted strengthening region in this study of the application of the modeling techniques developed in this work.
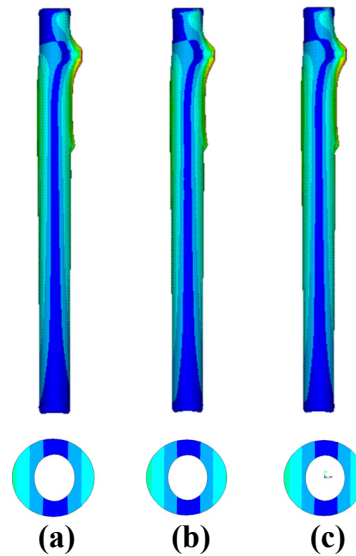
Figure 5.4 Representative von Mises stress distributions after shape optimization for different resultant force magnitudes but same direction. (a) 50N (b) 100N (c) 500N.

Of the two loading direction cases used in this preliminary study of the effect of magnitude of the resultant load, one met the convergence criteria while the other one reached a size limit before convergence could be achieved. For the case where a size limit was reached, the model stopped after a different number of iterations for each resultant force magnitude studied (variation about 10%), resulting in slightly more variation in the final geometry and nodal stresses amongst resultant force magnitudes studied for under this loading direction than for the loading direction where all optimization cases met the convergence criteria. For example, for loading direction when convergence was reached, the greatest variation in the nodal measures amongst the magnitudes studied was less than 1%, but for the loading direction which met the size limits before convergence, the same variation was <5%.

Some effect of the absolute individual muscle force magnitude was noted even though the relative amounts of individual muscle activity were the same for each magnitude case of a given loading direction. While, qualitatively, the von Mises stress (and, consequently, the strain energy density) distributions appeared to be nearly the same, slight variations in nodal values occurred. Figure 5.5a shows a representative case of the first iteration of calculated growth for each shape optimization under a given load direction for the magnitudes listed. The trends in the values of each followed those in Figure 5.5b of the ratio of element area weighted surface average to the element area weighted surface standard deviation. Recalling that growth is proportional to

$$\left(\frac{SED_k(l) - SED_k^{EleAWSurfAvg}}{SED_k^{EleAWSurfStDev}} \right),$$ it is clear that the trends in nodal growth in Figure 5.5a

followed the ratio of the average to standard deviation of the strain energy density over the optimizing surface. Because the data in Figure 5.5 is for the first iteration of calculated growth, it is a function directly of the state of stress in the bone due to the applied individual muscle forces, and is not related to the alterations in the stress state that occur due to the shape adaptation optimization process. Thus, the magnitude of the resultant force that is generated by the leg system does have a small (<10%) local effect on the stress (strain energy density) distribution resulting from the individual calculated magnitudes of the muscle forces even though their relative distribution is consistent over the resultant force magnitudes studied. These local stress effects slightly altered the surface average and standard deviation of the elemental strain energy density used in the growth equation and, therefore, causes slightly different amounts of nodal growth.
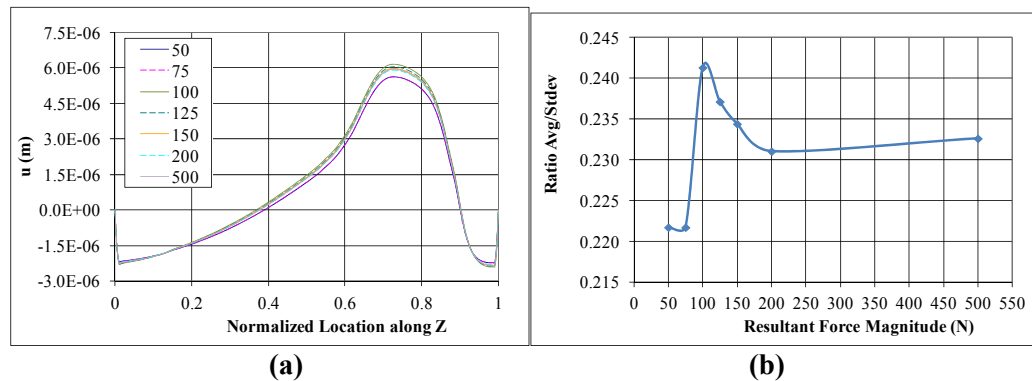
Figure 5.5 Effect of magnitude of resultant force on (a) local nodal growth and (b) global variation stress state over the surface for the first shape optimization iteration.

While the scaling of the individual muscle force magnitudes may have a small effect on the local state of stress and ensuing nodal growth, the overall changes in the shape, and, therefore, strength of the bone have been shown to not be altered significantly. Additionally, the collective effect of the relative magnitudes of these individual muscle forces, such as in their generation of a particular resultant force, has demonstrated a much greater effect on the bone shape strength adaptations, as seen in the differences in optimized geometry under different loading modes in Figure 4.1. Based on this preliminary investigation, the selected value of the magnitude of the net resultant force generated by the leg system was determined not to adversely affect the comparative studies of the relative differences in bone shape strength adaptations that result from the various system conditions investigated. Therefore, the loading conditions compared in the studies presented in this chapter are based on the generation of a 100N net static, isometric, resultant force by the leg between the toe and a fixed surface. This magnitude is consistent with that measured during similar static exercises of the leg in published studies [347] and is approximately one-third of the reported value of the isometric fatigue limit of the leg [348].

These two final preliminary investigations complete the model development and definition for its application in the comparative studies in this work. Because the relative values of the individual muscle force magnitudes have a significant effect on the bone's shape adaptations, the analysis of the results of the described comparative studies begins with an investigation of the individual muscle forces that are generated to create the prescribed net resultant forces in the three limb configurations examined (Figure 5.1).

5.2   Comparisons of Muscle Force Magnitudes

As discussed throughout this work, the mechanical environment of a bone is largely defined by the activity of the attached muscles that pull on the bone in response to more global environmental factors, such as the interaction between a system of muscles and bones and externally imparted forces. The activity of the muscles, represented by a set of individual muscle force vectors, therefore, depends not only on the externally imparted forces that they must resist or overcome, but also on the relative orientation and arrangement of the bone and muscles that comprise the system. By analyzing the effects of the system configuration and the externally applied loads on the activity of individual muscle forces, a better understanding of the mechanical environment of a bone system, which, in turn, drives the bone strength adaptations, is achieved. Accordingly, before the presentation of the changes in the shape of the tibia as a result of the net resultant forces and relative orientations of the leg bone segments in Figure 5.1 and Table 5.1, a discussion of the muscle activity generated for each of these conditions is required. As needed, refer to Figure 5.1, depicting the muscle force lines of action, orientation of the bony system components and the net resultant forces generated. Comparisons are made

amongst the sets of muscle forces that generate the four net resultant loading directions in the three system configurations studied.

5.2.1 Activity of Individual Muscles

As shown in the validation studies presented in Chapter 3, insight into the musculoskeletal system behavior can be gained by analyzing the activity of individual muscles based on their locations of attachment and actions induced in the system studied. Muscles with common actions are called functional groups, and there were six in this study: hip flexors, hip extensors, knee flexors, knee extensors, ankle flexors and ankle extensors. As their names imply the groups function either to increase (extend) or decrease (flex) the joint angles in the leg by moving the lower (more distal) segment towards the upper (more proximal) one. Based on the anatomy near the joints, the hip and ankle flexion occurs in the counterclockwise direction, through the pull of the muscles attached to the anterior (front) surfaces of the leg bones, while the knee flexion occurs in the clockwise direction, driven by the activity of the muscles on the posterior (back) surfaces of these bones.

Because the "function" of these groups is defined by the directions of the rotations they induce about each of the joints and because an angular momentum balance is used in the determination of the individual muscle forces, an analysis of the moments generated by each functional group and each muscle within each group is helpful in understanding the specific set of muscle activities that work together to create each net resultant force studied. In each case studied, a desired resultant force generated by the entire leg system between the toe and a fixed plate is defined. Based on the relative orientation of the bony components in the system, the foot, tibia, femur, and pelvis and their overall dimensions,

the moments the muscles must generate about the hip, knee and ankle joints to create and maintain this force against the fixed surface can be determined (Tables 5.2 through 5.5 for the four resultant force cases studied). The individual muscles needed to create these joint moments are then selected, through the optimization process described in Chapter 3, corresponding to their defined "function", and their intensities are determined through that optimization routine as a function of relative orientations the bony segments in the system and the directions of both the individual muscle forces and the net resultant force. The magnitudes of the forces generated by the individual muscles in this study (a representation of each muscle's activity and intensity during a particular system function) are shown in Figures 5.6a through 5.6d for the four studied directions of the net resultant force generated by the leg in each of the three configurations considered. In these figures, the functional groups and locations of attachment of each muscle are identified for a better understanding of its function within the system. The ability of these load sets to create a 100N force in the desired net resultant force direction at the toe of each system configuration studied will be discussed based on the respective functions of each individual muscle and its specific positioning within the systems studied. While a similar analysis could be performed examining the moments generated by each muscle about each joint, the muscle forces directly affect the local stress state of the bone, which drives the functional adaptations, and, therefore, is of greater interest in this work.

Some muscles considered in this developed model create moments about more than one joint. As described in Table 2.2, four of the ten muscles studied create moments about two joints. Therefore, while the force exerted by such a muscle may be generated with the main objective of producing a moment about one joint, its arrangement within

the system will cause it to create another moment about an additional joint. If this second moment is not needed for the generation of the net desired system function, other muscles must be activated with the opposing function to counter this extraneously generated moment. This "antagonistic" muscle activity is important to the system function, as, while it may reduce the moment generated about a joint, it increases the forces on the bones in the system, thus contributing to their overall stress state which drives the strength adaptations studied in this work.

While a static isometric loading condition is studied in this work, the muscle activity may be better understood when considering the "actions" each muscle and the resultant force direction induce. Therefore, in this way of understanding the muscle function, their actions may be described as "inducing a small rotation" about a joint even though no such action actually occurs under the conditions studied. Similarly, the anteriorly and posteriorly directed force (in the global x-direction in Figure 5.1) may be considered as actions to kick a ball, and the superiorly and inferiorly directed forces (in the global y-direction in Figure 5.1) may be considered as actions to climb a stair or stomp a foot. Figures are arranged in this chapter to allow for direct comparisons.
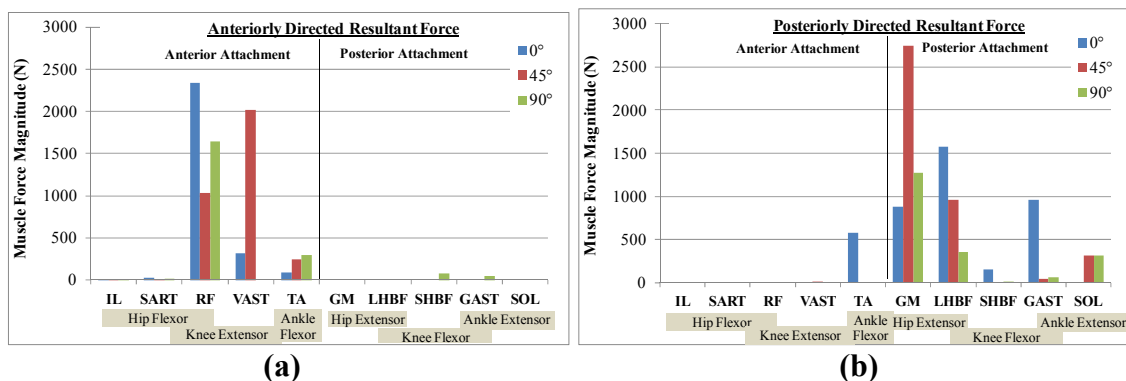
(a)   (b)

Figure 5.6 Comparison of muscle activity of the leg in the three configurations studied to create an (a) anteriorly (b) posteriorly (c) superiorly and (d) inferiorly directed static resultant force between the toe and a fixed surface.
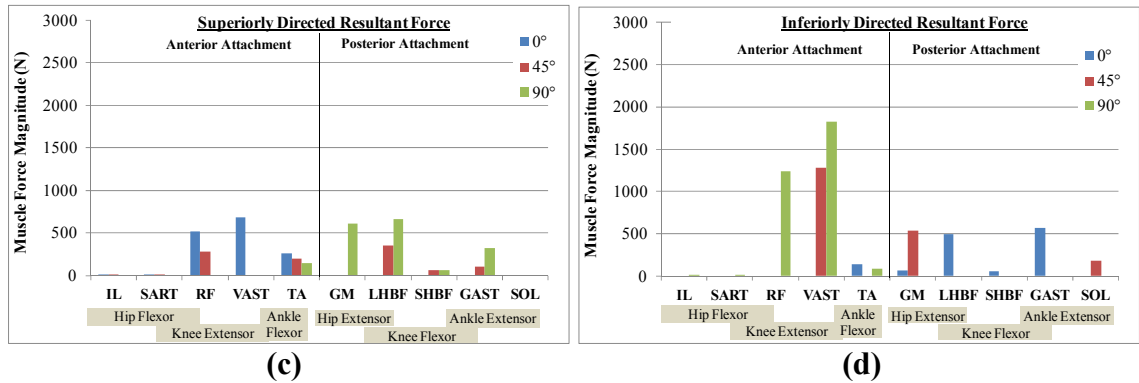
Figure 5.6 Comparison of muscle activity of the leg in the three configurations studied to create an (a) anteriorly (b) posteriorly (c) superiorly and (d) inferiorly directed static resultant force between the toe and a fixed surface. (Continued)

5.2.1.1 Anteriorly Directed Resultant Force. The anteriorly directed resultant force is caused by counterclockwise moments about each joint in each configuration studied (Table 5.2). Therefore, the main activity is in the hip and ankle flexor and knee extensor muscles (Figure 5.6a). The differences in the relative intensity of the individual muscles within each of these functional groups are related to the positioning of the muscles within the system. Of the four muscles that are active under this configuration, two act on both the hip and the knee joints. Because the sartorius muscle has a cross sectional area that is ten times smaller than that of the rectus femoris and the optimization process minimizes a function of muscle stresses, the sartorius creates a very small force compared to the dominant the rectus femoris muscle force, and its activity is nearly negligible.

The tibialis anterior muscle, ankle flexor, activity increases with increasing ankle moment (Table 5.2) in the progression through the 0°, 45°, and 90° configurations as the angle between the foot and tibia remained fixed, maintaining a constant moment arm between the tibialis anterior muscle and the joint center, while the orientation of the tibia transitions from parallel to the global y-axis to parallel to the global x-axis (Figure 5.1).

In the 0° configuration, the anteriorly directed muscle force is generated by progressively increasing moments about the ankle, knee and hip joints. The ankle moment generated by the tibialis anterior muscle has already been discussed in the previous paragraph. The large rectus femoris muscle contributes most significantly to the anteriorly directed resultant force in this configuration, with a force nearly two orders of magnitude more than that of any other muscle. It functions to generate the hip moment nearly completely itself, with only slight help from the sartorius muscle. The moment that the rectus femoris generates about the knee is amplified by a small amount of additional activity by the vastii, which acts only on the knee. From this load set, the anteriorly directed resultant force imparted by the straight leg on the fixed surface can be thought of as a ball being kicked forward at the foot mainly as a result of a counterclockwise rotation about the hip joint.

In the 45° configuration, with both hip flexed at 45° and the knee flexed at 90°, the knee extensor muscles dominate the generation of the anteriorly directed net resultant force. Both the rectus femoris and vastii muscles are very active, with the magnitude of the vastii twice that of the rectus femoris (Figure 5.6a). This smaller magnitude of the rectus femoris muscle force despite the larger magnitude of the moment about the hip compared to the knee (Table 5.2) is, in part, due to the increased moment arm between the rectus femoris muscle and the ankle joint with the flexion of the hip in this configuration (Figure 5.1).

The large knee extensor activity can be explained in terms of the "small rotations" induced about the hip and knee joints to create the anteriorly directed "kick" at the toe. With the femur at a 45° angle with the global y-axis, an increase in flexion

(counterclockwise rotation) at the hip caused by the rectus femoris muscle would tend to move the femur towards the global positive x-axis, making it more horizontal (parallel with the anteriorly directed net resultant force). This reduces the ability of the rectus femoris to contribute to the generation of an anteriorly directed resultant force simply through the rotation of the femur about the hip joint. In contrast, the tibia makes a -45° angle with the global y-axis, and an increase in extension (counterclockwise rotation) of the knee joint by the vastii and rectus femoris muscles would cause the tibia to approach the global y-axis, making it more vertical (normal to the anteriorly directed net resultant force). This increases the horizontal component of the muscle forces (or the forces generated by the movement of the foot at the end of the tibia rotating about the knee). This described activity is the desired resultant force direction. Therefore, from this load set, the anteriorly directed resultant force generated by the leg in the 45° configuration can be thought of mainly as a kicking a ball at the foot due to a counterclockwise rotation about the knee joint.

In the 90° configuration, the femur is in the same orientation as it is in the 0° configuration, but the knee is flexed at 90°, making the tibia parallel to the global x-axis (the anterior-posterior direction) (Figure 5.1). In this configuration, the rectus femoris muscle, which couples hip flexion and knee extension (or counterclockwise moments about each of these joints), dominates, and there is no additional individual knee extensor activity (Figure 5.6a). In fact, the antagonistic knee flexor muscles, the short head of the biceps femoris and the gastrocnemius that create opposing, clockwise moments about the knee joint, are slightly active to modulate the large moment generated about the knee due to the rectus femoris muscle.

As in the 45° configuration, the relative muscle activity can be understood when considering the relative orientations of the femur and tibia with respect to the direction of the resultant force. In this 90° configuration, the tibia is parallel to the global x-axis and pointed in the posterior direction with respect to the knee joint. When extending the knee from this position through a counterclockwise rotation, the force at the toe due to this rotation would initially have a very large vertical component and will not significantly contribute to the net anteriorly directed force at the toe, parallel to the global x-direction. With the femur aligned with the global y-direction, a small rotation about the hip joint would cause a force at the knee to have a very large horizontal component, which is the desired force direction. Therefore, the anteriorly directed resultant force in the 90° configuration can be thought of a forward "rolling" action of a ball at the toe by the foot mainly through a counterclockwise rotation about the hip joint.

Table 5.2 Moments Created About Joints by the Active Set of Muscles when Generating an Anteriorly Directed Net Resultant Force (CCW+) (N-m)

	0°	45°	90°
Ankle	6.4	18.3	19.5
Knee	46.6	46.7	19.5
Hip	88.6	76.4	61.5

5.2.1.2 Posteriorly Directed Resultant Force. The joint moments generated to create the posteriorly directed (negative global x-direction) resultant force are equal in magnitude and opposite in direction from the anteriorly directed (positive global x-direction) resultant force (Table 5.3). However, the muscle activity is more varied (Figure 5.6b). While the majority of the active muscles are on the posterior side of the bone system, there is some antagonistic ankle flexor activity. In all of the configurations

studied, the hip extensor muscles dominate the generation of the posteriorly directed force with varying contributions of the knee flexors and ankle extensor muscles, as the long head biceps femoris creates moments about both the knee and hip joints and the gastrocnemius causes moments about the knee and ankle.

In the 0° configuration, the hip extensors and knee flexors show nearly equal intensities of activity. The long head of the biceps femoris creates the largest force with the gluteus maximus and gastrocnemius generating about two-thirds of its magnitude, each amplifying the hip extension and knee flexion activity, respectively, of the long head biceps femoris muscle (Figure 5.6b). Because the gastrocnemius also acts to extend the ankle, the relatively large magnitude of this force creates a large moment about the ankle that is modulated through the antagonistic tibialis anterior ankle flexor activity. Therefore, the posteriorly directed force at the toe in this straight leg configuration can be thought to be generated by large hip extension (clockwise rotation) and knee flexion (clockwise rotation) to pull the entire leg backwards towards the heel (negative global x).

Under the 45° configuration, the hip extensors are dominant, with three times the total force of the knee flexors. This force distribution is driven by the very large gluteus maximus force. The large increase in this force over the 0° configuration is due, in part, to the decrease in its moment arm about the hip joint as the hip is flexed at the 45° angle (Figure 5.1b). Similarly, the decrease in the magnitude of the long head of the biceps femoris muscle force over that generated in the straight leg configuration is partly offset by the increase in the distance between its line of action and the center of the knee joint as described in Chapter 2 (Figure 5.1b). Because no additional moment about the knee is needed to create the net knee joint moment desired, the ankle moment is generated

completely by the soleus, which acts only on the ankle joint. The analysis of the relative intensity of the hip extensor to the knee flexor muscle forces in generating a posteriorly directed resultant force in this 45° configuration follows the descriptions of the conditions for the anteriorly directed force in this configuration. However, while the orientation of the bones with respect to the global coordinate system is the same in this analysis, the posteriorly directed force is generated by oppositely directed moments about the joints, resulting in opposite behavior of the system due to muscle activities.

The analysis proceeds with the similar "imaginary" small rotations about the joints. Further extension of the hip joint from this 45° position would bring the femur more vertical, increasing the horizontal component of the force generated by the motion of the knee (and below) resulting from the rotation of the hip, enhancing the resultant force generated in the desired direction. In contrast, the further flexion of the knee would bring the tibia more horizontal, increasing the vertical component of the resultant force generated at the ankle (and below) against the fixed surface, which is not the desired effect. This analysis helps to explain the dominance of the hip extension functional group when generating the posteriorly directed "back kick" in the 45° configuration.

A similar trend is seen in the 90° configuration with the posteriorly directed loading, which results in very high hip extensor muscle forces (Figure 5.6b). In this configuration, the gluteus maximus muscle generates a force more than three times that of the long head biceps femoris and soleus. As in the 45° configuration, the gastrocnemius has a minor, insignificant role relative to the other active muscles. No antagonistic muscle force activity is generated in this configuration.

Following the "small rotation" analysis, it is easy to see that a clockwise rotation of the hip joint in this configuration would create a horizontally directed force at the knee and below, while that of the knee would create a vertically directed force at the ankle and below. Thus, the "back kick" action seen in the 45° configuration is repeated in the 90° configuration. The ankle extensor (soleus) activity is used to translate forces generated by the hip and knee rotations from the ankle to the toe, the location of the resultant force generation, while maintaining the 90° orientation between the tibia and the foot.

Table 5.3 Moments Created About Joints by the Active Set of Muscles when Generating a Posteriorly Directed Net Resultant Force (CCW+) (N-m)

	0°	45°	90°
Ankle	-6.4	-18.3	-19.5
Knee	-46.6	-46.7	-19.5
Hip	-88.6	-76.4	-61.5

5.2.1.3 Superiorly Directed Resultant Force. The superiorly directed resultant force acting to pull the toe upwards, results in more variation in the active muscles among the three configurations studied and significantly smaller muscle force magnitudes (Figure 5.6b) than the anteriorly or posteriorly directed forces to create the much smaller resultant joint moments (Table 5.4). The generation of this resultant force direction in the 0° configuration is dominated by the anteriorly attached muscles while that in the 90° configuration is dominated by the posteriorly attached muscles. As can be deduced, the 45° configuration has the most diverse muscle activities for this resultant force direction.

In the 0° configuration, the leg is straight, and the superiorly directed force corresponds to the lifting of the toe, as in a toe tap. All the joint moments are the same because the joints are in line, parallel to the superiorly directed resultant force vector. Because the moment arm of the tibialis anterior muscle to the ankle joint is the largest, it

creates the smallest of the active muscle force magnitudes. With all the joint moments the same, the vastii generates the largest muscle force because it has the smallest moment arm about the joint on which it acts compared to the other active muscles in this condition. The vastii acts about the knee joint only and the line of action is parallel to that of the resultant force. Therefore, it contributes significantly to the "upwards" pulling of the foot. Finally, the rectus femoris generates the largest force of the muscles that act on hip joint. Although the iliacus and sartorius were also active, their cross-sectional areas were much smaller and, therefore, produced minimal forces.

The analysis used in the posteriorly and anteriorly directed resultant force under the 90° configuration can be applied to understand the muscle activity to direct the resultant force superiorly in this 90° configuration, where the hip and knee had equal magnitudes of clockwise joint moments (hips extension/knee flexion) and the ankle had a very slight extension moment. The superiorly directed resultant force at the toe in the 90° bent back configuration is generated mainly through knee flexor activity. Because of the relatively large moment arms of the knee flexor muscles about the knee joint in this configuration, the long head biceps femoris and gastrocnemius muscles produce forces of moderate magnitudes. Because the ankle does not require as large a moment as that which is generated by the gastrocnemius in its contribution to knee flexion activity, the antagonistic tibialis anterior muscle forces are activated to modulate the moment induced by this ankle extensor. The clockwise hip moment is enhanced by the gluteus maximus, which acts solely to further pull the toe upward.

In the 45° configuration, the superiorly directed load can be thought of as folding up the leg, as occurs when the toe is being pulled up off the ground to take a step.

Therefore, all flexor muscles are activated to pull the toe "inward" or more proximal. The most activity occurs about the knee joint since it is in the middle of the configuration, and the knee flexor activity must be sufficient to compensate for the knee extensor moment that is generated by the rectus femoris muscle as a secondary result of its produced hip joint flexion. Therefore, the rectus femoris and the long and short heads of the biceps femoris and the gastrocnemius and the tibialis anterior muscles all act in concert to create the superiorly directed force at the toe in this bent leg 45° configuration.

Table 5.4 Moments Created About Joints by the Active Set of Muscles when Generating a Superiorly Directed Net Resultant Force (CCW+) (N-m)

	0°	45°	90°
Ankle	19.5	9.3	-6.4
Knee	19.5	-19.1	-46.6
Hip	19.5	10.6	-46.6

5.2.1.4 Inferiorly Directed Resultant Force. As with the anteriorly and posteriorly directed resultant forces, the joint moments required to generate the inferiorly directed resultant force are equal in magnitude and opposite in direction to those which generate the superiorly directed force (Table 5.5). However, the resulting individual muscle activity is very different (Figure 5.5d). While it is expected that the active muscles used to create the inferiorly directed resultant force would generate opposite moments (antagonistic activity) to those that produce the superiorly directed one, the muscle force magnitudes to induce the moments are very different. In fact, the muscle force magnitudes required to generate the inferiorly directed force are three to four times greater than those to create the superiorly directed forces in the bent leg configurations. First, however, the straight leg configuration is discussed.

In the 0° configuration, the knee flexors dominate to push the toe down, with nearly equal intensities from the long head biceps femoris muscle pulling up on the tibia and gastrocnemius muscle pulling up on the heel, both creating clockwise rotations about the knee that result in the downward action at the toe. The activity of the gastrocnemius muscle also works to create the required clockwise ankle moment to further push the toe downward, in the desired resultant force direction. Because the gastricnemius activity produces a clockwise moment about the ankle greater than what is required to crate the net resultant force, the tibialis anterior muscle must generate an antagonistic, counterclockwise, modulating moment. The short head biceps femoris adds a little to the knee joint moment created by the long head of the biceps femoris as does the gluteus maximus muscle in creating a counterclockwise rotation about the hip joint.

It is interesting that the gastrocnemius and the long head of the biceps femoris both work to flex the knee but actually create opposing moments about the knee joint since one attaches on the femur side and the other attaches on the tibia side. This configuration has direct implications on the stress state that is created by when both of these muscles are active, as in these superiorly and inferiorly directed resultant forces, since the moments induced by one muscle on the tibia would oppose moments induced on the tibia by the other muscle.

In the 90° configuration, the activity is dominated by the knee extensor muscles that would rotate the lower leg counterclockwise and move the ankle downward, creating a large force parallel to the global negative y-direction at the toe. Thus, the vastii muscle force is very large, aided by the rectus femoris muscle force. The hip flexor force of this muscle would aid in the downward movement of the toe as the knee rotates forward. A

small tibialis anterior muscle force generates the small ankle flexor moment that prevents the ankle from extending in this fixed limb configurations under the forces generated by the other active muscles.

Finally, in the 45° configuration, in direct opposition to the muscle activity required to generate the superiorly directed resultant force, the hip, knee and ankle extensors work together to "unfold" the leg from this bent position as when climbing a stair or propelling during a run. The relatively large moment arms at the soleus and gluteus maximus in combination with the larger joint moment at the knee result in very large vastii muscle forces compared to the other two active muscles. It is interesting to note that because of the function of the muscles selected for inclusion in this study, the inferiorly directed force can be generated by muscles that act only on one joint each, eliminated the need for the modulation of the resulting joint moments with antagonistic muscle activity as was seen in the superiorly directed resultant force.

Table 5.5 Moments Created About Joints by the Active Set of Muscles when Generating an Inferiorly Directed Net Resultant Force (CCW+) (N-m)

	0°	**45°**	**90°**
Ankle	-19.5	-9.3	6.4
Knee	-19.5	19.1	46.6
Hip	-19.5	-10.6	46.6

5.2.1.5 Relative Muscle Force Intensity. In many experimental studies, the measurement of the electrical activity in an individual muscle is used as an estimate for the intensity of the activity of a muscle in the system investigated. To obtain a quantitative measure of this relative activity of the set of muscles within the system, the strength of the recorded electrical signals of each individual muscle is often normalized to the maximum value in the active set [126]. In Chapter 3, the usefulness of this

normization process in understanding the contribution of each individual muscle to the overall system function was demonstrated, even when the actual muscle force magnitudes were known. Therefore, such an analysis was performed with the predicted muscle force magnitudes for each of the cases modeled in this comparative phase of the work to better compare the relative intensities of the individual muscle forces for each of the conditions studied. The ratio of the individual muscle force magnitudes to maximum magnitude of all active muscles for each loading direction and limb configuration are presented in percentage form in Table 5.6.

Table 5.6 Relative Intensity of the Individual Muscle Force Magnitudes for the Set of Active Muscles in Each Loading Case Considered

		[1,0,0] Anterior			[-1,0,0] Posterior			[0,1,0] Superior			[0,-1,0] Inferior		
		0°	45°	90°	0°	45°	90°	0°	45°	90°	0°	45°	90°
Anterior Attachments	IL	0.3%	0.1%	0.4%	0.0%	0.0%	0.0%	0.2%	0.4%	0.0%	0.0%	0.0%	0.2%
	SART	1.0%	0.6%	1.0%	0.0%	0.0%	0.0%	0.8%	1.1%	0.0%	0.0%	0.0%	0.7%
	RF	100.0%	51.0%	100.0%	0.0%	0.0%	0.0%	75.4%	79.2%	0.0%	0.0%	0.0%	68.2%
	VAST	13.3%	100.0%	0.0%	0.0%	0.5%	0.0%	100.0%	0.0%	0.0%	0.0%	100.0%	100.0%
	TA	3.6%	12.1%	18.1%	36.8%	0.0%	0.0%	38.0%	57.6%	22.2%	23.9%	0.0%	4.7%
Posterior Attachments	GM	0.0%	0.0%	0.0%	55.5%	100.0%	100.0%	0.0%	0.0%	92.5%	11.2%	41.8%	0.0%
	LHBF	0.0%	0.0%	0.0%	100.0%	34.9%	28.1%	0.0%	100.0%	100.0%	86.6%	0.0%	0.0%
	SHBF	0.0%	0.0%	5.0%	9.5%	0.0%	0.1%	0.0%	17.6%	9.6%	9.3%	0.0%	0.0%
	GAST	0.0%	0.0%	3.0%	60.5%	1.6%	5.3%	0.0%	30.3%	48.4%	100.0%	0.0%	0.0%
	SOL	0.0%	0.0%	0.0%	0.0%	11.4%	24.4%	0.0%	0.0%	0.0%	0.0%	14.3%	0.0%

In the cases where the anteriorly attached muscle forces dominate, either the rectus femoris or the vastii consistently produced the largest forces while the sartorius and the iliacus provided only minor additions. This directly follows the relative sizes of their physiological cross-sectional areas and verifies that the model predicts force magnitudes that are capable of being generated by the individual muscles (as muscles with smaller areas cannot generate as great forces as can larger sized muscles). The tibialis anterior muscle, which is the sole ankle flexor on the anterior side of the bone system modeled, usually produces a force with a much lower magnitude than any of the knee flexor and hip extensor muscles acting on this "front" side of the bone, especially

when the others dominate. This could be due in part to its muscle size, as it is half the size of the rectus femoris and about one quarter that of the vastii. However, the relatively small tibialis activity is also due to its relatively large moment arm about the ankle joint when compared to similar distances for the other anteriorly attached muscles on the leg.

When the posteriorly attached muscles dominate, it is the long head of the biceps femoris or the gluteus maximus that provides the majority of the force intensity in most of the conditions examined. This is likely due to the relatively large size of these muscles (Table 2.3). The matching of antagonistic muscle force magnitudes is readily seen using this "normalization" analysis. For example, the ankle extensor function of the gastrocnemius is essentially eliminated by the greater ankle flexor tibialis anterior force in the superiorly directed load in the 45° configuration.

Presenting the muscle force magnitudes in this manner is also helpful in comparing cases. For instance, in the 0° configuration, the same muscles are active to produce a posteriorly and an inferiorly directed resultant force. However, their relative intensities are different, with the gluteus maximus and long head of the biceps femoris having a much greater influence in the posteriorly directed force and the gastrocnemius having dominance in the inferiorly directed force.

Through the use of the developed muscle force magnitude optimization model, the behavior of the individual muscle forces could be revealed and quantified. By analyzing the magnitudes of the forces generated by the ten muscles in this study, their contributions to overall system function could be better understood. In analyzing the changes in bone strength that these individual muscle forces induce, their effect on the stress distribution within the adapting region of the bone is important. While the local

stress state is affected by the behavior of the entire system in response to the combination of muscle forces and external forces, it is directly impacted by the forces of the muscles directly attached to the adapting bone by the activity of the muscles that act nearby.

5.2.2 Activity of Muscles Local to the Tibia Bone

Eight of the ten muscles in the selected system directly affect the tibia bone, the site of bone shape strength adaptation simulation in this work. Therefore, it is worthwhile to consider their behavior in the various conditions examined in this comparative study as a way to better understand the shape adaptations that occur. The attachment of muscle directly to the tibia occurs entirely in the upper one third of the bone, near the knee. Three knee extensors function in this proximal region. Two, the rectus femoris and the vastii, attach at the same location on the anterior side of the bone, while the third, the sartorius attaches just five millimeters below. Just slightly above this, towards the knee by one centimeter but on the opposite (posterior) side, both the long and short heads of the bicep femoris, the knee flexors, attach to the tibia. Five centimeters below this, also on the posterior side, acts the soleus, the ankle extensor. The ankle flexing anterior tibialis acts an additional five centimeters towards the ankle from the soleus but on the anterior side. Though not directly attached to the tibia bone, the gastrocnemius straddles it on the posterior side, attaching directly above the knee and below the ankle at the heel, thereby directly influencing the behavior of the tibia bone. Figures 5.7a through 5.7d depict the magnitudes of the forces generated by these muscles at each location at which they act upon the tibia bone.
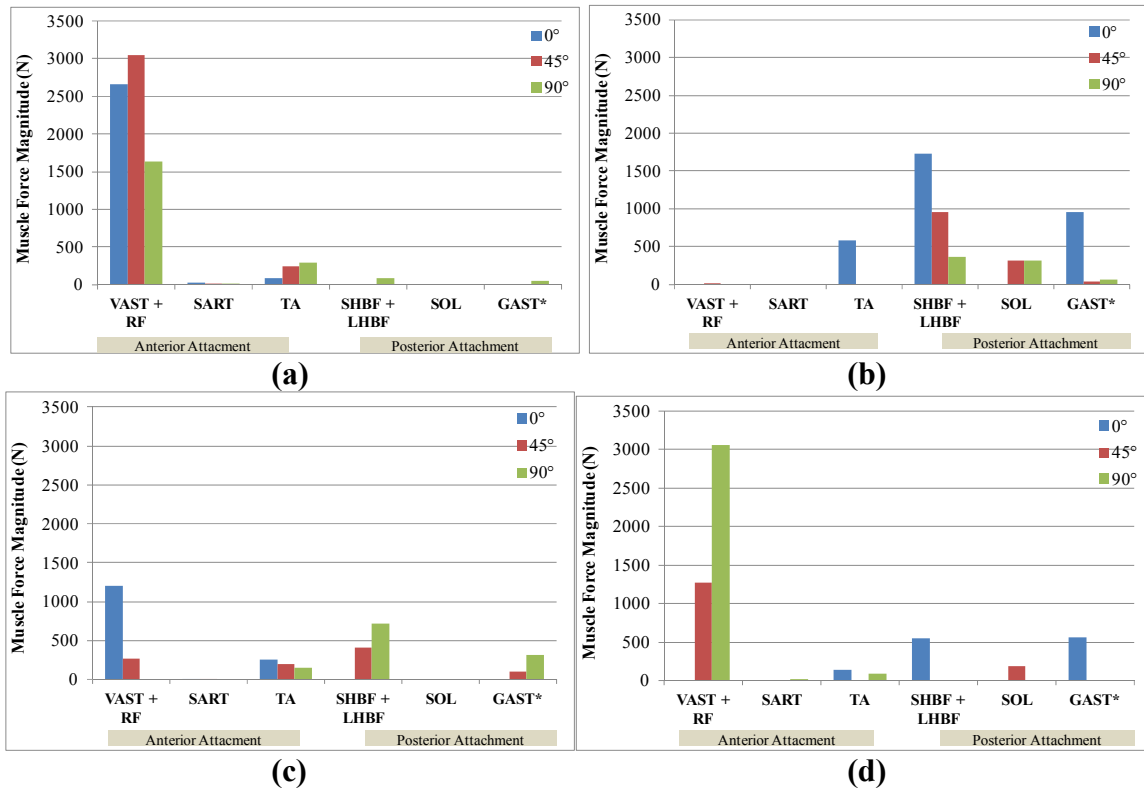
Figure 5.7 Comparison of magnitudes of the forces generated by the eight muscles directly influencing the behavior of the tibia bone in this investigation. The figure shows the activity under the three leg configurations specified that work together to create an (a) anteriorly (b) posteriorly (c) superiorly and (d) inferiorly directed static resultant force on a fixed surface at the toe. * does not attach directly to the tibia bone.

5.2.2.1 Anteriorly Directed Resultant Force. The knee flexors that act together on the tibia in the same location, the vastii and rectus femoris, produce substantially greater forces than any other active muscles that contribute to the anteriorly directed force for all three configurations. The net forces generated by these muscles are generally two to three orders of magnitude greater than any of the other active muscles on the anterior side of the bone (Figure 5.7a). The next largest forces are generated by the tibialis anterior.

5.2.2.2 Posteriorly Directed Resultant Force. The posteriorly directed load shows a slightly more distributed set of muscle force magnitudes across the muscles in the system studied, especially at the 90° configuration (Figure 5.7b). For this posteriorly directed

loading, the largest force in all configurations is usually at the location of attachment of the long and short head of the biceps femoris, the knee flexors. In the 0° configuration, the gastrocnemius and the tibialis anterior were also quite active, the first likely contributing to the knee flexion and the later modulating the secondary effect of the first, the ankle extension. The large gastrocnemius force likely induces a significant bending load on the tibial bone. In the 45° configuration, the biceps femoris muscle dominates, with the largest of all the forces applied to the tibia bone. The soleus adds to the posteriorly directed bending induced on the bone. In the 45° configuration, there are a number of small muscle forces. The gastrocnemius force likely does not induce much bending on the bone, and there are also very slight, likely inconsequential, forces applied by the vastii and rectus femoris. At the 90° configuration, only the soleus and biceps femoris muscles generate significant, nearly equal, forces on the tibia bone, with the magnitude of the long head of the biceps femoris generating the smallest force that it creates in all three configurations while the soleus produces a force nearly equal to what it generates under the 45° configuration.

5.2.2.3 Superiorly Directed Resultant Force. While the total magnitude of the muscle forces generated to create the superiorly directed resultant force are much smaller than those to create the anterior or posterior forces, the relative magnitudes of the forces on the tibia bone are similar to those found in the other loading directions. The vastii/rectus femoris muscles apply a combined force at their common attachment point that is almost an order of magnitude greater than that by the tibialis anterior muscle at the 0° orientation (Figure 5.7c). In the 90° orientation, the biceps femoris muscles are the only forces directly applied to the posterior side of the bone. The moderate gastrocnemius force

induces some effects by bending and the tibialis anterior likely generates a moment about the ankle to modulate its effect at that joint. The 45° orientation shows a more even distribution of forces with the posteriorly attached biceps femoris and the anteriorly attached knee extensors almost directly opposing, with less than half its magnitude. The tibialis anterior produces a slight but significant force on the anterior side of the bone, while the small gastrocnemius force produces a minor amount of bending.

5.2.2.4 Inferiorly Directed Resultant Force. Of the four loading conditions studied, the inferiorly directed force requires the most variation in the active muscles from one configuration to the next. In the straight leg, 0° configuration, only the biceps femoris muscle acts directly on the posterior side of the tibia, and a very slight force occurs on the anterior side, resulting from the tibialis anterior. The gastrocnemius muscle, acting on the posterior side of the leg but not directly on the tibia bone, generates a force almost equivalent in magnitude to that of the biceps femoris muscles, creating a substantial bending effect. In the 90° configuration, the majority of the forces acting on the tibia occur at the vastii/rectus femoris attachment location, with a slighter, two orders of magnitude smaller, force from the tibialis anterior muscle that act more distally but on the same side of the bone. The 45° configuration shows a similar but less intense dominance of the forces at the vastii/rectus femoris muscle attachment point. However, the 45° configuration requires an ankle extension action from the soleus rather than the ankle flexion moment from tibialis anterior that occurs in the 90° case.

5.2.3 Comparison Case

For completeness of the study of muscle activity for the conditions examined in this work, the loading conditions in the comparison (critical load) case described in Section 2.4 are presented. Refer to Figure 2.15 and Table 2.10 for a description of the system configuration and joint moments. In this mid-stance jogging loading condition, the leg was at a configuration between that of the 0° and the 45° cases used in the strength adaptation cases studied, with the hip joint flexed by 20°, the knee joint flexed by 45°, and the ankle joint flexed by 20°. Similar to the static, isometric shape adaptation studies, the comparison mid-stance jogging condition was assumed to be instantaneously static (See Chapter 2). However, because of the large momentum changes of the body just before and after this mid-stance stage of the jogging cycle, the joint moments, especially at the ankle and the knee, were much greater than any of the isometric activities generated by the thirty-three conditions studied, with a moment about the ankle of 160N-m, that about the knee of 180N-m and that about the hip of 30N-m. These moments were generated mainly by hip and knee extensor and ankle flexor muscles. Figure 5.8 shows the muscle force magnitude distribution.
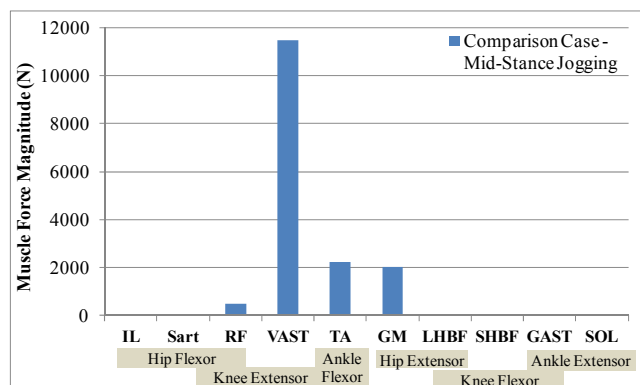
Figure 5.8 Magnitudes of muscle forces required to generate the hip, knee and ankle moments induced in the leg at the mid-stance point in a jogging cycle.

The main active muscles each function only about one joint, generating the necessary joint moments with relatively no antagonistic activity required.   At this mid-stance point in the jogging cycle, the active muscles must create the momentum change from landing to preparing for pushoff of the leg for the next cycle.   The vastii, knee extensor, exerts the greatest force in the entire system configuration.   The gluteus maximus acts alone to create the hip joint extensor moment, for if the long head biceps femoris muscle was active to aid in the creation of this clockwise moment about the hip joint, the knee extensor activity would have to increase even more than its already large force to counter the moments that would result from the second function of the biceps femoris as a knee flexor.   The sole ankle flexor in the study, the tibialis anterior muscle, creates a substantial force to generate the very large moment required to alter the body's momentum at this stage of the jogging cycle.   Because the model neither considered all of the leg muscles nor the effects of the soft tissues and ligaments in tempering the moments about the leg joints, the muscle force magnitudes predicted by the model in these conditions may be slightly greater than what actually is exerted by the muscles studied.   Nonetheless, this set of muscle forces gives a good indication of the extreme (critical design load) conditions that may induce stress fractures in the distal tibia. Therefore, this model is likely to be an effective tool in comparing the strength improvements predicted by the developed model that result from the various loading conditions examined in this phase of the current work.

This study of how the magnitudes of the individual muscle forces vary due to the change in the relative orientations of the bones to which they are attached and of the relationships of these magnitudes due to the variation in the direction of the net generated

resultant force for a given configuration of the leg is beneficial to the understanding the behavior of the entire system under investigation. Because local influences on the system drive the bone strength adaptive phenomena, this understanding is crucial to the analysis of the growth patterns and shape changes in the strength adaptation processes in a bone. As a result, the above analysis will be referred to within the descriptions of the results of the model-predicted shape/strength changes under the conditions studied.

The shape optimization (strength adaptation) model developed in this work was applied to the bone system described to convert an initially uniformly circular cylindrical tibia bone to shapes "optimized" to resist each of the thirty-three conditions (combinations of limb configurations and net resultant loads) studied. As described in previously, the effectiveness of these optimal bone shapes at improving the bone's strength in a region of the distal tibia susceptible to stress fractures was then evaluated by subjecting the leg system modeled, with each optimal tibial bone shape, to loading conditions thought to induce these stress fractures, those of mid-stance jogging. Comparisons of measures of the strength of each optimized bone shape, specifically at a location one-third of the tibial bone length from the ankle under this common loading condition (critical design load), were then made so that loading conditions that might be most beneficial at mitigating the risk for this kind of fracture might be identified. This evaluation is next discussed. The optimal bone shapes from each of the loading conditions examined will first be described followed by the changes in the von Mises stresses that they induce compared to the original initially circular cylindrical geometry at the targeted strengthening location. The correlations between the shape changes and the resulting stress changes under this comparison load will be emphasized.

5.3   Performance of Optimized Geometries under Mid-Stance Jogging

The developed shape strength optimization modeling method was applied to the tibia bone of the multibone multimuscle leg system described previously and depicted in Figure 5.1. The initial geometry of the region of this bone to be optimized was a uniformly circular hollow cylinder. Changes to the bone's shape from this regular geometry could, thus, be readily identified. To determine the changes in the bone strength due to these shape adaptations, an initial, baseline, static analysis was performed on this initial hollow circular cylindrical geometry under the same mid-stance jogging (critical load) conditions as was imposed on each of the "optimized" tibial bone geometries that resulted from each of the thirty-three loading conditions in this comparative study. The change in the maximum von Mises stress at the location susceptible to stress fracture under this comparison mid-stance jogging loading, the cross section of the bone at a distance one-third of the length of the tibia from the ankle, from that was occurred in the original uniform circular hollow cylinder, was selected as the quantitative measure of comparison of the effectiveness of each loading condition studied. Finally, the effect on the entire system performance was examined through comparisons of the von Mises stress distributions throughout the whole leg system.

5.3.1 Changes to the Cross-sectional Shape at the Fracture Prone Region

As reviewed in Chapter 2, the literature has suggested that the smaller the diameter of a tibia bone at a location one-third of the length of the bone away from the ankle, the more likely a stress fracture is to occur. Therefore, an initial measure of the effectiveness of a particular set of adaptation-inducing conditions at reducing the occurrence of a stress fracture is an examination of the change in size of the bone at this location. This analysis

was performed in two ways. First, a visual evaluation of the resulting shape changes was performed from using images taken from the adapted geometric mesh, indicating locations and relative amounts of growth and decay in the region of interest. Next, geometric measures of the resulting shapes of the cross-sectional area of the tibial bone at the one-third length targeted strengthening location were determined.

5.3.1.1 Qualitative Comparisons of "Optimized" Geometry at Targeted Region. A visual evaluation of the changes in bone strength at the selected comparison location gives a basic indication of the limb configurations and loading modes that may be more conducive to resisting stress fractures in the distal portion of the tibia bone. In Figures 5.9 through 5.11, the final cross sectional geometries that resulted from the bone shape optimization process under each of the eleven loading conditions studied for the 0°, 45°, and 90° configurations, respectively, is superimposed on that of the initial circular hollow cylindrical geometry from which the optimization began. In part (a) of each of these figures, the resulting geometry from all eleven loading conditions is presented for visual comparison. In part (b) of these figures, for only the single load cases, the resulting inner and outer boundary curves are plotted with dimensional reference to give a quantitative feel for the amounts of change that have occurred due to the optimization processes.

0° Configuration

 From the images in Figure 5.9a, it is clear that resorption (decay) occurred on both the endosteal (inner) and periosteal (outer) surfaces of the bone at this comparison location under nearly every loading condition imposed on the limb in the 0° configuration. In general, the predicted changes were greater on the inner surface. While many of the loading conditions imposed on this straight leg configuration resulted in resorption at all

points on both surfaces at the targeted region, those loadsets involving a posteriorly or inferiorly directed resultant force showed some accretion of bone material, causing slight growth, mainly on this inner surface (Figures 5.9a (c) and (d) and Figure 5.9b). The changes from the initially circular cylinder were quite small under this 0° configuration, especially in the sequential application of all four load directions. The relatively small amount of changes to the profile of the outer surface at this location compared to the alterations to the inner surface is noticeable in Figure 5.9b.

(a) Anterior   (b) Superior   (c) Posterior   (d) Inferior

(e) S-A   (f) P-S   (g) P-I   (h) A-I

(i) A-P   (j) S-I   (k) A-I-P-S

Figure 5.9a Comparison of change in shape at the transverse one-third tibial length cross-section for cases indicated for the 0° configuration. Note: Red curves are the initial geometry and black curves show the optimized shape.

Figure 5.9b Superimposed final geometries of four single load cases, the one four-load case (all around) and the initial geometry, for reference, at the one-third cross section for optimization under the 0° configuration.

45° Configuration

In contrast to the 0°, straight leg, configuration, larger amounts of growth (accretion) and decay (resorption) occurred at the location targeted for strengthening in response to most of the loading conditions investigated under the 45°, bent leg configuration. Almost all of the eleven loading conditions applied to this bent leg configuration showed the same basic patterns of shape change: growth on the endosteal (inner) and periosteal (outer) surfaces near the Θ=0° and Θ=180° locations (±x-directions in Figure 5.10) with decay on both surfaces at the Θ=90° and Θ=270° locations (±y-directions in Figure 5.10). The only case that did not follow this pattern was the posteriorly directed resultant force, which displayed decay along both inner and outer surfaces at all points of the studied cross section. In general, these 45° configuration cases showed slight asymmetry about the y-axis, with thicker regions (more growth/less decay) on the positive x-axis side. Some of the important observations about these shape changes are summarized below.

Aside from the posterior case, the resulting "optimal" geometries can be grouped by similar features that correspond to the varying relative amounts of growth at specific locations amongst the eleven loading cases studied. The anterior (Figure 5.10a(a)), inferior (Figure 5.10a(d)), and anterior-inferior (Figure 5.10a(h)) cases are nearly identical, with very large growth at the outer surfaces along the local x-axis ($\Theta=0°$ to $\Theta=180°$ locations) and very large amounts of decay along the local y-axis ($\Theta=90°$ to $\Theta=270°$ locations). Lesser amounts of the same direction of growth occurred on the inner surface for this group. The posterior-inferior (Figure 5.10a(g)) and anterior-posterior (Figure 5.10a(i)) cases shared many of the same features of the single load anterior and inferior cases, including the greater growth on the positive x-axis ($\Theta=0°$) location, but these cases presented less overall growth along the local x-axis on the outer surface and more decay along the local y-axis on the inner surface. Under the superiorly directed resultant force (Figure 5.10a(b)), the growth pattern at this targeted comparison cross-section was very similar to that under the anterior loading, but with the asymmetry reversed, where the larger amount of change is along the negative x-axis ($\Theta=180°$) rather than the positive x-axis ($\Theta=180°$). The multiload superior-inferior (Figure 5.10a(j)) and superior-anterior (Figure 5.10a(e)) then followed with more symmetric growth, but with the larger amount of growth and decay than what was seen in the single load anterior/inferior group. Finally, the posterior-superior (Figure 5.10a(f)), anterior-posterior (Figure 5.10a(i)), and four-load case (Figure 5.10a(k)) sets followed the patterns of the superior-inferior and superior-anterior sets with slightly more symmetric shapes and less overall amounts of growth or decay.

(a) Anterior **(b) Superior** **(c) Posterior** **(d) Inferior**

(e) S-A **(f) P-S** **(g) P-I** **(h) A-I**

(i) A-P **(j) S-I** **(k) A-I-P-S**
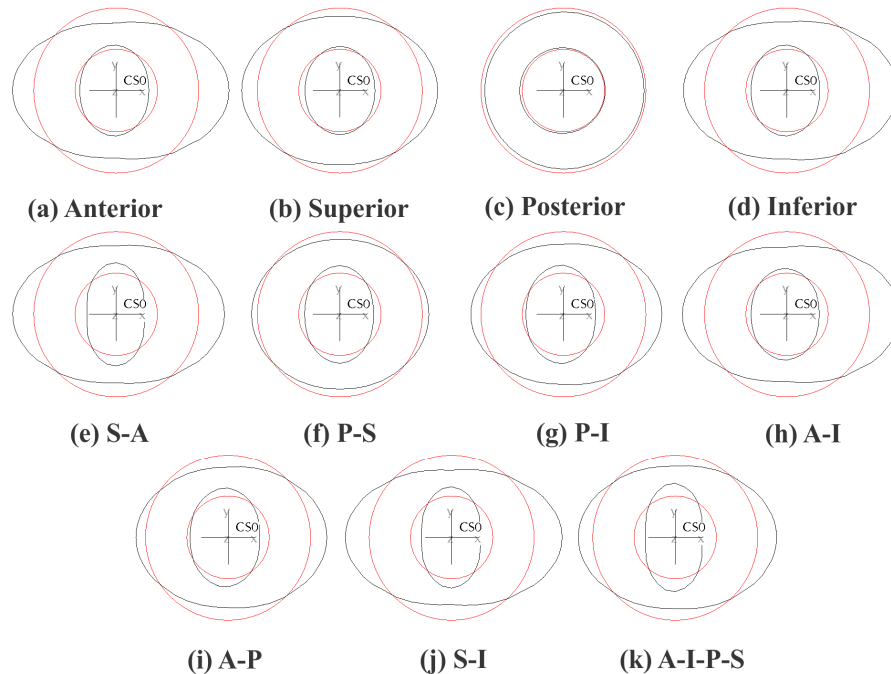
Figure 5.10a Comparison of change in shape at the transverse one-third tibial length cross-section for cases indicated under the 45° configuration. Note: Red curves are the initial geometry and black curves show the optimized shape.
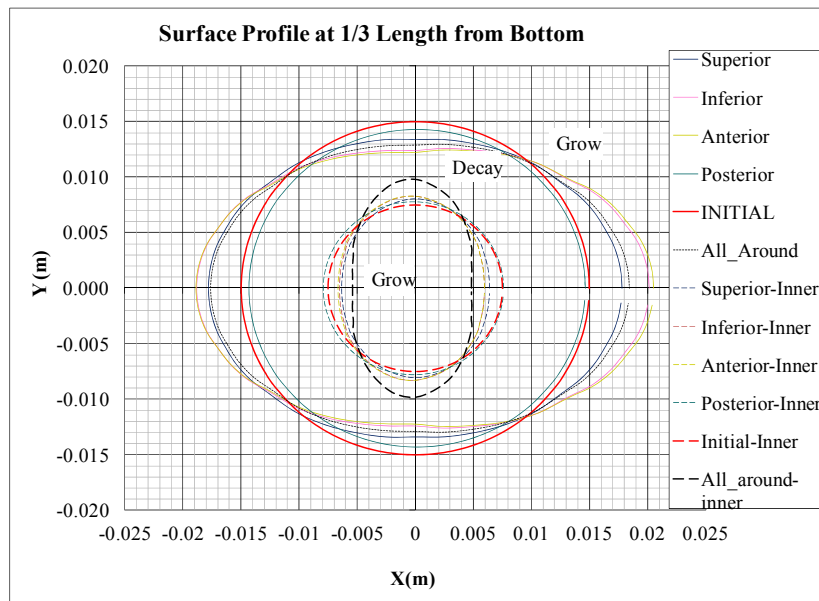
Figure 5.10b Superimposed final geometries of four single load cases, the one four-load case (all around) and the initial geometry at the one-third cross section under the 45° configuration.

90° Configuration

Many of the changes in the geometry from the initially uniform circular cylinder at this targeted strengthening region under the eleven loading sets imposed on the leg in the 90°, bent back, configuration were similar to those seen in the 45° and 0° configurations. The geometric changes resulting from the anterior (Figure 5.11a(a)) and inferior (Figure 5.11a(d)) loading were nearly identical to those seen in the 45° configuration. Similarly, the changes resulting from the posterior (Figure 5.11a(c)) and superior loading (Figure 5.11a(b)) under this 90° bent back configuration were similar to the superior and posterior loading, respectively, under the 0° straight leg configuration, with the posteriorly directed force resulting in slightly thicker region on the negative x-side and the superiorly directed force producing the opposite conditions. This follows the rotation of the tibia from the 0° configuration to the 90° configuration, as the globally defined posteriorly directed force[-1 0 0] in the 0° configuration points to the heel while the superior direction[0 1 0] also points to the heel in the 90° bent back configuration.

The multiload cases showed similar grouping patterns as the 45° bent leg configuration. The anterior, inferior and combined anterior-inferior cases were nearly identical to those in the 45° configuration. The anterior-posterior, posterior-inferior, superior-anterior and superior-inferior were also similar to anterior/inferior shape, but with less change to the overall outer surface profile. These cases followed the asymmetry of the non-anterior/inferior load set which it contained (For example, the anterior-posterior follows the posterior single case asymmetry). The posterior-superior (Figure 5.11a(g)) set showed the smallest amount of change in shape, as the opposing asymmetries seem to negate each other when applied in sequence. Finally, the four load

case (Figure 5.11a(k)) showed similar, but less extreme features as the cases combining the anterior or inferior loads with those of the posterior or superior sets and more overall symmetry as all four individual load cases contribute to this the final shape.

(a) Anterior   (b) Superior   (c) Posterior   (d) Inferior

(e) S-A   (f) P-S   (g) P-I   (h) A-I

(i) A-P   (j) S-I   (k) A-I-P-S
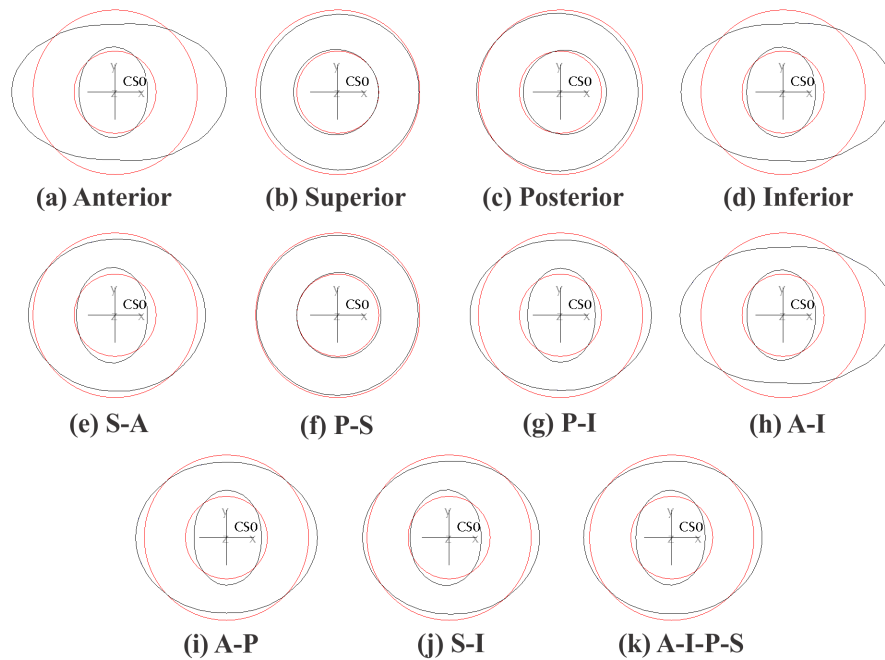
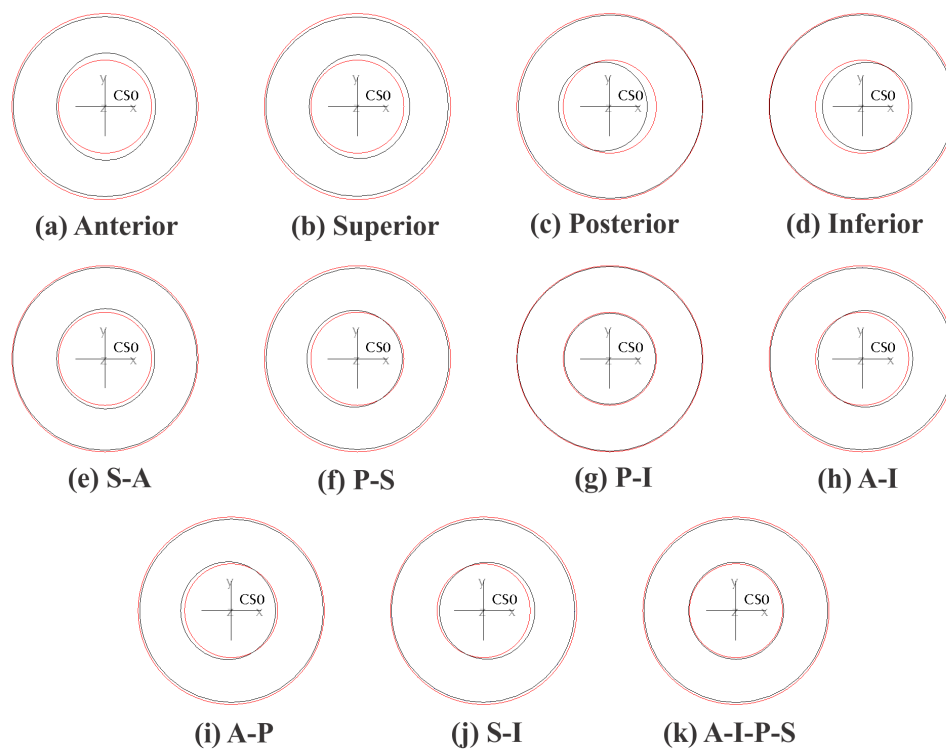**Figure 5.11a** Comparison of change in shape at the transverse one-third tibial length cross-section for cases indicated under the 90° configuration. Note: Red curves are the initial geometry and black curves show the optimized shape.
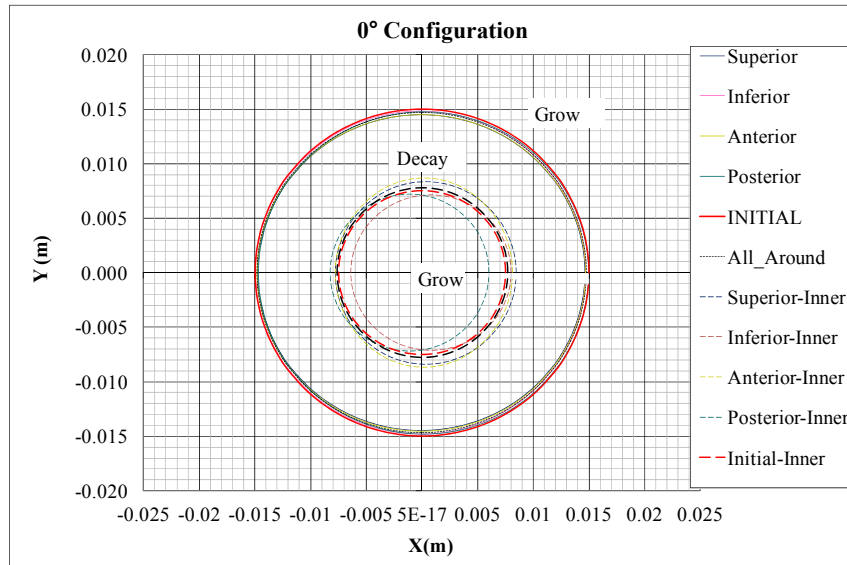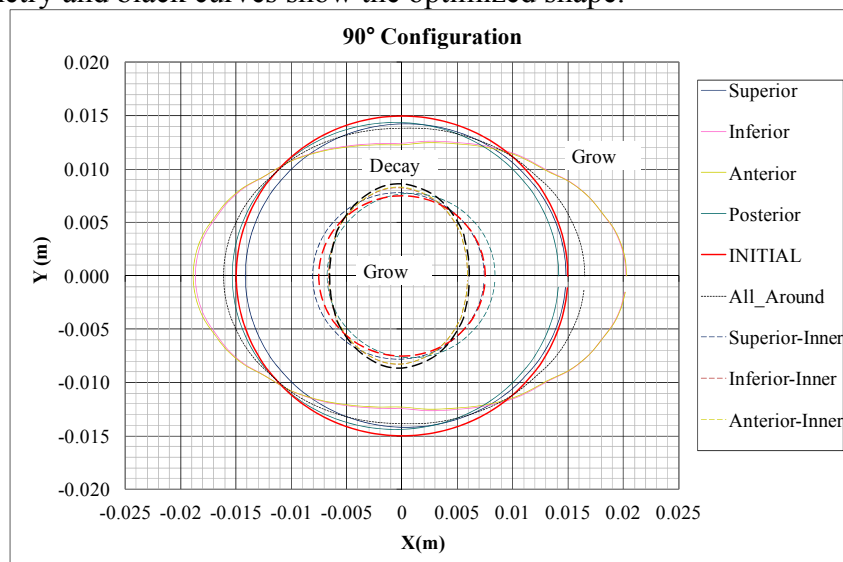

Figure 5.11b Superimposed final geometries of four single load cases, the one four-load case and the initial geometry at the one-third cross section under the 90° configuration.

5.3.1.2 Quantitative Comparisons of "Optimized" Geometry at Targeted Region.

To gain a better understanding of the relative amounts of change in the geometry of this fracture-prone region of the tibia bone in the shape optimized for each of the thirty-three conditions studied, geometric measures were calculated for each resulting cross-section. The area, moment of inertia, polar moment of inertia, maximum radial dimension and coordinates of the center of gravity were calculated for each "optimal shape" at the targeted one-third length location. Each of these measures gives an indication of the strength of a shape of this cross-section. However, because each geometry measure is related to the strength under a particular mode of loading, as discussed in Chapter 4, this information alone is not sufficient to predict the general strength or behavior of the bone under normal, varied, daily activities. Nonetheless, the amount of change in these measures from the initially circular cylinder gives an indication of the relative geometric alterations caused by the shape optimization and, hence, an indication of the potential strength improvement. The ratio of the value of each geometric measure of the targeted cross-section of the "optimal" geometry created from each of the imposed loading conditions in each leg configuration studied to that of the initially circular hollow cylinder was used as a quantitative measure of the geometric changes induced.

0° Configuration

In all of the loading conditions studied for this straight leg configuration, all conditions resulted in approximately 10% to 15% reductions in the measures of geometry at the one-third length from the ankle location susceptible to fracture (Figure 5.12b). In general, the moment of inertia about the x-axis decreased the most, due to the thinning along the y-axis ($\Theta = 90°$-$270°$ locations). The polar moment of inertia, which considers the changes

along both the x-axis and the y-axis, decreased the next greatest amount. Relative change in the moment of inertia about the y-axis (as a result of the decay at the ($\Theta = 0°$ and $\Theta = 180°$ locations) and the cross-sectional area from the initially circular hollow cylinder were typically similar to each other and less than the changes to the other moments of inertia. The maximum radial dimension changed very little from initial as noted through Figure 5.9. The center of gravity (Figure 5.18a) shifted anteriorly (positive x-direction $\Theta = 0°$) for the posteriorly directed loading, but it moved posteriorly for all the other loads, indicating a thickening on the anterior side of the bone compared to the posterior side of the bone at this cross section only for the posterior, anterior-posterior, and posterior-superior loading cases. This "asymmetry" was observed in the qualitative comparisons in Figure 5.9. The inferior, followed by the superior loading directions, produced the greatest shift to the posterior (negative x-direction $\Theta = 180°$) side of the bone, indicating that the combination of changes to the outer and inner surfaces of the bone at the cross section studied resulted in a shape that was thicker posteriorly than on the anterior side.

In comparing the single load cases, the inferiorly and the posteriorly directed resultant force conditions produced very similar geometries, with the inferior resulting in slightly less changes than the posterior. Similar trends were found for the superiorly and the anteriorly directed resultant force conditions, with the superior causing slightly more changes to the initial geometry than the anterior.

In each multiple load case, the sequential loading of different conditions produced more moderate changes in the shape and resulting geometric measures than the single load cases of which they were comprised. For example, the single load superior and anterior cases produced greater changes than the combination of either of these with any

other single load case. The exception to this observation was the combination of the posterior-inferior loading condition, which resulted in the least amount of change at this fracture prone location. As seen in the very small shift in center of gravity from the uniform circular cylinder for the posterior-inferior combined load in Figure 5.12a, the change in geometric measure in Figure 5.12b, and the images in the change in cross-section in Figure 5.9a, the opposing asymmetries of the single load posterior and inferior cases negate each other when applied sequentially. The trends in these geometric measures quantify the qualitative observations discussed in the previous section.
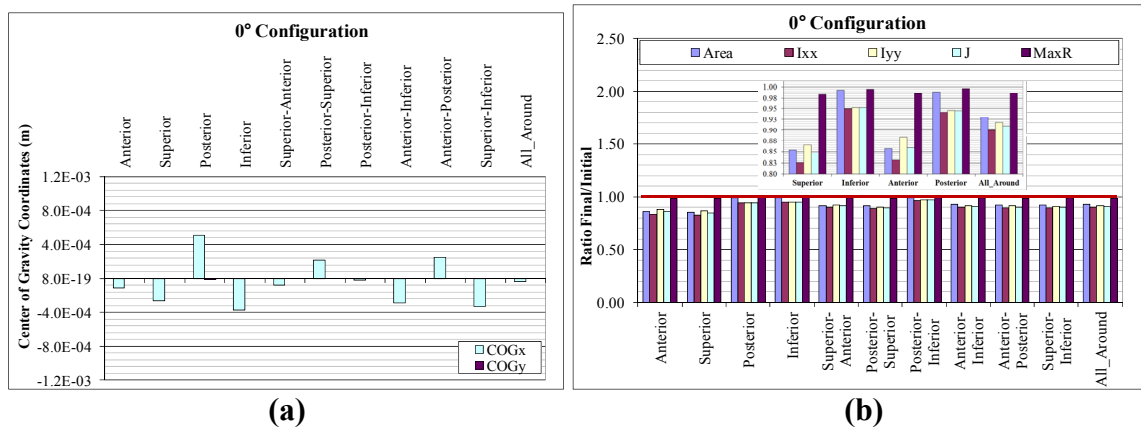
Figure 5.12 Change in geometric measures from initially circular cylinder for loading conditions studied in 0° configuration. (a) center of gravity (b) measures of cross-section.

45° Configuration

In the 45° configuration, similar correlations between the visual observations of shape change and the relative values of geometric measures were found as in the 0° configuration. The coordinates of the center of gravity (Figure 5.13a) confirm the observations of the relative amounts of asymmetry of growth under each of the loading cases. For example, the x-coordinate of the center of gravity for the anterior alone case shifts much more than for the combined anterior-superior loading conditions, resulting in

less "asymmetry" due to the combined case. The area, moments of inertia, and maximum radial dimension for the examined cross-sections under the 45° configuration changed more than under the 0° configuration (Figure 5.13b). The trends in the geometry matched the visual descriptions of the shape changes, with a very large, nearly two-fold, increase in the moment of inertia about the local y-axis in most cases, due to the large growth in the x-direction, and a significant (nearly 20%) decrease in that about the local x-axis, with the noted decay in the y-direction for many of the loading conditions studied. The more moderate, 10% to 20%, increases in area, polar moment of inertia, and maximum outer radial dimension followed, as there was a net material increase under these loading conditions.

The posteriorly directed case in the 45° configuration was unique, with growth patterns that did not follow the others. The geometric changes were more similar those created under many of the loading directions in the 0° leg configuration, with a decrease in all the geometric measures to coincide with the decay observed on all surfaces. Subtle differences between the geometric measurements of different load cases, reveal conditions which could not be ascertained from the visual inspections, including the slightly larger changes in growth under the anteriorly directed load compared to the inferiorly directed load and, likewise, the greater changes under the superior-inferior over the superior-anterior loading cases. These measurements can be used to compare the cases with a common loading direction. For example, the application of an inferiorly or anteriorly directed load after the application of a superiorly or posteriorly directed one increased the overall growth over either the superiorly or posteriorly directed loads alone but decreased that of the inferiorly or anteriorly directed loads.
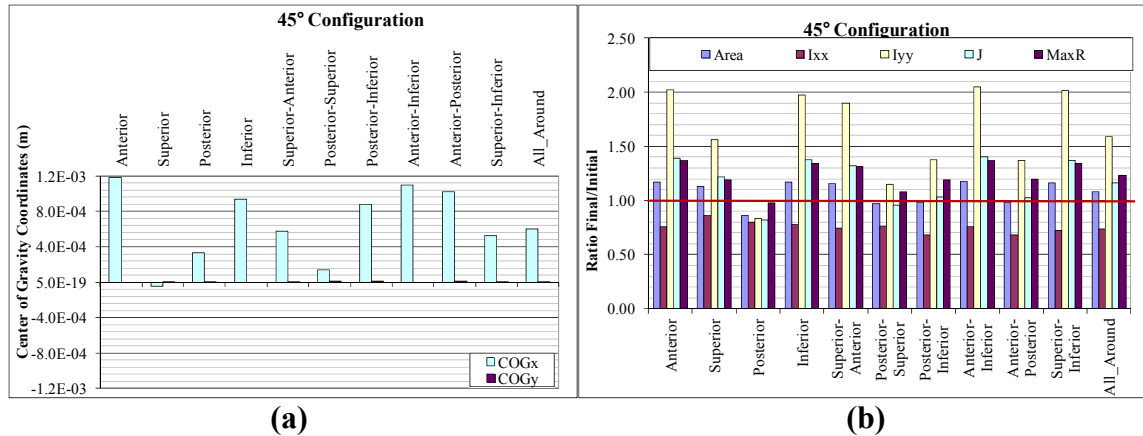
Figure 5.13 Change in geometric measures from initially circular cylinder for loading conditions studied in the 45° configuration. (a) center of gravity (b) measures of cross-section

90° Configuration

Similar trends as in the 0° and 45° configurations were revealed in the 90° configuration, though, in general, the shape changes were not as extreme as were seen in the 45° and 0° cases. The trends in the opposing direction of the asymmetric geometry resulting from the posterior and superior loading shown in Figure 5.11 were revealed in the measures of the location of the center of gravity (Figure 5.14a). The large growth in the anterior, inferior and anterior-inferior cases was clearly observed using the ratio of the change in the geometric measures from the initial to the "optimal" geometry in Figure 5.14b. Moreover, the nearly equivalent magnitudes of the geometric measures for these anterior/inferior cases under both the 90° and 45° configurations confirmed their visual similarities. The grouping of the results from the anterior and the inferior loading and from the posterior and superior loading was more distinct under the 90° loading than in the 45° loading, similar to the grouping of superior and anterior loading cases in the 0° conditions. Additionally, through these geometric measures, the similarity between the superiorly directed resultant force in the 90° configuration (Figure 5.14b) and the

posteriorly directed resultant force (Figures 5.13b) was deduced. Finally, the moderation of the extremes of the two groups using multiload cases, like the posterior-superior and posterior-anterior cases, is revealed through center of gravity measurements Figure 5.14a.
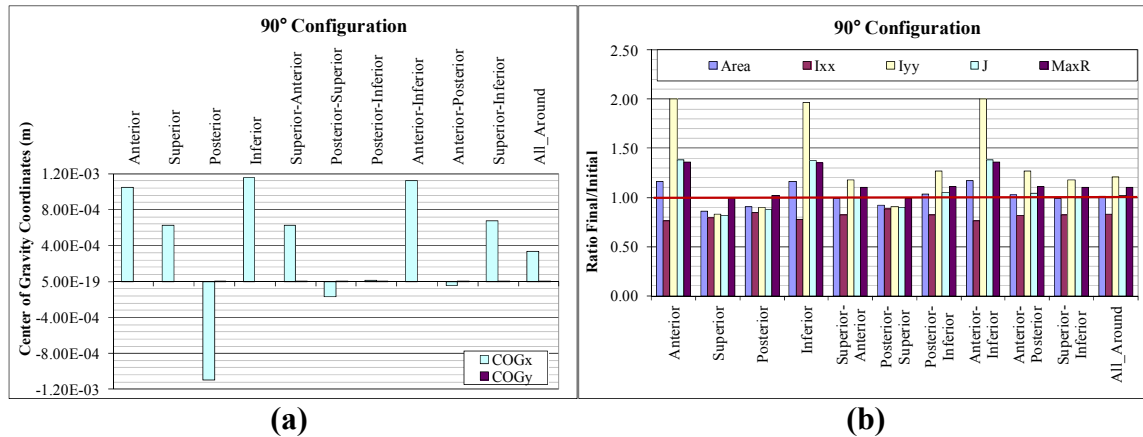
Figure 5.14 Change in geometric measures from initially circular cylinder for loading conditions studied in the 90° configuration. (a) center of gravity (b) measures of cross-section.

The general trends in the geometric changes from the initial circular cylinder at this targeted region as a result of the shape optimization (strength adaptation) presented above give a general indication of the changes to the mechanical response of each system to a particular loading condition that is dependent upon that geometric measure. For bending stress depends on the area moments of inertia, the stresses induced by torsion are related to the polar moment of inertia of its cross-section, and the resistance to an axially applied force is controlled by the cross-sectional area of an object. However, a specific system, biological or inert, rarely is subjected to only a single mode of loading. Therefore, these geometric measures are not sufficient as a general measure of the bone's overall strength, and alternative means of quantifying the change in the ability of the bone shape to resist failure at the location of interest are necessary.

5.3.2 Changes to State of Stress at the Fracture Prone Region

The bone shape adaptation model developed in this work is based on variations in the local measures of strain energy density. As discussed in Chapters 2 and 4, the strain energy density is used as a measure of the local state of combined stress in the bone that drives the shape strength adaptations, tying the energy transferred to the bone from externally applied loads to the energy used to perform the bone strength adaptation processes. Also as explained in Chapter 4, the von Mises stress is a measure of the stress generated in a body by an applied force that is related to the energy required to cause its failure by the distortion that occurs due to this transferred energy. Therefore, because the von Mises stress links the concepts of the strain energy density used to drive the optimization model with the predictions of resulting strength of the optimized object, changes to the von Mises stress in the targeted fracture prone were location from that of the pre-optimized uniform circular hollow cylinder were compared amongst the eleven loading sets imposed on each of the three limb configurations studied.

The use of a common comparison set of loading conditions (critical design load) can expose "optimal designs" from the various conditions studied that create the greatest decrease in the maximum von Mises stress in the stress fracture-prone targeted region under the mid-stance jogging conditions, which are believed to induce stress fractures in the region of interest. In addition to the nodal maximum von Mises stress, changes in the spread between the minimum and maximum von Mises stresses over the boundaries of the cross-section of interest helped to rank the cases examined by indicating change in uniformity.

5.3.2.1 0° Configuration. The von Mises stress distribution for the bone shapes created under the straight leg 0° configuration are shown in Figure 5.15. Most "optimized" shapes resulting from the eleven loading conditions for this configuration had in a larger maximum stress at the fracture-prone location than the initially circular cylinder and, therefore, did not improve the bone strength under the criteria defined in this model. The posteriorly directed resultant force, which predicted, uniquely amongst the conditions studied, material accretion on the inner surface of the anterior side of the bone, did result in a slightly smaller (by <5%) maximum von Mises stress than the original geometry at the location studied. Two cases produced maximum stresses at this location that were only slightly greater than the original geometry. The geometry from the inferiorly directed resultant force had a 5% greater maximum von Mises stress than original geometry, and the combination of these posterior and inferior cases produced a less than 1% increase. The superiorly directed load, closely followed by the anteriorly directed load, resulted in the greatest almost 50% increase in the von Mises stress. The remainder of the combined loads resulted less, but still significant, increases in the von Mises stress under the comparison conditions, increasing the likelihood of failure of the bone under the conditions specified. These trends within the resulting geometries were consistent both on the inner (Figure 5.15b) and outer surfaces (Figure 5.15a).

For each "optimized" tibia design at the fracture-prone cross-section targeted for strengthening, these observed changes from the initially circular cylinder in the stress distribution resulting from the "critical load" mid-stance jogging load were ranked. Specifically, the percentage change over the initially circular cylinder in the maximum nodal von Mises stress, minimum nodal von Mises stress, and the spread between these

two for each of the conditions studied, were considered (Table 5.7). Regardless of the measure: minimum, maximum, or spread, the ranking of the load cases under the straight leg configuration was the same. Only the posteriorly directed resultant load decreased the maximum von Mises stress as well as the variation of the stress over the cross-section's perimeter on both the inner and outer surface at the targeted stress fracture prone location. However, the improvement was very slight.

Table 5.7 Comparison of Changes in Extrema and Spread of Nodal von Mises Stress at the One-Third Tibial Length Comparison Location for Adaptations made under the 0° Configuration

Loading Case	Outer (Periosteal) Surface			Inner (Endosteal) Surface		
	MAX VMS	MIN VMS	MAX-MIN VMS	MAX VMS	MIN VMS	MAX-MIN VMS
Posterior	**-4%**	1%	**-5%**	**-13%**	**-78%**	**-9%**
Inferior-Posterior	0%	**-1%**	1%	**0%**	13%	**-1%**
Inferior	5%	**-10%**	6%	9%	102%	3%
Anterior-Posterior	28%	75%	25%	18%	159%	9%
Posterior-Superior	29%	75%	26%	20%	154%	12%
All_Around	30%	78%	27%	26%	106%	21%
Superior-Anterior	33%	85%	30%	31%	128%	25%
Anterior-Inferior	33%	85%	30%	31%	128%	25%
Superior-Inferior	35%	82%	32%	37%	56%	36%
Anterior	43%	107%	39%	43%	168%	35%
Superior	47%	101%	43%	50%	158%	44%

Interestingly, this improvement in strength could not be discerned from the geometric data alone at this cross section, as all measures of these "optimized cross-sectional geometries" had values that were smaller than the initially circular cylinder. Additionally, the geometry of the inferiorly directed load actually showed the least reduction in these measures geometric. The only measure where the posteriorly directed load was noticeably different than the other cases was in the center of gravity, where this measure indicated an increased asymmetry under the posteriorly directed load set.

Although the multiload cases containing the posteriorly directed load showed similar, though less significant, thickening in this region, a decrease in the von Mises stress did not result. Therefore, in this three-dimensional model, it is clear that the changes in a single cross-section are not the sole influence on the stress state in this section but are affected by that of the surrounding regions along the local tibial bone axial direction. The behavior in the surrounding regions is not considered when examining geometric measures of a singular slice of the bone and changes in the geometry and behavior of the system. This observation verifies the use of the modeling methods developed in this work as a means to evaluate the effectiveness of the strength changes in the bone over the standard two-dimensional geometric measurements that have traditionally been used.

Figure 5.15 Variation in von Mises stress under comparison load along the (a) outer and (b) inner perimeters at the one-third cross section for the straight leg 0° configuration. Note: In these graphs, the θ=0° position corresponds to the positive x-coordinate in Figure 5.9b.
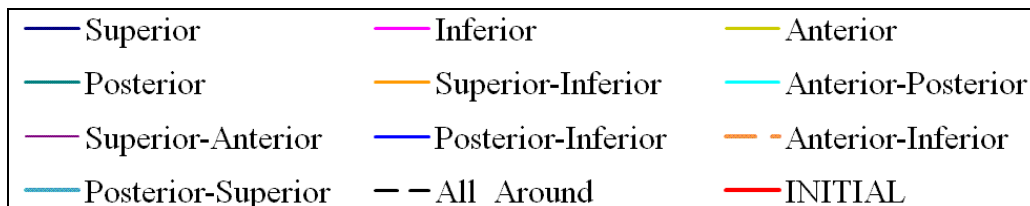
5.3.2.2 45° Configuration. The von Mises stress along the boundaries of this targeted cross-section for the various optimized geometries resulting from the loading conditions on the leg in the 45° configuration (Table 5.8, Figure 5.16) follow the groups defined based on their shapes (Figure 5.10). In general, there was a reduction in the maximum von Mises stress in almost all cases on both the inner and outer surfaces, with the inner surface having a greater reduction. Only the posterior alone case had a maximum von Mises stress on the inner surface that was more than that of the original geometry (20%, following that of the outer surface). The geometries resulting from the posterior alone and the posterior-superior loads had the largest increase in von Mises stresses under this comparison condition, 20% and 7% greater than the original uniform circular cylinder on the outer surface, respectively. The posterior-inferior and anterior-posterior group resulted in only a slight (3%) reduction in maximum von Mises stress on the outer surface. The superior-anterior and superior-inferior group showed a more significant reduction, 16% on outer surface. The optimal geometries from the anterior, inferior and combination of the two resulted in the greatest reduction of von Mises stress, 22%.

It is interesting to note that the anterior and inferior loading conditions resulted in optimal geometries at this cross-section (Figure 5.10a (a) and (d)) very similar to those which resulted under pure bending loads in the preliminary shape adaptation model develop studies presented in Figure 4.1. To better understand this, the behavior of the bone system under these loads was examined. The flexed knee and hip and the large knee extensor muscle forces at the proximal tibia pulled the knee towards the pelvis. With the constrained toe, this established conditions in the tibia very similar to the pure "beam" bending mode from that preliminary study. The anterior and inferior loading

conditions had a similar limb configuration and dominant knee extensor muscle activity acting directly on the tibia as the mid-stance jogging comparison condition. These similar system conditions may have contributed to the high ranking of the geometries optimized under the anteriorly and inferiorly directed resultant forces, as they were "designed" to resist loading conditions similar to those selected as the comparison state.

As in the 0° configuration, the ranking of the loading cases under the 45° configuration was consistent for minimum, maximum, and spread of von Mises stress, and also on the inner and the outer surfaces. The only difference noted between rankings on the inner and outer surface arises between the superior and all around cases where their ranking on the inner and outer surfaces is reversed, through very similar. In this tabular form of comparison, the qualitatively observed groupings amongst the similar optimized geometries at the given cross-section is noticeable, more so in the maximum values of the von Mises stress, which were more closely tied to the applied muscle forces, than in the minimum values.

All optimized geometries created under loads applied to the 45° configuration except the posterior alone and the posterior-superior cases improved the strength at this fracture prone location. Those resulting from the anterior and inferior loads, alone or in sequence, were most effective under this critical design load. Although the posterior-based loads under this 45° configuration were least effective at improving the local bone strength amongst the others formed under this bent leg arrangement, the stresses in these shapes were less than those created in most of the shapes optimized under the 0° straight leg configuration. This indicates that the bent leg configuration may be more conducive to strengthening the distal tibia than the straight leg configuration.
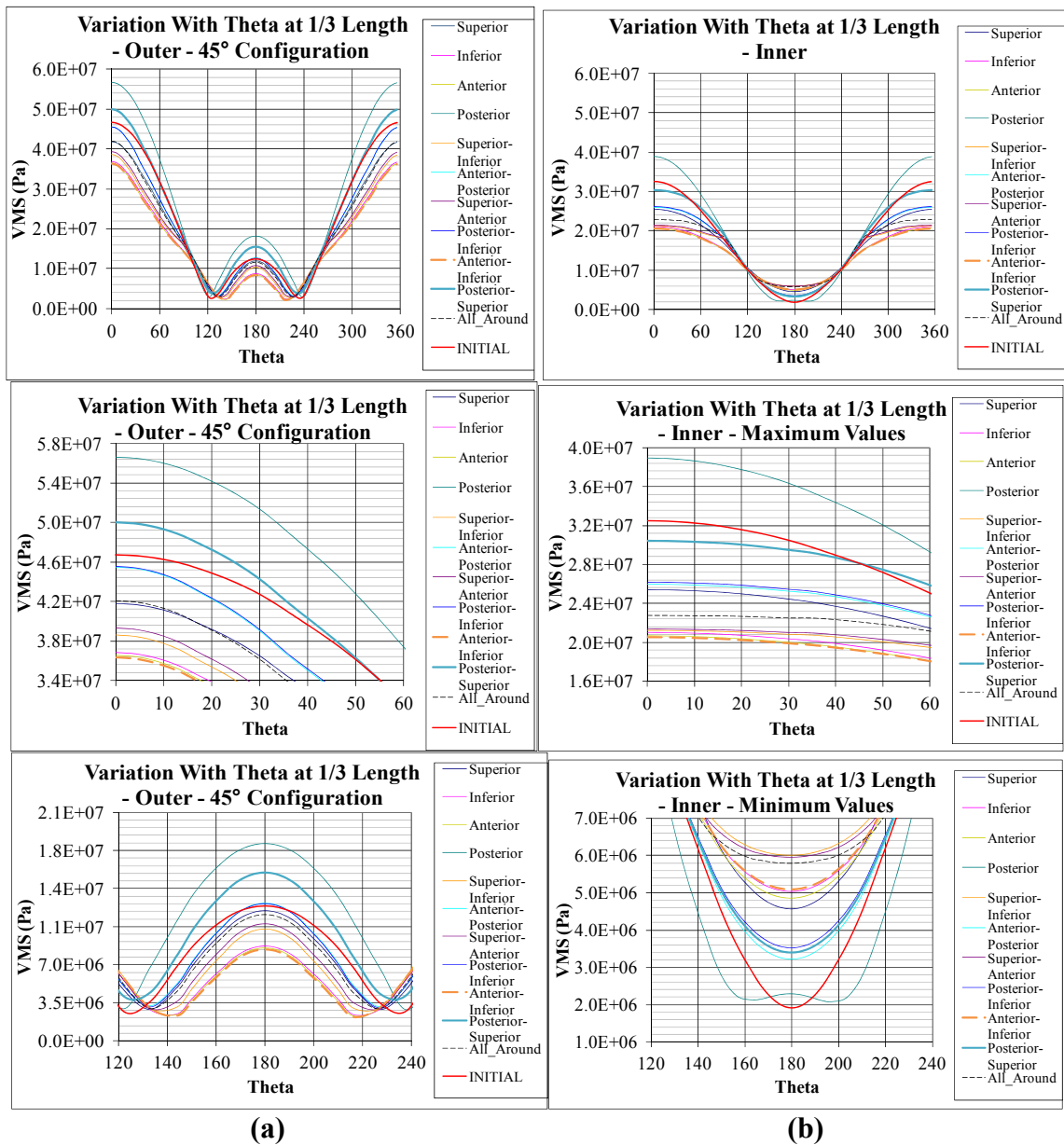
Figure 5.16 Variation in von Mises stress under comparison load along the (a) outer and (b) inner perimeters at the one-third cross section for the 45° configuration. Note: In these graphs, the θ=0° position corresponds to the positive x-coordinate in Figure 5.10b.
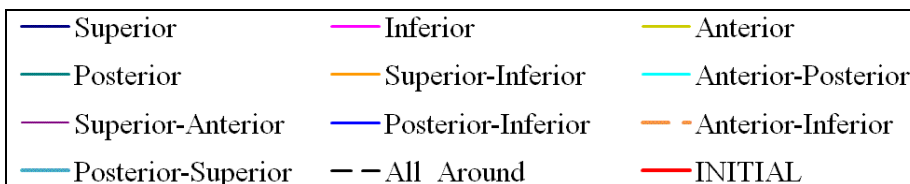
Table 5.8 Comparison of Changes in Extrema and Spread of Nodal von Mises Stress at the One-Third Tibial Length Comparison Location for Adaptations made under the 45° Configuration

Loading Case	Outer (Periosteal) Surface			Inner (Endosteal) Surface		
	MAX VMS	**MIN VMS**	**MAX-MIN VMS**	**MAX VMS**	**MIN VMS**	**MAX-MIN VMS**
Anterior-Inferior	**-22%**	**-18%**	**-23%**	**-37%**	166%	**-49%**
Anterior	**-22%**	**-14%**	**-22%**	**-36%**	154%	**-48%**
Inferior	**-21%**	**-11%**	**-22%**	**-35%**	163%	**-50%**
Superior-Inferior	**-17%**	13%	**-19%**	**-35%**	215%	**-48%**
Superior-Anterior	**-16%**	11%	**-17%**	**-34%**	211%	**-50%**
Superior	**-11%**	8%	**-12%**	**-22%**	139%	**-32%**
All Around	**-10%**	12%	**-11%**	**-30%**	203%	**-44%**
Anterior-Posterior	**-3%**	19%	**-4%**	**-20%**	68%	**-26%**
Inferior-Posterior	**-3%**	15%	**-4%**	**-19%**	85%	**-26%**
Posterior-Superior	7%	53%	4%	**-6%**	78%	**-12%**
Posterior	21%	9%	22%	20%	8%	21%

5.3.2.3 90° Configuration. The von Mises stress distributions resulting from the optimized shapes under the eleven loading conditions applied to the leg in the 90° configuration were similar to the 45° configuration; however, the grouping between the geometry resulting from the posteriorly directed and superiorly directed resultant load and that from the anteriorly and inferiorly directed loads was more distinct (Figure 5.17). Because of this closer grouping, multiload sets containing one load from each of these groups had more similar stresses as their optimized geometries were nearly identical, resulting in much less change than the single load cases comprising them (Figure 5.11). As in the 45° case, the posteriorly and posterior-superior combination (and now the superior alone as well) resulted in weaker bone structure at this one-third length comparison location under the selected comparison mid-stance jogging load. The optimized geometry from the posteriorly directed load showed a maximum von Mises stress at the targeted region 30% greater than that of the originally uniform hollow

circular cylinder. Similarly, the superiorly direct load increased the maximum stress by 20% and their combination did so by 15%. The difference in the increase in stress due to the posterior and superior load cases at the targeted region despite their very similar geometric measures (Figure 5.14b) can be deduced by the center of gravity measurement (Figure 5.14a). A visual inspection of their cross sections (Figure 5.11) showed nearly identical trends and amounts of geometry changes between these two cases but with oppositely directed asymmetry. The posterior case thinned more on the anterior (Θ=0°, positive local x-coordinate) side, weakening the bone where there were greater stresses in the comparison (critical design) case. In contrast, the superiorly directed load thinned more on the posterior (Θ=180°, negative local x-coordinate) side, leaving a slightly thicker and, therefore, stronger geometry where the stress was greater.

Similar to the 45° configuration, the anteriorly and inferiorly directed resultant forces and their sequential application resulted in a 22% reduction in the maximum von Mises stress on the outer surface. As noted in the above section, the resulting geometry under these loadings between these two bent leg configurations is similar (Figures 5.10 and 5.11). Also, as in the 45° configurations, the relative changes to the von Mises stress on the inner surface were almost double those on the outer surface, but followed the trends of the outer surface. The exception was the superior case, which showed a greater increase in von Mises stress on the outer than on the inner boundary of this cross-section.
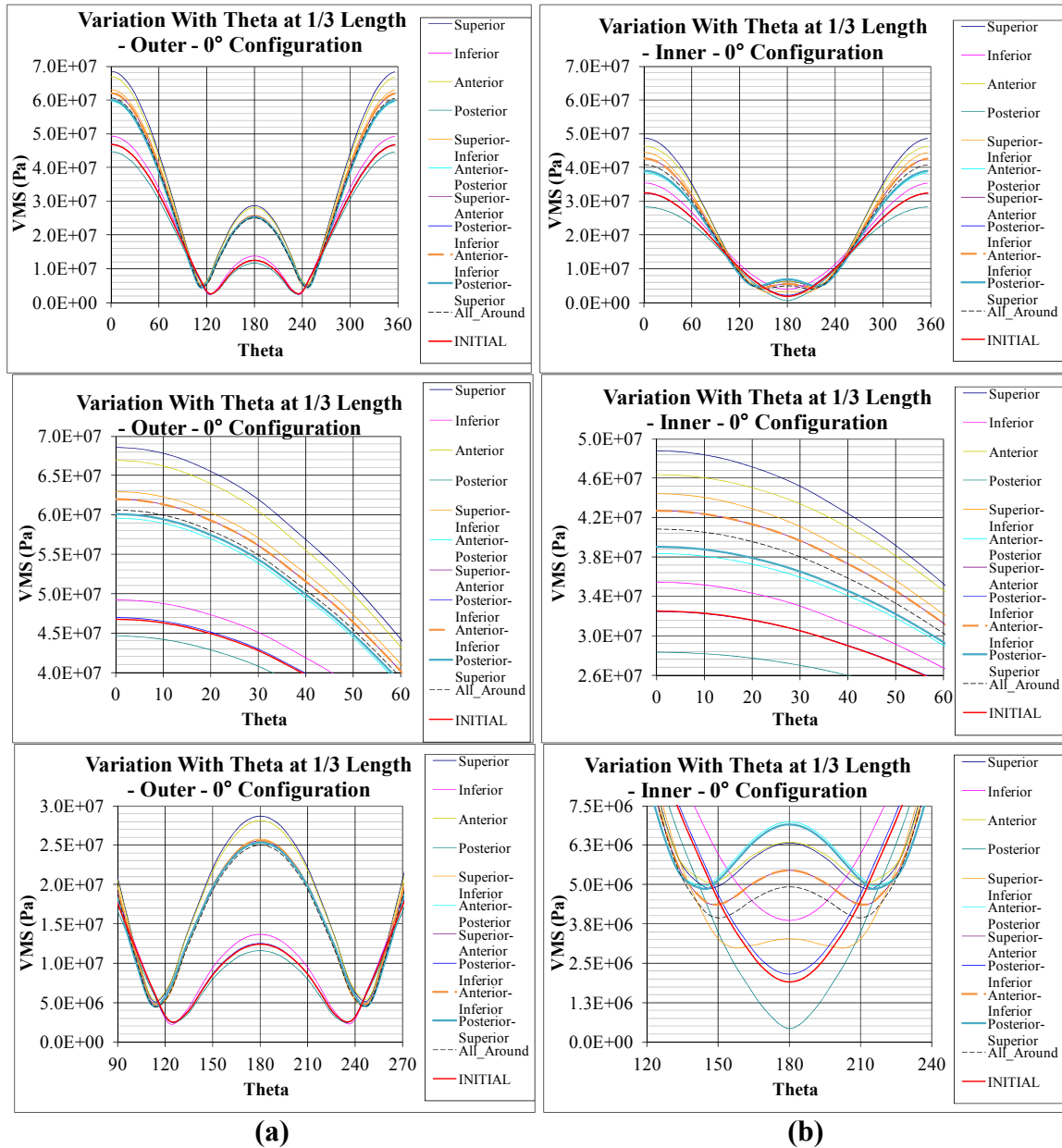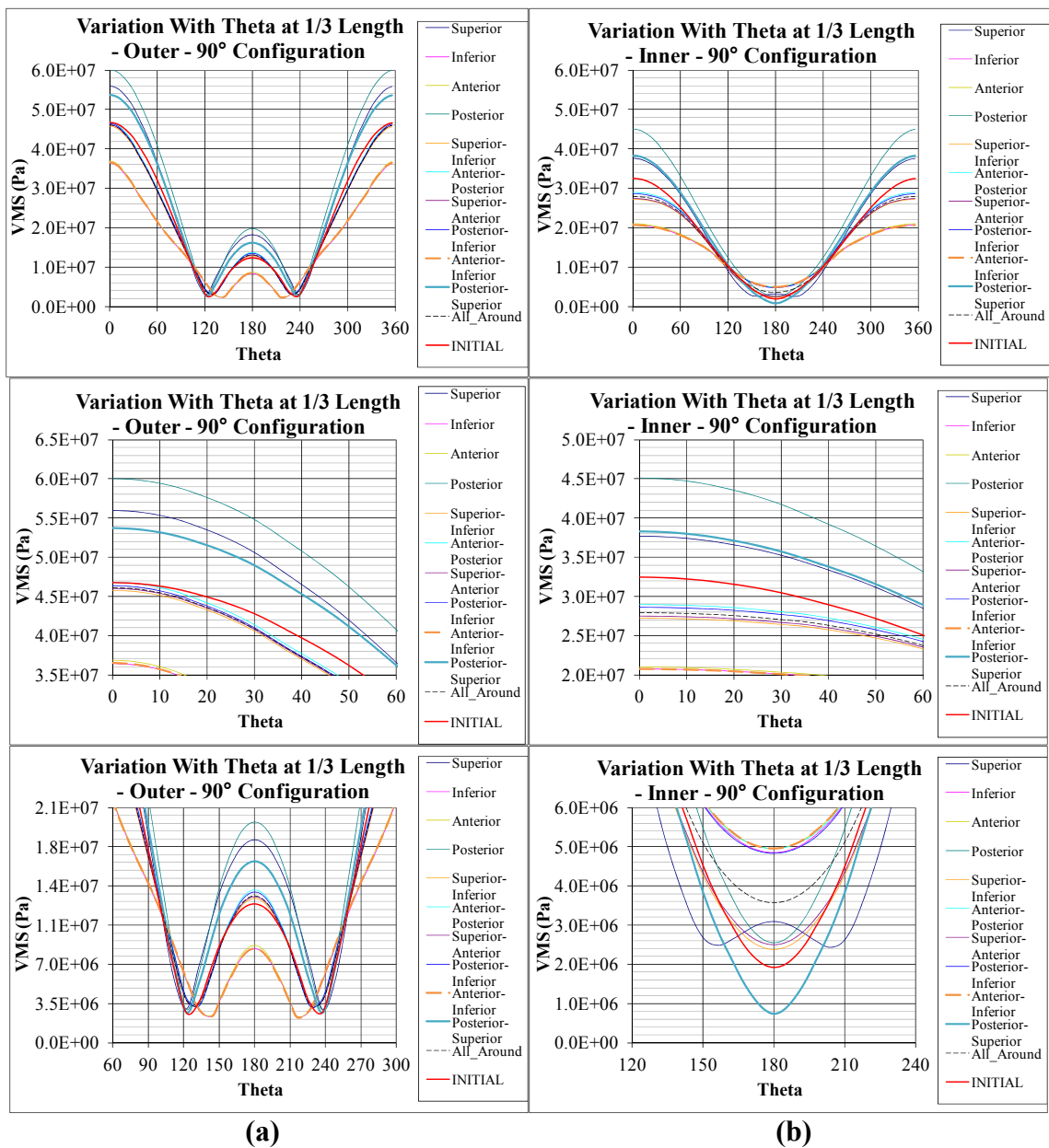
Figure 5.17 Variation in von Mises stress under comparison load along the (a) outer and (b) inner perimeters at the one-third cross section for the 90° configuration. Note: In these graphs, the θ=0° position corresponds to the positive x-coordinate in Figure 5.11b.
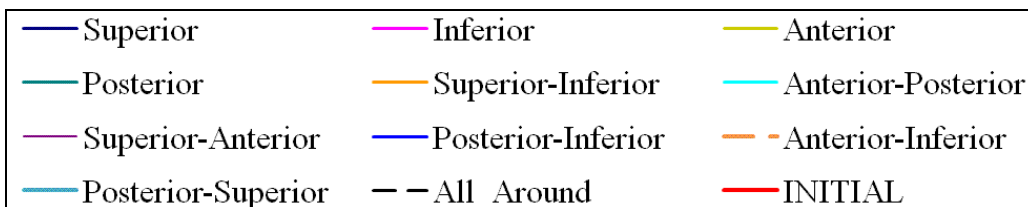
When listing the ranking (Table 5.8) of the effectiveness of the geometries optimized under the loading cases applied to the 90° configuration to reduce stresses at this fracture prone region, a pattern similar to that of the 45° case emerges with two main differences. First, the superiorly directed load had a higher ranking applied to the 45° configuration than in the 90° configuration. A small improvement in strength at this comparison location was seen under this loading in the 45° configuration, while the optimized geometry under this loading direction in the 90° configuration weakened the bone significantly. Second, despite their quite visible changes in geometry the multiload cases with combinations of single loads from each of the two main groups, resulted in nearly no change in strength over the initially uniform cylinder, as measured by the maximum von Mises stress on the outer surface.

Table 5.9 Comparison of Changes in Extrema and Spread of Nodal von Mises Stress at the One-Third Tibial Length Comparison Location for Adaptations made under the 90° Configuration

Loading Case	Outer (Periosteal) Surface			Inner (Endosteal) Surface		
	MAX VMS	MIN VMS	MAX-MIN VMS	MAX VMS	MIN VMS	MAX-MIN VMS
Anterior-Inferior	-22%	-16%	-22%	-36%	153%	-48%
Inferior	-22%	-13%	-23%	-36%	159%	-48%
Anterior	-21%	-14%	-22%	-35%	160%	-48%
Superior-Inferior	-2%	30%	-4%	-16%	24%	-19%
Superior-Anterior	-1%	25%	-3%	-16%	31%	-18%
All_Around	-1%	31%	-3%	-14%	87%	-20%
Inferior-Posterior	-1%	21%	-2%	-12%	153%	-22%
Anterior-Posterior	0%	21%	-1%	-11%	159%	-22%
Posterior-Superior	15%	1%	16%	18%	-62%	23%
Superior	20%	10%	20%	16%	27%	15%
Posterior	28%	12%	29%	39%	33%	39%

While the trends in the cross sectional geometry gave a good indication of the trends in the von Mises stress distributions at the particular cross section, because the shape adaptation method developed in this work is applied to a component of a complex assembly of three-dimensional geometries, not just a two dimensional cross-section of a single bone, the variations in local shape and state of stress in one location affected the conditions throughout the bone studied. Therefore, in understanding the trends discussed above, clarity can be gained by examining the shape changes and resulting von Mises stress distributions under the mid-stance jogging critical load condition throughout the tibia bone for each of these "optimized" geometries.

5.3.3 Changes to the Overall Shape of the Tibia

The trends in the von Mises stress at the fracture prone region discussed in the previous section did not directly follow those of the cross sectional geometry at that location, indicating that the shape of the bone being optimized as well as its interaction with the other bones within the system studied under the applied load affects the local stress state. Therefore, the investigation of more global variations in the optimized tibial geometries was required. In addition to aiding the understanding of the changes of strength in the targeted location of likely stress fracture, which was the goal of the comparative studies in this work, by examining these more global variations, a better appreciation of the changes in the stresses within the studied system under this comparison "critical design" load set that result from the inclusion of the optimized tibial bone shapes is also gained. While the adaptations in each optimized geometry analyzed resulted in a more uniform strain energy density under each of the thirty-three particular combination of load case and limb configuration studied, it is important to understand the effects that these changes

have on the overall bone strength under other "typical" loads before recommendations about their inclusion in strengthening routines are made. For while the changes to the bone shape due to a set of loading conditions may improve its strength one location of the tibia as desired, an undesirable weakening in another location may also result.

5.3.3.1 Effect of Optimal Geometries on Stress Distributions under Comparison Load. The von Mises stress distributions under the comparison loading conditions in the sagittal midplane of the leg modeled using all thirty-three the "optimal" tibial bone geometries that were created as a result of the various loading conditions studied under the 0°, 45° and 90° configurations are presented in Figures 5.18, 5.19 and 5.20, respectively. Through these cross sectional views, the alterations to the inner and outer surface profiles for each "optimized geometry" along the axial length of the bone are also shown. In addition, the von Mises stress distribution over the transverse cross-section of the bone at the one-third length comparison location is presented in these figures, as this location, prone to stress fractures under the jogging loading conditions simulated, was the focus of the study. While the profiles of the bone all around its boundary surfaces were altered during the shape optimization processes simulated in this work, because the muscle force vectors only functioned in this sagittal two-dimensional plane, the presented images well represent the variations in the behavior of the bone that result from the shape optimizations under the conditions studied. In the images in these figures, the local bone coordinate system shown is at the comparison location, where the transverse cross-section was taken. The bone geometry with the colored stress contours in these images also depict the (scaled) deflection behavior induced in the bone system under the critical design load jogging conditions, while the outlined images of the bone geometry portray

the undeformed shape and resulting stress contour lines, for reference. The same stress contour ranges (top left for sagittal section, top right for transverse section) are used for all images presented in these three figures, and all deflections are scaled by the same factor so that comparisons can be made directly. The loads applied to the tibia bone geometry during the mid-stance jogging behavior are depicted in red arrows, and the behavior of the original, uniform circular cylinder before optimization is shown at the top of each image for reference. The changes to the overall shape of the tibia bone under each of the loads are first described, followed by the effects that these changes have on the von Mises stress distributions throughout the tibia bone under the application of the comparison "critical design" load set.

In all optimization cases, the region of application of the largest muscle forces (vastii and rectus femoris muscles for the cases with active knee extensors and biceps femoris muscle for cases with active knee flexors) showed very localized, very significant growth. Regions of generally large, but less extreme growth were observed at the attachment areas of other active muscles acting directly on the tibia, such as the tibialis anterior (ankle flexor) and soleus (ankle extensor) muscles. This large growth is not likely to occur in actual bone system as the bone is naturally wider in the region where muscles attach, thereby reducing the stresses induced by these muscles. This initially wider region was not included in the current model simplification. However, since the focus of the study was on the distal region of the bone, away from these areas of muscle force application, the exclusion of this geometric feature did not adversely affect the results of the study.

In the 0° straight leg configuration, three main patterns of growth were identified due to the application of the single load sets (Figure 5.18). The anteriorly and superiorly directed loads (Figure 5.1a) showed similar patterns of thinning of the cortical wall in the distal end of the bone (near the ankle) and thickening in the proximal end (near the knee) on both the anterior ($\Theta=0°$) and posterior ($\Theta=180°$) sides of the bone. The posteriorly and inferiorly directed resultant forces produced shapes under the 0° configuration that had significant thinning on the posterior side of the proximal end of the bone, just under the region of large growth where the biceps femoris muscle attaches to the tibia bone. The inferiorly directed load case also exhibited thinning in the anterior distal region of the bone and thickening in the posterior distal and anterior proximal regions. Under the posteriorly directed resultant load in this 0° configuration, the posterior side of the bone became thinner than the anterior side of the bone, which displayed slight thickening throughout the length. As a result of the sequential application of two or more of these loads in this straight leg configuration, the geometric attributes discussed for the single load cases were combined, enhancing or maintaining common effects and reducing differences, and resulted in more moderate amounts of change throughout. For example, the opposing thinning and thickening in common regions of the bone under the posterior and superior load cases "cancel" each other in the combined sequential posterior-superior case (Figure 5.18).

Under the 45° configuration (Figure 5.19), the anteriorly and inferiorly directed loads had similar patterns of growth and decay over the surface of the tibia bone studied, with a thickening of the cortical wall that was the greatest at the most distal location, near the ankle, and gradually reduced proximally, towards the knee.   In these cases the

anterior side of the bone showed slightly more thickening than the posterior side of the bone. The superiorly directed load resulted in a similar shape, but with significantly more thinning on the proximal end of the bone and more prominent shaping near the tibialis anterior muscle attachment location. In contrast, the posteriorly directed load resulted in a thickening in the proximal region of the bone, near the knee, gradually thinning distally along the length of the tibia approaching the ankle. As with the 0° case, the combinations of these loads tempered these extreme effects. For example, by applying the anteriorly directed load after the superiorly directed load, the desired thickening in the distal region near the stress fracture prone area was retained, however, the detrimental extreme thickening in the proximal region near the knee was reduced (Figure 5.19). Similarly, the extreme distal thickening and proximal thinning of the anterior and inferior loading cases can be nearly fully neutralized through the sequential application of a loading case that, on its own, resulted in opposing shape alterations, such as the superior or posterior loads, so that a nearly uniform cortical wall thickness was maintained.

As described in the 0° configuration, the prominent muscle forces acting directly on the bone in each load case under the 45° configuration resulted in local "disturbances" to these general trends (Figure 5.19). The anterior and inferior cases produced large region of growth near the knee extensor (rectus femoris/vastii) muscle attachment on the anterior side of the bone. The superior load case also showed this effect due to the knee extensors, but was additionally affected by the knee flexor (biceps femoris muscles) and the ankle extensor (tibialis anterior) muscles. Finally, the posteriorly directed load

showed the direct effects of the knee flexor (biceps femoris) and the ankle extensor (soleus) muscles on the locally large amounts of bone growth.

Consistent with the observed trends at the one-third cross section, the anteriorly and inferiorly directed loads under the 90° configuration resulted in nearly identical shape patterns over the length of the tibia bone to those that occurred under the 45° configuration (Figure 5.20). In this bent back configuration, the posteriorly and superiorly directed resultant loads induced similar growth trends on the anterior (positive x-direction or $\Theta=0°$) side of the bone, with thickening in the proximal end of the tibia bone and thinning proceeding distally. Under the posteriorly directed load, this trend was followed on the anterior side only. It was reversed, on the posterior (negative x-direction $\Theta=180°$) side, with thickening in the distal end, and thinning proceeding proximally. Under the superiorly directed load, the variation in posterior side of the bone followed that of the anterior side but with less thickening and more thinning.   As reported the other limb configurations, the multiload cases showed a blending of characteristic features of the single loads results, with opposite trends offsetting each other while maintaining like trends. For example, the distal thinning and proximal thickening of the superior case is counterbalanced by the distal thickening and proximal thinning of the inferior case in the combined superior-inferior case to create near uniform thickness throughout the length of the bone (Figure 5.20).
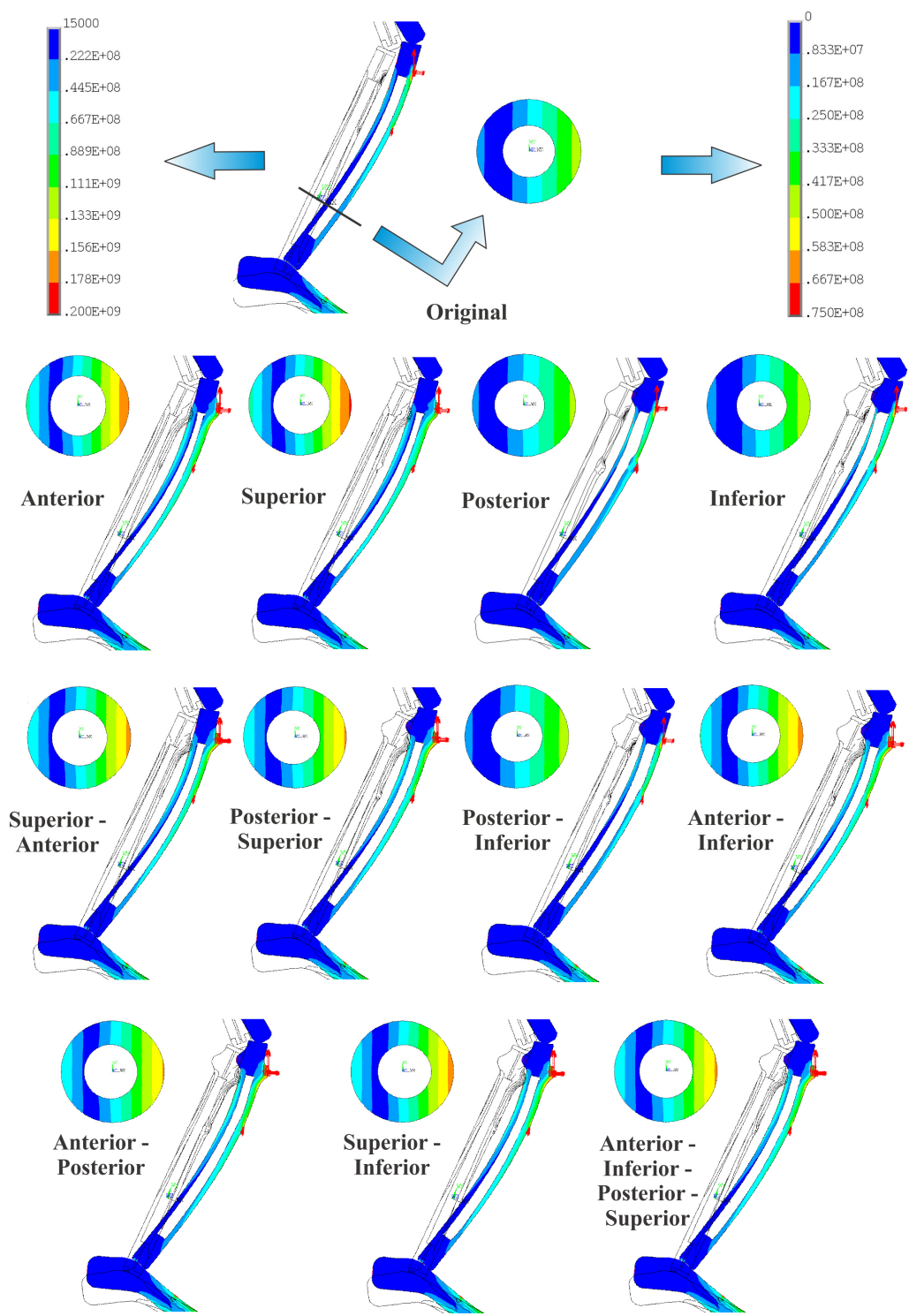
Figure 5.18 von Mises stress distribution under comparison load at sagittal mid-plane cross-section and transverse one-third length cross-section for 0° configuration for the "optimal geometry" resulting from the loading cases studied.
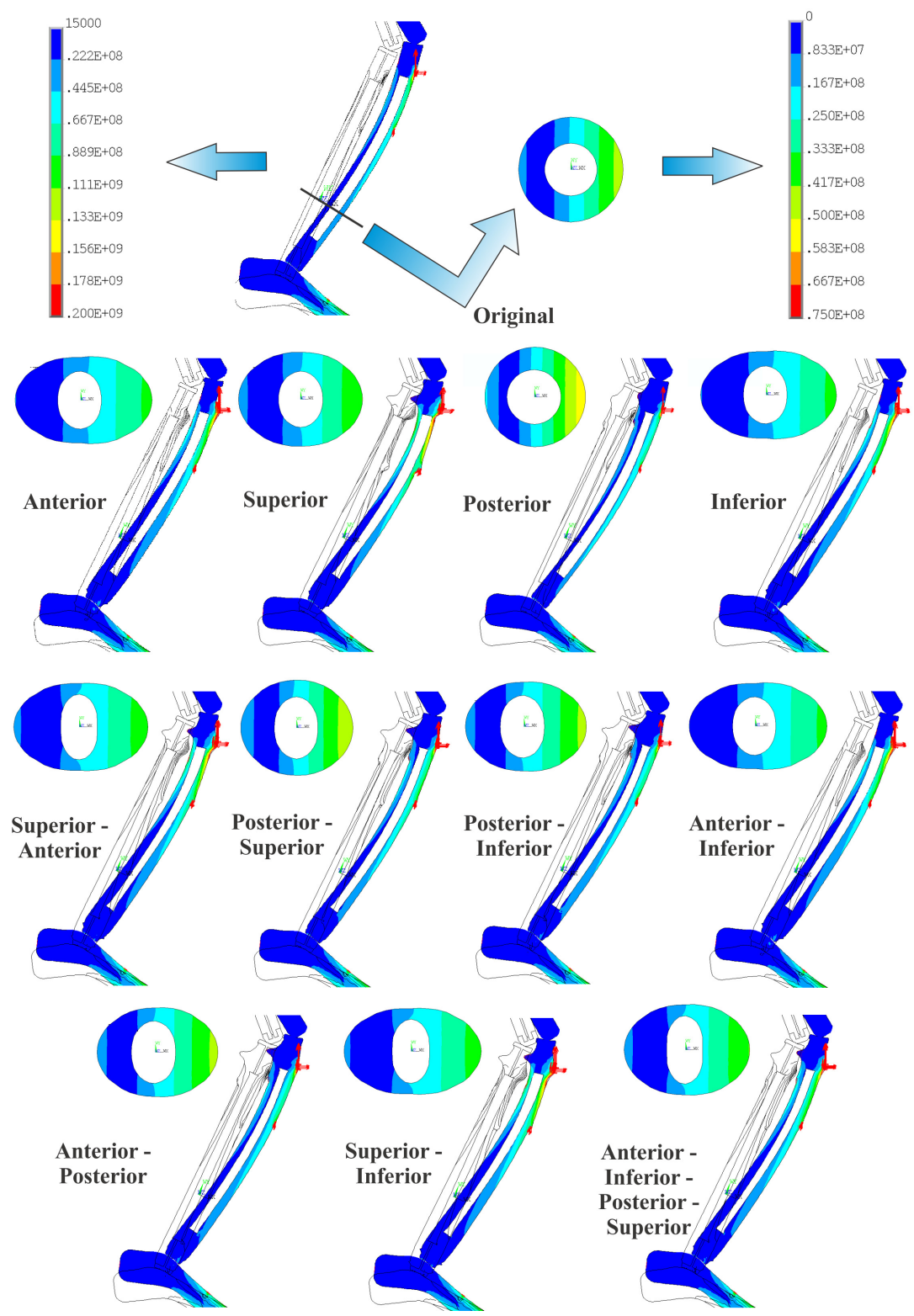
Figure 5.19 von Mises stress distribution under comparison load at sagittal mid-plane cross-section and transverse one-third length cross-section for 45° configuration for the "optimal geometry" resulting from the loading cases studied.
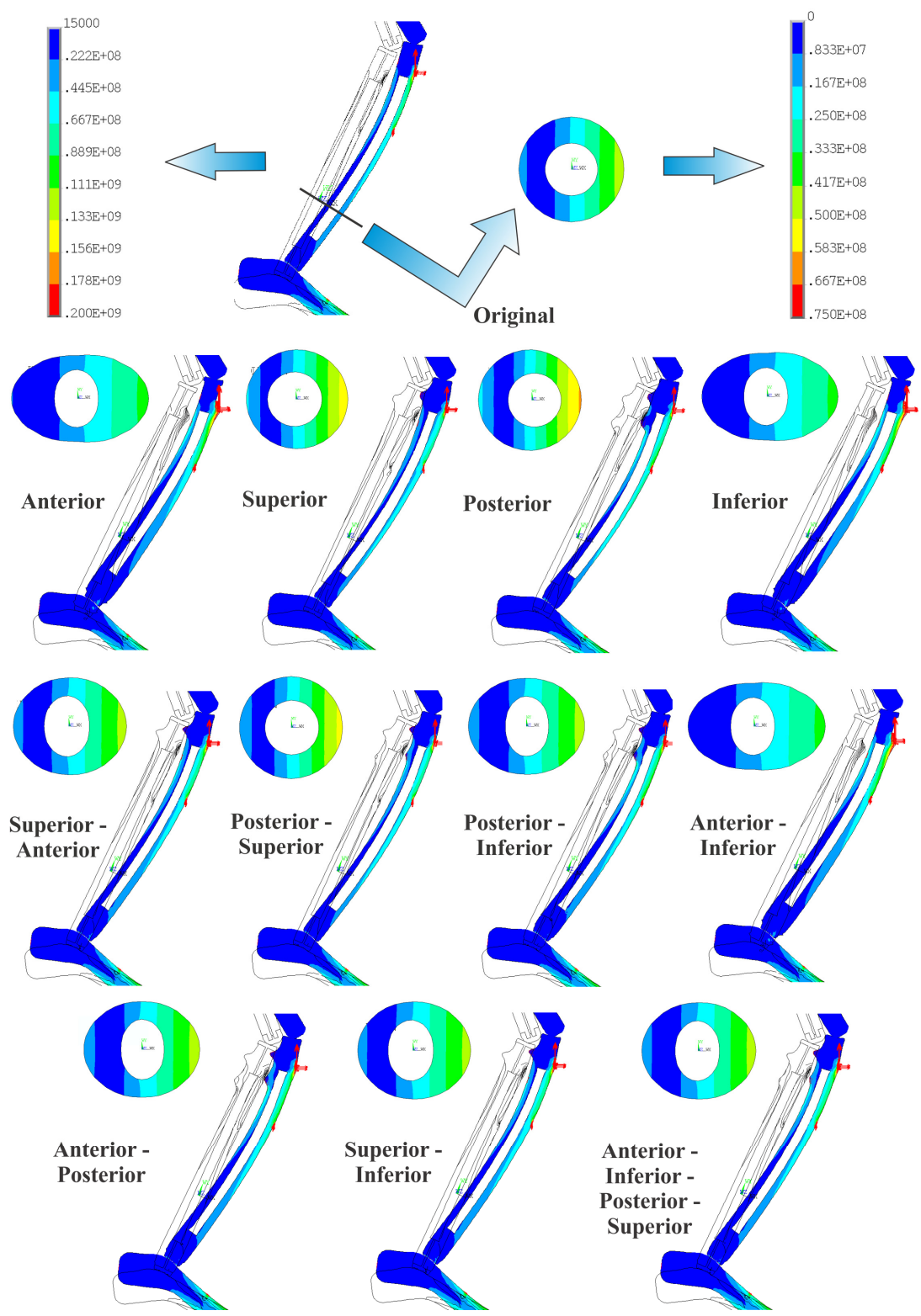
Figure 5.20 von Mises stress distribution under comparison load at sagittal mid-plane cross-section and transverse one-third length cross-section for 90° configuration for the "optimal geometry" resulting from the loading cases studied.

5.3.3.2 Change in Cortical Thickness along Length of "Optimized" Tibia Geometry.

For a more exact comparison between the changes to the geometric features and their effect on stresses developed under the "critical design" comparison condition of the mid-stance jogging, the changes with axial location in relative thickness and radial dimensions (total nodal growth) on the inner and outer surfaces of the "optimal" geometries created under the thirty-three conditions studied (Figure 5.1) can be examined. These axial changes in geometry were examined at three distinct locations on the perimeters of the bone: on the anterior ($\Theta=0°$ along the local positive x-direction), posterior ($\Theta=180°$ or along the local negative x-direction), and medial ($\Theta=90°$ along the local positive y-direction). Because of the symmetry of the geometry and the loading about the sagittal (local x-z) plane in this model (shown in Figures 5.18 through 5.20) assumed in this work, the changes to the lateral side of the bone were the same as those to the medial side and are, therefore, not presented. The focus in this review is on the similarities and differences in the optimal shapes under the various conditions studied. Figures 5.9, through 5.11 are useful to aid in understanding of Figures 5.18 through 5.20 and Figures 5.21 through 5.26.

Anterior ($\Theta=0°$) Side of the Bone

On the anterior $\Theta=0°$ side of the optimized tibial bone shape, some distinct trends in the cortical bone thickness in the hollow region are noted amongst the optimized geometries resulting from the single load sets under the three limb configurations studied (Figure 5.21). The anteriorly, superiorly, and inferiorly directed forces in the 0° configuration, the posteriorly directed force in the 45° configuration, and the posterior and superiorly directed forces in the 90° configuration all result in optimal shapes that are thinner than

the original geometry in the distal region and gradually thicken to greater than the original geometry in the proximal region. The inferior resultant force in the 0° configuration diverges from this trend in the proximal region (near normalized Z=0.67 in 5.21a) as the growth along this axial line is disturbed by the effects of the tibialis anterior muscle force which causes a spike in growth followed by a slight, brief, dip into decay just proximal to the muscle force. The posteriorly directed force in the 0° configuration follows that of the inferiorly directed force on this Θ=0° side of the bone except that there is no distal decay. The anteriorly and inferiorly directed loads in the 90° and 45° configurations, on the other hand, show opposing trends along the length of the bone on this Θ=0° side, with a thicker geometry on the distal end and a thinner geometry on the proximal end. The magnitudes of the thickness over the length of the bone in these four conditions are nearly identical. In the 45° configuration, the superiorly directed force follows a similar trend as these anterior and inferiorly but with less thickening distally and some thinning proximally after the disturbance caused by the tibialis anterior muscle (near the normalized Z = 0.67 location in Figure 5.21b).

Within this hollow bone region, the tibialis anterior muscle, when active, produces the local disturbance in the trend in the bone thickness at the normalized Z = two-thirds location seen in all plots in Figure 5.21. While not acting directly in the hollow region, the effect of the large knee extensor muscle forces results in the sharp increase in bone thickness just before the proximal cancellous region of the tibia bone (near the normalized Z = 0.83) in many of the cases examined at this (Θ=0°) location.
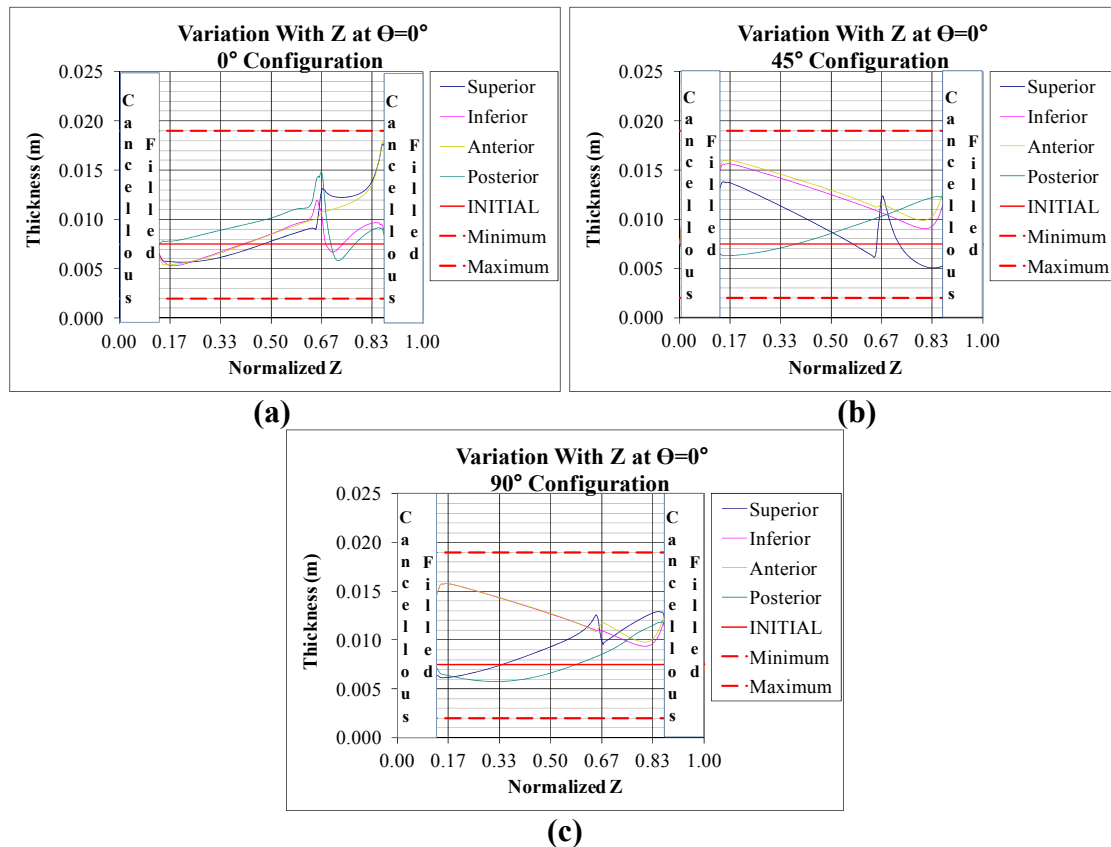
Figure 5.21 Change in thickness along the length of the hollow region of the tibia bone at the Θ=0° (anterior) side as a result of the shape adaptation optimization for the single load cases. (a) 0° (b) 45° (c) 90° configuration.

In examining the total amount of nodal growth along the inner and outer surfaces of the anterior (Θ=0°) side of the tibia bone (Figure 5.22), the significant local effect of the directly applied tibialis anterior and rectus femoris muscle forces is clearly seen in the proximal (normalized $Z > 0.5$) half of the bone as the two large spikes in total growth (near normalized $Z = 0.67$ and 0.83) on the outer surface plots (left side of Figure 5.22) and the small spikes at these locations and overall disturbance in the patterns of growth seen on the inner surface plots (right side of Figure 5.22) for many of the load cases in the three configurations studied, such as the superiorly directed load in the 0° or 45° configurations (blue curves). The more widespread effects seen in the gentler, smoother

regions of the growth curves, such as in the distal half (normalized $Z < 0.5$) of the bone away from the applied muscle forces results from the growth related to the indirect effects of the muscle force loading and bone constraints, such as the bending that was discussed above under the inferiorly and anteriorly directed resultant loads in the 45° or 90° configurations. This relationship between the stress distributions resulting from the thirty-three loading cases/limb configurations and the ensuing distributions of the local growth is discussed in more detail in Section 5.4.

Under the 45° and 90° configurations, the growth on the outer surface on this anterior ($\Theta=0°$) side of the bone was much greater than on the inner surface although the trends in growth and decay were the same on both surfaces (Figure 5.22b and 5.22c). This common trend in shape change on both inner and outer surfaces amplifies either the thickening or thinning that occurs under the particular conditions examined as the two surfaces work in harmony. Under the 0° configuration, however, (Figure 5.23a) the changes on the inner surface are much greater than those on the outer surface, and they dominate the overall changes in the bone's thickness (Figure 5.21). In fact, under the posterior loading in this 0° configuration, the thickening observed on the ($\Theta=0°$) anterior side of the bone at the one-third distal tibia length cross section in Figure 5.9 and Figure 5.21 is a result of the changes to the inner rather than the outer surface.

(a)

(b)

(c)
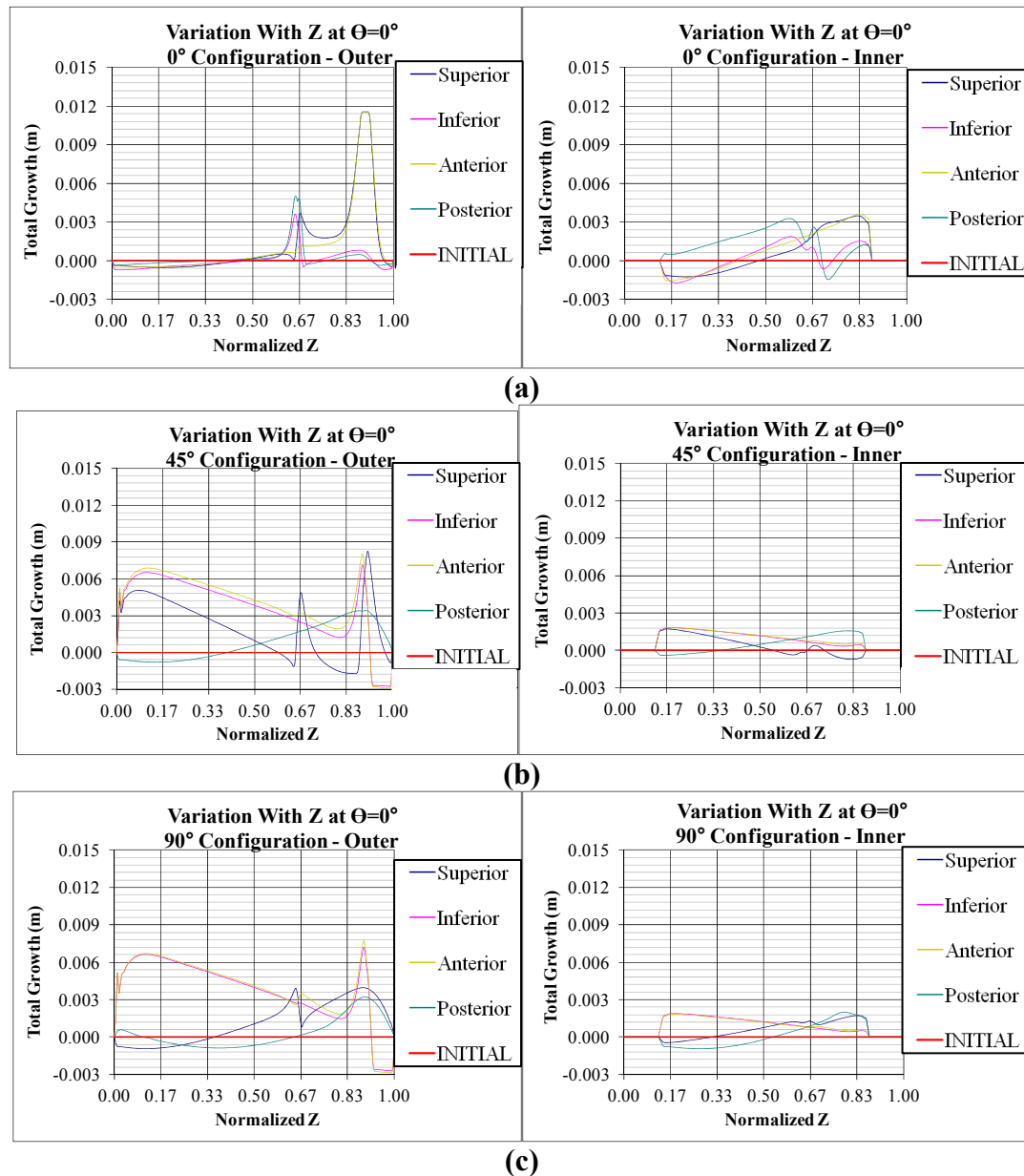
Figure 5.22 Total growth along the length of the tibia bone on the Θ=0° (anterior) side for the outer (left plots) and inner (right plots) surfaces as a result of the shape adaptation optimization for the single load cases (a) 0° (b) 45° (c) 90° configurations.

Posterior (Θ=180°) Side of the Bone

On the opposite (posterior, Θ=180°) side of the bone, the optimal shapes caused by the conditions studied also display some interesting trends (Figure 5.23). The inferiorly directed force in the 0° configuration as well as the posteriorly directed force in the 90°

configuration and the anterior and interior load sets in the 45° and 90° configurations all resulted in distal thickening (near the ankle) on this Θ=180° (posterior) side of the bone, gradually reducing to thinning near the proximal (near the knee) end of the hollow region of the tibia bone compared to the size of the initial cylinder. The posteriorly directed load in the 0° configuration followed the same trend of increased thinning from the ankle to the knee along the Θ=180° position, but throughout this hollow region, this load case resulted in decay, except for the very slight thickening at the start of the hollow region near the ankle (Figure 5.23a).

In contrast, a thinning in the distal region gradually increasing to a thickening in the proximal region is seen in the anteriorly and superiorly directed forces under the 0° configuration, the posteriorly directed force of the 45° configuration and the superiorly directed force under the 90° configuration at this Θ=180° (negative x-direction, posterior) side of the tibia bone. The posterior 45° and superior 90° cases result in nearly identical trends, with small changes in the thickness of the cortical wall in this hollow mid-shaft region of the tibia bone over much of the bone length. In all these cases, the initial thinning in the distal end converts to thickening near the knee. In most of the cases studied, in fact, all cases under the 45° configuration, the general trends on the anterior side of the bone match the trends in the posterior side of the corresponding load cases. However, the posteriorly directed load under the 90° and 0° configuration and inferiorly directed load under the 0° configuration show opposite trends in thickening and thinning on the anterior and posterior sides of the bone. This results in the very asymmetric geometry at the targeted comparison one-third cross-section as seen in Figures 5.9a (c) and (d), 5.11a (c), and the shifts in the center of gravity as shown in 5.12a and 5.14a.
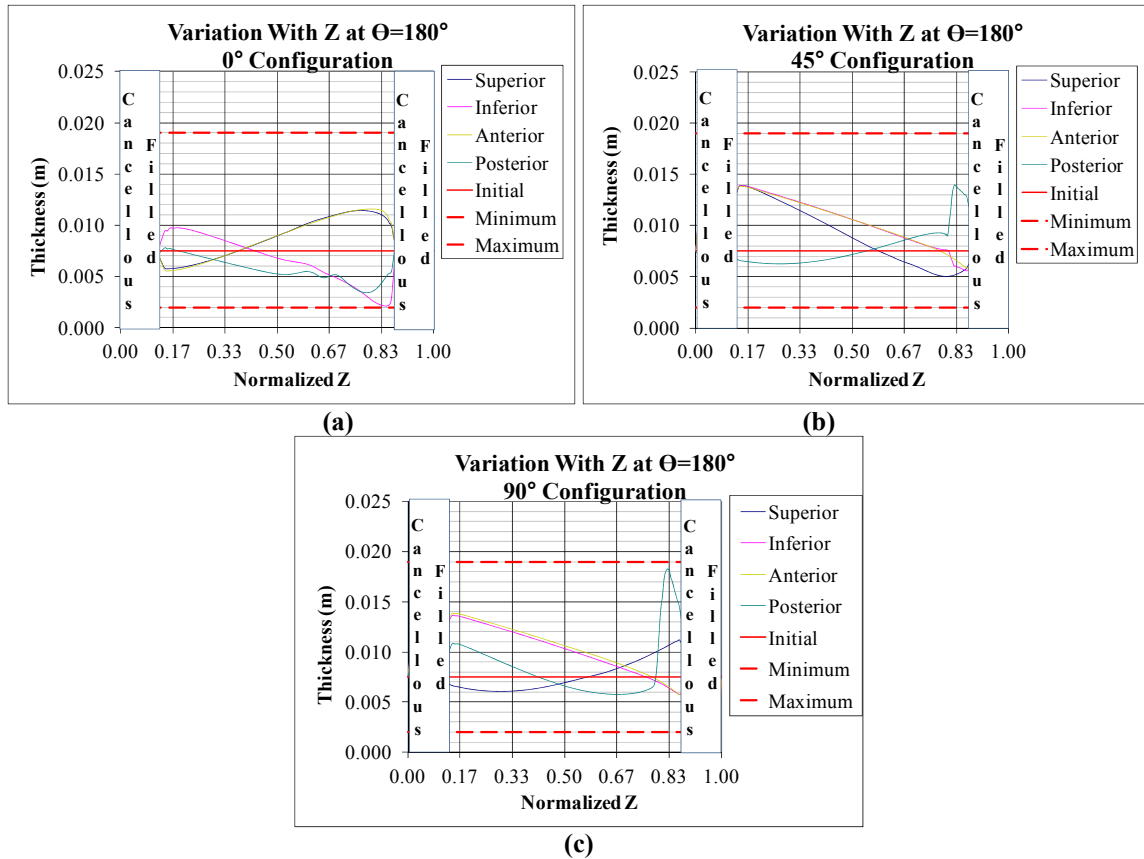
Figure 5.23 Change in thickness along the length of the hollow region of the tibia bone on the Θ=180° (posterior) side as a result of the shape adaptation optimization for the single load cases (a) 0° (b) 45° (c) 90° configuration.

Similar observations can be made in the nodal growth on the inner and outer surfaces of the posterior side of the bone that were used to explain the growth on the anterior side in the previous section regarding the relatively large amount of growth on the inner surface under the 0° leg configuration (5.22a and 5.24a). Similarly, the general trends of the growth on inner surface following that on the outer surface as seen in many of the plots on this posterior side of the bone such as the superior and anterior 45° and 90° cases (Figures 5.24b and 5.24c). It is interested that, as in the 45° case with the superiorly directed load on the Θ=0° anterior surface, in the 90° configuration on the posterior Θ=180° surface (5.24c), the posteriorly directed load (green lines) results in

much smaller total growth on the outer surface compared to the anterior (yellow lines) and inferior directions (pink lines), while on the inner surface all three have nearly the same amount of growth. This might be due to the number of shape adaptation iterations completed before achieving convergence and is examined in more detail in Section 5.4.

(a)

(b)

(c)
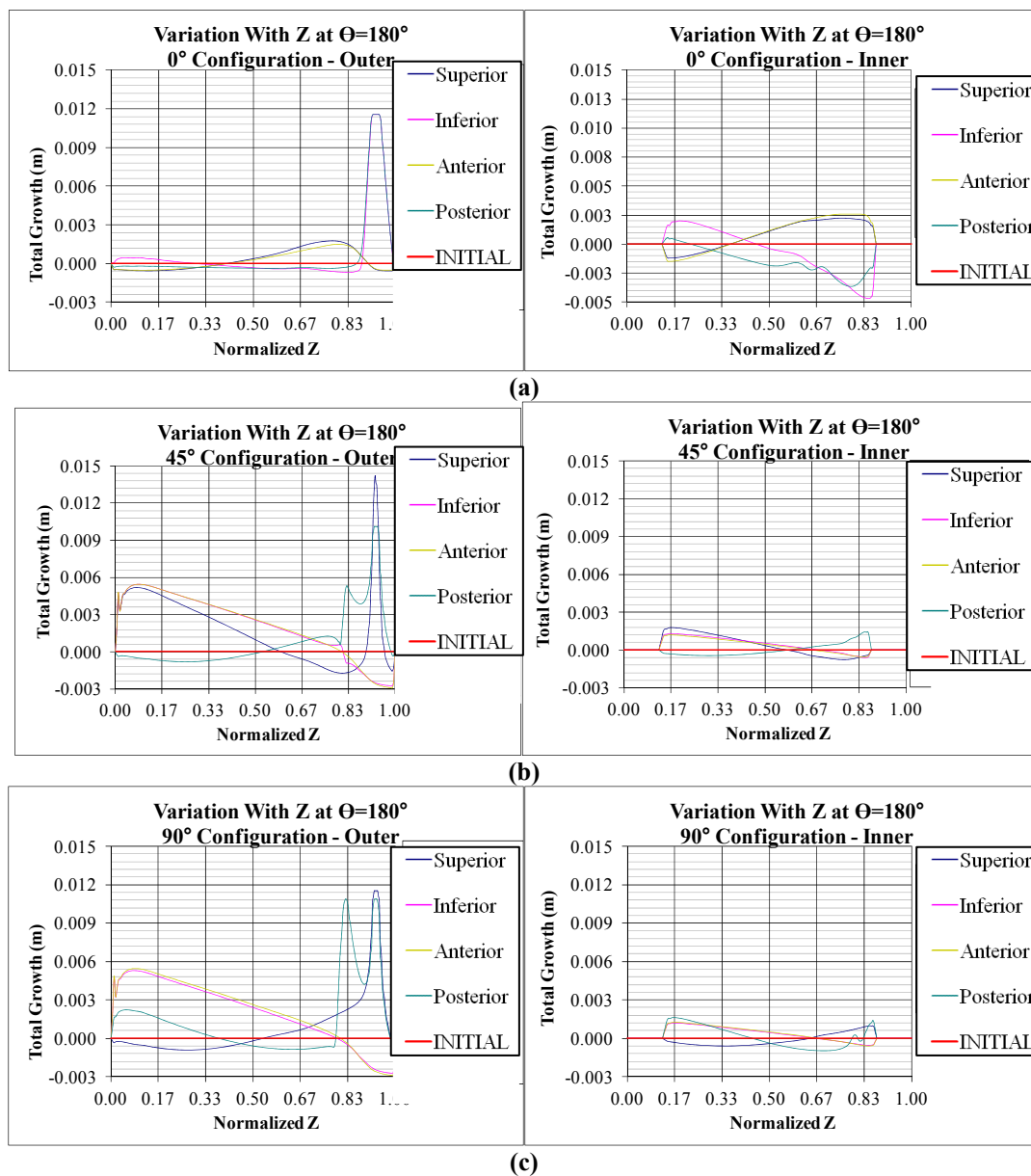
Figure 5.24 Total growth along the length of the tibia bone at Θ=180° (posterior) on the outer (left) and inner (right) surfaces as a result of the shape adaptation optimization for the single load cases (a) 0° (b) 45° (c) 90° configuration.

While less dramatic than on the anterior and posterior sides, the geometric on the medial Θ=90° and lateral Θ=270° sides of the bone are not inconsequential and have an important effect on the stresses developed in the optimized shape. These trends are less complex, mostly resulting in thinning over the length of the bone in the locations studied for all loading conditions and limb configurations (Figures 5.25 and 5.26). Slight growth was observed, however, on the inner surface of distal end on this medial side in the 0° configuration under the posterior and inferiorly directed resultant forces (Figure 5.9a (c),(d), Figure 5.25a, Figure 5.26a (right). This growth thickened this distal region of the bone contributing the high placement in the ranking of these cases in strength improvement amongst the loading cases studied in this straight leg configuration.

(a) (b)

(c)
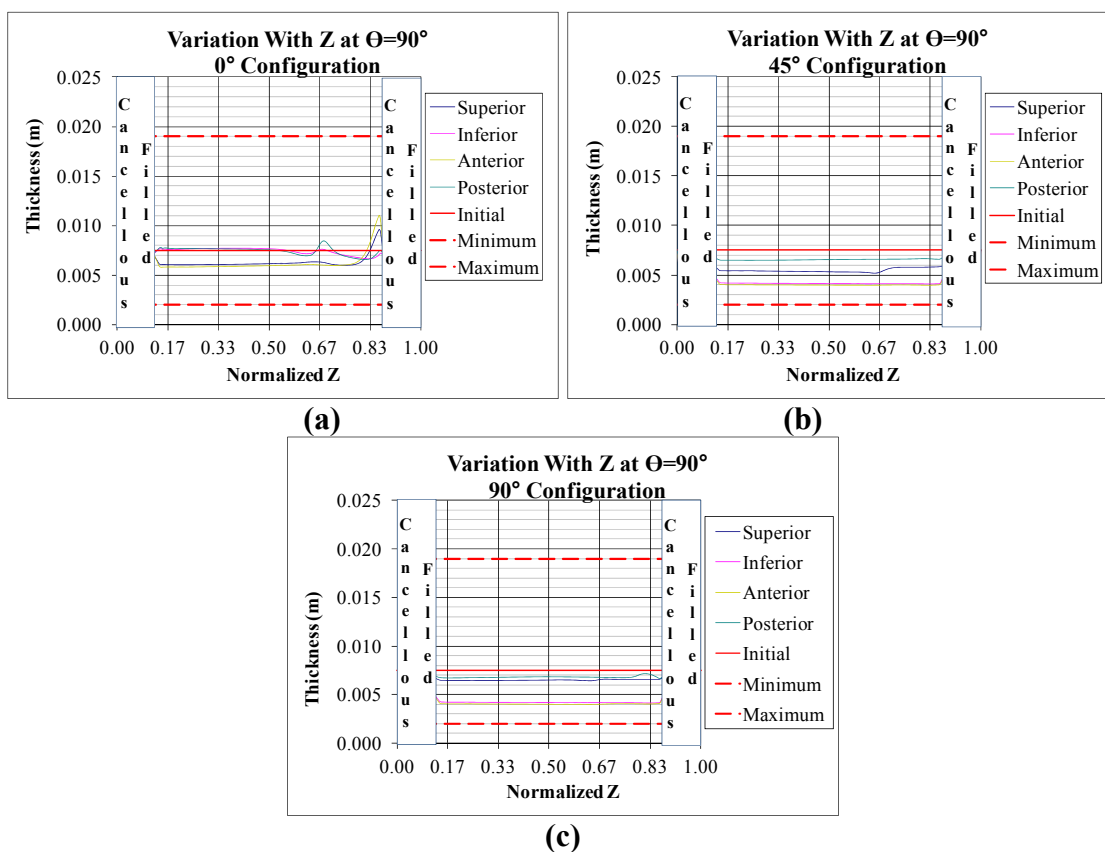
Figure 5.25 Change in thickness along the length of the hollow region of the tibia bone at Θ=90° as a result of the shape adaptation optimization for the single load cases (a) 0° configuration (b) 45° configuration (c) 90° configuration.
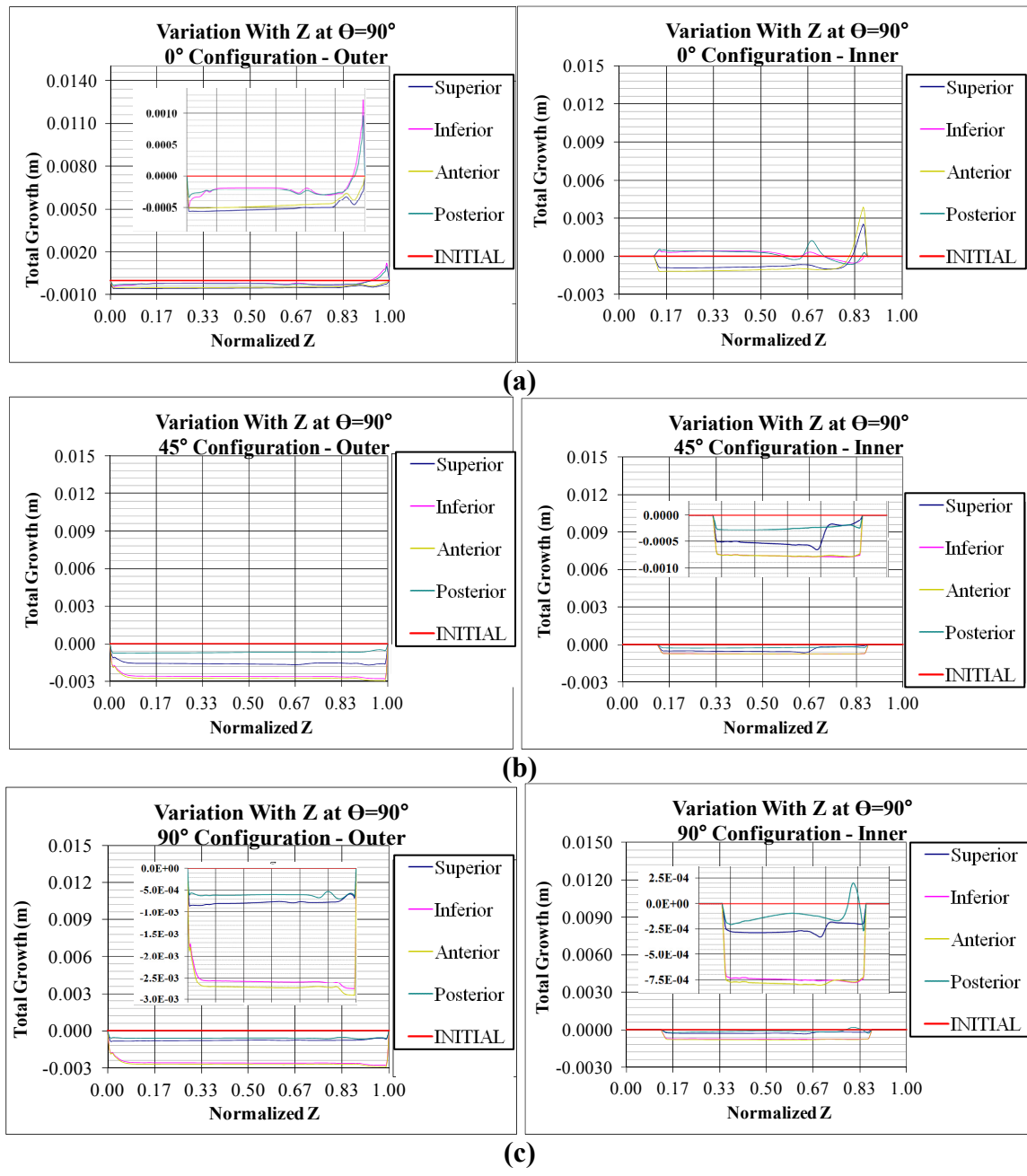
Figure 5.26 Total growth along the length of the tibia bone at Ѳ=90° (medial and lateral) side on the outer (left) and inner (right) surfaces as a result of the shape adaptation optimization for the single load cases (a) 0° (b) 45° (c) 90° configuration.

Sequential Load Application

As noted in the qualitative descriptions of the shape changes in Subsection 5.3.3.1, the sequential application of single loads that, separately, caused opposing trends in shape resulted in more moderate adaptations of the two. For example, (Figure 5.27a) while one single load may result in significant decay in a region of the bone, when included in sequential application with another single load that causes significant growth in the same region, the decaying effect of one is nearly completely offset by the growing effect of the other. The combination of a single load case that causes increasingly thickening with axial location with a case with causes increasing thinning over the same location results in nearly uniform shape over the surface studied (Figure 5.27b). Finally, in Figure 5.27c, the sequential application of two individual load cases with parallel trends with axial location but different amounts of growth results in a nearly averaged amount of the two.
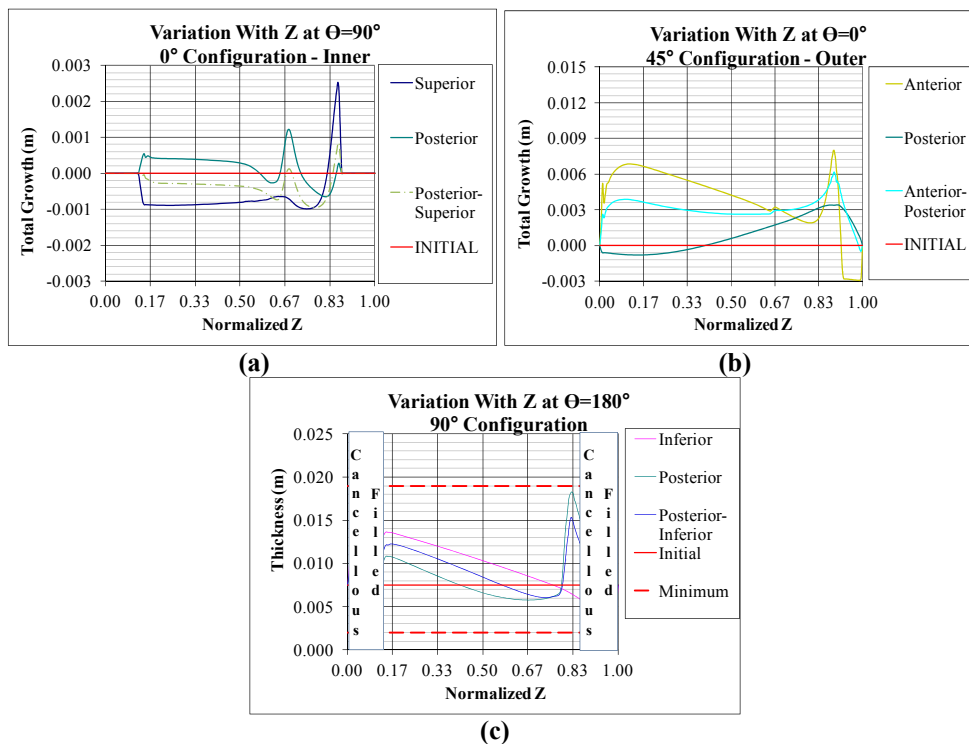
Figure 5.27 Tempering effect of sequential application of individual load sets on shape changes (a) 0° (b) 45° (c) 90° configuration.

5.3.4 Changes to the von Mises Stress Distribution in the Tibia Bone

The goal of any shape optimization problem is to use the alterations in the shape of an object to induce changes in its state of stress. As discussed in the previous section, significant deviations from the initially uniform hollow circular cylinder emerge as the result of the shape optimization processes performed on the tibia bone under the thirty-three conditions examined in this comparative study. While their effect on the von Mises stress distribution at the location targeted for strengthening was investigated in Subsection 5.3.2, the effect of the shape changes throughout the whole tibia bone on its stress distribution resulting from the application of the comparison (critical design load) mid-stance jogging conditions provides a better understanding of the overall strength of each optimized shape and gives insight into the effects of the various geometric features created within these optimized geometries in response to each loading set that was used to drive the shape adaptations. Trends in the changes in the nodal von Mises stress under the comparison conditions at the same representative locations along the optimizing surfaces as have been studied in the above subsections were examined.

In each configuration studied and under all load sets, the large amounts of growth in the regions of the applied muscle forces had a significant impact on the von Mises stress both at the location of muscle force application and in the bone material surrounding this region. When a load in the comparison configuration was applied near or at the same location on an optimal geometry, studied where significant growth occurred due to an applied muscle force during its shape optimization process, the von Mises stress significantly decreased, sometimes more than 50% over the stresses in that location for the initial uniform hollow circular cylinder. However, in the region of bone

immediately surrounding the load application site, the typically stresses increased nearly as much as they were reduced in the large growth region. This effect is pronounced in areas where the growth due to the load application transitioned very rapidly to decay. An example of this is in the area near the active tibialis anterior and knee extensor attachment locations under the 45° configuration (Growth under adaptive load see Figure 5.22b, von Mises stress under comparison case loads see Figure 5.28b) Also, in each location examined, the changes in the von Mises stress on the inner surface generally followed those on the outer surface (as seen in the above referenced figures). Following are some interesting observations regarding the changes in the nodal von Mises stress in the optimized bone compared to that of the initially circular cylinder and its relation to the shape changes along the length of the bone at the anterior ($\Theta=0°$), posterior ($\Theta=180°$) and medial/lateral ($\Theta=90°$) locations around the boundaries of each optimized bone.

While the trends in the changes in the von Mises stress (Figure 5.28) follow the trends in changes in bone thickness in the regions of large growth (Figure 5.21), such as where muscles forces acted in the shape optimization loading in the proximal region of the bone, the trends in these two features were not directly proportional in regions where the change in shape was more subtle, such as in the distal region of the bone, as the state of stress in this region was related to the more global response of the bone to the loading conditions exerted upon it. This is well represented along the anterior ($\Theta=0°$) face of the bone under the 0° straight leg configuration. All four single loading directions had nearly parallel changes in bone thickness (Figure 5.21a) in the distal region of the bone, with the anterior and inferior having the greatest amount of thinning, the posterior showing slight thickening, and the superior following in between. The von Mises stress under the

comparison conditions in the shape optimized under the posteriorly directed load, as expected, showed a decrease in this region due to the slight thickening (Figure 5.28b). Similarly, the inferiorly directed load showed a slight increase in stress due to the thinning in the most distal region of the bone, but then displayed a slight decrease as the optimized geometry became thicker than the original geometry near the middle of the bone. In contrast, while the trend in thickness in this region of the geometry optimized under the superiorly and anteriorly directed forces was very similar to that of the inferior case, the resulting changes in von Mises stress were very different, as they showed a constant increase in stress despite the eventual thickening over the original geometry. The stress in this distal region is directly related to the changes in the geometry in the proximal region, namely the very large growth that occurred due to the knee extensor muscle forces in the superior and anterior loading cases that created the geometry (Figure 5.22a). Because the knee extensor muscles are also active in the mid-stance jogging comparison case, their force is applied to the surface this very thickened region, creating a larger bending moment in the tibia that for the initial geometry, and contributing to the larger stresses in the distal tibia despite the shape changes in this region.

This undesired effect of increased applied moment with increased regional growth in the area of load application is a limitation of the current model. In the modeling method developed in this work, it was assumed that the loading imposed on the bones of the system due to the applied muscle forces was consistent for all optimized bone geometries under the comparison load. As just described, however, this was not the case when the shape optimization resulted in a region of very large growth where a muscle force is to be applied. The muscle force magnitudes applied to the bones in the mid-

stance jogging comparison model were the same in all cases compared, regardless of the tibial geometry. These muscle forces were calculated based on the moment arms in the initially uniform circular cylinder. When large growth occurred in these regions, as in the superior and anterior based loads in this 0° straight leg configuration and, similarly, in other configurations, the moment arm from the muscle force vector acting at this location to the joint about which acts is increased, creating a larger bending moment in the system and resulting in larger bending stresses simply due changes in the region of the muscle force application, not necessarily due to a weakening of the bone in the high stress region. It is this, rather than differences in the shape changes in the optimized geometry due to the anterior and superior loads over that of the inferior load, that is the likely cause of the significantly increased von Mises stress measured in these cases.

The significant (greater than two-fold) increase in the von Mises stress at this same anterior ($\Theta=0°$) due to the shape optimized under the superiorly directed resultant in the 45° configuration (Figure 5.28b), however, is not due to unintentional alterations in the applied load described above. Instead, it is directly related to the extreme thinning noted in Figure 5.18 and Figure 5.21b. A similar, though less intense, increase occurs on the opposite (posterior $\Theta=180°$) side of the bone also due to the thinning shown in Figure 5.15 and Figure 5.23b. This extreme weakening of the bone makes this optimization loading condition unfavorable despite the relatively significant nearly 10% decrease in stress at the fracture prone comparison one-third distal location. The thinning in this region was especially undesirable as it occurred near the stress concentration resulting from transition from the hollow to cancellous filled interior volume of the bone geometry.
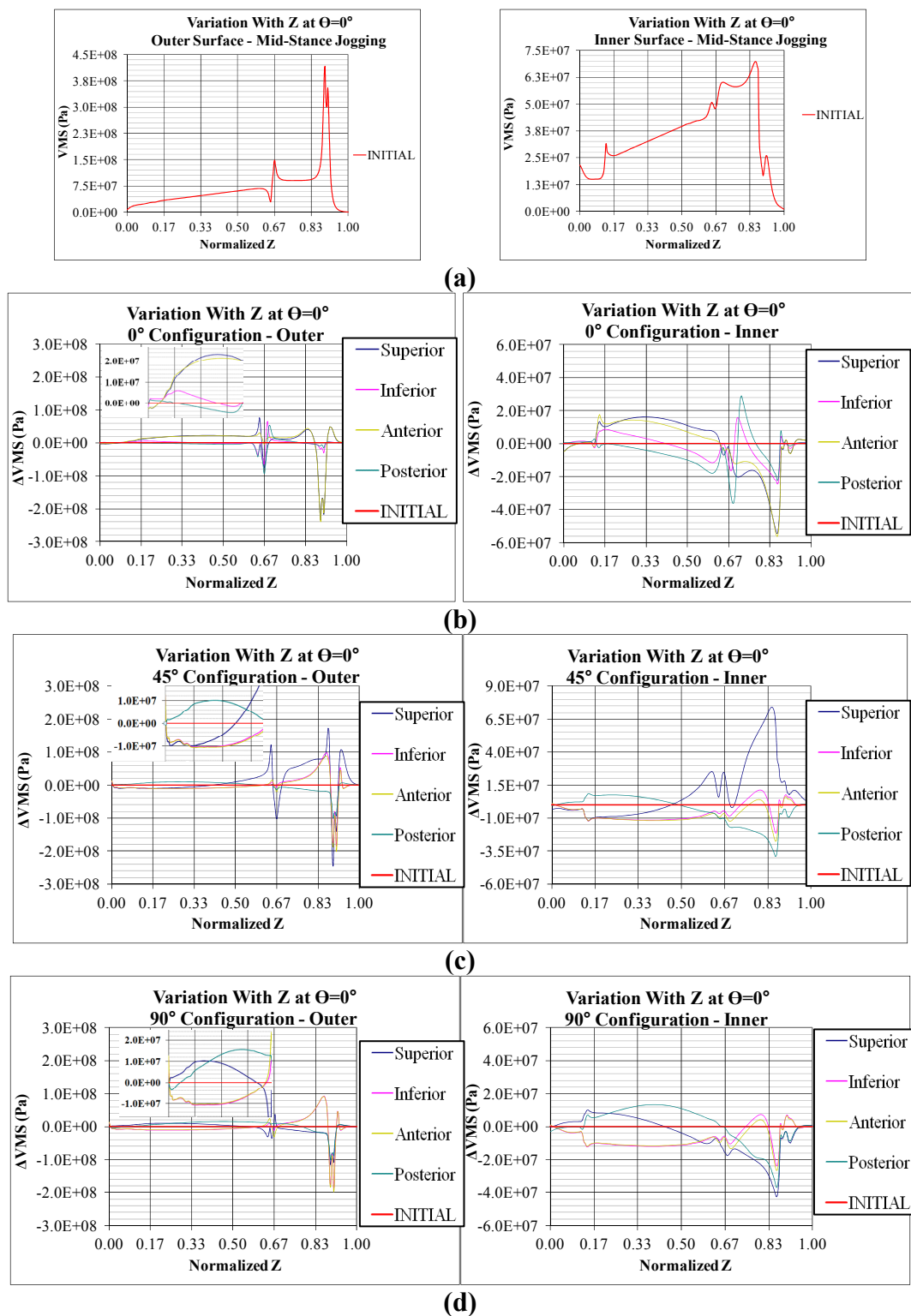
Figure 5.28 Change in nodal von Mises stress along the length of the tibia bone at the anterior (Θ=0°) side on the outer (left) and inner (right) surfaces as a result of the shape adaptation optimization for the single load cases (a) original von Mises stress distribution for reference (b) 0° configuration (c) 45° configuration (d) 90° configuration.

On the posterior (Θ=180°) side of the bone there was no direct loading in this comparison (critical design) case. As a result, the effect of the geometric changes could be more readily observed, unclouded by the extreme changes from the direct application of muscle forces. For example, for the bone geometry optimized under the superiorly directed resultant force in the 90° configuration (Figure 5.20), the gradual thickening of the bone on the proximal region of this posterior side (Figure 5.23c) resulted in a moderate decrease in a stress concentration in the original geometry, especially on the inner surface, (5.29d) due to transition from a hollow to a cancellous filled inner core of the bone under the bending loading in the tibia bone from the "critical" jogging condition.

Despite the relatively small stresses and changes in stress that occurred on the medial (Θ=90°) side of the bone, the changes in von Mises stress in this location are a strong example of the indirect effect of shape changes on alterations in local bone strength. The stresses in this region were nearly uniform for the initial geometry (Figure 5.30a). Likewise, changes in shape of the bone at this location were also relatively uniform over much of the optimizing region of the tibia bone (Figures 5.25 and 5.26). However, despite this uniformity, the resulting changes in the von Mises stress along this (Θ=90°) location normal to the loading plane, varied quite significantly (Figure 5.30 b, c, and d) for the shapes optimized in all conditions studied. These changes in stress at this medial location correlate well with the variations in stress that occurred along the axial length of the bone due to the shape changes on the anterior (Θ=0°) and posterior (Θ=180°) sides which were within the plane of loading and experienced greater alterations. This demonstrates the importance of using a three-dimensional representation of the bone geometry, even when a two-dimensional loading pattern is considered.

(a)

(b)

(c)

(d)
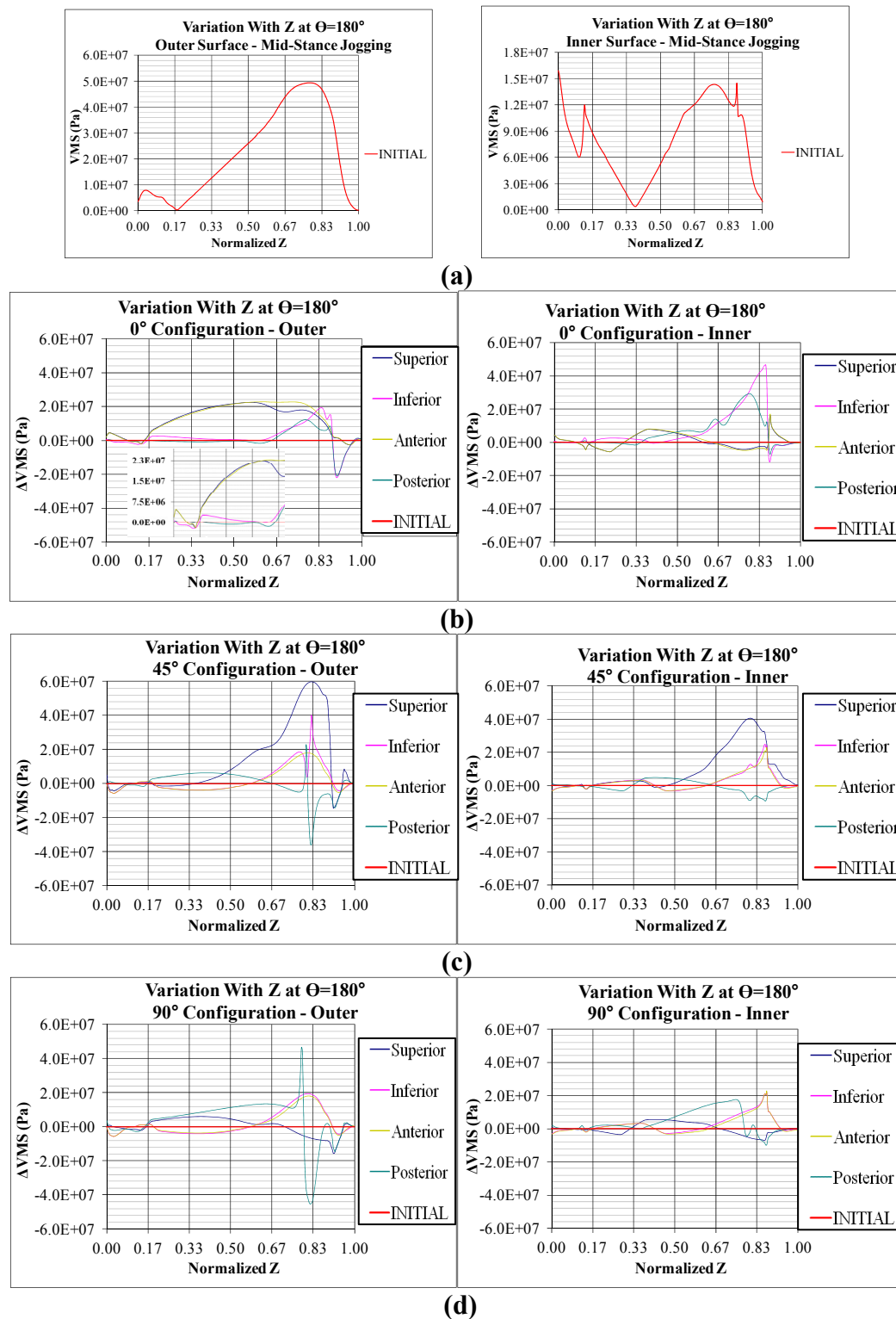
Figure 5.29 Change in nodal von Mises stress along the length of the tibia bone at the posterior (Θ=180°) side on the outer (left) and inner (right) surfaces as a result of the shape adaptation optimization for the single load cases (a) original von Mises stress distribution for reference (b) 0° configuration (c) 45° configuration (d) 90° configuration.
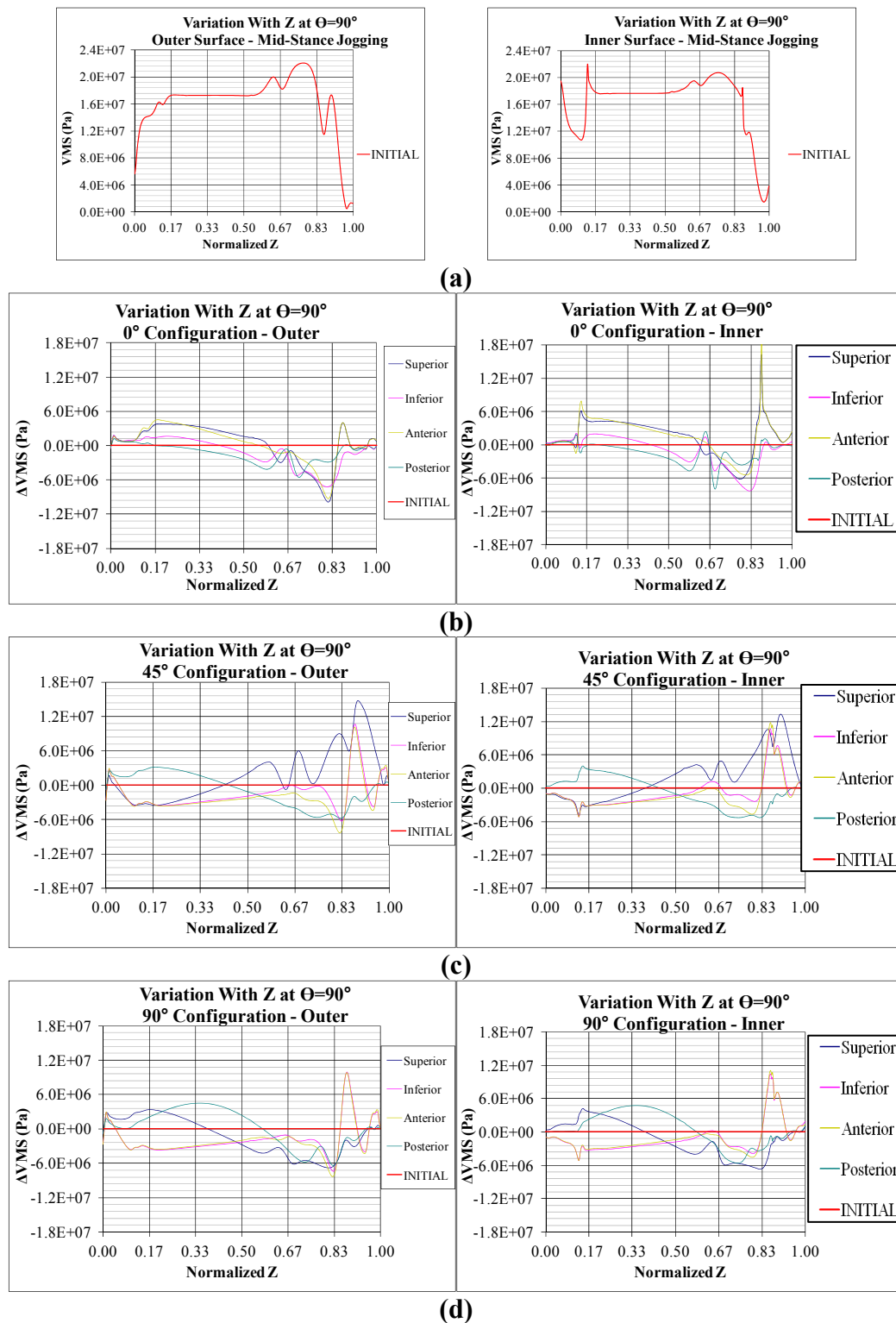
Figure 5.30 Change in nodal von Mises stress along the length of the tibia bone at medial (Θ=90°) on the outer (left) and inner (right) surfaces as a result of the shape adaptation optimization for the single load cases (a) original von Mises stress distribution for reference (b) 0° configuration (c) 45° configuration (d) 90° configuration.

The analysis of the effects of the shape changes over the whole adapting bone demonstrated the import of examining the whole stress field as a result of the optimization to ensure that undesirable effects do not develop at other locations while a beneficial improvement in strength is achieved at the targeted strengthening location. As in the qualitative descriptions of the overall shape changes and resulting von Mises stress distributions at the beginning of this section, the overall improvement of the bone strength, rather than the greatest improvement in one region, might be found through use of a multi-load set that maintains the beneficial strengthening in the target region, but mitigates the undesired weakening that may occur in other regions.

This discussion of the effects of shape change on the von Mises stresses under a particular load completes the objective of part of the second phase of this research, to use the developed model to directly compare the effects of various loading conditions on changes in bone strength. The final goal of this phase of the work was to use the results of the comparative case to understand the conditions within the function of the developed modeling method that led to the optimized shapes for the thirty-three conditions studied. Therefore, an analysis of the evolution of these "optimal" shapes was performed. Through this analysis, a better understanding of the relationship between the loading patterns and the shapes that reduce the variations in the local states of stress induced by them. Additionally, the function of the developed model under a wide range of loading modes and magnitudes is explored.

5.4   Evolution of the Optimal Shapes

The analysis of the function of the optimal shapes under the comparison "critical design load" mid-stance jogging conditions in Section 5.3 was used to solve the overall design problem examined in this work: finding a set of static loading conditions that would induce changes to the shape of a tibia bone such that it is "optimally" suited to resist stress fractures. However, the development of the alterations to the shape of the bone from the initially circular cylinder under each of the thirty-three static loading conditions studied as potential mechanisms for reducing the risk of fracture is essentially a set of thirty-three mechanical design problem. In each problem the "optimal" shape of the bone to function within a particular system configuration that best resists the particular set of loading conditions imposed is found. Therefore, each of these thirty-three design problems could be solved using the developed shape optimization/strength adaptation modeling method.

As described in Chapter 4, this optimization method was driven by the standardized nodal strain energy density, which considered how the difference between the nodal strain energy density and the average strain energy density over the surface being optimized compared to the standard deviation of the strain energy density over the surface. Further, the completion of the evolution of the optimal shape was defined based on either the achievement of a particular relative reduction in the variation of the strain energy density over the optimizing surface, which defined "convergence", or the approach to one of a number of defined size limits.   Therefore, to understand the evolution of each optimized shape, the manner in which the completion of the adaptations was signaled and the resulting changes to the surface average and standard deviation of

the local strain energy density should be examined. This section begins with a discussion of the convergence of each of the thirty-three cases studied. It then compares the more global changes in the mechanical state of the optimizing surface through measures of average and variation of the local strain energy density. Finally, the shape changes are examined through correlations between local nodal strain energy density, global strain energy density, and the ensuing changes in the positions of the surface nodes.

5.4.1 Convergence

The first step in the comparison of the convergence of each of the loading cases studied is the determination of the manner in which the simulation ended. Next, a comparison of the "path to convergence" as measured by the change in the Q14Spread, a measure of the variation in nodal strain energy density over the optimizing surface (see Chapter 4), from that of the initial case is considered for both inner and outer optimizing surfaces. Because the multiple load cases required the convergence of each of its components to signal the satisfaction of the optimization goal, the full data only for the single load cases is presented. Additional remarks are made about the alterations to the convergence trends resulting from the sequential application of multiple loads.

5.4.1.1 Stopping Criteria Achieved. The manner in which the "optimal" geometries used in the analysis in Sections 5.2 and 5.3 were reached may influence the conclusions drawn about its performance and selection for use in designed bone strengthening activities targeted at fracture prone regions. Therefore, the identification of the method of the completion of the simulation (achieved the defined convergence or size limit) is important.

0° Configuration

In this straight leg configuration, every case reached the maximum cortical wall thickness criteria before it achieved convergence on both the inner and the outer surfaces. This size limit was attained either at the region of the knee extensor (vastii and rectus femoris) attachment on the anterior side of the tibia or the region of knee flexor (short and long heads of biceps femoris) on the posterior side of the tibia, depending on the muscle activity for the particular conditions examined. In the single load cases, the full inner region of the muscle force application area (see Chapter 2 for description) grew uniformly to the maximum thickness. In the multiple load cases, however, due to the variation in the applied magnitude and distribution of muscle forces on the system, the maximum thickness criteria was achieved only at the single node in the center of the force application area.

Specifically, the superior, anterior, anterior-posterior, superior-anterior, and anterior-inferior cases reached a maximum thickness because of the knee extensor muscle forces, while the inferior, posterior, superior-inferior, posterior-inferior, posterior-superior, and all around loading cases reached the maximum thickness value due to the knee flexor muscle forces. This information provides insight into the loading mode that dominated the behavior of the bone shape changes under the sequential application of multiple loads. Under this straight leg configuration, for each single load case, the dominate muscles were identified as the knee extensors for the anteriorly and superiorly directed resultant loads and knee flexors for the posteriorly and inferiorly directed loads (Figure 5.7). All double load cases containing anterior loading, with its very large knee extensor muscle forces, reached maximum thickness value where these muscles attached.

However, all double load cases containing either posterior or inferior loads reached maximum thickness at the knee flexor attachment location. This was true even for the superior-inferior and all around cases where the muscle forces that generated the superiorly directed resultant were double in magnitude from those to create an inferiorly directed one, implying that the localized growth under regions of high stress was greater in these knee flexor based conditions than the knee extensor based ones.

The maximum number of iterations reached before the maximum thickness or convergence was achieved on each the inner and outer surfaces for all load cases studied in this 0° configuration is shown in Figure 5.31. Only the inner surface of the superiorly directed resultant load achieved the 50% reduction in the Q14Spread from that of the initial geometry (convergence criterion) in this straight leg configuration. Of the remaining surfaces and loading conditions, all single load cases reached the maximum thickness at nearly the same iteration. The majority of the double load cases achieved maximum thickness at common iteration count as well, slightly greater than the single load cases. Because maximum thickness was the stopping criterion and all cases stopped after approximately the same number of optimization iterations, it is likely that the maximum growth per node limit was reached for every iteration so that these regions of very high stress near the applied loads noted above grew at a constant rate, independent of the specific value of the strain energy density and particular load case studied. The two double load sets, superior-anterior and posterior-inferior, that had the smallest number of iterations to maximum thickness, likely reached the maximum growth limit under both loading conditions, despite the reduction of the step size per iteration based on the number of loadsets involved (i.e. $\alpha=\alpha/2$ in Equation 4.23 for double load case).
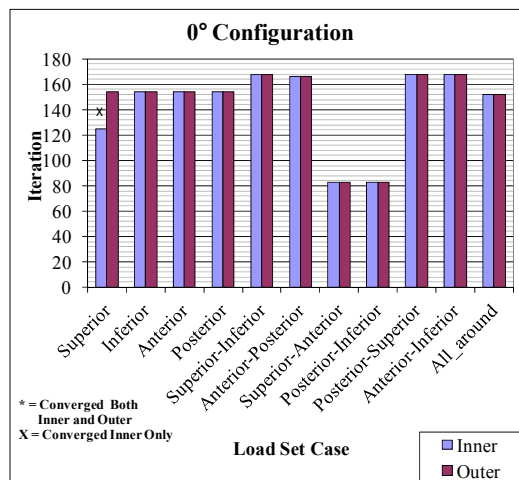
Figure 5.31 Iterations to convergence or size limit for the cases studied under the 0° straight leg configuration.

45° Configuration

In this 45° configuration, all single load cases as well as the anterior-inferior double load case reached convergence on both inner and outer surfaces. Additionally, all other double load cases reached convergence on the inner surface only, meaning both sets of loads reached convergence on the inner surface but not on the outer surface. Only the four-loadset case (all around) did not achieve the defined convergence on either surface. The convergence behavior for these cases is presented in Figure 5.32.
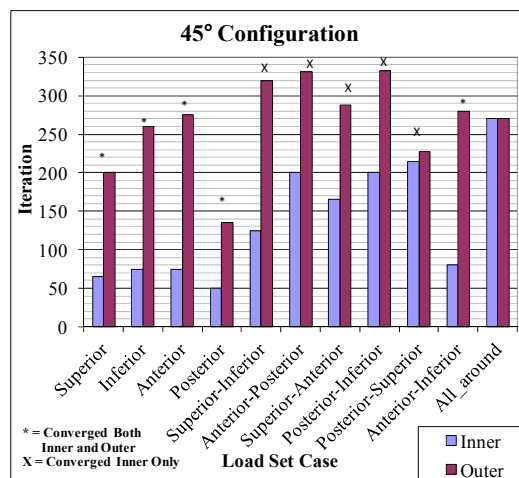
Figure 5.32 Iterations to convergence or size limit for the cases studied under the 45° conditions.

Of the cases that did not fully converge, the anterior-posterior, posterior-inferior and posterior-superior reached a maximum thickness limit at the attachment point of the short and long head of the biceps femoris just below the knee on the posterior side of the bone. The superior-inferior, superior-anterior and all around cases reached a minimum thickness limit at the Θ=270° location just above the cancellous filled region on the distal end (near the ankle). This region was noted as a high stress location under the bending loads in the comparison mid-stance jogging conditions (Section 5.3) due to the geometric transition from the cancellous filled solid to hollow geometry. The zone was also flagged as a potentially high stress location, requiring specially developed node smoothing methods to be applied (Chapter 4). The attainment of a minimum thickness at this Θ=270° location, which is not in the plane containing the applied muscle forces, parallels the adaptive behavior seen under a bending load (Figure 4.1), implying that bending may be the major loading mode in the tibia bone under these conditions.

90° Configuration

Under the 90° configuration, only three of the four single loading conditions, the inferiorly, anteriorly, and posteriorly directed resultant load sets achieved full convergence on both inner and outer surfaces before a size limit was reached. The superiorly directed case achieved the defined convergence only on the inner surface. Further, the combination of the anterior and inferior loads achieved full convergence while the four load set case and the posterior-superior case attained the convergence only on the inner surface (Figure 5.33). Similar to the 45° configuration, all cases that did not reach convergence met a maximum size limit at the attachment location for the biceps femoris muscles.
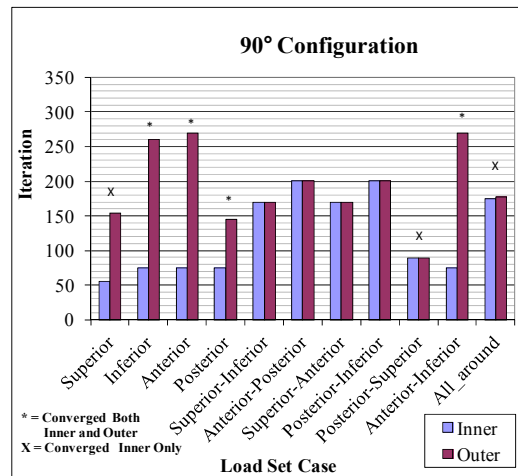
Figure 5.33 Iterations to convergence or size limit for the cases studied under the 90° conditions.

5.4.1.2 Trends in Convergence Measure. To better understand the convergence behavior of the load cases studied, plots of convergence measure with iteration were analyzed. From these convergence plots, the converging (increased uniformity) or diverging (increased variation) behavior of each set of conditions studied was identified by the slope of a plot of the convergence measure versus optimization iteration.

0° Configuration

While all outer surfaces moved towards increased uniformity, the inner surface of the posteriorly directed and inferiorly directed resultant forces did not (Figure 5.34). The behavior of the model at the interface between the hollow cortical shell and the cancellous filled region, with the discontinuities in materials and geometry may have been responsible for the nonconvergence of the inner surface in these cases. This zone has been identified as a high stress area, subject to additional smoothing. It may not be possible to reduce the stress in this region by shape changes alone. Interestingly, in contrast to the posteriorly and inferiorly directed forces, the inner surface converged faster than the outer for the anteriorly and superiorly directed resultant force cases in this

configuration, indicating a greater reduction in the variation of the stress state over the inner surface.
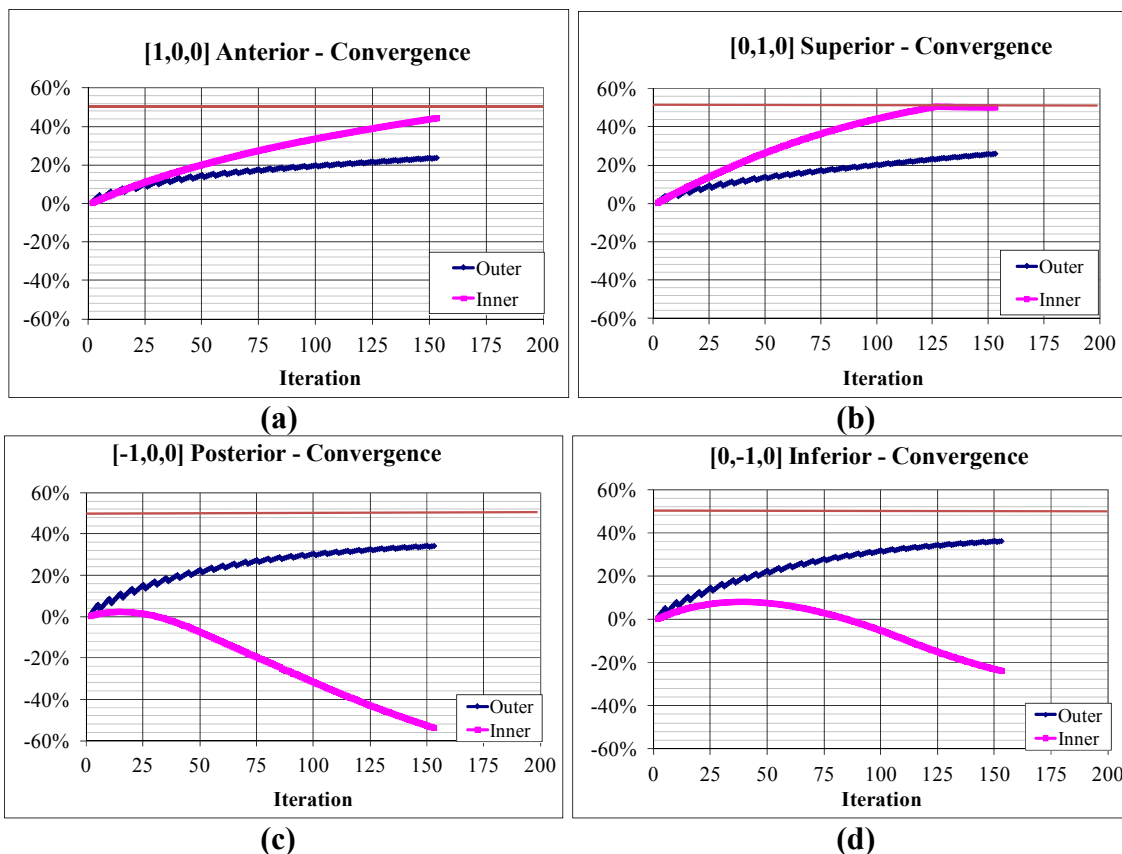
Figure 5.34 Convergence measure with iteration for the single load cases in the 0° configuration. (a) anteriorly (b) superiorly (c) posteriorly (d) inferiorly directed resultant forces.

Because the location of maximum thickness was found to vary with loading conditions, a further look into the convergence behavior of the multiload combinations of these individual load cases under this configuration was warranted. In the multiload cases, a sequence of applied loading conditions is iteratively repeated to create the shape changes (See Chapter 4 for details of this process). First, the shape changes due to the stress state under one loadset. Then, the next load is applied to the new shape, and it is further altered. Therefore, the resulting shape is not the optimal geometry to improve the

uniformity of the strain energy density under a single load condition. Rather, it is the "best" under all of the loads applied during the optimization process. In Figure 5.35, the convergence measure for all single and multiload cases containing an anteriorly directed load is presented. In the multiload cases, the data that is plotted is a measure of the variation of the nodal strain energy density values under the anteriorly directed resultant force loading condition for the geometry that was altered due to a the sequential application of a series of loadsets, only one of which was the anteriorly directed load under which this convergence measure was calculated. Instead of the gradual approach to constant state of uniformity as occurred under only one loading condition (Figure 5.35a), the diverging behavior in the multiload cases (Figures 5.35b through e) indicates that the sequence of multiple loads applied to this straight leg configuration did not make it stronger under the anteriorly directed loading condition, which was only one part of the total loading to which the bone was subjected. This exemplifies the need to study the independent loading conditions by which to compare the effectiveness of the particular prescribed loading sets in improving the bone's strength rather than the optimizing load itself. Additionally, although the location of the maximum thickness for the multiload sets containing the anterior load occurred at the same location as that which developed under the single load anterior case, the convergence trends clearly did not follow the single load case.
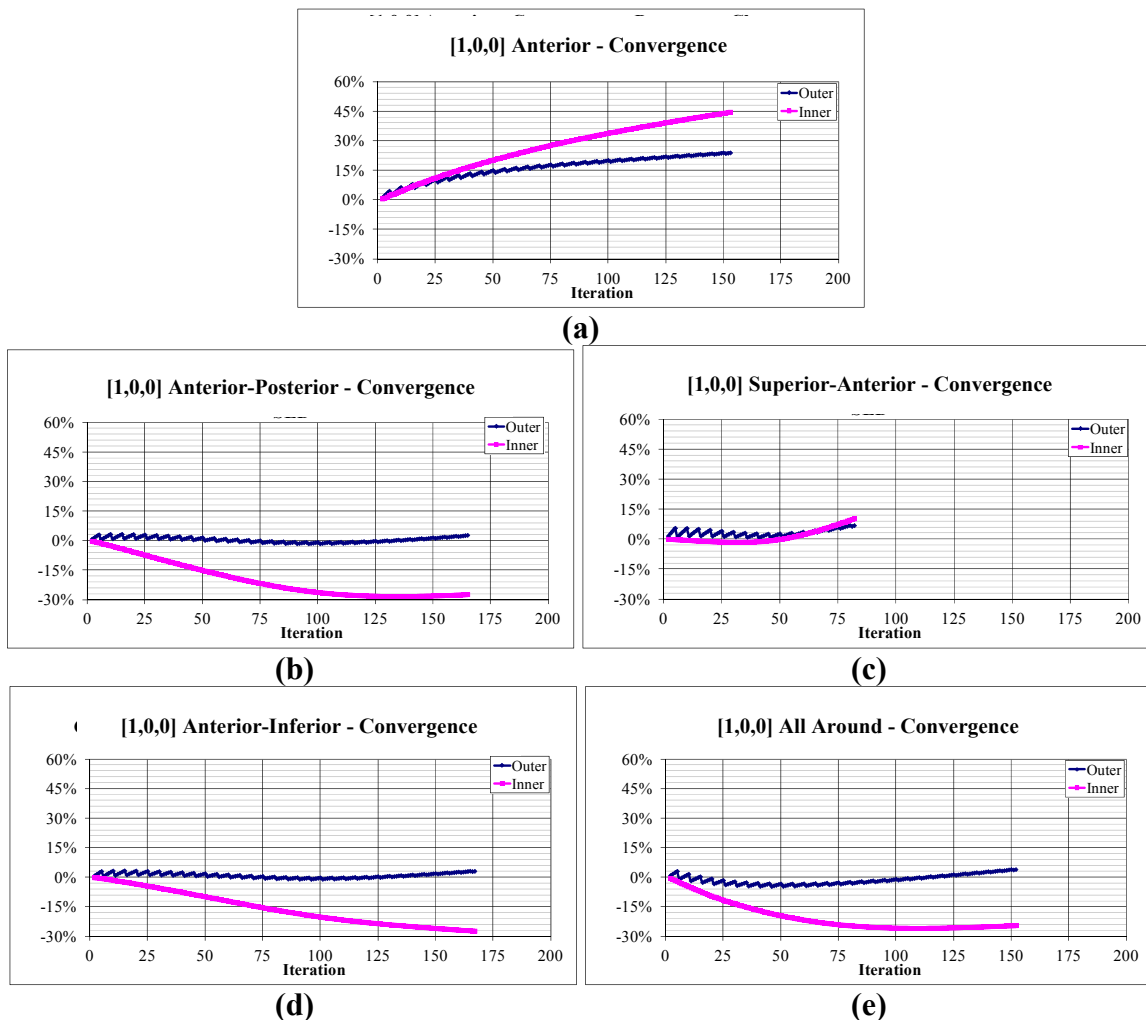
Figure 5.35 Convergence with iteration for the anteriorly directed resultant force component of any single or multiload case in the 0° configuration. (a) anterior (b) anterior-posterior (c) superior-anterior (d) anterior-inferior (e) all around.

In contrast, the same analysis performed on the posteriorly directed load showed similar trends from single to multiload (Figure 5.36). While none of the multiload cases achieved as high a convergence value as the single load case, and while the rate of change in the variation of the convergence differed between the cases, the basic trends were very similar, indicating that the effects of posterior loading conditions may have a dominant influence over the optimizing behavior of the bone in this 0° straight leg configuration.
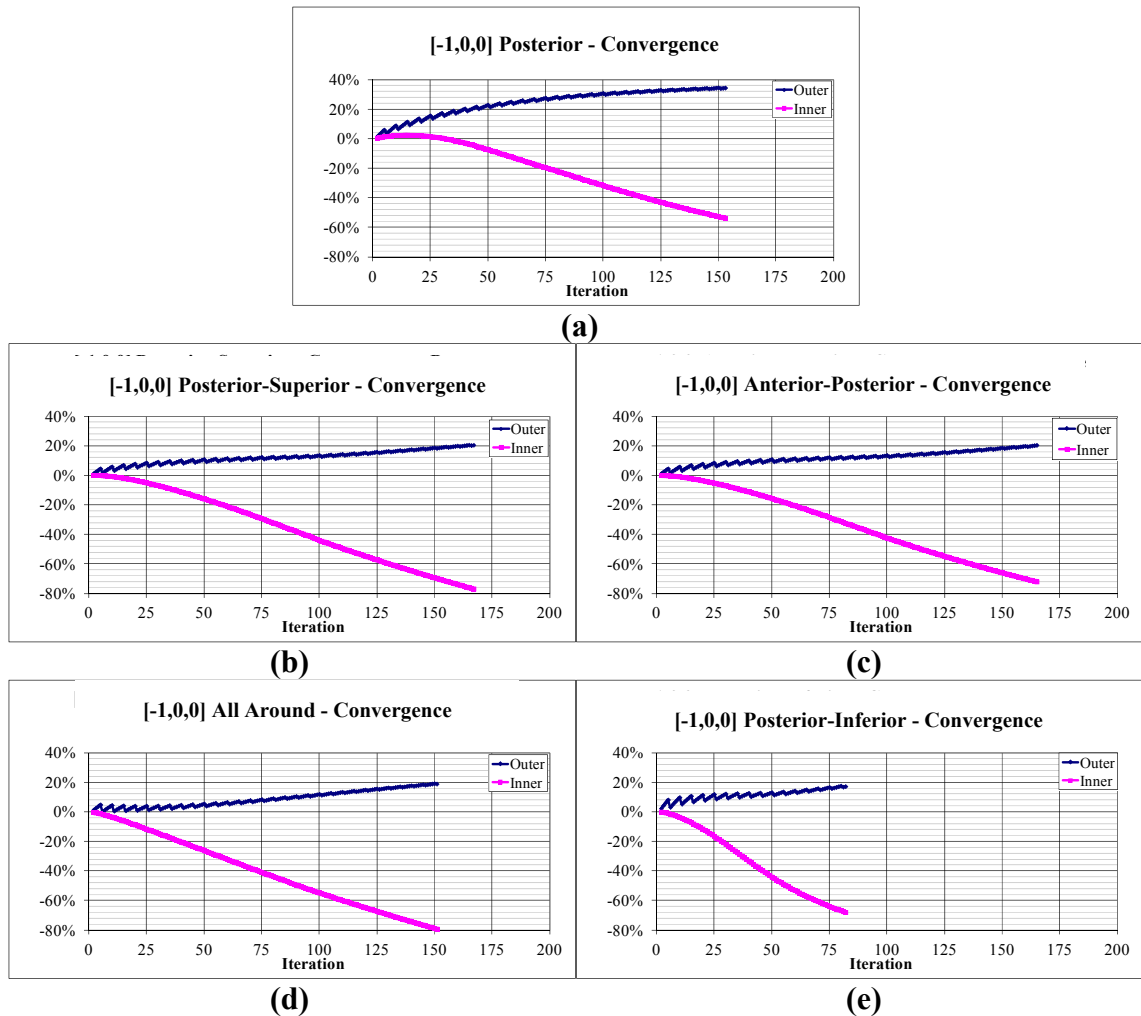
Figure 5.36 Convergence with iteration for the posteriorly directed resultant force component of any single or multiload case in the 0° configuration. (a) posterior (b) anterior-posterior (c) posterior-superior (d) posterior-inferior (e) all around.

45° Configuration

Unlike the 0° configuration, many of the load cases under the 45° configuration displayed strong convergence on both inner and outer surfaces (Figure 5.37). All surfaces showed converging trends even if the convergence criteria was not reached before a size limit was. In all cases, the inner surface convergence value was greater than that of the outer surface, and the inner surface converged more quickly than the outer surface, in as little as one-fifth of the number of iterations of outer surface convergence. Upon convergence,

the inner surface convergence measure did not become nearly as constant as in the 0°
configuration. Instead, it continued to increase, although at a decreasing rate nearly
parallel to the slope of the convergence measure for the outer surface..
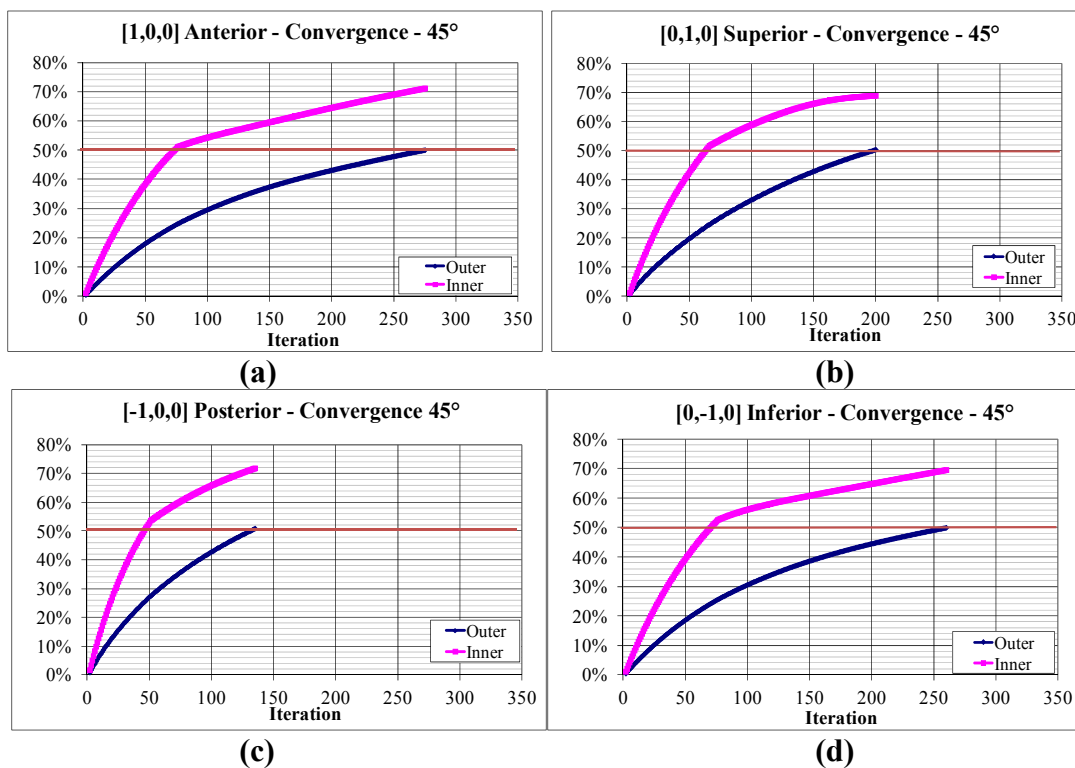
Figure 5.37 Convergence measure with iteration for the single load cases in the 45°
configuration. (a) anteriorly (b) superiorly (c) posteriorly (d) inferiorly directed resultant
forces.

The multiload cases followed the trends of the single load cases. Unlike in the 0°
configuration, however, the double load cases were not simply intermediate versions of
the two single load cases. Instead, some had very different behavior. For example,
because the surface strain energy density must converge under all loading conditions
before the bone stops changing shape, many convergence curves under one of the loads
in a load set increased well above the convergence criteria as they awaited the
convergence of another load set in their application sequence. The only load case, under
all the loads studied in this 45° configuration, to exhibit diverging behavior was the outer

surface under the posteriorly directed resultant force in the four-load set (all around) case, which showed a slight diverging trend initially, but then proceeded towards converging behavior, although this case never met the convergence criterion. These varying multiload behaviors are exhibited in the four-load all around case (Figure 5.38).
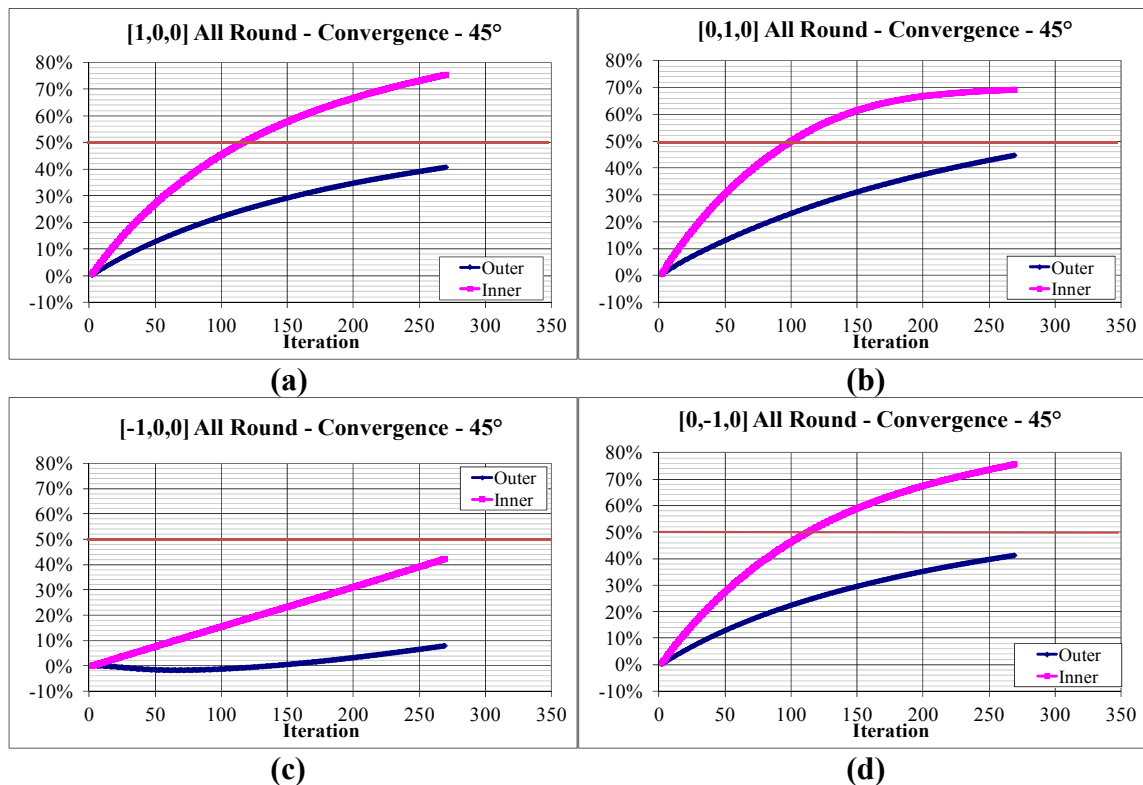
Figure 5.38 Convergence measure with iteration for the load sets of the all around four load case in the 45° configuration. (a) anteriorly (b) superiorly (c) posteriorly (d) inferiorly directed resultant forces.

90° Configuration

While not all cases reached the defined convergence criteria, none of the load cases imposed on the leg system in the 90° configuration, either alone or in a multiload set presented, any diverging behavior. While the superiorly directed load case did not reach the convergence threshold before it attained the maximum thickness, it was nearly at convergence and can be classified as converged (Figure 5.39). Similar to the 0°

configuration, the behavior of the individual cases within the mutliload set followed that of the corresponding single load case but with smaller slopes and, therefore, slower paths towards convergence. The only exception is the anterior-inferior case where, as noted for the comparison geometry and von Mises stress distributions, the convergence behavior for the single anterior and inferior cases and their combination were all nearly identical.
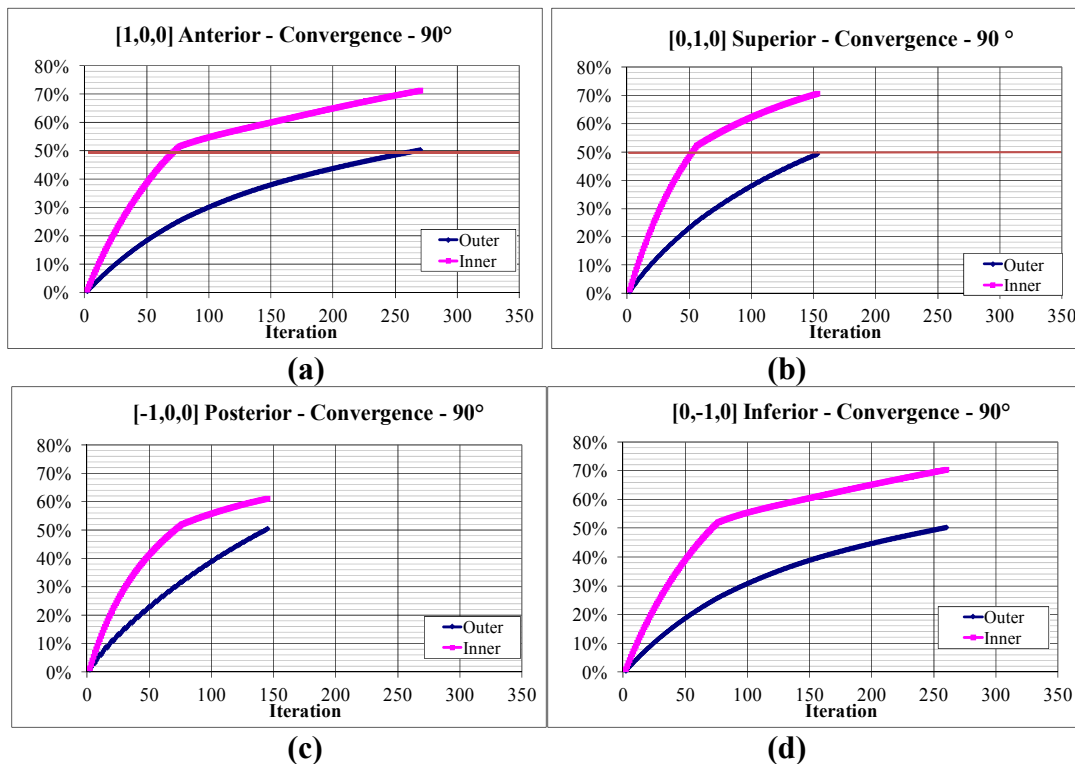
Figure 5.39 Convergence measure with iteration for the load sets of the four load case in the 90° configuration. (a) anteriorly (b) superiorly (c) posteriorly (d) inferiorly directed resultant forces.

5.4.1.3 Average and Variation of Elemental Strain Energy Density on Surfaces. The optimization goal of the developed bone shape strength adaptation model was to reduce the variation of the nodal strain energy density over the surface being optimized. In order to better understand the convergence behavior of the cases studied, trends in the average and standard deviation of the strain energy density over the optimizing surfaces were

studied. These measures are used in the statistical standardization of the nodal strain energy density that drives the shape adaptation model. Therefore, both their initial values and their change over the optimization process can provide information about progression of the model behavior towards the optimization goal. Because of the wide range of average and standard deviation values for the cases compared, a relative measure of the variation, the ratio of the standard deviation to the average, was used, in addition to the direct values of the average and standard deviation, to compare the cases studied. This ratio was intended to normalize the measure of the local strain energy density variation over the surface being optimized for a more consistent comparison between cases.

0° Configuration

While no surface reached the desired amount of improved uniformity of the stress state in the optimizing surface under the straight leg configuration except the inner surface for the superiorly directed load, it was desired to better understand the progress of each case studied towards the stated optimization goal. The trends in the change in average and standard deviation of the strain energy density over the optimizing surface for the single load cases were found to be representative of all eleven loading conditions in this straight leg configuration, as the trends in the multiload cases followed those of the single load, though with less pronounced features. The change in the average and standard deviation of the local strain energy density as a result of the optimization process for the periosteal (outer) and endosteal (inner) surfaces are presented in Tables 5.10 and 5.11, respectively.

Initially, the anteriorly directed load resulted in the largest average and standard deviation of the strain energy density over the outer surface by more than twice the value of the measures of the nearest load set, posterior loading. The inferiorly directed load

had the smallest average and standard deviation of the strain energy density by more than an order of magnitude. On the outer surface, all cases had values of the standard deviation much greater than those of the average of the strain energy density. On the inner surface, however, the inferior and posterior loading had the standard deviation of the strain energy density less than that of the average, indicating a fairly uniform initial distribution of strain energy density under those loads.

On completion of optimization, the standard deviation on the outer surfaces decreased by about 60% for all cases, while the average increased by almost 30% for the superiorly and anteriorly directed resultant loads and stayed about the same for inferiorly and posteriorly directed loads. The change in standard deviation on the inner surface was not as consistent. For the anterior and superior loads, the variation at the inner surface decreased by approximately 20%, but for the posterior load, the variation nearly doubled, while, for the inferior load, this value remained about the same. Despite the increases, all variations on the inner surface were of smaller magnitude than the average on the inner surface at the end of the optimization.

When comparing the change in the normalized measure of the surface variation (ratio of standard deviation to average of the local strain energy density), all cases had about the same level of improvement in the variation of the local strain energy density on the outer surface, with the inferiorly directed loadset having slightly more improvement and the anteriorly directed load having slightly less improvement. On the inner surface, however, only the superior and the anterior loads showed a reduction in the variation of the strain energy density while the variation under the inferior case did not change significantly, and that under the posterior case worsened.

      While the change in the variation of the strain energy density over the outer surface was greater than the inner surface, its overall variation was still significantly more than that of the inner surface, resulting in comparatively lower convergence values (Figures 5.34b and c). For the superior and anterior cases, the standard deviation of the strain energy density over the inner surface was initially greater than the average. Because the value of the standard deviation of the strain energy density eventually fell below that of the average, a greater "convergence", or reduction in extreme values was generated when compared to the outer surface, whose standard deviation of the strain energy density remained above the average value over the optimization process.

Table 5.10 Change in Element Area Weighted Average and Standard Deviation of SED on Outer Surface - Single Load Cases 0° Configuration

Outer 0° Configuration		Superior	Inferior	Anterior	Posterior
Initial	SEDAvg	199.6	55.8	801.5	306.2
	SEDstdev	1101.7	224.7	5335.1	2263.6
Final	SEDAvg	246.0	54.1	1073.7	325.2
	SEDstdev	449.8	77.0	2051.8	782.6
Final/Initial	SEDAvg	1.23	0.97	1.34	1.06
	SEDstdev	0.41	0.34	0.39	0.35
Initial STDEV/Avg		552%	403%	666%	739%
Final STDEV/Avg		183%	142%	191%	241%
Final/Initial STDEV/Avg		0.33	0.35	0.29	0.33

Table 5.11 Change in Element Area Weighted Average and Standard Deviation of SED on Inner Surface - Single Load Cases 0° Configuration

Inner 0° Configuration		Superior	Inferior	Anterior	Posterior
Initial	SEDAvg	49.4	38.9	176.6	135.8
	SEDstdev	65.8	11.4	238.4	38.8
Final	SEDAvg	51.6	37.6	213.9	132.1
	SEDstdev	40.6	12.4	164.9	70.8
Final/Initial	SEDAvg	1.04	0.97	1.21	0.97
	SEDstdev	0.62	1.09	0.69	1.82
Initial STDEV/Avg		133%	29%	135%	29%
Final STDEV/Avg		79%	33%	77%	54%
Final/Initial STDEV/Avg		0.59	1.14	0.57	1.86

45° Configuration

Under the 45° configuration, the averaged strain energy density and its standard deviation over both the inner and outer surfaces decreased during the optimization process for all load sets in all single and multiple load cases. The trends in the multiload cases generally followed those of the single load cases. The data for the single load cases are summarized in Tables 5.12 and 5.13.

There was a two orders of magnitude difference in the average and standard deviation of the local strain energy density over the outer surface amongst the four single load cases that were studied and almost a three orders of magnitude difference for the inner surfaces under the single load cases studied in this configuration. On both surfaces, the anteriorly directed force produced an average and standard deviation of strain energy density that was an order of magnitude greater than did the inferiorly directed forces, whose values, in turn, were an order of magnitude larger than those of the posterior case. The values for the posteriorly directed load case were approximately twice those of the inferiorly directed load.

Despite these large differences in magnitude, the average strain energy density on the outer surface decreased about the same amount for each case, approximately 35% to 40%, with the biggest changes occurring from the inferior and posterior load cases and smallest for the superior and anterior cases. The change in the standard deviation of the strain energy density over the surface was also about the same for all these single load cases in the 45° configuration, approximately 50%, corresponding to the 50% decrease in Q14Spread required for the convergence that was reached by all these cases, as discussed in the previous section. This decrease in both standard deviation and average of the strain

energy density over the surfaces being optimized implies that not only does this 45° configuration show more improvement in uniformity of the strain energy density over the cases in the 0° configuration, but it also decreases the maximum stress over the outer surface, both indicators of an overall improvement in strength of the bone. As seen in the convergence trends, the anteriorly and inferiorly directed forces displayed very similar behavior in the changes in both the average and standard deviation of strain energy density over the optimizing surface. Despite the large differences in magnitude of these measures, the ranking of these cases by the changes in these global surface measures as a result of the optimization process matched the ranking created in Table 5.8 of the strength improvement at the one-third location under the mid-stance jogging conditions.

Similar trends were seen for the single load cases on the inner surface as was described for the outer surface; however the changes in these strain energy density measures were larger, likely due to the lack of directly loaded nodes. The surface average strain energy density decreased over the optimization process by about 50% for all cases, with a greater decrease for the anterior and inferior load cases and a smaller decrease for the superior load case. The standard deviation of the local strain energy density over the inner surface for these individual load cases decreased approximately 75%, with the smallest decrease for anterior load case and greatest for posterior load case. This large decrease in the standard deviation of the strain energy density over the inner surface also corresponded with the plot of the convergence measure for the inner surface with optimization iteration (Figure 5.37). As the shape changes to the outer surface continued past the point of inner surface convergence, they continue to affect the local

stress state on this surface altering the overall variation (standard deviation) over the surface.

Table 5.12 Change in Element Area Weighted Average and Standard Deviation of SED on Outer Surface - Single Load Cases 45° Configuration

Outer 45° Configuration		Superior	Inferior	Anterior	Posterior
Initial	SEDAvg	196.0	7851.0	40434.2	339.6
	SEDstdev	273.2	8656.4	43855.9	675.7
Final	SEDAvg	129.4	4696.2	23788.2	221.2
	SEDstdev	131.6	4207.8	21292.4	339.8
Final/Initial	SEDAvg	0.66	0.60	0.59	0.65
	SEDstdev	0.48	0.49	0.49	0.50
Initial STDEV/Avg		139%	110%	108%	199%
Final STDEV/Avg		102%	90%	90%	154%
Final/Initial STDEV/Avg		0.73	0.81	0.83	0.77

Table 5.13 Change in Element Area Weighted Average and Standard Deviation of SED on Inner Surface - Single Load Cases

Inner 45° Configuration		Superior	Inferior	Anterior	Posterior
Initial	SEDAvg	49.2	2170.7	11334.4	96.2
	SEDstdev	53.3	2104.2	10879.8	126.4
Final	SEDAvg	30.1	923.8	4616.6	50.0
	SEDstdev	14.3	543.0	2691.8	37.5
Final/Initial	SEDAvg	0.61	0.43	0.41	0.52
	SEDstdev	0.27	0.26	0.25	0.30
Initial STDEV/Avg		108%	97%	96%	131%
Final STDEV/Avg		47%	59%	58%	75%
Final/Initial STDEV/Avg		0.44	0.61	0.61	0.57

In comparing the standard deviation of the local strain energy density normalized by the surface average of the strain energy density for each case, the posterior loading condition initially resulted in the largest variation over both the inner and outer surfaces, with the standard deviation of the local strain energy density nearly twice the average outer surface value and about one-third greater than the average value on the inner surface. In contrast, the anterior loading condition showed the least initial variation in the local strain energy density, with the standard deviation only 10% greater than the surface average on the outer surface and nearly equal to the average (5% less) on the inner surface.

90° Configuration

For the four single loading conditions studied in the 90° configuration, similar trends as the 45° configuration were seen in the magnitudes of the surface average and variation of strain energy density but with a more distinct grouping in the load cases. Also, as with the 45° configuration, both the average and standard deviation of the local strain energy density over the surface decreased for all cases studied on both surfaces optimized.

The inferior and anterior load cases had values of average and standard deviation of the local strain energy density more than two orders of magnitude greater than the posterior and the superior load cases. The average and standard deviation of the strain energy density over the outer surface of the geometry under the inferior load were three times those of the anterior load case, while the superior load case's were also about three times those of the posterior load case. However, when normalizing the initial standard deviation with these initial outer surface average values, the superior and posterior cases showed twice the variation of the inferior and anterior. These two groups, which were also seen in the geometric comparisons of Section 5.3, were well matched, with nearly equivalent ratios for the superior and posterior load cases and for the inferior and anterior load cases. While the measures of the decrease in absolute average showed a 10% greater decrease for the cases with the larger values of the strain energy density (anterior and inferior), the opposite was true when looking at the standard deviation normalized by the surface average, where the superior and posterior cases showed a greater reduction in surface variation over the anterior and inferior cases. Similar trends were found for the inner surface. In contrast to the conclusions drawn for the 45° configuration, the direct measurement of the decrease in average and variation of the standard deviation, rather

than the use of this normalized value, resulted in a ranking of load cases that matched those of the maximum von Mises stress at the targeted one-third cross section (Table 5.9).

While correlations between the use of global measures of the optimizing loadset and the performance of the optimized geometry under a different common critical design loadset were noted, they were inconsistent in predicting the ability of the optimized geometry to improve the strength in a local region, which was the goal of the studies in Section 5.3. Therefore, the global measures presented in this section cannot be used to universally predict the local behavior of the optimized geometry under loads different than that under which it was optimized. Thus, the comparison studies used in this work of the performance of the geometries, that were optimized under different load conditions, under a common, critical design, loadset was shown to be necessary.

Table 5.14 Change in Element Area Weighted Average and Standard Deviation of SED on Outer Surface - Single Load Cases = 90° Configuration

Outer 90° Configuration		Superior	Inferior	Anterior	Posterior
Initial	SEDAvg	168.6	45201.0	12280.4	62.4
	SEDstdev	337.6	49774.0	13266.9	129.3
Final	SEDAvg	115.9	26661.6	7166.0	42.5
	SEDstdev	170.1	23908.5	6395.6	61.4
Final/Initial	SEDAvg	0.69	0.59	0.58	0.68
	SEDstdev	0.50	0.48	0.48	0.47
Initial STDEV/Avg		200%	110%	108%	207%
Final STDEV/Avg		147%	90%	89%	144%
Final/Initial STDEV/Avg		0.73	0.81	0.83	0.70

Table 5.15 Change in Element Area Weighted Average and Standard Deviation of SED on Inner Surface - Single Load Cases - 90° Configuration

Inner 90° Configuration		Superior	Inferior	Anterior	Posterior
Initial	SEDAvg	53.5	12637.7	3439.0	22.6
	SEDstdev	60.6	12373.4	3251.6	21.6
Final	SEDAvg	30.8	5250.0	1404.0	15.6
	SEDstdev	19.8	3082.2	811.1	9.6
Final/Initial	SEDAvg	0.58	0.42	0.41	0.69
	SEDstdev	0.33	0.25	0.25	0.45
Initial STDEV/Avg		113%	98%	95%	96%
Final STDEV/Avg		64%	59%	58%	62%
Final/Initial STDEV/Avg		0.57	0.60	0.61	0.64

As compared to the normalized ratios of the standard deviation to the surface average strain energy density for the load cases in the 0° configuration, the initial variation of the strain energy density over the outer surface for the 90° configuration was more uniform. The magnitude of the standard deviation of the strain energy density on both optimizing surfaces for both the 45° and 90° configurations were smaller than for the 0° configuration for all load sets studied. The optimization processes in the 45° and the 90° configuration resulted in better convergence for the cases studied compared to those for the 0° configuration. Additionally, both the 45° and 90° configurations resulted in a decrease in the overall surface average standard deviation, while the straight leg configurations showed an increase in the surface averaged strain energy density as a result of the optimization process. These results could indicate that there may be a limit to the effectiveness of the shape adaptations in improving the strength of an object based on the initial amount of variation over the surface imposed by the applied loading conditions. The shape changes may be more effective at improving the strength where the initial variation of the local stress state of the optimizing surface is moderate, where the initial global measures of the stress state of the optimizing inner and outer surfaces of the hollow cylinder are similar, and where the initial conditions of the system being optimized are within a certain range of the local optima. These findings follow the suggestions that have been made in the literature about the appropriate use of gradientless optimization methods being limited only to systems whose initial state is close to a local optimal value (see Chapter 4).

The discussions of the convergence behavior of the shape optimization model under the thirty-three conditions studied in this phase of the research and of the changes

in average and standard deviation of strain energy density over each surface provided insight into the progress each "shape design problem" made towards its optimization goal of improved uniformity of the local stress state on the optimizing surface under each given applied set of muscle loads. This can help identify the physical design features that are useful in improving this uniformity under a given set of loading conditions. In order to identify how these physical design features arose during the optimization process, however, the study of relationships between the changes to the local stress state, global state of stress, and variation of the stress state over the optimizing surface that drive these local shape changes is necessary.

5.4.2 Similar Stress Distributions under Load Sets Studied

The shape optimization model developed in this work is driven by the variation in the distribution of strain energy density (stress) over the surface being optimized. Therefore, as shown in Section 5.1, load sets that induce similar von Mises stress distributions over the optimizing domain, even if scaled by orders of magnitude, result in similar alterations to the shape both in the magnitude and distribution of local growth. In the evaluation of the effectiveness of optimal tibial shapes derived from various loading conditions on improving the bone's resistance to stress fractures under the "critical design" mid-stance jogging conditions (Section 5.3), similar states of stress under this common load were observed in optimal shapes with similar geometric features, even if they were formed using different sets of muscle activities and even limb configurations. In order to understand these similarities, the stress distributions in the tibia bone under the loading conditions from which the optimal shapes were derived were examined. The groups of bone shapes compared in this analysis are based on observations discussed in Section 5.3.

0° Configuration

Under the 0° configuration, the optimal tibia shapes and resulting alterations in strength for the four single load conditions were distinctly separated into two groups: the anteriorly and superiorly directed resultant forces and the posteriorly and inferiorly ones (Table 5.7). A comparison of the relative muscle activities described in Section 5.2 that together create these resultant loads under this leg configuration (Table 5.6) revealed similar active muscles although different relative magnitudes of the forces generated by these muscles for the members of each group so that one was not simply a scaled version of the other. Additionally, previous subsection showed that the average strain energy density differed four- to six-fold and the standard deviation of the local strain energy density over the surface varied almost an order of magnitude between group members (Tables 5.10 and 5.11). Therefore, the analysis of the individual muscle activity in Section 4.2 was consulted to determine the loading features responsible for inducing the similar shape changes amongst these group members in this straight leg configuration.

Anteriorly and Superiorly Directed Resultant

First examined was the anterior/superior load case group that resulted in the thinning of the cortical wall (Figures 5.18, 5.21, 5.23, 5.25) at the distal one-third region in this straight leg configuration, causing an overall increase in maximum stress at the targeted region under the comparison critical design jogging conditions (Table 5.7) and making these conditions the least effective of all studied at preventing stress fractures. Both load cases used all of the anteriorly attached muscles included in the model to create these net resultant force directions in this straight leg configuration (Table 5.6). The largest of these forces were generated by the rectus femoris, the vastii and the tibialis anterior

muscles (Figure 5.6). As described in Section 5.2, the anteriorly directed resultant force was dominated by hip flexion, resulting in the very large rectus femoris muscle force, generating more than 80% of the sum of the active muscle force magnitudes. Also, as previously described, the superiorly directed load required significant moments about all three joints. Therefore, the active muscle force magnitudes were more diverse, with large forces both from the rectus femoris and the vastii and a significant contribution from the tibialis anterior of about 35% of the maximum (vastii) muscle force, compared to the 5% (of maximum rectus femoris force) contribution in the anteriorly directed case. However, because the vastii and the rectus femoris muscles attach to the tibia at same location, they act as a single force with a magnitude equal to the sum of the forces generated by each one, making their combined generated force two orders of magnitude greater than that which is generated by the tibialis anterior muscle, and making and relative effect of the tibialis anterior muscle between these two load cases negligible. The common resulting, stress contours (Figure 5.40), therefore, form the nearly identical "optimal" shapes described in Section 5.3.

Figure 5.40 Similarities between von Mises stress distribution and displacement under (a) anteriorly and (b) superiorly directed resultant force at toe for 0° configuration. Note: von Mises stress contours and deflection scales on each are different.

Posteriorly and Inferiorly Directed Resultant

The posteriorly and inferiorly directed resultant directions were created, not surprisingly, by mainly posteriorly attached muscles in this 0° configuration (Table 5.6). The posteriorly directed force was created by a combination of hip extension and knee flexion (Figure 5.6) with dominant forces on the tibia bone from the biceps femoris and secondarily by the gastrocnemius (Figure 5.7), acting against the fixed toe and pelvis to deflect the knee joint anteriorly (towards the toe) in a cantilever like manner (Figure 5.41). In this load case, the tibialis anterior aided in the forward pull of the knee.

The inferiorly directed resultant force was dominated by the direct flexion of the knee, with large gastrocnemius and biceps femoris muscle forces. With a smaller contribution from the tibialis, the bending from the gastrocnemius dominated. Despite these small local differences, the overall deflection patterns and the resulting stress distributions were very similar between these two cases (Figure 4.51) and resulted in similar "optimal" shapes. Because of the slightly larger stresses near the ankle, these two cases cause slight improvements in the bone's strength in the distal one-third region.

(a)   (b)
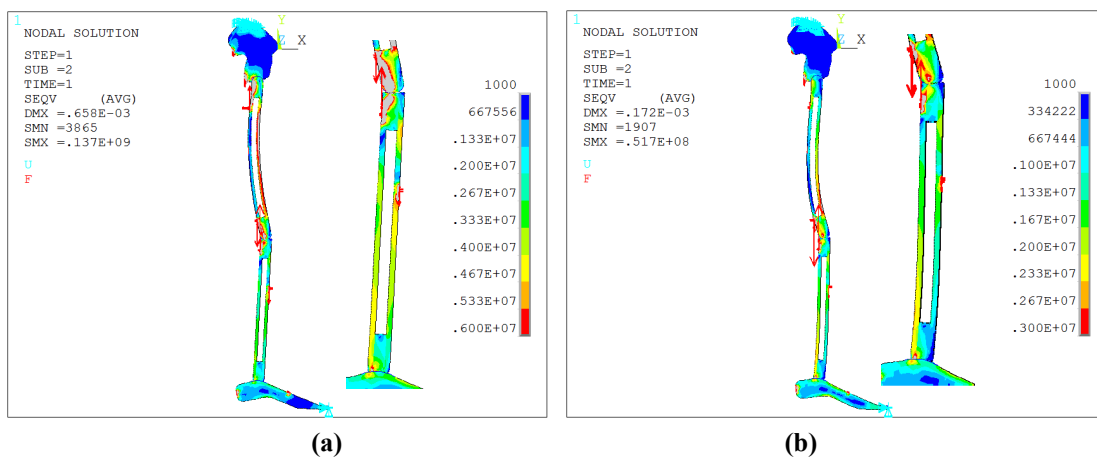
Figure 5.41 Similarities between von Mises stress distribution and displacement under (a) posteriorly and (b) inferiorly directed resultant force at toe for 0° configuration. Note: von Mises stress contours and deflection scales on each are different.

45° Configuration

The anteriorly and inferiorly directed resultant load cases applied to the 45° configuration caused very similar predicted shape changes in the tibia (Figures 5.10 and 5.19) despite requiring rather different active muscles and relative intensities of these muscles (Table 5.6). Specifically, the anteriorly directed resultant force required activity in all of the anteriorly attached muscles, dominated by the knee extensor, to "kick" the foot forward. These muscles, acting at a common location on the tibia, generated more than 90% of the sum of the active muscle force magnitudes (Figure 5.6, Table 5.6). In contrast, the inferiorly directed force required muscles on both the anterior and posterior sides of the system, with active knee, hip, and ankle extensors working to "unfold" the bent leg and direct the force at the toe downward (Table 5.6, Figure 5.6). As in the anteriorly directed load case, the knee extensor dominated both cases, with almost an order of magnitude greater force than the only other active muscle acting on the tibia, the ankle extensor.

As in the anterior and superior load cases in the 0° configuration, the stresses within the system at the 45° configuration generated by the anteriorly and inferiorly resultant force directions were dominated by the effects of the knee extensor muscle forces (Figure 5.41), pulling the tibia bone, at the knee, anteriorly, along its cylindrical axis, inducing significant bending in the tibia and femur bones and rotating the foot up about the toe as the deflection of the system is resisted by the constraints at the toe and the pelvis. Despite a five-fold difference in both the surface average and standard deviation of the local strain energy densities and significantly different active muscles, because of the dominant knee flexors, the adaptive response of these two cases was nearly identical.
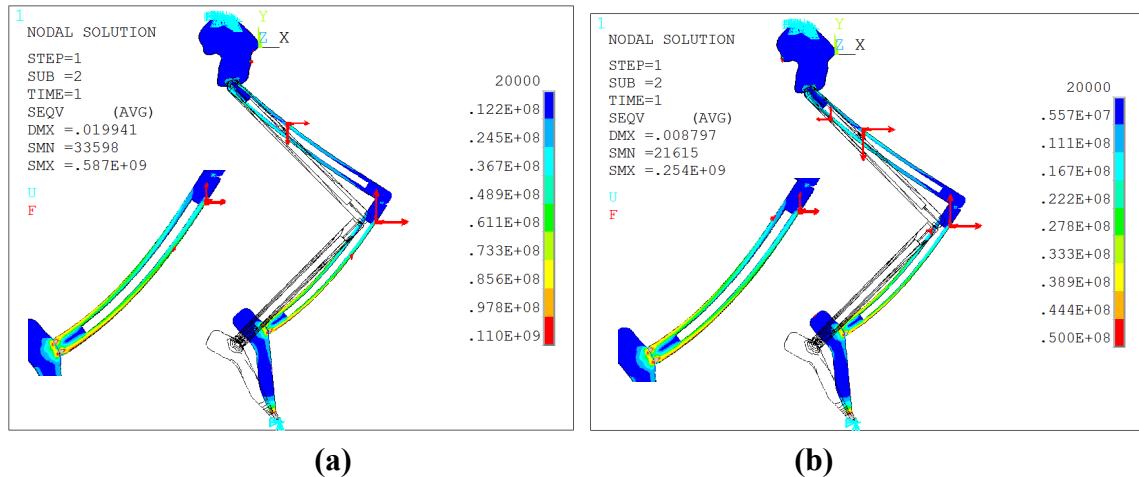
Figure 5.42 Similarities between von Mises stress distribution and displacement under (a) anteriorly and (b) inferiorly directed resultant force at toe for 45° configuration. Note: von Mises stress contours and deflection scales on each are different.

90° Configuration

The anteriorly and inferiorly directed resultant forces also produced similarly adapted shapes when applied to the leg arranged in the 90° configuration. As described in Section 5.2, in this 90° arrangement, the anteriorly directed force is achieved mainly through activity about the hip joint, resulting from significant forces generated by the rectus femoris muscle on the anterior side of the system, despite the slight activity on the posterior side of the bone (Table 5.6). In contrast, the inferiorly directed resultant force is generated mainly through the knee extensor vastii muscle despite having activity in all of the anteriorly attached muscles modeled (Figures 5.6 and 5.7). However, as described for the other configurations, because the vastii and rectus femoris act at the same location, they induce the same effect on the system modeled (Figure 5.43). As in the 45° configuration, this dominant system force pulls the tibia at the knee along its cylindrical axis, against the constraints at the foot at the pelvis, creating a significant bending in the tibia, forming similar stress distributions and invoking a similar adaptive response.
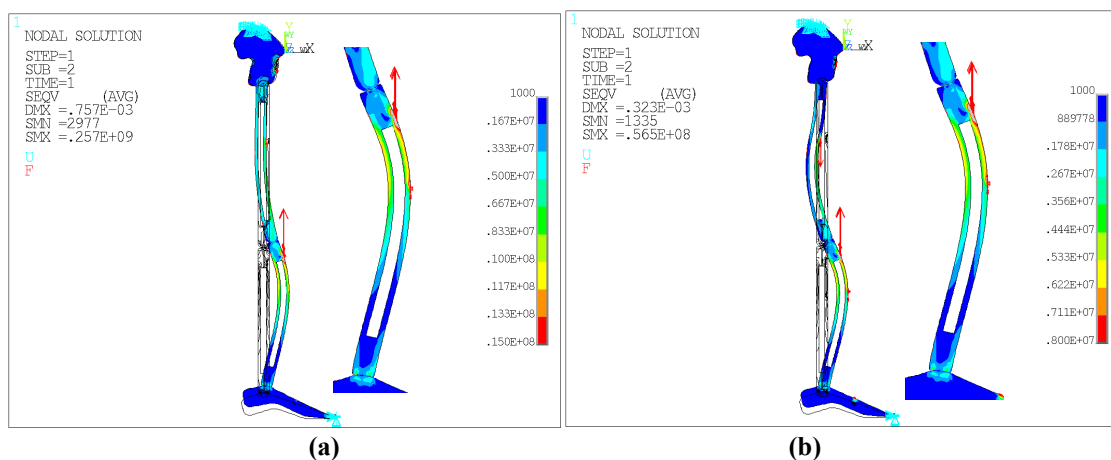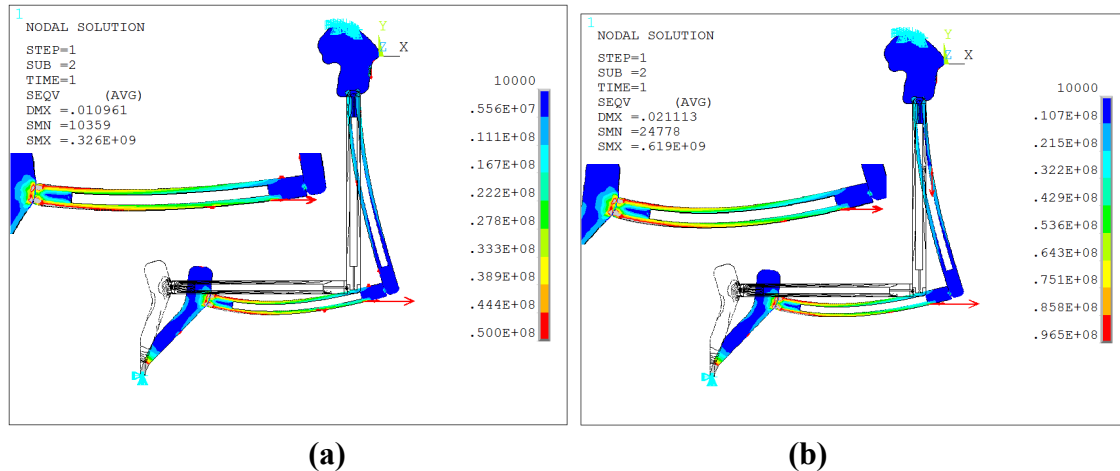
Figure 5.43 Similarities between von Mises stress distribution and displacement under (a) anteriorly and (b) inferiorly directed resultant force at toe for 90° configuration. Note: von Mises stress contours and deflection scales on each are different.

These noted similarities in the predicted shape strength adaptations that occur despite the differences in the individual muscle forces acting on the bone system and the orders of magnitude differences in the surface averaged strain energy densities induced in these varied cases highlight the importance of two features in the developed model. The first is the ability to study a wide range of loading conditions and magnitudes without the need to adjust any of the model parameters or functions. The second is the necessity of analyzing a complete musculoskeletal model with multiple bone segments and individual muscles, including the appropriate simulation of their contact interaction between bones. The common behavior of the different optimized bones to an applied load likely would not have been revealed without inclusion of the interactions of the other components of the leg system studied. Because of the similarities, only one from each group included in the study of relationships between the nodal strain energy density and nodal growth that caused the evolution of each of the optimal shapes analyzed.

5.4.3 Shape Adaptation Optimization Process Under Conditions Studied

The determination of loading conditions most conducive to preventing stress fractures consists of a series of structural optimization problems, where the best (optimal) bone shapes to resist each of the particular loading/configuration conditions examined is first found. The effectiveness of each of these shapes at resisting a common load is then calculated to identify loading conditions that create bone shapes that can withstand this extreme "critical design load". The evolution of each of these "optimal bone designs" occurs through the use of the developed shape optimization model, which is based on the statistically standardized nodal strain energy density, which considered local and global measures of the stress state, and its standard deviation state over the optimizing surface.

To better understand the relationships between these local and global measures of the state and variation of the stress over the optimizing surface and the ensuing changes in the local shape that drive the bone towards the "optimal" shape under the particular set of conditions, a detailed examination of the progressive changes in the local nodal strain energy density within the tibia bone and the alterations in the positions of the surface nodes during the simulated adaptation processes was undertaken. Because the standardized value of the nodal strain energy density was used to drive the growth, the changes to the average and standard deviation of the strain energy density over the optimizing surfaces due to the ensuing shape changes had a significant effect on the amount of nodal growth per iteration and were likewise tracked and analyzed. Additionally, these measures were tracked with each optimization iteration at representative locations along the optimizing surfaces. Specifically, as in Section 5.3, three positions on the perimeter of the bone were analyzed along the axial length of the

adapting surface: anterior side ($\Theta=0°$, positive local x-axis), the medial side ($\Theta=90°$, positive local y-axis), and the posterior side ($\Theta=180°$, negative local x-axis). Particular nodes were also selected along these angular coordinates on the optimizing surfaces at lengths one-sixth of the total tibial length apart. These analyses were performed for the shape optimization processes of both the endosteal (inner) and periosteal (outer) surfaces of the tibial bone. Representative cases of the eleven loading cases in the three leg conditions studied are presented. Additional data can be obtained from the author.

5.4.3.1 Shape Optimization under the 0° Configuration. Based on the analyses in Subsection 5.4.2, two unique stress distributions arose from the eleven loading conditions studied in the straight leg 0° configuration, that of the posteriorly and of the superiorly directed resultant force. From this 0° configuration, these two cases were the best and worst performers, respectively, at reducing the potential for stress fracture in the distal region of the tibia bone under the jogging, critical comparison, load case. Therefore, they were subjected to this investigation to understand the differences in their local and global stress states that drove the shapes to these relative extremes under the 0° configuration.

As found in the comparisons of the optimized shapes from the mutliload sets in Section 5.3, the adaptations resulting from each load set in the sequential series of multiple resultant forces both complemented and countered each other to create more moderate changes than either single load cases. To better understand this behavior, the combination of the posterior and superior loadcases was also studied. These cases are representative of the modeled shape optimization behavior of the system studied. While the discussions are particular to these three cases, the analysis methods and insight gained can be applied to similar features resulting from any similar studied conditions.

Changes in Global Stress State during Surface Optimization

To understand the state of stress within the tibia bone being optimized, it is important to understand the loads imposed on it both directly through attached muscles and indirectly through the interaction with neighboring bony components, each with their own directly attached muscles. While the muscle activities for each set of conditions studied were described in detail in Section 5.2, they are summarized for each case studied.

Posteriorly Directed Resultant

The posteriorly directed resultant force in this straight leg configuration had four active muscles near the tibia: three acting in two locations directly on the tibia bone, the tibialis anterior on the anterior surface one third the length of the tibia from the knee joint and the short and long heads of the biceps femoris on the posterior side directly under the knee joint, and one, the gastrocnemius, straddling the tibia bone, connecting the posterior side of the femur, just above the knee joint, to the heel. The gluteus maximus indirectly influenced the behavior at the tibia through the contacting interface at the knee joint between the femur and the tibia. This lead to a fairly complex state of stress within the entire leg system, particularly within the tibia bone, as seen in Figure 5.44a.

Superiorly Directed Resultant

All three main active muscles that create the superiorly directed resultant load in this straight leg 0° configuration acted directly on the tibia bone at two unique locations on the anterior side of the bone: the tibialis anterior described above and the rectus femoris and vastii muscles acting at the same point just below the knee joint. This lead to a simpler stress state in the tibia bone under this load set (Figure 5.45a).
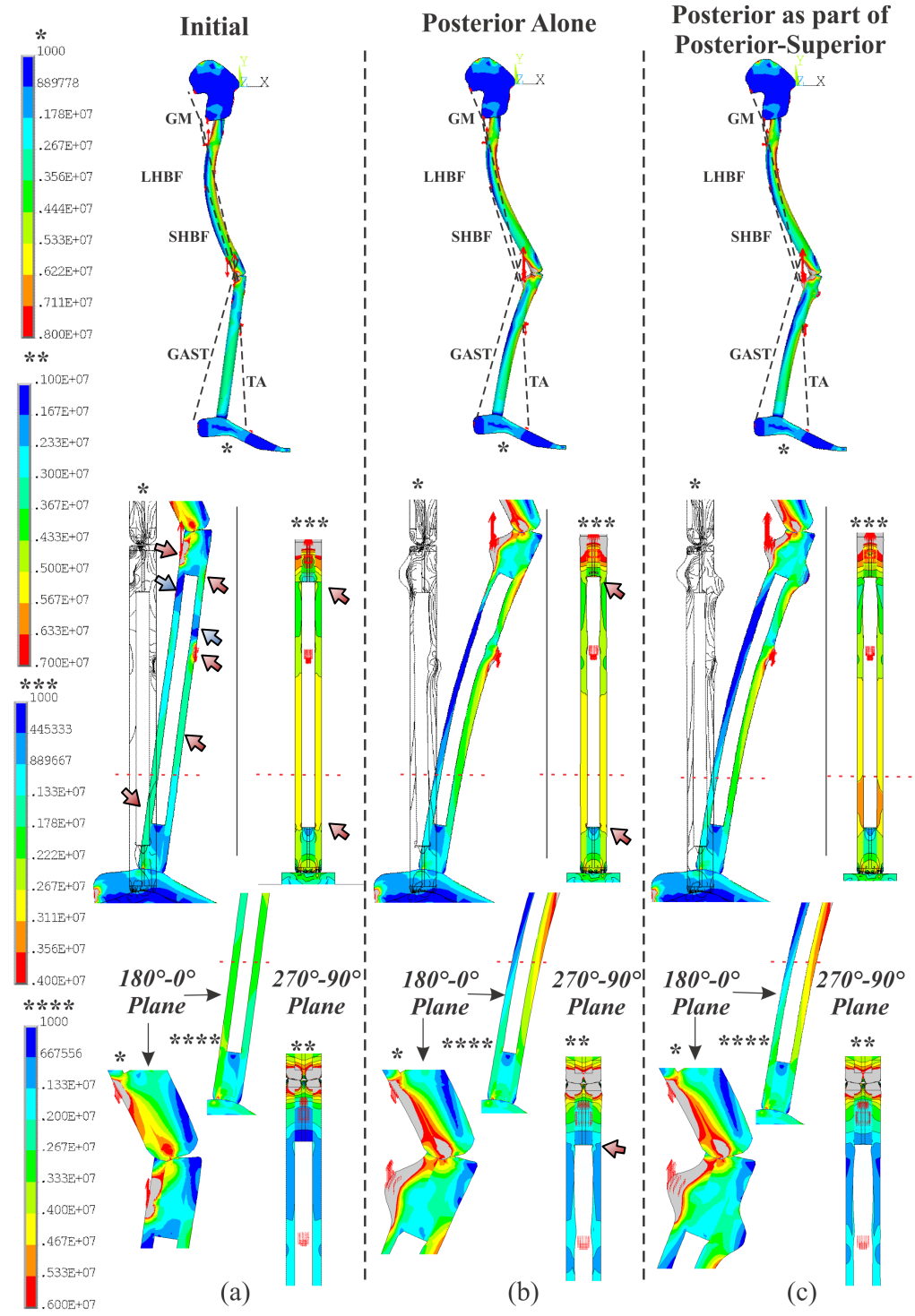
Figure 5.44 Comparison of von Mises stress distributions under posteriorly directed resultant force in the 0° configuration for (a) initial geometry and final geometry created by (b) superior alone and (c) posterior-superior loading cases.

Notes: Red dashed line indicates targeted strengthening location. Legends used for each contour plot identified by matching "*"'s.
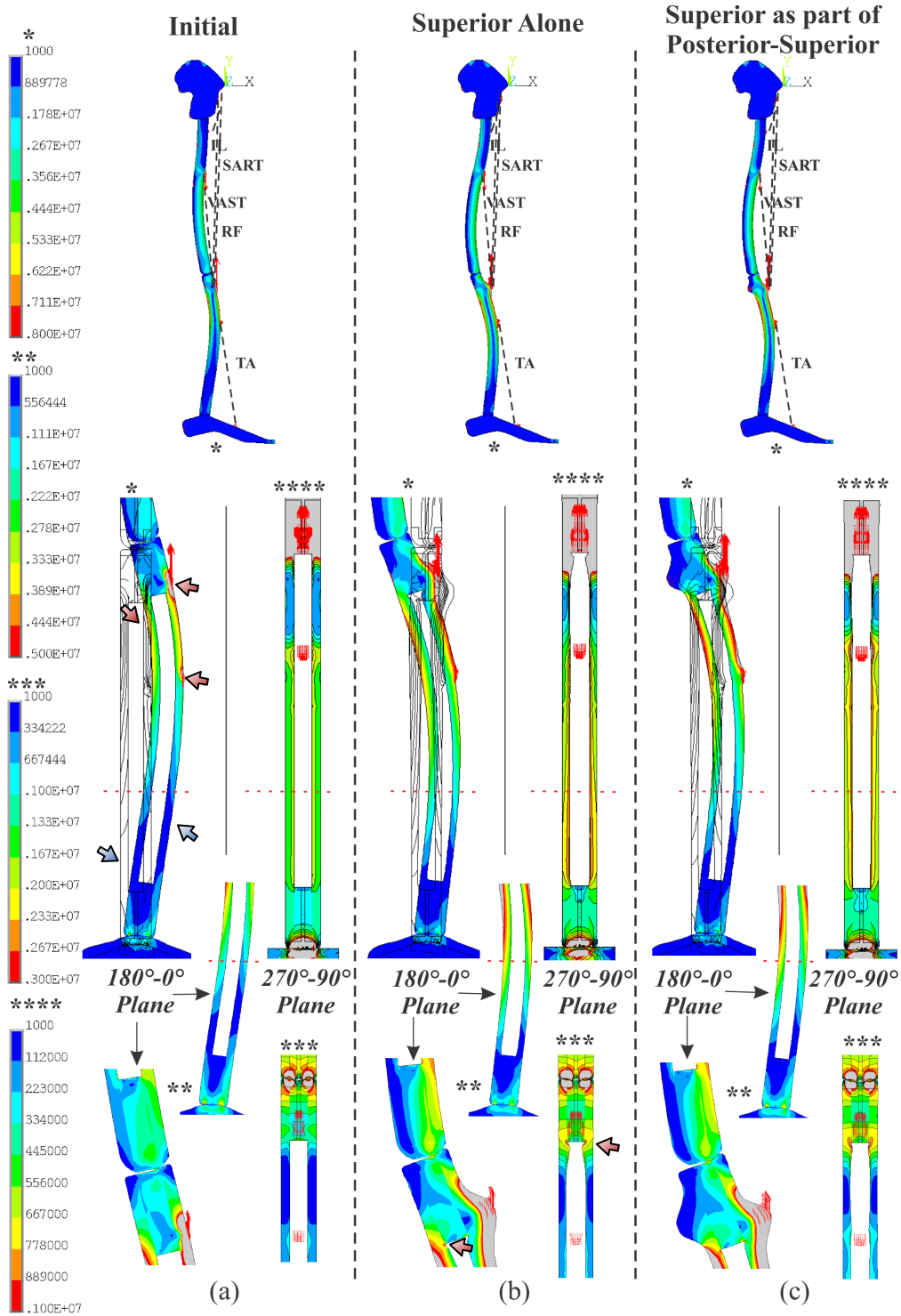
Figure 5.45 Comparison of von Mises stress distributions under superiorly directed resultant force in the 0° configuration for (a) initial geometry and final geometry created by (b) superior alone and (c) posterior-superior loading cases.

Notes: Red dashed line indicates targeted strengthening location. Legends used for each contour plot identified by matching "*"'s.

A general understanding of the effective progression of the shape to create a state of uniform stress can be gained by tracking the average and standard deviation of the local strain energy density over each surface during its optimization. Through the growth driver function (Equation 4.23), the nodal growth is directly dependent on the difference between the nodal strain energy density and the average of the local strain energy density over the surface being optimized and inversely dependent on the standard deviation of this strain energy density over this surface. While the overall change in each measure as a result of the optimization was compared as an indicator of achievement of the optimization goal in Section 5.4.1, the trends in these measures are now discussed in relation to their contribution to the evolution of the optimized shape.

The changes in the surface average and standard deviation of the strain energy density over the course of the optimization under the posterior and superior load cases are presented in Figures 5.46a and 5.46b, respectively, for the outer surface and in Figures 5.47a and 5.47b for the inner surface. These plots show both of these measures for each loading direction as part of a single load case and also as part of the sequential application of the two in a multiload case. The relative changes in the average and standard deviation of the strain energy density directly affect the nodal growth, and their combined effects drive the converging or diverging behavior shown in Figures 5.34(b) and (c) and 5.36(b). Alterations in the von Mises stress distributions under these two loads due to the resulting shape changes are shown in Figures 5.44 and 5.45.

Posteriorly Directed Resultant

In general, the average strain energy density of the outer surface increased only 10% over the course of the optimization under the posteriorly directed load alone (Figure

5.46a(top)). In contrast, the standard deviation under this single load case on the outer surface decreased over 70% (Figure 5.46b(top)). This lead to a trend towards "convergence" (Figure 5.34c) and to a decrease in the overall measure of surface variation (ratio of standard deviation to average in Table 5.10).

The trends in the changes with optimization iteration of the average and standard deviation of the strain energy density over the inner surface under this single load posteriorly directed case in the 0° configuration differed slightly from those of the outer surface. The average strain energy density over the inner surface decreased only slightly over the optimization process (5%) while the standard deviation nearly doubled. Therefore, the surface variation (ratio standard deviation to average in Table 5.11) increased, resulting in a diverging trend of the convergence measure in Figure 5.34c.

<u>Superiorly Directed Resultant</u>

The changes of the global measures of stress state on the tibial surfaces due to the shape optimization under the superiorly directed load were quite different than those for the posteriorly directed load. The average strain energy density under this loading condition increased, nearly linearly, by approximately 25% on the outer surface (Figure 5.46a(bottom)). This contrasts with the decrease and then increase trend that was seen under the posterior load may be related to the differences in complexity of the surface state of stress for each case described above. Because the posteriorly directed load case had many direct and indirect forces of similar magnitudes acting on the tibia, changes in the geometry might give each one varying amounts of dominance over the course of the shape optimization. Like in the posteriorly directed load, the standard deviation of the strain energy density on the outer surface decreased under the superiorly directed load

more than two-fold from its initial value. The scaled trends of standard deviation with iteration are nearly identical for the posterior and superior cases (Figure 5.46b). This increase in average and decrease in standard deviation lead to an overall decrease in the measure of the surface variation of the strain energy density (ratio of standard deviation to average in Table 5.10) and a trend towards convergence (Figure 5.34b) for the outer surface under the superiorly directed load.

The nearly constant average strain energy density on the inner surface over the course of the optimization, similar to the posteriorly directed load, was coupled with a decreasing standard deviation of the strain energy density, rather than the increasing one of the posteriorly directed load (Figure 5.47), to lead to a trend in convergence under the superiorly directed load for the inner surface (Figure 5.34b). In fact, the inner surface under the superiorly directed load was the only one to reach full convergence under the 0° configuration.

Sequential Loading of Posteriorly and Superiorly Resultants

On the outer surface, the sequential generation of the posteriorly directed and superiorly directed loads resulted in an increase in the surface average, a decrease in the surface standard deviation, and an overall trend towards convergence under each loading condition, though this trend was very slight for the superior portion of the sequential load (Figure 5.46 and 5.36b). In general, the strain energy densities on bone surfaces were less uniform under either load after optimization from the combined loads than from the single loads alone. The multiload case resulted in slower rates of decrease of the standard deviation of the strain energy density over the surface, leading to a larger increase of the surface averaged value. These trends quantify the observation previously stated that

under the multiload sets, the resulting geometry is optimized for neither load set in particular but for the combination of the sets used. It is interesting to note that while the values were different, the trends in the average strain energy density over the outer surface for the posterior portion of the sequential posterior-superior case and the superior portion of the multiload posterior-superior case were very similar. Even more interesting is the fact that the trends in standard deviation of the strain energy density on the outer surface for both the single load posterior and superior cases and their respective single load components of the multiload case were almost indistinguishable despite the values of the superior cases being half the values of the posterior cases.
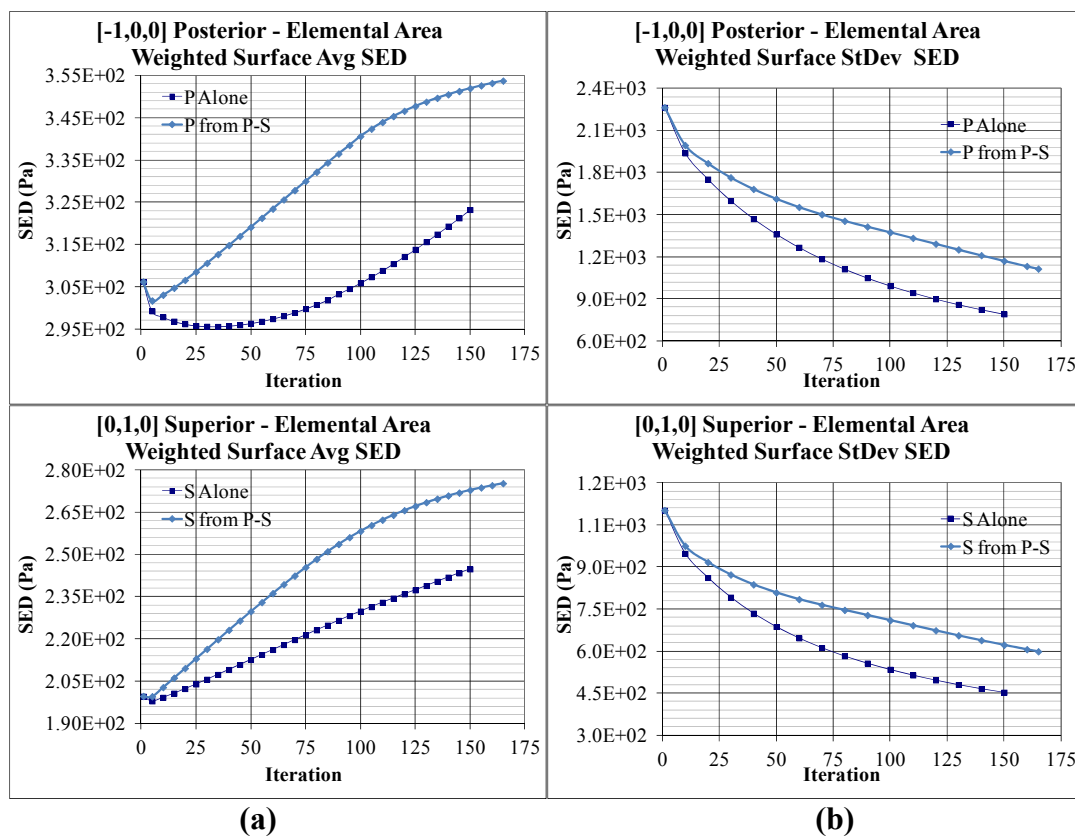
Figure 5.46 Comparison of (a) element area weighted average and (b) standard deviation of strain energy density on the outer surface for the single load case by itself and as part of a double load case. Posterior alone and posterior component of the sequential posterior-superior load set (top). Superior alone and superior part of the sequential posterior-superior load set (bottom). Note each plot has a different scale so features of each curve can be revealed.
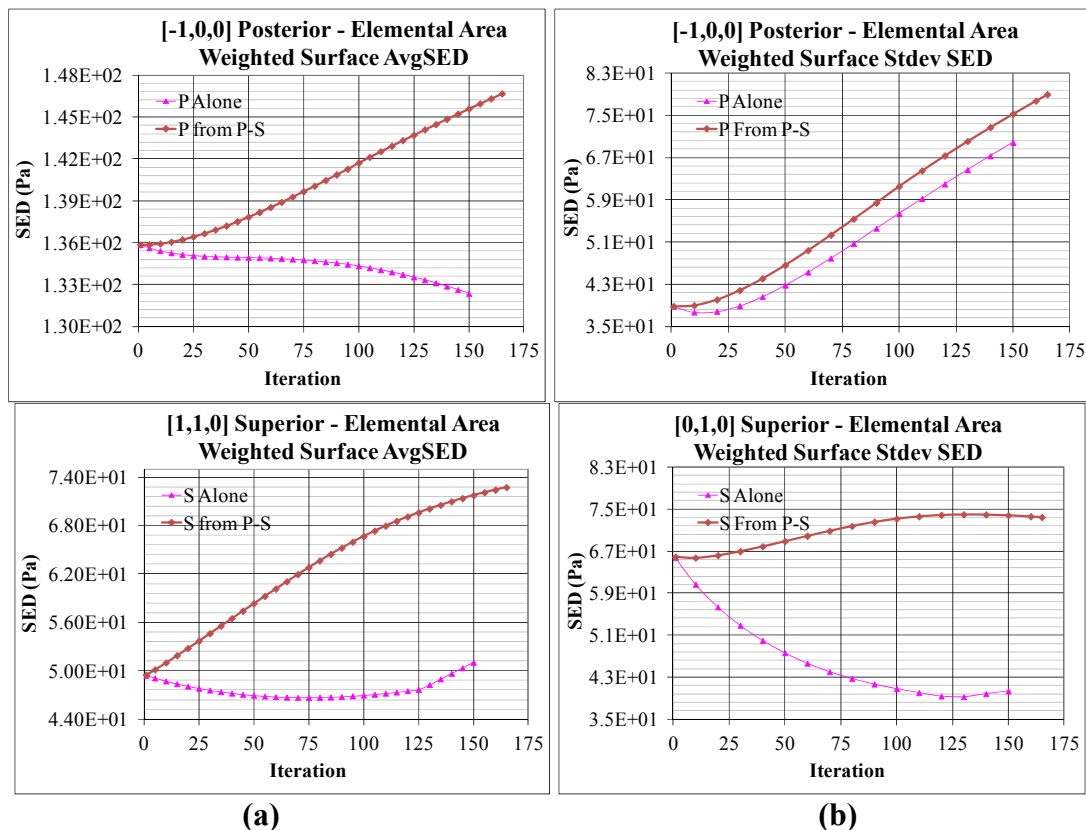
Figure 5.47 Comparison of (a) element area weighted average and (b) standard deviation of strain energy density on the inner surface for the single load case by itself and as part of a double load case. Posterior alone and posterior component of the sequential posterior-superior load set (top). Superior alone and superior part of the sequential posterior-superior load set (bottom). Note each plot has a different scale so features of each curve can be revealed.

Unlike the outer surface, the trends in the standard deviation and average of the local stress state over the inner surface under the posterior and superior loads due to multiload sets were significantly different from those of the single load cases (Figure 5.47). The sequential loading caused an increase in both the surface average and the standard deviations of the strain energy density over the inner surface under the posterior as well as the superior cases. The relative amounts of increase, however, caused the posteriorly directed load from the multiload case to follow the convergence trends of the single load (Figure 5.36b). That of the superior load was quite different, however, with a diverging trend under the multiload conditions despite the fact that it was the only case to

reach full convergence under the single load application. Therefore, the trends indicate that the multiload case affected the inner surface more strongly than it did the outer surface and caused the "optimal" shape to be "less optimal" for either load case than the shapes generated by each loadset alone but best suit both loads comprising the set.

Changes to Stress Distributions and Shape

The trends in the changes to the global measures of the state of stress on the optimizing surface, the surface average and standard deviation of the strain energy density, described above, can be considered in combination with trends in local nodal strain energy density to reveal the ability of the developed shape optimization model to locally altering the surface profile of the bone geometry so that a more uniform state of stress is approached. The examination of the relationships between these values over the optimization process can help explain the specific conditions in the tibia bone and leg system that led to the "optimal designs" considered in Section 5.3 and how these optimal designs perform under the load for which they were optimized. Such an analysis was undertaken using the posteriorly directed resultant force alone and as part of a multiload set where it is applied in sequence with a superiorly directed load case. A similar study was completed for the superiorly directed load case.

Posteriorly Directed Resultant Load

Because the shape adaptations are driven by the variations of the local stress state over the optimizing surface, it is first important to understand the variations in the original initially circular geometry due to the "optimizing" load sets studied. These result from the directly applied muscle forces (explained above) and the interactions between the bone segments (which result from the limb configuration).

The bone system in the 0° configuration under the posteriorly directed resultant load generation is depicted in Figure 5.44. The stress distributions over the deflected geometries for the initial, uniformly circular hollow cylindrical geometry, that optimized under the posterior load case alone, and the optimized geometry from the multiload posterior-superior case are depicted along with the active muscles acting on the bones. The regions of high stress of importance in the tibia under these conditions are indicated by red arrows, and regions of locally low stress of importance are identified by blue arrows. The stress states near the hip and knee joints are also depicted in this figure.

In the initial geometry in the straight leg configuration under the posterior loadcase (Figure 5.44a), locally high stresses occur near the knee flexor load application area on the posterior ($\Theta=180°$) side of the bone just below the knee and on the anterior ($\Theta=0°$) side of the bone where the ankle flexor tibialis anterior muscle acts. Locally high regions of stress, though at much lower magnitudes than the regions under the direct load application, also occur near the transition from the hollow to cancellous filled internal region of the bone. Additionally, locally high stresses are related to the bending stresses in the tibia induced by the applied muscle forces. These occur on the midshaft anterior side and on the distal posterior side near the end of the hollow portion of the bone. A region of locally low von Mises stress occurs on the anterior side of the bone just above the tibialis anterior muscle force as the direction of the stresses in the bone changes from being pulled down and front by the tibialis anterior muscle to being pulled up and back by the biceps femoris muscles. A similar region is located on the posterior side.

The correspondence between the regions of locally high von Mises stress, strain energy density, and growth can be seen by comparing the plots in Figures 5.44 and 5.48.

The regions of initially high and low stress can easily be identified as the large peaks and valleys of the blue curves in the plots of the axial distribution of the strain energy density at the three locations along the outer surface of the tibia bone in Figure 5.48a. The initial changes to the shape due to this initial stress state in the uniform circular cylinder under this posteriorly directed resultant load are shown in analogous blue curves in Figure 5.48b. For example, the strain energy density caused by the biceps femoris muscle on the 180° (posterior) side of the bone (Figure 5.48b, bottom, near normalized Z=1) was so large that it resulted in the attainment of the maximum growth limit throughout the optimization process (Figure 5.48b, bottom).

In the final optimization iteration (pink lines in Figure 5.48) significant growth per iteration remained at the locations of direct muscle force application (right side). This large amount of growth over the optimization process resulted in an almost fourfold decrease in the strain energy density (left side of figure) at these locations. Despite the decrease, the strain energy density (and von Mises stress) in these muscle force application area still remained relatively high, even in the "optimal" bone shape (5.48 and 5.44). Because of the hollow geometry, the relatively large tibialis anterior muscle force caused a locally high strain energy density (and stress) region near its attachment (normalized z=0.67). This propagated around the bones surface, though at significantly less intensity than at the force application point, as seen by location A in Figure 5.48 at the 90° (medial) location and at the 180° (posterior) location and remained throughout the optimization process (Figures 5.48 and 5.44). The end (boundary) effects are also prominently shown in the plots of nodal strain energy density with axial location, especially at the proximal end (normalized z=1 in Figure 5.48a) at the 90° location, likely

due to the large biceps femoris load just below and the no-growth constraint just above where the cylindrical geometry transitions to that of the knee joint. A smaller effect is also seen at the bottom of the tibia near the ankle (normalized z=0 in Figure 5.48a), especially at the 180° location, likely due to bending stresses induced by the gastrocnemius muscle and by the no-growth constraint on this end of the growth region.

Away from these effects of the applied boundary conditions, between the one-sixth and one-half length axial locations, the stresses transition more gradually and the shape changes are less dramatic (Figures 5.48 and 5.44). It is important to note that the selected targeted strengthening region is in the middle of this zone, and it is, therefore, not directly affected by the applied force and constraint boundary conditions. In this region, the stresses (strain energy density) on the anterior ($\Theta=0°$) side increase proximally, from the ankle towards the knee, resulting in a gradual thickening of the bone from ankle to knee on this anterior ($\Theta=0°$) side. In contrast, the region of high stress in the distal region of the posterior ($\Theta=180°$) side of the bone near the ankle gradually decreases moving proximally towards the knee. The relative magnitudes between this nodal strain energy density and the surface averaged and standard deviation values control the amount and direction of the trains. Nearly uniform decay occurs on the medial and lateral sides of the bone in this mid-shaft region, resulting from the near uniform, relatively low magnitudes of the local strain energy density.

The shape alterations resulted in an improvement of the uniformity of the stresses away from the boundary conditions and a reduction in the very large stresses induced by the muscle forces near these boundary conditions. However, some of the shape changes adversely increased the stresses induced in regions far away from the directly applied

boundary conditions. For example, the thinning in the posterior side of the of the bone under these loading conditions allowed it to flex more under the applied load, increasing the stress near that material and geometric transition to the cancellous-filled region (point B in Figure 5.48 and red contours in Figure 5.44b).

Both the posteriorly directed resultant force alone and in sequence with the superiorly directed resultant load induced very similar changes to the nodal strain energy density and amount of growth at the final iteration (nonconverged) at locations far from the applied loads in this mid-shaft region where the targeted strengthening region is located (Figure 5.48 pink solid (single load) versus dashed (multiload) lines). The changes, however, were generally more moderate than those of the single load case. For example, near the location of the tibialis anterior attachment, the single load case caused a greater reduction in the locally high strain energy density from the anterior tibialis muscle activity in the posteriorly directed resultant case than occurred in the two-load set. For this multiload set, the region above the tibialis anterior muscle force grew thicker and so the region surrounding the muscle force application grew less prominently than under the single load case. This is because the superiorly directed loadset induced large stresses in this region (Figure 5.45a), causing a relatively large amount of growth that offset and overcome the decay in this region described above due to the posterior case (Figure 5.44b and c and Figure 5.48 (top)). Similar phenomena occurred on the posterior ($\Theta=180°$) side of the bone, tempering the extreme decay in the region on this side of the bone that results in the very thin shape under the single posterior load case (Figure 5.44b and 5.48b) and improving the stress in the region just below the knee flexor biceps femoris muscle force (Figure 5.44c).

Figure 5.48 Posterior load, case 0° configuration, outer surface: Variation of (a) nodal strain energy density and (b) growth with axial location Z at three locations along the surface: anterior side (Θ=0°), medial side (Θ=90°), and posterior side (Θ=180°) due to shape optimization single load or in series with superior load case.

The tracking of the nodal strain energy density and growth per iteration at discrete points along the axial lines studied in Figure 5.49 can provide addition insight into the shape optimization process and resulting adaptations to the bone's strength. The direct

correlation between the amount of nodal growth per shape optimization iteration and the difference between the nodal strain energy density and the average of this measure over the design surface is clear, such as in the large growth seen in regions of very high stress. However, the dependence of the amount of nodal growth on the inverse of the surface standard deviation results in some interesting trends that are not as easily discerned.

On the anterior ($\Theta=0°$) side of the bone, Figure 5.49a (top), it is quite apparent that the trend in the nodal strain energy density with iteration at the two-thirds length location, where the tibialis anterior muscle acts, is almost opposite that of the growth at the same node Figure 5.49b (top) for the single load posterior case. The nodal strain energy density is approximately an order of magnitude larger than the surface averaged value for this load case, but it is approximately the same order of magnitude as the initial surface standard deviation (Table 5.10 and Figure 5.46). Therefore, following Equation 4.23, the initial growth (Figure 5.49b (top)) is essentially proportional to the ratio of the nodal strain energy density (Figure 5.49a(top) and the surface standard deviation (Figure 5.46b(top)) (the growth rate factor α was selected as 1e-5 in this study). While the surface standard deviation decreases rapidly (Figure 5.46), the nodal strain energy density and surface average remain relatively constant, leading to a large amount of growth per iteration driven by the large decrease in the standard deviation in the denominator of Equation 4.23. As the optimization progresses, the large growth leads to a decrease in the node's strain energy density. At the same time, the surface averaged strain energy density begins to increase significantly and at an increasing rate while the change in the standard deviation slows. This causes the magnitude of the numerator and denominator of the

growth driver to be comparable and slows the growth at this node to a near constant value as seen in Figure 5.46b(top).

At this same location, it is also quite noticeable that while the trend and magnitude of the nodal strain energy density for the multiload case (dashed lines) is very similar to that of the single load case (solid lines) over the optimization process, the resulting growth is very different (Figure 5.49 top). From Equation 4.23, this can be explained by to the differences in the trends in surface average and standard deviation of the strain energy density for these two cases (Figure 5.46). Both the single and the multiload cases start the same with the very high strain energy density driving the growth, resulting in a relatively large initial amount of growth. However, the combined greater increase in the average value and slower decrease in the standard deviation seen for the multiload case (Figure 5.46), with the slightly greater decrease in the nodal strain energy density with iteration, allow the numerator (difference between nodal and average strain energy density) and denominator (standard deviation) of the growth driver expression (ratio of the two in Equation 4.23) to become more comparable earlier in the optimization process. This leads to the constant growth seen at this location over most of the optimization process for the multiload case.

On the medial side 90° position (Figure 5.49(a)middle and 5.44b), both the nodal strain energy density and the surface averaged value are closer in magnitude and trend, leading to a near constant difference between these two values over the course of the optimization. The amount of growth (or here decay) with iteration, however, continually gets larger (Figure 5.49b(middle)). This change directly follows the trend of the inverse of the standard deviation of strain energy density, for as the standard deviation gets

smaller with iteration (Figure 5.46 b(top)), the amount of growth per iteration increases (Figure 5.49).

In some instances, the effect of the average value dominates the trending nodal growth during part of the optimization process and that of the standard deviation controls another part of the optimization. For example, on the outer surface at the 180° location, the trend in the five-sixths location is very different from that of the other locations (Figure 5.49(bottom)). Initially, the nodal strain energy density at that location is very small, as this is in the low stress region identified above (Figures 5.44a and 5.49a). The numerator of the growth driver portion of Equation 4.23, the difference between the nodal strain energy density and the surface average value, is, therefore, negative and relatively large compared to the other nodes depicted in Figure 5.49a, which have values closer to the surface average. This leads to a relatively large amount of initial decay at this location (Figure 5.49b(bottom)) compared to the other nodes in the plot. Yet, the decrease in the standard deviation is sufficient enough to still influence the increasingly decaying rate of growth per iteration. As the cortical wall gets thinner in this region, the nodal strain energy density increases (Figure 5.49a(bottom)) and the value of the numerator gets smaller, decreasing the amount of decrease in the growth per iteration. Eventually, as the nodal strain energy density increased enough towards the average value and the rate of change of the standard deviation declined enough with the increased uniformity of the stress state, the influence of the numerator increases (Figures 5.49 and 5.46 and 5.44b). Eventually, the increasing nodal strain energy density in this thinning region is large enough that the numerator takes control over the growth per iteration trend as the switch to growth at this location is approached just before the size limit is reached

(Figure 5.49). Simply put, the bone in this originally low stress region was getting "too thin" (stresses "too high") requiring a switch from decay to growth to reduce the possibility of fracture at this point.
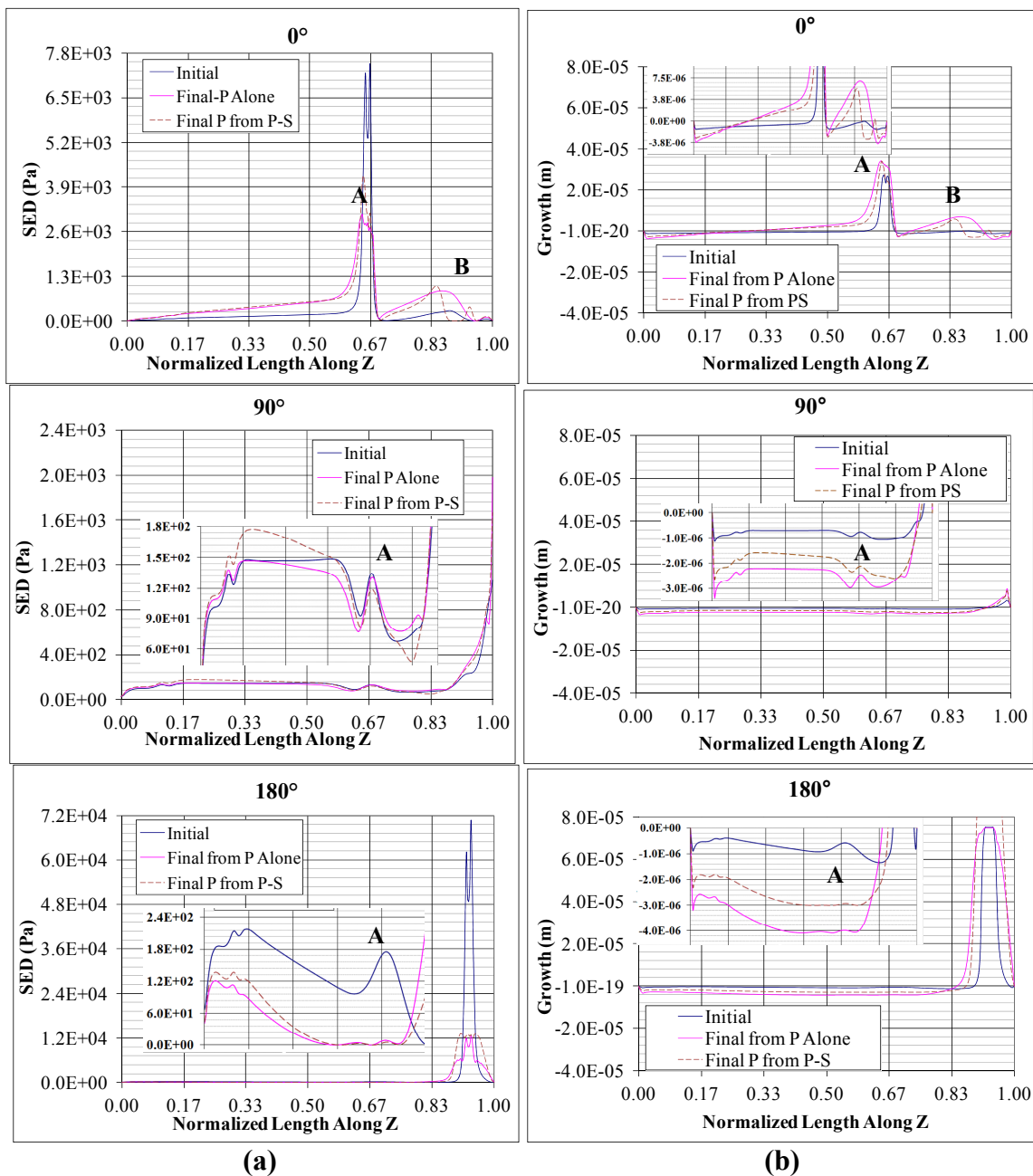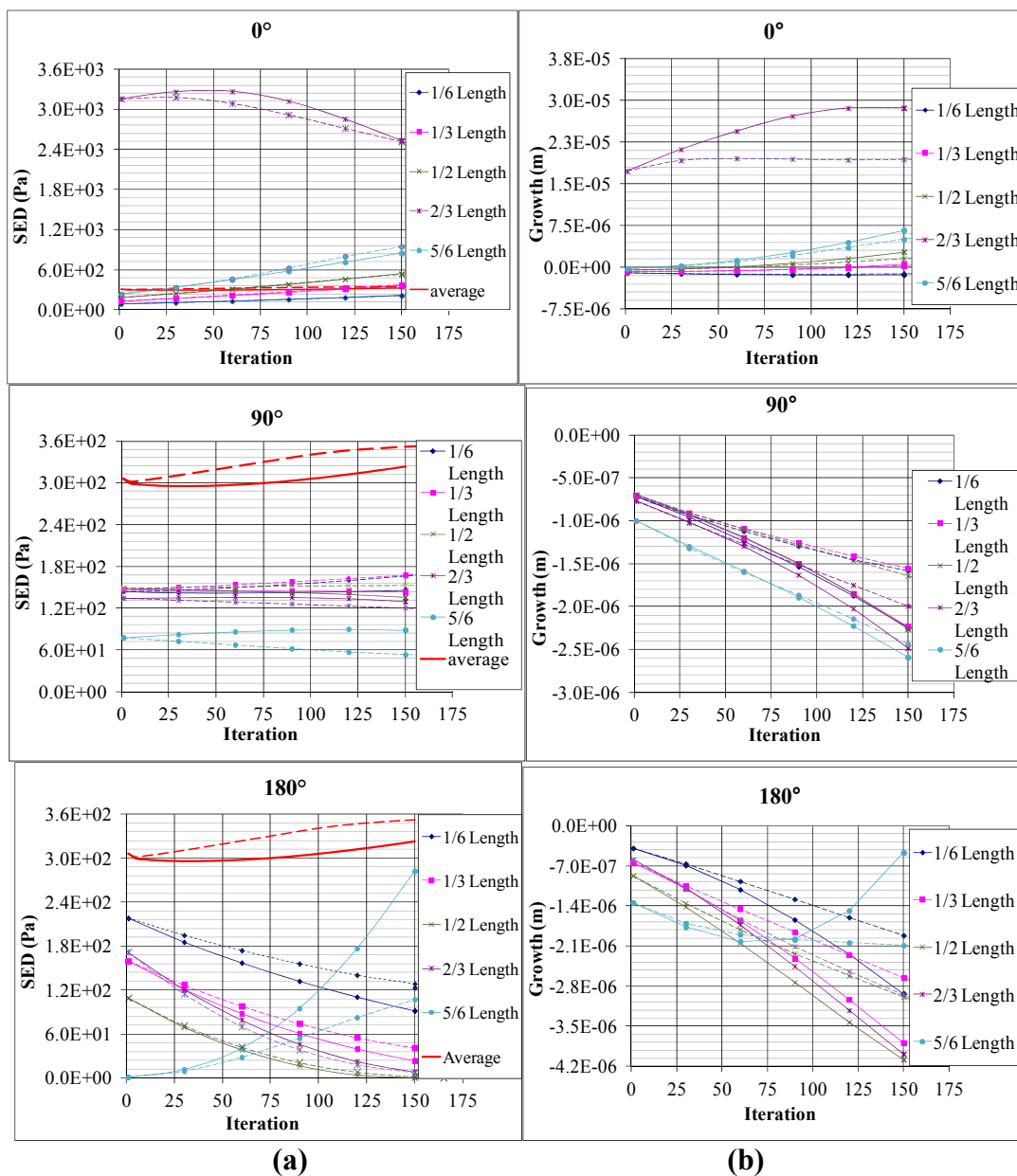

Figure 5.49 Posterior load case, 0° configuration, outer surface: Variation of (a) nodal strain energy density and (b) growth with optimization iteration at discrete axial locations (% total tibial length) and three locations along the surface: anterior side (Θ=0°), medial side (Θ=90°), and posterior side (Θ=180°) due to shape optimization due to single load or in series with the superior load case. Note: The "alone" case is identified by solid lines and the component of the multiload case by dashed lines.

A similar analysis can be performed on the inner surface. On this surface, the trends are similar to the outer surface, but less extreme due to the lack of directly applied loads. While the increased uniformity of nodal strain energy density over the surface is evident in the trends of strain energy density over the optimization process in Figure 5.50 and 5.51, the convergence measure (Table 5.11 and Figure 5.47) indicated an overall increase in the variation over the surfaces as a result of the shape changes. This is likely due to the stress concentrations that develop in the corners of the inner surface's transition to the cancellous-filled region, shown as local spikes in strain energy density and growth in the plots in Figure 5.50 near the one-sixth and five-sixths locations and in the small region of relatively large von Mises stress Figure 5.44b (red arrow). It is interesting to note that, as seen on the outer surface, the tibialis anterior muscle affects the stresses and growth on inner surface at the 90° (medial) and 180° (posterior) sides (regions of slightly higher growth and strain energy density near the two-thirds location in Figure 5.50).

On this inner surface, the sequential loading brought more variation in the strain energy density of the "optimal" design under the posterior loadset than did the single case alone under the same loads (Figure 5.50). These observed trends are likely due to the alterations in the deflection patterns and stress states under the applied load that occur due to differences in active muscle sets and resulting large growth regions for the posterior and superior load cases. These indirect effects of the addition of significantly increased thickness without increased load (either on the anterior side for the posteriorly directed loading or the posterior side on the superiorly directed loading) alter the behavior of the bone under the applied load sets (Figure 5.44).

Figure 5.50 Posterior load, case 0° configuration, inner surface: Variation of (a) nodal strain energy density and (b) growth with axial location Z at three locations along the surface: anterior side (Θ=0°), medial side (Θ=90°), and posterior side (Θ=180°) due to shape optimization single load or in series with superior load case.

When examining the change in the nodal values with iteration, more uniform trends with location along the inner surface are seen than on the outer surface (Figure 5.51 vs Figure 5.49). Opposite to the trends on the outer surface, the surface average strain energy density decreased with iteration on the inner surface (3%) while the standard deviation increased (more than two-fold) (Figure 5.51, Table 5.11). The decreased average value on the inner surface is related to the lack of directly applied loads to the surface so that the shape changes can have more of an effect on the local stresses. The increased standard deviation is likely due to the stress concentration near the transition to the cancellous filled region described above and the increasing uniformity elsewhere on the bone, creating a wider range of values over the surface.

There are two important differences in the relative values of the average and standard deviation in this inner surface compared to the outer (Figure 5.47(top)). First, the average strain energy density was twice that of the standard deviation over the inner surface during the optimization process, showing much less variation compared to the outer surface, where the standard deviation was up to eight times the average. Second, aside from the locations concentrations near the transition to the cancellous region, the nodal and average values of the strain energy density were very similar on the inner surface. Because the nodal strain energy density and its average and standard deviation over the inner surface had relatively equal weight by magnitude alone, the combined relationships between the values of the nodal strain energy density and the average and standard deviation of the strain energy density over the inner surface had a relatively direct influence on the amount of growth at each iteration. This contrasts the behavior on the outer surface under the loading conditions studied, where the differences between

these values were up to an order of magnitude and the growth was driven mainly by the changes to this very large magnitude of standard deviation of the nodal strain energy density over the surface.

The interrelationships between these measures with comparable values are shown through an example tracking the nodal strain energy density and its surface average and standard deviation with the nodal growth per iteration over the optimization process. Specifically, the changes in a single node were examined on the anterior ($\Theta=0°$) side of the inner surface at a location far from the applied muscle forces and constraints, at an axial location one-third of the tibial length from the ankle, during the optimization process under the single load posteriorly directed loadcase. The inner surface average strain energy density remains nearly constant during the optimization at a magnitude near that of the initial nodal strain energy density of many of the points on this anterior surface of the tibia bone. The standard deviation over the surface is initially about three times less than this magnitude, but slightly greater than initial difference between the nodal and surface averaged strain energy density (Figures 5.47 and 5.51a(top)). The trend in growth on the anterior ($\Theta=0°$) surface can be explained as follows. Because the standard deviation (denominator of the growth driver expression of Equation 4.23) is greater than the difference between the nodal strain energy density and the surface average strain energy density (numerator of the growth driver expression of Equation 4.23), initially, there is a relatively small amount of growth at this node. Over the first few iterations, the standard deviation changes little (Figure 5.47b(top)); however, the nodal strain energy density increases relatively rapidly (Figure 5.51a(top)), moving away from the nearly constant surface average value and increasing the numerator value over that of the

standard deviation in the denominator of the growth driver expression. Thus, the nodal growth initially follows the change in nodal strain energy density (Figure 5.51(top)). As the change in the standard deviation increases from its initial rate (Figure 5.47), it gains a slightly greater influence over the growth, reducing the rate of increase of growth from the linearly increasing difference between the nodal strain energy density and surface average. Eventually, as both the standard deviation and the nodal strain energy change linearly with iteration, and as the surface average remains relatively constant, the change in both the numerator and denominator of the growth rate expression is constant over the optimization process and the amount of growth per iteration at this node stops changing. This results in a nearly constant amount of growth at this node for each iteration for the remainder of the optimization process.

The influence of the increasing value of the standard deviation of the strain energy density is also shown through the study of the changes of a specific node on the inner surface with optimization iteration. At the ($\Theta=90°$) medial location, the nodal strain energy density remains nearly constant throughout the optimization process (Figure 5.51a(middle)). Because the surface average of the strain energy density also remains constant (Figure 5.47a(top)), the numerator of the growth driver expression does not change. Therefore, the progression of the amount of nodal growth with iteration over the optimization process depends only on the changes to the standard deviation of the strain energy density over the inner surface. Because it increases nearly linearly (Figure 4.47), the amount of growth per iteration decreases nearly linearly (Figure 5.51b(middle)) as it is proportional to the inverse of the standard deviation.

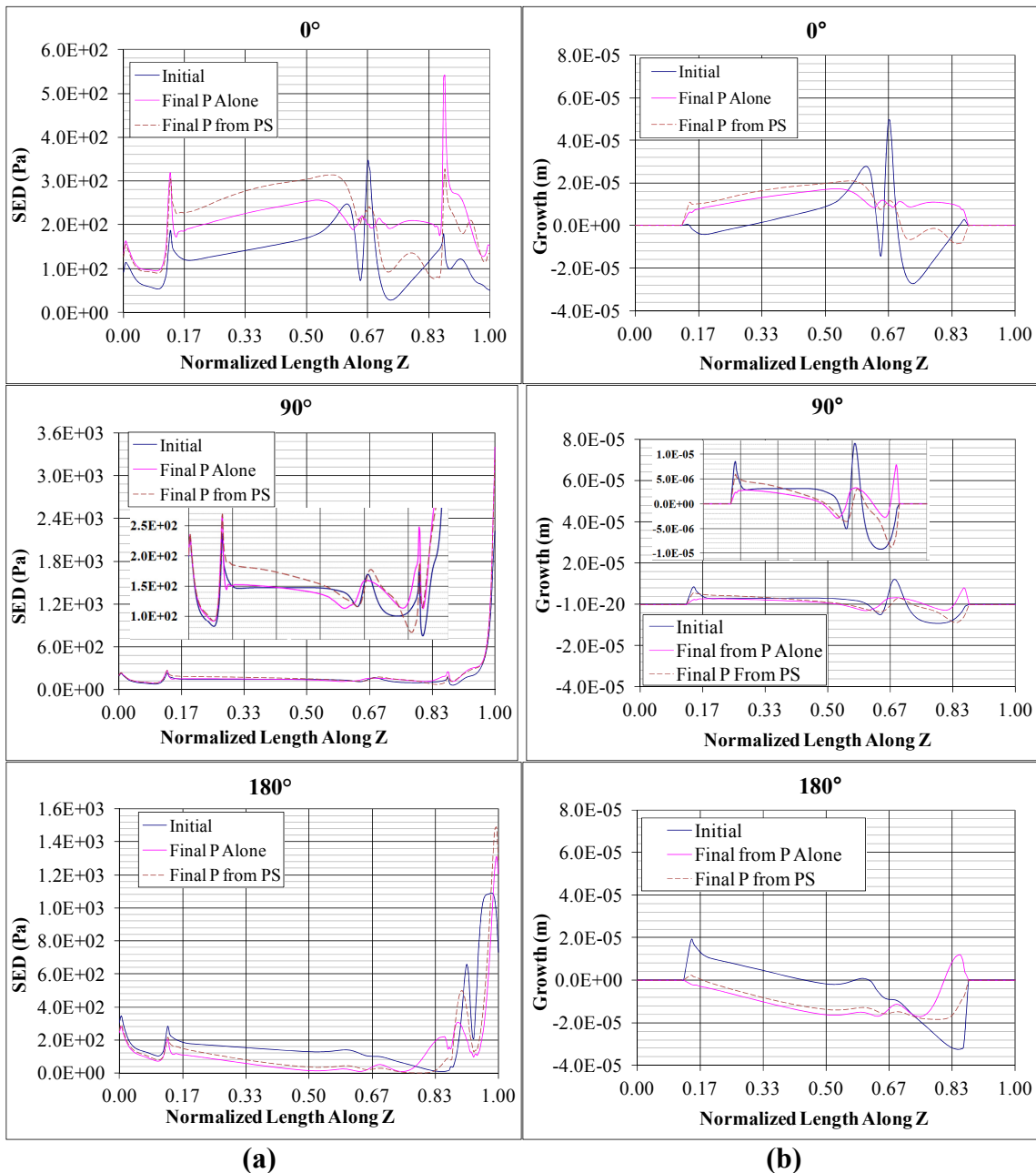**Figure 5.51** Posterior load case, 0° configuration, inner surface: Variation of (a) nodal strain energy density and (b) growth with optimization iteration at discrete axial locations (% total tibial length) and three locations along the surface: anterior side (Θ=0°), medial side (Θ=90°), and posterior side (Θ=180°) due to shape optimization due to single load or in series with the superior load case. Note: The "alone" case is identified by solid lines and the component of the multiload case by dashed lines.

As was observed for the outer surface, the addition of the sequential application of the nearly opposite loading conditions of the superiorly directed loadcase to the optimization of the bone shape under the posteriorly directed loadcase did not significantly alter the trends in the nodal strain energy density and resulting local growth on the inner surface except at regions nearby the areas of application of muscles that were active under either of these loading conditions. In these regions the trends in strain energy density and growth with iteration on the inner surface were more significantly influence as the effects of the alterations to the strain energy density and profile described previously for the outer surface propagated inward to affect the stress state on the inner surface.

A similar analysis follows for the superiorly directed load set. The concepts used to relate the changes to the average and standard deviation of the strain energy density over the optimizing surface, the changes to the nodal strain energy density, and the resulting nodal growth could be applied to any situation modeled. The detailed presentation using the posteriorly applied load provided a good understanding of the model function. As such, a detailed analysis of these relationships will not be presented for further load sets examined. Instead, differences will be highlighted between cases studied and interesting phenomena will be noted.

Superiorly Directed Load

The tibia bone had a simpler state of stress under the superiorly directed loading than under the posteriorly directed resultant loadcase that was described above (Figure 5.45a). Under this loading condition in the straight leg configuration, there were three regions of relatively higher stress that occurred on the anterior face at the proximal end of the bone.

The first two were at the locations of attachment of the knee extensor muscles and the tibialis anterior muscle (red arrows). The third location of high stress was in the area between these muscle force application regions. High stresses occurred there directly as the two muscle forces pulled nearby regions of bone in opposite directions because the directions of the muscle forces were nearly parallel to the global y-coordinate in this straight leg configuration. While the stresses induced on the anterior side of the bone were large due to the directly applied muscle forces, a region of relatively high stress also occurred on the posterior side of the bone in response to the bending induced by the muscles on the anterior side in the straight leg configuration. The stresses on both sides of the bones then gradually decrease proceeding distally towards the ankle.

Plots of axial variation of nodal strain energy density (Figure 5.52) followed the observed trends in the von Mises stress contours described above (Figure 5.45a). At the 0° (anterior) location, two local maxima, one at the two-thirds spot and the other just above the five-sixth location, were observed, corresponding to the regions of attachment of the tibialis anterior and the active knee extensor muscles to the tibia bone, with the strain energy density at the knee flexor attachment location, an order of magnitude greater than that at the tibialis anterior location. A nearly uniform region of elevated strain energy density, through less so than at the locations of direct muscle force attachment, was shown between the two local maxima corresponding to the observed high stress region in the contour plot. On the 180° side of the bone, with no direct load application, the trend in strain energy density followed an asymmetric skewed parabolic-like curve, with the peak correlating to the region of high von Mises stress in Figure 5.45 (red arrow on posterior side near end of the hollow region). This is related to high stress

region is that of maximum deflection in the hollow bone induced by the direct pull of the muscles on the opposite (anterior) side. The gradual decline of the strain energy density from this region towards the ankle, noted in the stress contours is clearly seen in the plot of the strain energy density in Figure 5.52a. As in the posteriorly directed load, the 90° (medial) location showed a transition between the anterior and posterior sides through a relatively low, nearly uniform, strain energy density, similar to the stresses that would be found a bending axis. A local region of high stress at the same axial location as the area of muscle force application demonstrates the dispersion of the muscle's effects throughout the region and serves, in part, to transition some of these stresses to the posterior side of the bone.

The geometry optimized under this single load case successfully reduced the stresses related to the muscle force through large amounts of local growth (Figure 5.52), with the location of knee extensor force application reaching the maximum growth limit throughout the optimization process. As typical to the shape adaptation model function, regions of high stress (and strain energy density) showed increased growth while the regions of low strain energy density in the distal region showed decay. When applied in sequential series with the posteriorly directed load, the changes in the bone shape due to the multiload case resulted in growth patterns and von Mises stress distributions under the superiorly directed component of the load set that were more similar to the superior alone case than was seen for the posteriorly directed load case. In the 90° location, the geometry generated by the sequentially applied posterior and superior load sets (dashed pink line) resulted in a more uniform stress distribution that the superiorly directed alone (solid pink line) far from the load application regions (Figure 5.52a(middle)).

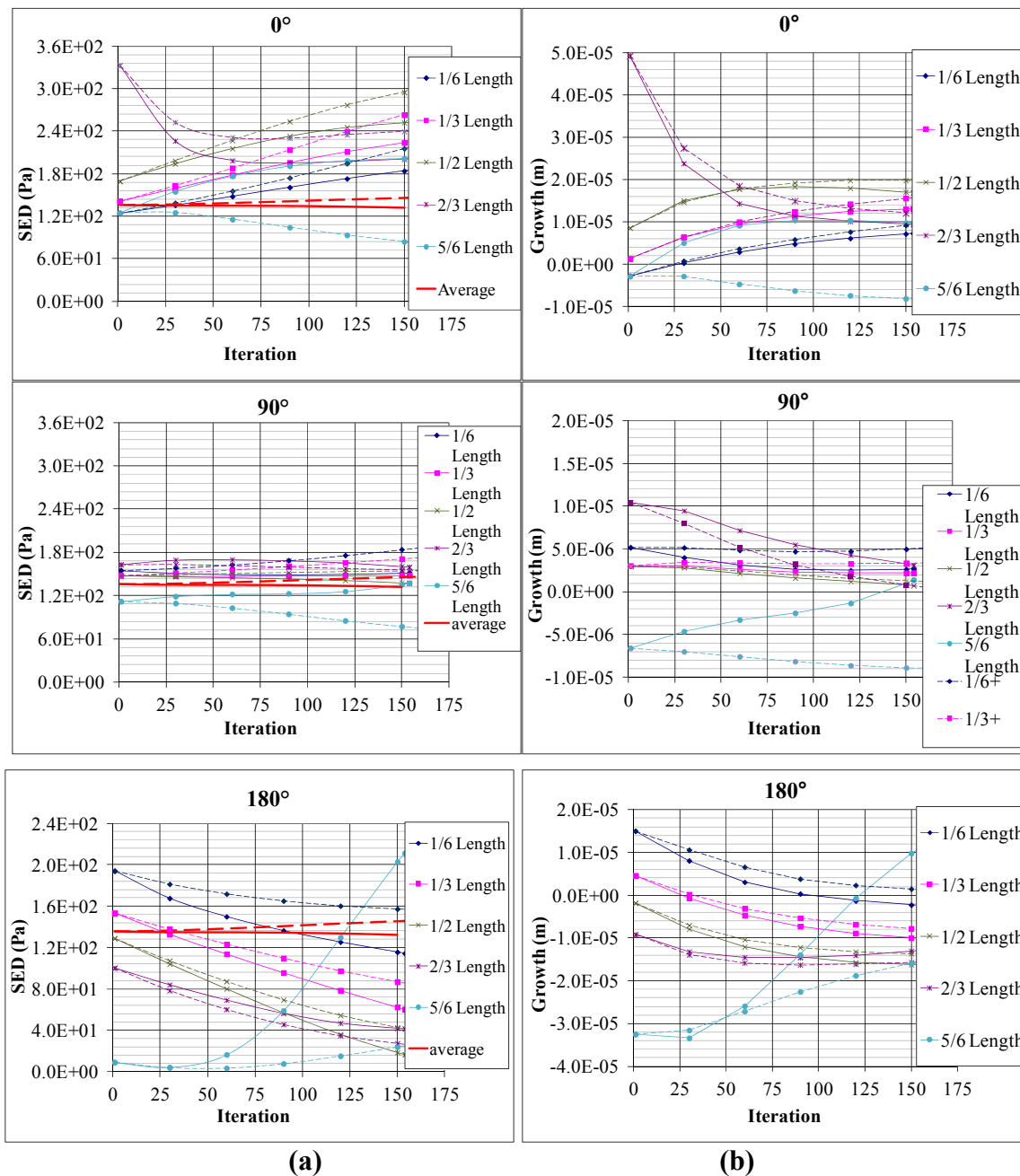**Figure 5.52** Superior load, case 0° configuration, outer surface: Variation of (a) nodal strain energy density and (b) growth with axial location Z at three locations along the surface: anterior side (Θ=0°), medial side (Θ=90°), and posterior side (Θ=180°) due to shape optimization single load or in series with posterior load case.

While the general correlation between regions of high stress and large growth (and between low stress and small amounts of growth) are valid in the conditions studied, in tracking the nodal strain energy density and growth with iteration, it is clear, as has

been seen in the other cases presented, that the trends in these two measure do not always follow. Because the trends in the standard deviation and the average of the strain energy density over the outer surface of the bone studied are different for this superiorly directed resultant force case than for the posterior case, an illustrative example of their relative effect is presented.

Over the outer surface, the average strain energy density increased linearly and significantly (25%) under the superiorly directed loadcase. This is in contrast to the posteriorly directed load case where the strain energy density first slightly decreased before it eventually results in a maximum 8% increase over the initial state (Figure 5.46). Unlike the trends in the surface average value, the trends in the standard deviation of the strain energy density over the surface under the superiorly directed load was nearly indistinguishable from that of the posteriorly directed loadcase, aside from magnitude. When comparing the magnitudes of these global measures of the state of stress over the outer surface from the two single load cases, the superiorly directed loadcase had a standard deviation that was more similar in magnitude to the surface average than occurred under the posteriorly directed load by almost 25% (also confirmed by ratios presented in Table 5.10).

The ways in which these two features of the global stress state affect the growth of the bone and the resulting changes in strength can be seen at the 0° location (anterior side) at the two-thirds location, near the attachment point of the tibialis anterior (Figure 5.53(top)). Initially, there was a relatively large difference between the nodal strain energy density at this point and the average of this measure over the surface, compared to the values at the other locations along the anterior surface of the bone. Therefore, despite

the even larger standard deviation of the strain energy density over the surface, the numerator in the growth driver expression of Equation 4.23, corresponding to the how different the stress state at a particular node is from the average over the surface, had a greater influence on the growth of the node because, although there is much variation over the surface (large standard deviation), this node is "more different" than the rest. As the cortical wall thickness increased near this node (Figure 5.21), the strain energy density in this location decreased. Despite this decrease, the corresponding thinning in other parts of the bone shape (Figure 5.21) increased the strain energy density such that the overall average increased (Figure 5.46), making the conditions at the examined node more similar to the average surface conditions than under the initial geometry. This results in a smaller numerator in the growth driver expression of Equation 4.23. As the nodes over the surface approach a more common value through relative changes in the local thickness over bone volume, the standard deviation of the strain energy density (denominator in Equation 4.23) also decreased.

The decrease in the standard deviation, with a nearly exponential decay (Figure 5.46b (bottom)), was initially much faster than that of the relative difference between the nodal strain energy density and the reference value, which progressed more linearly (Figure 5.53a(top) and Figure 5.46a(bottom)). This resulted in a slight increase in the amount of growth per iteration (Figure 5.53b(top)) despite the decreasing nodal strain energy density because the decrease in the standard deviation of the strain energy density drove the changes in the growth at this location. As the optimization progressed and the strain energy density of the surface nodes became more uniform (Figure 5.34b) the rate of change of the standard deviation decreased, resulting in slightly less growth per

iteration, as both the numerator and denominator varying nearly linearly with iteration. As the rates of change in both the numerator and denominator become more similar, the amount of growth per iteration at this location changed less between iterations and a constant amount of growth eventually resulted. Note that the growth itself did not stop, as the nodal strain energy density was still far from equaling the surface average value. The analysis simply showed how the growth per iteration became constant, meaning that the relationships between the nodal strain energy density, surface averaged strain energy density and the standard deviation of this measure over the surface remained constant.

Under the combined loading condition, the changes in the growth and strain energy density under a single load set were similar to those of the multi-load sets with slightly different magnitudes due to the modifications to the stress state from the growth caused by the influences of the second loadset on the alterations to the bone shape. For example, under the posterior loading conditions (Figure 5.48a(bottom)) the location of the biceps femoris attachment on the 180° side had a large reduction in strain energy density under both the single and the mulitload conditions. However, the high stress and high growth region occurred over a greater area when combined with the superiorly directed load. This is related to the more gradual variations of the strain energy density along 180° side from the bending induced under the superiorly directed load (Figure 5.52a(bottom)). This smoother growth over the length of the cylinder under the superiorly directed loading also helped to reduce the significant thinning directly distal to this high growth knee flexor muscle force application region on the posterior (180°) side of the bone that was caused by the posteriorly directed loading (Figure 5.45).

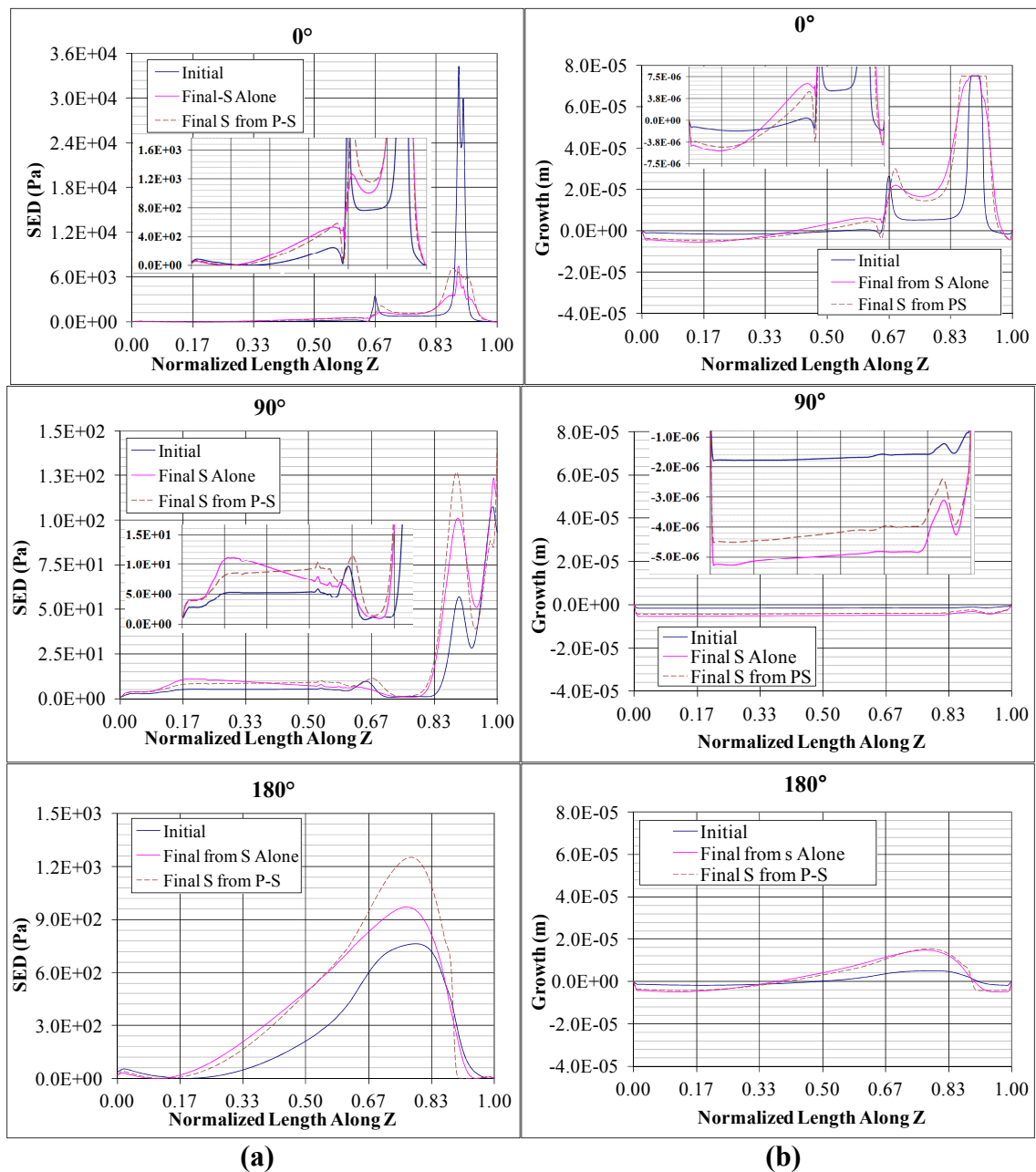**Figure 5.53** Superior load case, 0° configuration, outer surface: Variation of (a) nodal strain energy density and (b) growth with optimization iteration at discrete axial locations (% total tibial length) and three locations along the surface: anterior side (Θ=0°), medial side (Θ=90°), and posterior side (Θ=180°) due to shape optimization due to single load or in series with the posterior load case. Note: The "alone" case is identified by solid lines and the component of the multiload case by dashed lines.

Under this superiorly directed resultant force, the trends in the strain energy density and growth on the inner surface were similar to those on the outer surface, though less extreme. For this reason more uniformity over the distal surface near the ankle, between approximately the one-sixth and two-thirds locations on this inner surface, was achieved as a result of the single superiorly directed resultant force in all three locations examined (Figure 5.54 (solid pink line)). Due to the shape changes under the superiorly directed load, the influence of the muscle application forces, which caused a relatively large amount of growth initially (blue lines, Figure 5.54b) on this inner surface as the stresses (strain energy) propagated through the cortical bone thickness, was nearly eliminated (solid pink lines Figure 5.54b), and the growth in the force application region on the inner surface was nearly the same as that in other regions on that surface that were outside the influence of the boundary conditions. Even the local peaks in the nodal strain energy density at ends of the interior node growth region that have been seen in all studied cases due to the transition to the cancellous filled region were significantly reduced under this superiorly directed loading direction in the straight leg configuration. Thus, all over the inner surface, the variation of the strain energy density was reduced, resulting in the achievement of convergence for the inner surface under this single mode of loading, the only of its kind in this straight leg configuration study.

This improved uniformity of the strain energy density on the inner surface under the single superiorly directed load case, however, was not maintained when followed directly by a posteriorly directed load case in the sequential series of these two loads, particularly on the posterior (180°) side. While under the superiorly directed load, this location had no directly applied loads and a smooth, gradual increase in strain energy

density (and growth) from the distal end of the bone near the ankle to the proximal end near the knee. This gradual transition from one end to the other was eventually reduced to nearly a constant value over the length of the bone due to the shape optimization under the superiorly directed load (Figure 5.54 (bottom), Pink line or Figure 5.24a (superior - dark blue line)). In contrast, the posteriorly directed load resulted in thinning in this region (Figure 5.50 (bottom), Figure 5.24a (posterior -green line)). The combined load, therefore, created a geometry that did not have as thickened a cortical bone to resist the bending-type loading than the geometry created by the superior alone did. With geometry resulting from the combined load having an increased amount of overall deflection compared to the geometry created from the superiorly directed force alone, the stress concentration at the transition to the cancellous fill region was no longer reduced in the combined superior-posterior case as was seen under the single superiorly directed load case, and the variation over the surface of this "optimal geometry" under the superiorly directed load increased, accordingly (Figure 5.54a(bottom)).

Figure 5.54 Superior load, case 0° configuration, inner surface: Variation of (a) nodal strain energy density and (b) growth with axial location Z at three locations along the surface: anterior side (Θ=0°), medial side (Θ=90°), and posterior side (Θ=180°) due to shape optimization single load or in series with posterior load case.
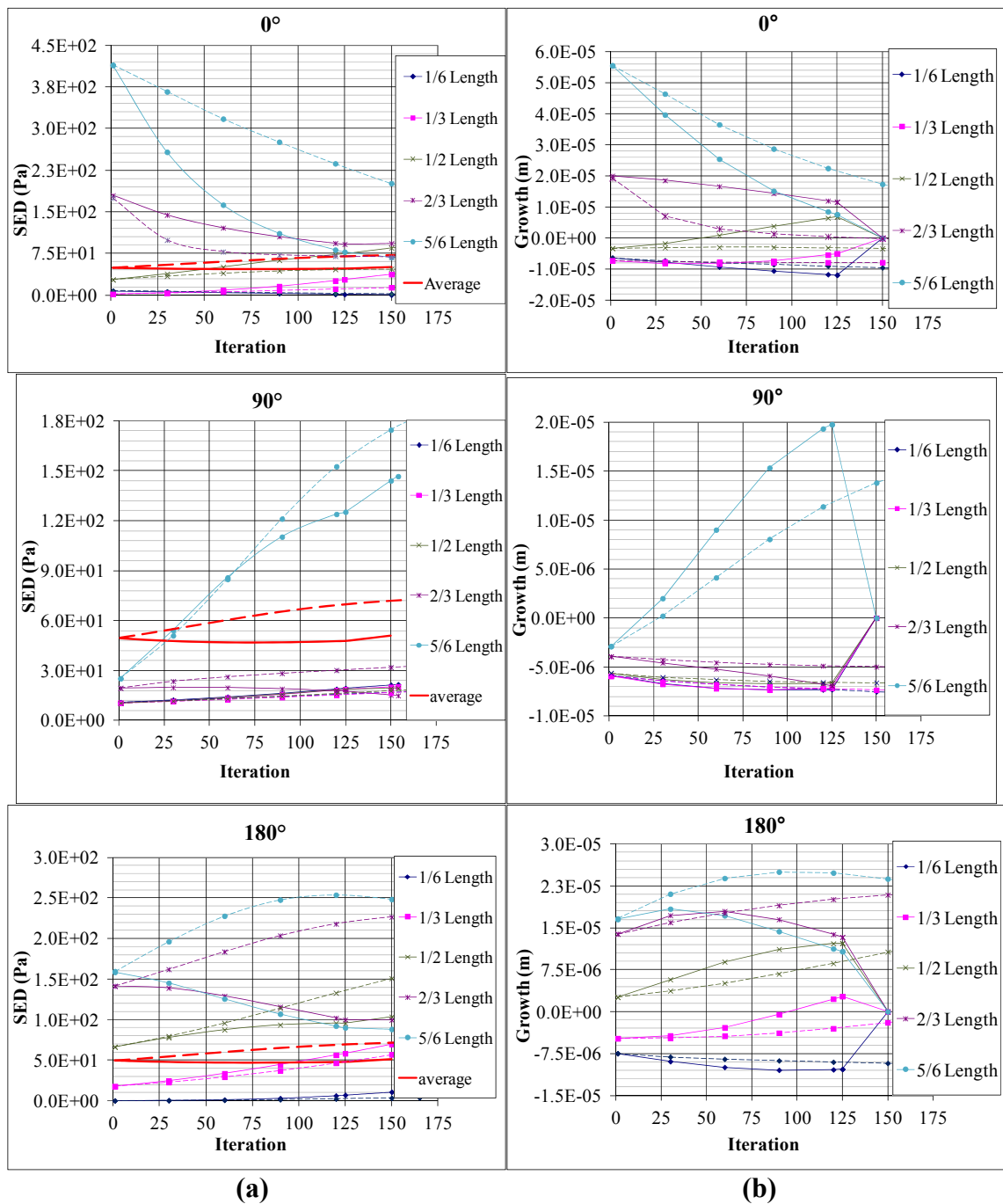
Figure 5.55 Superior load case, 0° configuration, inner surface: Variation of (a) nodal strain energy density and (b) growth with optimization iteration at discrete axial locations (% total tibial length) and three locations along the surface: anterior side (Θ=0°), medial side (Θ=90°), and posterior side (Θ=180°) due to shape optimization due to single load or in series with the posterior load case. Note: The "alone" case is identified by solid lines and the component of the multiload case by dashed lines.

Under the 0° configuration, muscle forces acted in directions closely aligned with the components of the global coordinate system, and, therefore, also aligned with the four main resultant loading directions studied. As a result, the stress state in the tibia was often directly related to the application of the muscle forces generated to create the desired resultant force. This more regional effect of the muscle forces resulted in locally very high stresses (strain energy densities) causing large averages and standard deviations over the surface being optimized and, consequently, localized regions of very large growth. Because of these isolated regions of very large growth, the average was biased towards these outliers despite the element area weighted factors used to reduce the variations. Accordingly, decay (bone resorption) occurred in many locations over the length of the bone, especially away from the regions where the muscle forces acted. With no directly applied loads and a smaller standard deviation of the strain energy density over the inner surface, there was no extreme local growth and widespread decay, and convergence was achieved on the inner surface for the superiorly directed force.

While local variations in growth occurred between the load cases studies from the varied relationships between nodal strain energy density and the average and standard deviation of the strain energy density over the optimizing surface, the characteristics of the "optimized" bone geometry under all load sets in the straight leg 0° configuration was the same: proximal and anterior thickening and distal and posterior thinning as the region of large growth was localized to the region of muscle main force application. Because the targeted fracture prone region was in the distal end of the bone, none of the loading modes applied to this straight leg configuration significantly improved the bone's strength in this region and, under many of the loads, the strength actually worsened.

In the 45° and 90° configurations, the tibia bone was rotated the named amount with respect to the global y-coordinate. Therefore, the directions of the muscle forces in the leg system studied are not fully aligned with the global coordinate system (and resultant force directions) as occurred in the 0° configuration. More complex loading on the tibia bone typically result as compared to the 0° configuration, which may be beneficial to the strengthening of the distal tibia, the optimization goal in this study. As discussed in Subsection 5.4.2, a number of the loading sets studied resulted in similar stress distributions for each of these configurations. Therefore, like in the straight leg configuration, only loading modes that result in unique stress states are presented. For the 45° configuration, these were the anteriorly, posteriorly, and superiorly directed resultant forces. For the 90° configuration, these were the inferiorly, posteriorly, and superiorly directed resultants. Because of the combined similarities, the evolution of the optimal tibial bone shapes under all six unique loading conditions for both the 45° and 90° configuration are discussed together.

5.4.3.2 Shape Optimization under the 45° and 90° Configurations. When the resulting "optimal" tibial bone geometries from these individual load cases were examined under the comparison loading condition in Section 5.3, it was found that the anteriorly and inferiorly directed resultant forces generated under both the 45° configuration and the 90° resulted in very changes to the bone geometry from the uniform initially circular cylinder, and, therefore, changes to the stress state under the common critical design load jogging comparison case. The same was found to be true for geometries resulting from the posteriorly directed resultant load generated by the leg in the 45° configuration and the superiorly directed resultant load in the 90° configuration.

Amongst these groups, the convergence behaviors during the optimization processes under each limb configuration and load set (Figures 5.37 and 5.39) and the relative changes in the surface average and standard deviation of the strain energy density resulting from the loads on the initially circular uniform cylinder to the same loads on the optimal shape (in Tables 5.12 through 5.15) were also very similar. Specifically, the changes in the average and standard deviation of the strain energy densities varied no more than 1% over both the inner and outer surfaces resulting from the four single load cases comprised of the inferiorly and anteriorly directed loads in the 45° and 90° configurations. Similarly, these measures varied less than 5% between the posteriorly directed load in the 45° and those from the superiorly directed load in the 90° configurations. While these measures of the changes on the outer surface for the superiorly directed resultant in the 45° configuration and the posteriorly directed force in the 90° configuration were similar ($< 5\%$), these measures for their inner surfaces varied by almost 20%. Representing their group, the anteriorly directed resultant force in the 45° configuration and the inferiorly directed force for the 90° configuration were plotted together. Similarly, the posteriorly directed resultant force in 45° configuration and the superiorly directed force in the 90° configuration were presented together. Because of their inner surface differences, the superiorly directed load in the 45° configuration and the posteriorly directed load in the 90° configuration were plotted separately.

While the trends in the global measures of the stress state and muscle activity for each of these loading conditions was studied in detail above, the similarities among the members of each group defined here are highlights so that trends in their growth patterns could be discovered.

Average and Standard Deviation of Strain Energy Density over the Optimizing Surface

In general, for the 45° and 90° configurations, the magnitudes of the average and standard deviation of the strain energy density over the optimizing surface were more comparable than they were in the 0° configuration described above, where the measure of standard deviation of the strain energy density was orders of magnitude greater than the surface average. Unlike in the 0° configuration, for all cases in these two bent leg configurations, both of these measures of the global state of stress decreased with optimization iteration. However, their magnitudes and exact trends varied. Because the magnitudes of the average and standard deviation of the strain energy density over the surface were of similar order in these bent leg configurations compared to those in the straight leg case, the relative dominance of the average and standard deviation of the strain energy density (numerator and denominator in the growth driver expression of Equation 4.23) often changed over the course of the optimization. The specific trends in these global measures over the optimizing surfaces for each loadset studied are shown in Figure 5.56. These relationships are used to understand the relative changes in growth with respect to the local and global measures of stress state on the optimizing surface.

Anterior-45° and Inferior-90°

The anteriorly directed load in the 45° configuration and the inferiorly directed load in the 90° configuration resulted in similar magnitudes and trends of the average and standard deviation of the strain energy density over the optimizing surfaces (Figure 5.56a and Figure 5.56b). The magnitudes of these measures were slightly greater for the inferior-90° case than the anterior-45° case over the course of the optimization case for both the inner and outer surfaces. For both loading conditions, the standard deviation of

the strain energy density on the outer surface was initially greater than the average. However, because the outer surface standard deviation initially decreased at a more rapid rate than the average, its magnitude eventually became less than that of the average. While similar trends occurred on the inner surface, with the initial rapid decrease at different rates followed by the slower parallel changes with iteration, the average of the strain energy density always remained greater than the standard deviation on the inner surface, and the difference in their magnitudes increased over the optimization. Both global measures of the stress state on the inner surface for both the inferior-90° and anterior-45° cases decreased parallel to each other after both cases attained inner surface convergence. The rate of change of these measures on the outer surface also became parallel for both cases upon the completion of the inner surface shape changes.

Posterior-45° and Superior-90°

The trends in the global stress state measures for the posteriorly directed resultant force in the 45° configuration and the superiorly directed resultant force in the 90° configuration were nearly identical. However, their magnitudes were significantly different, with the measures of the posterior-45° case nearly double those of superior-90° (Figures 5.56c and 5.56d). Additionally, in these cases, the standard deviation of the strain energy density over the outer surface was initially almost twice the corresponding average value. Over the course of the optimization process, this difference decreased, ending with about a 50% difference. This is directly related to the greater rate of reduction of the standard deviation than that of the average on the outer surface. In contrast, the average and standard deviation on the inner surface, started closer in magnitude. As the standard

deviation of the strain energy density on this surface decreased at a greater rate than the average, its magnitude eventually became less than that of the average.

Superior-45°

This superiorly directed resultant under the 45°configuration had a standard deviation of the strain energy density on the outer surface that initially was 25% greater in magnitude than the surface average. Similar to all of the cases reviewed, the standard deviation fell at a greater rate than did the average, ending with a magnitude approximately the same as the average (Figure 5.56e). On the inner surface, the magnitude of the surface average remained greater than that of the standard deviation of the strain energy density throughout most the optimization process (Figure 5.56h). With no directly applied forces on the inner surface, the magnitude of the standard deviation, though initially greater than the average, rapidly became smaller. At completion, the standard deviation of the inner surface strain energy density was approximately 50% less than the average. The magnitude of both measures on the inner surface was nearly constant after convergence.

Posterior-90°

The trends in the global measures of stress state for the posteriorly directed load in the 90° configuration were similar to those of the superior-45° with a few notable differences. Throughout the outer surface optimization the standard deviation of the strain energy density remained greater than the surface average, although their difference progressively decreased nearly 70%. In contrast, the standard deviation of the strain energy density over the inner surface was consistently less than the average, and their difference increased from nearly the same value to almost a 50% difference. The overall global measure changes in these conditions were less than those for the superior-45° case.
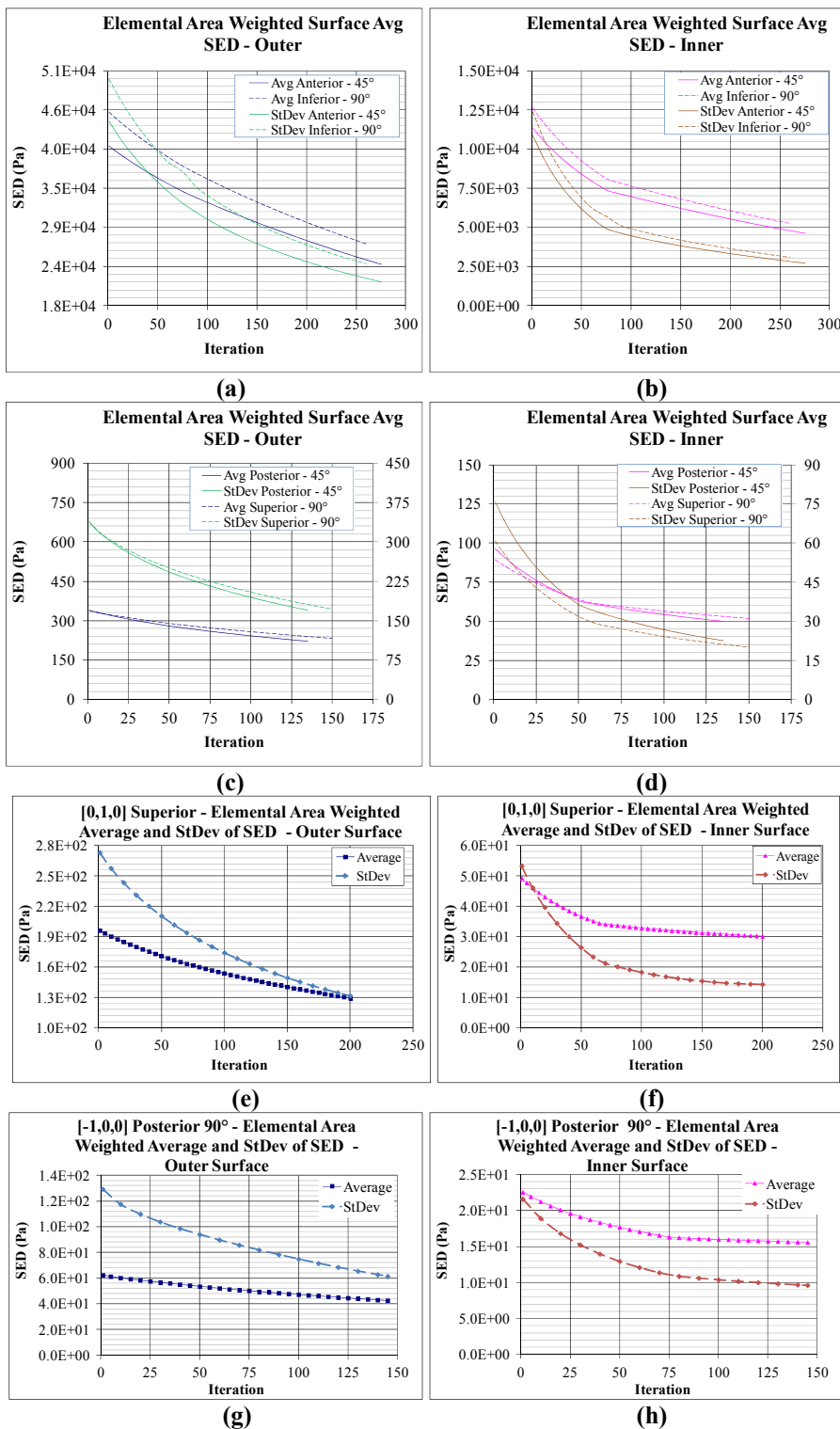
Figure 5.56 Surface average and standard deviation for the following resultant load directions and joint configurations (a) anterior 45°/inferior 90° outer surface (b) anterior 45°/inferior 90° inner surface (c) posterior 45°/superior 90° outer surface (d) posterior 45°/superior 90° inner surface   (e) superior 45° outer surface (f) superior 45° inner surface (g) posterior 90° outer surface (h) posterior 90° inner surface.

Active Muscles and Resulting von Mises Stress Distribution

The similarities between the loading cases in the various configurations can be better understood through a comparison of their active muscles. As with the trends in the standard deviation and average of the strain energy density over the optimizing surfaces, while the muscle activity was already reviewed in Section 5.2, a comparison of the muscle forces related to loading conditions that resulted in common optimal shapes may help understand the system features that lead to the similarly evolved geometries.

Anterior-45° and Inferior-90°

To create the anteriorly directed net resultant load in the 45° configuration, the vastii, rectus femoris and tibialis anterior muscles were most active, with the vastii muscle generating the greatest force. These three muscles also were most active in the creation of the inferiorly directed resultant force in the 90° leg configuration (Figures 5.57a(a) and 5.58a(a)). In this inferior-90° case, while the vastii muscle force still had the greatest magnitude, the rectus femoris muscle contributed slightly more and the tibialis anterior slightly less than in the anterior-45° configuration. Nonetheless, the dominant vastii muscle force was opposed by the fixed constraints at the toe and pelvis, rotating the foot clockwise and bending the tibia bone, inducing the greatest tibial stresses in the anterior (front 0°) distal (near ankle) region. The optimal shape, therefore, was created to resist this mainly bending load through a thickening in the distal portion and a thinning in the proximal (near the knee) end of the modeled bone (Figures 5.57b(a) and 5.58b(a)).

Posterior-45° and Superior-90°

To create the posteriorly directed force in the 45° configuration, the hip extensor gluteus maximus muscle force was greatest, pulling the leg backwards and indirectly affecting

the tibia through the contact with the femur and bending induced throughout the constrained leg bone system modeled. Of the forces directly affecting the tibia bone, the biceps femoris and the soleus muscles acted on the proximal region (near the knee) of the posterior side of the bone, the tibialis anterior muscle acted on the anterior side (Figure 5.57a(b)). While the biceps femoris muscle created the largest force magnitude, all of these muscle forces were significant, combining to create a local, posteriorly directed bending of the tibia bone just below the knee with regions of relatively large stresses on the proximal one-third of the bone, directly related to the forces of the attached muscles. This stress pattern lead to proximal growth and distal decay (Figure 5.58b(b)), similar to many loading conditions in the 0° configuration.

The superiorly directed load in the 90° configuration resulted in a similar loading patterns as the posterior-45° case, with slightly different stress distributions due to different patterns and intensities of muscle forces. Under these loading conditions, the biceps femoris muscles was dominant, and the gastrocnemius, rather than the soleus, acted as the main ankle extensor, countered by a smaller magnitude force by the tibialis anterior muscle. This lead to slightly more bending, though generally the same distribution of stresses, in the tibia bone and the same prediction of greater growth near the knee near the active muscles and less near the ankle far from the high load region (Figure 5.57a and b(b) and 5.58a and b(c)).

Posterior-90°

The muscles used to create the posteriorly directed resultant force in the 90° configuration were similar to that that created this force in the 45° configuration excluding the tibialis anterior muscle. As in the 45° configuration, the gluteus maximus

dominated the overall muscle function in the whole leg system. The biceps femoris and soleus muscles contributed to the majority of the loading directly on the tibia bone, with the biceps femoris generating a slightly greater force (Figure 5.57a (b)). This lead to a slight bending about the ankle and growth in both the proximal and the distal ends of the bone, with more growth more on posterior than on the anterior side. (Figure 5.58b(b)).

Superior-45°

The superiorly directed force in the 45° configuration resulted from a more complex system of muscle forces than the other load sets reviewed, with significant muscle activity both on the anterior and posterior sides of the bone, resulting in a sort of combination of all of the above discussed loading modes. While the biceps femoris muscle generated the greatest force magnitude to flex the knee and extend the hip, it was countered by nearly as great a magnitude of the rectus femoris muscle force opposing this action. Similarly, the gastrocnemius functioned to pull the heel towards the femur to extend the ankle, while the tibialis anterior muscle acted on the foot in the opposing rotation (Figure 5.57a (c)). This combined loading pattern lead to a somewhat sinusoidal bending of the tibia. With the proximal region pulled towards the femur and the distal region bent towards the toe, it contained features of the loading patterns and their resulting stress from all of the groups studied. Specifically significant stresses were developed near the ankle, in the distal region of the tibia, due to the knee flexor muscle forces similar to those found under the anterior and inferior load cases in both the 45° and 90° configurations, and smaller, but relatively significant, stresses from the activity of the knee flexor muscle seen in the posterior-45° case were developed in the proximal region of the bone near the knee. Because the magnitudes of the forces generated by the active

muscles were similar and because many of the muscles with opposing functions were active, their effects were more regionalized than the previously discussed cases that had one clear dominant muscle action that caused a single major effect over the whole bone. The combination of these muscle forces acting directly on the bones and the contact behavior at the joints transferring their effects from one region to the next, resulted in the complex state of stress, and hence, shape changes, due to this loading mode.

The comparison of the muscle force patterns, with emphasis on the dominant muscle force or actions in each load set, helped to understand the similarities that were identified in the stress distributions and optimal shapes between seemingly different loading conditions. How the distributions of these muscle forces and bone stresses were converted to the variations in bone shape for these configurations is next discussed. In many of the figures depicting trends in nodal values, plots for all the common conditions or locations discussed are arranged on the same page to allow for direct comparisons.
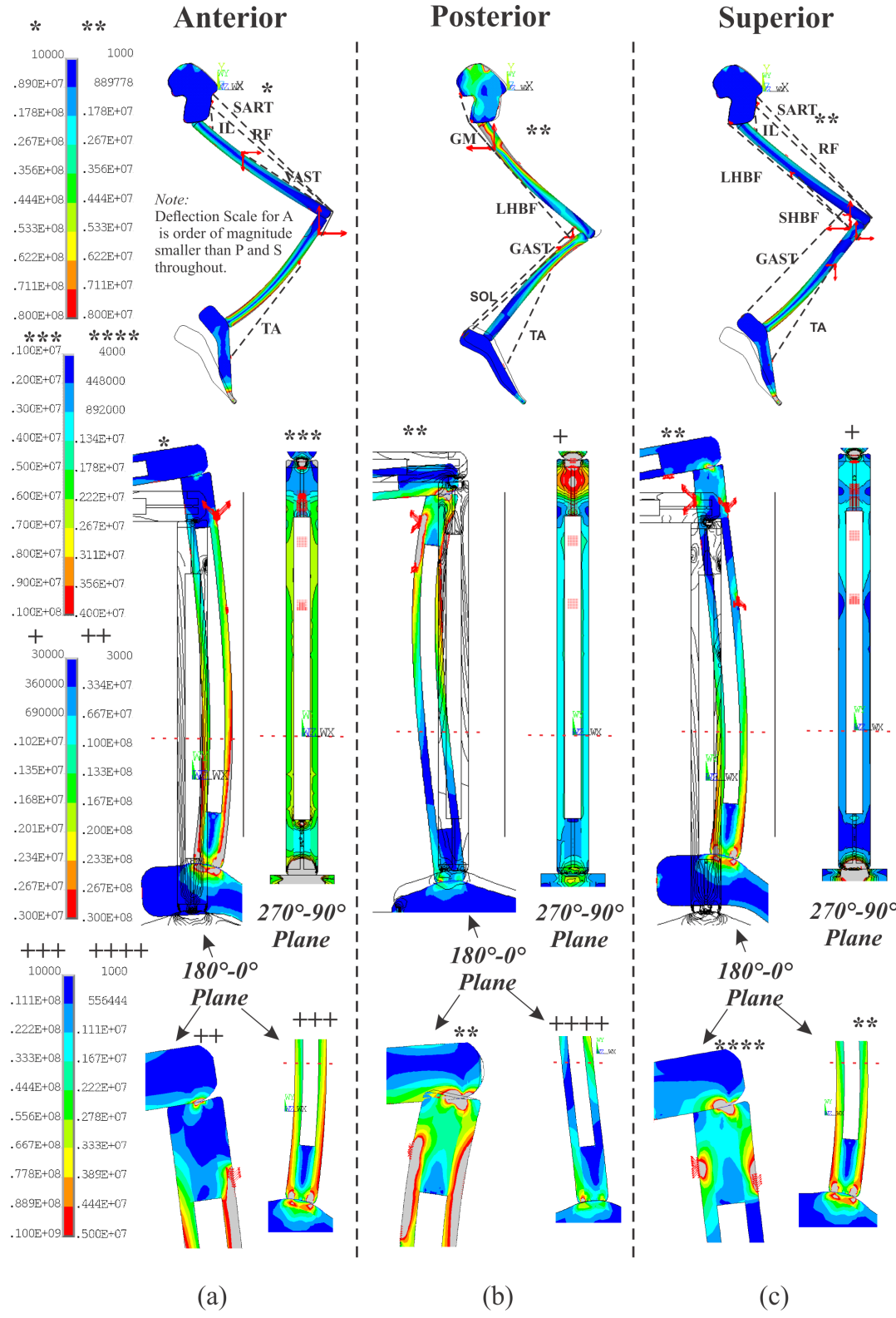
Figure 5.57a von Mises stress distributions on leg system with initial tibial bone geometry in the 45° configuration for the (a) anteriorly (b) posteriorly (c) superiorly directed resultant force.
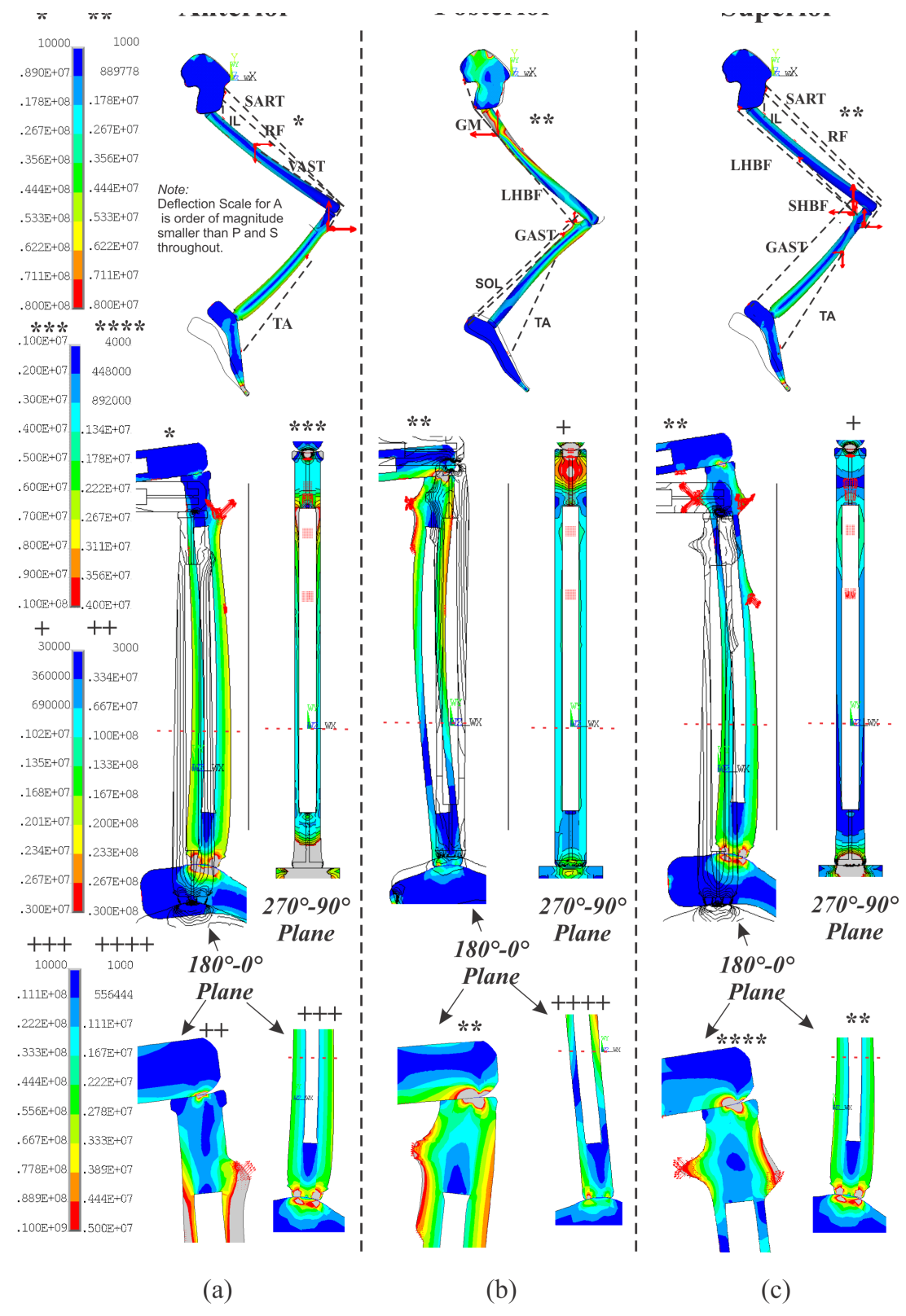
Figure 5.57b von Mises stress distributions on leg system with optimal tibial bone geometry in the 45° configuration for the (a) anteriorly (b) posteriorly (c) superiorly directed resultant force.
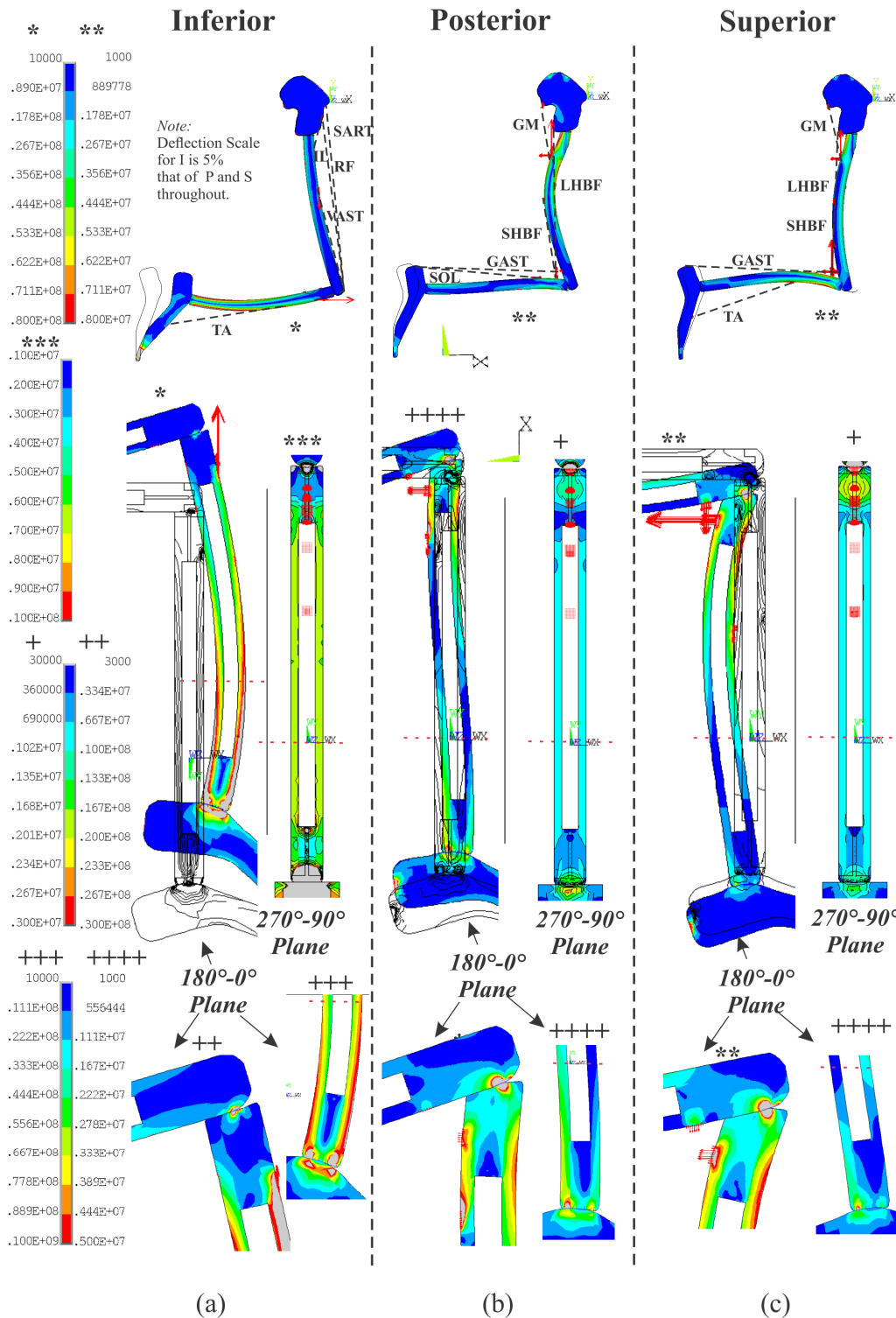
Figure 5.58a von Mises stress distributions on leg system with initial tibial bone geometry in the 90° configuration for the (a) inferiorly (b) posteriorly (c) superiorly directed resultant force.
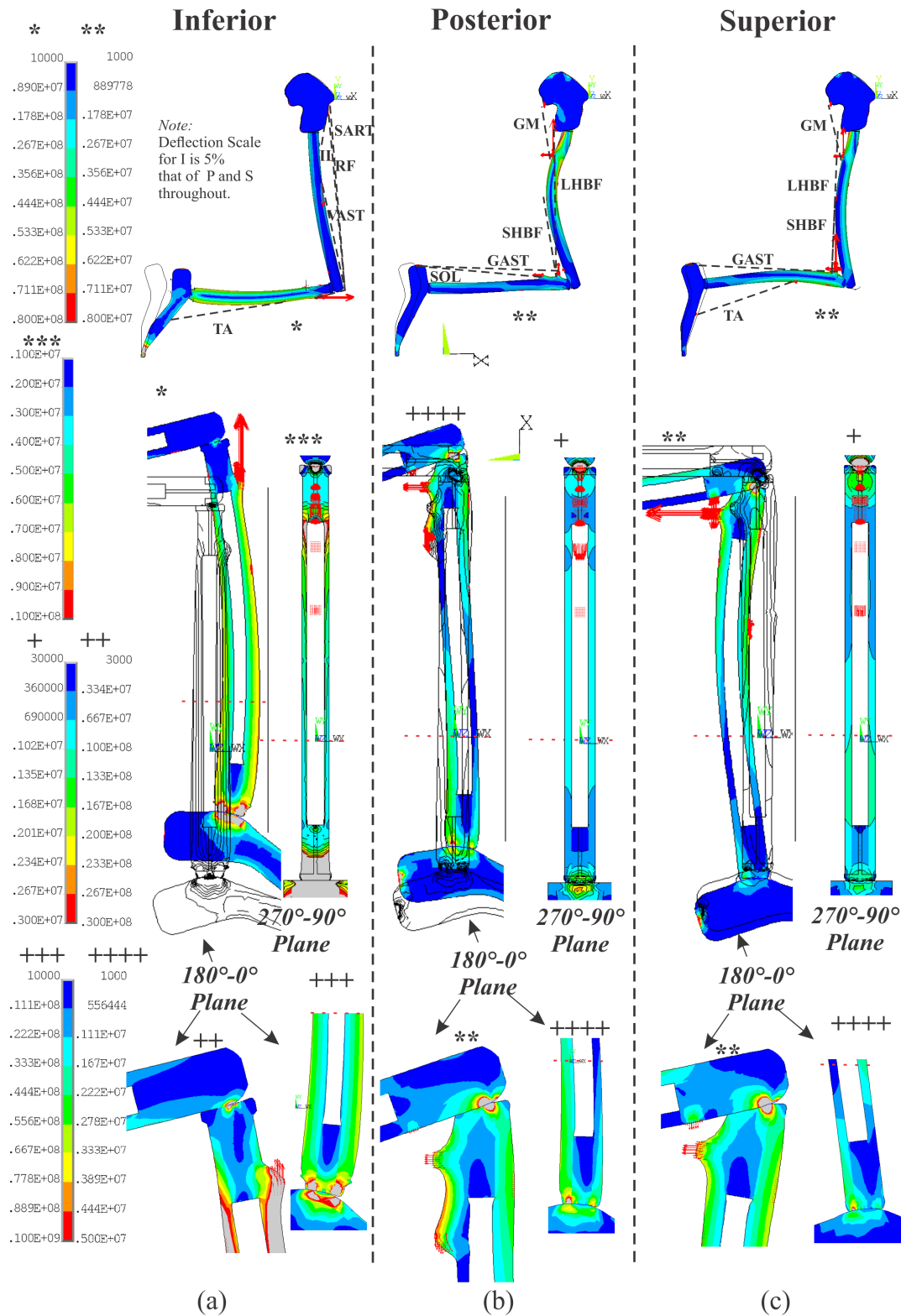
Figure 5.58b von Mises stress distributions on leg system with optimal tibial bone geometry in the 90° configuration for the (a) inferiorly (b) posteriorly (c) superiorly directed resultant force.

Trends in Nodal Strain Energy Density and Growth with Location and Iteration

Similar to the analysis performed for the 0° configuration, the study of the relationships between the changes in the state of stress and shape under loading conditions in these bent leg configurations can reveal information about the conditions studied and provide insight into the common system features that resulted in similar growth, and, therefore, strength, patterns. While many of the features described in the previous section for the 0° configuration, such as the basic interrelationships between the local and global stress state and variations, the effects of the abrupt geometric and material transitions, and the local effects of the large stresses induced by the directly applied muscles, are also observed for these bent leg conditions, some trends specific to these bent leg conditions have been revealed. Their understanding can lead to better control of strength distributions of bone through a better design of the imposed loading conditions.

Anterior-45°/Inferior-90°

As described in the section above comparing the muscle activity required to generate these loading conditions in these two limb configurations, under the mainly bending loading induced in the tibia by the dominant knee extensor muscles under these condition, the strain energy density was greatest in the distal end, near the ankle and decreased almost linearly towards the knee on both the anterior (0°) and posterior (180°) sides of the tibia bone (blue lines in Figure 5.59). The growth in the bone followed this relatively simple strain energy density distribution (Figure 5.59), with material accretion on the distal end and resorption on the proximal end, resulting in the final shape (Figure 5.57b(a)) that resembled a uniform stress beam. This near uniformity in the strain energy density distribution, resulting from the induced shape changes, is shown in the

representative plots of the nodal strain energy density distribution along the axial length of the "optimal" bone geometry (pink lines in Figure 5.59). As in the straight leg 0° configuration, locally large amounts of strain energy density and growth occur where the muscle forces act directly, and the propagation of these local effects is demonstrated in the plots at the 90° (medial) location where slight increases in growth and strain energy density result in the final geometry near the region of applied knee extensor muscle forces, despite being out of the loading plane and away from directly applied forces.

The changes of the nodal strain energy density and growth at the surface locations studied with optimization iteration (Figure 5.60) demonstrate their convergence toward uniformity. To understand this trend, the factors driving these changes were analyzed. Initially, both the nodal growth and strain energy density change rather rapidly following similar rapid changes in the standard deviation of the strain energy density (Figure 5.56a). The nodal locations with the biggest difference between the local strain energy density and the surface average value (numerator in the growth driver Equation 4.23) then result in the largest relative amount of growth to create greater changes in the locations that are further away from the reference (average) value. As the nodal strain energy density approaches a more common value, the changes in the average and standard deviation of the strain energy density begin to occur at the same rate and the changes in the growth per iteration begin to follow those of the nodal strain energy density, driving the nodal growth to common value (Figure 5.60). It is interesting to note that while the nodal strain energy density under the inferior-90° case are slightly larger than those induced by the anterior-45° case, so are the surface average and standard deviation values that complete the growth driver expression, leading to nearly equal

growth between the cases seen in Figures 5.59 and 5.60, verifying the model dependence on variations of the local stress state rather than absolute magnitudes.
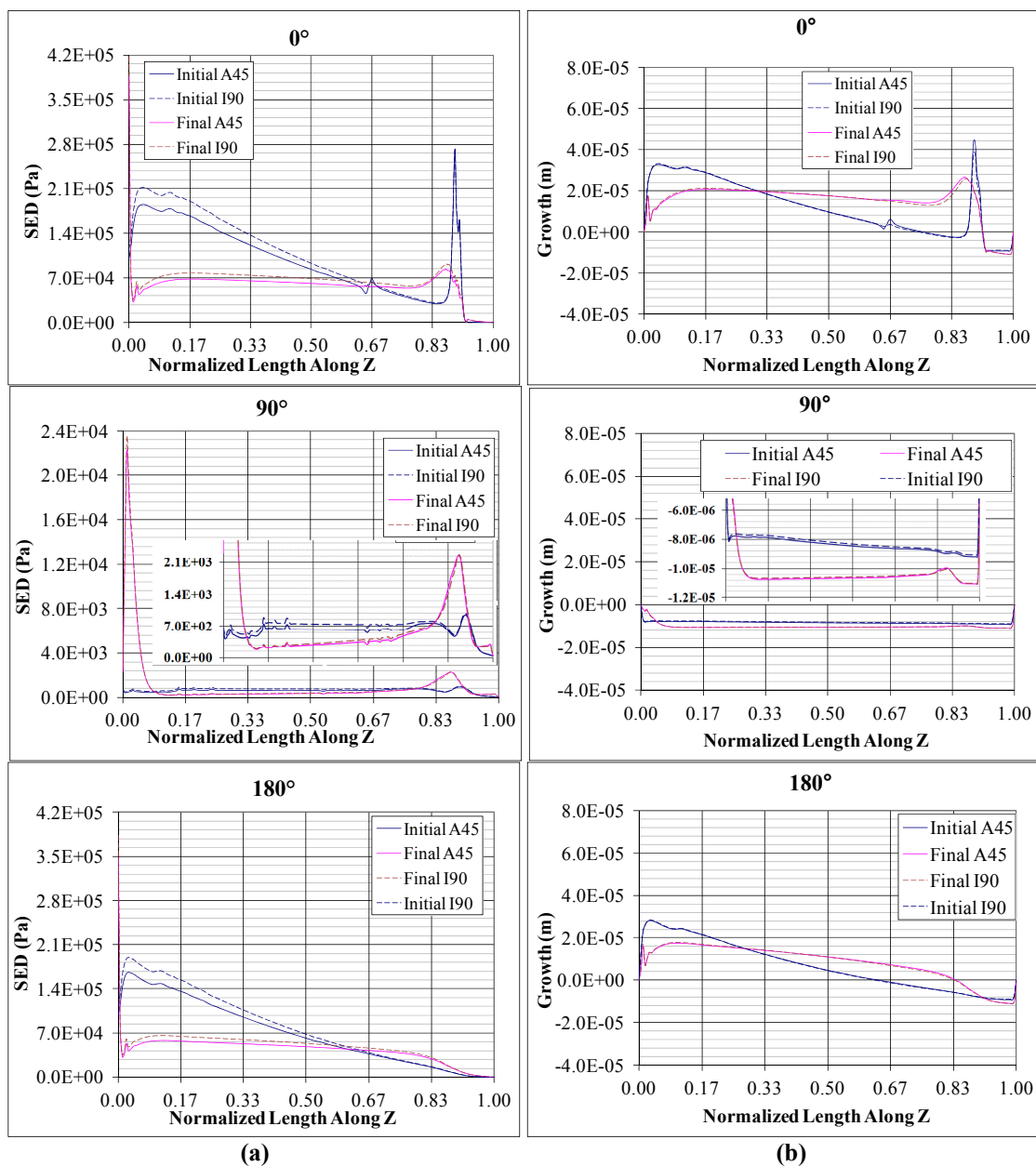
Figure 5.59 Outer surface variation of (a) nodal strain energy density and (b) growth with axial location Z at three locations along the surface: anterior side ($\Theta=0°$), medial side ($\Theta=90°$), and posterior side ($\Theta=180°$) due to shape optimization under the anteriorly directed resultant load in the 45° configuration (solid lines) and the inferiorly directed resultant load in the 90° configuration (dashed lines).
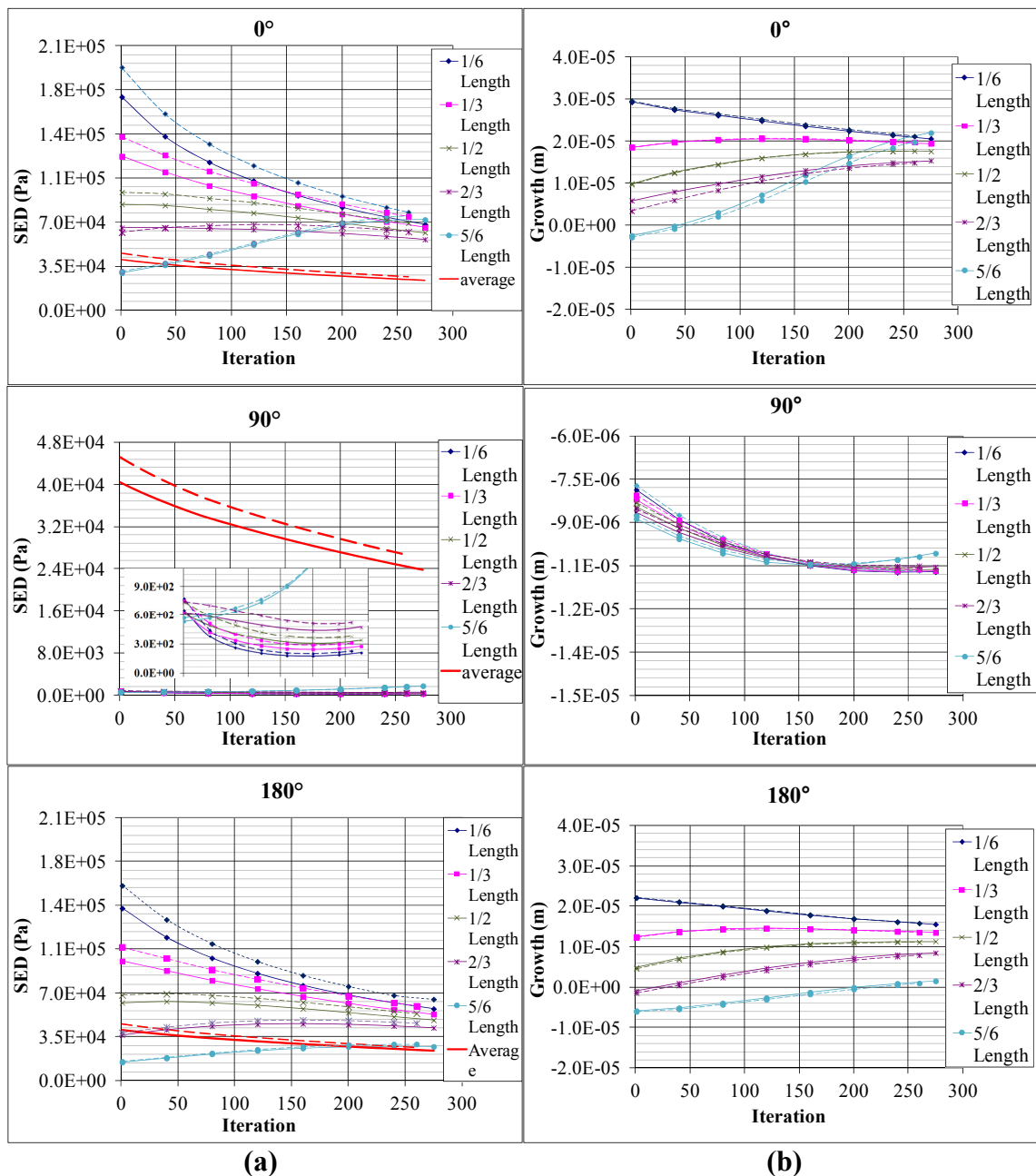
Figure 5.60 Outer surface variation of (a) nodal strain energy density and (b) growth with optimization iteration at discrete axial locations (% total tibial length) at three locations along the surface: anterior side (Θ=0°), medial side (Θ=90°), and posterior side (Θ=180°) due to shape optimization under the anteriorly directed resultant load in the 45° configuration (solid lines) and the inferiorly directed resultant load in the 90° configuration (dashed lines).

Other than the spikes in the strain energy density at the transition from the hollow to the cancellous region under this anterior or inferior loading case, which are the largest of all seen in this 90° configuration, the trends in the strain energy density and growth on the inner surface (Figure 5.61) follow those described for the outer surface (Figure 5.59). While the effect of directly applied loads is not as significant on the inner surface, the propagation of the high stresses induced by the muscle loads through the bone volume is noticeable, for example in the slight disturbance at the two-thirds location along 0° line due to the activity of the tibialis anterior muscle in the anterior-45° case.

In the trends of changes in the nodal growth and strain energy density with iteration in Figure 5.62, the more rapid decrease in the strain energy density on the inner surface compared to that on the outer surface (Figure 5.61), resulting in the more rapid convergence for the inner surface in these cases (Figures 5.37 and 5.39). Note that Figure 5.62 depicts the change in strain energy density over the course of the nearly 300 optimization iterations, but growth only in the first 80 before convergence. Because the surface average strain energy density on the inner surface was always greater than its standard deviation but the standard deviation changed (decreased) at a greater rate than the average did, the nodal growth on the inner surface was driven by the difference from surface averaged strain energy density for nodes with stress states far from that of the average average and by the changes to the standard deviation for nodes with stress states more similar to that of the average.

Figure 5.61 Inner surface variation of (a) nodal strain energy density and (b) growth with axial location Z at three locations along the surface: anterior side (Θ=0°), medial side (Θ=90°), and posterior side (Θ=180°) due to shape optimization under the anteriorly directed resultant load in the 45° configuration (solid lines) and the inferiorly directed resultant load in the 90° configuration (dashed lines).

Figure 5.62 Inner surface variation of (a) nodal strain energy density and (b) growth with optimization iteration at discrete axial locations (% total tibial length) at three locations along the inner surface: anterior side (Θ=0°), medial side (Θ=90°), and posterior side (Θ=180°) due to shape optimization under the anteriorly directed resultant load in the 45° configuration (solid lines) and the inferiorly directed resultant load in the 90° configuration (dashed lines).

Posterior-45°/Superior 90°

This next pair of loads that was shown to have similar stress distributions and loading patterns is the posterior-45° and the superior-90° loadcases. Unlike the anterior/inferior group, the magnitudes of these stresses and resulting strain energy densities for these two cases were very different, with the posterior-45° case values nearly double those of the superior-90° case. Therefore, their presentation on the same graph involves two different scales with the posterior-45° case on the left hand scale and the superior-90° case on the right hand scale. Once scaled, the similar trends in strain energy density and growth were revealed. For ease of comparison, plots of common measures for different locations or conditions are arranged on the same page in this work.

In addition to the magnitudes discussed there were some differences in the muscles active in these two conditions (Table 5.6). The biggest difference between the two cases was in the activity of the tibialis anterior and the soleus muscles. The tibialis anterior (ankle flexor) muscle was only active in the superior-90° case as seen in the large spike at the two-thirds location at the $\Theta=0°$ location in Figure 5.63a(top). This local disturbance, however, did not significantly alter the trend in strain energy density along the axial line at the $\Theta=0°$ from following the same curve as that of the posterior-45° case which had no anteriorly attached muscles (compare dashed to solid lines in this figure). Similar trends are seen due to the soleus (ankle extensor) muscle, which was only active in the posterior-45° case as can be seen as a local disturbance in the $\Theta=180°$ location near the five-sixths location (Figure 5.63a(bottom)). The local differences between the two cases related to the activity of two muscle forces are also revealed in the plots of change in growth and strain energy density with iteration at the tracked nodes near their region of

application: Θ=0°, two-thirds length and and Θ=180°, five-sixths locations (Figure 5.64). While these local differences are significant on the proximal end of the tibia bone where the muscles act, they have little effect far from the region of load application, such as near the distal end of the bone, the targeted strengthening region.

Trends in growth with iteration on the outer surface showed decay in the distal region and varying amounts of growth in the proximal region of the bone for both of these conditions (Figure 5.64). Under these posterior-45° and superior-90° loading conditions the standard deviation of the strain energy density over the outer surface was greater than the average throughout the optimization but the decrease in this variation was greater than that for the average, causing change in the dominant global value during the optimization process and based on local nodal conditions. For example the change in nodal strain energy density at the 0°, five-sixths location (Figure 5.64a(top)) deceased at about the same rate as the standard deviation. Because the average value was relatively comparatively constant, the change in the numerator in the growth driver expression in Equation 4.23 essentially followed the change in the nodal strain energy density, which was the same as that of the denominator in the growth driver equation, resulting in a nearly constant amount of growth at this location with iteration.

The trends on the inner surface (Figures 5.65 and 5.66) generally followed those on the outer surface. As in some of cases in the 0° configuration, because the standard deviation was relatively smaller and was decreasing faster than the average surface strain energy density, larger amounts of growth ensued on the inner surface compared to the outer surface where the global conditions were more similar (Figure 5.56. The disturbances from the applied muscle forces on the outer surface that propagated to the

inner surface for the initial geometry and the large the strain energy density at the proximal end near the knee near the cancellous bone region was significantly reduced due to the inner surface shape adaptations.
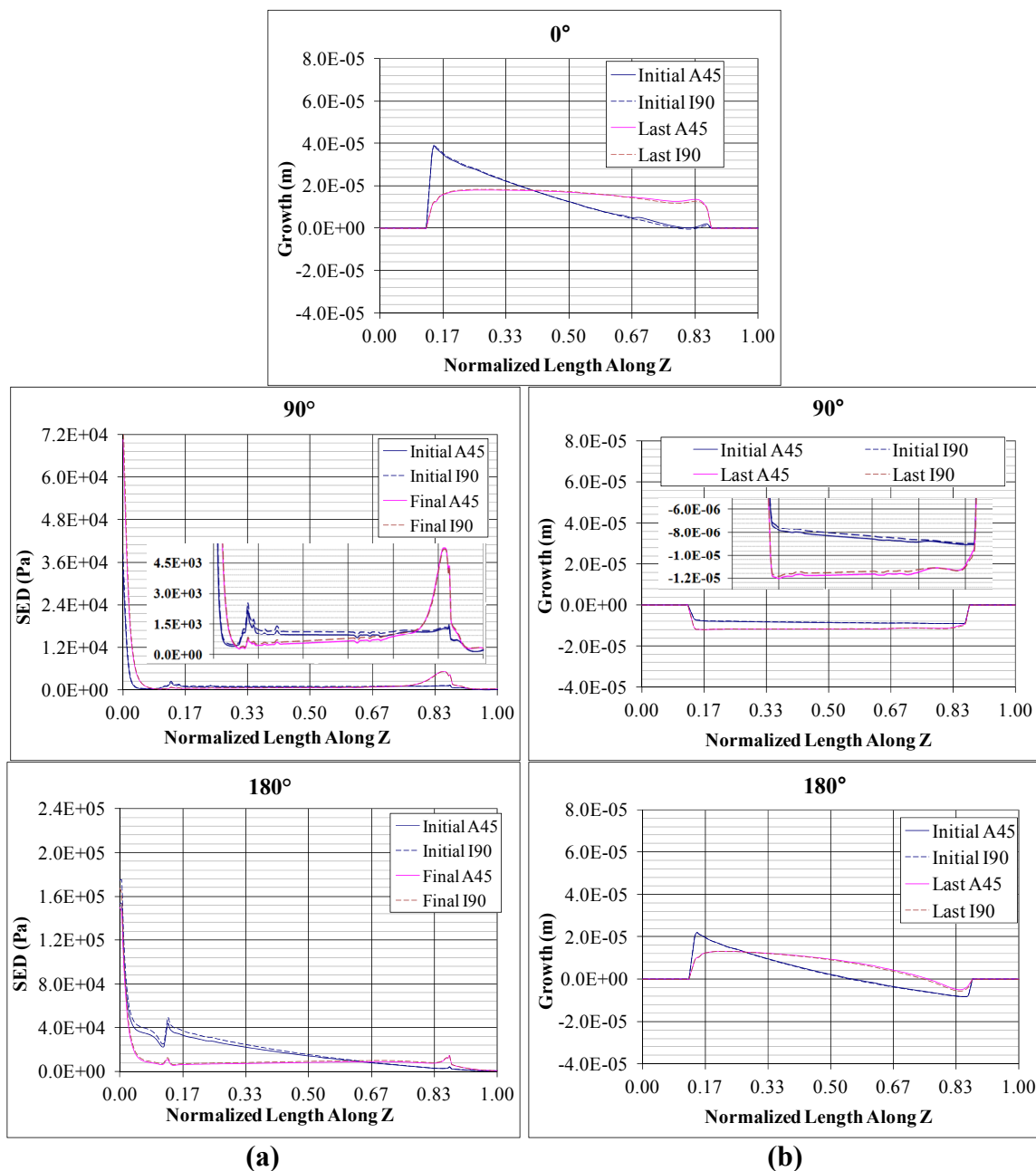

Figure 5.63 Outer surface variation of (a) nodal strain energy density and (b) growth with axial location Z at three locations along the surface: anterior side (Θ=0°), medial side (Θ=90°), and posterior side (Θ=180°) due to shape optimization under the posteriorly directed resultant load in the 45° configuration (solid lines) and the superiorly directed resultant load in the 90° configuration (dashed lines).
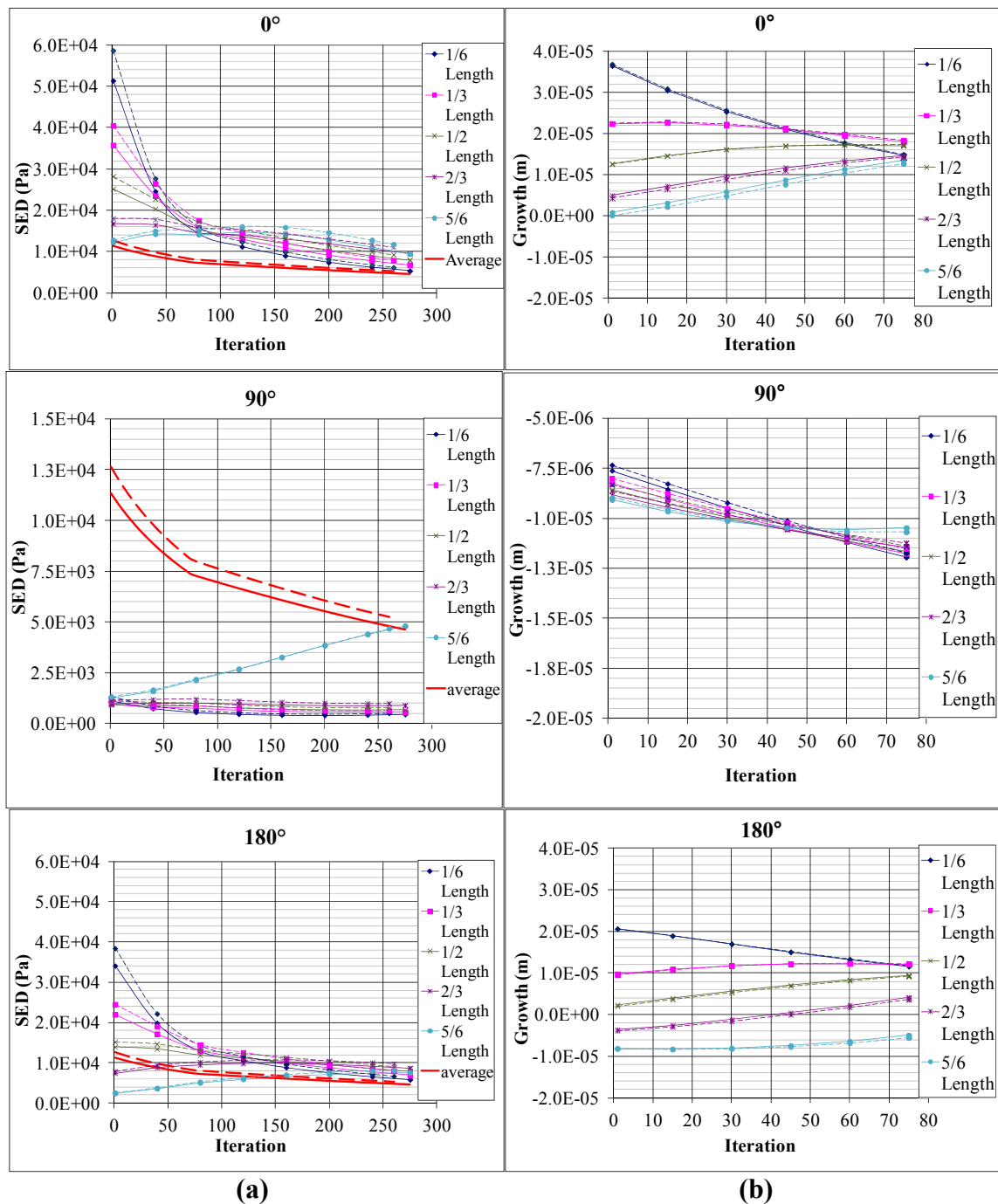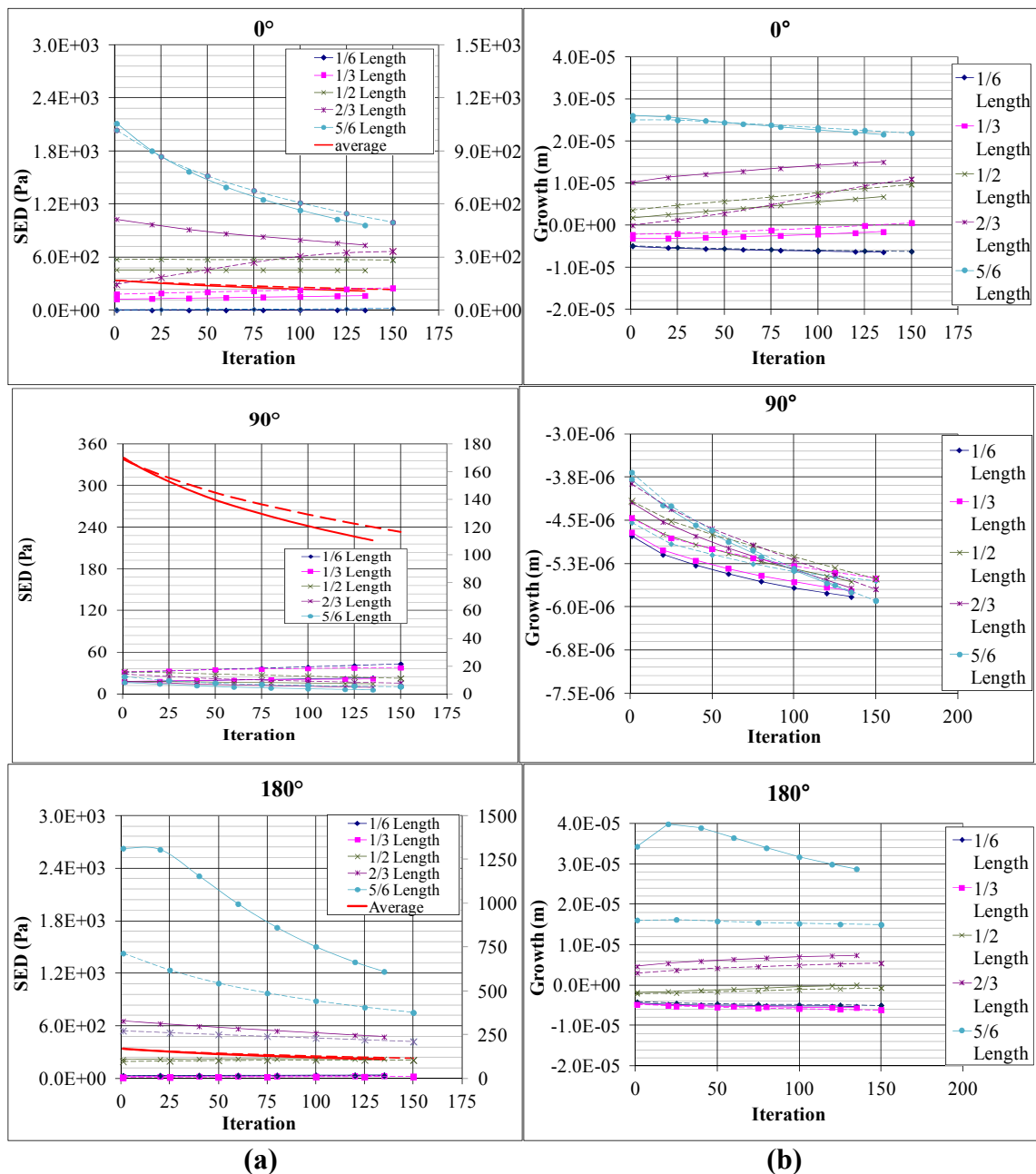
Figure 5.64 Outer surface variation of (a) nodal strain energy density and (b) growth with optimization iteration at discrete axial locations (% total tibial length) at three locations along the surface: anterior side (Θ=0°), medial side (Θ=90°), and posterior side (Θ=180°) due to shape optimization under the posteriorly directed resultant load in the 45° configuration (solid lines) and the inferiorly directed resultant load in the 90° configuration (dashed lines).

Figure 5.65 Inner surface variation in (a) nodal strain energy density and (b) growth with axial location Z at three locations along the surface: anterior side (Θ=0°), medial side (Θ=90°), and posterior side (Θ=180°) due to shape optimization under the posteriorly directed resultant load in the 45° configuration (solid lines) and the superiorly directed resultant load in the 90° configuration (dashed lines).

(a)

(b)

Figure 5.66 Inner surface variation of (a) nodal strain energy density and (b) growth with optimization iteration at discrete axial locations (% total tibial length) at three locations along the surface: anterior side (Θ=0°), medial side (Θ=90°), and posterior side (Θ=180°) due to shape optimization under the posteriorly directed resultant load in the 45° configuration (solid lines) and the superiorly directed resultant load in the 90° configuration (dashed lines).

Posterior-90°

The posteriorly directed load under the 90° configuration had loading conditions and resulting stress distributions that were unique among the cases studied. The strength adaptations in the tibia were driven by the effects of the posteriorly attached muscles. Specifically, the nearly equivalent effects of the long head biceps femoris pulling the proximal posterior region of the bone towards the pelvis and the soleus pulling the same region to the heel (Figure 5.67a(bottom) and Figure 5.58a(b)) caused a locally high stress region near their locations of attachment and between these regions as the material is stretched in the two opposing regions by these muscles. Additionally, more disperse effects occur as their forces displaced the system bones against the constraints on the top of the pelvis and at the toe resulting in a sinusoidal-like deflection curve along the length of the bone. The high stress region was found on the anterior side of the bone near the transition from the hollow mid-shaft to the cancellous filled volume (Figure 5.58a (b) red arrow) is a direct result of this deflection as are the large strain energy densities on either end on anterior side of the bone and a near zero stress region between the one-third and one-half locations as the bone behavior switches from flexing anteriorly to flexing posteriorly (Figures 5.58a and b). The shape changes follow with slight growth on the distal end near the ankle, significant growth near the knee, and a region of decay from the one-sixth to the two-thirds locations (Figure 5.67a and b).

On the posterior (180°) side of the tibia bone, the bending behavior caused by the soleus was dominant over the majority of the length and the local effects of the two applied muscle forces controlled the adaptations in the proximal region. Because these were the only forces acting directly on the adapting bone and they were nearly equal in

value, the growth in both of these regions was very high, meeting the maximum growth per iteration criterion throughout the optimization process (Figure 5.67b(bottom)).

As in the other conditions studied, the 90° (medial) location incorporated the effects of the applied loads on the posterior side with disturbances to match the location and trend in peak strain energy density at the axial level of muscle force application. The effect of the decay in the mid-region was also apparent in this 90° location as the strain energy density that was initially uniform becomes parabolic over the length of the bone as a result of this decay at the Θ=0° location (Figure 5.67).

The trends in growth per iteration showed a nearly constant state of stress and decay in the region from one-sixth to two thirds, with the smallest stress and largest decay near the one-third location under this posterior-90 configuration (Figure 5.68). This was likely the transition point in the deflection curve from bending "towards the toe" in the distal region of the bone, driven by the soleus, to bending the "towards the heel" in the proximal region of the bone, driven by the biceps femoris muscle. The significantly different trend in strain energy density and growth at the five-sixths level can be related to the activity of the soleus muscle that attaches near this location. On the plot of growth with axial location (Figure 5.67), this five-sixths level is at the end of the region of muscle force application and is one of large changes in growth and strain energy density over short distances. Therefore, the tracking of changes at this single point (Figure 5.68) may not be representative of the true trends in this area of large gradients in the strain energy density except that the relatively large strain energy density in this region resulted in a large amount of growth. The slight changes in growth were related to the relatively small changes in the nodal and global strain energy density in the nodal locations studied.
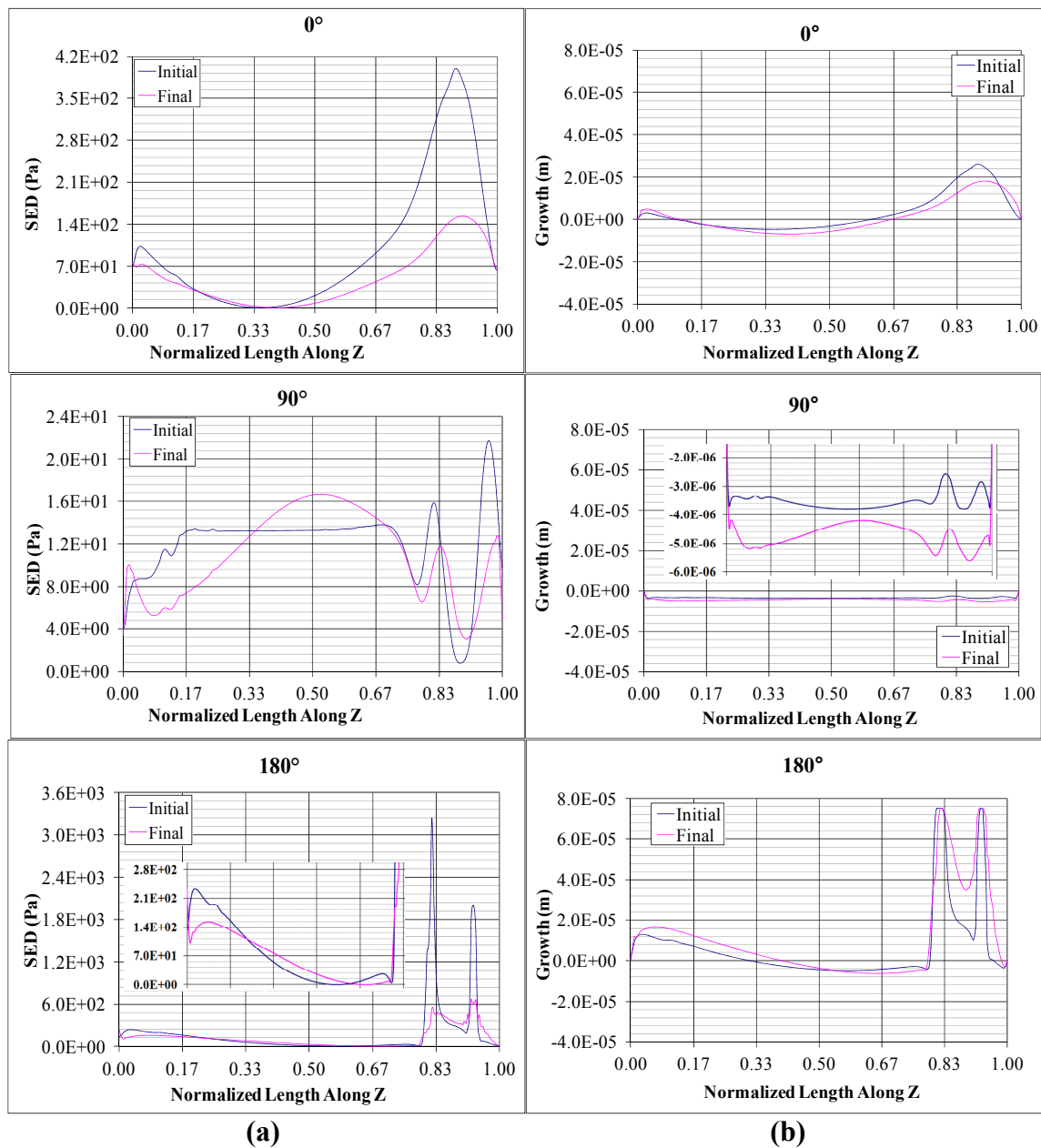
Figure 5.67 Posterior load, 90° configuration, outer surface: Variation of (a) nodal strain energy density and (b) growth with axial location (% total tibial length) at three locations along the surface: anterior side (Θ=0°), medial side (Θ=90°), and posterior side (Θ=180°) due to shape optimization.
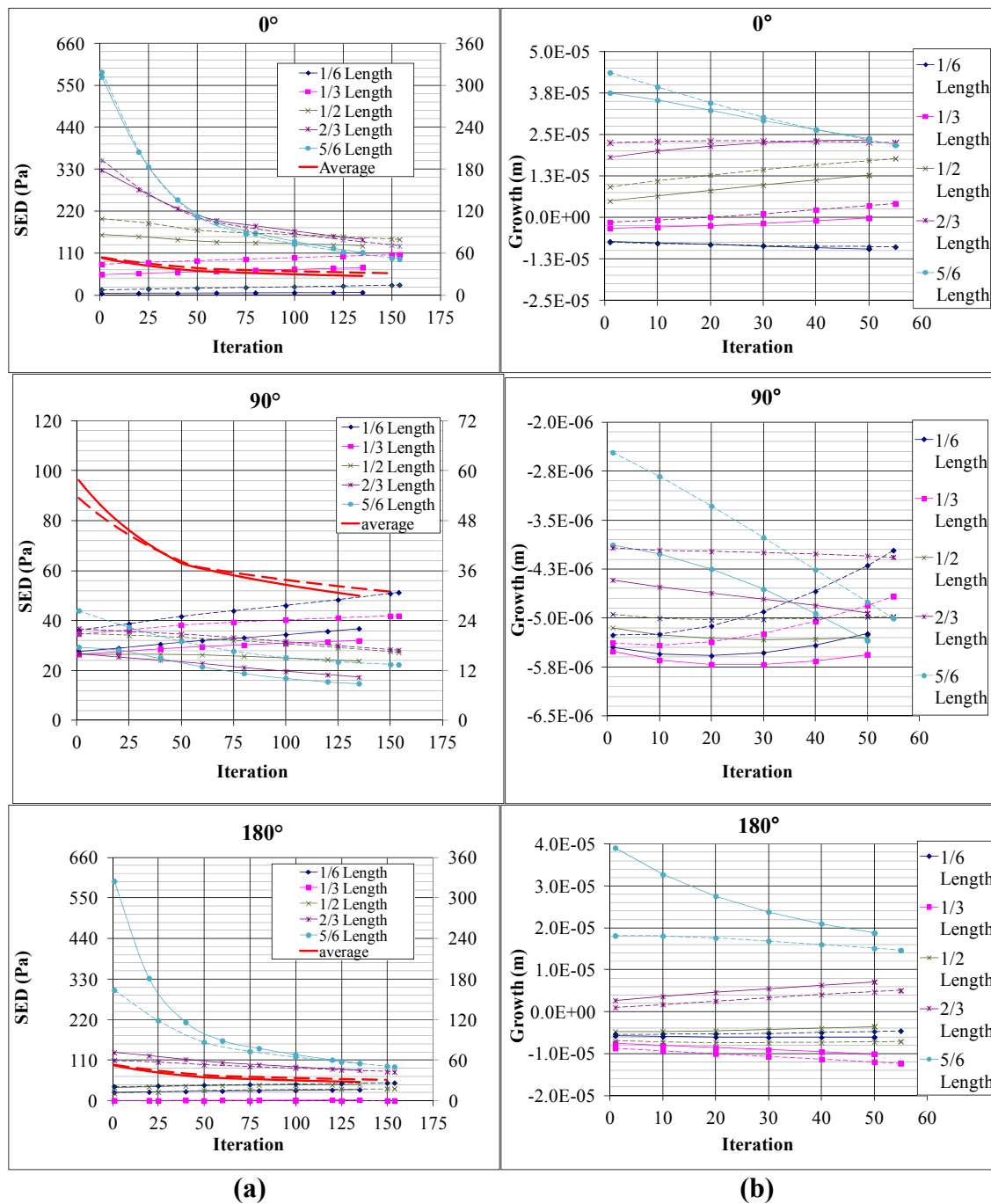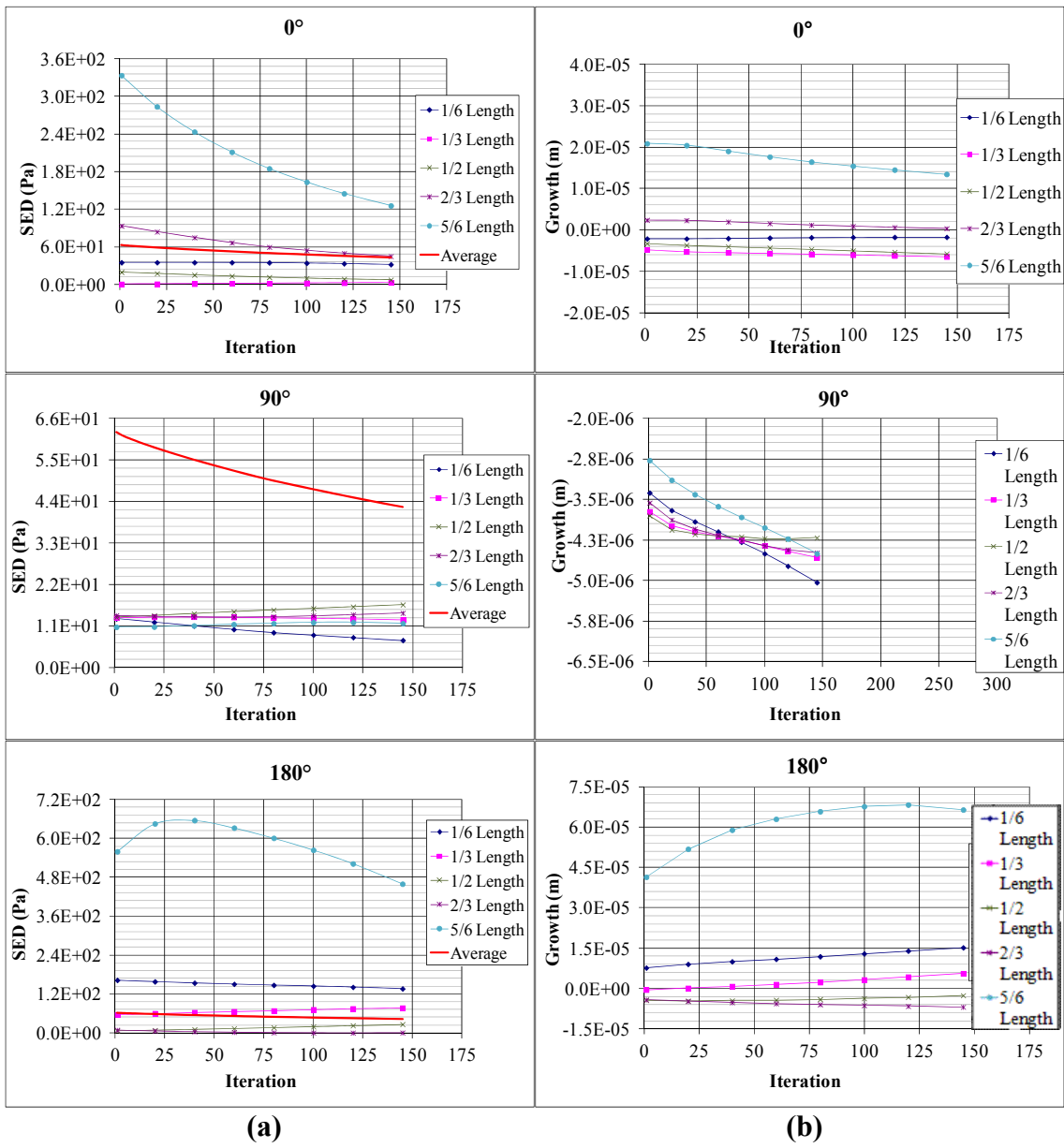
Figure 5.68 Posterior load case, 90° configuration, outer surface: Variation of (a) nodal strain energy density and (b) growth with optimization iteration at discrete axial locations (% total tibial length) at three locations along the surface: anterior side (Θ=0°), medial side (Θ=90°), and posterior side (Θ=180°) due to shape optimization.

The trends over the inner surface due to this posterior-90° condition generally followed the behavior in this region of the outer surface with the exception of the noted spikes from the transition from hollow to the cancellous region. With changes in shape only from approximately the one-sixth to the five-sixths locations, the inner surface escaped the main effects of the applied muscles as they occurred more proximal to this region. Nonetheless, the effects of the muscle forces close to this region (soleus on the 180° location) were clearly seen and significantly reduced during the optimization process so that, unlike on the outer surface, the proximal, posterior region went from extremely large amount of growth per iteration to slight decay per iteration region before the convergence criteria was met and all shape changes stopped.

On the inner surface (Figures 5.69 and 5.70), the value of the average strain energy density was greater than that of its standard deviation. Although both of these measures had similar initial magnitudes, the standard deviation decreased at a faster rate with iteration (Figure 5.56h). As convergence was approached, the variation over the surface was, therefore, smaller. Although the difference between the nodal and average strain energy density was also reduced as both measures decreases as convergence was approached, the very small standard deviation dominated the growth driver expression caused the larger amount of growth on the inner surface(Figure 5.69b) compared to outer surface (Figure 5.67b). This is similar to the behavior demonstrated under some loading conditions in both of the other limb configurations, especially that of the straight leg.

Figure 5.69 Posterior load case, 90° configuration, inner surface: Variation of (a) nodal strain energy density and (b) growth with axial location Z at three locations along the surface: anterior side (Θ=0°), medial side (Θ=90°), and posterior side (Θ=180°) due to shape optimization.

Figure 5.70 Posterior load case, 90° configuration, inner surface: Variation of (a) nodal strain energy density and (b) growth with optimization iteration at discrete axial locations (% total tibial length) at three locations along the surface: anterior side (Θ=0°), medial side (Θ=90°), and posterior side (Θ=180°) due to shape optimization.

Superior-45°

As described above, the superiorly directed force acting on the leg in the 45° configuration resulted from a large number of active muscles with many different functions and areas of attachment. Additionally, with their relatively small and more comparable magnitudes all had a significant effect on the behavior of the tibia bone in this load case and the resulting shape alterations. As described in Section 5.2, to create the superiorly directed force in the 45° configuration is to fold the leg inward, flexing the hip, knee, and ankle joints, using a wide range of active muscles, many of which act on or near the tibia, creating a quite complex state of stress in this bone being optimized.

Along the anterior surface, the rectus femoris created a relatively large force near the knee, inducing a bending moment on the bone tibia bone from this load application point at the knee toward the foot, which was constrained at the toe. This caused the large stresses, and, therefore, growth near the ankle joint at the distal end of the bone (Figure 5.57a (c)) and an overall deflection pattern similar to that of the anterior and inferior cases (Figure 5.57a(a)).

On the posterior side, however, the long head biceps femoris, acting at nearly the same elevation of the rectus femoris (both within the cancellous region) generated the greatest force magnitude, pulling in a direction normal to the bone surface and causing a deflection in the proximal region of the bone near the knee joint that was similar to that which was seen in the posterior-90° case (Figure 5.58a(b)). Unlike the posterior-90° case, however, in the superior-45° case, the tibialis anterior muscle also produced a relatively significant force pulling the bone towards the toe, approximately at a 45° angle from its surface. The component of this force acting normal to the bone surface, in

combination with the bending load, countered the deflection caused by the opposing pull of the biceps femoris muscles in this slightly more distal location and caused a region of very low stress at an axial location between these two forces, at the start of the hollow (and more flexible) region of the bone.

This combination of the generally local behavior of muscle forces acting at various locations over the surface in the "sinusoidal" deflection described above and seen on the plots of strain energy density and growth with axial location (Figures 5.71 and 5.72). On the anterior and posterior surfaces, the higher strain energy density near the ankle was reduced proceeding towards the knee, resulting in relatively large growth near the ankle and decay as this proximal muscle force region was approached. Large local spikes in strain energy density and growth occurred near the locations of attachment of the biceps and rectus femoris and tibialis anterior muscle forces, and the region of very low stress between the tibialis anterior and rectus femoris muscle forces resulted in decay (Figure 5.71). In the final shape (Figure 5.57b (c)), the location of this thinning cortical wall at the beginning of the hollow region further would likely weaken an area that is already a subject to larges stresses and strains and potential fracture as it was in a hollow region right near a solid, cancellous filled one, whose cortical shell grew additionally thicker as a result of the local influences of the biceps and rectus femoris muscle forces acting this region.

At the 90° location, the initially nearly uniform strain energy density away from the boundary conditions converged in a similar manner as the anterior/inferior load cases previously discussed, with decay occurring over the length of the bone at this location. The patterns in the stain energy density and growth in the proximal region at this medial

location was affected by the muscle loads acting on the anterior and posterior sides of this region near the knee. Additionally, a region of significantly less decay occurred at this medial location at the same axial location as the extreme thinning on the anterior surface, resulting from an increase in stress in this location.

An examination of the trends in strain energy density and growth at points along these curves with iteration reveals the consolidation of the strain energy densities and growth in the distal two-thirds of the bone and the nearly constant decay at the five-sixths locations. The shape optimization process significantly reduced the stresses at the locations of muscle force application, and drove the distal one-third of the bone to near uniformity, with the generally increasing amounts of growth just below the muscle force application region and decreasing amounts of growth more distally.

Trends on the inner surface followed those on the outer surface without the extremes from the direct muscle force application. Although, as in the other cases, with magnitude lost from propagation through the cortical shell, the effects of these muscle forces were still prevalent. The nearly parallel changes to the nodal strain energy density, surface averaged strain energy density, and standard deviation of strain energy density over the surface with iteration (Figure 5.56f, Figure 5.74) caused a constant amount of growth over much of the inner surface with optimization iteration. However, if the change in the nodal strain energy density was large enough, the nodal growth could generally follow that of the strain energy density over most of the optimization (Figure 5.74) as, based on the growth driver expression in Equation (4.23), the effect of the standard deviation was greatest only in the early iterations when its change per iteration was most significant.
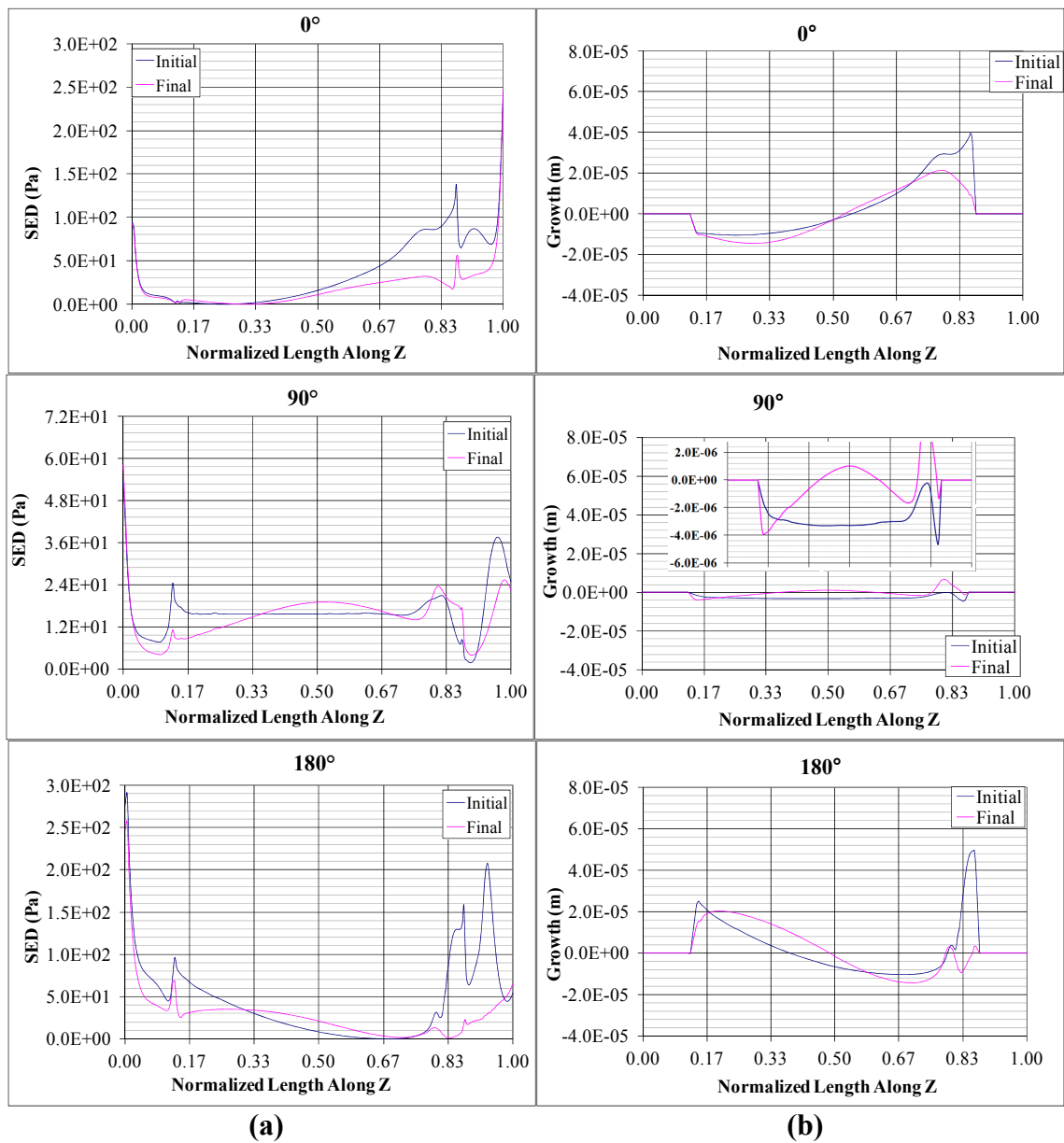
Figure 5.71 Superior load case, 45° configuration, outer surface: Variation of (a) nodal strain energy density and (b) growth with axial location Z at three locations along the surface: anterior side (Θ=0°), medial side (Θ=90°), and posterior side (Θ=180°) due to shape optimization.
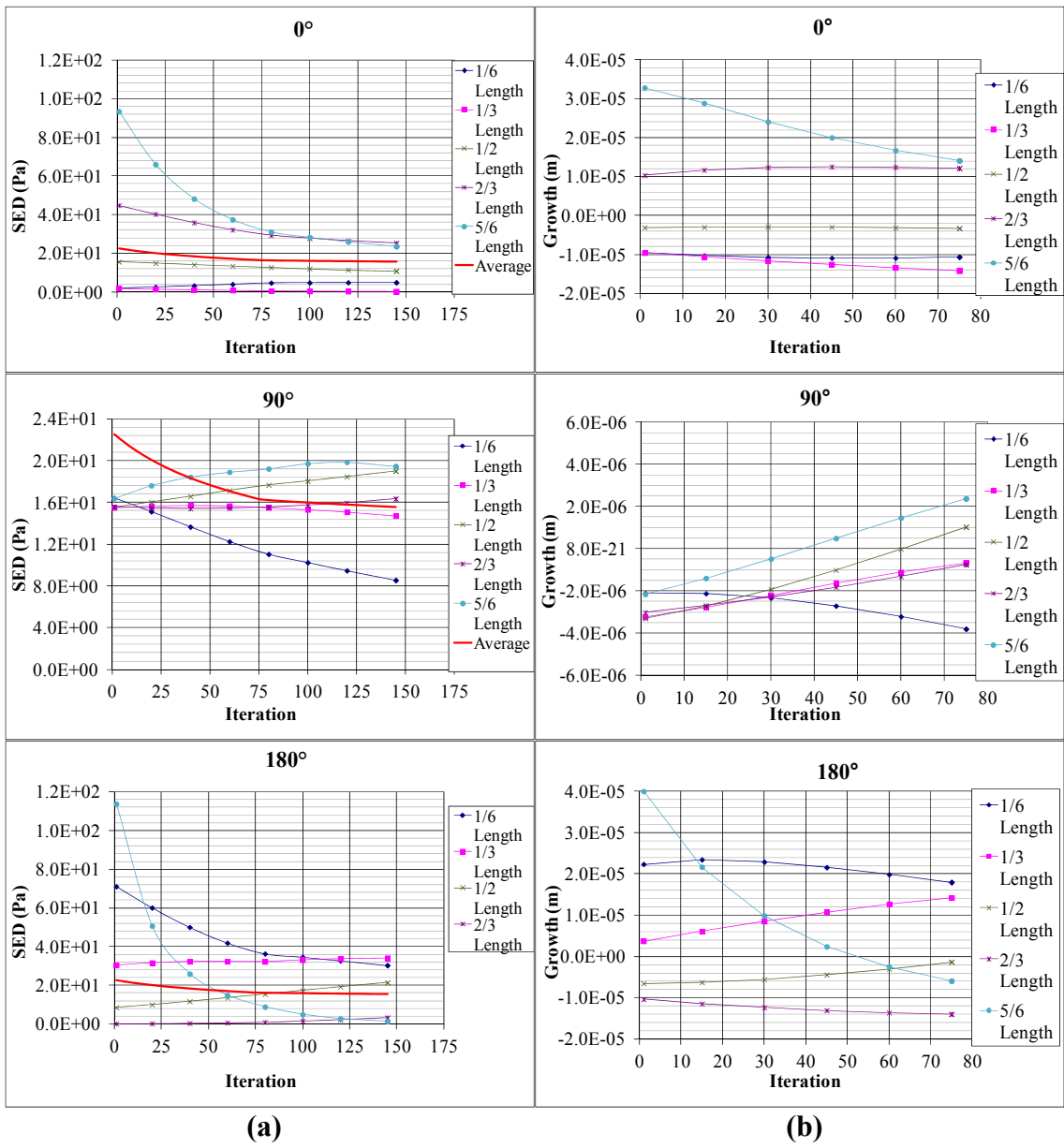
Figure 5.72 Superior load case, 90° configuration, outer surface: Variation of (a) nodal strain energy density and (b) growth with optimization iteration at discrete axial locations (% total tibial length) at three locations along the surface: anterior side (Θ=0°), medial side (Θ=90°), and posterior side (Θ=180°) due to shape optimization.

Figure 5.73 Superior load case, 45° configuration, inner surface: Variation of (a) nodal strain energy density and (b) growth with axial location Z at three locations along the surface: anterior side (Θ=0°), medial side (Θ=90°), and posterior side (Θ=180°) due to shape optimization.

Figure 5.74 Superior load case, 45° configuration, inner surface: Variation of (a) nodal strain energy density and (b) growth with optimization iteration at discrete axial locations (% total tibial length) at three locations along the surface: anterior side (Θ=0°), medial side (Θ=90°), and posterior side (Θ=180°) due to shape optimization.

5.5   Overall Performance

In this chapter, the implementation of the model developed through the work described in the previous chapters was discussed. The application of the developed model to solve a specific design problem was beneficial in two ways. First, a quantitative comparison of the effectiveness of varied mechanical influences (derived from sets of active muscle forces and relative orientations of the bone system component) at improving the strength in a targeted fracture prone region of a bone in the system studied can aid in the development of exercise regimens for people that may be especially susceptible to fracture of this targeted region. Second, the use of the developed model to study a wide range of conditions can not only verify that the model successfully analyzes the type of system for which it was designed, but can lead to a better understanding of its function in predicting the "optimal" bone shape and of its modeling and simulation capabilities.

5.5.1 Stress Fracture Resistance

In this second phase of work, the developed model was used to analyze exercise-based means for reducing the risk of stress fractures in the distal tibia that may occur under a jogging-based load. Specifically, the strength adaptations in this fracture-prone region of the tibia bone under various loading conditions (Table 5.1) and with the leg positioned in different configurations (Figure 5.1) were found using the developed coupled muscle force optimization/bone shape strength adaptation model.   The conditions studied involved static isometric loads created in the leg system modeled by generating a resultant force at the toe against a fixed surface in various directions at a given consistent magnitude. Both the repeated generation of a single load direction and the sequential generation of loads in a series of directions were evaluated.

The optimized bone shape designs were then subjected to the "critical design loading" conditions within the full leg model positioned appropriately for the mid-stance phase of jogging. The muscle forces to generate the typical joint moments at this point of moderate jogging were calculated and applied to bone system. The maximum von Mises stress under these jogging conditions at the targeted region, a distance one-third of the length of each "optimized" tibia "design" from the ankle, were compared. Based on the resulting change in the maximum von Mises stress at this location compared to that generated in the initially uniform circular hollow cylindrical geometry, the bone geometries that "strengthened" the bone significantly were selected and the loading conditions used to generate these "optimal" geometries were identified. Specifically, for each limb configuration studied (Figure 5.1), the best performing "optimal" tibial bone design generated by the optimization process due to one of the eleven loading cases considered (Table 5.1) was selected for comparison to the other "winners" to determine the "overall" best performing tibial bone geometry (design) and the conditions which induced these changes. Similarities and differences among all the "optimal tibial designs" generated by each of the thirty-three conditions studied as well as among the features of the conditions themselves were examined so that recommendations linking mechanical influences to beneficial shape adaptations could be made.

5.5.2 Conditions that Improved the Bone Strength in the Targeted Region

Of the three limb configurations studied, the distal tibia region was best strengthened when the knee was flexed. The most beneficial conditions occurred under the majority of the eleven loading conditions analyzed in the 45° configuration with the knee flexed at 90° and the hip flexed at 45°. Likewise, the same loads generated by the leg positioned

in the 0° straight leg configuration were generally least effective at strengthening the distal region of the tibia bone. There was more division between effective and ineffective load sets when examining the leg positioned at the 90° configuration with the knee flexed 90° and the hip in the neutral (straight leg) position.

The optimal bone geometries formed due to the anteriorly and inferiorly directed resultant forces generated by the leg in 45° and 90° configurations as well as the sequential generation of these two loads by the leg in these two configurations were nearly identical and all resulted in a 22% reduction in the maximum von Mises stress under the jogging conditions studied, over those induced by in the initially circular uniform cylindrical geometry. These represented the best overall performance of all of the conditions evaluated. A number of other loading conditions resulted in improved performance. Six other loading conditions generated by the leg in the 45° configuration caused improvement in the strength of the targeted distal region of the bone. Four improved the strength by 10% to 20% while the remaining two showed only a 3% reduction in the maximum von Mises stress under the comparison jogging conditions. In the 90° configuration, four other loading direction sets resulted in geometry that slightly reduced (1% to 2%) the stresses in the tibia bone under the potentially stress-fracture inducing mid-stance jogging conditions. Only one loading condition in the 0° configuration generated an optimal geometry that successfully reduced the maximum von Mises stress at the selected comparison location: the posteriorly directed resultant force, with a decrease in maximum von Mises stress of 5% over the initial circular uniform cylinder.

5.5.3 Conditions that Weakened the Bone in the Targeted Region

Many varied loading conditions in the three leg configurations evaluated failed to decrease the von Mises stress at this targeted region under the critical design load chosen. Under the 0° straight leg configuration most of the cases resulted in decay in the comparison region as they functioned mainly to strengthen isolated regions near the muscle forces attachment areas in the proximal region of the bone. While the inferiorly directed load and the sequential combination of the inferiorly and posteriorly directed resultant forces only showed slight weakening (less than 5% increase in von Mises stress), the von Mises stress generated in the optimal bone geometry created under the remaining nine cases were 30% to 50% greater than the initial uniform circular cylinder. In fact, the geometry optimized under the superiorly directed resultant force, followed closely by the anteriorly directed resultant force, in this straight leg configuration performed the worst of the optimal shapes resulting from all of the loads in all the leg configurations studied under the comparison jogging conditions in this stress fracture prone region.

Under the 45° configuration, only two cases, the posteriorly directed resultant force and the sequential generation of the posteriorly and superiorly directed resultant forces failed to reduce the von Mises stress in the targeted region of the tibia bone. The bone shape optimized under the posteriorly directed force increased the maximum von Mises stress in this region by 20% while the combination case caused a 7% increase over that induced in the initially circular uniform cylinder under the same loading conditions.

Under the 90° configuration, these posteriorly and superiorly directed resultant forces again failed to produce geometries stronger in the targeted region than the initially

uniform hollow circular cylinder. The geometry optimized under the single posteriorly directed resultant force increased the stresses by 28% while that of the superiorly directed load increased the stress by 20% and their sequential combination by 15%. The remaining load sets in this 90° configuration were all combinations of one of the winning loading directions (anterior and inferior) and one of the losing loading directions (posterior and superior). Each of these mixed combinations resulted in a geometry that showed negligible (less than 2%) changes in the bone strength at the targeted region.

The resulting performance of these multiload cases followed the observations that the individual values and trends in the nodal von Mises stress, strain energy density, and growth on surfaces of geometries generated by the combination of the basic loading directions were tempered, somewhat averaged, versions of each of the individual load sets combined to create the sequential multiload condition. It was observed that, in these multiload cases, similar features remained while opposing features offset each other, resulting in the less extreme changes in the stresses under the comparison critical design loading condition for "optimal" geometries created by the multiload cases compared to those created by the single load cases.

5.5.4 Common Features of Effective Strengthening Conditions

A comparison of geometric features of the best and worst performing tibial bone geometries optimized under the thirty-three conditions studied did not reveal a single geometric measure that correlated directly with the results of the comparison case. However, there were some general trends noted. Typically, the best performing geometries had a thickened cortical wall on the anterior side of the tibial bone at the cross section targeted for strengthening, which generally resulted in a shift of the center of

gravity in this direction. The inverse was generally true for the worst performers. However, this was not an absolute rule. For example, the superiorly directed resultant force case in the 90° configuration resulted in a tibial design geometry that increased the stress under the jogging load by 20%. However, it had a substantial anterior shift in its center of gravity, as this shift occurred from significant decay on the posterior side of the bone rather than growth on the anterior side (Figure 5.20). Additionally, under the 0° configuration, both the inferiorly and posteriorly directed loads resulted in nearly the same changes in cross sectional area and moments of inertia. However, the posterior load resulted in a 5% decrease in maximum stress in the jogging conditions while the inferiorly directed load resulted in a 5% increase. This can be directly related to anterior thickening of the geometry under the posteriorly directed load and the posteriorly thickening of the inferiorly directed load (Figure 5.18). The region of beneficial thickening corresponded to the region of maximum stress under the critical design load mid-stance jogging comparison condition.

Further insight into the conditions that induced alterations to the bone shape resulting in beneficial changes to the targeted fracture prone region was gained when examining the response of the tibia bone to each of the thirty-three conditions studied. The anterior and inferior cases under the 45° and 90° configurations resulted in nearly pure bending in the tibia bone, with the main load applied near the knee joint and the constraint at the toe resisting the most deflection near the ankle. In these conditions, the anterior surface of the tibia bone is deflected anteriorly with the greatest deflection near the comparison location (as in Figure 5.57a(a)). In fact the final optimized geometry under these loading conditions closely resembles a uniform stress cantilever beam

(Figures 5.57b(a) and 5.58b(a)). This deflection pattern is very similar to that which occurred under the comparison jogging loading condition. In fact, this bending, said to be due to the very large muscle forces during midstance jogging, has been thought to be the condition that induces a distal tibia stress fracture in a sufficiently weak bone [233]. Based on the observations of the multiload cases, it is not surprising that the geometries optimized to resist the loading conditions similar to the one used to compare the strengthening effectiveness would perform better that those optimized under different or more mixed mode conditions.

The comparisons of the changes over the length of the tibia revealed the importance of examining the effects of the optimized shape on the stress state over the entire bone surface. Many of the cases that resulted in significantly increased bone strength in the distal targeted region also induced significant thinning and decreased strength in the proximal region of the bone. Therefore, mixed multiload loadsets that have similar, desirable performance in the targeted region but opposing strengthening abilities in regions that may be adversely affected by either alone may be more beneficial than singly targeted loading conditions.

5.5.5 Overall Model Performance

In the analysis of the thirty-three loadsets in this comparative study, the developed coupled muscle force-bone shape adaptation model was subjected to a large array of conditions. Muscle forces magnitudes were calculated ranging from 2N to 10e3N. In each case, the predicted muscle activity and individual muscle force intensities that worked together to properly generated the correct joint moments and resultant forces. The muscle forces were appropriately scaled to their abilities based on their sizes and the

active muscles predicted were a proper mix of synergistic and antagonistic forces when required. Additionally, they resulted in reasonable muscle stresses, within the functional ranges most reported for muscle tissue material.

Similarly, the shape adaptation model handled the conditions induced by these muscle forces over bone surfaces that had standard deviations in the resulting strain energy density ranging from 100Pa to 50e3Pa with no alterations to the functional features or parameters. This indicated that the model could handle not only a wide range of loading conditions but a large variation of local stress state under a single loading condition without having to make manual or even automated adjustments to the model scheme. Because the model predicted adaptations to an initially uniform circular cylindrical tibial bone geometry under the near full cantilever bending that resembled the uniform stress beam, the ability of the developed model to improve the uniformity of the stress state over the optimizing surface was validated.

The developed convergence criteria consistently stopped the model, and, together with the use of the common comparison case, allowed for the direct quantitative comparisons of the strengthening effectiveness of various conditions as presented in this chapter. Finally, the node smoothing routines appropriately prevented extreme mesh distortion during the shape optimization process, allowing the finite element solution methods to properly predict the stress states that drove the bone shape adaptation simulations. Through these comparison cases, the powerful capabilities of the developed modeling method were revealed.

CHAPTER 6

SUMMARY, CONCLUSIONS, AND FUTURE WORK

6.1   Summary and Conclusions

In this work, new modeling techniques were developed and implemented to investigate the effects of mechanical factors on bone strength.   These methods determine the forces acting on a bone within a multibone, multimuscle system, simulate the ensuing alterations to the bone shape, and predict the effects that these shape adaptations have on the ability of the bone to resist the loads imposed on it during typical activities that may induce fractures in weakened regions of the bone. This was accomplished through the coupling of computational optimization techniques with finite element methods. The intent of the work was to develop a tool with which to quantitatively analyze, compare, and develop techniques to counteract the losses of bone strength that occur with disuse or age by identifying weak regions in the bone structure and targeting them for strengthening. This tool can help improve the understanding of the relationships between variations in loading conditions and alterations in bone strength as many currently available models that simulate bone strength adaptation are limited in their universal application because of their extensive reliance upon parameters based on experimental or clinical observations.

6.1.1 Model Development

The long bones studied in this model were considered mechanical components of the complete mutisegment musculoskeletal system that operates within the whole body system to provide the system with movement and force resistance.   Therefore, the stresses within the bone volumes are a result of the complex mixture of both direct and

indirect forces. The direct forces acting on a bone are generated by the muscles that are attached to it. Indirect forces on a bone come from within the musculoskeletal system studied, imposed by the interactions between the bones of the system and by the muscle forces acting upon these other bones that result in a whole system response. Indirect forces can also come from external sources applied to the whole body system or from bone or muscle components not part of the particular system studied. Because these stress distributions drive the shape and strength adaptations being simulated in this work, the model used included the bony segments of the complete bone system that surrounded the targeted bone (the entire leg) as well as the major muscles acting on these system bones to produce the desired resultant forces or activities studied. Additionally, the effects of the externally applied forces to this subsystem of the whole body musculoskeletal system were represented through the appropriate application of constraints to the modeled geometry.

The computational techniques developed couple the determination of the muscle forces acting within the system studied, the stresses they induce within the bone, and the ensuring shape adaptations of the bone studied which alter its strength. Using knowledge from the field of structural analysis, gradient based optimization methods were employed to solve the indeterminate system of angular momentum balance equations for the magnitudes of the forces generated by individual muscles modeled that work together to generate a net resultant static force by the leg against a fixed surface. Using knowledge from the field of structural design, gradientless optimization techniques were employed to determine the "optimal" bone designs that reduced the variations of the stress state over the optimizing surfaces. The bone designs developed included alterations to both the

outer (periosteal) surface of the long bone studied and the inner (endosteal) surface of its central hollow (diaphyseal) region. Customized code was written to perform these optimizations. They worked directly within a commercial finite element code, which was used to perform the structural analysis of the leg bone system studied based on the applied individual muscle forces. Using the structural shape optimization model developed, the nodes of the meshed bone geometry in this finite element model were moved based on the stress distributions resulting from the modeled muscle activity. This process was iteratively repeated until a sufficient reduction in the surface stress variation was achieved or a size limit was reached. The effectiveness of each of the resulting optimal bone geometries created under varying load conditions at improving the maximum stress at a desired location during a particular, critical design load, activity, or action of the system studied was then compared. The varying loading conditions studied to induce the shape strength changes in this model could be anything from different net resultant forces generated to the alteration of the relative orientations of the bony components of the system studied.

For the model to be able to compare the effects of a wide range of conditions, it had to be independent of load case specific model parameters or features and needed a common, consistent stopping or convergence criteria in both the determination of the muscle forces and the changes to the bone shape. This was achieved in the muscle force optimization model through the selection of the optimization goal and the numerical optimization solution method for a gradient-based optimization routine. However, because gradientless optimization methods were employed for the shape optimization of the bone, due to their efficient implementation in analyzing complex three-dimensional

design surface, an absolute optimum could not be identified by the optimization solution method used alone. While many similar published bone shape adaptation models have selected arbitrary parameters to control the growth per iteration and define the completion of the optimization process, for the modeled developed in this work to function consistently to directly compare a wide range of conditions, it required no arbitrarily selected or experimentally determined model parameters to drive the model function. Instead, nodal growth in the developed model was based on the current stress state of the bone surface being optimized. Additionally, a measure of the overall change in the variation of the stress over the surface being optimized was development to explicitly define when "sufficient" improvement in stress uniformity was achieved. These features complied with the design objectives of universal applicability and the independence from experimentally based model parameters.

The muscle force optimization portion of this model was based on one previously developed in the literature. Specifically, the sum of the squares of the muscle stresses was minimized through the use of a gradient projection optimization method. The optimization goal essentially used the size of a muscle as a weighting factor for its generated force magnitude, thus ensuring that each muscle was capable of generating the magnitude of the force predicted for it by the model. Because this optimization function (sum of the muscle stresses) was convex, the gradient projection optimization method resulted in global optima, and a unique solution was found. This eliminated the need for the repeated solution of the optimization problem with various initial guesses to ensure a global optimum was found, which would have prohibited its automatic, coupled use in the modeling method developed in this work. The computational implementation of the

gradient projection method was modified slightly in this model to improve its numerical stability.

Many gradientless optimization methods that have been developed for both bone strength adaptation and structural shape optimization were explored for their use in the developed modeling methods. These methods are generally based on the iterative progression of the value of a measure of the stress state of the particular system modeled towards that obtained from a reference system. However, most of these previously developed models were designed to solve a single specific problem and, therefore, incorporated model parameters that were satisfactory for the problem investigated without regard to its function in optimizing another system. Additionally, because the gradientless optimization methods are less mathematically rigorous than the gradient based ones used in this work to determine the individual muscle forces, they do not necessarily reach a global or even a local optimum. Instead, these models are typically stopped when the measure of the mechanical state of the system studied is sufficiently close to the selected threshold value. While this is adequate for the study of a single, particular system, it lacks the consistency necessary for use in comparative studies.

To allow for a more universal application of the model developed in this work, three main modeling features were developed. First, the optimization model was driven not by a selected threshold value as many of its predecessors, but by one that represented the global state of stress on the surface being optimized. Based on the statistical standardization of a set of data, this growth driver threshold value was the surface averaged value and the growth driver expression was normalized by the standard deviation of the measure of the stress state over the optimizing surface. Therefore, the

growth at each node was proportional to the ratio of the difference between the value of a measure of the state of stress at the particular node and the average of this measure over the surface to the variation (standard deviation) of that stress state measure over the entire surface being optimized.   Second, the convergence of the model, which measured the progression of the optimization towards uniformity of the stress state over the surface being optimized, was based on a statistical method of identifying groups of extreme values. Through the use of quartiles, the progress of the set of measures of the nodal stress states towards uniformity was quantified by tracking the difference between the "effective extremes" over the optimizing surface, the difference between the average of the lower 25% of the surface nodes and the average of the upper 25% of the surface nodes. The uniformity was said to be sufficiently improved when this difference was reduced 50% from its value at the start of the optimization process. Last, because of the potential for large changes in the shape of the model over the optimizations performed using this developed model, surface as well as internal nodal smoothing methods were developed and implemented for this work to maintain the integrity of the meshed representation of the bone volume being optimized during the course of the study, ensuring the accuracy of the results of the structural analysis that drives the shape adaptation predictions. These features allowed the developed model to be used to compare a wide range of conditions without the need to alter any component of the optimization model. In this work, the measure of the state of stress used to drive the shape optimization model was the strain energy density.

6.1.2 Model Implementation

While the modeling techniques developed could be applied to any system, to understand its capabilities, the leg was the focus of study in this work as the muscles of the leg can generate a wide range of force magnitudes. The tibia bone was the targeted of the strength adaptation, specifically, the distal portion of this bone, near the ankle. This region of the tibia has been shown to be significantly affected by the reduction of strength that occurs with disuse. Additionally, it is often the site of stress fractures, even in bones with normal densities. Therefore, methods to mitigate the risk of stress fractures in both normal and weakened bones would be beneficial to both "weakened" and "healthy" bones. The musculoskeletal model used included bony segments representing the pelvis, femur, tibia, and foot, and the ten major muscles that cause the flexion and extension actions of the hip, knee and ankle joints. The isometric activity generated by this leg system was assumed to be resisted at the foot and was represented by a fixed constraint, and the effects of the rest of the body on the leg system studied were simulated by a fixed constraint at the top of the pelvis.

In a series of parametric studies, the developed modeling techniques were used to determine a number of tibial bone "designs" optimized under a variety of potentially bone strengthening activities. The effectiveness of each of these bone "designs" in resisting the conditions thought to induce stress fractures, those of mid-stance jogging, was then studied as the "comparison critical design load case". The specific loading conditions compared were based on the leg arranged in three unique positions or "configurations": a straight leg arrangement (0° configuration), a bent leg configuration (45° configuration) with hip flexed 45° and knee flexed 90°, and a bent back configuration (90°

configuration) with the hip in its neutral, neither flexed nor extended, position and its knee flexed at 90°. A net static isometric force was generated by the leg against a fixed surface at the toe. Eleven loading cases were then considered, each with the same magnitude of the resultant force of 100N but with varying directions and number of loads applied. Four single load cases with the resultant load directed in each of the four global coordinate directions, six double load cases with the sequential generation of pairs of these four basic directions, and one four-load case with all four basic directions sequentially applied in a clockwise order. The leg was arranged so that, in the straight leg 0° coordinate system, its long axis was aligned with the global y-coordinate (superior-inferior direction as positive-negative y-axis), the toe pointed toward the global positive x-axis (anterior direction) and the heel toward the global negative x-axis (posterior direction). The cylindrical axis of the tibia was aligned with the global z-axis.

Of all the arrangements studied, the 45° configuration resulted in more loading conditions that improved the tibia bone's strength in the fracture prone region. This was followed by the 90° configuration. The 0° straight leg configuration resulted in only one case with a slight improvement in the strength of the fracture prone region.

Of all the cases considered, the tibial bone design geometries that were optimized under the anteriorly directed resultant force, the inferiorly directed resultant force, and their sequential combination in both the 45° and 90° leg configurations all produced a 22% improvement in the targeted region over an uniformly circular hollow cylindrical geometry. Though all producing nearly identical optimal geometry, they differed over an order of magnitude in their surface averages and standard deviations of the strain energy density. None of these "winning" conditions were derived from the same set of active

muscles. Additionally, even in the active muscles that were common to each of these loading conditions, no similarities in absolute or relative magnitudes of their generated forces could be found. What was noticed among these common performing loading conditions were very similar ratios of initial average to standard deviation of the strain energy density over the optimized surface (a measure of the initial variation of the parameter over the surface being optimized). In addition, all of these cases had a very large knee extensor force that resulted in almost pure bending of the tibia bone about a point near the ankle joint. These loading conditions lead to a thickening of the cortical bone geometry near the ankle (distal) end of the bone in the region of highest stress and a gradual thinning of the cortical bone shell toward the location of the load application near the knee (proximal) end of the bone. This gradual transition between the thickened and thinned region of the bone had the tapered look of a uniform stress beam.

Similarly the "worst" performers, such as the posteriorly directed resultant force in the 45° and 90° configurations, had more complex loading patterns and stress distributions in the tibia bone, with smaller stresses near the ankle and larger stresses near the knee. The distribution of stress resulting from these loading conditions induced the greatest growth near the knee and caused decay in the distal tibia, the targeted strengthening region in this study. These cases also tended to have a bending deflection towards the posterior side of the bone (towards the heel) as opposed to more deflection toward the toe (anterior side) which occurred under the loadsets found to be more "beneficial" at strengthening this region.

In addition to features relating to loading patterns or stress distributions, there was a trend found with the resulting asymmetry in growth at the region of interest. It was

observed that a thickening on the anterior side of the bone was shown to be beneficial over its inverse, thickening on the posterior side. An example of this is a comparison between the posteriorly directed loading in the 0° configuration which resulted in anterior thickening and a slight (5%) improvement in strength (decrease in resulting stresses) and the inferiorly directed loading in the same configuration, which, while resulting in the very similar geometric measures such as cross sectional area and moments of inertia, but demonstrated anterior thinning and posterior thickening, resulting in a slight (5%) increase in the stresses at the comparison location.

Therefore, the common features to suggest improved strengthening of a bone (or even similar shape adaptation trends) are not related to patterns of muscle activity, limb configurations, magnitudes of muscle forces, or even geometric measures. Instead, the similarities in stress distributions, represented by stress contour patterns, were shown to be the best indicator of general performance. Thus, unlike muscle strength, where there is only one mode of loading (tensile stress), the strength of a bone cannot be directly inferred by the magnitude of the force acting on it. Because of the complex states of stress that arise in most bones, a number of combinations of loads acting on the bone (through various combinations of muscle forces and limb configurations) can create similar patterns in stress. This explains the nearly identical strength improvements resulting from significantly different sets of muscle activities and limb configurations in the comparative studies in this work. While this reasoning is helpful in understanding and predicting the general adaptive behavior in a musculoskeletal system, the comparison of the relative improvements in the bone strength can only be achieved through the use of a comparison load case method, such as the one used in this work.

Based on this analysis, combinations of loading modes and limb configurations that induce bending stresses in the tibia bone, similar to what occurs in the jogging "critical design load" comparison case, were most beneficial at improving the strength in the distal tibia where stress fractures can occur, especially during mid-stance jogging. However, the optimal geometries developed under these loading modes, as stated, are similar to uniform stress beams. Therefore, while they can improve the strength in the distal region near the ankle, they can have significant amounts of decay in the proximal region near the knee. This decay is undesirable in many loading conditions, as it occurs where many of the muscles act directly on the tibia bone and a thicker geometry would be more beneficial. In this study, while the single load cases generally resulted in more extreme shape changes, making them the "best" and "worst" performers based on the design criteria in this parametric study of strengthening the distal one-third of the tibia, the combinations of the loading modes showed more moderate changes. Specifically, similar features were maintained, such as in the multiload case of the anteriorly and inferiorly directed loads in the 45° configuration, where the same changes in shape and bone strength were produced as were in the single load anterior or inferior cases implemented separately in this study. In contrast, opposing features at common locations, such as the thickening of the tibia under the anteriorly directed load in the 45° configuration and the thinning under the posteriorly directed load in the same configuration, tend to cancel each other, reducing the effect of either one. Thus, the desired features, such the thickening of the fracture prone region, created under one loading condition may be maintained, and its undesirable consequences of the optimization, such as the thinning in another region that may increase its risk of fracture,

may be mitigated through the sequential application of an appropriately selected second load case that thickens both regions. While the bone may not have as uniform a stress state as would occur under a single load, the bone would not be weakened in one area just so that the targeted area could be strengthened.

Many of the 0° configuration cases showed poor improvement in strength and reached the growth limit before attaining the desired reduction in surface variation of the strain energy density. In contrast, many in the 45° configuration succeeded in both of these tasks. There were no distinct trends in the set of active muscles or the magnitudes of the muscle between these two configurations. Additionally, there was no trend in magnitude of average or standard deviation of the strain energy density over the optimizing surface, as many of the cases that proved beneficial in the 45° configuration had averages and standard deviations of the nodal strain energy densities that were two orders of magnitude greater than those of the 0° configuration. The difference, however, appeared to lie in the relative magnitude between the average and the standard deviation of the strain energy density over the optimizing surface. The cases that failed to converge using the developed model and resulted in poor strengthening performance were the ones that had a very large variation of the strain energy density over the optimizing surface compared to the surface average value of the strain energy density (ratio standard deviation to average). This essentially means that if the initial state of the model (as measured by the diversity of the nodal strain energy density strain energy density) is very far from its optimization goal (defined as a uniform strain energy density over the surface being optimized), then final shape would have to be very different from the initial shape to achieve the desired reduction (meaning that much to the initial shape would be

required), which may not occur before the size limit is reached. It has been said that because these gradientless optimization methods are not mathematically rigorous, the initial conditions must be close to the desired optimal conditions for the method to properly find the optimal state desired. Thus, under some loading conditions, it seems that there may be a limit to the effectiveness that the changes in shape from an initially circular cylinder have on changes in strength.

The use of this developed model to study the effects of mechanical conditions on changes in bone shape and strength allows the tracking of the relative influence of the local measures of the stress state of the bone, the global measure of the overall state of stress, and the global variations in the stress state over the surface being optimized on the local changes to the bone shape. The use of the statistical standardization of the nodal strain energy density as the driver of growth essentially changes the local shape based on the ratio of the variance of the local nodal strain energy density from the surface averaged value to the variation (standard deviation) of all of the nodes on the surface being optimized. Thus, when one of these three measures, local strain energy density, average strain energy density or its standard deviation over the surface is much larger than the others, it dominates the shape changes. This was demonstrated in the description of some of the conditions in the comparison studied in Chapter 5, especially for the 0° configuration cases, which had a very large standard deviation of the strain energy density in relation to the nodal and average strain energy density values and resulted in the relatively small amounts of growth in most areas of the bone studied. In contrast, when the magnitudes of these three measures are more similar, the dominate measure of

stress can alter throughout the optimization process, modifying the resulting growth patterns on its way to convergence.

The limitations of the current model are related to the assumptions used in its development and should be noted. Because the model is optimization based, not time based, it cannot be used to predict exact amounts of changes in bone shape or strength over the course of an experimental or clinical study. It can only be used to quantify the relative effectiveness of one loading mode over another. While a three-dimensional bone geometry was used, the loading applied only acted in the two-dimensional plane and the effects of out of plane forces were not considered. Additionally, the developed model currently only simulates static loading conditions. Although static, resistance-based exercises have been shown to significantly improve bone strength over more dynamic modes such as walking, the changes in the bone shape and strength due to dynamic loading might still be of interest. Finally, as discussed above, the model developed has a limit to the range of ratios of standard deviation to the average of the local stress state of the optimizing surface over which it can effectively predict shape changes to improve the uniformity of the mechanical state (stresses or strain energy density) within the region being considered.

The implementation of the developed modeling technique demonstrated its effectiveness at comparing the varying abilities of a wide range of loading conditions to strengthen a targeted region of a bone within a multisegment musculoskeletal system. Because the model determines the magnitudes of the individual muscle forces within this multisegment system, its use to analyze each of the loading conditions studied gave insight into the function of the model as well as the effects of variations in the local

mechanical environment on bone strength and shape adaptation. Thus, it enhances the currently available capabilities to predict bone shape adaptation, allowing for more thorough studies of this phenomenon. Therefore, the developed modeling method can be a useful tool in analyzing and developing mechanical means for targeted bone strengthening. It can be used to develop new exercise regimes or to understand the effects of current ones in order to refine the wide array of currently available techniques to counteract the loss of bone strength that can occur due to age or disuse both on Earth and in Space.

6.2   Future Work

The future implementation and further development of the model can improve the understanding and modeling of bone strength adaptation. In addition to the study of basic loading conditions, like the ones investigated in this work, the developed modeling techniques can be used to study loading patterns that more closely represent typically suggested bone strengthening exercises so that the regions of bone that these exercises target could be identified and the relative effectiveness of the proposed exercises could be determined. The model can be employed to study other systems, such as the arm, or other bones within the current leg system modeled, such as the femur.

Means of improving the current function of the developed model can be suggested. The current methods for surface nodal smoothing in the developed could be enhanced to eliminate some small regions of zigzagging that were noticed near the areas of very large stresses and stress gradients, such as near the boundary constraints. Additionally, the values of the muscle force moment arms used in the muscle force magnitude optimization methods could be adjusted with the progression of the

optimization model to modify the muscle forces so that consistent joint moments are produced despite the growth that may occur in their areas of muscle force application. To potentially reduce these large amounts of growth, the geometry of the modeled bone shape could be modified to be more similar to that of a natural bone, with a general widening in the regions near the joints where many of the muscles act. This would likely reduce the stresses in the region and the resulting extreme, and unrealistic, local growth predicted by the model. The region of high stress on the inner surface directly neighboring the cancellous filled region could be eliminated from the convergence calculations, or its effect could be modified, so that the convergence measure is more representative of the change in mechanical state for most of the surface studied rather than being driven by these stress concentration areas. Finally, alterations in the developed computational code could be performed to allow the model to run more efficiently, reducing the overall runtimes.

In addition to the function of the numerical optimization and structural analyses models, alterations to the current geometric system model can be suggested. More realist bone geometry or the incorporation of the effects of other soft tissues, such as cartilage or ligaments at the joints, could alter the high stresses that resulted in these regions using the current model. Muscles that produce forces out of the sagittal plane could be included in the model so that their effect on the changes in bone strength could be identified. Finally, the geometry of the bone system studied, the optimization model used to determine the muscle forces, and the methods to perform the structural analysis could be altered to allow for the simulation and prediction of the effects of dynamic loading.

Despite being studied for centuries, the observed adaptations of bone shape and strength with age, load, and disuse that has fascinated researchers and laypeople alike is still of great interest. Yet, the difficulties in separating the desired mechanical effects on the alterations to bone shape and strength from all the other mechanical impositions on a bone during normal daily activities through experimental means have limited the progression of the understanding of the relationships between specific mechanical influences and the observed adaptations. Computational tools such as the ones developed in this model eliminate these difficulties and provide means for improving the understanding and, ultimately, the better control of these adaptive phenomena.

APPENDIX A

ORTHOGONAL PROJECTIONS AND QR FACTORIZATION

This Appendix explains the mathematical concepts of orthogonal projections and QR factorization, and their application to determining the eigenvalues results from a set of linear least squares equations. These concepts were used in this work in the development of the code to perform the gradient projection optimization used to find the individual muscle force magnitudes as described in Chapter 3.

A.1 Orthogonal Projections

A projection method moves all the points along a vector "**a**" in a particular direction until the points encounter a subspace. In an orthogonal projection the projection direction is orthogonal, or normal, to the subspace. An orthogonal projection of a vector onto a subspace can be used to find the point on the subspace closest to the vector [349]. This can be achieved through the application of an orthogonal basis of a subspace as described here. Although the method is valid for complex space, the present application is a physical problem in real space and so this discussion is limited to real space.

Defining χ to be a subspace of real space. Let **Q** be an orthonormal basis for χ. For reference, a basis is a set of linearly independent vectors that span a subspace [251, 349]. An orthonormal basis is a set of linearly independent vectors that are all orthogonal to one another and that span a subspace [251]. Let **z** be a vector defined within the real space.

$$\mathbf{z}_\chi = \mathbf{Q}\mathbf{Q}^T\mathbf{z} \qquad (A.1)$$

$$\text{and } \mathbf{P}_\chi \equiv \mathbf{Q}\mathbf{Q}^T \qquad (A.2)$$

$\mathbf{z}_\chi$ is the projection of $\mathbf{z}$ onto the subspace χ. In the more familiar two-dimensional space, this is analogous to determining the orthogonal x- and y- components of a vector $\mathbf{z}$ by projecting it onto the orthogonal planes through the use of dot products between $\mathbf{z}$ and the unit normals for each of these planes [251].

Similar to this "dot product" example, the vector $\mathbf{z}$ can be written as a linear combination of two orthogonal vectors $\mathbf{z}_\chi$ and $\mathbf{z}_\perp$ that lie in two generalized (not necessarily planar) subspaces χ and $\chi_\perp$, where $\chi_\perp$ is the orthogonal complement of χ. Therefore the projection of $\mathbf{z}$ onto $\chi_\perp$ is (from [349]):

$$\mathbf{z}_\perp = \left(\mathbf{I} - \mathbf{Q}\mathbf{Q}^T\right)\mathbf{z} \qquad (A.3)$$

$$\text{And } \mathbf{P}_\perp \equiv \mathbf{I} - \mathbf{Q}\mathbf{Q}^T \qquad (A.4)$$

where I is the identity matrix.

Orthogonal projections are used in the gradient projection optimization method to determine the direction in which to search for the optimal solution. The search direction is defined as the projection $\mathbf{P}$ of the negative of the gradient of the optimization goal, F, or $-\nabla Z(\mathbf{F})$, onto the surface comprised of the constraints that are exactly satisfied (equal to zero) or "active". The surface comprised of this subset of constraints is used in determining the search direction, as it defines the boundary of the feasible region where extreme (or optima) values would likely be located. The gradient of the optimization goal is used because it defines the largest rate of change of the optimization function. The

negative of the gradient is used to reduce the value of the optimization function (in a minimization problem). An orthogonal projection is used to establish the search for the point that minimizes the optimization goal specifically amongst the set of points most likely to be an optimum (this subspace defined by the active constraints) as described above. [114, 203]

Because gradients are normal to their functions, if the constraint functions are linear, and thus their gradients are scalar, then the gradients of these constraints form a set of vectors that establish a basis of the subspace normal, or orthogonal, to the space formed by the constraints. So if the projection onto the space defined by the gradients of the constraints is given by:

$$-\nabla Z(\mathbf{F})_\chi = -\mathbf{P}_\chi \nabla Z(\mathbf{F}) \tag{A.5}$$

then the desired projection onto the subspace of the constraints themselves is :

$$-\nabla Z(\mathbf{F})_\perp = -\left(\mathbf{I} - \mathbf{P}_\chi\right) \nabla Z(\mathbf{F}) \tag{A.6}$$

Even though $\mathbf{P}_\perp$, or $\left(\mathbf{I} - \mathbf{P}_\chi\right)$, is desired, the projection onto its orthogonal complement, $\mathbf{P}_\chi$, is used because it is convenient to calculate the gradients of the constraint functions. The gradients of the constraints, while normal to the constraints, may not be normal to each other, and so typically do not form an orthonormal basis of the orthogonal complement of the subspace of the active constraints. However, an orthonormal version of this set of vectors can be found through $\mathbf{QR}$ factorization.

A.2   QR Factorization

QR factorization is used in the model described in Chapter 3 to calculate the orthogonal projections as described above. The **QR** factorization (or decomposition) process factors an n x p matrix **X** into the product of an n x p orthogonal matrix **Q** and a p x p upper triangular matrix **R** with positive diagonal elements [349]. Similar outcomes can be achieved by factoring the matrix to an orthogonal matrix **Q** and a lower triangular matrix **L**. This is called **LQ** factorization [258]. However, only **QR** is described in this appendix based on [349]. In general it takes the form:

$$\mathbf{X} = \mathbf{QR} \tag{A.7}$$

or because the inverse of an orthogonal matrix is equal to its transpose:

$$\mathbf{Q}^T\mathbf{X} = \begin{pmatrix} \mathbf{R} \\ \mathbf{0} \end{pmatrix} \tag{A.8}$$

The first p columns of **Q** form an orthonormal basis for the subspace of **X,** χ, called $\mathbf{Q}_\chi$. The last p-k columns of **Q** form a basis of the complementary subspace whose vectors are orthogonal to **X,** $\chi_\perp$, called $\mathbf{Q}_\perp$. Therefore Equation A.1 can be written as :

$$\mathbf{Q}^T\mathbf{X} = \begin{pmatrix} \mathbf{Q}_\chi^T\mathbf{X} \\ \mathbf{Q}_\perp^T\mathbf{X} \end{pmatrix} = \begin{pmatrix} \mathbf{R} \\ \mathbf{0} \end{pmatrix} \tag{A.9}$$

or

$$\mathbf{Q}_\chi^T\mathbf{X} = \mathbf{R} \tag{A.10}$$

$$\mathbf{Q}_\perp^T \mathbf{X} = \mathbf{0} \tag{A.11}$$

$\mathbf{Q}_X$ and $\mathbf{R}$ are unique, but $\mathbf{Q}_\perp$ is not. It can be any orthonormal basis of the orthogonal complement of $\mathbf{X}$, $\chi_\perp$.

In this work, specific code was not developed for $\mathbf{QR}$ factorization. Instead a pre-programmed built-in function in MATLAB was implemented.

The $\mathbf{QR}$ factorization is applicable to the calculation of orthogonal projections. As mentioned above, a matrix of the gradients of the constraint functions is formed in the gradient projection optimization method to form a basis of the orthogonal complement of the subspace of active constraints. If the constraints take the general form of Equation 3.3:

$$g_j(\mathbf{F}_k) = \mathbf{A}_j^T \mathbf{F}_k - \mathbf{b}_j \tag{A.12}$$

where j are only the "active constraints" and $\mathbf{F}$ is the unknown, in this case the muscle force magnitudes, then

$$\nabla g_j(\mathbf{F}_k) = \mathbf{A}_j^T \equiv \mathbf{N}^T \tag{A.13}$$

The columns of $\mathbf{N}$ contain the gradient of the active constraints and form a basis for the orthogonal complement of the subspace of active constraints. The symbol $\mathbf{N}$ is most commonly used, but $\mathbf{A}_j$ is also widely implemented. [114]

To find the orthonormal basis of the gradients of the constraints, **QR** factorization can be used to find the orthonormal factor of **N**. Applying Equation A.8 to **N** with $\mathbf{Q}_\chi \mathbf{R} = \mathbf{N}$ gives:

$$\mathbf{Q}_\chi^T \mathbf{N} = \mathbf{R} \tag{A.14}$$

$$\text{where } \mathbf{Q}_\chi = \mathbf{N}\mathbf{R}^{-1} \tag{A.15}$$

$$\text{Thus, } \mathbf{Q}_\chi^T = \left(\mathbf{N}\mathbf{R}^{-1}\right)^T = \mathbf{R}^{-T}\mathbf{N}^T \tag{A.16}$$

From Equation A.5, the projection of **F** onto the subspace of the constraints is [114]:

$$-\nabla Z(\mathbf{F})_\perp = -\left(\mathbf{I} - \mathbf{P}_\chi\right)\nabla Z(\mathbf{F}) \tag{A.17}$$

$$\text{where } \mathbf{P}_\chi \equiv \mathbf{Q}_\chi \mathbf{Q}_\chi^T \tag{A.18}$$

from Equation A.2. Using Equations A.7 and A.16 in Equation A.18 [349]

$$\text{Then, } \mathbf{P}_\chi \equiv \mathbf{N}\mathbf{R}^{-1}\mathbf{R}^{-T}\mathbf{N}^T \tag{A.19}$$

$$\text{or rewriting } \mathbf{P}_\chi = \mathbf{N}\left(\mathbf{R}^T\mathbf{R}\right)^{-1}\mathbf{N}^T \tag{A.20}$$

Putting Equation A.7 in terms of **N**[349]:

$$\mathbf{N} = \mathbf{Q}_\chi \mathbf{R} \tag{A.21}$$

$$\text{So, } \mathbf{N}^T = \left(\mathbf{Q}_\chi \mathbf{R}\right)^T = \mathbf{R}^T \mathbf{Q}_\chi^T \tag{A.22}$$

$$\text{Therefore, } \mathbf{N}^T\mathbf{N} = \mathbf{R}^T\mathbf{Q}_\chi^T\mathbf{Q}_\chi\mathbf{R} \tag{A.23}$$

But, because $\mathbf{Q}_\chi$ is orthogonal, $\mathbf{Q}_\chi^T \mathbf{Q}_\chi = 1$ and:

$$\mathbf{N}^T \mathbf{N} = \mathbf{R}^T \mathbf{R} \qquad\qquad (\text{A.24})$$

Substituting Equation A.24 into Equation A.20:

$$\mathbf{P}_\chi = \mathbf{N}\left(\mathbf{N}^T \mathbf{N}\right)^{-1} \mathbf{N}^T \qquad\qquad (\text{A.25})$$

Then, substituting Equation A.25 into Equation A.17 gives :

$$-\nabla Z(\mathbf{F})_\perp = -\left(\mathbf{I} - \mathbf{N}\left(\mathbf{N}^T \mathbf{N}\right)^{-1} \mathbf{N}^T\right)\nabla Z(\mathbf{F}) \qquad\qquad (\text{A.26})$$

Often the projection term $\left(\mathbf{I} - \mathbf{N}\left(\mathbf{N}^T \mathbf{N}\right)^{-1} \mathbf{N}^T\right)$ is simply called $\mathbf{P}$. Therefore, Equation A.26 defines the search direction $\mathbf{S}$ for the gradient projection optimization method (Projection of the gradient of the optimization function onto the orthogonal complement of the solution space) described in Chapter 3's Equations 3.11 and 3.12 [114] shown here for reference.

$$\mathbf{S} = -\mathbf{P}\nabla Z(\mathbf{F}) \qquad\qquad (3.11)$$

$$\mathbf{P} = \mathbf{I} - \mathbf{N}(\mathbf{N}^T \mathbf{N})^{-1}\mathbf{N}^T \qquad\qquad (3.12)$$

A.3 Linear Least Square and Eigenvectors by QR Factorization

To more efficiently solve the eigenvalue problem for least squares problems, **QR** factorization is often used. The method is applied in the gradient projection method to the following components of the current model: to solve for the Lagrange multipliers,

which are eigenvalues [188], in checking for satisfaction of the Kuhn-Tucker conditions when determining if a feasible solution is an optima, and in adding or removing active constraints to the system (See Chapter 3). A linear least squares method is also used to numerically solve for Lagrange multipliers in order to reduce susceptibility of error amplification. [203]

In general, the linear least squares problem is a sort of optimization of the form [349]:

$$\text{find } \mathbf{b} \text{ where } \|\mathbf{y} - \mathbf{Xb}\|_2^2 = \text{minimum} \tag{A.27}$$

where $\mathbf{X}$ is a known n x p matrix of rank p and $\mathbf{y}$ is a known vector of length n

$\mathbf{QR}$ factorization of the $\mathbf{X}$ matrix leads to an n x n orthonormal matrix $\mathbf{Q}$ and p x p upper triangular matrix $\mathbf{R}$ (Equation A.9) so that :

$$\mathbf{Q}^T\mathbf{X} = \begin{pmatrix} \mathbf{Q}_\chi^T\mathbf{X} \\ \mathbf{Q}_\perp^T\mathbf{X} \end{pmatrix} = \begin{pmatrix} \mathbf{R} \\ \mathbf{0} \end{pmatrix} \tag{A.28}$$

$\mathbf{z}$ can be defined as

$$\mathbf{z} = \mathbf{Q}^T\mathbf{y} = \begin{pmatrix} \mathbf{Q}_\chi^T\mathbf{y} \\ \mathbf{Q}_\perp^T\mathbf{y} \end{pmatrix} = \begin{pmatrix} \mathbf{z}_\chi \\ \mathbf{z}_\perp \end{pmatrix} \tag{A.29}$$

In this equation, $\mathbf{Q}^T$ is an orthogonal (orthonormal) matrix and whose Euclidian norm is unitarily invariant or:

$$\|\mathbf{y} - \mathbf{Xb}\|_2^2 = \|\mathbf{Q}^T\left(\mathbf{y} - \mathbf{Xb}\right)\|_2^2 \tag{A.30}$$

Substituting in Equations A.28 and A.29 into Equation A.30 yields:

$$\left\| \mathbf{y} - \mathbf{Xb} \right\|_2^2 = \left\| \mathbf{Q}^T \mathbf{y} - \mathbf{Q}^T \mathbf{Xb} \right\|_2^2 = \left\| \begin{pmatrix} \mathbf{z}_\chi \\ \mathbf{z}_\perp \end{pmatrix} - \begin{pmatrix} \mathbf{R} \\ \mathbf{0} \end{pmatrix} \mathbf{b} \right\|_2^2 = \left\| \mathbf{z}_\chi - \mathbf{Rb} \right\|_2^2 + \left\| \mathbf{z}_\perp \right\|_2^2 \tag{A.31}$$

Since $\left\| \mathbf{z}_\perp \right\|_2^2$ is a constant, $\left\| \mathbf{y} \text{ - } \mathbf{Xb} \right\|_2^2$ minimized when $\left\| \mathbf{z}_x - \mathbf{Rb} \right\|_2^2$ is minimized. Therefore,

$\left\| \mathbf{z}_\chi - \mathbf{Rb} \right\|_2^2$ is minimized when it is equal to zero or $\mathbf{z}_\chi = \mathbf{Rb}$.

Thus, solving for the unknown **b** (which could be, for example, the Lagrange multipliers λ in the Kuhn-Tucker conditions) :

$$\mathbf{Rb} = \mathbf{z}_\chi = \mathbf{Q}_\chi^T \mathbf{y} \tag{A.32}$$

R is an upper triangular square matrix. Hence, solving for **b** is straightforward with $\mathbf{Q}_\chi^T$ and **y** known. Recall that $\mathbf{Q}_\chi^T$ consists of the first p rows of $\mathbf{Q}^T$ so that $\mathbf{Q}_\chi^T$ is a p x n matrix.

The method described was used in the program written in this work for the gradient projection optimization to eliminate the need to calculate the inverses of matrices that may be ill-conditioned when determining the of eigenvalues of the system [203].

APPENDIX B

MATHEMATICAL TOOLS EMPLOYED IN COMPUTATIONAL MODELING OF BONE SHAPE ADAPTATION

This appendix explains the mathematical tools used in the developed model of bone shape adaptation. The means to transform the definition of nodal positions between various coordinate systems is first discussed. Next, efficient means for sorting a large array of data, used in a number of applications in the developed model is described. Finally, the calculation of the weighting factor for the surface node smoothing method implemented in this shape adaptation model, the magnitude of the gradient of the nodal strain energy density, is presented.

B.1 Coordinate Transformations

The transformations of the definition of a point from a global coordinate system to a local coordinate systems requires both a rotation to reorient the coordinate directions and a translation to adjust the location of the origin. A rotation matrix $\mathbf{R}$ and a translation matrix $\mathbf{S}$ were defined so that for the Cartesian coordinate system,

$$\vec{\mathbf{L}} = \mathbf{R}\mathbf{S}\vec{\mathbf{G}} \qquad \text{(B.1)}$$

where $\vec{\mathbf{L}}$ represents the position vector of a point relative to the local bone Cartesian coordinate system and $\vec{\mathbf{G}}$ represents the position vector of the same point relative to the global coordinate system. The $\mathbf{R}$ rotation matrix and the $\mathbf{S}$ translation matrix are derived below.

The rotation used in the coordinate transformation in this work was performed in order to preserve the x, y, z unit vector right handedness of the global Cartesian coordinate system. This maintains the same orientation between different transformations so that the local x-direction always points anteriorly and the local z-direction always points axially along the length of the bone. Because the z-direction is aligned with the axis of the tibia bone (cylinder), the z-direction is considered the "driver" direction. Therefore, the local coordinate system is rotated about a fixed point without introducing any extraneous spin until the global z-coordinate becomes aligned with the local z-coordinate [341]. Physically, this can be represented by using the global z-coordinate as a joystick with the global x- and y-Cartesian axes firmly attached and moving the joystick to the local coordinate system where no relative rotation is possible about the axis of the joystick [341]. The presentation of this coordinate transformation follows that explained in [341].

The local z-coordinate is known. Therefore, it can be proposed that the unit vector in the local y-direction is normal to the plane formed by the global Cartesian coordinate x-direction and the local z-direction, or the cross-product of these two:

$$\overline{e}_y^L = \frac{\overline{e}_z^L \times \overline{e}_x^G}{\left|\overline{e}_z^L \times \overline{e}_x^G\right|} \tag{B.2}$$

where the superscript L represents the local bone coordinate system and the superscript G represents the global system coordinate system and $\overline{e}$ are unit vectors.

The unit vectors $\overline{e}_z^L$, $\overline{e}_x^G$ and $\overline{e}_y^L$ form a right handed system of this order such that $\overline{e}_y^L$ is normal to both $\overline{e}_z^L$ and $\overline{e}_x^G$ as well as the projection of $\overline{e}_z^L$ onto the $\overline{e}_z^G$ $\overline{e}_y^G$ plane.

The local x-direction can then be found because it must form an orthogonal right handed system in the order, $\overline{e}_y^L \; \overline{e}_z^L \; \overline{e}_x^G$ so that :

$$\overline{e}_x^L = \overline{e}_y^L \times \overline{e}_z^L \tag{B.3}$$

Based on Equations B.2 and B.3, if a point on the local z-coordinate axis has coordinates represented by (A,B,C) in the global coordinate system, then a vector along this local z-direction in the global system is:

$$\overline{e}_z^L = \frac{A\overline{e}_x^G + B\overline{e}_y^G + C\overline{e}_z^G}{R1} \tag{B.4}$$
$$R1 = \sqrt{A^2 + B^2 + C^2}$$

Following Equation B.2, the unit vector along the local y-axis is:

$$\overline{e}_y^L = \frac{0\overline{e}_x^G + C\overline{e}_y^G - B\overline{e}_z^G}{R2} \tag{B.5}$$
$$R2 = \sqrt{B^2 + C^2}$$

Following Equation B.3, the unit vector along the local x-axis is:

$$\overline{e}_x^L = \frac{\left(B^2 + C^2\right)\overline{e}_x^G - AB\overline{e}_y^G + AC\overline{e}_z^G}{R1R2} \tag{B.6}$$

Arranging this into matrix form so that:

$$\bar{e}^L = \mathbf{R}\bar{e}^G \tag{B.7a}$$

$$\mathbf{R} = \begin{pmatrix} \dfrac{C^2 + B^2}{R1R2} & \dfrac{-AB}{R1R2} & \dfrac{-AC}{R1R2} \\ 0 & \dfrac{C}{R2} & \dfrac{-B}{R2} \\ \dfrac{A}{R1} & \dfrac{B}{R1} & \dfrac{C}{R1} \end{pmatrix} \tag{B.7b}$$

In this work, the point (A,B,C) on the local z-axis used in the determination of this rotation matrix was a point created to define this cylindrical axis as described in Section 4.4.1.1.

The final step in the transformation from global to local coordinate systems is the translation of the origin. The translation is defined as the vector from the old to the new and so is defined as the vector :

$$\mathbf{S} = \mathbf{P}_O^G - \mathbf{P}_O^L \tag{B.8}$$

where $\mathbf{P}_O^G$ and $\mathbf{P}_O^L$ are the origins of the global and local coordinate systems as defined in the global system. So if $\mathbf{P}_O^L$ is defined as $\left[P_O^X, P_O^Y, P_O^Z \right]$ and $\mathbf{P}_O^G$ is [0,0,0] then

$$\mathbf{S} = \begin{bmatrix} -P_O^X \\ -P_O^Y \\ -P_O^Z \end{bmatrix} \tag{B.9}$$

Putting this all into matrix form, the coordinate transformation becomes:

$$
\begin{bmatrix} X^L \\ Y^L \\ Z^L \\ 1 \end{bmatrix} = \begin{pmatrix} \dfrac{C^2+B^2}{R1R2} & \dfrac{-AB}{R1R2} & \dfrac{-AC}{R1R2} & 0 \\ 0 & \dfrac{C}{R2} & \dfrac{-B}{R2} & 0 \\ \dfrac{A}{R1} & \dfrac{B}{R1} & \dfrac{C}{R1} & 0 \\ 0 & 0 & 0 & 1 \end{pmatrix} \begin{pmatrix} 1 & 0 & 0 & -P_O^X \\ 0 & 1 & 0 & -P_O^Y \\ 0 & 0 & 1 & -P_O^Z \\ 0 & 0 & 0 & 1 \end{pmatrix} \begin{bmatrix} X^G \\ Y^G \\ Z^G \\ 1 \end{bmatrix}
\tag{B.10}
$$

with all terms defined above.

B.2   Heap Sorting

Heap sorting was applied extensively in the numerical modeling methods developed in this work [258]. Unlike many other common sorting methods, such as bubble sorting, heap sorting is very efficient because it sorts in place rather than requiring auxiliary storage space to temporarily hold the data being rearranged. In general, it uses a "sift-up" and "sift-down" process to rearrange the data by direct comparison of neighbors to result in a list of data sorted in ascending order. Each data point is either moved down or up from its initial "slot" in a method that has been compared to the retirement of an executive and the promotion of the next capable subordinate [258]. The method works by comparing the value of a datapoint at the halfway point from the first unsorted value from the top of a list to the bottom of the list. If this lower slotted point has a smaller value, then the algorithm takes the data in that first unsorted upper slot and puts it at the bottom of the heap of unsorted values. The algorithm then looks at the next two lower slots in the data list to see which one has a smaller value. The smaller one is put at the top of the heap and the comparisons are repeated. As the lowest value datapoints begin

filling in the top slots, the "half way" comparison point shifts down in the data list, decreasing the size of the unsorted heap. The process is repeated until there is only one data slot remaining, which will be filled with the largest valued datapoint.

B.3 Calculation of the Gradient of the Strain Energy Density

As presented in Chapter 4, the gradients of the nodal strain energy density, which were used in the surface node smoothing method code written for this work, were calculated using finite difference based discrete approximations [342] of $\frac{\partial SED}{\partial r}$, $\frac{\partial SED}{\partial \theta}$, and $\frac{\partial SED}{\partial z}$ based on the nodal values of the local strain energy density and the relative locations of the nodes themselves. Depending on the location and number of neighboring nodes, different approximations were implemented. For example, for all gradients in θ and for all gradients in z at nodal positions at least three nodes away from the ends of the optimizing surface, the approximations were fourth order accurate:

$$\frac{\partial SED(l)}{\partial \theta} = \frac{-SED(l+2)+8SED(l+1)-8SED(l-1)+SED(l-2)}{12\Delta\theta}$$

$$\frac{\partial SED(l)}{\partial z} = \frac{-SED(l+2)+8SED(l+1)-8SED(l-1)+SED(l-2)}{12\Delta z}$$

(B.11)

The ends of the optimizing surface were considered to be the top and bottom of the cylindrical growth region of the outer surface of the bone and the start of the cancellous filled region on the inner surface of the bone. To handle the gradients in z near the ends of the optimizing surface, other discrete approximations were necessary because there were no longer enough local nodes on either side of the desired node to compute the fourth-order accurate approximation. Specifically, for the last node at the

ends of the optimizing surface, a second order accurate approximation was used. For the bottom of the optimizing surface, the following approximation using the two nodes above the final row was implemented:

$$\frac{\partial SED(l)}{\partial z} = \frac{-3SED(l) + 4SED(l+1) - SED(l+2)}{2\Delta z}$$

(B.12)

For nodes at the top of the optimizing surface a similar approximation was made using the value at the top row and the two nodes lower this top row:

$$\frac{\partial SED(l)}{\partial z} = \frac{3SED(l) - 4SED(l-1) + SED(l-2)}{2\Delta z}$$

(B.13)

When nodes were one row in from the end surface, they still did not have enough nodes on either side to implement the fourth-order accurate method. In these situations, a central difference approximation was used:

$$\frac{\partial SED(l)}{\partial z} = \frac{SED(l+1) - SED(l-1)}{2\Delta z}$$

(B.14)

In the radial direction, only the gradients of the surface nodes were of interest. Therefore, Equation B.13 was applied:

$$\frac{\partial SED(l)}{\partial r} = \frac{3SED(l) - 4SED(l-1) + SED(l-2)}{2\Delta r}$$

(B.15)

For each of these gradients, the Δr, Δz, and $\Delta \theta$ terms were assumed to be the average distance between the neighboring nodes used in the calculation. This was

required because the mesh spacing was not always uniform. For example, in calculating

the gradient in the theta direction in Equation B.11:

$$\Delta\theta = \frac{1}{4}\left[\left(\theta(l)-\theta(l-1)\right)+\left(\theta(l-1)-\theta(l-2)\right)+\left(\theta(l+1)-\theta(l)\right)+\left(\theta(l+2)-\theta(l+2)\right)\right] \qquad \text{(B.16)}$$

And in calculating the central difference approximation in Equation B.14:

$$\Delta z = \frac{1}{2}\left[\left(z(l)-z(l-1)\right)+\left(z(l+1)-z(l)\right)\right] \qquad \text{(B.17)}$$

Similarly, in Equations B.13 and B.12 the Δz was calculated as Equations B.18 and B.19,

respectively :

$$\Delta z = \frac{1}{2}\left[\left(z(l)-z(l-1)\right)+\left(z(l-1)-z(l-2)\right)\right] \qquad \text{(B.18)}$$

$$\Delta z = \frac{1}{2}\left[\left(z(l+2)-z(l+1)\right)+\left(z(l+1)-z(l)\right)\right] \qquad \text{(B.19)}$$

REFERENCES

[1] Vander, A., Sherman, J., and Luciano, D., 1998, Human Physiology: The Mechanisms of Body Function, McGraw-Hill, New York, NY.

[2] Campbell, N. A., 1993, Biology, The Benjamin/Cummings Publishing Company, New York, NY.

[3] Roesler, H., 1981, "Some Historical Remarks on the Theory of Cancellous Bone Structure," Mechanical Properties of Bone at the Joint ASME-ASCE Applied Mechanics, Fluids Engineering and Bioengineering Conference, Boulder, Colorado June 22-24, 1981, S. C. Cowin, ed., American Society of Mechanical Engineers, Boulder, CO, pp. 27-42.

[4] Mattheck, C., 1990, "Design and Growth Rules for Biological Structures and Their Application to Engineering," Fatigue and Fracture of Engineering Materials and Structures, 13(5), pp. 535-550.

[5] Mattheck, C., 2006, "Teacher Tree: The Evolution of Notch Shape Optimization from Complex to Simple," Eng. Fract. Mech., 73(12), pp. 1732-1742.

[6] Archer, R. R., 1976, "On the Distribution of Tree Growth Stresses - Part II: Stresses Due to Asymmetric Growth Strains," Wood Science and Technology, 10(4), pp. 293-309.

[7] Archer, R. R., and Wilson, B. F., 1970, "Mechanics of the Compression Wood Response," Plant Physiol., 46, pp. 550-556.

[8] Zhang, S., Garbutt, V., and McBride, J. T., 1996, "Strain-Induced Growth of the Immature Lung," J. Appl. Physiol., 81(4), pp. 1471-1476.

[9] Cowan, M. J., and Crystal, R. G., 1975, "Lung Growth after Unilateral Pneumonectomy: Quantitation of Collagen Synthesis and Content," Am. Rev. Respir. Disease, 111, pp. 267-276.

[10] Fung, Y. C., 2004, Biomechanics: Mechanical Properties of Living Tissues, Springer, New York, NY.

[11] Humphrey, J. D., Eberth, J. F., Dye, W. W., and Gleason, R. L., 2009, "Fundamental Role of Axial Stress in Compensatory Adaptations by Arteries," J. Biomech., 42(1), pp. 1-8.

[12] Prior, B. M., Yang, H. T., and Terjung, R. L., 2004, "What Makes Vessels Grow with Exercise Training?," J. Appl. Physiol., 97(3), pp. 1119-1128.

[13] Currey, J. D., 2002, Bones: Structure and Mechanics, Princeton University Press, Princeton, NJ.

[14] Martin, R. B., Burr, D. B., and Sharkey, N. A., 1998, Skeletal Tissue Mechanics, Springer, New York, NY.

[15] Doblare, M., Garcia, J., and Gomez, M., 2004, "Modelling Bone Tissue Fracture and Healing: A Review," Eng. Fract. Mech., 71, pp. 1809-1840.

[16] Cowin, S. C., ed., 2008, Bone Mechanics Handbook, Informa Healthcare, New York, NY.

[17] Martin, R. B., and Burr, D., 1989, Structure, Function and Adaptation of Compact Bone., Raven Press, New York, NY.

[18] Roesler, H., 1987, "The History of Some Fundamental Concepts in Bone Biomechanics," J. Biomech., 20(11/12), pp. 1025-1034.

[19] Evans, F. G., 1973, Mechanical Properties of Bone, Charles C. Thomas, Springfield, IL.

[20] Frost, H. M., 2001, "From Wolff's Law to the Utah Paradigm: Insights About Bone Physiology and Its Clinical Applications," The Anatomical Record, 262, pp. 398-419.

[21] Cowin, S. C., ed., 1989, Bone Mechanics, CTC Press, Boca Raton, FL.

[22] Dequeker, J., 1971, "Periosteal and Endosteal Surface Remodeling in Pathologic Conditions," Invest. Radiol., 6(4), pp. 260-265.

[23] Milgrom, C., and Giladi, M., 1989, "The Area Moment of Inertia of the Tibia: A Risk Factor for Stress Fractures," J. Biomech., 22(11/12), pp. 1243-1248.

[24] Beck, T. J., Ruff, C. B., Mourtada, F. A., Shaffer, R. A., Maxwell-Williams, K., et al., 1996, "Dual-Energy X-Ray Absorptiometry Derived Structural Geometry for Stress Fracture Prediction in Male U.S. Marine Corp Recruits," J. Bone Miner. Res., 11(5), pp. 645-653.

[25] Ackerman, K. E., Putman, M., Guereca, G., Taylor, A. P., Pierce, L., et al., 2012, "Cortical Microstructure and Estimated Bone Strength in Young Amenorrheic Atheletes, Eumenorrheic Athletes and Non-Athletes," Bone Miner., 51, pp. 680-687.

[26] Crossley, K., Bennell, K. L., Wrigley, T., and Oakes, B., 1999, "Ground Reaction Forces, Bone Characteristics, and Tibial Stress Fracture in Male Runners," Med. Sci. Sports Exerc., 31(8), pp. 1088-1093.

[27] Frost, H. M., 2004, "A 2003 Update of Bone Physiology and Wolff S Law for Clinicians," Angle Orthod., 74(1), pp. 3-15.

[28] Ferretti, J. L., Frost, H. M., Gasser, J. A., High, W. B., Jee, W. S. S., et al., 1995, "Perspectives on Osteoporosis Research: Its Focus and Some Insights from a New Paradigm," Calcif. Tissue Int., 57(6), pp. 399-404.

[29] Frost, H. M., 2003, "Bone's Mechanostat: A 2003 Update," Anatomical Record - Part A Discoveries in Molecular, Cellular, and Evolutionary Biology, 275(2), pp. 1081-1101.

[30] Akkus, O., Polyakova-Akkus, A., Adar, F., and Schaffler, M. B., 2003, "Aging of Microstructural Compartments in Human Compact Bone," J. Bone Miner. Res., 18(6), pp. 1012-1019.

[31] Burr, D. B., 1997, "Muscle Strength, Bone Mass, and Age-Related Bone Loss," Journal of Bone and Mineral Research : The Official Journal of the American Society for Bone and Mineral Research, 12(10), pp. 1547-1551.

[32] Frost, H. M., 2000, "Muscle, Bone, and the Utah Paradigm: A 1999 Overview," Med. Sci. Sports Exerc., 32(5), pp. 911-917.

[33] Pavy-Le Traon, A., Heer, M., Narici, M. V., Rittweger, J., and Vernikos, J., 2007, "From Space to Earth: Advances in Human Physiology from 20 Years of Bed Rest Studies (1986-2006)," Eur. J. Appl. Physiol., 101, pp. 143-197.

[34] Rittweger, J., and Felsenberg, D., 2009, "Recovery of Muscle Atrophy and Bone Loss from 90 days Bed Rest: Results from a One-Year Follow-Up," Bone, 44(2), pp. 214-224.

[35] Evans, C. A., Robinson, J. A., Tate-Brown, J., Thumm, T., Crespo-Richey, J., et al., 2009, "International Space Station Science Research Accomplishments During the Assembly Years: An Analysis of Results from 2000-2008," Report No. NASA/TP-2009-213146-Revision A, NASA, Houston, TX.

[36] LeBlanc, A. D., Spector, E. R., Evans, H. J., and Sibonga, J. D., 2007, "Skeletal Responses to Space Flight and the Bed Rest Analog: A Review," Journal of Musculoskeletal Neuronal Interactions, 7(1), pp. 33-47.

[37] Oganov, V. S., 2004, "Modern Analysis of Bone Loss Mechanisms in Microgravity," Journal of Gravitational Physiology : a Journal of the International Society for Gravitational Physiology, 11(2).

[38] Sibonga, J. D., Cavanagh, P. R., Lang, T. F., LeBlanc, A. D., Schneider, V. S., et al., 2007, "Adaptation of the Skeletal System During Long-Duration Spaceflight," Clin. Rev. Bone. Miner. Metab., 5(4), pp. 249-261.

[39] Vico, L., Collet, P., Guignandon, A., Lafage-Proust, M. H., Thomas, T., et al., 2000, "Effects of Long-Term Microgravity Exposure on Cancellous and Cortical Weight-Bearing Bones of Cosmonauts," Lancet, 355(9215), pp. 1607-1611.

[40] LeBlanc, A. D., Lin, C., Shackelford, L. C., Sinitsyn, V., Evans, H., et al., 2000, "Muscle Volume, MRI Relaxation Times (T2), and Body Composition after Spaceflight," J. Appl. Physiol., 89(6), pp. 2158-2164.

[41] di Prampano, P. E., and Narici, M. V., 2003, "Muscles in Microgravity: From Fibres to Human Motion," J. Biomech., 36, pp. 403-412.

[42] Giangregorio, L., and Blimkie, C. J. R., 2002, "Skeletal Adaptations to Alterations in Weight-Bearing Activity: A Comparison of Models of Disuse Osteoporosis," Sports Med., 32(7), pp. 459-476.

[43] Covertino, V. A., 1989, "Considerations for an Exercise Prescription," Report No. 19910001272, NASA.

[44] Whalen, R., 1993, "Musculoskeletal Adaptation to Mechanical Forces on Earth and in Space," Physiologist, 36(1 Suppl), pp. S127-S130.

[45] Schneider, V., Oganov, V., LeBlanc, A., Rakmonov, A., Taggart, L., et al., 1995, "Bone and Body Mass Changes During Space Flight," Acta Astronaut., 36(8-12), pp. 463-466.

[46] Berg, H. E., Eiken, O., Miklavcic, L., and Mekjavic, I. B., 2007, "Hip, Thigh and Calf Muscle Atrophy and Bone Loss after 5-Week Bedrest Inactivity," Eur. J. Appl. Physiol., 99(3), pp. 283-289.

[47] Smith, S. M., Wastney, M. E., O'Brien, K. O., Morukov, B. V., Larina, I. M., et al., 2005, "Bone Markers, Calcium Metabolism, and Calcium Kinetics During Extended-Duration Space Flight on the Mir Space Station," J. Bone Miner. Res., 20(2), pp. 208-218.

[48] Cann, C. E., 2000, "Is Bone Loss in Space a Problem?," American Astronautical Society, Scientific Technology Series(97), pp. 71-84.

[49] Felbeck, D. K., and Atkins, A. G., 1984, Strength and Fracture of Engineering Solids, Prentice-Hall, Inc., Englewood Cliffs, NJ.

[50] Hawkey, A., 2007, "Low Magnitude, High Frequency Signals Could Reduce Bone Loss During Spaceflight," JBIS - Journal of the British Interplanetary Society, 60(8), pp. 278-284.

[51] Turner, C. H., 1991, "Homeostatic Control of Bone Structure: An Application of Feedback Theory," Bone, 12(3), pp. 203-217.

[52] Shackelford, L. C., LeBlanc, A. D., Driscoll, T. B., Evans, H. J., Rianon, N. J., et al., 2004, "Resistance Exercise as a Countermeasure to Disuse-Induced Bone Loss," J. Appl. Physiol., 97(1), pp. 119-129.

[53] Deitrick, J. E., Whedon, G. D., and Shorr, E., 1948, "Effects of Immobilization Upon Various Metabolic and Physiologic Functions of Normal Men," The American Journal of Medicine, 4(1), pp. 3-36.

[54] Jaworski, Z. F. G., Liskova-Kiar, M., and Uhthoff, H., K., 1980, "Effect of Long Term Immobilization on the Pattern of Bone Loss in Older Dogs," Journal of Bone and Joint Surgery - Series B, 62B(1), pp. 104-110.

[55] Uhthoff, H., K., and Jaworski, Z. F. G., 1978, "Bone Loss in Response to Long-Term Immobilisation," Journal of Bone and Joint Surgery - Series B, 60B, pp. 420-429.

[56] Spector, E. R., Smith, S. M., and Sibonga, J. D., 2009, "Skeletal Effects of Long-Duration Head-Down Bed Rest," Aviat. Space Environ. Med., 80(5), pp. A23-A28.

[57] Hert, J., Liskova, M., and Landa, J., 1971, "Reaction of Bone to Mechanical Stimuli. Part 1. Continuous and Intermittent Loading of Tibia in Rabbit," Folia Morphol. (Praha). 19(3), pp. 290-371.

[58] Liskova, M., and Hert, J., 1971, "Reaction of Bone to Mechanical Stimuli. Part 2. Periosteal and Endosteal Reaction of Tibial Diaphysis in Rabbit to Intermittent Loading," Folia Morphol. (Praha). 29(3), pp. 301-317.

[59] Lanyon, L. E., and Rubin, C. T., 1984, "Static Vs Dynamic Loads as an Invluence on Bone Remodelling," J. Biomech., 17(12), pp. 897-905.

[60] Lanyon, L. E., Goodship, A. E., Pye, C. J., and MacFie, J. H., 1982, "Mechanically Adaptive Bone Remodelling," J. Biomech., 15(3), pp. 141-154.

[61] Borer, K. T., and Kuhns, L. R., 1977, "Radiographic Evidence for Acceleration of Skeletal Growth in Adult Hamsters by Exercise," Growth, 41(1), pp. 1-13.

[62] Steinberg, M. E., and Trueta, J., 1981, "Effects of Activity on Bone Growth and Development in the Rat," Clin. Orthop. Relat. Res., No. 156, pp. 52-60.

[63] Woo, S. L.-Y., Kuei, S. C., Amiel, D., Gomez, M. A., Hayes, W. C., et al., 1981, "The Effect of Prolonged Physical Training on the Properties of Long Bone: A Study of Wolff's Law," Journal of Bone and Joint Surgery - Series A, 63A(5), pp. 780-787.

[64] Warner, S. E., Shea, J. E., Miller, S. C., and Shaw, J. M., 2006, "Adaptations in Cortical and Trabecular Bone in Response to Mechanical Loading with and without Weight Bearing," Calcif. Tissue Int., 79(6), pp. 395-403.

[65] Pearson, O. M., and Lieberman, D. E., 2004, "The Aging of Wolff's "Law": Ontogeny and Responses to Mechanical Loading in Cortical Bone," Yb Phys Anthrop, 47, pp. 68-99.

[66] Engelke, K., Kemmler, W., Lauber, D., Beeskow, C., Pintag, R., et al., 2006, "Exercise Maintains Bone Density at Spine and Hip. EFOPS: A 3-Year Longitudinal Study in Early Postmenopausal Women," Osteoporosis Int., 17(1), pp. 133-142.

[67] Guadalupe-Grau, A., Fuentes, T., Guerra, B., and Calbet, J. A. L., 2009, "Exercise and Bone Mass in Adults," Sports Med., 39(6), pp. 439-468.

[68] Vainionpaa, A., Korpelainen, R., Sievanen, H., Vihriala, E., Leppaluoto, J., et al., 2007, "Effect of Impact Exercise and Its Intensity on Bone Geometry at Weight-Bearing Tibia and Femur," Bone, 40, pp. 604-611.

[69] Nikander, R., Kannus, P., Dastidar, P., Hannula, M., Harrison, L., et al., 2009, "Targeted Exercises against Hip Fragility," Osteoporosis Int., 20(8), pp. 1321-1328.

[70] Greenleaf, J. E., Bulbulian, R., Bernauer, E. M., Haskell, W. L., and Moore, T., 1989, "Exercise-Training Protocols for Astronauts in Microgravity," J. Appl. Physiol., 67(6), pp. 2191-2204.

[71] Smith, S. M., Zwart, S. R., Heer, M., Lee, S. M. C., Baecker, N., et al., 2008, "Wise-2005: Supine Treadmill Exercise within Lower Body Negative Pressure and Flywheel Resistive Exercise as a Countermeasure to Bed Rest-Induced Bone Loss in Women During 60-Day Simulated Microgravity," Bone, 42(3), pp. 572-581.

[72] Bentley, J. R., Leach, M. A., McCleary, F., Smith, C., Norcross, J., et al., 2006, "Advanced Resistive Exercise Device (ARED) Man-in-the Loop Test (MILT)," Report No. NASA/TP-2006-213717, NASA, Houston, TX.

[73] Moore, A. D., Amonette, W., Bentley, J. R., Blazine, K. L., Loehr, J. A., et al., 2004, "Results of the International Space Station Interim Resistance Exercise Device Man-in-the-Loop Test," Report No. NASA/TP-2004-212062, NASA, Houston, TX.

[74] NASA Tech Briefs, 2007, "Article 2311: Advanced Resistive Device," http://www.techbriefs.com/component/content/article/2311, Accessed on 10/18/2009.

[75] English, K. L., Loehr, J. A., Lee, S. M. C., Laughlin, M. A., and Hagan, R. D., 2008, "Reliability of Strength Testing Using the Advanced Resistive Exercise Device and Free Weights," Report No. NASA/TP-2008-214782, NASA, Houston, TX.

[76] Keim, B., 2009, "High-Tech Weights for Space Workout," http://www.wired.com/wiredscience/2009/04/astromuscles2/, Accessed on 11/17/09.

[77] Ploutz-Snyder, L., 2009, "An Evidence-Based Approach to Exercise Prescriptions on ISS," Report No. JSC-18070 NASA, Houston, TX.

[78] LeBlanc, A., Matsumoto, T., Jones, J., Shapiro, J., Lang, T. F., et al., 2013, "Bisphosphonates as a Supplement to Exercise to Protect Bone During Long-Duration Spaceflight," Osteoporosis Int., 24(7), pp. 2105-2114.

[79] Smith, S. M., Heer, M. A., Shackelford, L. C., Sibonga, J. D., Ploutz-Snyder, L., et al., 2012, "Benefits for Bone from Resistance Exercise and Nutrition in Long-Duration Spaceflight: Evidence from Biochemistry and Densitometry," J. Bone Miner. Res., 27(9), pp. 1896-1906.

[80] Ruff, C., Holt, B., and Trinkaus, E., 2006, "Who's Afraid of the Big Bad Wolff?: "Wolff's Law" and Bone Functional Adaptation," Am. J. Phys. Anthropol., 129, pp. 484-498.

[81] Keaveny, T. M., Hoffmann, P. F., Singh, M., Palermo, L., Bilezikian, J. P., et al., 2008, "Femoral Bone Strength and Its Relation to Cortical and Trabecular Changes after Treatment with Pth, Alendronate, and Their Combination as Assessed by Finite Element Analysis of Quantitative Ct Scans," J. Bone Miner. Res., 23(12), pp. 1974-1982.

[82] Annicchiarico, W., Martinez, G., and Cerrolaza, M., 2007, "Boundary Elements and [Beta]-Spline Surface Modeling for Medical Applications," Appl. Math. Model., 31(2), pp. 194-208.

[83] Cai, R., Cai, S., Yang, X., and Lu, F., 1998, "A Novel Method of Structural Shape Optimization Coupling BEM with an Optimization Method Based on Biological Growth," Structural Optimization, 15(3-4), pp. 296-300.

[84] Sadegh, A. M., Luo, G. M., and Cowin, S. C., 1993, "Bone Ingrowth: An Application of the Boundary Element Method to Bone Remodeling at the Implant Interface," J. Biomech., 26(2), pp. 167-182.

[85] Cowin, S. C., 1987, "Bone Remodeling of Diaphyseal Surfaces by Torsional Loads: Theoretical Predictions," J. Biomech., 20(11-12), pp. 1111-1120.

[86] Cowin, S. C., and Firoozbakhsh, K., 1981, "Bone Remodeling of Diaphysial Surfaces under Constant Load: Theoretical Predictions," J. Biomech., 7, pp. 471-484.

[87] Cowin, S. C., and Van Buskirk, W. C., 1979, "Surface Bone Remodeling Induced by a Medullary Pin," J. Biomech., 12(4), pp. 269-276.

[88] Hart, R. T., Davy, D. T., and Heiple, K. G., 1984, "A Computational Method for Stress Analysis of Adaptive Elastic Materials with a View toward Applications in Strain-Induced Bone Remodeling," J. Biomech. Eng., 106(4), pp. 342-350.

[89] Cowin, S. C., Hart, R. T., Balser, J. R., and Kohn, D. H., 1985, "Functional Adaptation in Long Bones: Establishing in Vivo Values for Surface Remodeling Rate Coefficients," J. Biomech., 18(9), pp. 665-671.

[90] Huiskes, R., Weinans, H., Grootenboer, H. J., Dalstra, M., Fudala, B., et al., 1987, "Adaptive Bone-Remodeling Theory Applied to Prosthetic-Design Analysis," J. Biomech., 20(11-12), pp. 1135-1150.

[91] Beaupre, G. S., Orr, T. E., and Carter, D. R., 1990, "An Approach for Time-Dependent Bone Modeling and Remodeling - Theoretical Development," J. Orth. Res., 8, pp. 651-661.

[92] Van der Meulen, M. C. H., Beaupre, G. S., and Carter, D. R., 1993, "Mechanobiologic Influences in Long Bone Cross-Sectional Growth," Bone, 14, pp. 635-342.

[93] Levenston, M. E., Beaupre, G. S., and Carter, D. R., 1998, "Loading Mode Interactions in Simulations of Long Bone Cross-Sectional Adaptation," Comput. Methods Biomech. Biomed. Eng., 1(4), pp. 303-319.

[94] Mattheck, C., and Burkhardt, S., 1990, "A New Method of Structural Shape Optimization Based on Biological Growth," Int. J. Fatigue, 12(3), pp. 185-190.

[95] Mittlmeier, T., Mattheck, C., and Dietrich, F., 1994, "Effects of Mechanical Loading on the Profile of Human Femoral Diaphyseal Geometry," Med. Eng. Phys., 16(1), pp. 75-81.

[96] Brown, T. D., Pedersen, D. R., Gray, M. L., Brand, R. A., and Rubin, C. T., 1990, "Toward an Identification of Mechanical Parameters Initiating Periosteal Remodeling: A Combined Experimental and Analytic Approach," J. Biomech., 23(9), pp. 893-897.

[97] Gardner, T. N., Stoll, T., Marks, L., Mishra, S., and Knothe Tate, M., 2000, "The Influence of Mechanical Stimulus on the Pattern of Tissue Differentiation in a Long Bone Fracture -- an FEM Study," J. Biomech., 33(4), pp. 415-425.

[98] Pettermann, H. E., Reiter, T. J., and Rammerstorfer, F. G., 1997, "Computational Simulation of Internal Bone Remodeling," Archives of Computational Methods in Engineering, 4(4), pp. 295-323.

[99] Main, R. P., 2007, "Ontogenic Relationships between in Vivo Strain Environment, Bone Histomorphometry and Growth in the Goat Radius," J. Anat., 210, pp. 272-293.

[100] Judex, S., Gross, T. S., and Zernicke, R. F., 1997, "Strain Gradients Correlate with Sites of Exercise-Induced Bone-Forming Surfaces in the Adult Skeleton," J. Bone Miner. Res., 12(10), pp. 1737-1745.

[101] Luo, G., Cowin, S. C., Sadegh, A. M., and Arramon, Y. P., 1995, "Implementation of Strain Rate as a Bone Remodeling Stimulus," J. Biomech. Eng., 117(3), pp. 329-338.

[102] Xu, W., and Robinson, K., 2008, "X-Ray Image Review of Bone Remodeling around an Osseointegrated Trans-Femoral Implant and a Finite Element Simulation Case Study," Ann. Biomed. Eng., 36(3), pp. 435-443.

[103] Turner, C. H., Anne, V., and Pidaparti, R. M. V., 1997, "A Uniform Strain Criterion for Trabecular Bone Adaptation: Do Continuum-Level Strain Gradients Drive Adaptation?," J. Biomech., 30(6), pp. 555-563.

[104] Koontz, J. T., Charras, G. T., and Guldberg, R. E., 2001, "A Microstructural Finite Element Simulation of Mechanically Induced Bone Formation," J. Biomech. Eng., 123, pp. 607-612.

[105] Gross, T. S., Edwards, J. L., McLeod, K. J., and Rubin, C. T., 1997, "Strain Gradients Correlate with Sites of Periosteal Bone Foramtion," J. Bone Miner. Res., 12(6), pp. 982-988.

[106] Carter, D. R., 1984, "Mechanical Loading Histories and Cortical Bone Remodeling," Calcif. Tissue Int., 36(SUPPL. 1), pp. S19-S24.

[107] Guo, X.-D., and Cowin, S. C., 1992, "Periosteal and Endosteal Control of Bone Remodleing under Torsional Loading," J. Biomech., 12(6), pp. 645-650.

[108] Schulte, F. A., Ruffoni, D., Lambers, F. M., Christen, D., Webster, D. J., et al., 2013, "Local Mechanical Stimuli Regulate Bone Formation and Resorption in Mice at the Tissue Level," PLoS ONE, 8(4).

[109] Chen, G., Pettet, G., Pearcy, M., and McElwain, D. L. S., 2007, "Comparison of Two Numerical Approaches for Bone Remodelling," Med. Eng. Phys., 29(1), pp. 134-139.

[110] Jang, I. G., and Kim, I. Y., 2008, "Computational Study of Wolff's Law with Trabecular Architecture in the Human Proximal Femur Using Topology Optimization," J. Biomech., 41(11), pp. 2353-2361.

[111] Vossou, C. G., Savva, G. S., and Provatidis, C. G., 2008, "The Influence of Different Bone Remodeling Equations on a 2-D Vertebra Model in the Final Bone Density Distribution," 8th IEEE International Conference on BioInformatics and BioEngineering, BIBE 2008.

[112] Kumar, N. C., Dantzig, J. A., Jaisuk, I. M., Robling, A. G., and Turner, C. H., 2010, "Numerical Modeling of Long Bone Adaptation Due to Mechanical Loading: Correlation with Experiments," Ann. Biomed. Eng., 38(3), pp. 594-604.

[113] Kolda, T. G., Lewis, R. M., and Torczon, V., 2003, "Optimization by Direct Search: New Perspectives on Some Classical and Modern Methods," SIAM Review, 45(3), pp. 385-482.

[114] Fox, R. L., 1971, Optimization Methods for Engineering Design, Addison-Wesley Publishing Company, Reading, MA.

[115] Gallagher, R., and Zienkiewicz, O., eds., 1973, Optimal Structural Design: Theory and Applications, John Wiley and Sons, New York, NY.

[116] Marom, S. A., and Linden, M. J., 1990, "Computer Aided Stress Analysis of Long Bones Utilizing Computed Tomography," J. Biomech., 23(5), pp. 399-404.

[117] Viceconti, M., Testi, D., Taddei, F., Martelli, S., Clapworthy, G., et al., 2006, "Biomechanics Modeling of the Musculoskeletal Apparatus: Status and Key Issues," Proceedings of the IEEE, 94(4), pp. 725-739.

[118] Ezquerro, F., Simon, A., Prado, M., and Perez, A., 2004, "Combination of Finite Element Modeling and Optimization for the Study of Lumbar Spine Biomechanics Considering the 3d Thorax-Pelvis Orientation," Med. Eng. Phys., 26(1), pp. 11-22.

[119] Phillips, A. T. M., 2009, "The Femur as a Musculo-Skeletal Construct: A Free Boundary Condition Modelling Approach," Med. Eng. Phys., 31(6), pp. 673-680.

[120] Fischer, K. J., Jacobs, C. R., and Carter, D. R., 1995, "Computational Method for Determination of Bone and Joint Loads Using Bone Density Distributions," J. Biomech., 28(9), pp. 1127-1135.

[121] Fischer, K. J., Jacobs, C. R., Levenston, M. E., and Carter, D. R., 1996, "Different Loads Can Produce Similar Bone Density Distributions," Bone, 19(2), pp. 127-135.

[122] Bitsakos, C., Kerner, J., Fisher, I., and Amis, A. A., 2005, "The Effect of Muscle Loading on the Simulation of Bone Remodelling in the Proximal Femur," J. Biomech., 38(1), pp. 133-139.

[123] Speirs, A. D., Heller, M. O., Duda, G. N., and Taylor, W. R., 2007, "Physiologically Based Boundary Conditions in Finite Element Modelling," J. Biomech., 40(10), pp. 2318-2323.

[124] Jang, I. G., and Kim, I. Y., 2010, "Computational Simulation of Simultaneous Cortical and Trabecular Bone Change in Human Proximal Femur During Bone Remodeling," J. Biomech., 43(2), pp. 294-301.

[125] Sibonga, J. D., Evans, H. J., Sung, H. G., Spector, E. R., Lang, T. F., et al., 2007, "Recovery of Spaceflight-Induced Bone Loss: Bone Mineral Density after Long-Duration Missions as Fitted with an Exponential Function," Bone, 41, pp. 973-978.

[126] Wells, R., and Evans, N., 1987, "Functions and Recruitment Patterns of One- and Two-Joint Muscles under Isometric and Walking Conditions," Human Movement Science, 6(4), pp. 349-372.

[127] Pedotti, A., Krishnan, V. V., and Stark, L., 1978, "Optimization of Muscle-Force Sequencing in Human Locomotion," Math. Biosci., 38(1-2), pp. 57-76.

[128] McNeil, C. J., Raymer, G. H., Doherty, T. J., Marsh, G. D., and Rice, C. L., 2009, "Geometry of a Weight-Bearing and Non-Weight-Bearing Bone in the Legs of Young, Old and Very Old Men," Calcif. Tissue Int., 85, pp. 22-30.

[129] Allen, M. D., Johnstone, J., Rice, C. L., and Marsh, G. D., 2011, "Differences in Leg Bone Geometry in Young, Old and Very Old Women," Eur. J. Appl. Physiol., 111, pp. 2865-2871.

[130] Wilks, D. C., Winwood, K. L., Gulliver, S. F., Kwiet, A., Chatfield, M., et al., 2009, "Bone Mass and Geometry of the Tibia and the Radius of Master Sprinters, Middle and Long Distance Runners, Race-Walkers, and Sedentary Control Participants: A Pqct Study," Bone, 45, pp. 91-97.

[131] White, S. C., Yack, J., and Winter, D. A., 1989, "A Three-Dimensional Musculoskeletal Model for Gait Analysis, Anatomical Variability Estimates," J. Biomech., 22(8/9), pp. 885-893.

[132] Reynolds, H. M., Snow, C. C., and Young, J. W., 1981, "Spatial Geometry of the Human Pelvis," Report No. AAC-119-81-5, Protection and Survival Laboratory, Civil Aeromedical Institute, Mike Monroney Aeronautical Center, Federal Aviation Administration, Oklahoma City, OK.

[133] Weinhandl, J. T., and O'Connor, K. M., 2010, "Assessment of a Greater Trochanter-Based Method of Locating the Hip Joint Center," J. Biomech., 43.

[134] Högler, W., Blimkie, C. J. R., Cowell, C. T., Inglis, D., Rauch, F., et al., 2008, "Sex-Specific Developmental Changes in Muscle Size and Bone Geometry at the Femoral Shaft," Bone, 42(5), pp. 982-989.

[135] Stephenson, P., and Seedhom, B. B., 1999, "Cross-Sectional Geometry of the Human Femur in the Mid-Third Region," Proceedings of the Institution of Mechanical Engineers, Part H: Journal of Engineering in Medicine, 213(2), pp. 159-166.

[136] Stein, I. D., and Granik, G., 1979, "The Human Tibia: A Simplified Method of Radiographic Analysis of Its Cross-Section with Anthropometric Correlations," Ann. Biomed. Eng., 7, pp. 103-116.

[137] Évinger, S., Suhai, B., Bernáth, B., Gerics, B., Pap, I., et al., 2005, "How Does the Relative Wall Thickness of Human Femora Follow the Biomechanical Optima? An Experimental Study on Mummies," J. Exp. Biol., 208(5), pp. 899-905.

[138] Macdonald, H. M., Kontulainen, S. A., MacKelvie-O'Brien, K. J., Petit, M. A., Janssen, P., et al., 2005, "Maturity- and Sex-Related Changes in Tibial Bone Geometry, Strength and Bone-Muscle Strength Indices During Growth: A 20-Month Pqct Study," Bone, 36(6), pp. 1003-1011.

[139] Sommers, M. B., Fitzpatrick, D. C., Madey, S. M., Vande Zanderschulp, C., and Bottlang, M., 2007, "A Surrogate Long-Bone Model with Osteoporotic Material Properties for Biomechanical Testing of Fracture Implants," J. Biomech., 40(15), pp. 3297-3304.

[140] Varghese, B. A., Miller, M. E., and Hangartner, T. N., 2008, "Estimation of Bone Strength from Pediatric Radiographs of the Forearm," Journal of Musculoskeletal Neuronal Interactions, 8(4), pp. 379-390.

[141] ANSYS Inc., ANSYS, Version 12.0, Canonsburg, PA.

[142] Anatomical Chart Company, 2005, "Muscular System Anatomical Chart," Lippencott, Williams, and Wilkins, Baltimore, MD.

[143] Anatomical Chart Company, 2005, "Skeletal System Anatomical Chart," Lippencott, Williams, and Wilkins, Baltimore, MD.

[144] Anatomical Chart Company, 2005, "Hip and Knee Anatomical Chart," Lippencott, Williams, and Wilkins, Baltimore, MD.

[145] Raichlen, D. A., Armstrong, H., and Lieberman, D. E., 2011, "Calcaneus Length Determines Running Economy: Implications for Endurance Running Performance in Modern Humans and Neandertals," J. Hum. Evol., 60(3), pp. 299-308.

[146] Anatomical Chart Company, 2005, "Foot and Ankle Anatomical Chart," Lippencott, Williams, and Wilkins, Baltimore, MD.

[147] Mason, M., Belisle, A., Bonutti, P., Kolisek, F. R., Malkani, A., et al., 2006, "An Accurate and Reproducible Method for Locating the Joint Line During a Revision Total Knee Arthroplasty," J. Arthroplasty, 21(8), pp. 1147-1153.

[148] Heegaard, J. H., Leyvraz, P. F., and Hovey, C. B., 2001, "A Computer Model to Simulate Patellar Biomechanics Following Total Knee Replacement: The Effects of Femoral Component Alignment," Clin. Biomech., 16(5), pp. 415-423.

[149] Fernandez, J. W., and Hunter, P. J., 2005, "An Anatomically Based Patient-Specific Finite Element Model of Patella Articulation: Towards a Diagnostic Tool," Biomechanics and Modeling in Mechanobiology, 4(1), pp. 20-38.

[150] 2004, "ANSYS Contact Technology Guide: ANSYS Release 9.0," ANSYS, Inc., Canonsburg, PA.

[151] Nigg, B. M., and Herzog, W., eds., 2006, Biomechanics of the Musculo-Skeletal System, John Wiley and Sons, New York, NY.

[152] Brand, R. A., Crowninshield, R. D., Wittstock, C. E., Pedersen, D. R., Clark, C. R., et al., 1982, "A Model of the Lower Extremity Muscular Anatomy," J. Biomech. Eng., 104, pp. 304-310.

[153] Anderson, F. C., and Pandy, M. G., 2001, "Static and Dynamic Optimization Solutions for Gait Are Practically Equivalent," J. Biomech., 34(2), pp. 153-161.

[154] Erdemir, A., McLean, S., Herzog, W., and van den Bogert, A. J., 2007, "Model-Based Estimation of Muscle Forces Exerted During Movements," Clin. Biomech., 22(2), pp. 131-154.

[155] Pandy, M. G., 2001, "Computer Modeling and Simulation of Human Movement," Annu. Rev. Biomed. Eng., 3, pp. 245-273.

[156] Yamaguchi, G. T., 2001, Dynamic Modeling of Musculoskeletal Motion, Klower Academic Publishers, Boston, MA.

[157] Trent, P. S., Walker, P. S., and Wolf, B., 1976, "Ligament Length Patterns, Strength and Rotation Axes of the Knee Joint," Clinical Orthopedics, 117, pp. 263-270.

[158] Maganaris, C. N., Reeves, N. D., Rittweger, J., Sargeant, A. J., Jones, D. A., et al., 2006, "Adaptive Response of Human Tendon to Paralysis," Muscle Nerve, 33(1), pp. 85-92.

[159] Arampatzis, A., Karamanidis, K., and Albracht, K., 2007, "Adaptational Responses of the Human Achilles Tendon by Modulation of the Applied Cyclic Strain Magnitude," J. Exp. Biol., 210(15), pp. 2743-2753.

[160] Seireg, A., and Arvikar, R. J., 1973, "A Mathematical Model for the Evaluation of Forces in Lower Extremeties of Teh Musculo-Skeletal System," J. Biomech., 8, pp. 313-326.

[161] Mow, V., and Hayes, W., 1997, "Basic Orthopedic Biomechanics," Lippencott-Ravin, New York, NY.

[162] Brand, R. A., Pedersen, D. R., and Friederich, J. A., 1986, "The Sensitivity of Muscle Force Predictions to Changes in Physiologic Cross-Sectional Area," J. Biomech., 19(8), pp. 589-596.

[163] Raikova, R. T., and Prilutsky, B. I., 2001, "Sensitivity of Predicted Muscle Forces to Parameters of the Optimization-Based Human Leg Model Revealed by Analytical and Numerical Analyses," J. Biomech., 34(10), pp. 1243-1255.

[164] Pierrynowski, M. R., 1982, "A Physiological Model for the Solution of Individual Muscle Forces During Normal Human Walking," Ph.D. Dissertation, Simon Fraser University, Vancouver, B.C., Canada.

[165] Wickiewicz, T. L., Roy, R. R., and Powell, P. L., 1984, "Muscle Architecture and Force-Velocity Relationships in Humans," Journal of Applied Physiology Respiratory Environmental and Exercise Physiology, 57(2), pp. 435-443.

[166] Friederich, J. A., and Brand, R. A., 1990, "Muscle Fiber Architecture in the Human Lower Limb," J. Biomech., 23(1), pp. 91-95.

[167] Yamaguchi, G. T., Sawa, A. G. U., Moran, D. W., Fessler, M. J., and Winters, J. M., 1990, "A Survey of Humon Musculotendon Actuator Parameters " Multiple Muscle Systerms: Biomechanics and Movement Organization, J. M. Winters, and L. Y. Woo, eds., Springer Verlag, Berlin, Germany, pp. 718-773.

[168] Fukunaga, T., Roy, R. R., Shellock, F. G., Hodgson, J. A., Day, M. K., et al., 1992, "Physiological Cross-Sectional Area of Human Leg Muscles Based on Magnetic Resonance Imaging," J. Orth. Res., 10(6), pp. 926-934.

[169] Akima, H., Kuno, S., Suzuki, Y., Gunji, A., and Fukunaga, T., 1997, "Effects of 20 Days of Bed Rest on Physiological Cross-Sectional Area of Human Thigh and Leg Muscles Evaluated by Magnetic Resonance Imaging," Journal of gravitational physiology : a journal of the International Society for Gravitational Physiology, 4(1), pp. S15-21.

[170] Prilutsky, B. I., and Gregor, R. J., 1997, "Strategy of Coordination of Two- and One-Joint Leg Muscles in Controlling an External Force," Motor Control, 1, pp. 92-116.

[171] Horsman, M. D. K., Koopman, H. F. J. M., Van der Helm, F. C. T., Prose, L. P., and Veeger, H. E. J., 2007, "Morphological Muscle and Joint Parameters for Musculoskeletal Modelling of the Lower Extremity," Clin. Biomech., 22, pp. 239-247.

[172] PTC, Pro/Engineer, Wildfile 4.0, Needham, MA.

[173] An, K. N., Takahashi, K., Harrigan, T. P., and Chao, E. Y., 1984, "Determination of Muscle Orientation and Moment Arms," J. Biomech. Eng., 106, pp. 280-282.

[174] Bobbert, M. F., and van Ingen Schenau, G. J., 1988, "Coordination in Vertical Jumping," J. Biomech., 21, pp. 249-262.

[175] Visser, J. J., Hoogkamer, J. E., Bobbert, M. F., and Huijing, P. A., 1990, "Length and Moment Arm of Human Leg Muscles as a Function of Knee and Hip-Joint Angles," Eur. J. Appl. Physiol., 61, pp. 453-460.

[176] Knets, I., 2002, "Peculiarities of the Structure and Mechanical Properties of Biological Tissues," Meccanica, 37(4-5), pp. 375-384.

[177] Ascenzi, A., and Bonucci, E., 1976, "Mechanical Similarities between Alternate Osteons and Cross Ply Laminates," J. Biomech., 9(2), pp. 65-71.

[178] Reilly, D. T., and Burstein, A. H., 1974, "The Mechanical Properties of Cortical Bone," Journal of Bone and Joint Surgery - Series A, 56(5), pp. 1001-1022.

[179] Carter, D. R., and Hayes, W. C., 1977, "Compact Bone Fatigue Damage. A Microscopic Examination," Clin. Orthop. Relat. Res., NO. 127, pp. 265-274.

[180] Viceconti, M., Testi, D., Taddei, F., Martelli, S., Clapworthy, G. J., et al., 2006, "Biomechanics Modeling of the Musculoskeletal Apparatus: Status and Key Issues," Proceedings of the IEEE, 94(4), pp. 725-738.

[181] Main, R. P., 2007, "Ontogenetic Relationships between in Vivo Strain Environment, Bone Histomorphometry and Growth in the Goat Radius," J. Anat., 210(3), pp. 272-293.

[182] Winwood, K. L., Zioupos, P., Currey, J. D., Cotton, J. R., and Taylor, M., 2006, "The Importance of the Elastic and Plastic Components of Strain in Tensile and Compressive Fatigue of Human Cortical Bone in Relation to Orthopaedic Biomechanics," Journal of Musculoskeletal Neuronal Interactions, 6(2), pp. 134-141.

[183] Hoffmeister, B. K., Smith, S. R., Handley, S. M., and Rho, J. Y., 2000, "Anisotropy of Young's Modulus of Human Tibial Coritcal Bone," Med. Biol. Eng. Comput., 38, pp. 333-338.

[184] Ebacher, V., Tang, C., Mc Kay, H., Oxland, T. R., Guy, P., et al., 2007, "Strain Redistribution and Cracking Behavior of Human Bone During Bending," Bone, 40, pp. 1265-1275.

[185] Dong, X. N., and Guo, X. E., 2004, "The Dependence of Transversely Isotropic Elasticity of Human Femoral Cortical Bone on Porosity," J. Biomech., 37(8), pp. 1281-1287.

[186] Ugural, A. C., and Fenster, S. K., 1995, Advanced Strength and Applied Elasticity, Prentice Hall PTR, Upper Saddle River, NJ.

[187] Gonzalez, O., and Stuart, A. M., 2008, A First Course in Continuum Mechanics, Cambridge University Press, New York, NY.

[188] Holzapfel, G. A., 2000, Nonlinear Solid Mechanics: A Continuum Approach for Engineering, John Wiley and Sons, New York, NY.

[189] Moran, M. J., and Shapiro, H. N., 1996, Fundamentals of Engineering Thermodynamics, John Wiley and Sons, New York, NY.

[190] Moaveni, S., 2008, Finite Element Analysis: Theory and Application with ANSYS, Prentice Hall, Upper Saddle River, NJ.

[191] Ghista, D. N., Toridis, T. G., and Srinivasan, T. M., 1976, "Human Gait Analysis: Determination of Instantaneous Joint Reactive Forces, Muscle Forces and the Stress Distribution in Bone Segments. Part II," Biomed. Tech. (Berl). 21(3), pp. 66-74.

[192] Dul, J., Townsend, M. A., Shiavi, R., and Johnson, G. E., 1984, "Muscular Synergism--I. On Criteria for Load Sharing between Synergistic Muscles," J. Biomech., 17(9), pp. 663-673.

[193] Crowninshield, R. D., and Brand, R. A., 1981, "A Physiologically Based Criterion of Muscle Force Prediction in Locomotion," J. Biomech., 14(11), pp. 793-801.

[194] Herzog, W., and Leonard, T. R., 1991, "Validation of Optimization Models That Estimate the Forces Exerted by Synergistic Muscles," J. Biomech., 24(Supplement 1), pp. 31-39.

[195] Kaufman, K. R., An, K. N., Litchy, W. J., and Chao, E. Y. S., 1991, "Physiological Prediction of Muscle Forces - I. Theoretical Formulation," Neuroscience, 40(3), pp. 781-792.

[196] Pedersen, D. R., Brand, R. A., Cheng, C., and Arora, J. S., 1987, "Direct Comparison of Muscle Force Predictions Using Linear and Nonlinear Programming," J. Biomech. Eng., 109, pp. 192-199.

[197] Arjmand, N., and Shirazi-Adl, A., 2006, "Sensitivity of Kinematics-Based Model Predictions to Optimization Criteria in Static Lifting Tasks," Med. Eng. Phys., 28(6), pp. 504-514.

[198] Buchanan, T. S., and Shreeve, D. A., 1996, "An Evaluation of Optimization Techniques for the Prediction of Muscle Activation Patterns During Isometric Tasks," J. Biomech. Eng., 118(4), pp. 565-574.

[199] Li, G., Kaufman, K. R., Chao, E. Y. S., and Rubash, H. E., 1999, "Prediction of Antagonistic Muscle Forces Using Inverse Dynamic Optimization During Flexion/Extension of the Knee," J. Biomech. Eng., 121(3), pp. 316-322.

[200] Cowin, S. C., and Hegedus, D. H., 1976, "Bone Remodeling I: Theory of Adaptive Elasticity," Journal of Elasticity, 6(3), pp. 313-326.

[201] Baiotto, S., and Zidi, M., 2004, "Theoretical and Numerical Study of a Bone Remodeling Model: The Effect of Osteocyte Cells Distribution," Biomechanics and Modeling in Mechanobiology, 3(1), pp. 6-16.

[202] Mullender, M. G., Huiskes, R., and Weinans, H., 1994, "A Physiological Approach to the Simulation of Bone Remodeling as a Self-Organizational Control Process," J. Biomech., 27(11), pp. 1389-1394.

[203] Haftka, R. T., Gurdal, Z., and Kamat, M. P., 1990, Elements of Structural Optimization, Kluwer Academic Publishers, Boston, MA.

[204] Imam, M. H., 1982, "Three-Dimensional Shape Optimization," International Journal for Numerical Methods in Engineering, 18(5), pp. 661-673.

[205] Mattheck, C., Baumgartner, A., and Walther, F., 1994, "Optimization Procedures by Use of the Finite Element Method," American Society of Mechanical Engineers, Petroleum Division (Publication) PD, A. Faghri, and M. A. Yaghoubi, eds., Publ by ASME, London, Engl, pp. 27-32.

[206] Chen, G., Pettet, G. J., Pearcy, M., and McElwain, D. L. S., 2007, "Modelling External Bone Adaptation Using Evolutionary Structural Optimisation," Biomechanics and Modeling in Mechanobiology, 6(4), pp. 275-285.

[207] Ding, Y., 1986, "Shape Optimization of Structures: A Literature Survey," Computers and Structures, 24(6), pp. 985-1004.

[208] Sonmez, F. O., 2007, "Shape Optimization of 2d Structures Using Simulated Annealing," Computational Methods in Applied Mechanics and Engineering, 196, pp. 3279-3299.

[209] Meske, R., Sauter, J., and Schnack, E., 2005, "Nonparametric Gradient-Less Shape Optimization for Real-World Applications," Structural and Multidisciplinary Optimization, 30(3), pp. 201-218.

[210] Burr, D. B., Martin, R. B., Schaffler, M. B., and Radin, E. L., 1985, "Bone Remodelling in Response to in Vivo Fatigue Microdamage," J. Biomech., 18(3), pp. 189-200.

[211] Umetani, Y., and Hirai, S., 1975, "An Adaptive Shape Optimization Method for Structural Material Using the Growing-Reforming Procedure," The 1975 Joint JSME-ASME Applied Mechanics Western Conference, The Japan Society of Mechanical Engineers, Ilikai Hotel, Honolulu, Hawaii, pp. 359-365.

[212] Schnack, E., 1979, "Optimization Procedure for Stress Concentrations by the Finite Element Technique," International Journal for Numerical Methods in Engineering, 14(1), pp. 115-124.

[213] Le, C., Bruns, T., and Tortorelli, D., 2011, "A Gradient-Based Parameter-Free Approach to Shape Optimization," Computational Methods in Applied Mechanics and Engineering, 200, pp. 985-996.

[214] Carter, D. R., van der Meulen, M. C. H., and Beaupre, G. S., 1996, "Mechanical Factors in Bone Growth and Development," Bone, 18(1), pp. 5S-10S.

[215] Warden, S. J., Hurst, J. A., Sanders, M. S., Turner, C. H., Burr, D. B., et al., 2005, "Bone Adaptation to a Mechanical Loading Program Significantly Increases Skeletal Fatigue Resistance," J. Bone Miner. Res., 20(5), pp. 809-816.

[216] Carpenter, R. D., and Carter, D. R., 2008, "The Mechanobiological Effects of Periosteal Surface Loads," Biomechanics and Modeling in Mechanobiology, 7, pp. 227-242.

[217] Robling, A. G., Hinant, F. M., Burr, D., and Turner, C. H., 2002, "Improved Bone Structure and Strength after Long-Term Mechanical Loading Is Greatest If Loading Is Separated into Short Bouts," J. Bone Miner. Res., 17(8), pp. 1545-1554.

[218] Armelagos, G. J., Mielke, J. H., Owen, K. H., Van Gerven, D. P., Dewey, J. R., et al., 1972, "Bone Growth and Development in Prehistoric Populations from Sudanese Nubia," J. Hum. Evol., 1(1).

[219] Carlson, D. S., Armelagos, G. J., and Van Gervan, D. P., 1976, "Patterns of Age Related Cortical Bone Loss (Osteoporosis) within the Femoral Diaphysis," Hum. Biol., 48(2), pp. 295-314.

[220] Lazenby, R. A., 1990, "Continuing Periosteal Apposition II: The Significance of Peak Bone Mass, Strain Equilibrium, and Age-Related Activity Differentials for Mechanical Compensation in Human Tubular Bones," Am. J. Phys. Anthropol., 82(4), pp. 473-484.

[221] Warden, S. J., Galley, M. R., Richard, J. S., George, L. A., Dirks, R. C., et al., 2013, "Reduced Gravitational Loading Does Not Account for the Skeletal Effect of Botulinum Toxin-Induced Muscle Inhibition Suggesting a Direct Effect of Muscle on Bone," Bone, 54(1), pp. 98-105.

[222] Zlatkin, M. B., Bjorkengren, A., Sartoris, D. J., and Resnick, D., 1987, "Stress Fractures of the Distal Tibia and Calcaneus Subsequent to Acute Fractures of the Tibia and Fibula," AJR. Am. J. Roentgenol., 149, pp. 329-332.

[223] Speed, C. A., Fordham, J. N., and Cunningham, J. L., 1996, "Simultaneous Bilateral Tibial Stress Fractures in a 15-Year-Old Milkman- a Case Report," Br. J. Rheumatol., 35(9), pp. 905-907.

[224] Orava, S., Puranen, J., and Ala-Ketola, L., 1978, "Stress Fractures Caused by Physical Exercise," Acta Orthop. Scand., 49, pp. 19-27.

[225] Milgrom, C., Giladi, M., Simkin, A., Rand, N., Kedem, R., et al., 1998, "Analysis of Biomechanical Mechanisms of Tibial Stress Fractures among Israeli Infantry Recruits," Clin. Orthop. Relat. Res., 231, pp. 216-221.

[226] Milgrom, C., Giladi, M., Simkin, A., Rand, N., Kedem, R., et al., 1989, "The Area Moment of Inertia of the Tibia: A Risk Ractor for Stress Fractures," J. Biomech., 22(11/12), pp. 1243-1248.

[227] Giladi, M., Ahronson, Z., and Stein, M., 1985, "Unusual Distribution and Onset of Stress Fractures in Soldiers," Clin. Orthop. Relat. Res., 192, pp. 142-146.

[228] Crossley, K., Bennell, K. L., Wrigley, T., and Oakes, B. W., 1999, "Ground Reaction Forces, Bone Characteristics, and Tibial Stress Fracture in Male Runners," Med. Sci. Sports Exerc., 31(8), pp. 1088-1093.

[229] Ross, R. A., and Allsopp, A., 2002, "Stress Fractures in Royal Marines Recruits," Mil. Med., 167(7), pp. 560-565.

[230] Gross, D. L., and Gross, M. T., 2012, "A Review of Mechanics and Injury Trends among Various Running Styles," The United States Army Medical Department Journal, July - September 2012, pp. 62-71.

[231] Milgrom, C., Finestone, A., Levi, Y., Simkin, A., Ekenman, I., et al., 2000, "Do High Impact Exercises Produce Higher Tibial Strains Than Running?," Br. J. Sports Med., 34(3), pp. 195-199.

[232] Burr, D. B., 1997, "Bone, Exercise, and Stress Fractures," Exerc. Sport Sci. Rev., 25, pp. 171-194.

[233] Phuah, A. H., Schache, A. G., Crossley, K., Wrigley, T., and Creaby, M. W., 2010, "Sagittal Plane Bending Moments Acting on the Lower Leg During Running," Gait Posture, 31, pp. 218-222.

[234] Creaby, M. W., and Dixon, S. J., 2008, "External Frontal Plane Loads May Be Associated with Tibia Stress Fracture," Med. Sci. Sports Exerc., 40(9), pp. 1669-1674.

[235] Scott, S., and Winter, D. A., 1990, "Internal Forces at Chronic Running Injury Sites," Med. Sci. Sports Exerc., 22(3), pp. 357-369.

[236] Cavanagh, P. R., 1987, "The Biomechanics of Lower Extremity Action in Distance Running," Foot Ankle, 7(4), pp. 197-217.

[237] Miller, R. H., Caldwell, G. E., Van Emmerik, R. E. A., Umberger, B. R., and Hamill, J., 2009, "Ground Reaction Forces and Lower Extremity Kinematics When Running with Suppressed Arm Swing," J. Biomech. Eng., 131(12).

[238] Bus, S. A., 2003, "Ground Reaction Forces and Kinematics in Distance Running in Older-Aged Men," Med. Sci. Sports Exerc., 35(7), pp. 1167-1175.

[239] Munro, C. F., Miller, D. I., and Fuglevand, A. J., 1987, "Ground Reaction Forces in Running: A Reexamination," J. Biomech., 20(2), pp. 147-155.

[240] De Wit, B., De Clercq, D., and Aerts, P., 2000, "Biomechanical Analysis of the Stance Phase During Barefoot and Shod Running," J. Biomech., 33(3), pp. 269-278.

[241] Winter, D. A., 1983, "Moments of Force and Mechanical Power in Jogging," J. Biomech., 16(1), pp. 91-97.

[242] Bresler, B., and Frankel, J. P., 1950, "The Forces and Moments in the Leg During Level Walking," Transactions of the ASME, 72, pp. 27-36.

[243] Wells, R., 1981, "The Projection of the Ground Reaction Force as a Predictor of Internal Joint Moments," Bull. Prosthet. Res., 18(1), pp. 15-19.

[244] Cavanagh, P. R., and Laforture, M. A., 1980, "Ground Reaction Forces in Distance Running," J. Biomech., 13, pp. 397-406.

[245] Winter, D. A., 1990, Biomechanics and Motor Control of Human Movement, John Wiley and Sons, Inc., New York, NY.

[246] Dul, J., Johnson, G. E., Shiavi, R., and Townsend, M. A., 1984, "Muscular Synergism--II. A Minimum-Fatigue Criterion for Load Sharing between Synergistic Muscles," J. Biomech., 17(9), pp. 675-684.

[247] Goel, V. K., Kong, W., Han, J. S., Weinstein, J. N., and Gilbertson, L. G., 1993, "A Combined Finite Element and Optimization Investigation of Lumbar Spine Mechanics with and without Muscles," Spine, 18(12), pp. 1531-1541.

[248] Van Bolhuis, B. M., and Gielen, C. C. A. M., 1999, "A Comparison of Models Explaining Muscle Activation Patterns for Isometric Contractions," Biol. Cybern., 81(3), pp. 249-261.

[249] Herzog, W., and Binding, P., 1992, "Predictions of Antagonistic Muscular Activity Using Nonlinear Optimization," Math. Biosci., 111, pp. 217-229.

[250] Herzog, W., 1987, "Individual Muscle Force Estimations Using a Non-Linear Optimal Design," J. Neurosci. Methods, 21(2-4), pp. 167-179.

[251] Kreyszig, E., 1999, Advanced Engineering Mathematics, John Wiley and Sons, New York, NY.

[252] Venkataraman, P., 2002, Applied Optimization with MATLAB Programming, John Wiley and Sons, New York, NY.

[253] Haug, E. J., and Arora, J. S., 1979, Applied Optimal Design: Mechanical Structures and Systems, John Wiley and Sons, New York, NY.

[254] Gill, P. E., Murray, W., and Wright, M. H., 1986, Practical Optimization, Elsevier Academic Press, New York, NY.

[255] Mathworks Inc., 2008, Matlab 2008a Documentation.

[256] Mathworks Inc., 2009, MATLAB, 2009a, Natick, MA.

[257] Rosen, J. B., 1960, "The Gradient Projection Method for Nonlinear Programming Part 1. Linear Constraints," Journal of the Society for Industrial and Applied Mathematics, 8(1), pp. 181-217.

[258] Press, W. H., Flannery, B. P., Teukolsky, S. A., and Vetterling, W. T., 1986, Numerical Recipes: The Art of Scientific Computing, Cambridge University Press, New York, NY.

[259] Raikova, R. T., and Prilutsky, B. I., 2001, Static Optimization MATLAB Source Code, http://www.clbme.bas.bg/projects/motco/.

[260] Christensen, P. W., and Klarbring, A., 2009, An Introduction to Structural Optimization, Springer.

[261] Haftka, R. T., and Grandhi, R. V., 1986, "Structural Shape Optimization - a Survey," Computer Methods in Applied Mechanics and Engineering, 57, pp. 91-106.

[262] Kuhl, E., Menzel, A., and Steinmann, P., 2003, "Computational Modeling of Growth," Compuatational Mechanics, 32, pp. 71-88.

[263] Gerhard, F. A., Webster, D. J., Van Lenthe, G. H., and Muller, R., 2009, "In Silico Biology of Bone Modelling and Remodelling: Adaptation," Philosophical Transactions of the Royal Society A: Mathematical, Physical and Engineering Sciences, 367(1895), pp. 2011-2030.

[264] Jacobs, C. R., Simo, J. C., Beaupre, G. S., and Carter, D. R., 1997, "Adaptive Bone Remodeling Incorporating Simultaneous Density and Anisotropy Considerations," J. Biomech., 30(6), pp. 603-613.

[265] Jang, I. G., Kim, I. Y., and Kwak, B. M., 2009, "Analogy of Strain Energy Density Based Bone-Remodeling Algorithm and Structural Topology Optimization," J. Biomech. Eng., 131(1), pp. 011012-011017.

[266] Fischer, K. J., Jacobs, C. R., Levenston, M. E., and Carter, D. R., 1997, "Observations of Convergence and Uniqueness of Node-Based Bone Remodeling Simulations," Ann. Biomed. Eng., 25, pp. 261-268.

[267] Harrigan, T. P., and Hamilton, J. J., 1992, "An Analytical and Numerical Study of the Stability of Bone Remodelling Theories: Dependence on Microstructural Stimulus," J. Biomech., 25(5), pp. 477-488.

[268] Jacobs, C. R., Levenston, M. E., Beaupré, G. S., Simo, J. C., and Carter, D. R., 1995, "Numerical Instabilities in Bone Remodeling Simulations: The Advantages of a Node-Based Finite Element Approach," J. Biomech., 28(4), pp. 449-459.

[269] Zienkiewicz, O. C., and Campbell, J. S., 1973, "Shape Optimization and Sequential Linear Programming," Optimum Structural Design: Theory and Applications, R. H. Gallagher, and O. C. Zienkiewicz, eds., Wiley, New York, NY.

[270] Ramakrishnan, C. V., and Francavilla, A., 1975, "Structural Shape Optimization Using Penalty Functions," Journal of Structural Mechanics, 3(4), pp. 403-422.

[271] Bennett, J. A., and Botkin, M. E., 1985, "Structural Shape Optimization with Geometric Description and Adaptive Mesh Refinement," AIAA J., 23(3), pp. 458-465.

[272] Belegundu, A. D., and Rajan, S. D., 1988, "A Shape Optimization Approach Based on Natural Design Variables and Shape Functions," Computer Methods in Applied Mechanics and Engineering, 66(1), pp. 87-106.

[273] Chang, K.-H., and Choi, K. K., 1992, "An Error Analysis and Mesh Adapation Method for Shape Design of Structural Components," Computers and Structures, 44(6), pp. 1275-1289.

[274] Banichuk, N. V., Barthold, F. J., Falk, A., and Stein, E., 1995, "Mesh Refinement for Shape Optimization," Structural Optimization, 9(1), pp. 46-51.

[275] Banichuk, N. V., Barthold, F. J., Falk, A., and Stein, E., 1996, "Finite Element Analysis with Mesh Refinement for Shape Optimization," Control and Cybernetics, 25(3), pp. 657-664.

[276] Zhang, S., and Belegundu, A. D., 1993, "Mesh Distortion Control in Shape Optimization," AIAA J., 31(7), pp. 1360-1362.

[277] Schleupen, A., Maute, K., and Ramm, E., 2000, "Adaptive Fe-Procedures in Shape Optimization," Structural and Multidisciplinary Optimization, 19(4), pp. 282-302.

[278] Wilke, D. N., Kok, S., and Groenwold, A. A., 2006, "A Quadratically Convergent Unstructured Remeshing Strategy for Shape Optimization," International Journal for Numerical Methods in Engineering, 65, pp. 1-17.

[279] Francavilla, A., Ramakrishnan, C. V., and Zienkiewicz, O. C., 1975, "Optimization of Shape to Minimize Stress Concentration," Journal of Strain Analysis 10(2), pp. 63-70.

[280] Quea, J. P., and Trompette, P., 1980, "Two-Dimensional Shape Optimization by the Finite Element Method," International Journal for Numerical Methods in Engineering, 15, pp. 1603-1612.

[281] Heller, M., Kaye, R., and Rose, L. R. F., 1999, "Gradientless Finite Element Procedure for Shape Optimization," J. Strain Anal. Eng. Des., 34(5), pp. 323-336.

[282] Tortorelli, D., and Wang, Z., 1993, "A Systematic Approach to Shape Sensitivity Analysis," International Journal of Solids and Structures, 30(9), pp. 1181-1212.

[283] van Keulen, F., Haftka, R. T., and Kim, N. H., 2005, "Review of Options for Structural Design Sensitivity Analysis. Part 1: Linear Systems," Computer Methods in Applied Mechanics and Engineering, 194, pp. 3213-3243.

[284] Hsu, Y.-L., 1994, "A Review of Structural Shape Optimization," Computers in Industry, 26, pp. 3-13.

[285] Archer, R. R., and Byrnes, F. E., 1974, "On the Distribution of Tree Growth Stresses - Part I: An Anisotropic Plane Strain Theory," Wood Science and Technology, 8(3), pp. 184-196.

[286] Archer, R. R., and Wilson, B. F., 1982, "Apical Control of Branch Movements in White Pine: Compression Wood Action," Wood Science and Technology, 16(3), pp. 181-191.

[287] Martinez, G., and Cerrolaza, M., 2003, "External Bone Remodeling Using the Boundary Element Method," Biomechanica Acta Cientifica Venezolana, 54, pp. 76-84.

[288] Krishnapillai, K., and Jones, R., 2009, "Structural Optimisation of 3d Damage Tolerant Components Comparing the Biological and Genetic Algorithm Solutions," Eng. Failure Anal., 16(3), pp. 713-727.

[289] Tekkaya, A. E., and Guneri, A., 1996, "Shape Optimization with the Biological Growth Method: A Parameter Study," Engineering Computations (Swansea, Wales), 13(8), pp. 4-18.

[290] Wessel, C., Cisilino, A., and Sensale, B., 2004, "Structural Shape Optimisation Using Boundary Elements and the Biological Growth Method," Structural and Multidisciplinary Optimization, 28(2-3), pp. 221-227.

[291] Archer, R. R., 1989, "On the Origin of Growth Stresses in Trees - Part 2: Stresses Generated in a Tissue of Developing Cells," Wood Science and Technology, 23(4), pp. 311-322.

[292] Socci, L., Pennati, G., Gervaso, F., and Vena, P., 2007, "An Axisymmetric Computational Model of Skin Expansion and Growth," Biomechanics and Modeling in Mechanobiology, 6(3), pp. 177-188.

[293] Tanaka, H., Hirose, M., Osada, T., Miwa, H., Watanabe, S., et al., 2000, "Implications of Mechanical Stretch on Wound Repair of Gastric Smooth Muscle Cells in Vitro," Dig. Dis. Sci., 45(12), pp. 2470-2477.

[294] Lintilhac, P. M., and Vesecky, T. B., 1984, "Stress-Induced Alignment of Division Plane in Plant Tissues Grown in Vitro," Nature, 307(5949), pp. 363-364.

[295] Weinans, H., Huiskes, R., and Grootenboer, H. J., 1992, "The Behavior of Adaptive Bone-Remodeling Simulation Models," J. Biomech., 25(12), pp. 1425-1441.

[296] Lanyon, L., 1987, "Functional Strain in Bone Tissue as an Objective, and Controlling Stimulus for Adaptive Bone Remodelling," J. Biomech., 20(11/12), pp. 1083-1093.

[297] Lanyon, L. E., 1976, "The Measurement of Bone Strain 'in Vivo'," Acta Orthop. Belg., 42(sup1), pp. 98-108.

[298] Lanyon, L. E., Goodship, A. E., and Baggott, D. G., 1976, "The Significance of Bone Strain 'in Vivo'," Acta Orthop. Belg., 42(sup1), pp. 109-122.

[299] Frost, H. M., 1992, "Perspectives: Bone's Mechanical Usage Windows," Bone Miner., 19(3), pp. 257-271.

[300] Skedros, J. G., Hunt, K. J., Hughes, P. E., and Winet, H., 2003, "Ontogenetic and Regional Morphologic Variations in the Turkey Ulna Diaphysis: Implications for Functional Adaptation of Cortical Bone," Anatomical Record - Part A Discoveries in Molecular, Cellular, and Evolutionary Biology, 273(1), pp. 609-629.

[301] Skedros, J. G., Mason, M. W., Nelson, M. C., and Bloebaum, R. D., 1996, "Evidence of Structural and Material Adaptation to Specific Strain Features in Cortical Bone," Anat. Rec., 246(1), pp. 47-63.

[302] Guo, X.-D., and Cowin, S. C., 1992, "Periosteal and Endosteal Control of Bone Remodeling under Torsional Loading," J. Biomech., 25(6), pp. 645-650.

[303] Kummer, B. K. F., 1972, "Biomechanics of Bone: Mechanical Properties, Functional Structure, and Functional Adaptation," Biomechanics: Its Foundations and Objectives, Y. C. Fung, N. Perrone, and M. Anliker, eds., Prentice Hall, Englewood Cliffs, NJ.

[304] Carter, D. R., Fyhrie, D., and Whalen, R., 1987, "Trabecular Bone Density and Loading History: Regulation of Connective Tissue Biology by Mechanical Energy," J. Biomech., 20(8), pp. 785-794.

[305] Morris, C. E., 1990, "Mechanosensitive Ion Channels," J. Membr. Biol., 113(2), pp. 93-107.

[306] Ko, K. S., and McCulloch, C. A. G., 2000, "Partners in Protection: Interdependence of Cytoskeleton and Plasma Membrane in Adaptations to Applied Forces," J. Membr. Biol., 174(2), pp. 85-95.

[307] Mikic, B., and Carter, D. R., 1995, "Bone Strain Gage Data and Theoretical Models of Functional Adaptation," J. Biomech., 28(4), pp. 465-469.

[308] Chennimalai Kumar, N., Dantzig, J. A., Jasiuk, I. M., Robling, A. G., and Turner, C. H., 2009, "Numerical Modeling of Long Bone Adaptation Due to Mechanical Loading: Correlation with Experiments," Ann. Biomed. Eng., pp. 1-11.

[309] Fridez, P., Rakotomanana, L., Terrier, A., and Leyvraz, P. F., 1998, "Three Dimensional Model of Bone External Adaptation," Comput. Methods Biomech. Biomed. Eng., 2, pp. 189-196.

[310] Pedersen, P., 2000, "On Optimal Shapes in Materials and Structures," Structural and Multidisciplinary Optimization, 19(3), pp. 169-182.

[311] Gross, T. S., Edwards, J. L., McLeod, K. J., and Rubin, C. T., 1997, "Strain Gradients Correlate with Sites of Periosteal Bone Formation," J. Bone Miner. Res., 12(6), pp. 982-988.

[312] Mi, L. Y., Fritton, S. P., Basu, M., and Cowin, S. C., 2005, "Analysis of Avian Bone Response to Mechanical Loading - Part One: Distribution of Bone Fluid Shear Stress Induced by Bending and Axial Loading," Biomechanics and Modeling in Mechanobiology, 4(2-3), pp. 118-131.

[313] Xu, W., and Robinson, K., 2008, "X-Ray Image Review of the Bone Remodeling around an Osseointegrated Trans-Femoral Implant and a Finite Element Simulation Case Study," Ann. Biomed. Eng., 36(3), pp. 435-443.

[314] Boerckel, J. D., Dupont, K. M., Kolambkar, Y. M., Lin, A. S. P., and Guldberg, R. E., 2009, "In Vivo Model for Evaluating the Effects of Mechanical Stimulation on Tissue-Engineered Bone Repair," J. Biomech. Eng., 131(8).

[315] Florio, C. S., and Narh, K. A., 2013, "Effect of Modeling Method on Prediction of Cortical Bone Strength Adaptation under Various Loading Conditions," Meccanica, 48(2), pp. 393-413.

[316] Martens, M., Van Audekercke, R., De Meester, P., and Mulier, J. C., 1981, "The Geometrical Properties of Human Femur and Tibia and Their Importance for the Mechanical Behaviour of These Bone Structures," Arch. Orthop. Trauma Surg., 98(2), pp. 113-120.

[317] Martin, R. B., and Atkinson, P. J., 1977, "Age and Sex-Related Changes in the Structure and Strength of the Femoral Shaft," J. Biomech., 10, pp. 223-231.

[318] Figliola, R. S., and Beasley, D. E., 1995, Theory and Design for Mechanical Measurements, John Wiley and Sons, New York, NY.

[319] Terrier, A., Rakotomanana, L., Ramaniraka, A. N., and Leyvraz, P. F., 1997, "Adaptation Models of Anisotropic Bone," Comput. Methods Biomech. Biomed. Eng., 1(1), pp. 47-59.

[320] Roberts, M. D., and Hart, R. T., 2005, "Shape Adaptation of Long Bone Structures Using a Contour Based Approach," Comput. Methods Biomech. Biomed. Eng., 8(3), pp. 145-156.

[321] Harrigan, T. P., and Hamilton, J. J., 1994, "Necessary and Sufficient Condiitons for Global Stability and Uniqueness in Finite Element Solutions of Adaptive Bone Remodeling," International Journal of Solids and Structures, 31(1), pp. 97-107.

[322] Sugiyama, T., Meakin, L. B., Browne, W. J., Galea, G. L., Price, J. S., et al., 2012, "Bones' Adaptive Response to Mechanical Loading Is Essentially Linear between the Low Strains Associated with Disuse and the High Strains Associated with the Lamellar/Woven Bone Transition," J. Bone Miner. Res., 27(8), pp. 1784-1793.

[323] Wu, Z., 2005, "An Efficient Approach for Shape Optimization of Components," International Journal of Mechanical Sciences, 47(10), pp. 1595-1610.

[324] Das, R., Jones, R., and Peng, D., 2006, "Optimization of Damage Tolerant Structures Using a 3d Biological Algorithm," Eng. Failure Anal., 13, pp. 362-379.

[325] Yang, R. J., and Chen, C. J., 1996, "Stress-Based Topology Optimization," Structural Optimization, 12, pp. 98-105.

[326] Ruff, C. B., and Hayes, W. C., 1983, "Cross-Sectional Geometry of Pecos Pueblo Femora and Tibiae - a Biomechanical Investigation: I. Method and General Patterns of Variation," Am. J. Phys. Anthropol., 60(359-381).

[327] Ruff, C. B., and Hayes, W. C., 1983, "Cross-Sectional Geometry of Pecos Pueblo Femora and Tibiae - a Biomechanical Investigation: II. Sex, Age, and Side Differences," Am. J. Phys. Anthropol., 60, pp. 383-400.

[328] Ruff, C. B., and Hayes, W. C., 1988, "Sex Differences in Age-Related Remodeling of the Femur and Tibia," J. Orth. Res., 6, pp. 886-896.

[329] Das, R., and Jones, R., 2009, "Development of a 3d Biological Method for Fatigue Life Based Optimisation and Its Application to Structural Shape Design," Int. J. Fatigue, 31, pp. 309-321.

[330] Bedair, O., 1997, "The Application of Indirect Boundary Element Method to Optimum Shape Design," Computers and structures, 65(5), pp. 651-668.

[331] Pathak, K. K., and Sehgal, D. K., 2010, "Gradientless Shape Optimization Using Artificial Neural Networks," Structural and Multidisciplinary Optimization, 41, pp. 699-709.

[332] Cheng, J.-H., 1988, "Automatic Adaptive Remeshing for Finite Element Simulation of Forming Processes," International Journal for Numerical Methods in Engineering, 26(1), pp. 1-18.

[333] Kikuchi, N., Chung, K. Y., Torigaki, T., and Taylor, J. E., 1986, "Adaptive Finite Element Methods for Shape Optimization of Linearly Elastic Structures," General Motors Research Laboratories Symposia Series, Plenum Press, Warren, MI, USA, pp. 139-169.

[334] Luo, Y., 2010, "R-Adaptation Algorithm Guided by Gradients of Strain Energy Density," International Journal for Numerical Methods in Biomedical Engineering, 26(8), pp. 1077-1086.

[335] George, P. L., 1991, Automatic Mesh Generation: Application to Finite Element Methods, John Wiley and Sons, New York, NY.

[336] Salagame, R. R., and Belegundu, A. D., 1994, "Distortion, Degeneracy and Rezoning in Finite Elements - a Survey," Sadhana, 19(2), pp. 311-335.

[337] Batina, J. T., 1990, "Unsteady Euler Airfoil Solutions Using Unstructured Dynamic Meshes," AIAA J., 28(8), pp. 1381-1388.

[338] Zhang, D., Cowin, S. C., and Weinbaum, S., 1997, "Electrical Signal Transmission and Gap Junction Regulation in a Bone Cell Network: A Cable Model for an Osteon," Ann. Biomed. Eng., 25(2), pp. 357-374.

[339] Wainwright, S. A., Biggs, W. D., Currey, J. D., and Gosline, J. M., 1976, Mechanical Design in Organisms, Edward Arnold Publishers, London, England.

[340] Montgomery, D. C., and Runger, G. C., 2003, Applied Statistics and Probability for Engineers, John Wiley and Sons, Inc., New York, NY.

[341] Florio, P. J., 1983, Eg-202: Computer Graphics Package, NJIT Bookstore, Newark, NJ.

[342] Peyret, R., and Taylor, T. D., 1983, Computational Methods for Fluid Flow, Springer-Verlang, New York, NY.

[343] Noble, P. C., Box, G. G., Kamaric, E., Fink, M., Alexander, J. W., et al., 1995, "The Effect of Aging on the Shape of the Proximal Femur," Clin. Orthop. Relat. Res., 316, pp. 31-44.

[344] Lee, S. C., Coan, B. S., and Bouxsein, M. L., 1997, "Tibial Ultrasound Velocity Measured in Situ Predicts the Material Properties of Tibial Cortical Bone," Bone, 21(1), pp. 119-125.

[345] Croker, S. L., Clement, J. G., and Donlon, D., 2009, "A Comparison of Cortical Bone Thickness in the Femoral Midshaft of Humans and Two Non-Human Mammals," HOMO - Journal of Comparative Human Biology, 60(6), pp. 551-565.

[346] Uzel, A.-P., Deloumeaux, J., Rouvillain, J.-L., Laflamme, G.-Y., Durandeau, A., et al., "Comparative Study of Femoral Diaphyseal Morphometry in Two Male Populations, in France and a French West Indies Island: An Example of Clinical Relevance of Comparative Anatomy for Orthopedic Practice," Surg. Radiol. Anat., 33(3), pp. 235-240.

[347] Remaud, A., Cornu, C., and Guevel, A., 2010, "Neuromuscular Adaptation to 8-Week Strength Training: Isotonic Versus Isokinetic," Eur. J. Appl. Physiol., 108, pp. 59-69.

[348] Hunter, S. K., Yoon, T., Farinella, J., Griffith, E. E., and Ng, A. V., 2008, "Time to Task Faiure and Muscle Activation Vary with Load Type for Sumbaximal Fatiguing Contraction with Lower Leg," J. Appl. Physiol., 105, pp. 463-472.

[349] Stewart, G. W., 1998, Matrix Algorithms Volume I: Basic Decompositions, SIAM, Philadelphia, PA.